FIBROUS ASSEMBLIES: FROM SYNTHESIS AND NANOSTRUCTURE CHARACTERIZATION TO MATERIALS DEVELOPMENT AND APPLICATION

EDITED BY: Cinzia Giannini, Ulf Olsson, Dimitrios I. Zeugolis and Maria Grazia Raucci

PUBLISHED IN: Frontiers in Bioengineering and Biotechnology

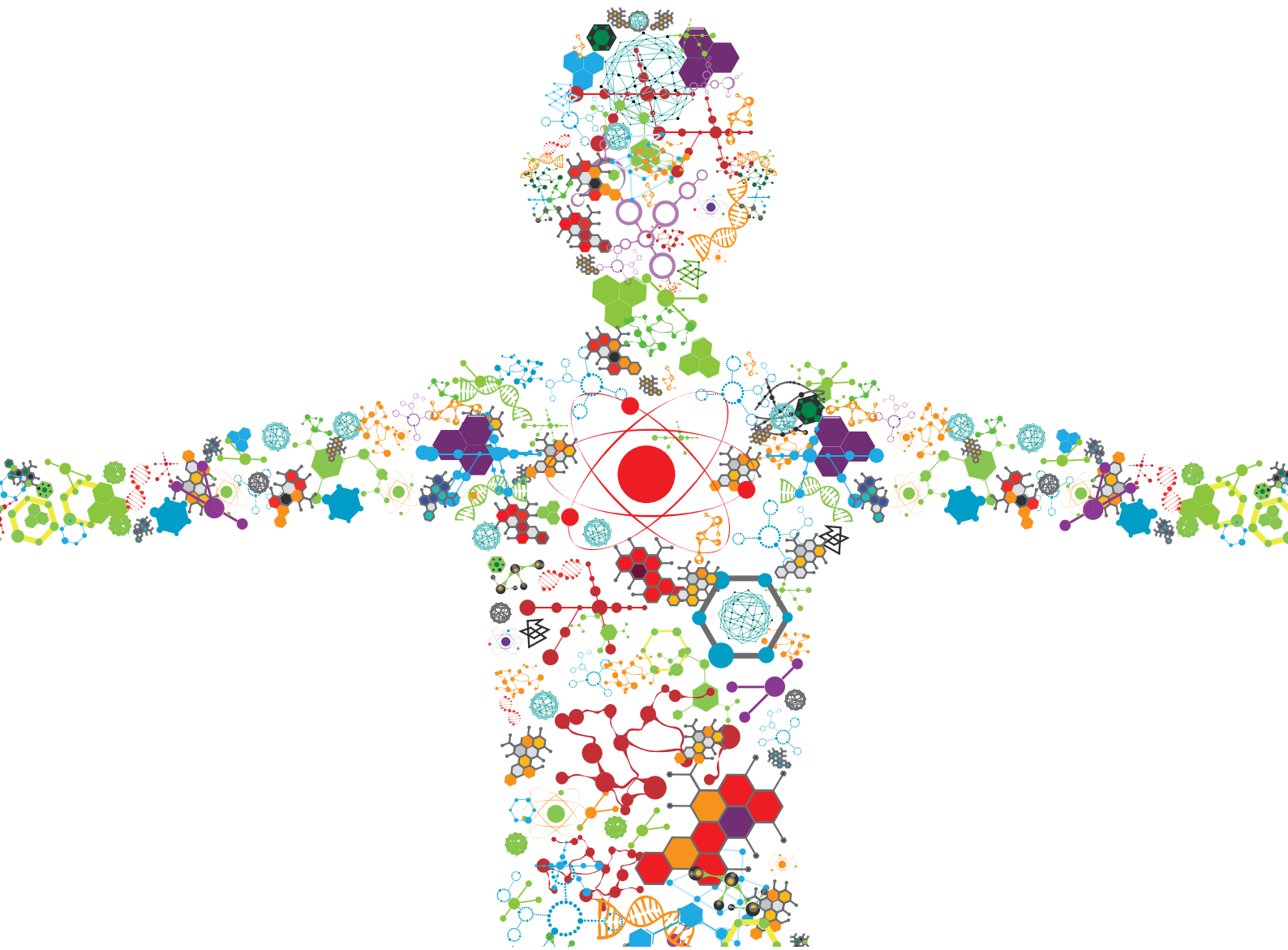

frontiers Research Topics

ISSN 1664-8714
ISBN 978-2-88971-722-4
DOI 10.3389/978-2-88971-722-4

About Frontiers

Frontiers is more than just an open-access publisher of scholarly articles: it is a pioneering approach to the world of academia, radically improving the way scholarly research is managed. The grand vision of Frontiers is a world where all people have an equal opportunity to seek, share and generate knowledge. Frontiers provides immediate and permanent online open access to all its publications, but this alone is not enough to realize our grand goals.

Frontiers Journal Series

The Frontiers Journal Series is a multi-tier and interdisciplinary set of open-access, online journals, promising a paradigm shift from the current review, selection and dissemination processes in academic publishing. All Frontiers journals are driven by researchers for researchers; therefore, they constitute a service to the scholarly community. At the same time, the Frontiers Journal Series operates on a revolutionary invention, the tiered publishing system, initially addressing specific communities of scholars, and gradually climbing up to broader public understanding, thus serving the interests of the lay society, too.

Dedication to Quality

Each Frontiers article is a landmark of the highest quality, thanks to genuinely collaborative interactions between authors and review editors, who include some of the world's best academicians. Research must be certified by peers before entering a stream of knowledge that may eventually reach the public - and shape society; therefore, Frontiers only applies the most rigorous and unbiased reviews.
Frontiers revolutionizes research publishing by freely delivering the most outstanding research, evaluated with no bias from both the academic and social point of view. By applying the most advanced information technologies, Frontiers is catapulting scholarly publishing into a new generation.

What are Frontiers Research Topics?

Frontiers Research Topics are very popular trademarks of the Frontiers Journals Series: they are collections of at least ten articles, all centered on a particular subject. With their unique mix of varied contributions from Original Research to Review Articles, Frontiers Research Topics unify the most influential researchers, the latest key findings and historical advances in a hot research area! Find out more on how to host your own Frontiers Research Topic or contribute to one as an author by contacting the Frontiers Editorial Office: frontiersin.org/about/contact

FIBROUS ASSEMBLIES: FROM SYNTHESIS AND NANOSTRUCTURE CHARACTERIZATION TO MATERIALS DEVELOPMENT AND APPLICATION

Topic Editors:
Cinzia Giannini, Institute of Crystallography, Italian National Research Council, Italy
Ulf Olsson, Lund University, Sweden
Dimitrios I. Zeugolis, University College Dublin, Ireland
Maria Grazia Raucci, Institute of Polymers, Composites and Biomaterials, National Research Council (IPCB-CNR), Italy

Citation: Giannini, C., Olsson, U., Zeugolis, D. I., Raucci, M. G., eds. (2021). Fibrous Assemblies: From Synthesis and Nanostructure Characterization to Materials Development and Application. Lausanne: Frontiers Media SA.
doi: 10.3389/978-2-88971-722-4

Table of Contents

frontiers in Bioengineering and Biotechnology

EDITORIAL
published: 01 October 2021
doi: 10.3389/fbioe.2021.778094

Editorial: Fibrous Assemblies: From Synthesis and Nanostructure Characterization to Materials Development and Application

Cinzia Giannini[1]*, *Ulf Olsson*[2], *Maria Grazia Raucci*[3] and *Dimitrios I Zeugolis*[4]

[1]Institute of Crystallography, National Research Council (IC-CNR), Bari, Italy, [2]Physical Chemistry Department, Lund University, Lund, Sweden, [3]Institute of Polymers, Composite and Biomaterials, National Research Council (IPCB-CNR), Naples, Italy, [4]Regenerative, Modular & Developmental Engineering Laboratory (REMODEL), Charles Institute of Dermatology, Conway Institute of Biomolecular & Biomedical Research and School of Mechanical & Materials Engineering, University College Dublin, Dublin, Ireland

Keywords: fibers, SAXS, WAXS, amyloids, Type1 collagen, elastin, fibroin

Editorial on the Research Topic

Fibrous Assemblies: From Synthesis and Nanostructure Characterization to Materials Development and Application

Fibrous assemblies are ubiquitous in living organisms, providing mechanical stability, elasticity and conservation of shape from cells to tissue and the full organism. In the human body, microtubules and actin filaments shape cells through the cytoskeleton and support the long projected axons of neurons. Collagen is the most abundant extracellular matrix protein in mammals. This structural protein is an important component, responsible for the unique mechanical properties of skin, tendon, cornea, cartilage, and bone. Elastin is responsible for the elastic properties of connective tissue. Actin and myosin filaments are basic components of skeletal muscle fibres. These amazing tissue materials have for a very long time inspired scientists to develop various biomimetic materials and to utilise such materials in tissue engineering. Other than physiological function, fibrous assemblies in our body can also be pathogenic. For example, the formation of peptide amyloid fibrils in the brain is associated with a number of different neurodegenerative diseases, the two most common of which being Alzheimer's disease and Parkinson's disease. Understanding these natural fibrous assemblies, on a fundamental level, is thus important for the development of biocompatible and biomimetic materials for a diverse range of clinical indication and to combat neurodegenerative diseases.

In the research topic *Fibrous Assemblies: From Synthesis and Nanostructure Characterization to Materials Development and Application*, research advances and limitations of fibrous assemblies are discussed. In a way, this research topic goes very much back to Leonardo da Vinci's work 600 years ago, and this is the reason for our choice of the figure which illustrates the topic. Leonardo was, fascinated by bones and muscles, and interested in analysing the human body in mechanical terms. In the winter of 1,510–1,511, he participated in a number of autopsies at the University of Pavia, from which he skilfully produced many beautiful and fundamental tutorial drawings that also tell us how close Leonardo actually came to today's modern medical thinking. Contributions to the topic cover different aspects of fibrous assemblies, ranging from their characterisation to contribution to reparative medicine and disease manifestation and progression. Fichman and Schneider discuss ways to increase the mechanical rigidity of supramolecular peptide-based gel systems using Frémy's salt. Liu et al. assess *in vivo* fibrous

OPEN ACCESS

Edited and reviewed by:
Gianni Ciofani,
Italian Institute of Technology (IIT), Italy

***Correspondence:**
Cinzia Giannini
cinzia.giannini@ic.cnr.it

Specialty section:
This article was submitted to Nanobiotechnology, a section of the journal Frontiers in Bioengineering and Biotechnology

Received: *16 September 2021*
Accepted: *20 September 2021*
Published: *01 October 2021*

Citation:
Giannini C, Olsson U, Raucci MG and Zeugolis DI (2021) Editorial: Fibrous Assemblies: From Synthesis and Nanostructure Characterization to Materials Development and Application. Front. Bioeng. Biotechnol. 9:778094. doi: 10.3389/fbioe.2021.778094

collagen dura substitutes. Nitti et al. demonstrate the potential of a magnesium doped hydroxyapatite/collagen scaffold in bone tissue engineering . Balasco et al. present a comprehensive review of amyloid-like aggregation in disease and biomaterials. Ozsvar et al. and Rodriguez-Cabello et al. provide a comprehensive review in tropoelastin and elastin assembly and the use of elastin-based biomaterials in regenerative medicine. Salvatore et al. discuss the utilisation of collagen-based materials in tissue repair and regeneration. Rizzo et al. investigates the behaviour of degummed silk fibroin in the presence of lanthanide ions. In a more fundamental level, Narayanan et al. conduct multiscale structural analysis of peptide nanotubes using X-Ray scattering methods and investigate amyloid peptide nanotube assembly using SAXS/WAXS methods (Narayanan et al.). Evidently, fibrous assemblies are fundamental in tissue genesis, disease and repair. Understanding the mechanism involved in these processes will enable us to develop tissue-specific facsimiles with enhanced therapeutic capacity.

AUTHOR CONTRIBUTIONS

All authors listed have made a substantial, direct and intellectual contribution to the work, and approved it for publication.

Conflict of Interest: The authors declare that the research was conducted in the absence of any commercial or financial relationships that could be construed as a potential conflict of interest.

Publisher's Note: All claims expressed in this article are solely those of the authors and do not necessarily represent those of their affiliated organizations, or those of the publisher, the editors and the reviewers. Any product that may be evaluated in this article, or claim that may be made by its manufacturer, is not guaranteed or endorsed by the publisher.

frontiers in Bioengineering and Biotechnology

BRIEF RESEARCH REPORT
published: 05 January 2021
doi: 10.3389/fbioe.2020.594258

Utilizing Frémy's Salt to Increase the Mechanical Rigidity of Supramolecular Peptide-Based Gel Networks

*Galit Fichman and Joel P. Schneider**

Chemical Biology Laboratory, National Cancer Institute, National Institutes of Health, Frederick, MD, United States

Peptide-based supramolecular gels are an important class of biomaterials that can be used for biomedical applications ranging from drug delivery to tissue engineering. Methodology that allows one to readily modulate the mechanical properties of these gels will allow yet even a broader range of applications. Frémy's salt is an inorganic salt and long-lived free radical that is known to oxidize phenols. Herein, we show that Frémy's salt can be used to dramatically increase the mechanical rigidity of hydrogels formed by tyrosine-containing self-assembling β-hairpin peptides. When Frémy's salt is added to pre-formed gels, it converts tyrosine residues to o-quinones that can subsequently react with amines present within the lysine side chains of the assembled peptide. This results in the installation of chemical crosslinks that reinforce the gel matrix. We characterized the unoxidized and oxidized gel systems using UV-Vis, transmission electron microscopy and rheological measurements and show that Frémy's salt increases the gel rigidity by nearly one order of magnitude, while retaining the gel's shear-thin/recovery behavior. Thus, Frémy's salt represents an on-demand method to modulate the mechanical rigidity of peptide-based self-assembled gels.

Keywords: hydrogel, peptide, self-assembly, Frémy's salt, crosslinking, quinone

OPEN ACCESS

Edited by:
Ulf Olsson,
Lund University, Sweden

Reviewed by:
Martin Malmsten,
University of Copenhagen, Denmark
Karin Akerfeldt,
Haverford College, United States
Luciano Galantini,
Sapienza University of Rome, Italy

***Correspondence:**
Joel P. Schneider
Schneiderjp@mail.nih.gov

Specialty section:
This article was submitted to Nanobiotechnology, a section of the journal Frontiers in Bioengineering and Biotechnology

Received: *12 August 2020*
Accepted: *07 December 2020*
Published: *05 January 2021*

Citation:
Fichman G and Schneider JP (2021) Utilizing Frémy's Salt to Increase the Mechanical Rigidity of Supramolecular Peptide-Based Gel Networks. Front. Bioeng. Biotechnol. 8:594258. doi: 10.3389/fbioe.2020.594258

INTRODUCTION

Hydrogels are considered promising biomaterials for various biomedical and biotechnological applications (Kopecek and Yang, 2007). Peptide-based supramolecular hydrogels formed by self-assembly (Fichman and Gazit, 2014; Du et al., 2015; Draper and Adams, 2017; Raymond and Nilsson, 2018; Li et al., 2019) represent one class that has been proven to be suitable for applications such as drug delivery (Li and Mooney, 2016; Li et al., 2016; Majumder et al., 2018), wound healing (Carrejo et al., 2018; Zhou et al., 2019; Thota et al., 2020), and tissue engineering, serving as extracellular matrix mimetics for cell growth and differentiation (Kisiday et al., 2002; Jayawarna et al., 2009; Collier et al., 2010; Alakpa et al., 2016; Ghosh et al., 2017; Hellmund and Koksch, 2019). In specific applications, the ability to modulate and fine tune the mechanical properties of these gels is highly desirable. For example, Alakpa et al. have shown that tuning the hydrogel stiffness can direct perivascular stem cell differentiation, where the expression of neural, chondrogenic, or osteogenic markers were observed according to gel rigidity (1, 13, and 32 kPa, respectively) (Alakpa et al., 2016). Indeed, the ability to modify the mechanical properties of peptide-gels has become an

impetus in peptide molecular design (Pashuck et al., 2010; Geisler and Schneider, 2012; Micklitsch et al., 2015; Clarke et al., 2018; Basavalingappa et al., 2019; Hiew et al., 2019). Moreover, efforts have been made to improve the mechanical properties of established supramolecular peptide-based gels, focusing mainly in developing methods to enhance the mechanical rigidity of the gel, as these gels are typically only moderately stiff (Yan and Pochan, 2010; Li et al., 2014). Such efforts include, among others, the introduction of crosslinks into the gel network (Hu et al., 2019) using physical (Greenfield et al., 2010; DiMaio et al., 2017; Bairagi et al., 2019; Scelsi et al., 2019), enzymatic (Bakota et al., 2011; Li et al., 2013), or chemical (Seow and Hauser, 2013; Khalily et al., 2015) crosslinking mechanisms. Interestingly, only limited success has been reported for chemical crosslinking of peptide-based gels (Li et al., 2014). However, one example was recently described by Wang and co-workers, who used a photocrosslinking approach to improve the mechanical stability of tyrosine-containing gels, based on the ruthenium complex ($Ru(bpy)_3Cl_2$)-catalyzed conversion of tyrosine to di-tyrosine that occurs upon light irradiation (Ding et al., 2013). Since tyrosine-containing peptide materials are widely used in various applications (Lee et al., 2019), we wanted to further expand the arsenal of chemical crosslinking strategies that exploit the intrinsic chemistry of phenolic tyrosine. Here, we present a simple *in vitro* post-self-assembly approach to introduce covalent crosslinks into the gel network using potassium nitrosodisulfonate (Frémy's salt), **Figure 1A**, a long-lived free radical that has been used to chemically convert tyrosine to reactive o-quinone for many decades (Zimmer et al., 1971). The use of Frémy's salt to oxidize tyrosine residues complements the use of enzymes (e.g., tyrosinase). However, Frémy's salt may provide an advantage for use on an established gel network. In contrast to enzymes whose diffusion could be limited if a gel's mesh size is small, nitrosodisulfonate can better penetrate the network.

We had previously developed a class of amphiphilic peptides that can undergo triggered self-assembly into supramolecular hydrogels (Schneider et al., 2002). These peptide gelators are well-characterized over several length scales. For example, using cryo-TEM, Pochan et al. showed that soon after self-assembly is triggered, clusters of well-defined fibrils are formed throughout the sample volume (Yucel et al., 2008). Individual clusters contain dangling fibril ends that grow and interpenetrate neighboring clusters as the network evolves. The exact time at which the clustered fibril network percolates the entire sample volume and the solution becomes a gel is fast (<1 min at 1 wt% peptide) and concentration dependent (Veerman et al., 2006). After the gel point, the network continues to grow, filling the voids, to further rigidify the gel. Cryo-TEM suggests that the final network contains fibrils that entangle and form branch-points, both are physical crosslinks that help define the gel's mechanical properties. The mesh size of the network can be varied (∼20–50 nm) by adjusting the peptide concentration or the rate of self-assembly (Ozbas et al., 2004; Branco et al., 2009). TEM and AFM were used to characterize the local morphology of the fibrils affording width and height measurements of 3 and 2 nm, respectively, suggesting that the peptide folds and is stacked when assembled. Solid state NMR later showed that these amphiphilic peptides do indeed fold into a well-defined β-hairpin conformation in their self-assembled state, forming a bilayer cross-β structure within each fibril (Nagy-Smith et al., 2015). Importantly, the fibrils formed are monomorphic indicating that the peptide used in the NMR study, and presumably others in this hairpin class, assembles into a unique arrangement within the fibril. Thus, a structure-based approach can be used to design new gelators that display regiospecific functionality within the fibrils they form, ultimately imbibing targeted properties to the gel. Here, a new peptide gelator is designed to display both lysine and tyrosine residues on the solvent-exposed surface of the fibrils it ultimately forms (**Figure 1B**). As will be shown, on demand addition of Frémy's salt to the newly-designed gel system results in a chemical conversion of the phenolic-tyrosine into a highly reactive o-quinone (Zimmer et al., 1971). In the lysine rich environment of the assembled peptide, o-quinone can readily react with amines present within the lysine side chains, introducing covalent crosslinks to the system (Yang et al., 2014), **Figure 1C.** These covalent crosslinks directly contribute to the cohesion of the network, increasing the mechanical rigidity of the gel.

RESULTS AND DISCUSSION

The designed peptide incorporates nine valine residues that drive self-assembly via the hydrophobic effect, arranged in an amphiphilic $(AB)_n$ repeat with lysine, where A is a hydrophobic residue and B is hydrophilic with the exception of a sole tyrosine residue at position 15. Based on the previously determined solid-state NMR structure (Nagy-Smith et al., 2015), the peptide should self-assemble as depicted in the model shown in **Figure 1B**. The model at left shows only a portion of a fibril containing eight folded peptides where each peptide adopts an amphiphilic β-hairpin conformation. Peptides are assembled into a bilayer, sequestering their valine-rich faces from water. The hydrophilic face of each peptide displays its lysine and tyrosine side-chains into solvent and are thus accessible to chemical reagents. The panel at right at **Figure 1B** shows only two peptides within the fibril to better visualize the relative position of tyrosine and lysine residues. This 20-residue peptide is readily dissolved in water, where repulsive interactions between the protonated lysine side chains prevent it from self-assembling. Peptide assembly is triggered by the addition of saline buffer (pH 7.4), which increases the solution pH and ionic strength, reducing the inter-lysine electrostatic interactions. Assembly leads to a bi-layered cross β-sheet fibrillar network, giving rise to a macroscopic self-supporting gel. Again, since both tyrosine and lysine side chains are displayed from the hairpin's hydrophilic face, those residues are repetitively presented along the solvent-exposed surfaces of the fibrils within the gel system. Having the functional residues exposed to the solvent within the gel matrix provides one the ability to increase gel rigidity on demand, by simply adding Frémy's salt exogenously to a pre-formed gel. We first examined macroscopically how the addition of the oxidant affects the pre-formed gel (**Figure 2A**). We observed that the addition of the salt

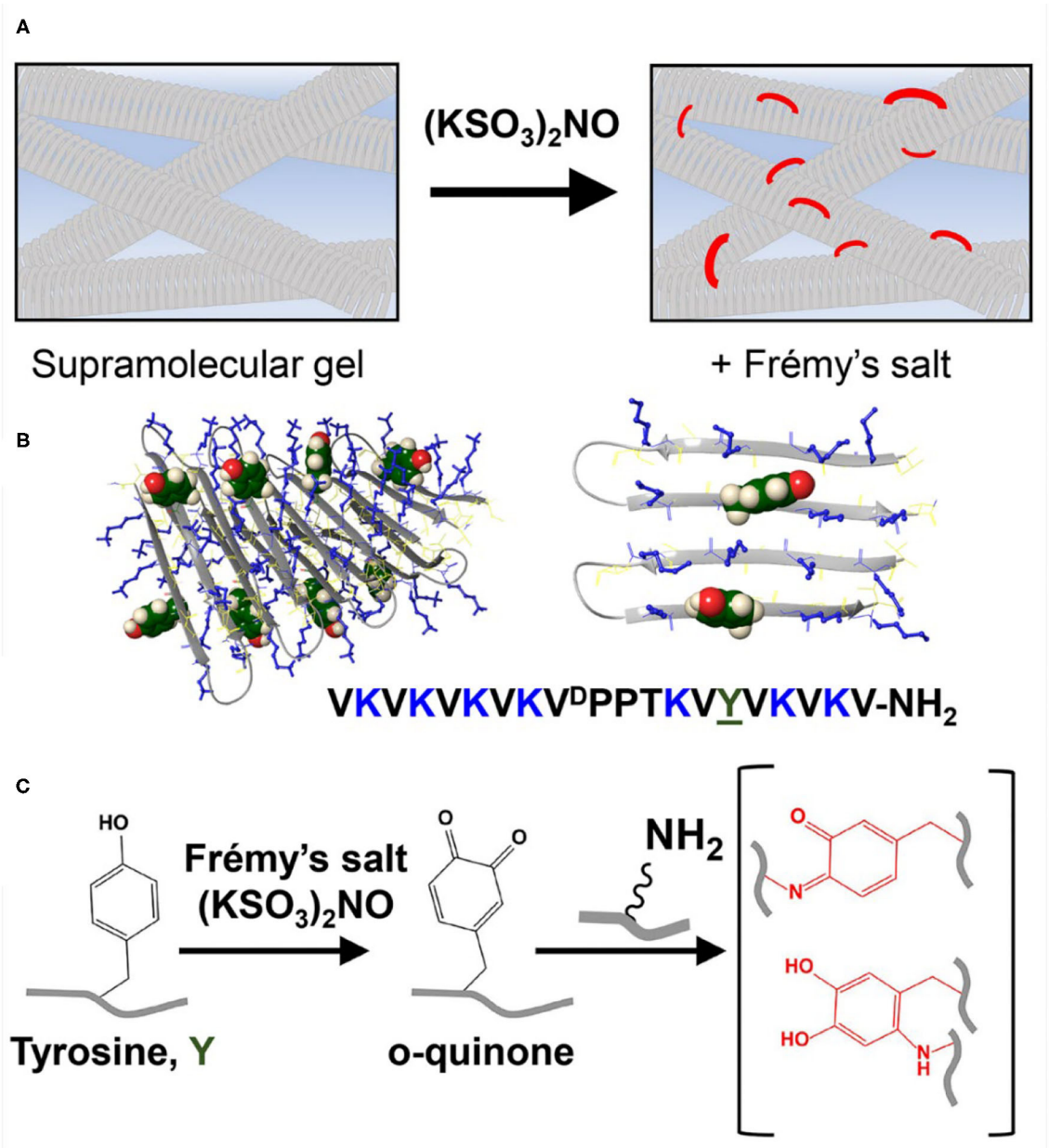

FIGURE 1 | (A) Conceptual scheme showing reinforcement of a supramolecular gel scaffold by introducing covalent crosslinks into a non-covalent network using Frémy's salt. **(B)** A tyrosine-functionalized lysine-rich peptide gelator. This peptide self-assembles into a bi-layered cross β-sheet fibrillar network, adopting an amphiphilic β-hairpin conformation in its self-assembled state. At left, eight peptides are shown as part of a fibril. At right, only two adjacent peptides from one monolayer are shown so that the relative positions of the tyrosine and lysine residues can be seen more clearly. Tyrosine side chains are displayed from the hairpin's hydrophilic face and thus the solvent-exposed surfaces of the fibrils. Tyrosine residues are shown in green CPK rendering and lysine side chains are shown as blue sticks. **(C)** The addition of Frémy's salt to the pre-formed gel results in chemical conversion of tyrosine to ortho-quinone, enabling the subsequent formation of covalent crosslinks within the network via the reaction of lysine and ortho-quinone functional groups.

did not affect the gel's integrity, as it retained its macroscopic 3D shape. However, when Frémy's salt was added to the colorless gel, the material eventually turned an orange-like color. The observed color change represents a clear indication of tyrosine oxidation. **Figure 2B** shows the time-dependent coloration of gel, supporting the assertion that an oxidative process within the gel is occurring. When Frémy's salt is initially dissolved in buffer, it is purple in color due to the presence of monomeric nitrosodisulfonate ions. Overtime, the nitrosodisulfonate ions decompose and the purple color of the Frémy's salt solution is discharged (Murib and Ritter, 1952), resulting in a light yellowish solution (**Supplementary Figures 1**, **2**). In the first

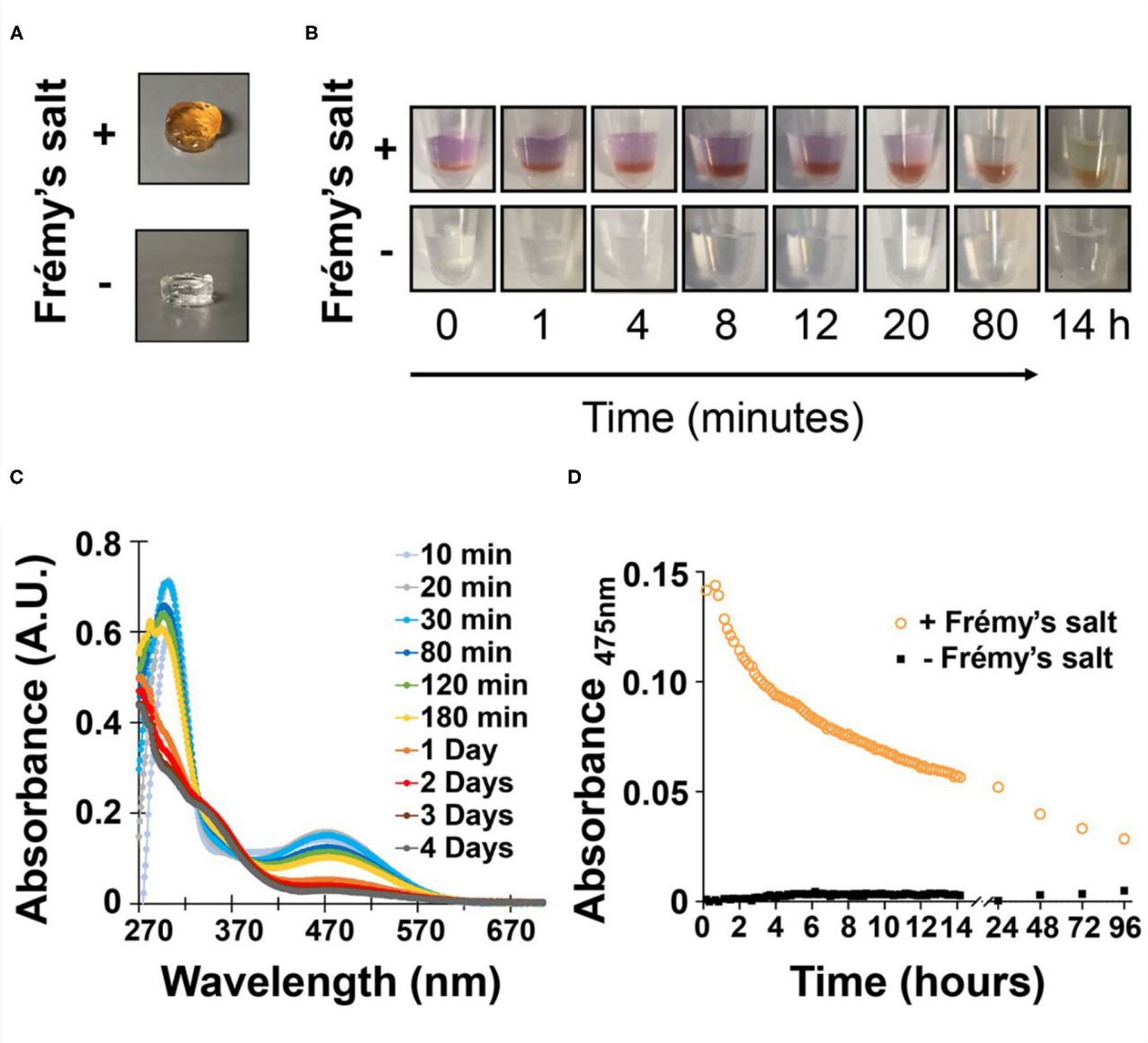

FIGURE 2 | (A) Images of pre-formed gels following overnight incubation in the presence or absence of Frémy's salt. Changes in gel color observed only in the presence of Frémy's salt overtime, were monitored by **(B)** the naked eye as well as **(C)** UV-Vis spectroscopy. **(D)** Change in gel absorbance at 475 nm as a function of time and presence or absence of oxidant.

20 min following the addition of Frémy's salt solution, the purple color of the solution on top of the gels is clearly observed. Interestingly, during this time period we also observed an initial red layer at the gel-solution interface, at the upper part of the gel. Frémy's salt is a radical that is known to selectively oxidize phenol to quinones (Zimmer et al., 1971). The initial conversion of phenol to o-quinone is typically characterized with the appearance of a red color that later dissipates, giving rise to other secondary colored products (Siegel and Siegel, 1958). The rapid red coloration suggests that the tyrosine residues found at the gel's surface are immediately oxidized by the Frémy's salt solution. As time passes, the oxidant penetrates the gel, completely permeating the material in 20 min, with the entire gel turning red. The change in gel color after an overnight incubation from a red to an orange-yellowish color indicates that the quinone further reacted, forming other end products. UV-Vis spectroscopy was also used to follow the oxidation reaction (**Figure 2C**). In these studies, to avoid light scattering, a lower peptide concentration of 0.125 wt% was used. At this concentration, the peptide assembles into fibers but does not form gel. In the absence of Frémy's salt, the UV-Vis spectra of the tyrosine-functionalized peptide in HEPES buffer is characterized by a single peak with λ_{max} around 278 nm whose wavelength maximum does not change over 4

days (**Supplementary Figure 3**). In contrast, we observe that in the presence of the Frémy's salt solution, initial stages of the reaction are characterized by the formation of dopachrome intermediate products, showing absorption maxima at 300 and 475 nm (Dukler et al., 1971). This spectrum resembles other spectra reported in the literature that describe the oxidation of NH_2-terminal tyrosine and tyrosine-containing peptides either by Frémy's salt (Dukler et al., 1971) or enzymatically by tyrosinase (Yasunobu et al., 1959). After about 30 min both the 300 and 475 nm peaks start to gradually decrease (**Figure 2D**, **Supplementary Figure 4A**), and a shoulder around 350 nm appears (**Figure 2C**, **Supplementary Figure 4B**). Similar spectral changes were reported previously where Frémy's salt was used to oxidize oligopeptides that contain both lysine and tyrosine residues in their sequence (Wilchek and Miron, 2015). After 1 day the spectrum ceased to change and remained constant for at least 3 days, the last time point assessed. From the UV-Vis data and the qualitative color-change observations we conclude that the oxidation reaction and subsequent crosslinking reactions are complete following an overnight incubation. We envision that the majority of covalent crosslinks are introduced to the system by the reaction of o-quinone with lysine, given its large concentration in the network. It is possible that dityrosine adducts could also form. However, within a given fibril, tyrosine residues are not close enough to react, **Figure 1B** (right panel) so any dityrosines formed would do so from the reaction of residues located on different fibrils that have entangled within the network.

We then wanted to examine how tyrosine oxidation affected the local morphology of the fibrils and the mechanical properties of the gel matrix. First, TEM was used to study the underlying structural characteristics of the fibrils. Fibrils were isolated from gel via diluting the gel with water to allow visualization of distinct fibrils. As seen in **Figure 3A** and **Supplementary Figure 5A,** in the absence of Fremy's salt, the fibrils that constituted the gel network display well-defined uniform morphology of mostly discrete long fibrillar structures that are approximately 3 nm in width. In contrast, following an overnight oxidation with Frémy's salt, though the gel was water-diluted, most of the fibrils were no longer distinct from each other and rather appear as clusters of entangled fibrils (**Figure 3B**, **Supplementary Figure 5B**). The fibrils were of inconsistent length (**Supplementary Figure 5B**), mostly shorter than fibrils isolated from an unoxidized gel, but with a similar characteristic width of about 3 nm. Collectively, the TEM data suggests that the local morphology of fibrils defined by the arrangement of assembled peptides is not influenced by oxidation. Although we cannot rule out surface-effects by the grid, oxidation does seem to influence the interactions between fibrils, as evident by their clumping. Thus, introducing the Frémy's salt to the established gel does not compromised the already assembled fibril, rather most likely introduces inter- or intra-fibril covalent crosslinks via oxidized phenol groups. Preservation of ordered molecular nanostructures was also reported in other post-self-assembly crosslinking systems (Zhang et al., 2012; Wei et al., 2016). Since introducing such covalent crosslinks can increase the cohesion of the supramolecular network, we wanted to examine the effect of Frémy's salt on the mechanical rigidity of the gels. Rheological studies were performed on oxidized and unoxidized tyrosine gels (**Figure 4**). To ensure homogenous oxidation of tyrosine throughout the gel, 300 μL of concentrated Frémy's salt solution (100 mM; ∼95 eq) was added to the top of the gels. To account for any possible contribution of an increase in ionic strength to gel rigidity, 300 μL of a 100 mM NaCl solution was added to the control gels containing no Frémy's salt. Prior to each measurement the salt solutions above the gels (either Frémy or NaCl) were removed, and the gels were washed. Measurements of storage and loss modulus (G' and G'', respectively) of pre-formed gels, collected in the linear viscoelastic (LVE) regime (0.2% strain, 6 rad/s, **Supplementary Figure 6**) display a significant increase in gel rigidity once the gel is oxidized by Frémy's salt, as indicated by the differences in G' between unoxidized and oxidized gel. Initial G' values of oxidized gels were about eight times higher than G' values of unoxidized gels (25,470 ± 6,723 vs. 2,932 ± 401 Pa, respectively). Repetitive shear-thinning cycles were also performed to study the material's ability to recover after thinning. Here, following examination of the gel G'/G'' within the LVE, high strain (1,000% strain) is applied to shear-thin the gel. The high strain is then decreased and the gel G'/G'' values are recorded again within the LVE regime. Upon performing several shear cycles (**Figure 4A**), we observe that both the oxidized and the unoxidized gels were capable of shear-thin/recovery behavior. While the unoxidized gel fully recovered to its pre-sheared G' values (105 ± 3%), the oxidized gels did not, showing about 60% recovery in the first shearing cycle with greater deviation between the samples (61 ± 13%). This gradual decrease in G' as a function of thinning cycles indicates that the crosslinked network, although more rigid than non-chemically crosslinked material, losses some of its mechanical integrity when shear-thinned. Yet, it is worth mentioning that the recorded recovered rigidity values of the oxidized gels were still higher than the unoxidized gels. Further, this rheological behavior is conducive to syringe-delivery of the crosslinked gel for applications that demand its local placement.

The enhancement of the storage modulus is dependent on the concentration of Frémy's salt used for crosslinking. **Figure 4B** shows that at low concentrations (1.6 and 6.3 mM), only a small enhancement is realized, which increases with increasing concentrations of the salt. As discussed above, a change in material color from red to orange-yellow indicates the installment of crosslinks. Thus, the spatial distribution of coloration within the gel provides insight into the distribution of crosslinks throughout the material. When an excess amount of Frémy's salt (molar ratio of 33:1; Frémy's salt:Tyr) is used, uniform coloration is observed suggestion that crosslinks have been installed homogenously throughout the gel (**Figure 2A**, **Supplementary Figure 7**). In contrast, when a molar ratio of ∼1:1 or 4:1 is used, coloration is only observed near the surface of the gel, **Figure 4B**. This indicates that at low concentrations of oxidant there is not enough to permeate the entire gel volume and crosslinks are only installed proximal to the solution-gel interface, **Supplementary Figure 7**.

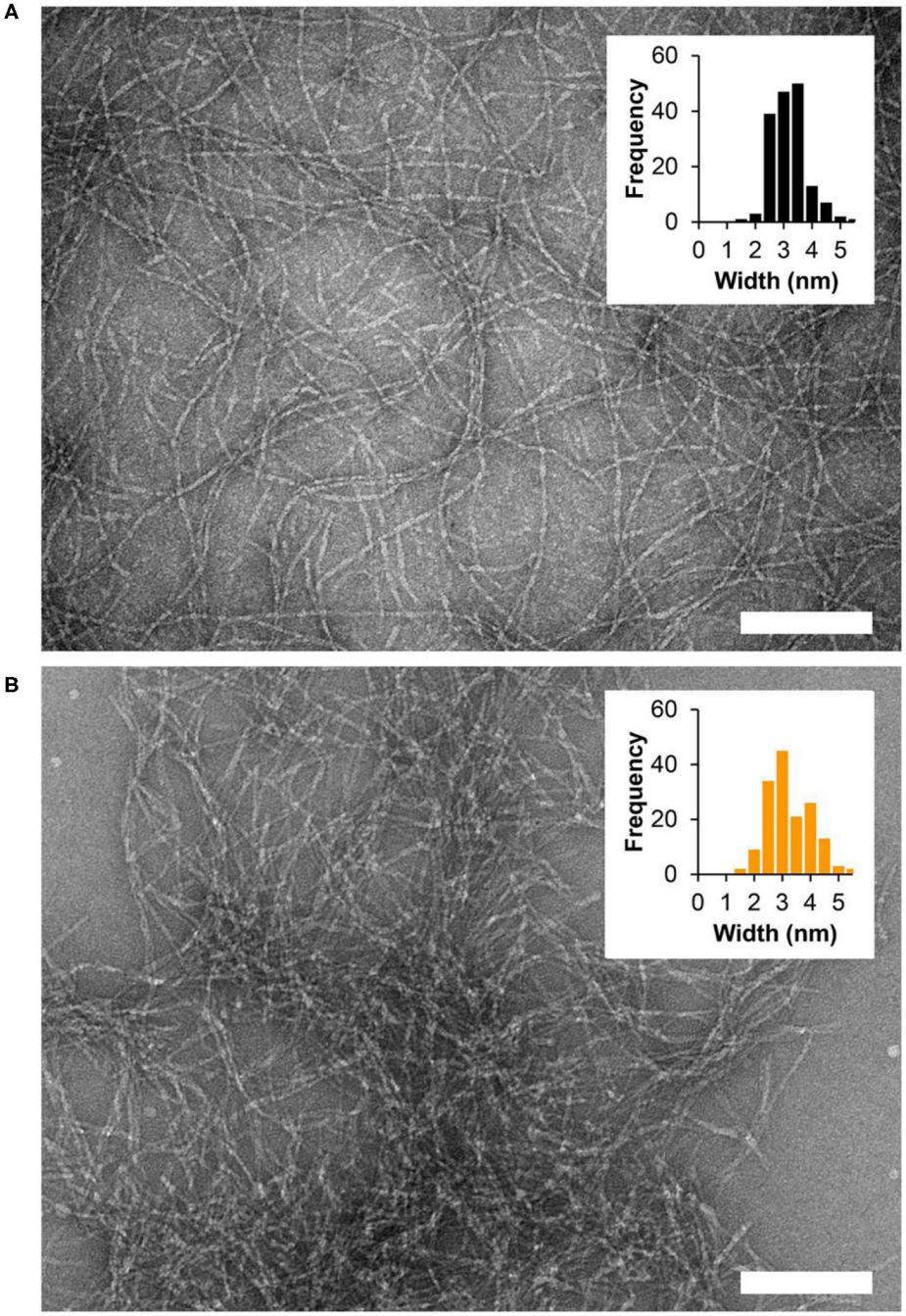

FIGURE 3 | TEM micrographs showing fibrils isolated from 1 wt% fibrillar gel networks **(A)** in the absence of oxidant or **(B)** following overnight oxidation with Frémy's salt. Scale bar = 100 nm. Widths of individual fibrils were determined using ImageJ software, $n = 164$ and $n = 156$ for the non-oxidized and oxidized gel, respectively.

Lastly, we evaluated the cytocompatibility of Frémy's salt-treated gels toward human dermal fibroblast (HDF). Frémy's salt is intended to increase the mechanical rigidity of tyrosine gels upon demand, *in vitro*, prior to the ultimate usage of the gels. For example, one can use Frémy's salt to increase the rigidity of gel matrix for 2D cell growth. Here, Frémy's salt can be added to the gel to increase its rigidity and simply removed before plating cells on the material. **Figure 5A** shows a Live/Dead cytocompatibility assay performed with Frémy's salt-treated or untreated tyrosine gels. In this assay, HDF cells are incubated on top of the gels and cell viability is assessed using fluorescence microscopy and fluorescent dyes, where live cells fluoresce green and dead cells fluoresce red. As seen in **Figure 5A**, cells are viable on both surfaces. Interestingly, cell

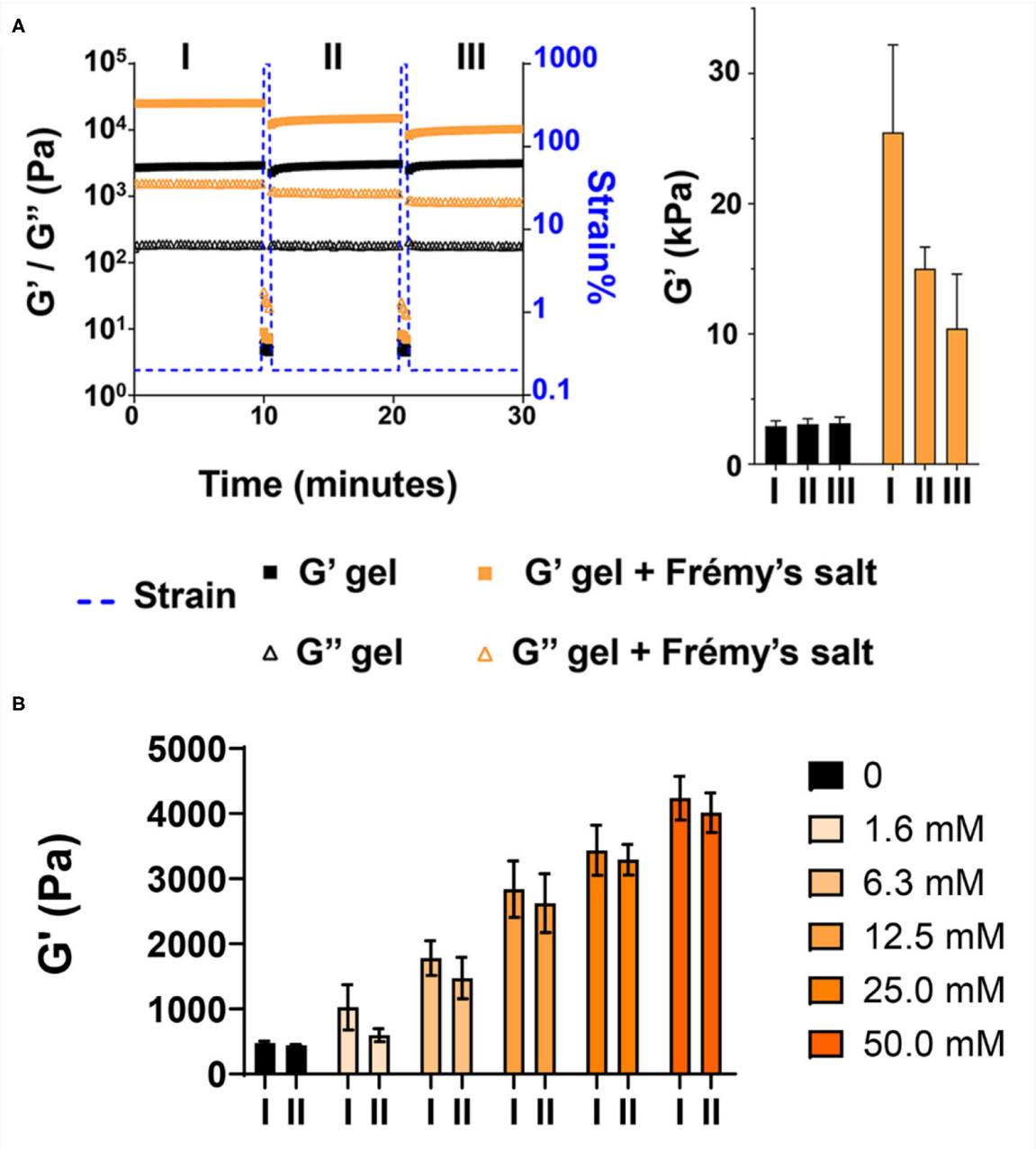

FIGURE 4 | Frémy's salt increases the rigidity of tyrosine-functionalized gels. **(A)** Rheological characterization of 1 wt% gels after overnight incubation with or without Frémy's salt. Gels were subjected to repetitive shear-thinning cycles. In each cycle the storage (G′) and loss (G″) modulus of the gels were monitored as follows: 10 min of measurements within the linear viscoelastic regime (LVE, 0.2% strain, 6 rad/s), then 30 s under high strain that rupture the gel network (1,000% strain, 6 rad/s), following by 10 min measurements of the G′/G″ again within the LVE regime (0.2% strain, 6 rad/s) where the gel recovers. The bar graph at right displays G′ values obtained at the end of each 10 min measurement (marked as I, II, III). **(B)** Rheological characterization of 0.5 wt% gels after overnight incubation with different concentrations of Frémy's salt. Bar graph marked as I displays G′ values obtained at the end of the first 10 min measurement. Bar graph marked as II, displays recovery G′ values of the gels obtained 10 min after applying high strain (1,000%) to thin the gel network.

morphology and spreading on each surface are slightly different. This might be attributed to changes in gel properties such as surface topography and/or mechanical rigidity that result from gel oxidation. We should note that Frémy's salt on its own is cytotoxic, so the gels must be washed before cells are introduced to the material. We also examined the enzyme-mediated degradation of Frémy's salt treated gels by measuring their storage modulus after 2 days of incubation with trypsin. **Figure 5B** demonstrates that both oxidized and unoxidized gels are relatively stable. However, the oxidized gel is more

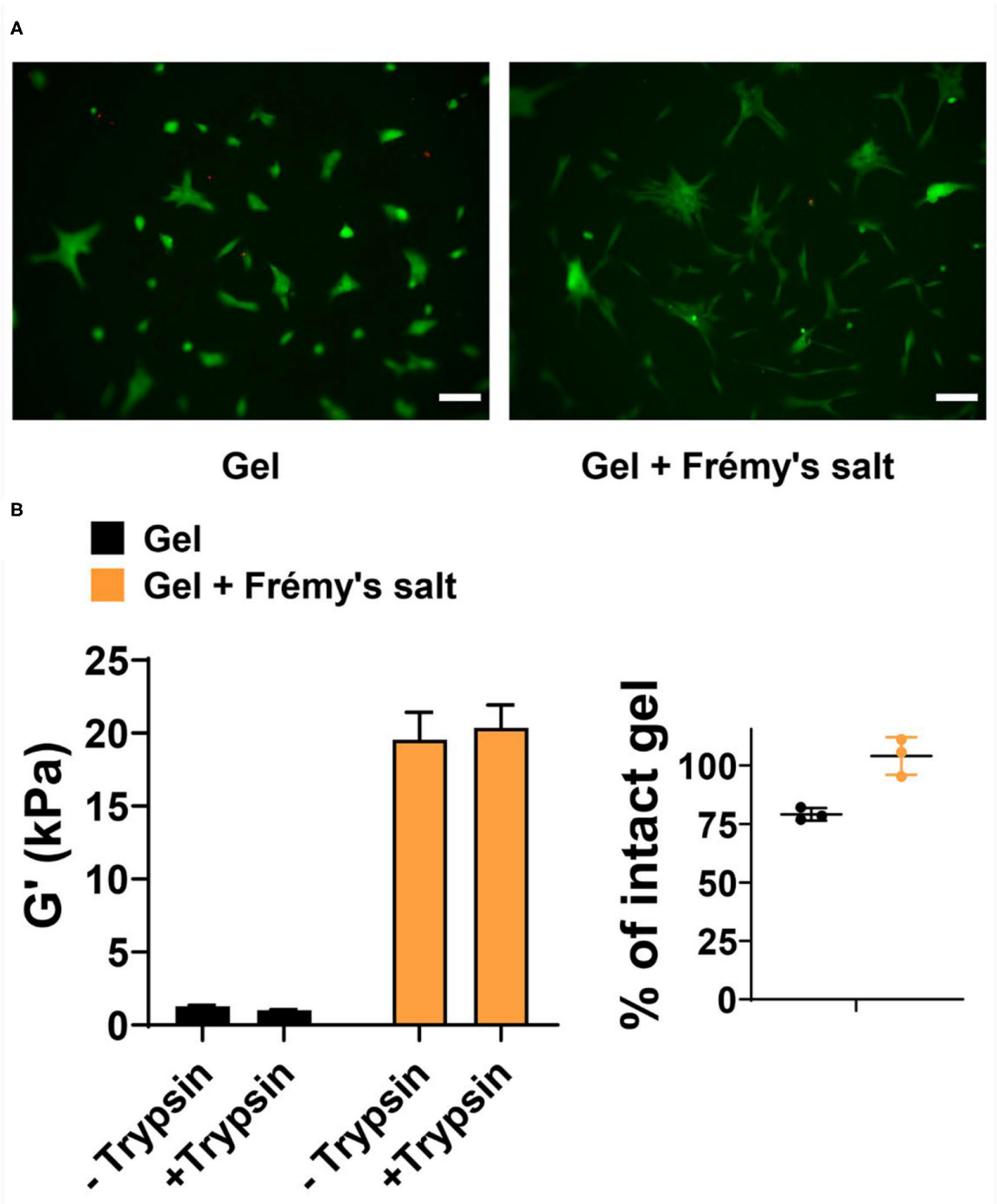

FIGURE 5 | (A) Live/Dead assay of human dermal fibroblasts 48 h after being seeded onto 1 wt% tyrosine-gels untreated or treated with Frémy's salt (left and right panels, respectively). In live cells enzymatic conversion of non-fluorescent calcein-AM to calcein produce green fluorescence, whereas dead cells are labeled with ethidium homodimer-1 and fluoresce red. Scale bar is 100 μm. **(B)** Degradation of Frémy's salt-treated or untreated gels by trypsin. Rheological measurements were performed on 1 wt% gels following 2 days of incubation with trypsin or buffer as a control. Percentage of intact gel was calculated by dividing the G′ value of trypsin treated gel with the average of untreated control gels. Individual values of trypsin-treated gels are plotted with the mean and standard deviation.

stable having not degraded significantly at day 2. Although not investigated here, longer times most likely would result in further degradation.

In conclusion, we present the design and characterization of a peptide-based gel system whose mechanical rigidity can be increased on demand, by chemically introducing

covalent crosslinks within the supramolecular gel network. The addition of Frémy's salt to the gel enhanced its rheological properties, while conserving its shear-thinning behavior and local morphological fibrillar structure. Moreover, the Frémy's salt-treated gels are cytocompatible toward HDF cells and therefore may find future uses in biomedical applications such as scaffolds for cell growth. In general, this simple chemical approach can be used to modulate the mechanical rigidity of peptide-based self-assembled gels and complements the use of enzymes (e.g., tyrosinase) to oxidize tyrosine residues within gel systems. Future directions will include examination of Frémy's salt contribution to the mechanical rigidity of tyrosine gels as a function of tyrosine content and location within the peptide gelator.

MATERIALS AND METHODS

Materials

Rink amide ChemMatrix® resin, Oxyma, and all other Fmoc-protected amino acids were purchased from Novabiochem®. 2-(6-Chloro-1H-benzotriazole1-yl)-1,1,3,3-tetramethylaminium hexafluorophosphate (HCTU) was purchased from Chem Impex International. Piperidine was purchased from Alfa Aesar. Ethanedithiol (98+%) was purchased from Fluka. Trifluoroacetic acid (TFA, 97%), anisole (99%), thioanisole (>=99%), 4-(2-hydroxyethyl)-1-piperazineethanesulfonic acid (HEPES), and potassium nitrosodisulfonate (Frémy's Salt, 220930) were purchased from Sigma Aldrich. N,N′-Diisopropylcarbodiimide (DIC, 99%), N,N-Diisopropylethylamine (DIEA), Dimethylformamide (DMF, 99.9%), Dichloromethane (DCM, >=99.8%), Diethyl ether and acetonitrile were purchased from Fisher Scientific.

Peptide Synthesis

The tyrosine-containing peptide was synthesized by standard Fmoc-solid phase peptide synthesis using a Liberty Blue™ automated microwave peptide synthesizer (CEM) with H-Rink amide ChemMatrix® resin. Resin-bound peptide was cleaved and side chain-deprotected using a cleavage cocktail of TFA:thioanisole:ethanedithiol:anisole (90:5:3:2) for 3 h under argon. Crude peptide was purified by RP-HPLC using a preparative Vydac C18 peptide column at 40°C. Solvents for RP-HPLC consisted of standard A (0.1% TFA in water) and standard B (0.1% TFA in 9:1 acetonitrile/water). Gradients were used as follows: an isocratic gradient from 0 to 2 min at 0% standard B, a linear gradient from 0 to 20% standard B for 10 min and a linear gradient of 20 to 100% standard B over an additional 160 min. The peptide eluted at approximately 34% B, lyophilized and then analyzed using analytical HPLC and LC-MS. Analytical HPLC chromatograms and ESI (+) mass spectra of the pure peptide are provided in **Supplementary Figure 8**.

Gel Preparation

Gels were prepared by dissolving lyophilized peptide in water to obtain 2X concentrated (wt%) peptide stock solution. Peptide assembly was initiated by mixing together equal volumes of peptide stock solution and chilled 2X HEPES buffer solution (150 mM HEPES, 300 mM NaCl, pH 7.4) on ice. The final mixed solution (1X wt% peptide in 75 mM HEPES, 150 mM NaCl, pH 7.4) was then incubated for 2 h at 37°C, resulting with a self-supporting gel.

Gel Oxidation by Frémy's Salt

Tyrosine gels were prepared as described, where following 2 h incubation at 37°C, Frémy's salt in HEPES buffer (75 mM HEPES, 150 mM NaCl, pH 7.4) was added on top of the gel and incubated overnight at 37°C. Typically, the Frémy's salt solution was added at molar concentration that is about 32 times higher than the final molar concentration of the peptide and in a volume that is 3 times higher than the final gel volume [e.g., on top of 100 μL of 1 wt% gel (∼3.15 mM), 300 μL of 100 mM Frémy's salt in HEPES buffer were added].

Monitoring Color Change in Oxidized Gels

To monitor color change in oxidized gels using the naked eye, 1 wt% tyrosine-gel in HEPES buffer was prepared as described above where 10 μL aliquots were transferred to Eppendorf tubes for 2 h incubation at 37°C. Thirty microliter of either 100 mM Frémy's salt or 100 mM NaCl, as a control, dissolved in HEPES buffer (75 mM HEPES, 150 mM NaCl, pH 7.4) were added on top of the gels and pictures of the tubes were taken at different time points. To monitor color change using UV-Vis 0.125 wt% tyrosine-peptide gel in HEPES were prepared as described above in a 96-well plate (each well had a final volume 80 μL). Following 2 h incubation at 37°C, 8.33 mM Frémy's salt in HEPES buffer was added to each well and absorption spectra were collected from 270 to 700 nm using a plate reader (Epoch™ Microplate Spectrophotometer, Biotek).

Transmission Electron Microscopy

1 wt% gels were prepared as described above in Eppendorf tubes, incubated overnight at 37°C with or without 100 mM Frémy's salt. The samples were prepared by diluting the gels X50 into water to allow visualization of distinct fibers. A 5 μL drop of peptide solution was placed on a 200-mesh copper grid covered by carbon film (Electron Microscopy Science) for 1 min, then blotted by filter paper. Subsequently, 5 μL of 0.75% uranyl formate was added to the grid and allowed to stand for 1–2 min, then blotted with a filter paper and left to air dry. Images were taken with a Hitachi 7650 at 80 kv accelerating voltage. Average fibril width was measured via ImageJ software by taking 164 and 156 independent measurements of distinct fibrils of the non-oxidized and oxidized gel, respectively.

Rheology

Rheological measurements were performed on pre-formed gels using an AR G2 rheometer (TA Instruments) equipped with an 8-mm stainless steel parallel plate geometry tool. Hundred microliter of 1 wt% tyrosine-gels in HEPES buffer were prepared as described above in Corning® Costar® Transwell® cell culture inserts positioned in a 24-well plate. Following the 2 h incubation at 37°C 300 μL of either 100 mM Frémy's salt or 100 mM NaCl solutions (75 mM HEPES buffer containing 150 mM NaCl, pH 7.4) were added on top of the gels for overnight incubation (∼16 h) at 37°C. The next day, the solution on top of the gel was

removed, the gels were washed, and the rheological properties of the gels were determined. Shear-thinning/recovery cycles were performed as follows: 10 min time-weep at the LVE regime (0.2% strain, 6 rad/s), then shearing for 30 s under high strain (1,000% strain, 6 rad/s), following by a 10 min time-sweep at the LVE regime (0.2% strain, 6 rad/s). A dynamic frequency sweep in the frequency range of 0.1–100 rad/s was collected at 0.2% strain and a dynamic strain sweep (0.1–1,000 strain%) was collected at a constant frequency of 6 rad/s. Rheological data represent the average G′ and G″ obtained from at least three independent measurements. Frémy's salt concentration dependent studies were done similarly with pre-formed 0.5 wt% tyrosine gels and different concentrations of Frémy's salt dissolved in HEPES buffer. The control tyrosine-gel (0 mM Frémy's salt) was supplemented with additional 50 mM NaCl.

Cell Viability Assay

1 wt% gels were prepared as described above in a 96-well plate (50 μL per well). Following 2 h of incubation at 37°C, 200 μL of HEPES buffer (75 mM HEPES, 150 mM NaCl, pH 7.4) either with or without 100 mM Frémy's salt were added on top of the gels for overnight incubation (∼16 h) at 37°C. Buffer solution from the top of the gels was removed and gels were washed several times with fresh HEPES buffer (25 mM HEPES, 150 mM NaCl, pH 7.4). Human dermal fibroblast (HDF, ATCC® PCS-201-010™) cells were trypsinized and counted using Bio-Rad TC20™ Automated Cell Counter. The resulting cell suspension was diluted with serum containing Dulbecco's Modified Eagle's Medium (DMEM, Gibco™ GlutaMAX™, 10567-014 supplemented with 50 mg/mL gentamicin). Two hundred microliter of 10,000 HDF cells were placed on top of each gel and on a control tissue-culture treated polystyrene surface. After 48 h of incubation at 37°C and 5% CO_2, the medium was removed, and each well was washed with serum-free DMEM medium. Cell viability was evaluated using LIVE/DEAD™ Viability/Cytotoxicity assay (Molecular Probes, L3224) according to manufacture instructions. Typically, 100 μL serum-free DMEM medium containing both 1 μM calcein AM and 2 μM ethidium homodimer was added into each well and incubated at 37°C for 15 min. Cells were imaged using fluorescence microscopy (EVOS FL Cell Imaging System, Thermo Fisher Scientific). Samples were prepared in quadruplicate with two biological repeats. Images of merged green and red channels were prepared using ImageJ software. Brightness and contrast were adjusted for the figures as follows: minimum and maximum displayed values of 10 and 65 for the red channel. Minimum and maximum displayed values of 10 and 130 for the green channel.

Proteolytic Degradation of Gels

Eighty microliter of 1 wt% tyrosine-gels in HEPES buffer were prepared as described above in Corning® Costar® Transwell® cell culture inserts positioned in a 24-well plate. Following the 2 h incubation at 37°C, 300 μL of HEPES buffer (75 mM HEPES, 150 mM NaCl, pH 7.4) with or without 100 mM Frémy's salt were added on top of the gels for overnight incubation (∼16 h) at 37°C. The next day, buffer solution was removed from the gels and all gels were washed with HEPES buffer supplemented with EDTA (25 mM HEPES, 150 mM NaCl, 1 mM EDTA pH 7.8). Bovine pancreatic trypsin (Sigma, T9201) was prepared in buffer (50 mM BTP 150 mM NaCl 1 mM EDTA pH 7.8) and introduced to the top of the gels yielding a final trypsin concentration of 125 nM upon equilibrium. Gels were incubated for 2 days at 37°C. Control gels (oxidized and non-oxidized) were prepared in the same manner in the absence of trypsin. Following 2 days, solution from the gel was removed and rheological measurements were performed.

DATA AVAILABILITY STATEMENT

The original contributions presented in the study are included in the article/**Supplementary Materials**, further inquiries can be directed to the corresponding author.

AUTHOR CONTRIBUTIONS

GF and JS designed the experiments and prepared the manuscript. GF performed the experiments. All authors contributed to the article and approved the submitted version.

FUNDING

This research was supported by the Center for Cancer Research (CCR), National Cancer Institute (NCI), the National Institutes of Health (NIH).

ACKNOWLEDGMENTS

GF and JS would like to thank members of the Schneider laboratory for helpful discussions.

SUPPLEMENTARY MATERIAL

The Supplementary Material for this article can be found online at: https://www.frontiersin.org/articles/10.3389/fbioe.2020.594258/full#supplementary-material

REFERENCES

Alakpa, E. V., Jayawarna, V., Lampel, A., Burgess, K. V., West, C. C., Bakker, S. C. J., et al. (2016). Tunable supramolecular hydrogels for selection of lineage-guiding metabolites in stem cell cultures. *Chem* 1, 298–319. doi: 10.1016/j.chempr.2016.08.001

Bairagi, D., Biswas, P., Basu, K., Hazra, S., Hermida-Merino, D., Sinha, D. K., et al. (2019). Self-assembling peptide-based hydrogel: regulation of mechanical stiffness and thermal stability and 3D cell culture of fibroblasts. *ACS Appl. Bio Mater.* 2, 5235–5244. doi: 10.1021/acsabm.9b00424

Bakota, E. L., Aulisa, L., Galler, K. M., and Hartgerink, J. D. (2011). Enzymatic cross-linking of a nanofibrous peptide hydrogel. *Biomacromolecules* 12, 82–87. doi: 10.1021/bm1010195

Basavalingappa, V., Guterman, T., Tang, Y., Nir, S., Lei, J., Chakraborty, P., et al. (2019). Expanding the functional scope of the fmoc-diphenylalanine

hydrogelator by introducing a rigidifying and chemically active urea backbone modification. *Adv. Sci.* 6:1900218. doi: 10.1002/advs.201900218

Branco, M. C., Pochan, D. J., Wagner, N. J., and Schneider, J. P. (2009). Macromolecular diffusion and release from self-assembled beta-hairpin peptide hydrogels. *Biomaterials* 30, 1339–1347. doi: 10.1016/j.biomaterials.2008.11.019

Carrejo, N. C., Moore, A. N., Silva, T. L. L., Leach, D. G., Li, I. C., Walker, D. R., et al. (2018). Multidomain peptide hydrogel accelerates healing of full-thickness wounds in diabetic mice. *ACS Biomater. Sci. Eng.* 4, 1386–1396. doi: 10.1021/acsbiomaterials.8b00031

Clarke, D. E., Parmenter, C. D. J., and Scherman, O. A. (2018). Tunable pentapeptide self-assembled beta-sheet hydrogels. *Angew. Chem. Int. Ed. Engl.* 57, 7709–7713. doi: 10.1002/anie.201801001

Collier, J. H., Rudra, J. S., Gasiorowski, J. Z., and Jung, J. P. (2010). Multi-component extracellular matrices based on peptide self-assembly. *Chem. Soc. Rev.* 39, 3413–3424. doi: 10.1039/b914337h

DiMaio, J. T. M., Doran, T. M., Ryan, D. M., Raymond, D. M., and Nilsson, B. L. (2017). Modulating supramolecular peptide hydrogel viscoelasticity using biomolecular recognition. *Biomacromolecules* 18, 3591–3599. doi: 10.1021/acs.biomac.7b00925

Ding, Y., Li, Y., Qin, M., Cao, Y., and Wang, W. (2013). Photo-cross-linking approach to engineering small tyrosine-containing peptide hydrogels with enhanced mechanical stability. *Langmuir* 29, 13299–13306. doi: 10.1021/la4029639

Draper, E. R., and Adams, D. J. (2017). Low-molecular-weight gels: the state of the art. *Chem* 3, 390–410. doi: 10.1016/j.chempr.2017.07.012

Du, X. W., Zhou, J., Shi, J. F., and Xu, B. (2015). Supramolecular hydrogelators and hydrogels: from soft matter to molecular biomaterials. *Chem. Rev.* 115, 13165–13307. doi: 10.1021/acs.chemrev.5b00299

Dukler, S., Wilchek, M., and Lavie, D. (1971). Oxidation of tyrosine and its peptides with potassium nitrosodisulphonate. *Tetrahedron* 27, 607–614. doi: 10.1016/S0040-4020(01)90729-X

Fichman, G., and Gazit, E. (2014). Self-assembly of short peptides to form hydrogels: design of building blocks, physical properties and technological applications. *Acta Biomater.* 10, 1671–1682. doi: 10.1016/j.actbio.2013.08.013

Geisler, I. M., and Schneider, J. P. (2012). Evolution-based design of an injectable hydrogel. *Adv. Func. Mater.* 22, 529–537. doi: 10.1002/adfm.201102330

Ghosh, M., Halperin-Sternfeld, M., Grigoriants, I., Lee, J., Nam, K. T., and Adler-Abramovich, L. (2017). Arginine-presenting peptide hydrogels decorated with hydroxyapatite as biomimetic scaffolds for bone regeneration. *Biomacromolecules* 18, 3541–3550. doi: 10.1021/acs.biomac.7b00876

Greenfield, M. A., Hoffman, J. R., de la Cruz, M. O., and Stupp, S. I. (2010). Tunable mechanics of peptide nanofiber gels. *Langmuir* 26, 3641–3647. doi: 10.1021/la9030969

Hellmund, K. S., and Koksch, B. (2019). Self-assembling peptides as extracellular matrix mimics to influence stem cells fate. *Front. Chem.* 7:172. doi: 10.3389/fchem.2019.00172

Hiew, S. H., Mohanram, H., Ning, L. L., Guo, J. J., Sanchez-Ferrer, A., Shi, X. Y., et al. (2019). A short peptide hydrogel with high stiffness induced by 3(10)-helices to beta-sheet transition in water. *Adv. Sci.* 6:1901173. doi: 10.1002/advs.201901173

Hu, W. K., Wang, Z. J., Xiao, Y., Zhang, S. M., and Wang, J. L. (2019). Advances in crosslinking strategies of biomedical hydrogels. *Biomater. Sci.* 7, 843–855. doi: 10.1039/C8BM01246F

Jayawarna, V., Richardson, S. M., Hirst, A. R., Hodson, N. W., Saiani, A., Gough, J. E., et al. (2009). Introducing chemical functionality in Fmoc-peptide gels for cell culture. *Acta Biomater.* 5, 934–943. doi: 10.1016/j.actbio.2009.01.006

Khalily, M. A., Goktas, M., and Guler, M. O. (2015). Tuning viscoelastic properties of supramolecular peptide gels via dynamic covalent crosslinking. *Organ. Biomol. Chem.* 13, 1983–1987. doi: 10.1039/C4OB02217C

Kisiday, J., Jin, M., Kurz, B., Hung, H., Semino, C., Zhang, S., et al. (2002). Self-assembling peptide hydrogel fosters chondrocyte extracellular matrix production and cell division: implications for cartilage tissue repair. *Proc. Natl. Acad. Sci. U.S.A.* 99, 9996–10001. doi: 10.1073/pnas.142309999

Kopecek, J., and Yang, J. Y. (2007). Hydrogels as smart biomaterials. *Polym. Int.* 56, 1078–1098. doi: 10.1002/pi.2253

Lee, J., Ju, M., Cho, O. H., Kim, Y., and Nam, K. T. (2019). Tyrosine-rich peptides as a platform for assembly and material synthesis. *Adv. Sci.* 6:1801255. doi: 10.1002/advs.201801255

Li, J. L., Xing, R. R., Bai, S., and Yan, X. H. (2019). Recent advances of self-assembling peptide-based hydrogels for biomedical applications. *Soft Matter.* 15, 1704–1715. doi: 10.1039/C8SM02573H

Li, J. Y., and Mooney, D. J. (2016). Designing hydrogels for controlled drug delivery. *Nat. Rev. Mater.* 1:16071. doi: 10.1038/natrevmats.2016.71

Li, Y., Ding, Y., Qin, M., Cao, Y., and Wang, W. (2013). An enzyme-assisted nanoparticle crosslinking approach to enhance the mechanical strength of peptide-based supramolecular hydrogels. *Chem. Commun.* 49, 8653–8655. doi: 10.1039/c3cc45127e

Li, Y., Qin, M., Cao, Y., and Wang, W. (2014). Designing the mechanical properties of peptide-based supramolecular hydrogels for biomedical applications. *Sci. China Phys. Mech. Astron.* 57, 849–858. doi: 10.1007/s11433-014-5427-z

Li, Y., Wang, F., and Cui, H. (2016). Peptide-based supramolecular hydrogels for delivery of biologics. *Bioeng. Transl. Med.* 1, 306–322. doi: 10.1002/btm2.10041

Majumder, P., Baxa, U., Walsh, S. T. R., and Schneider, J. P. (2018). Design of a multicompartment hydrogel that facilitates time-resolved delivery of combination therapy and synergized killing of glioblastoma. *Angew. Chem. Int. Ed.* 57, 15040–15044. doi: 10.1002/anie.201806483

Micklitsch, C. M., Medina, S. H., Yucel, T., Nagy-Smith, K. J., Pochan, D. J., and Schneider, J. P. (2015). Influence of hydrophobic face amino acids on the hydrogelation of beta-hairpin peptide amphiphiles. *Macromolecules* 48, 1281–1288. doi: 10.1021/ma5024796

Murib, J. H., and Ritter, D. M. (1952). Decomposition of nitrosyl disulfonate ion .1. products and mechanism of color fading in acid solution. *J. Am. Chem. Soc.* 74, 3394–3398. doi: 10.1021/ja01133a052

Nagy-Smith, K., Moore, E., Schneider, J., and Tycko, R. (2015). Molecular structure of monomorphic peptide fibrils within a kinetically trapped hydrogel network. *Proc. Natl. Acad. Sci. U.S.A.* 112, 9816–9821. doi: 10.1073/pnas.1509313112

Ozbas, B., Rajagopal, K., Schneider, J. P., and Pochan, D. J. (2004). Semiflexible chain networks formed via self-assembly of beta-hairpin molecules. *Phys. Rev. Lett.* 93:268106. doi: 10.1103/PhysRevLett.93.268106

Pashuck, E. T., Cui, H. G., and Stupp, S. I. (2010). Tuning supramolecular rigidity of peptide fibers through molecular structure. *J. Am. Chem. Soc.* 132, 6041–6046. doi: 10.1021/ja908560n

Raymond, D. M., and Nilsson, B. L. (2018). Multicomponent peptide assemblies. *Chem. Soc. Rev.* 47, 3659–3720. doi: 10.1039/C8CS00115D

Scelsi, A., Bochicchio, B., Smith, A., Workman, V. L., Diaz, L. A. C., Saiani, A., et al. (2019). Tuning of hydrogel stiffness using a two-component peptide system for mammalian cell culture. *J. Biomed. Mater. Res. A* 107, 535–544. doi: 10.1002/jbm.a.36568

Schneider, J. P., Pochan, D. J., Ozbas, B., Rajagopal, K., Pakstis, L., and Kretsinger, J. (2002). Responsive hydrogels from the intramolecular folding and self-assembly of a designed peptide. *J. Am. Chem. Soc.* 124, 15030–15037. doi: 10.1021/ja027993g

Seow, W. Y., and Hauser, C. A. E. (2013). Tunable mechanical properties of ultrasmall peptide hydrogels by crosslinking and functionalization to achieve the 3D distribution of cells. *Adv. Healthc. Mater.* 2, 1219–1223. doi: 10.1002/adhm.201200463

Siegel, S. M., and Siegel, B. Z. (1958). Autoxidation of pyrogallol - general characteristics and inhibition by catalase. *Nature* 181, 1153–1154. doi: 10.1038/1811153a0

Thota, C. K., Berger, A. A., Elomaa, L., Nie, C., Bottcher, C., and Koksch, B. (2020). Coassembly generates peptide hydrogel with wound dressing material properties. *ACS Omega* 5, 8557–8563. doi: 10.1021/acsomega.9b04371

Veerman, C., Rajagopal, K., Palla, C. S., Pochan, D. J., Schneider, J. P., and Furst, E. M. (2006). Gelation kinetics of beta-hairpin peptide hydrogel networks. *Macromolecules* 39, 6608–6614. doi: 10.1021/ma0609331

Wei, Q. C., Xu, M. C., Liao, C. A., Wu, Q., Liu, M. Y., Zhang, Y., et al. (2016). Printable hybrid hydrogel by dual enzymatic polymerization with superactivity. *Chem. Sci.* 7, 2748–2752. doi: 10.1039/C5SC02234G

Wilchek, M., and Miron, T. (2015). Mussel-inspired new approach for polymerization and cross-linking of peptides and proteins containing tyrosines by fremys salt oxidation. *Bioconjug. Chem.* 26, 502–510. doi: 10.1021/bc5006152

Yan, C., and Pochan, D. J. (2010). Rheological properties of peptide-based hydrogels for biomedical and other applications. *Chem. Soc. Rev.* 39, 3528–3540. doi: 10.1039/b919449p

Yang, J., Stuart, M. A. C., and Kamperman, M. (2014). Jack of all trades: versatile catechol crosslinking mechanisms. *Chem. Soc. Rev.* 43, 8271–8298. doi: 10.1039/C4CS00185K

Yasunobu, K. T., Peterson, E. W., and Mason, H. S. (1959). Oxidation of tyrosine-containing peptides by tyrosinase. *J. Biol. Chem.* 234, 3291–3295.

Yucel, T., Micklitsch, C. M., Schneider, J. P., and Pochan, D. J. (2008). Direct observation of early-time hydrogelation in beta-hairpin peptide self-assembly. *Macromolecules* 41, 5763–5772. doi: 10.1021/ma702840q

Zhang, Y., Li, N., Delgado, J., Gao, Y., Kuang, Y., Fraden, S., et al. (2012). Post-self-assembly cross-linking of molecular nanofibers for oscillatory hydrogels. *Langmuir* 28, 3063–3066. doi: 10.1021/la203923d

Zhou, S. T., Hokugo, A., McClendon, M., Zhang, Z. Y., Bakshi, R. E. N., Wang, L. X., et al. (2019). Bioactive peptide amphiphile nanofiber gels enhance burn wound healing. *Burns* 45, 1112–1121. doi: 10.1016/j.burns.2018.06.008

Zimmer, H., Lankin, D. C., and Horgan, S. W. (1971). Oxidations with potassium nitrosodisulfonate (fremys radical). Teuber reaction. *Chem. Rev.* 71, 229–246. doi: 10.1021/cr60270a005

Conflict of Interest: The authors declare that the research was conducted in the absence of any commercial or financial relationships that could be construed as a potential conflict of interest.

frontiers in Bioengineering and Biotechnology

ORIGINAL RESEARCH
published: 04 February 2021
doi: 10.3389/fbioe.2021.631177

Enhancing Bioactivity of Hydroxyapatite Scaffolds Using Fibrous Type I Collagen

Paola Nitti[1]*, *Sanosh Kunjalukkal Padmanabhan*[1], *Serena Cortazzi*[1], *Eleonora Stanca*[2], *Luisa Siculella*[2], *Antonio Licciulli*[1] and *Christian Demitri*[1]

[1] Biomaterials Laboratory, Department of Engineering for Innovation, University of Salento, Lecce, Italy, [2] Laboratory of Biochemistry and Molecular Biology, Department of Biological and Environmental Sciences and Technologies, University of Salento, Lecce, Italy

In the field of bone tissue regeneration, the development of osteoconductive and osteoinductive scaffolds is an open challenge. The purpose of this work was the design and characterization of composite structures made of hydroxyapatite scaffold impregnated with a collagen slurry in order to mimic the bone tissue structure. The effect of magnesium and silicon ions enhancing both mechanical and biological properties of partially substituted hydroxyapatite were evaluated and compared with that of pure hydroxyapatite. The use of an innovative freeze-drying approach was developed, in which composite scaffolds were immersed in cold water, frozen and then lyophilized, thereby creating an open-pore structure, an essential feature for tissue regeneration. The mechanical stability of bone scaffolds is very important in the first weeks of slow bone regeneration process. Therefore, the biodegradation behavior of 3D scaffolds was evaluated by incubating them for different periods of time in Tris-HCl buffer. The microstructure observation, the weight loss measurements and mechanical stability up to 28 days of incubation (particularly for HA-Mg_Coll scaffolds), revealed moderate weight loss and mechanical performances reduction due to collagen dissolution. At the same time, the presence of collagen helps to protect the ceramic structure until it degrades. These results, combined with MTT tests, confirm that HA-Mg_Coll scaffolds may be the suitable candidate for bone remodeling.

Keywords: hydroxyapatite, magnesium, silicon, collagen, freeze - drying, bone regeneration, biodegradability

OPEN ACCESS

Edited by:
Cinzia Giannini,
Institute of Crystallography (CNR), Italian National Research Council, Italy

Reviewed by:
Alberta Terzi,
Institute of Crystallography (CNR), Italian National Research Council, Italy
Ugo D'Amora,
Institute of Polymers, Composite and Biomaterials (CNR), Italian National Research Council, Italy

***Correspondence:**
Paola Nitti
paola.nitti@unisalento.it

Specialty section:
This article was submitted to Nanobiotechnology, a section of the journal Frontiers in Bioengineering and Biotechnology

Received: *19 November 2020*
Accepted: *11 January 2021*
Published: *04 February 2021*

Citation:
Nitti P, Kunjalukkal Padmanabhan S, Cortazzi S, Stanca E, Siculella L, Licciulli A and Demitri C (2021) Enhancing Bioactivity of Hydroxyapatite Scaffolds Using Fibrous Type I Collagen. Front. Bioeng. Biotechnol. 9:631177. doi: 10.3389/fbioe.2021.631177

INTRODUCTION

The use of 3-dimensional (3D) scaffolds is an approach of bone tissue engineering for the reconstruction of massive bone defects such as diseased or damaged bones (Karp et al., 2003). Scaffolds should be biocompatible and provide a temporal and spatial three-dimensional framework to form the designed tissues; also, they should act as an artificial extracellular matrix to support cell growth, proliferation and ultimately the deposition of regenerated tissue and simultaneously supply structural support to the newly formed tissue (O'Brien et al., 2007). To perform this function, scaffolds should have similar mechanical properties to those of bone repair site, biocompatibility, biodegradability, pore size between 200 and 800 μm (for bone tissue) and an open and interconnected pore structure (with a porosity >90%) (Jones, 2013).

The high porosity allows supplying adequate amount of nutrients, to dispose of metabolic waste by flow transportation and to achieve tissue regeneration through tissue in-growth and then vascularization (Freed et al., 1994).

The native bone tissue consists of an organic component made mostly of collagen and an inorganic crystalline mineral component such as hydroxyapatite (HA) (Hartwig, 1990). Organic components provide flexibility, whereas inorganic components ensure strength and toughness (Wang et al., 2016). Collagen-based scaffolds are widely used because of the collagen bioactivity, which offers excellent biological performance (Salvatore et al., 2018). These scaffolds exhibited high porosity and permeability; nevertheless, they also showed poor mechanical properties and rapid enzymatic degradation, thus limiting their use when high mechanical strength is required (Akkouch et al., 2011). Therefore, due to its favorable biological properties, Collagen (Coll) could be mixed with other material such as HA to improve its mechanical properties. HA is both biocompatible and osteoconductive, although poor resorbability and brittle constructs are problems that occur when using micron-sized HA particles (Wei and Ma, 2004). One strategy to enhance resorbability is doping HA powder with biological active ions. Under *in vivo* conditions, the bone apatite has a crystalline structure allowing the substitution of constitutive bone ions (Ca^{2+}, PO_4^{3-}, and OH^-) with other ions present in natural bone tissue (such as Na^+, Zn^{2+}, CO_3^{2-}, Mg^{2+}, SiO_4^{4-}) (Takata et al., 2005). These substitutions cause changes in crystallinity, solubility (Farzadi et al., 2014) and in bone homeostasis driving osteogenesis, angiogenesis, degradation dynamics, osteoclastogenesis, etc. (Bose et al., 2013, Hoppe et al., 2011). Starting from this evidence, more scientific works reported the fabrication of ions doped apatite (Aina et al., 2012; Padmanabhan et al., 2014; Scalera et al., 2017; Rasskazova et al., 2019; Scalera et al., 2020). Among ions found in the natural bone tissues, magnesium and silicon play an important role in the development of new bone tissue, allowing the control of bioresorption and facilitating the biomineralization and the formation of bone stock on the surface of the material (Landi et al., 2008; Munir et al., 2011).

Based on these considerations, this paper focuses on the development of novel composite scaffolds for bone regeneration using the combination of two major constituents of native bone: collagen type I and hydroxyapatite, to alleviate the problems encountered with Coll alone and HA alone (Soriente et al., 2018). Furthermore, to improve the osseointegration, bioceramic scaffolds with an open and interconnected porosity > 90% were synthesized using polymer sponge replica method (Gervaso et al., 2011), using Hydroxyapatite (HA), magnesium doped HA (HA-Mg) and silicon doped HA (HA-Si). Subsequently, to increase the bioactivity, these scaffolds were impregnated with a collagen matrix and freeze-dried, using a new approach that led to the formation of open pores on composite scaffolds surface. Therefore, the two freeze-drying approaches (new and traditional) and three composite scaffold types (HA-Coll, HA-Mg_Coll, HA-Si_Coll) were compared from a morphological and mechanical point of view. The degradation behavior of bone scaffolds is crucial for cell growth, host response and tissue regeneration (Mikos et al., 1998). Ideal scaffolds should have a degradation rate matching the regeneration rate of new bone tissue (Gervaso et al., 2016). For this reason, the scaffolds stability in aqueous buffer that simulates physiological condition was evaluated, measuring the weight loss, analyzing morphology and mechanical stability. Moreover, preliminary biological tests were assessed to demonstrate favorable cell-material interactions implying physiological responses in terms of viability and proliferation.

MATERIALS AND METHODS

Pure and Doped Hydroxyapatite Synthesis

Pure and substituted (magnesium and silicon) HA were synthesized by aqueous precipitation reaction using $Ca(NO_3)_2{\cdot}4H_2O$, H_3PO_4 (85w/v), $Mg(NO_3)_2.\ 6.H_2O$, $Si(CH_3CH_2O)_4$ (TEOS) and NH_4OH precursors. The amounts of reactants were calculated on the assumption that calcium would be substituted by magnesium and phosphorus would be substituted by silicon. Pure HA powder was synthesized by dissolving proper amounts of $Ca(NO_3)_2 \cdot 4H_2O$ and H_3PO_4 in distilled water separately and then slowly adding $Ca(NO_3)_2 \cdot 4H_2O$ solution to H_3PO_4 solution while stirring. In solution, Ca/P ratio fixed at 1.67. After mixing, NH_4OH was added until pH reached a value of 10. The solution was kept on stirring for 2 h and then transferred to a borosilicate glassware and the liquid part was slowly evaporated by heating up to 400°C in a ventilated oven. After drying, the powder lumps were crushed in a ball mill and calcined to 900°C in an electric furnace to get the final powder.

For magnesium and silicon substituted HA, two compositions were prepared with nominal formula $Ca_{(10-x)}Mg_x(PO_4)_6(OH)_2$, with $x = 0.4$ and $Ca_{10}(PO_4)_{6-y}(SiO_4)_y(OH)_{2-y}$, with $y = 0.7$ for nano-Mg-HA and nano-Si-HA samples, respectively. For Mg-HA synthesis, appropriate amounts of $Ca(NO_3)_2{\cdot}4H_2O$ and $Mg(NO_3)_2.\ 6.H_2O$ were dissolved in water and added to H_3PO_4 solution and precipitated using NH_4OH. For silicon substituted HA, firstly, appropriate amount of TEOS was hydrolyzed in distilled water using few drops of HCl and this silica sol was added to H_3PO_4 solution. $Ca(NO_3)_2 \cdot 4H_2O$ solution was added to the phosphorous/ silica mixture and the pH was adjusted to 10 by adding NH_4OH. After precipitating, pure HA synthesis procedure was carried out to obtain the final powders.

X-ray Diffraction Analysis

The crystallinity of Hydroxyapatite calcinated powders was evaluated by X-ray diffraction (XRD). XRD analysis was performed on calcined powders using a D-Max/Ultima diffractometer (Rigaku, Tokyo, Japan). The particles crystallite size (D) was calculated from the Scherrer equation applied to the diffractogram (Sanosh et al., 2009):

$$D = \frac{0.89\,\lambda}{(\beta \cos\theta)} \tag{1}$$

where λ is the wavelength (Cu Kα), β is the full width at the half-maximum of the HA (2 1 1) line and θ is the diffraction angle. The percentage of secondary phases in HA-Mg powder was evaluated according to the following equation (Sanosh et al., 2009):

$$\nu \text{ secondary phase } = \frac{(I_1 + I_2)}{(I_{HA} + I_1 + I_2)} \quad (2)$$

were I_1 and I_2 represent the intensity of highest peaks present in secondary phases while I_{HA} is the intensity of the highest peak of HA.

Scaffolds Fabrication

The Hydroxyapatite powders synthesized by precipitation method were used to obtain bioceramic porous scaffold by polyurethane sponge replica method. Three different slurries were made with the three types of apatite powders (HA, HA-Mg, HA-Si). In all slurries, the powder was added up to a final concentration of 70 wt% and polyvinyl alcohol (PVA) was used as binder at 1%wt. A poly electrolyte (Dolapix CE64, Zschimmer-Schwarz, Germany) was used as deflocculating agent and the mixture was milled in a planetary mill using zirconia balls to get a suitable ceramic suspension for infiltration. The polyurethane (PU) sponge cubes (1 cm^3, density 30 kg/m^3) were immersed in the slurry for impregnation, gently squeezed to remove the excess suspension and dried at 60°C overnight. The infiltrated sponges were heated to 500°C for 1 h (heating rate at 0.5°C/min) in order to burnout the polyurethane foam, following the sintering phase at 1,300°C for 3 h (heating rate at 3°C/min) and the cooling phase at room temperature (4°C/min).

A collagen slurry (0.5 % w/v) was prepared by dissolving equine tendon collagen type I (kindly provide by Typeone srl, Lecce, IT) (Raucci et al., 2019; Salvatore et al., 2020) in aqueous acetic acid solution at pH 3.8 and impregnated with hydroxyapatite scaffolds under vacuum. The impregnated scaffolds were prepared for freeze-drying (LIO-5P, Cinquepascal, Italy) using different approaches: (i) traditional method in which samples were cooled to −20°C and (ii) innovative method, in which scaffolds were placed on ice plates, immersed in cold distilled water (0°C) and cooled to −20°C.

For comparison, neat collagen scaffolds were also prepared. Briefly, the collagen suspension was mixed by a magnetic stirrer for 2 h, and then the resulting slurry was poured into an aluminum multi-well (single well diameter = 8 mm), frozen at −20°C and then lyophilized.

After lyophilizing, all scaffolds (Coll, HA_Coll, HA-Mg_Coll, HA-Si_Coll) were dehydrothermally (DHT) crosslinked (under vacuum) for 24 h at 121°C.

Scaffold Characterization

Surface Morphology and Composition

The morphology of the scaffolds was studied using scanning electron microscopy (SEM) (SEM EVO® 40, Carl Zeiss AG, Oberkochen, Germany) with an accelerating voltage of 20 kV. SEM micrographs were then processed and analyzed with ImageJ 1.50c. software (National Institute of Health, USA; http://rsb.info.nih.gov/ij) to determine the pore diameter by taking the average values from 20 measurements chosen randomly in the images of each sample. The diameters were reported as mean ± SEM (standard error of the mean).

Additionally, doping of Mg and Si ions in the substituted hydroxyapatite scaffolds were analyzed using Micro XRF spectrometer (Bruker M4 Tornado, Berlin, Germany).

Mechanical Properties

The mechanical properties of the scaffolds were evaluated by compression tests using a universal testing machine (Lloyd LR5K instrument, Fareham Hants, UK), equipped with a 1 kN load cell. The scaffolds were immersed for 2 h in PBS 1X at room temperature prior testing (T_0). The thickness, length and width of hydrated cube specimens were measured (∼1 cm^3). The samples were placed between two parafilm layers and compressed at a crosshead speed of 0.5 mm/min. The samples ($n = 6$) from each batch of scaffolds were tested to obtain stress at failure (σ_{max}), calculated as the ratio between the maximum fracture load reached and the cross-sectional area of the scaffolds. The results were expressed as mean ± SEM (standard error of the mean).

Stability Test

The physical integrity of composite scaffolds in simulated physiological conditions was evaluated by soaking the samples ($n = 6$) from each batch of scaffolds in 50 mL of TRIS-HCl buffer (Trizma base 0.05 M, NaCl 0.15 M, Sodium azide 0.01% w/v, pH 7.4) at 37°C (Julabo GmbH, Seelbach, Germany). The pH of the solution was maintained at 7.4 by adding 1 M HCl. At scheduled time intervals (3, 7, 14, and 28 days), the samples were recovered and gently washed with water and ethanol several times before drying. All samples were dried in oven at 60°C for 24 h and then weighed (Gervaso et al., 2016). The weight loss percentages were calculated as

$$\%\ Weight\ loss = \frac{W_i - W_f}{W_i} \quad (3)$$

where W_i is the initial weight of sample and W_f the final weight of sample after soaking in Tris solution. The results were expressed as mean ± SEM (standard error of the mean). Moreover, post-immersion morphology of the scaffolds was qualitatively analyzed by SEM, and compression tests in wet conditions were carried out to verify possible changes in mechanical properties.

Cell Culture and Proliferation Assay

Human Bone Marrow-Derived Mesenchymal Stem Cells (BMSC) (ATCC-PCS-500-012, Milan, Italy) were cultured in Mesenchymal Stem Cell Basal Medium (BM) supplemented with 7% FBS, 100 IU/mL penicillin/streptomycin, 2.4 mM, 125 pg/mL FGF-b and 15 ng/mL IGF-1, at a density of 5×10^3 cells/cm^2 and incubated for 24 h at 37°C under 5% CO_2. BMSC were used between the third and the sixth passages. Scaffolds were sterilized under UV light overnight, followed by 75% ethanol for 1 h, washed with PBS for 1 h and then incubated with culture medium overnight. Cells were seeded on the top of each scaffold at a density of 1×10^4 cells per scaffold in a final volume of 50 μL. After 1.5 h, the culture medium

was added to cover the scaffolds. The medium was changed every 3 days. Cell proliferation was determined using the 3-(4, 5-dimethylthiazolyl-2)-2,5-diphenyltetrazolium bromide (MTT) assay at different time points. MTT is a commonly used method to evaluate the presence of metabolically viable cells, based on the ability of viable cells to convert MTT, a soluble tetrazolium salt, into an insoluble formazan precipitate, which is quantified spectrophotometrically. Briefly, the scaffolds were first transferred into a new 24-well plate. Then 0.5 mL of culture medium containing 50 μl of MTT stock solution, 5 mg/mL of phosphate-buffered saline (PBS) solution were added to each well. After 2 h incubation, the MTT solution was removed, and 0.5 mL of 0.01 N HCl in isopropyl alcohol were added to solubilize formazan crystals. Absorbance was measured at 570 nm through a spectrophotometer.

Statistical Analysis

For proliferation assay and compression test, values were expressed as mean ± SD for the indicated number of experiments. Differences between two groups were settled by unpaired Student's t test. In all comparisons, $P < 0.05$ was considered as statistically significant.

RESULTS AND DISCUSSION

Evaluation of Ceramic Powders Crystallinity

The XRD analysis (**Figure 1**) reveals the differences in crystallite size, crystallinity and different phases present in powders synthesized (Palazzo et al., 2011). Pure HA and HA-Mg shows a mean crystallite size of 50–60 nm, whereas HA-Si shows crystallite size of 25 nm. Pure HA shows a crystallinity around 89%. Mg doping in HA crystals resulted in an increase in crystallinity of 91% whereas Si doping decreased crystallinity to 74%. However, by examining the peaks associated with secondary phase β-tricalcium phosphate (β-TCP), it has been noticed that β-TCP was formed only in HA-Mg sample. The fraction of β-TCP calculated in HA-Mg powder is around 33%. These results indicate that Mg and Si substitution in HA crystal structure affects it crystallite size, crystallinity, and phase transformation.

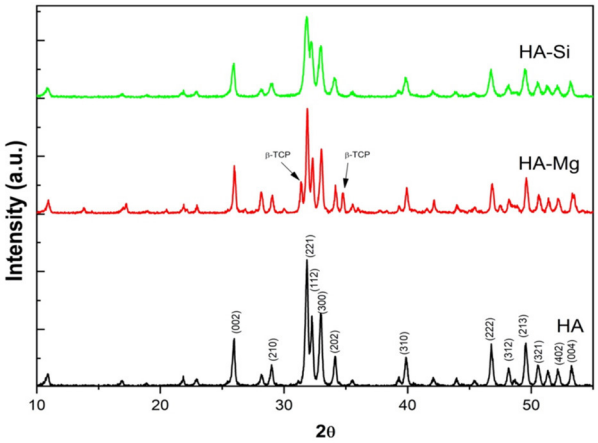

FIGURE 1 | The XRD spectrum of calcined powders.

Morphological and Mechanical Analysis of Composite Scaffolds

The freeze-drying is considered as a representative technique for the fabrication of porous foam-like scaffolds. The process consists of three steps: (i) freezing of the aqueous solution, (ii) primary drying to remove ice by sublimation and (iii) secondary drying to remove unfrozen or sorbed water by desorption (Zhang, 2018). The freezing step governs several critical parameters that influence the texture of the frozen matrix and, hence, the porosity and the specific surface of the final scaffold (Abdelwahed et al., 2006). Indeed, ice is used as a template in order to produce the desired template structures. A controlled freezing process is usually required in order to control the orientation, size, and morphology of the ice crystals (Zhang, 2018) and hence the porous structure. The dimensions of ice crystals are strictly correlated with the cooling rate. At lower cooling rates, few larges ice crystals are formed compared to the higher cooling rates, where more small ice crystals are formed. The size of the ice crystals determines the size of the pores in the dried matrix, indeed scaffolds produced at high temperature results in large mean pore size (O'Brien et al., 2004; Geidobler and Winter, 2013).

During the crystallization of ice, a thin skin layer usually formed at the top surface of freeze-dried samples. Such skin layer may prevent the transfer of water vapor during sublimation and slow down the sublimation rate, resulting in heating the product and its fusion (Abdelwahed et al., 2006), causing the formation of closed pores at scaffolds surface. Therefore, in this work, a new approach was used. The aim of the proposed technique was to avoid the skin layer formation (which is one of the common drawbacks of this process), in order to create an open porous structure at the top surface of scaffold, thus promoting cell migration and proliferation. Using the principle in which ice is used as a template, collagen-impregnated scaffolds were first immersed in cold water and then frozen. This aims to promote the nucleation of ice crystals on the edge between the external and the internal surfaces of the samples, leading to the formation of more open and interconnected pores. **Figure 2** shows the SEM images of samples prepared with traditional and innovative freeze-drying approaches. The use of this new approach seems to confirm the presence of a more open surface porosity. The formation of ice crystals on the scaffolds surface increases the presence of open pores on the outer layer of the scaffold which will come into contact with the tissues (**Figures 2d–f**). This represents an important advantage with respect to what is obtained with a traditional lyophilization in which collagen skin layer formed results in the absence of pores on the surface (**Figures 2a–c**). The open pore characteristic would promote cells migration from the outside to the inside of the scaffold and could result in an improved bone tissue growth in *in-vivo* applications. Furthermore, the pore diameters on the composite scaffolds' surface (between 200 and 600 μm) (**Table 1**) and average porosity around 92% of bulk ceramic scaffolds will allow cells to infiltrate,

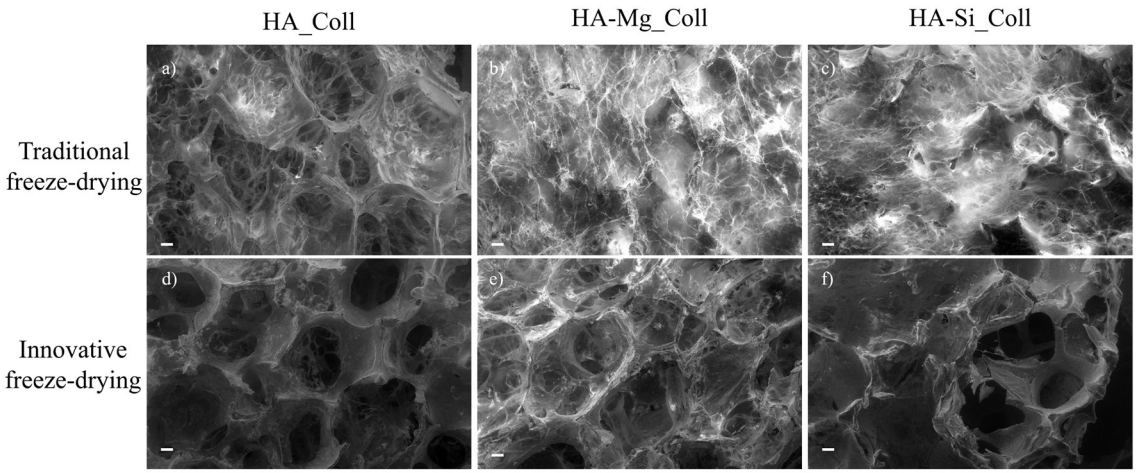

FIGURE 2 | SEM images (scale bar: 200 μm) of the HA_Coll, HA-Mg_Coll, and HA-Si_Coll scaffolds freeze-dried with traditional **(a–c)** and innovative **(d–f)** approach.

TABLE 1 | Pore size and maxim stress at failure of collagen and composite scaffolds.

Samples	Pore size (μm)	σ_{max} (MPa)
Coll	110 ± 0.05	0.007 ± 0.002
HA_Coll	602 ± 0.04	0.05 ± 0.01
HA-Mg_Coll	482 ± 0.03	0.22 ± 0.07
HA-Si_Coll	524 ± 0.06	0.09 ± 0.02

migrate and attach to the scaffold (Kramschuster and Turng, 2013). The macrostructure of bulk ceramic scaffolds exhibited open and interconnected pores and was an exact replica of PU sponge used (Queiroz et al., 2004). Elemental mapping of doped HA scaffold showed uniform distribution of Mg and Si ion in the scaffold structure (**Figures 3A,B**). These results proved that the doping effectively takes place during powder synthesis and remains stable during further scaffold preparation and sintering.

The assessment of the mechanical strength of composite scaffolds was carried out through compression tests. The stress–strain compression test results are in agreement with the literature (**Figure 3C**) (Gervaso et al., 2011). The samples exhibit a fragile behavior in compression, typical of ceramic materials, with a slight decrease in the total stress that rapidly increases as the displacement increases. In order to evaluate the mechanical resistance of scaffolds, the maximum stress at failure (σ_{max}) for all samples was evaluated. All samples showed low average stress values (**Table 1**), probably due to the poor compressive strength of type I collagen fibrils (0.007 ± 0.002) (Gervaso et al., 2012), because the high ratio between length and diameter makes them more unstable as the load to which they are subjected increases. However, among the three types, the HA-Mg_Coll scaffold showed the best performance, thanks to the presence of the Mg^{2+} ion that enhances the sinterabilty of HA powder.

Evaluation of Scaffolds Stability

Biodegradability is an essential feature of bioactive scaffolds, because the degradation rate must be synchronous with the bone tissue regeneration rate. Therefore, low degradation could induce an inflammatory response in the body; on the other hand, an excessively high rate will not allow the scaffold to provide a mechanical support for new tissue. To this aim, the stability of composite scaffolds in aqueous environment was evaluated and the samples were immersed in TRIS-HCl buffer (pH 7.4) at 37°C. At scheduled time intervals, i.e., after 3, 7, 14, and 28 days of soaking, stability performances of samples were checked through morphological, weight loss and mechanical evaluations (Nitti et al., 2020).

Degradation data corresponding to neat Coll scaffolds were not reported due to the rapid rate of degradation under test conditions. The composite scaffolds after soaking, as showed in **Figure 4**, exhibited a gradual degradation of the collagen component. After 3 days in Tris-HCl, HA_Coll scaffolds resulted in an increased reduction of collagen at the top surface of the scaffold than the HA-Mg_Coll and HA-Si_Coll scaffolds. After a week of soaking, HA-Mg_Coll showed higher collagen dose than those in HA_Coll and in HA-Si_Coll. However, at 14 and finally at 28 days, collagen decrease continued for all scaffold types, until the collagen disappeared from the surface of the scaffold, thus showing only the ceramic component. This degradation trend was also confirmed by weight loss % measurements (**Figure 5A**). Samples exhibited different degradation behavior, as assessed by 28-day stability test. The HA-Mg_Coll scaffolds were almost stable in physiological conditions and revealed a significantly lower dissolution rate than HA-Coll and HA-Si_Coll scaffolds (weight loss %: 0.36 ± 0.05; 1.61 ± 0.23 and 1.17 ± 0.05 after 28 days, respectively). While for HA-Mg_Coll and HA-Si_Coll scaffolds, the percentage of weight loss remained almost the same after 3 days in solution. For the HA_Coll scaffolds, there was a first sharp increase of weight loss % after 7 days and successively after 28 days. This degradation trend of HA_Coll scaffolds was also confirmed by mechanical analysis

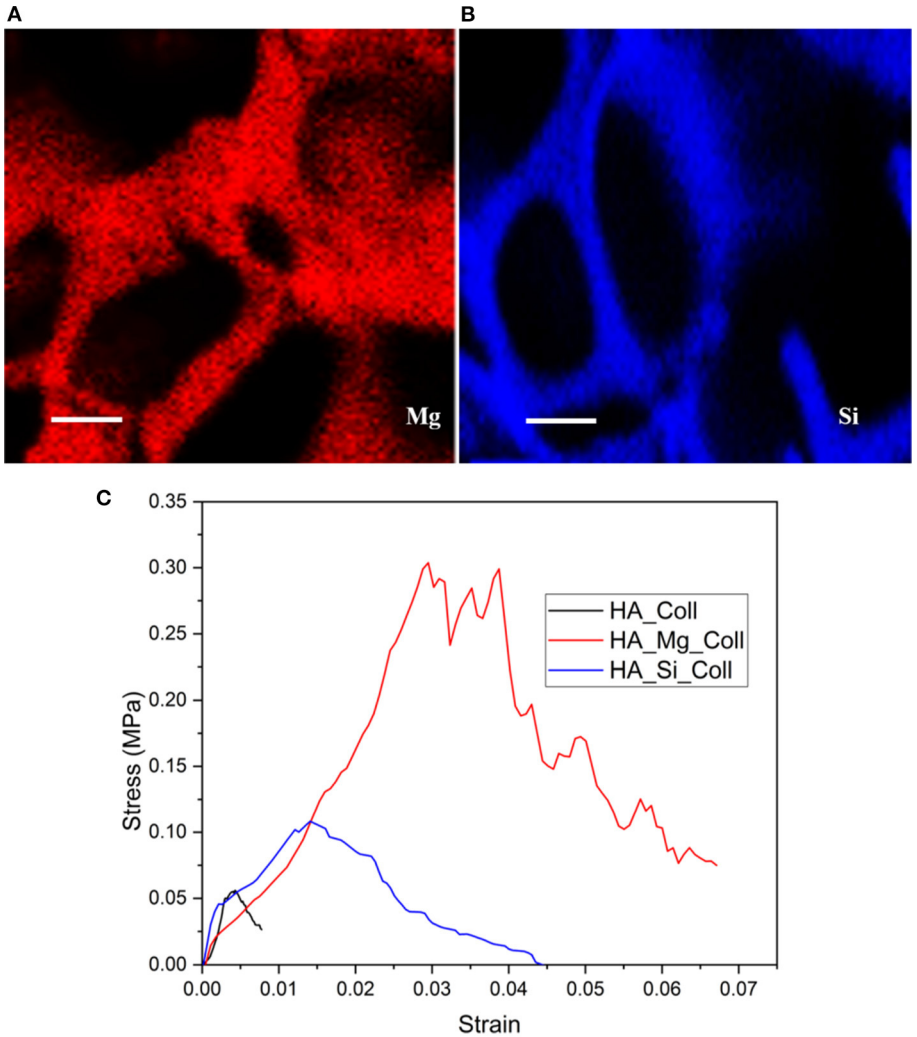

FIGURE 3 | The distribution of Mg (blue signal) and Si (red signal) elements on the surface of **(A)** HA-Mg and **(B)** HA-Si ceramic scaffolds (scale bar: 100 μm) and representative stress-strain plot of composite scaffolds **(C)**.

(**Figure 5B**). After a week of soaking, the loss of the collagen component from the scaffolds made the ceramic component prevail, thus leading to an increase in σ_{max}. After 28 days, a sharp decrease of stress at failure was present, which is similar to the observed weight loss. This is due to the initiation of degradation of the ceramic component, caused by the presence of impurities or structural defects (LeGeros, 2008). The same trend of HA_Coll scaffolds was observed in HA-Si_Coll scaffolds, although with higher σ values. During soaking, a continuous increase of stress at failure was observed due to progressive loss of collagen from the scaffold (from 0.09 ± 0.02 MPa before immersion to 0.20 ± 0.05 MPa at 28 days of soaking). However, unlike HA_Coll scaffolds at 28 day of immersion loss of ceramic component seems to be absent in Si_Coll scaffolds. Although the HA-Mg_Coll scaffolds showed better mechanical performance before immersion (0.22 ± 0.07 MPa), after immersion they presented a continuous and significant decrease of maximum stress (0.05 ± 0.01 MPa at 28 soaking days). This phenomenon could be caused by simultaneous degradation of collagen and HA-Mg due to presence of secondary phase (β-TCP) in Hydroxyapatite doped with Mg, which is more soluble and deteriorate the strength of the scaffold (Scalera et al., 2017).

Preliminary Cell Viability Evaluation

Cell proliferation on different scaffolds was determined using MTT assay (**Figure 6**). Collagen scaffolds are widely used to support the growth of many cell types (Iordache et al., 2014; Salvatore et al., 2020), since they have excellent properties for tissue engineering. For this reason, collagen scaffolds were selected as positive control for BMSC proliferation (Fasolino et al., 2019). The number of viable and metabolically active BMSC increased in a time-dependent manner until 21 days in Coll scaffolds (control). HA_Coll scaffolds exhibited a gradual

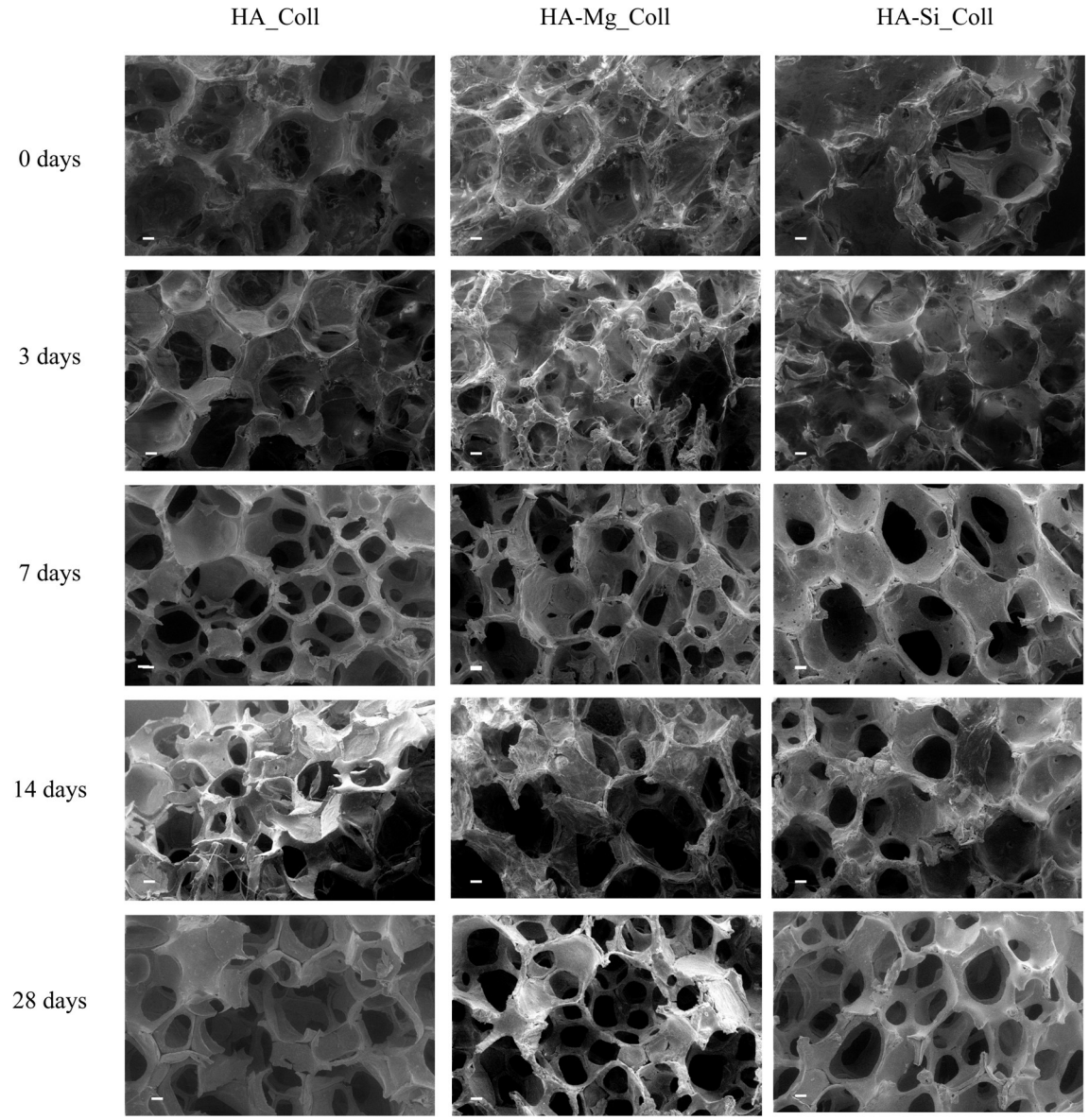

FIGURE 4 | SEM micrographs (scale bar: 200 μm) of HA_Coll, HA-Mg_Coll, and HA-Si_Coll scaffolds after 0, 3, 7, 14, and 28 days in TRIS-HCl pH 7.4 at 37°C.

increase of cell proliferation throughout time but it was lower with respect to control until 21 days. After 28 days of cell seeding, BMSC viability on HA_Coll scaffolds was increased by approximately 30% with respect to control. Conversely, HA-Mg_Coll scaffolds exhibited greater cell proliferation, while HA-Si_Coll showed lower cell proliferation compared to the control. This growing increase in cell proliferation, particularly for HA-Mg_Coll scaffold could be due to the lower degradation rate, as previously reported, and also to a more stable structure during cell incubation. The superior properties of HA-Mg_Coll scaffolds are attributable to a synergic effect of collagen bioavailability at shorter time and of Mg contribution on long term incubation. This combination of factors for HA-Mg_Coll scaffolds seems to elicit a metabolic boost for cell proliferation activities compared to both the control and the other investigated samples.

CONCLUSIONS

The development of suitable bioactive scaffolds that mimic the structure and biological characteristics of native tissue is a fundamental requirement for the treatment of injuries and diseases through a tissue engineering approach. In this study, bioactive scaffolds were fabricated successfully using a new freeze-drying approach. The proposed scaffolds presented a composite structure made with ceramic (HA, HA-Mg, and HA-Si) and collagen. The ceramic structure provides mechanical

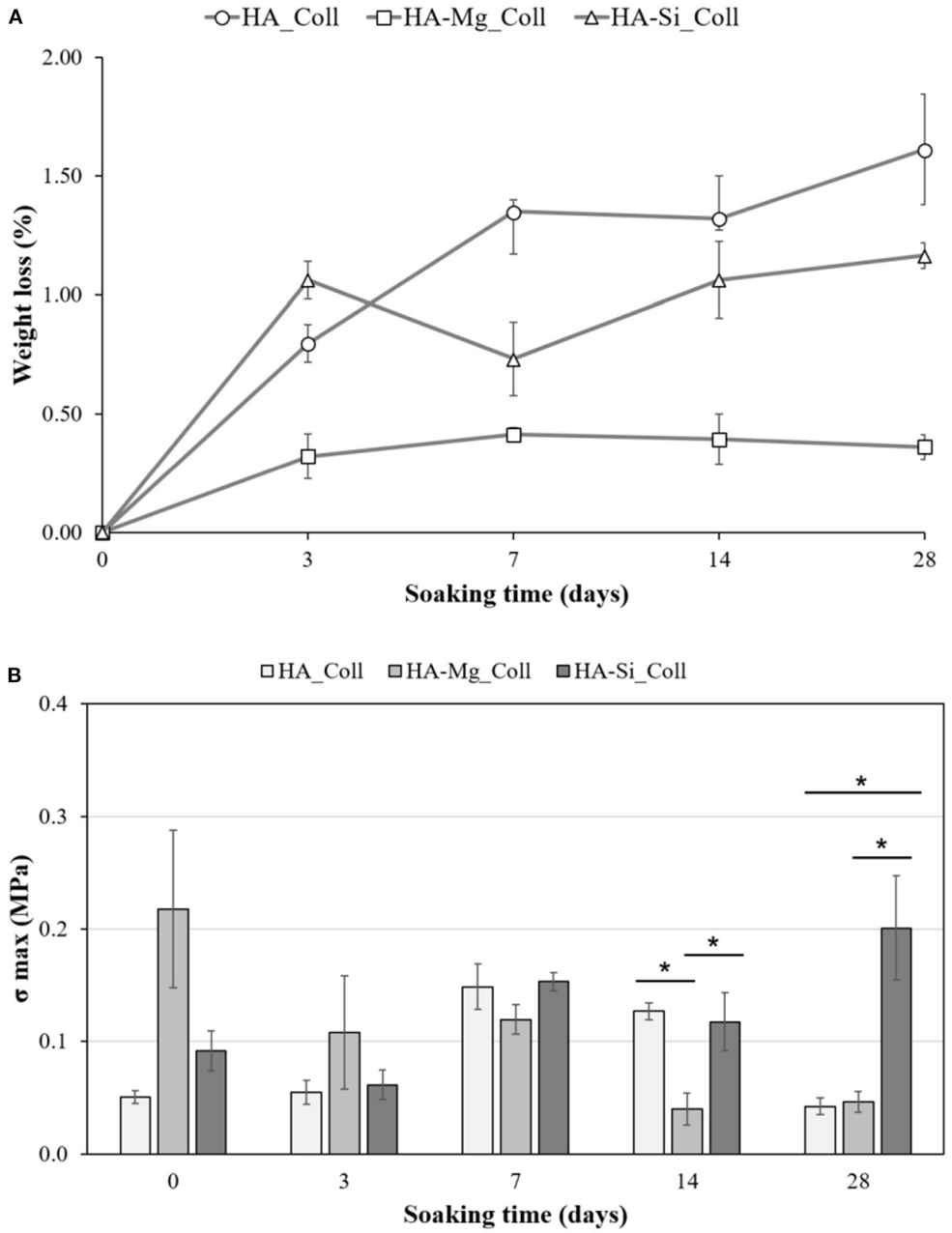

FIGURE 5 | Stability test on HA_Coll, HA-Mg_Coll, and HA-Si_Coll scaffolds. Plot of weight loss % **(A)** and stress at failure (σ_{max}) **(B)** after 0, 3, 7, 14, and 28 days of aging in TRIS-HCl pH 7.4 at 37°C (average values ± SEM, $n = 6$, $^*P < 0.05$).

support, while collagen guarantees the biomimetic and bioactive stimuli. Porosity, degradation rate and compressive strength are fundamental aspects for the choice of a good device for bone tissue regeneration. Therefore, in this study, scaffolds with a high porosity core and open and interconnected pores on the surface were developed. When using a traditional freeze-drying approach, a collagen skin layer is present on the top surface; hence, there are no open and interconnected pores. For this reason, a new approach of lyophilisation, in which ice crystals are used as templates to create pores, was successfully developed. This resulted in open pores on top surface of the composite scaffolds, making them more suitable for the cells to colonize and migrate inside the core scaffold. Furthermore, composite scaffolds in which ceramic part was made using pure HA, HA-Mg and HA-Si were fabricated and compared, revealing best performance in terms of weight loss for HA-Mg_Coll; whereas, HA-Si_Coll scaffolds showed better mechanical resistance before and after immersion in

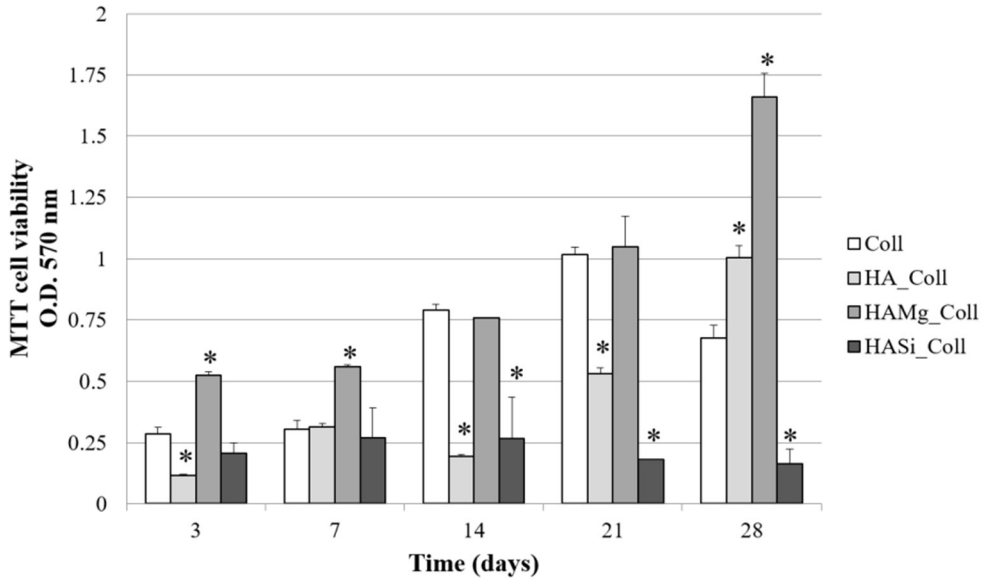

FIGURE 6 | Viability of BMSC on Coll, HA_Coll, HA-Mg_Coll, and HA-Si_Coll scaffolds assessed by MTT assay after 3, 7, 14, 21, and 28 days of cell seeding. Collagen scaffolds (Coll) are used as control. Data represent the means ± SD of duplicate measurements from three independent experiments. *$P < 0.05$.

physiological solution. However, in preliminary cell viability assays, Mg^{2+} seems to give best contribution when substituted into the structure of hydroxyapatite compared to SiO_4^{4-}. Mg improves the morphological, mechanical, stability properties and cell proliferation of the HA-based bioactive scaffolds, making those scaffolds suitable candidates for bone remodeling process.

DATA AVAILABILITY STATEMENT

The raw data supporting the conclusions of this article will be made available by the authors, without undue reservation.

AUTHOR CONTRIBUTIONS

PN: conceptualization, methodology, validation, investigation, and writing—original draft. SK: conceptualization, methodology, validation, investigation, and writing—review and editing. SC: validation and investigation. ES: methodology, validation, investigation, and writing. LS and AL: resources and supervision. CD: conceptualization, methodology, writing—review and editing, resources, and supervision. The manuscript and all the changes were written through contributions of all authors. All authors have given approval to the final version of the manuscript.

FUNDING

This research was funded by Ministero dello Sviluppo Economico project PON-MISE OSTEO-CARE, Prog. no. F/050370/03/X32 and by Ministero dell'Istruzione, Università e Ricerca (MIUR) project PRIN-SAPIENT, Prog. no. 2017CBHCWF.

ACKNOWLEDGMENTS

The authors are grateful to Mr. Donato Cannoletta of Department of Engineering for Innovation for the assistance with the SEM imaging. The authors acknowledge TypeOne Srl for providing type I collagen material.

REFERENCES

Abdelwahed, W., Degobert, G., Stainmesse, S., and Fessi, H. (2006). Freeze-drying of nanoparticles: formulation, process and storage considerations. *Suppl. Nonthematic Collect.* 58, 1688–1713. doi: 10.1016/j.addr.2006.09.017

Aina, V., Lusvardi, G., Annaz, B., Gibson, I. R., Imrie, F. E., Malavasi, G., et al. (2012). Magnesium- and strontium-co-substituted hydroxyapatite: the effects of doped-ions on the structure and chemico-physical properties. *J. Mater. Sci. Mater. Med.* 23, 2867–2879. doi: 10.1007/s10856-012-4767-3

Akkouch, A., Zhang, Z., and Rouabhia, M. (2011). A novel collagen/hydroxyapatite/poly(lactide-co-ε-caprolactone) biodegradable and bioactive 3D porous scaffold for bone regeneration. *J. Biomed. Mater. Res. Part A* 96A, 693–704. doi: 10.1002/jbm.a.33033

Bose, S., Fielding, G., Tarafder, S., and Bandyopadhyay, A. (2013). Understanding of dopant-induced osteogenesis and angiogenesis in calcium phosphate ceramics. *Trends Biotechnol.* 31, 594–605. doi: 10.1016/j.tibtech.2013.06.005

Farzadi, A., Bakhshi, F., Solati-Hashjin, M., Asadi-Eydivand, M., and Osman, N. A. (2014). Magnesium incorporated hydroxyapatite: synthesis and structural properties characterization. *Ceram. Int.* 40, 6021–6029. doi: 10.1016/j.ceramint.2013.11.051

Fasolino, I., Raucci, M. G., Soriente, A., Demitri, C., Madaghiele, M., Sannino, A., et al. (2019). Osteoinductive and anti-inflammatory properties of chitosan-based scaffolds for bone regeneration. *Mater. Sci. Eng. C Mater. Biol. Appl.* 105:110046. doi: 10.1016/j.msec.2019.110046

Freed, L. E., Vunjak-Novakovic, G., Biron, R. J., Eagles, D. B., Lesnoy, D. C., Barlow, S. K., et al. (1994). Biodegradable polymer scaffolds for tissue engineering. *Bio/Technology* 12, 689–693. doi: 10.1038/nbt0794-689

Geidobler, R., and Winter, G. (2013). Controlled ice nucleation in the field of freeze-drying: fundamentals and technology review. *Eur. J. Pharm. Biopharm.* 85, 214–222. doi: 10.1016/j.ejpb.2013.04.014

Gervaso, F., Padmanabhan, S. K., Scalera, F., Sannino, A., and Licciulli, A. (2016). Mechanical stability of highly porous hydroxyapatite scaffolds during different stages of *in vitro* studies. *Mater. Lett.* 185, 239–242. doi: 10.1016/j.matlet.2016.08.139

Gervaso, F., Scalera, F., Kunjalukkal, S., Licciulli, A., Deponti, D., Di Giancamillo, A., et al. (2012). Development and mechanical characterization of a collagen/hydroxyapatite bilayered scaffold for ostechondral defect replacement. *Key Eng. Mater.* 493–494, 890–895. doi: 10.4028/www.scientific.net/KEM.493-494.890

Gervaso, F., Scalera, F., Kunjalukkal, S., Sannino, A., and Licciulli, A. (2011). High-performance hydroxyapatite scaffolds for bone tissue engineering applications. *Int. J. Appl. Ceram. Technol.* 9, 507–516. doi: 10.1111/j.1744-7402.2011.02662.x

Hartwig, W. C. (1990). The anatomy and biology of the human skeleton by D. Gentry Steele and Claud A. Bramblett. Texas A & M University Press, College Station, 1988. *Clin. Anat.* 3, 151–153. doi: 10.1002/ca.980030210

Hoppe, A., Güldal, N. S., and Boccaccini, A. R. (2011). A review of the biological response to ionic dissolution products from bioactive glasses and glass-ceramics. *Biomaterials* 32, 2757–2774. doi: 10.1016/j.biomaterials.2011.01.004

Iordache, F., Constantinescu, A., Andrei, E., Curu?iu, C., Grumezescu, A. M., Voicu, G., et al. (2014). In vitro cytocompatibility evaluation of collagen based scaffolds using human endothelial progenitor cells for vascular tissue engineering. *Biomater. Tissue Eng. Bull.* 1, 10–16. doi: 10.33263/BTEB114.010016

Jones, J. R. (2013). Review of bioactive glass: from hench to hybrids. *Acta Biomater.* 9, 4457–4486. doi: 10.1016/j.actbio.2012.08.023

Karp, J. M., Dalton, P. D., and Shoichet, M. S. (2003). Scaffolds for tissue engineering. *MRS Bull.* 28, 301–306. doi: 10.1557/mrs2003.85

Kramschuster, A., and Turng, L-S. (2013). "Fabrication of tissue engineering scaffolds" in *Handbook of Biopolymers and Biodegradable Plastics*, ed S. Ebnesajjad (Norwich, NY: William Andrew Publishing), 427–446.

Landi, E., Logroscino, G., Proietti, L., Tampieri, A., Sandri, M., and Sprio, S. (2008). Biomimetic Mg-substituted hydroxyapatite: from synthesis to in vivo behaviour. *J. Mater. Sci. Mater. Med.* 19, 239–247. doi: 10.1007/s10856-006-0032-y

LeGeros, R. Z. (2008). Calcium phosphate-based osteoinductive materials. *Chem. Rev.* 108, 4742–4753. doi: 10.1021/cr800427g

Mikos, A. G., McIntire, L. V., Anderson, J. M., and Babensee, J. E. (1998). Host response to tissue engineered devices. *Adv. Drug Deliv. Rev.* 33, 111–139. doi: 10.1016/S0169-409X(98)00023-4

Munir, G., Koller, G., Di Silvio, L., Edirisinghe, M. J., Bonfield, W., and Huang, J. (2011). The pathway to intelligent implants: osteoblast response to nano silicon-doped hydroxyapatite patterning. *J. R. Soc. Interface* 8, 678–688. doi: 10.1098/rsif.2010.0548

Nitti, P., Gallo, N., Palazzo, B., Sannino, A., Polini, A., Verri, T., et al. (2020). Effect of l-arginine treatment on the *in vitro* stability of electrospun aligned chitosan nanofiber mats. *Polym. Test.* 91:106756. doi: 10.1016/j.polymertesting.2020.106758

O'Brien, F., Harley, B., Yannas, I., and Gibson, L. (2004). Influence of freezing rate on pore structure in freeze-dried collagen-GAG scaffolds. *Biomaterials* 25, 1077–1086. doi: 10.1016/S0142-9612(03)00630-6

O'Brien, F. J., Harley, B. A., Waller, M. A., Yannas, I. V., Gibson, L. J., and Prendergast, P. J. (2007). The effect of pore size on permeability and cell attachment in collagen scaffolds for tissue engineering. *Technol. Health Care* 15, 3–17. doi: 10.3233/THC-2007-15102

Padmanabhan, S. K., Ul Haq, E., and Licciulli, A. (2014). Rapid synthesis and characterization of silicon substituted nano hydroxyapatite using microwave irradiation. *Curr. Appl. Phys.* 14, 87–92. doi: 10.1016/j.cap.2013.08.022

Palazzo, B., Gallo, A., Casillo, A., Nitti, P., Ambrosio, L., and Piconi, C. (2011). Fabrication, characterization and cell cultures on a novel composite chitosan-nano-hydroxyapatite scaffold. *Int. J. Immunopathol. Pharmacol.* 24, 73–78. doi: 10.1177/03946320110241S214

Queiroz, A. C., Teixeira, S., and Monteiro, F. (2004). Production of porus hydroxyapatite with potential for controlled drug delivery. *Mater. Sci. Forum* 455–456, 358–360. doi: 10.4028/www.scientific.net/MSF.455-456.358

Rasskazova, L., Zhuk, I., Korotchenko, N., Brichkov, A., Chen, Y.-W., Paukshtis, E., et al. (2019). Synthesis of magnesium- and silicon-modified hydroxyapatites by microwave-assisted method. *Sci. Rep.* 9:14836. doi: 10.1038/s41598-019-50777-x

Raucci, M. G., D'Amore, U., Ronca, A., Demitri, C., and Ambrosio, L. (2019). Bioactivation routes of gelatin-based scaffolds to enhance at nanoscale level bone tissue regeneration. *Front. Bioeng. Biotechnol.* 7:27. doi: 10.3389/fbioe.2019.00027

Salvatore, L., Carofiglio, V. E., Stufano, P., Bonfrate, V., Calò, E., Scarlino, S., et al. (2018). Potential of electrospun poly(3-hydroxybutyrate)/collagen blends for tissue engineering applications. *J. Healthc. Eng.* 2018:6573947. doi: 10.1155/2018/6573947

Salvatore, L., Gallo, N., Aiello, D., Lunetti, P., Barca, A., Blasi, L., et al. (2020). An insight on type I collagen from horse tendon for the manufacture of implantable devices. *Int. J. Biol. Macromol.* 154, 291–306. doi: 10.1016/j.ijbiomac.2020.03.082

Sanosh, K. P., Chu, M. C., Balakrishnan, A., Lee, Y. J., Kim, T. N., and Cho, S. J. (2009). Synthesis of nano hydroxyapatite powder that simulate teeth particle morphology and composition. *Curr. Appl. Phys.* 9, 1459–1462. doi: 10.1016/j.cap.2009.03.024

Scalera, F., Gervaso, F., Palazzo, B., Scialla, S., Izzo, D., Cancelli, N., et al. (2017). Strategies to improve bioactivity of hydroxyapatite bone scaffolds. *Key Eng. Mater.* 758, 132–137. doi: 10.4028/www.scientific.net/KEM.758.132

Scalera, F., Palazzo, B., Barca, A., and Gervaso, F. (2020). Sintering of magnesium-strontium doped hydroxyapatite nanocrystals: towards the production of 3D biomimetic bone scaffolds. *J. Biomed. Mater. Res. Part A* 108, 633–644. doi: 10.1002/jbm.a.36843

Soriente, A., Fasolino, I., Raucci, M. G., Demitri, C., Madaghiele, M., Giuri, A., et al. (2018). Effect of inorganic and organic bioactive signals decoration on the biological performance of chitosan scaffolds for bone tissue engineering. *J. Mater. Sci. Mater. Med.* 29:62. doi: 10.1007/s10856-018-6072-2

Takata, M., Saiki, M., Sumita, N., Saldiva, P., and Pasqualucci, C. (2005). Trace element determinations in human cortical and trabecular bones. *J. Radioanal. Nucl. Chem.* 264, 5–8. doi: 10.1007/s10967-005-0666-0

Wang, X., Xu, S., Zhou, S., Xu, W., Leary, M., Choong, P., et al. (2016). Topological design and additive manufacturing of porous metals for bone scaffolds and orthopaedic implants: a review. *Biomaterials* 83, 127–141. doi: 10.1016/j.biomaterials.2016.01.012

Wei, G., and Ma, P. (2004). Structure and properties of nano-hydroxyapatite/polymer composite scaffolds for bone tissue engineering. *Biomaterials* 25, 4749–4757. doi: 10.1016/j.biomaterials.2003.12.005

Zhang, H. (2018). "Introduction to freeze-drying and ice templating" in *Ice Templating and Freeze-Drying for Porous Materials and Their Applications*, ed A. Jungbauer (Weinheim: Wiley-VCH), 1–27.

Conflict of Interest: The authors declare that the research was conducted in the absence of any commercial or financial relationships that could be construed as a potential conflict of interest.

The handling editor CG declared a past co-authorship with one of the authors, CD.

frontiers in Bioengineering and Biotechnology

ORIGINAL RESEARCH
published: 18 February 2021
doi: 10.3389/fbioe.2021.628129

In vivo Evaluation of Fibrous Collagen Dura Substitutes

*Wenbo Liu[1], Xin Wang[2], Jinlei Su[3], Qingsong Jiang[3], Jing Wang[3], Yang Xu[3], Yudong Zheng[1], Zhihui Zhong[2] and Hai Lin[3]**

[1] School of Material Science and Engineering, University of Science and Technology Beijing, Beijing, China, [2] Laboratory of Nonhuman Primate Disease Modeling Research, State Key Laboratory of Biotherapy, West China Hospital, Sichuan University, Chengdu, China, [3] National Engineering Research Center for Biomaterials, Sichuan University, Chengdu, China

Dura substitutes are applied in duraplasty to repair lost or damaged dura. Collagen-based dura substitutes are mainstream products in both the US and Chinese markets. In this study, dura substitute devices with potential dura regeneration ability are evaluated. The dura substitutes are composed of fibrous type I collagen that were purified from bovine tendon. Physical and chemical characterization demonstrated that the tested dura substitute has desirable porous scaffolding structures and is composed of highly purified type I collagen. The collagen dura substitutes were further investigated *in vivo* with a rabbit model for 6 months to evaluate their safety and performance to repair and regenerate dura. No inflammation or infection was observed during the course of *in vivo* study. The integration of the collagen dura substitutes with surrounding tissue was normal as compared to native tissue. The macroscopic and microscopic histological assessments of the sampled animal tissue showed that the damaged dura were regenerated. The collagen dura substitutes were resorbed between 3 and 6 months along with newly regenerated dura. Both tissue adhesion and dura repair was the worst in blank control group as compared to those in the collagen dura substitutes. Taken together, regenerative collagen dura substitutes demonstrated with suitable physicochemical properties. The *in vivo* evaluation in a rabbit model further demonstrated the safety and performance of such substitutes for dura repair and regeneration.

Keywords: collagen, dura substitute, animal study, preclinical (*in vivo*) studies, safety and efficacy

OPEN ACCESS

Edited by:
Maria Grazia Raucci, National Research Council (CNR), Italy

Reviewed by:
Fulvio Ratto, National Research Council (CNR), Italy
Christian Demitri, University of Salento, Italy

****Correspondence:***
Hai Lin
linhai028@scu.edu.cn

Specialty section:
This article was submitted to Nanobiotechnology, a section of the journal Frontiers in Bioengineering and Biotechnology

Received: *11 November 2020*
Accepted: *29 January 2021*
Published: *18 February 2021*

Citation:
Liu W, Wang X, Su J, Jiang Q, Wang J, Xu Y, Zheng Y, Zhong Z and Lin H (2021) In vivo Evaluation of Fibrous Collagen Dura Substitutes. Front. Bioeng. Biotechnol. 9:628129. doi: 10.3389/fbioe.2021.628129

INTRODUCTION

As an important tissue of central nerve system, dura mater works as natural protective barrier of brain tissue (Adeeb et al., 2012; Zwirner et al., 2019). Defects or damages of dura mater may be caused by trauma, inflammatory or neoplastic processes, or surgical procedures, which include but not limited to standard operation procedures of craniotomy in treatment of cranial injury, and thoroughly resection of cancer-related dura mater (Bartosz and Vasterling, 1994). The incomplete dura mater could not protect brain tissue, leading to complications such

as cerebrospinal fluid (CSF) leakage, intracranial infection, encephalocele, tissue adhesion, and epilepsy. Therefore, the need to close dura defects has promoted a quest for the ideal dura substitute (Wang and Ao, 2019; Go et al., 2020).

According to the guidance documents issued by the National Medical Products Administration of China (NMPA) (NMPA, 2020) and U.S. Food and Drug Administration (FDA) (U. S. Food and Drug Administration, 2000), the requirements for a dura substitute should include the following attributes: biocompatibility without induction of an immune or inflammatory response; controlled risks of infection or disease; appropriate mechanical properties, resistant to tear, and anti-leakage of cerebrospinal fluid. Dura substitutes made of non-degradable materials should be bio-inert and could replace the damaged dura permanently (Nagata et al., 1999; Ström et al., 2011; Matsumoto et al., 2013). Dura substitutes made of degradable materials should have suitable degradation properties with micro-environment for tissue remodeling and possible regeneration (Costantino et al., 2000; Yamada et al., 2002; Wang and Ao, 2019). Such degradable substitutes with appropriate pore size and porosity could be resorbed matching with the development of new tissue (Neulen et al., 2011; Sandoval-Sanchez et al., 2012). In addition, the abundance and availability of raw materials for dura substitutes would reduce the cost of the device and be economically attractive. Finally, easy-handling characteristics, convenient storage conditions and stable shelf life would be other important criteria for the dura substitute devices.

In history, autogenous membrane tissue was applied as dura substitute, which caused damage of donor sites and had limitation of size and shape (Dufrane et al., 2002; Tachibana et al., 2002; Sabatino et al., 2014; Morales-Avalos et al., 2017). Membrane-like allografts from donators was used to overcome some shortcomings of autografts (Parízek et al., 1997; Azzam et al., 2018; Turchan et al., 2018). However, the allograft was not widely applied in clinic owing to the lack of donor resources, and concerns over tissue quality, ethics, and immunogenic diseases. With the development of material science and medical technologies in recent decades, a series of dura substitutes based on synthetic polymers and nature-originated materials were developed and tested to investigate their potential in clinical applications (Pogorielov et al., 2017; Vecera et al., 2018). Some of the above devices were successfully commercialized (Schmalz et al., 2018).

Based on a search by November 10th, 2020 *via* public databases of NMPA and FDA, 14 dura substitutes from 11 companies were approved by NMPA as class III devices. 41 devices from 16 companies were cleared by FDA as 510(k) devices. The dura substitute devices and their associated materials are listed in **Supplementary Table 1**.

Based on the material properties and their interactions with host tissue, dura substitutes could be classified to degradable and non-degradable devices that are composed of synthetic or nature-originated materials. The non-degradable dura substitutes physically set barrier for brain tissue (including piamater, arachnoid membrane) from other tissues and prevented the leakage of cerebrospinal fluid. The degradable dura substitute gradually degraded and absorbed in host after the implantation (Zerris et al., 2007; Jing et al., 2020). For degradable dura substitutes with potential regeneration properties, during the degrading period, the endogenous cells would migrate and proliferate in the regenerative device with porous scaffolding structures, gradually reconstruct of extracellular matrix and vascularize to form new dura mater till the final repair and regeneration of damaged or lost dura mater.

Commercialized dura substitutes in **Supplementary Table 1** are made of diversified polymers which possess merits and drawbacks. Non-degradable dura substitutes made of synthetic polymers such as polyurethanes generally have preferable mechanical properties and anti-leakage performance (Wong et al., 2018), but they are recognized as foreign bodies after implantation (Maehara et al., 2020). The non-degradable, crosslinked animal-derived dura substitutes such as bovine/porcine pericardium have superior mechanical strength (Sun et al., 2018), but they may cause varying degrees of rapid or delayed immune or inflammatory response after implantation. Although biological safety like infectious pathogen and immunogenic disease is an inevitable issue for acellular matrix-based dura substitutes including porcine small intestinal submucosa and bovine dermis, many measures could be carried out to control the risk under a limited degree via virus inactivation treatments and immunogen elimination methods (Li et al., 2019).

Degradable dura substitutes made of absorbable synthetic polymer avoid exogenous virus and immune reaction (MacEwan et al., 2018; Chuan et al., 2020; Ramot et al., 2020), but they face other safety and performance issues. For example, the remaining of monomer or chemical residues could affect their biocompatibility. The design of their porous microstructure and quality control requirements could increase the difficulty of their manufacturing processes. The regulation of their degradability could determine their final results of tissue repair at an extensive extent (Hemstapat et al., 2020).

Because native dura mater is primary composed by type I collagen, the purified and reconstituted fibrous type I collagen-based dura substitute could meet the biological safety requirement and potential to regenerate the dura tissue via appropriate structure design. In the fully degradable dura substitutes based on natural materials, many products are based on type I collagen derived from different animal tissues. This predominated data suggests that the collagen-based dura substitutes are acceptable for clinical applications with satisfactory results.

Type I collagen is a fibrillar and structural protein which is expressed in almost all connective tissues. Because dura mater is composed primarily of type I collagen, a reconstituted bovine collagen-based scaffold is likely to be a suitable dura substitute candidate to repair and regenerate damaged or lost dura mater (Esposito et al., 2008, 2013; Calikoglu et al., 2019). In this study, a rabbit model was applied to evaluate the *in vivo* safety and dura repair performance of two dura substitutes, while blank was set as control. Furthermore, the feasibility and potential of dura regeneration by using the fibrous type I collagen dura substitute devices were investigated and discussed.

MATERIALS AND METHODS

Materials

All medicine or chemicals including IgG and IgM ELISA kit (Abnova, United States, Cat: KA2017 and KA2040), pentobarbital sodium (Sigma, United States, Cat: #020M2298V), saline for injection (Kelun, Sichuan China, Cat: W116051504), iodophor disinfectant (Yijieshi, Sichuan China, Cat: 15.10.22) were used as received without further treatment unless otherwise stated.

Collagen Dura Substitutes

Dura substitutes were acquired as commercial products. DuraPair was designated as the experiment device and DuraMax as the control of animal study are from Beijing Bonsci Technology Co., Ltd. (Beijing, China) (Nie and Zhang, 2018, 2020) and Tianxinfu Co., Ltd. (Beijing, China) (Li et al., 2013), respectively. Both devices were made of type I collagen fibrils from native bovine tendon and terminally sterilized by ethylene oxide gas. Please note that manufacturing processes are proprietary and product-specific. For both DuraPair and DuraMax, type I collagen fibrils were prepared from purified Achilles tendon followed by freeze-drying processes. Because the physico-chemical properties of DuraMax were reported previously (Xia et al., 2017), the current research studied the composition and microstructure of DuraPair before focusing on the *in vivo* study which investigated both fibrous type I collagen dura substitutes for dura repair and regeneration.

Characterization of Dura Substitutes

Composition Analysis: Purity and Amino Acid Analysis

The purity of collagen dura substitute (DuraPair) was defined as the ratio of type I collagen in the product. Since type I collagen can be affinitive recognized and fully degraded by type I collagenase, the comparison on electrophoresis strips of protein samples before and after the enzyme hydrolysis will indicate the type I collagen content in the sample. Accordingly, sodium dodecyl sulfate—polyacrylamide gel electrophoresis (SDS-PAGE) was applied to measure the type I collagen purity and protein impurity in collagen dura substitute. Briefly, the solid dura substitute sample was cut into small pieces around 1 mm^3, homogenized in 0.2 M HAc and stirred to attain a final sample solution (sample A). The 1.25 Unit/mL collagenase solution was prepared by dissolving the enzyme in 20 mmol/L NaH_2PO_4 (pH 7.4, contained 0.1 mmol/L $CaCl_2$). The collagen dura substitute was digested in the collagenase solution at 37°C for 4h, to acquire the digestion solution (sample B). The collagenase solution itself was labeled as sample C. To understand the lower limit value of protein can be detected by this method, BSA solutions with gradient concentrations were tested in advance and the lower limit of BSA (LL_{BSA}) was loaded as sample D. Meanwhile, protein molecular weight ladder and type I collagen control was served as sample E and F, respectively. All the samples were equal volume mixed with sample-loading buffer and cooked for 2 min in boiled water bath in sealed 0.5 mL centrifuge tubes. Subsequently, all the samples were loaded 20 μL in the spacer gel lanes, and further followed the standard SDS-PAGE protocol using Bio-rad Mini-Protean Tetra Cell gel electrophoresis system and dyed by coomassie brilliant blue. The concentrations of spacer and separation gels were 4 and 7%, respectively. The final acquired gel with electrophoresis strips of protein samples was imaged and further analyzed.

Amino acid analysis was applied to understand the amino acid components of collagen dura substitute and estimate the proportions of different amino acids as well. Around 40 mg collagen dura substitute was carefully and accurately weighed, and fully degraded in 6 mol/L HCl at 110°C for 22 h. The dried degraded outcome was dissolved to a quantified volume, and further analyzed by Hitachi L-8900 automatic amino acid analyzer.

Structural Analysis: Morphology and Porosity

The morphology of the collagen dura substitute was observed by scanning electron microscopy (SEM), and the porosity was further estimated. Sample was first frozen in liquid nitrogen and the brittle fracture surface was coated with an ultrathin layer of Au/Pt in anion sputtering, and further observed by Hitachi S-4800 scanning electron microscopy.

In vivo Animal Study

The animal study was approved by the Animal Care and Use Committee of Sichuan University (IACUC-2016-R-001). The animal study is complied with General Considerations for Animal Studies for Medical Device (FDA, United States) and Guidance Document for Dura Substitute Devices; Guidance for Industry (FDA, United States).

Surgical Procedure

Thirty-six female SPF New Zealand white rabbits (Animal Farm of Sichuan Laboratory Animal Committee, SCXK 2013-14) weighing 2.0–3.0 kg ± 20% were used for *in vivo* study of collagen dura substitute. All the animals were randomly assigned into three groups (i.e., experiment, control and blank control) and were feed 5 days to adapt to the environment before the surgery. The surgical procedures are shown as **Figure 1**. Briefly, the animals were general anesthesia with 3% pentobarbital sodium (25 mg/kg) *via* auricular vein and intramuscular injected with 100 kU penicillin, and placed in prone position. Through a 4 cm long calvarium midline incision, the skull was exposed. Behind the crest of the skull and distant around 6 mm to the midline on the right, a round opening with diameter of 12 mm was created by high-speed electric drill. The dura mater was exposed and a defect around 8 mm in diameter was made. The dura substitutes with 9 mm in diameter were applied to repair the defects in both experimental and control groups. Finally, the periosteum, subcutaneous tissue and skin were successively closed with absorbable suture. In blank control group, the defects were left without any implants but only suture. After the surgery the animals were kept in individual cages at room temperature on a 12 h light/dark cycle. Standard balanced food and water were available for freely intake. The penicillin (100 kU/kg) has been intramuscular introduced 30 min before surgery, and prolonged 3 days after the surgical procedure.

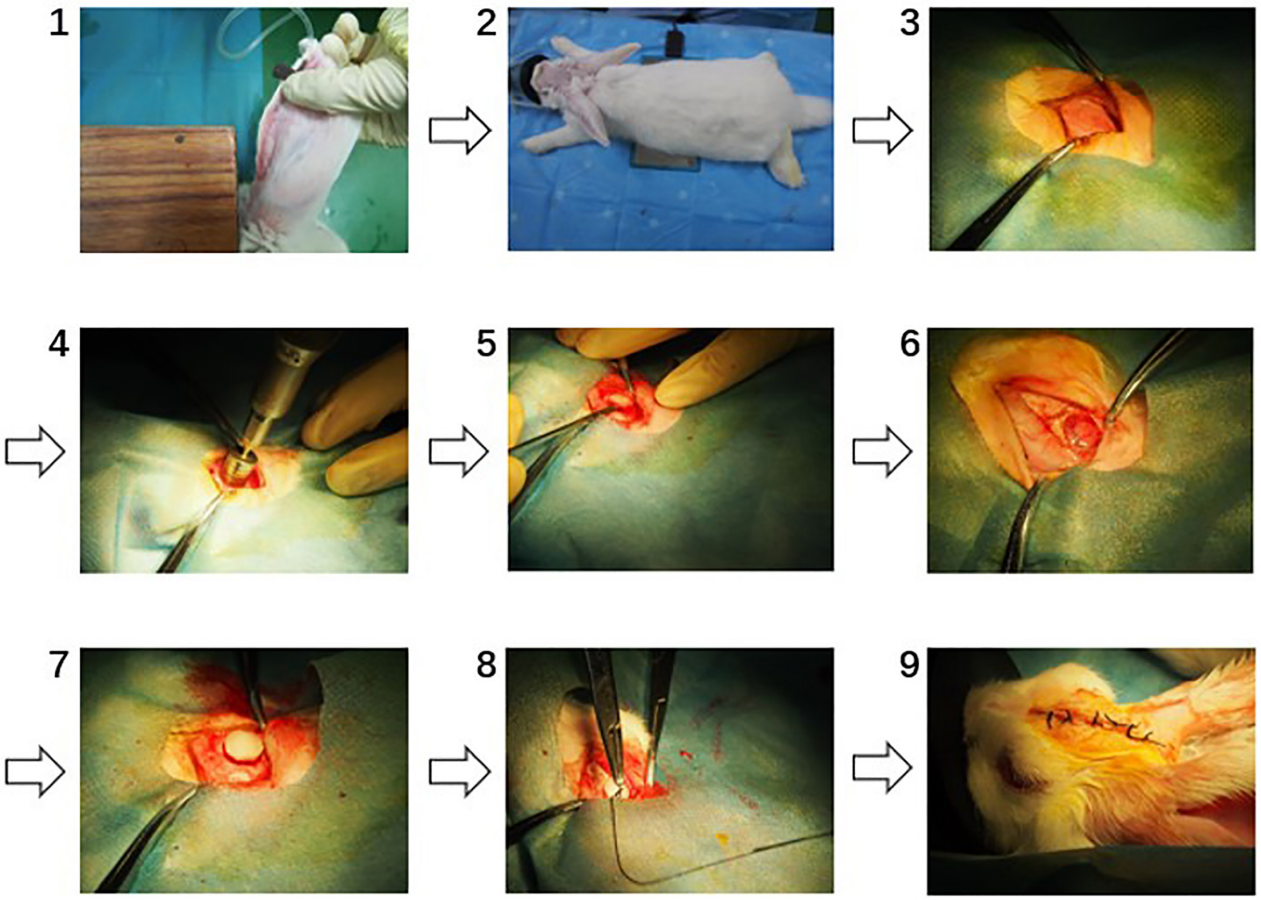

FIGURE 1 | The surgical procedures of dura mater implantation (1: anaesthetization, 2: exposure of surgical site, 3: exposure of the skull, 4: round opening on the skull, 5: establishing of dura mater defect, 6: established dura mater defect, 7: dura substitute implantation, 8: suturing, 9: post-operation).

Observation and Harvest Procedure

One week after the operation, all the animals were daily inspected on surgical site, including the wound healing, cerebrospinal fluid (CSF) leakage and infection situation. Especially, the surgical site, middle ear cavity and accessory nasal sinuses were carefully checked as possible CSF leakage sites.

Leukocyte count in complete blood was applied at three sampling time points: before the operation, 1 week post-operation and before the sacrifice. Leukocyte count in CSF was applied with CSF was collected just before animal sacrifice. The method used for leukocyte counts was microscopic visual counting.

Immunoglobulin G (IgG) and immunoglobulin M (IgM) in serum which was collected before the operation and before the sacrifice were detected with quantitative assay kits. The testing kits used for IgG (Catalog No. KA2017) and IgM (Catalog No. KA2040) were purchased from Abnova Inc. (United States).

After the sacrifice, the tissue materials were sampled and fixed in 10% buffered formalin for 10 days, following the decalcification in decalcifying fluid. Conventional histological sample treatments and staining were applied. Briefly, representative tissue sections were placed in histopathological cassettes, and processed in the tissue processor, where the material was dehydrated gradually in series of ethyl alcohol with increasing concentrations (80–99.8%), subsequently cleared in the series of xylenes, and embedded in paraffin. The formed paraffin blocks were cut using rotary microtome (Thermo Scientific HM340E) into 5 μm paraffin tissue sections, placed on slides and stained with H&E.

The animals were sacrificed at 30, 90, and 180 days postoperatively in all three groups (experiment group, control group and blank control group) by intravenous administration of a pentobarbital overdose (50 mg/kg).

The tissue adhesion of decalcified tissue samples and tissue sections were both double-blind rated by four senior researchers.

Grading System

A quantitative grading system was applied to score the tissue adhesion to the implants in both macroscopic and microscopic assessments, as previously described (Shackelford et al., 2002; NMPA, 2019). Macroscopic assessment of adhesion to surrounding tissue was graded from 0 = none, 1 = minimal, easy to separate, 2 = moderate, can separate without any break, 3 = multiple, difficult to separate and some tissue integrate with

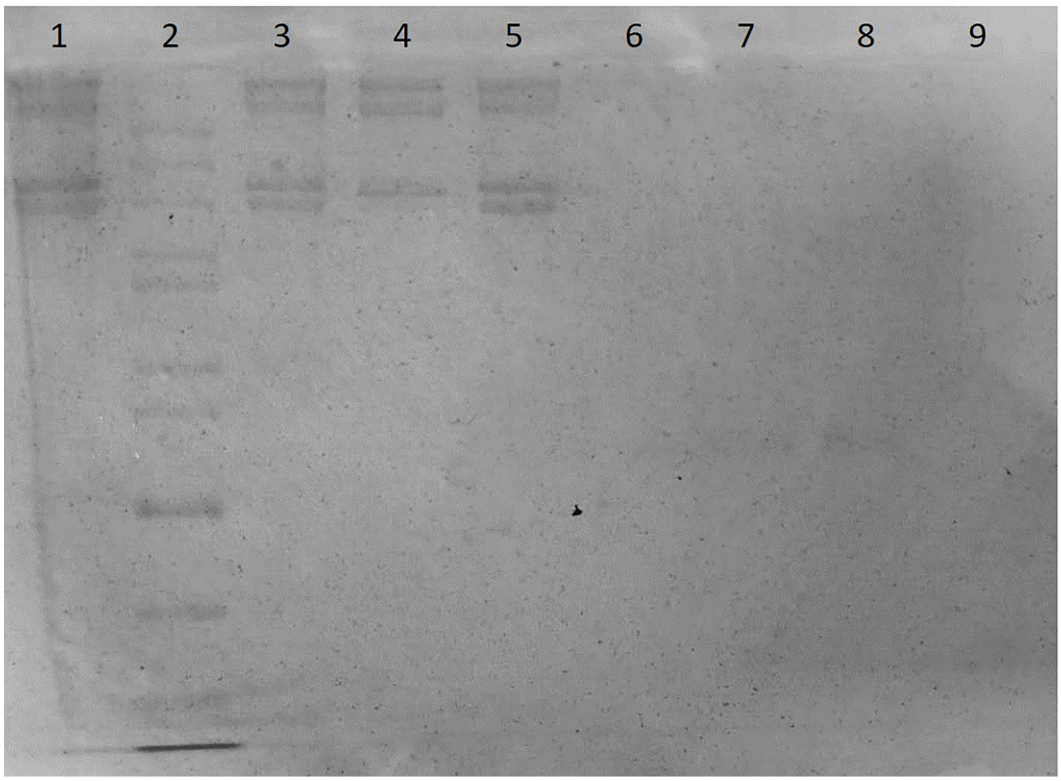

FIGURE 2 | The SDS-PAGE of dura substitute (Lane 1, 3, 5: sample A, collagen solution; Lane 2: sample E, molecular weight ladder; Lane 4: sample F, control type I collagen; Lane 6: sample B, digested collagen solution; Lanes 7, 8: sample D, BSA; Lane 9: sample C, collagenase solution).

the graft, and 4 = extensive, hardly to separate and lots of tissue integrate with the graft. Microscopic assessment of adhesion and inflammation of the graft were graded from 0 = none, 1 = minimal (<1%), 2 = mild (1–25%), 3 = moderate (26–50%), 4 = moderately severe (51–75%), and 5 = severe.

Statistical Analysis

All the experimental data were presented as mean ± standard deviations, and analyzed for significant by Kruskal-Wallis test, followed by Mann-Whitney U test. Data were analyzed using SPSS Statistics Software (version 17.0). Statistically significant differences were defined as having $p < 0.05$.

RESULTS

Characterization of Dura Substitutes

Composition Analysis

The SDS-PAGE image was shown as **Figure 2**, and the meanings of sample codes and lane numbers were specified in **Table 1**. According to the electrophoresis strips in the lanes loaded with different samples, dura substitute sample (sample A, lane 1, 3, 5) had similar molecular weights and distribution with type I collagen control (sample F, lane 4). Also, no strips were observed of collagenase digested dura substitute (sample B, lane 6) and collagenase (sample C, lane 9), which indicated the dura substitute was fully digested by collagenase. Thus, the amount of impurities in dura substitute samples was no larger than the detection limit measured with BSA. Since 20 μL of 0.01 mg/mL BSA solution was loaded as sample D (lane 7, 8), the purity of collagen dura substitute could be calculated as the following equation.

TABLE 1 | The meaning meanings of sample codes and lane numbers.

Sample code	Lane number	Meaning
A	1, 3, 5	Dura substitute samples
B	6	Collagenase digested dura substitute
C	9	Collagenase
D	7, 8	BSA
E	2	Protein molecular weight ladder
F	4	Type I collagen control

$$X = \frac{V * C - LL_{BSA}}{V * C} \times 100\%$$

Where LL_{BSA} is the lower limit of BSA (μg), V is the loaded sample volume (μL) and C is the sample concentration (μg/μL). In this study, C was 2.64 mg/mL, V was 20 μL, and LL_{BSA} was 0.2 μg. Accordingly, the purity was 99.62% and the non-collagen impurity content was less than 0.40%.

TABLE 2 | The amino acid analysis of dura substitute.

AA	Molar ratio		AA	Molar ratio		AA	Molar ratio	
	dura	Bovine I α 1		dura	Bovine I α 1		dura	Bovine I α 1
Asp	4.73%	4.26%	Val	2.26%	1.61%	Lys	1.87%	3.60%
Thr	1.79%	1.61%	Met	0.11%	0.66%	His	0.13%	0.28%
Ser	3.31%	3.60%	Ile	1.18%	0.85%	Arg	5.21%	5.02%
Glu	7.58%	7.48%	Leu	2.69%	2.08%	Pro	11.24%	22.82%
Gly	34.06%	32.77%	Tyr	0.27%	0.47%	Hyp	9.37%	0.00%
Ala	12.45%	11.65%	Phe	1.75%	1.23%	Trp	0.00%	0.00%
Cys	0.00%	0.00%						

AA, Amino Acid Total 100.00%

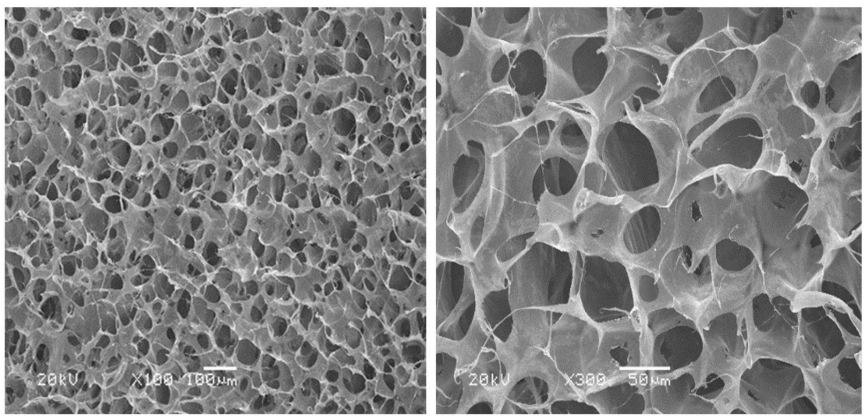

FIGURE 3 | The microstructure of dura substitute.

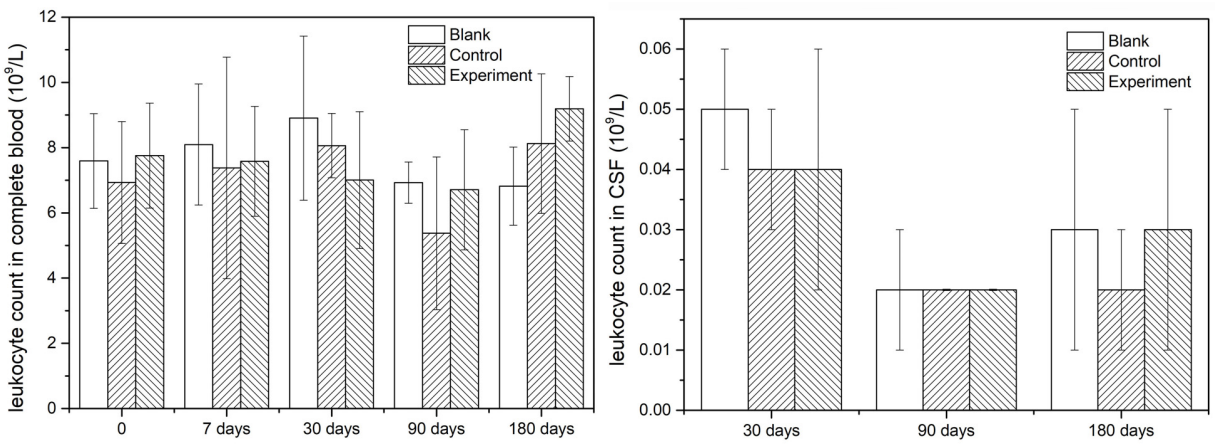

FIGURE 4 | The leukocyte counts in complete blood and CSF.

The result of amino acid analysis was given in **Table 2**, which included the molar ratios of different amino acids in collagen dura substitute. Also, the amino acid compositions of bovine collagen alpha-1(I) chain (UniProtKB entry: P02453) were shown as control according to the data from UniProtKB (UniProt, 2020). It is obvious to find that the collagen dura substitute met the main composition features of type I collagen, such as around 1/3 of glycine, no cysteine and tryptophan, and close total content of proline and hydroxyproline.

Structural Characterization

The microstructure of the collagen dura substitute was shown in **Figure 3**, which demonstrated a three dimensional network

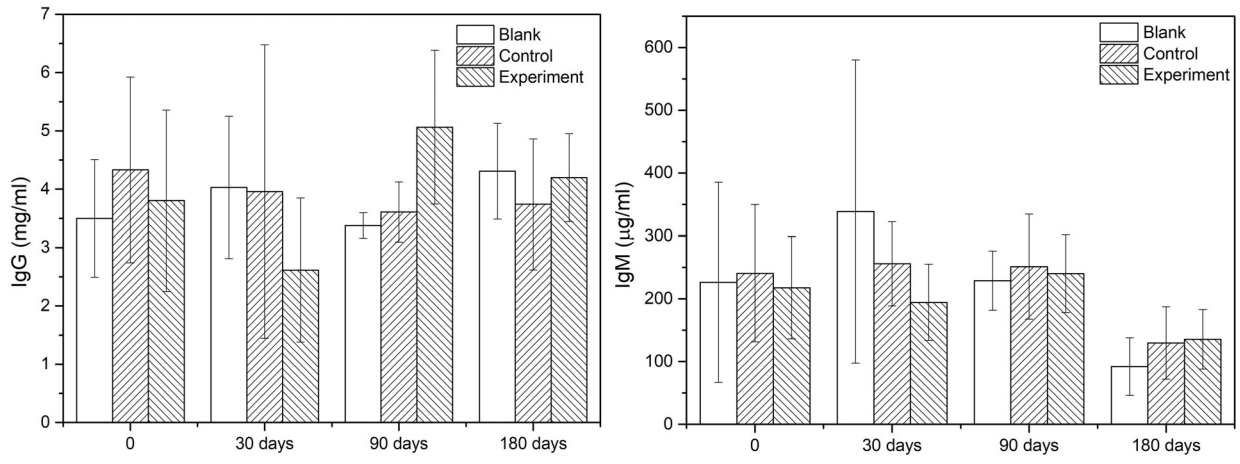

FIGURE 5 | The IgG and IgM contents in serum.

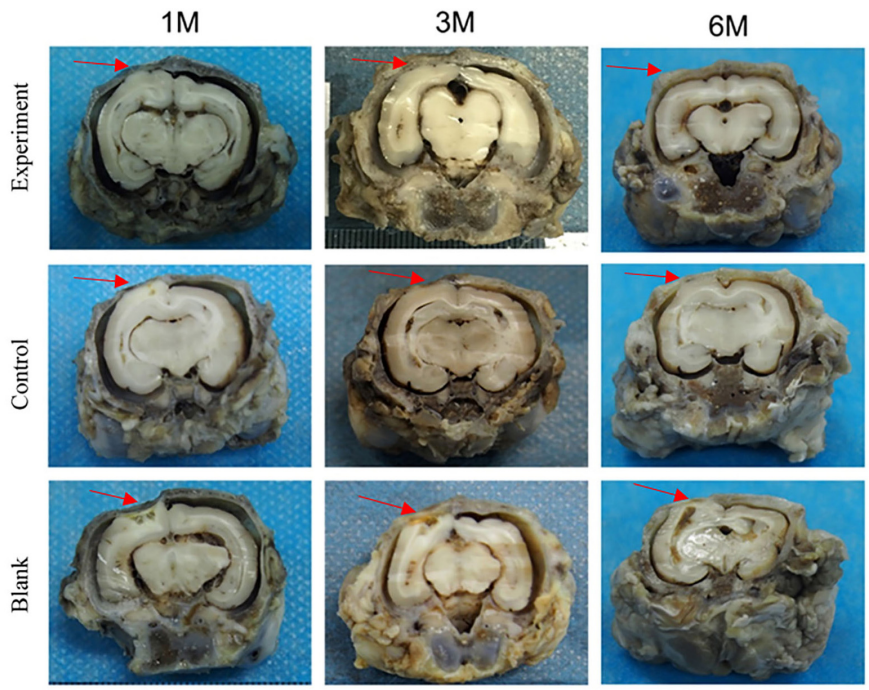

FIGURE 6 | The macroscopic examination of the implants (arrow: implant position).

structure with inter-connected pores of diameters ranged from a few to 150 μ m.

In vivo Animal Study

Gross Observation and Fluid Examination

All the animals had normal intakes and behavior post-operation. The body weight of each animal increased gradually and showed insignificant difference among groups (data not shown). The body temperature of each animal was in normal range during the observation period and showed insignificant difference among groups (data not shown).

For experiment and control groups, no irritation or inflammation, nor fluid or discharge was observed at the surgical site. More importantly, no CSF was observed postoperatively till the sacrifice of animals.

Inflammatory Evaluation

Since leukocytes were considered as one of the main response results when there is an inflammatory response, the leukocyte count was detected both in complete blood and CSF in this study. The results were shown in **Figure 4** and they indicated that the leukocyte counts in both complete and CSF had insignificant

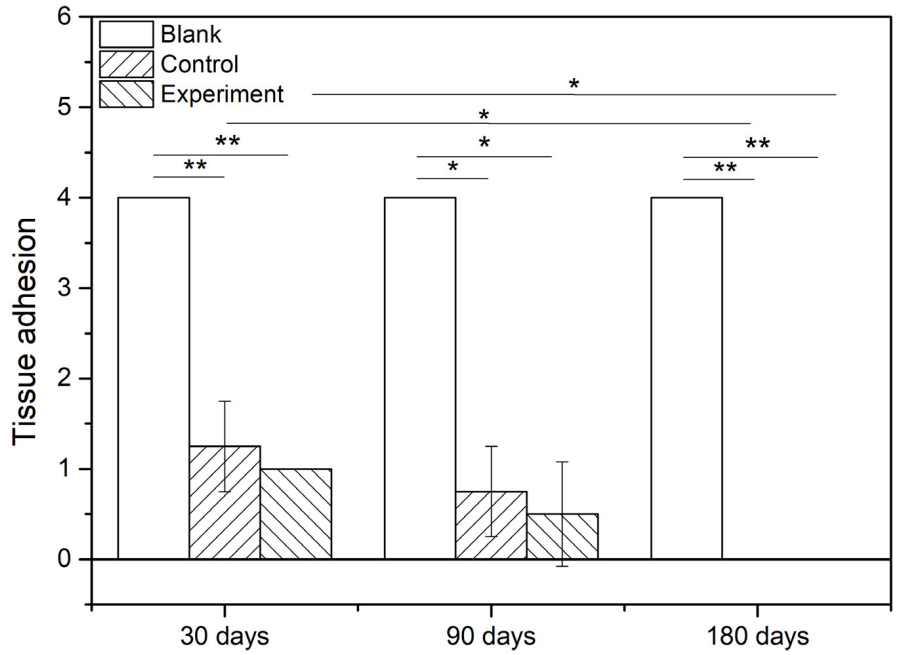

FIGURE 7 | The adhesion grading of implants with tissue (*$P < 0.05$, **$P < 0.01$).

difference at different sampling time points, which meant no inflammatory caused by the implant or the operation.

Immunological Response

As the main indicators of immunological response, the IgG and IgM contents in serum of different groups at given sampling times were showed in **Figure 5**. According to the results, there was no significant difference among the groups comparing the values at sampling time and those acquired before the operation. Therefore, it was reasonable to confirm that there was no early or delayed infection owing to the operation or the implant.

Macroscopic Examination

The tissue adhesion of dura substitutes is one of the critical aspects in the safety evaluation. Since there is no guidance document for tissue adhesion for animal study of dura substitutes, intraperitoneal hernia repair guidance document from NMPA and its referred evaluation standard on tissue adhesion is applied in this study. The macroscopic examination results of the implants at different sampling times were shown as **Figure 6**, and the adhesion grading results were given in **Figure 7**. For blank control group, the results showed that the adhesion of brain tissues was so severe that they were very difficult to be separated from the skull and lot of brain tissue were attached after the separation, no matter the examination time was 30, 90, or 180 days post-operation. The tissue adhesion in groups with dura substitute implantation was significant improved according to the results at the first sampling time (30 days). In both experiment and control groups, slight adhesion was found and was easy to be separated. 180 days after the implantation, there was no adhesion was observed in both experiment and control groups.

The histological results of tissue samples were shown as **Figure 8**. According to the microscopic images of tissues sampled at 30 days, the implants in both experiment and control groups were closely integrated with the surrounding dura tissue. At the same time, attachment and migration of fibroblasts into the implants were clearly identified while no abnormality was observed in arachnoid and brain tissues. The implants were partially degraded, and entangled with the newly formed extracellular matrix as repaired tissue. In blank control group, an obvious dura defect and disorderly fibroblastic proliferation in lateral dura was observed. Meanwhile, the arachnoid structure was incomplete and the brain tissue was shown as necrosis.

After 90 days of implantation, a large number of fibroblasts were observed in both experiment and control groups. The implanted dura substitutes were mostly degraded in both groups. The newly formed tissue with characteristic dura structure had no clear boundary with surrounding brain tissue, while the contacting sides of skull and meningeal tissue showed fine condition and no abnormality was observed in both arachnoid and brain tissue. Thus it is possible to consider that the regenerated dura had mainly replaced the implanted dura substitute. Comparatively, the blank control group exhibited obvious dura defect and loss of arachnoid structure. Also, the brain tissue was partially liquefied or necrotic, while it had visible adhesion with newly formed tissue at the edge of defect, accompanying with noticeable scar tissue.

One hundred and Eighty days after the surgery, the implants were completely degraded and the regenerated dura fully substituted the implants in both experiment and control groups.

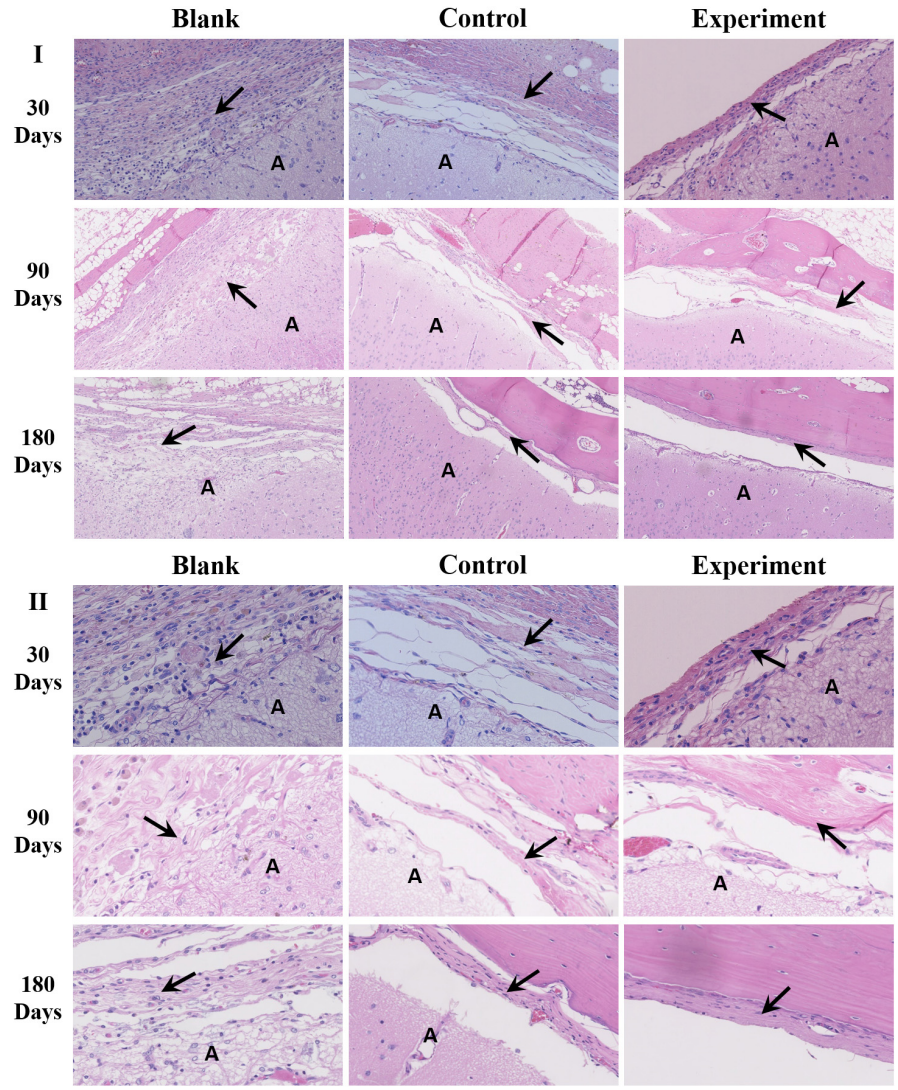

FIGURE 8 | The histological observation of the implants (A: brain tissue; the arrow → pointed to the repaired tissue; I: ×100, II: ×400).

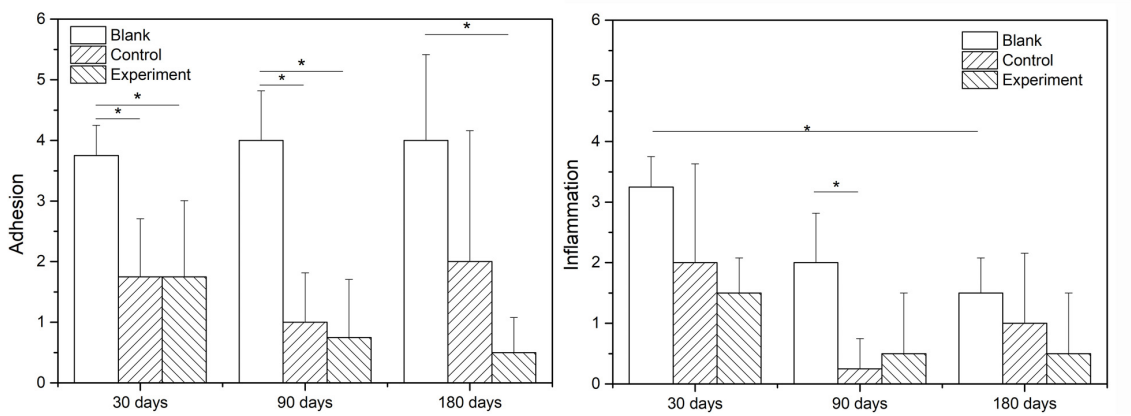

FIGURE 9 | The grade scoring of adhesion and inflammation on microscopic assessment (*$P < 0.05$).

The surrounding tissues were in good conditions as previous and the skull insufficiently covered the surgery zone was mostly regenerated as well. In blank control group, dura deficiency was obvious and tissues were in similar conditions with what were observed in the same group after 90 days of the implantation.

Figure 9 show the scoring results of histological evaluation of different groups at 30, 90, and 120 days after implantation. Thirty days after surgery, the tissue adhesion in blank control group was extensive and severe, which was significantly higher than those in experiment and control groups ($P < 0.05$). And this condition continued to 90 and 180 days after the surgery. The difference between experiment and control groups was insignificant at 30 and 90 days after the implantation, but the adhesion was insignificantly higher in control group than that in experiment group at 180 days after implantation ($P > 0.05$).

The inflammatory reactions in all groups were evaluated to be mild to moderate without obvious different at 30 days after the surgery. At 90 and 180 days after the implantation, the inflammatory cell infiltration in both experiment and control groups were reduced and significant lower than that in blank control group ($P < 0.05$), but the difference between experiment and control groups were insignificant ($P > 0.05$).

DISCUSSION

The composition analysis indicated the fibrous collagen prepared from bovine tendon was highly purified type I collagen (>99.5%) and the amino acid ratios met the main features of bovine collagen alpha-1(I) chain. Thus, the dura substitutes prepared by highly purified type I collagen in this study showed essential composition requirement for dura repair and potential regeneration as well. The dura substitutes possessed with excellent porous network structure which was critical to influence cell behaviors as an ideal biomimetic scaffold (Xu et al., 2017; Wang and Ao, 2019). The pores were inter-connected and the diameters ranged from a few to 150 μm, which was beneficial to the cell attachment, migration and proliferation. Also, the mass transfer, including delivery of nutrient and removal of metabolite in the dura substitute was unhindered, which was suitable for regeneration of extracellular matrix as well. Therefore, the highly purified chemical composition as well as biomimetic microstructure of the experiment dura substitute in this study is favorable niche for host fibroblasts to further regenerate damage or lost dura (Calikoglu et al., 2019).

All medical devices need to demonstrate their safety and efficacy *via* scientific evidence (Bi et al., 2020). For dura substitute devices expected to regenerate dura mater, the systematic design verification tests include, but not limited to, physical and chemical characterizations; biocompatibility evaluation per ISO 10993 standards which could include acute and chronic systemic toxicity, local tissue response, and genotoxicity tests; biological safety evaluation includes immunogenicity and infectious pathogen test of animal-derived devices. Animal studies are important to validate the *in vivo* safety as well as performance of the device per intended uses. For dura substitute devices, animal studies could provide data and evidence to prove their tissue repair and potential regeneration properties *in situ* of the damaged or lost dura mater.

In vivo safety and performance of collagen-based dura substitutes was investigated *via* animal studies. Multiple approaches were applied to conduct a comprehensive evaluation of the dura substitute for its ability to repair and regenerate dura mater. The gross observation, such as body weight and body temperature of the animal indicated the surgery and implant didn't cause abnormal body reaction or pyrogen reaction. The insignificant difference of leukocyte counts in both complete blood and CSF in all three groups implied the implants caused no systematical inflammatory in short (7 days) or long (180 days) term without any encapsulation or use of antibiotic (Xu et al., 2020). Furthermore, the immunogenicity of type I collagen has been related to the end of its triple helix structure, which is composed of non-helical telopeptides. Removing these non-helical components via specially designed processes has been shown to reduce the immunogenicity of type I collagen. As a result, the immunological responses showed no infection caused by the implants, which may owe to their highly purified fibrous type I collagen that has removed non-helical telopeptide in the molecule (Lynn et al., 2004). The macroscopic examination and histological observation suggested that the collagen-based dura substitute was tissue anti-adhesion and had suitable degradation rate which was appropriate for aggregation of newly secreted extracellular matrix in a gradual and order pattern to achieve desirable regeneration effect (Wang and Ao, 2019; Ramot et al., 2020). The highly purified type I collagen fibrils and porous microstructures were important to mimic the natural tissues for triggering the native mechanisms to regenerate new host tissue, while the desirable degradation rate to match the progress of newly formed extracellular matrix was critical for dura regeneration too.

CONCLUSION

The *in vivo* safety and performance of fibrous collagen dura substitutes composed of highly purified type I collagen and biomimetic porous microstructure were investigated using a rabbit model, which was feasible and reliable. Compared with the blank control, the collagen dura substitutes significantly improved the outcome of the dura repair. The collagen dura substitutes exhibited excellent *in vivo* performance in terms of anti-leaking of CSF, tissue anti-adhesion and degradability. Furthermore, the collagen dura substitutes also demonstrated dura regeneration ability during the course of animal study. In summary, the fibrous type I collagen dura substitutes in this animal study were safe and showed excellent performance for dura repair and regeneration.

DATA AVAILABILITY STATEMENT

The original contributions presented in the study are included in the article/**Supplementary Material**, further inquiries can be directed to the corresponding author/s.

ETHICS STATEMENT

The animal study was reviewed and approved by the Animal Care and Use Committee of Sichuan University (IACUC-2016-R-001).

AUTHOR CONTRIBUTIONS

HL: conceptualization and funding acquisition. WL, XW, ZZ, and HL: methodology. XW, ZZ, YZ, and HL: validation. WL, JS, QJ, JW, YX, and ZZ: investigation. WL and HL: writing–original draft preparation. YZ and HL: supervision. All authors contributed to the article and approved the submitted version.

FUNDING

This work was financially supported by the Key Science and Technology Program of Guangxi Province (Grant No. AA17204085-2), which was granted by the Department of Science and Technology of Guangxi Zhuang Autonomous Region, China.

SUPPLEMENTARY MATERIAL

The Supplementary Material for this article can be found online at: https://www.frontiersin.org/articles/10.3389/fbioe.2021.628129/full#supplementary-material

REFERENCES

Adeeb, N., Mortazavi, M. M., Tubbs, R. S., and Cohen-Gadol, A. A. (2012). The cranial dura mater: a review of its history, embryology, and anatomy. *Childs Nerv. Syst.* 28, 827–837. doi: 10.1007/s00381-012-1744-6

Azzam, D., Romiyo, P., Nguyen, T., Sheppard, J. P., Alkhalid, Y., Lagman, C., et al. (2018). Dural repair in cranial surgery is associated with moderate rates of complications with both autologous and nonautologous dural substitutes. *World Neurosurg.* 113, 244–248. doi: 10.1016/j.wneu.2018.01.115

Bartosz, D. K., and Vasterling, M. K. (1994). Dura mater substitutes in the surgical treatment of meningiomas. *J. Neurosci. Nurs.* 26, 140–145. doi: 10.1097/01376517-199406000-00006

Bi, X. W., Liu, B., Mao, Z. N., Wang, C. Y., Dunne, N., Fan, Y. B., et al. (2020). Applications of materials for dural reconstruction in pre-clinical and clinical studies: advantages and drawbacks, efficacy, and selections. *Mater. Sci. Eng. C Mater. Biol. Appl.* 117:111326. doi: 10.1016/j.msec.2020.111326

Calikoglu, C., Cakir, M., and Tuzun, Y. (2019). Histopathological investigation of the effectiveness of collagen matrix in the repair of experimental spinal dura mater defects. *Eurasian J. Med.* 51, 133–138. doi: 10.5152/eurasianjmed.2018.17422

Chuan, D., Wang, Y. L., Fan, R. R., Zhou, L. X., Chen, H. F., Xu, J. G., et al. (2020). Fabrication and properties of a biomimetic dura matter substitute based on stereocomplex poly (Lactic Acid) nanofibers. *Int. J. Nanomed.* 15, 3729–3740. doi: 10.2147/ijn.s248998

Costantino, P. D., Wolpoe, M. E., Govindaraj, S., Chaplin, J. M., Sen, C., Cohen, M., et al. (2000). Human dural replacement with acellular dermis: clinical results and a review of the literature. *Head Neck* 22, 765–771. doi: 10.1002/1097-0347(200012)22:8<765::aid-hed4<3.0.co;2-7

Dufrane, D., Cornu, O., Delloye, C., and Schneider, Y. J. (2002). Physical and chemical processing for a human dura mater substitute. *Biomaterials* 23, 2979–2988. doi: 10.1016/S0142-9612(02)00027-3

Esposito, F., Cappabianca, P., Fusco, M., Cavallo, L. M., Bani, G. G., Biroli, F., et al. (2008). Collagen-only biomatrix as a novel dural substitute. *Exam. Efficacy Saf. Outcome* 110, 343–351. doi: 10.1016/j.clineuro.2007.12.016

Esposito, F., Grimod, G., Cavallo, L. M., Lanterna, L., Biroli, F., and Cappabianca, P. (2013). Collagen-only biomatrix as dural substitute: what happened after a 5-year observational follow-up study. *Clin. Neurol. Neurosur.* 115, 1735–1737. doi: 10.1016/j.clineuro.2013.03.013

Go, K. O., Hwang, K., and Han, J. H. (2020). Surgical nuances to reduce and manage cerebrospinal fluid leaks after microvascular decompression. *J. Clin. Med.* 9:902. doi: 10.3390/jcm9040902

Hemstapat, R., Suvannapruk, W., Thammarakcharoen, F., Chumnanvej, S., and Suwanprateeb, J. (2020). Performance evaluation of bilayer oxidized regenerated cellulose/poly epsilon-caprolactone knitted fabric-reinforced composites for dural substitution. *Proc. Inst. Mech. Eng. Part H J. Eng. Med.* 234, 854–863. doi: 10.1177/0954411920926071

Jing, Y., Ma, X., Xu, C., Tian, H. L., and Chen, S. W. (2020). Repair of dural defects with electrospun bacterial cellulose membranes in a rabbit experimental model. *Mater. Sci. Eng. C Mater. Biol. Appl.* 117:111246. doi: 10.1016/j.msec.2020.111246

Li, Q., Zhang, F. H., Wang, H. M., and Pan, T. (2019). Preparation and characterization of a novel acellular swim bladder as dura mater substitute. *Neurol. Res.* 41, 242–249. doi: 10.1080/01616412.2018.1550139

Li, W. D., Tao, B. P., He, Q. Z., Ding, Y., Yuan, J., and Li, Q. (2013). Clinical application the freesuture, absorbable artificial dura mater "DuraMax" for repairing dura defects. *Ant. Clin.* 18, 227–229.

Lynn, A. K., Yannas, I. V., and Bonfield, W. (2004). Antigenicity and immunogenicity of collagen. *J. Biomed. Mater. Res. Part B Appl. Biomater.* 71B, 343–354. doi: 10.1002/jbm.b.30096

MacEwan, M. R., Kovacs, T., Osbun, J., and Ray, W. Z. (2018). Comparative analysis of a fully-synthetic nanofabricated dura substitute and bovine collagen dura substitute in a large animal model of dural repair. *Interdiscipl. Neurosurg. Adv. Tech. Case Manag.* 13, 145–150. doi: 10.1016/j.inat.2018.05.001

Maehara, N., Morioka, T., Shimogawa, T., Suzuki, S. O., Mizoguchi, M., and Haga, S. (2020). Massive ossification with hematopoietic marrow on both surfaces of the expanded polytetrafluoroethylene artificial dura mater. *World Neurosurg.* 139, 405–409. doi: 10.1016/j.wneu.2020.04.068

Matsumoto, Y., Aikawa, H., Tsutsumi, M., Narita, S., Yoshida, H., Etou, H., et al. (2013). Histological examination of expanded polytetrafluoroethylene artificial dura mater at 14 years after craniotomy: case report. *Neurol. Med. Chirurgica* 53, 43–46. doi: 10.2176/nmc.53.43

Morales-Avalos, R., Soto-Domínguez, A., García-Juárez, J., Saucedo-Cardenas, O., Bonilla-Galvan, J. R., Cardenas-Serna, M., et al. (2017). Characterization and morphological comparison of human dura mater, temporalis fascia, and pericranium for the correct selection of an autograft in duraplasty procedures. *Surg. Radiol. Anat. SRA* 39, 29–38. doi: 10.1007/s00276-016-1692-z

Nagata, K., Kawamoto, S., Sashida, J., Abe, T., Mukasa, A., and Imaizumi, Y. (1999). Mesh-and-glue technique to prevent leakage of cerebrospinal fluid after implantation of expanded polytetrafluoroethylene dura substitute–technical note. *Neurol. Medico-chirurgica* 39, 316–319. doi: 10.2176/nmc.39.316

Neulen, A., Gutenberg, A., Takacs, I., Weber, G., Wegmann, J., Schulz-Schaeffer, W., et al. (2011). Evaluation of efficacy and biocompatibility of a novel semisynthetic collagen matrix as a dural onlay graft in a large animal model. *Acta Neurochirurg.* 153, 2241–2250. doi: 10.1007/s00701-011-1059-5

Nie, H., and Zhang, K. (2018). *USA Patent No. 10034961*. Alexandria, VA: U. S. P. A. T. Office.

Nie, H., and Zhang, K. (2020). *USA Patent No. 10736994*. Alexandria, VA: U. S. P. A. T. Office.

NMPA (2019). *Guidance of Technical Review for Animal Experiment of Intraperitoneal Hernia Mesh. (NMPA No. 18). (in Chinese)*. Beijing: NMPA.

NMPA (2020). *Guidance of Technical Review for Product Registration of Dura Substitute (NMPA No. 48). (in Chinese)*. Beijing: NMPA.

Parízek, J., Mericka, P., Husek, Z., Suba, P., Spacek, J., Nemecek, S., et al. (1997). Detailed evaluation of 2959 allogeneic and xenogeneic dense connective tissue grafts (fascia lata, pericardium, and dura mater) used in the course of 20 years for duraplasty in neurosurgery. *Acta Neurochirurg.* 139, 827–838. doi: 10.1007/bf01411400

Pogorielov, M., Kravtsova, A., Reilly, G. C., Deineka, V., Tetteh, G., Kalinkevich, O., et al. (2017). Experimental evaluation of new chitin-chitosan graft for duraplasty. *J. Mater. Sci. Mater. Med.* 28:34. doi: 10.1007/s10856-017-5845-3

Ramot, Y., Harnof, S., Klein, I., Amouyal, N., Steiner, M., Manassa, N. N., et al. (2020). Local tolerance and biodegradability of a novel biodegradable artificial dura mater graft following implantation onto a dural defect in rabbits. *Toxicol. Pathol.* 48, 738–746. doi: 10.1177/0192623320947075

Sabatino, G., Della Pepa, G. M., Bianchi, F., Capone, G., Rigante, L., Albanese, A., et al. (2014). Autologous dural substitutes: a prospective study. *Clin. Neurol. Neurosurg.* 116, 20–23. doi: 10.1016/j.clineuro.2013.11.010

Sandoval-Sanchez, J. H., Ramos-Zuniga, R., de Anda, S. L., Lopez-Dellamary, F., Gonzalez-Castaneda, R., Ramirez-Jaimes, J. D., et al. (2012). A New Bilayer chitosan scaffolding as a dural substitute: experimental evaluation. *World Neurosurg.* 77, 577–582. doi: 10.1016/J.Wneu.2011.07.007

Schmalz, P., Griessenauer, C., Ogilvy, C. S., and Thomas, A. J. (2018). Use of an absorbable synthetic polymer dural substitute for repair of dural defects: a technical note. *Cureus* 10:e2127. doi: 10.7759/cureus.2127

Shackelford, C., Long, G., Wolf, J., Okerberg, C., and Herbert, R. (2002). Qualitative and quantitative analysis of nonneoplastic lesions in toxicology studies. *Toxicol. Pathol.* 30, 93–96. doi: 10.1080/01926230252824761

Ström, J. O., Boström, S., Bobinski, L., and Theodorsson, A. (2011). Low-grade infection complicating silastic dural substitute 32 years post-operatively. *Brain Injury* 25, 250–254. doi: 10.3109/02699052.2010.542431

Sun, H. T., Wang, H. D., Diao, Y. F., Tu, Y., Li, X. H., Zhao, W. Y., et al. (2018). Large retrospective study of artificial dura substitute in patients with traumatic brain injury undergo decompressive craniectomy. *Brain Behav.* 8:e00907. doi: 10.1002/brb3.907

Tachibana, E., Saito, K., Fukuta, K., and Yoshida, J. (2002). Evaluation of the healing process after dural reconstruction achieved using a free fascial graft. *J. Neurosurg.* 96, 280–286. doi: 10.3171/jns.2002.96.2.0280

Turchan, A., Rochman, T. F., Ibrahim, A., Fauziah, D., Wahyuhadi, J., Parenrengi, M. A., et al. (2018). Duraplasty using amniotic membrane versus temporal muscle fascia: a clinical comparative study. *J. Clin. Neurosci.* 50, 272–276. doi: 10.1016/j.jocn.2018.01.069

U. S. Food and Drug Administration (2000). *Guidance Document for Dura Substitute Devices - Guidance for Industry*. Silver Spring, MD: U. S. Food and Drug Administration.

UniProt (2020). *UniProt P02453 (CO1A1_BOVIN). UniProtKB.* Available online at: https://www.uniprot.org/uniprot/P02453 (accessed December 2, 2020).

Vecera, Z., Krejci, O., Houdek, M., Lipina, R., and Kanta, M. (2018). Dural reconstruction with usage of xenogenic biomaterial. *Ceska Slovenska Neurol. Neurochirurg.* 81, 686–690. doi: 10.14735/amcsnn2018686

Wang, W. Z., and Ao, Q. (2019). Research and application progress on dural substitutes. *J. Neurorestoratol.* 7, 161–170. doi: 10.26599/jnr.2019.9040020

Wong, S. T., Ho, W. N., He, Z. X., and Yam, K. Y. (2018). Epidural multi-slitted microporous non-absorbable patch in decompressive craniectomy to facilitate cranioplasty: a preliminary study. *Br. J. Neurosurg.* 32, 400–406. doi: 10.1080/02688697.2018.1480749

Xia, L., Chen, Y., Men, F., Zhang, Y., Chen, W., Zheng, X., et al. (2017). Comparative study on physical properties of different tissue-derived collagen biomaterials. *Mater. Sci.* 7, 431–439.

Xu, C., Zhao, J. W., Gong, Q. Y., and Chen, S. W. (2020). Sustained release of vancomycin from bacterial cellulose membrane as dural substitutes for anti-inflammatory wound closure in rabbits. *J. Biomater. Appl.* 34, 1470–1478. doi: 10.1177/0885328220908027

Xu, Y., Cui, W. G., Zhang, Y. X., Zhou, P. H., Gu, Y., Shen, X. F., et al. (2017). Hierarchical micro/nanofibrous bioscaffolds for structural tissue regeneration. *Adv. Healthcare Mater.* 6:1601457. doi: 10.1002/adhm.201601457

Yamada, K., Miyamoto, S., Takayama, M., Nagata, I., Hashimoto, N., Ikada, Y., et al. (2002). Clinical application of a new bioabsorbable artificial dura mater. *J. Neurosurg.* 96, 731–735. doi: 10.3171/jns.2002.96.4.0731

Zerris, V. A., James, K. S., Roberts, J. B., Bell, E., and Heilman, C. B. (2007). Repair of the dura mater with processed collagen devices. *J. Biomed. Mater. Res. Part B Appl. Biomater.* 83B, 580–588. doi: 10.1002/jbm.b.30831

Zwirner, J., Scholze, M., Waddell, J. N., Ondruschka, B., and Hammer, N. (2019). Mechanical properties of human dura mater in tension - an analysis at an age range of 2 to 94 years. *Sci. Rep.* 9:16655. doi: 10.1038/s41598-019-52836-9

Conflict of Interest: The authors declare that the research was conducted in the absence of any commercial or financial relationships that could be construed as a potential conflict of interest.

frontiers in Bioengineering and Biotechnology

REVIEW
published: 25 February 2021
doi: 10.3389/fbioe.2021.643110

Tropoelastin and Elastin Assembly

Jazmin Ozsvar[1,2], Chengeng Yang[3†], Stuart A. Cain[4†], Clair Baldock[4], Anna Tarakanova[3,5] and Anthony S. Weiss[1,2,6]*

[1] Charles Perkins Centre, The University of Sydney, Sydney, NSW, Australia, [2] School of Life and Environmental Sciences, The University of Sydney, Sydney, NSW, Australia, [3] Department of Biomedical Engineering, University of Connecticut, Storrs, CT, United States, [4] Wellcome Trust Centre for Cell-Matrix Research, Division of Cell-Matrix Biology and Regenerative Medicine, Faculty of Biology, Medicine and Health, School of Biological Sciences, Manchester Academic Health Science Centre, University of Manchester, Manchester, United Kingdom, [5] Department of Mechanical Engineering, University of Connecticut, Storrs, CT, United States, [6] Sydney Nano Institute, The University of Sydney, Sydney, NSW, Australia

Elastic fibers are an important component of the extracellular matrix, providing stretch, resilience, and cell interactivity to a broad range of elastic tissues. Elastin makes up the majority of elastic fibers and is formed by the hierarchical assembly of its monomer, tropoelastin. Our understanding of key aspects of the assembly process have been unclear due to the intrinsic properties of elastin and tropoelastin that render them difficult to study. This review focuses on recent developments that have shaped our current knowledge of elastin assembly through understanding the relationship between tropoelastin's structure and function.

Keywords: elastin, elastic fibers, tropoelastin, computational modeling, assembly

OPEN ACCESS

Edited by:
Maria Grazia Raucci, National Research Council (CNR), Italy

Reviewed by:
Jessica E. Wagenseil, Washington University in St. Louis, United States
Alfredo Ronca, National Research Council (CNR), Italy

***Correspondence:**
Anthony S. Weiss
tony.weiss@sydney.edu.au

† These authors have contributed equally to this work

Specialty section:
This article was submitted to Nanobiotechnology, a section of the journal Frontiers in Bioengineering and Biotechnology

Received: *17 December 2020*
Accepted: *08 February 2021*
Published: *25 February 2021*

Citation:
Ozsvar J, Yang C, Cain SA, Baldock C, Tarakanova A and Weiss AS (2021) Tropoelastin and Elastin Assembly. Front. Bioeng. Biotechnol. 9:643110. doi: 10.3389/fbioe.2021.643110

ELASTIC FIBERS AND ELASTIN

Elastic fibers are present in the extracellular matrix (ECM) of vertebrate tissues, such as the skin, lungs, cardiovascular system, cartilage, and tendons. They are ubiquitous across most vertebrates other than lower vertebrates such as species from the superclass *Agnatha* (jawless fish) (Debelle and Tamburro, 1999). Elastic fibers provide tissues with mechanical resilience, durability, and cell interactivity, which support a diverse range of specialized functionality.

Elastic fibers are composed of approximately 90% elastin, whilst the remaining components are primarily comprised of fibrillin glycoproteins (Mecham, 1991). Thus, elastin is responsible, in great part, for the properties of elastic fibers. The most crucial of these properties is the ability to undergo many stretch-recoil cycles whilst maintaining the structural and functional integrity of elastic tissues over an organism's lifetime. The ability to stretch and recoil arises from the biochemical properties of elastin's monomer, tropoelastin (discussed below). Additionally, elastin is remarkably durable as it is primarily deposited during prenatal development and childhood, and is rarely synthesized during adulthood. Its estimated half-life of 70 years (Shapiro et al., 1991) is due to its extensive cross-linking and high hydrophobicity, which render it resistant to degradation (Vrhovski and Weiss, 1998; Schrader et al., 2018; Hedtke et al., 2019).

TROPOELASTIN

Elastin's subunit, tropoelastin, is a soluble 60–70 kDa protein which has been intensely studied over the past three decades. Tropoelastin is a spring-like molecule that is extremely extensible prior to

cross-linking. A single tropoelastin molecule can stretch up to eight times its resting length and has a Young's modulus (tensile stiffness) of ∼ 3 kPa (Baldock et al., 2011) in comparison to elastin's extensibility of 150% and stiffness of ∼1 mPa (Aaron and Gosline, 1981). Tropoelastin undergoes minimal energy loss during extension, similar to other polymers such as rubber and resilin (Elvin et al., 2005; Cordier et al., 2008; Baldock et al., 2011). These remarkable properties arise from its sequence and structure, which render tropoelastin structurally highly flexible but not disordered (Tarakanova et al., 2018). In addition to its involvement in molecular elasticity, the flexibility of tropoelastin also a key requirement for self-assembly into elastin, with mutations that perturb this having detrimental effects on tissue (Yeo et al., 2016, 2017). Together, these two properties can be tuned and exploited to give rise to an increasing number of novel biomaterials for tissue engineering and regenerative medicine, which have been recently reviewed elsewhere (Wang et al., 2020; Wen et al., 2020).

TROPOELASTIN GENE AND EXPRESSION

Tropoelastin is encoded by the ELN gene, which is present in all vertebrates except jawless fish (Chung et al., 2006). Most organisms contain one copy of ELN, other than teleosts and amphibians which notably possess two distinct types of ELN genes (He et al., 2007; Miao et al., 2007, 2009). The human ELN gene is located on the long arm of chromosome 7q11.2 and comprises of 34 exons nestled between lengthy introns (Indik et al., 1987, 1989; Bashir et al., 1989). Human ELN gives rise to a broad variety of splice isoforms, with alternative splicing being observed with exons 22, 23, 24, 26A, 32, and 33 (Fazio et al., 1988; Parks et al., 1992) that result in 13 known human isoforms of the mature tropoelastin protein (Reichheld et al., 2019). The most commonly investigated isoform contains domain 26A and lacks domain 22, and is predominantly found in elastic tissues (Indik et al., 1987; Vrhovski et al., 1997).

Variations in the relative abundance of alternatively spliced ELN mRNA transcripts have been observed between tissues, and this diversity is thought to be necessary for the fine tuning of the mechanical characteristics of tissues to suit their unique functional requirements (Reichheld et al., 2019). Indeed, studies examining the consequences of domain insertions and deletions note changes in the intrinsic functionality of tropoelastin, corroborating the hypothesis that domain insertions and deletions result in altered tissue mechanics (Jensen et al., 2000; Kozel et al., 2003; Yeo et al., 2016; Miao et al., 2017). The isoform-function theory is further reinforced by the presence of two different ELN genes within teleosts that are differentially expressed both spatially and temporally during development (Miao et al., 2007). The self-assembly properties and nanostructure of these extra teleost isoforms are yet to be investigated.

SEQUENCE

Tropoelastin's domains each arise from single exons of the ELN gene. They can be categorized as either "hydrophobic" or "cross-linking" based on their functionality and amino acid content (**Figure 1**). Tropoelastin's primary sequence is low in complexity and contains repetitive motifs. Furthermore, tropoelastin's hydrophobic and cross-linking domains are arranged in alternating patterns throughout the majority of the molecule, giving rise to both inter- and intra-domain level repetition.

Tropoelastin's amino acid sequence predominantly consists of non-polar residues including glycine, valine, alanine, and proline (Debelle and Tamburro, 1999). The hydrophobic domains contain repetitions and variations of Val-Pro-Gly-Val-Gly motifs (**Figure 1**), resulting in the aforementioned low complexity of sequence (Foster et al., 1973; Gray et al., 1973). The hydrophobic domains vary in length, with the majority of the shorter (9–5 residues) domains occurring near the N-terminus, while the longer (up to 55 residues) domains are found within tropoelastin's central and C-terminal regions (Indik et al., 1989). The hydrophobic domains have been extensively studied and are responsible for facilitating tropoelastin's ability to self-assemble (Vrhovski et al., 1997; Toonkool et al., 2001).

The cross-linking domains are defined by lysines, which are responsible for the formation of durable bi-, tri-, and tetrafunctional cross-links within mature elastin. Cross-linking domains can be subdivided into KP or KA domains, which denote the amino acids (proline or alanine, respectively) that are adjacent to the lysines (**Figure 1**). KP domains are found closer toward the N-terminus, whereas KA domains are closer to the C-terminus and include alanine tracts (Indik et al., 1987). Unlike hydrophobic domains, cross-linking domains in isolation are unable to self-assemble; thus, they have been studied in the context of the cross-linking of elastin-derived biomaterials (Annabi et al., 2017; Yue et al., 2017). Cross-linking domains are capable of modulating self-assembly when incorporated into peptides and biomaterials derived from tropoelastin's hydrophobic domains. For example, their inclusion in peptides derived from hydrophobic domains confers decreased times taken for self-assembly, most likely due to their favorable interaction with aqueous solvent (Miao et al., 2003). Modulative effects are also observed within full length tropoelastin, where disruptions to domain 26 diminish self-assembly (Jensen et al., 2000), highlighting the context of primary sequence on higher order structures.

Another region of note is domain 36, which contains lysines but does not participate in cross-linking (Hedtke et al., 2019). The amino acid sequence of domain 36 is unique; furthermore, its sequence confers a positively charged C-terminus comprising lysines between positively charged arginines, forming a RKRK sequence (Vrhovski et al., 1997). In addition to the RKRK sequence, domain 36 contains tropoelastin's sole two cysteines and only disulfide bond. Perturbation of either of these components greatly reduces tropoelastin's ability to self-assemble *in vitro* and interact with the microfibril scaffold of elastic fibers (Nonaka et al., 2014), indicating that an intact domain 36 is required for correct assembly.

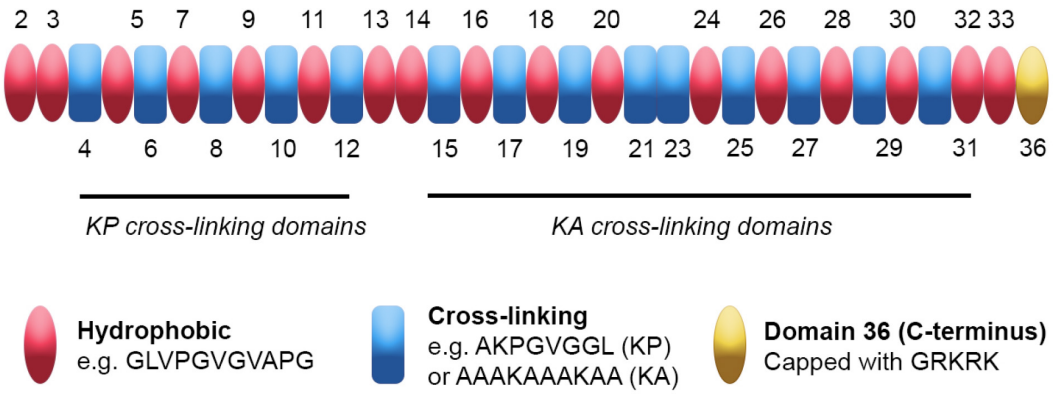

FIGURE 1 | Tropoelastin's sequence and domain arrangement. Tropoelastin is a low complexity protein on both primary and secondary sequence levels. Its hydrophobic (pink) and cross-linking (blue) domains consist of repetitive motifs that contribute uniquely to elastin assembly. The hydrophobic domains contain aliphatic amino acids with proline variations that provide flexibility and the ability to assemble into higher order structures. The cross-linking domains are enriched for either Lys-Pro (KP) or Lys-Ala (KA) motifs and form cross-links that link growing tropoelastin chains during elastogenesis; note that exon 6 encodes a KA domain. Tropoelastin's C-terminal domain 36 (yellow) does not fall into either category as it contains a distinct sequence capped with a Gly-Arg-Lys-Arg-Lys (GRKRK) motif and is primarily involved in cell interactions.

STRUCTURE

The understanding of tropoelastin's structure has been hindered by numerous intrinsic properties of the molecule. Of most importance, the inability to acquire large quantities of pure tropoelastin historically presented a significant obstacle to experimentally characterizing its structure. Elastin is extensively cross-linked and difficult to break apart into monomers even under harsh conditions, thus, initial strategies included feeding animals a copper deficient diet to prevent lysyl oxidase (LOX) cross-linking of tropoelastin; however, this proved inefficient and time consuming (Wise and Weiss, 2009; Tarakanova et al., 2018).

Even after being able to produce recombinant tropoelastin at scales suited to characterization studies, traditional techniques have not yet produced an experimentally verified atomistic structure (Martin et al., 1995; Tarakanova and Buehler, 2013). Tropoelastin's flexibility does not allow it to pack into a crystal lattice and its size renders it too complex to assign atomic interactions using nuclear magnetic resonance (NMR) on a global level (Tamburro et al., 2003, 2006; Bochicchio et al., 2004; Pepe et al., 2008). Cryo-electron microscopy is a rapidly developing method and likely to contribute to structural knowledge of tropoelastin. Indeed, cryo-EM was recently reported to have a lower molecular size limit of approximately 50 kDa, however, it has not yet been successfully applied to characterize tropoelastin (Murata and Wolf, 2018).

Due to the lack of a full-atomistic structure, a number of elastin derivatives, including isolated tropoelastin domains (Toonkool et al., 2001; Mackay et al., 2005; Dyksterhuis et al., 2007; Dyksterhuis and Weiss, 2010) and synthetic elastin-derived peptides (EDPs) (Luan et al., 1990; Tamburro et al., 1992; Kentsis and Sosnick, 1998; Kumashiro et al., 2006; Reichheld et al., 2014, 2017; Muiznieks et al., 2015; MacEwan et al., 2017; Tarakanova et al., 2017) have been studied to understand tropoelastin's domain level properties. Attempts to characterize tropoelastin's structure have seen a gradual shift from the belief that tropoelastin's domains have fixed structures, to understanding that the majority of its domains are capable of transitioning between random coils and transient ordered structures. These ordered structures can include α-helices and β-structures (Vrhovski et al., 1997), which depend on the amino acid content and arrangement of domains (He et al., 2012; Reichheld et al., 2014, 2017; Muiznieks et al., 2015) and the choice of solvent (Reiersen and Rees, 2000; Muiznieks et al., 2015).

Tropoelastin's hydrophobic domains are predominantly responsible for the random coil content of the monomer, and are the result of the unique pairing of proline and glycine pairs that are interspersed throughout the majority of hydrophobic domains (Rauscher and Pomes, 2017). The smallest amino acid, glycine is known to promote flexibility within local structures due to lack of steric hindrance, whereas proline's restrictive sidechain inhibits conformational sampling and disrupts the formation of prolonged secondary structures (Roberts et al., 2015). Combinations of these two amino acids result in domains that undergo rapid conformational sampling (Rauscher and Pomes, 2017), which, if perturbed toward a conformation that gravitate toward stability, will assemble into highly ordered amyloid-like fibrils that are not elastomeric (Rauscher et al., 2006; Roberts et al., 2015).

More surprisingly, tropoelastin's cross-linking domains are also capable of similar transitions between ordered and disordered structures. KA domains were initially thought to form α-helices and poly-proline II helices (PPII) due to the presence of cross-links which require a lysine arrangement that was postulated to be achieved via α-helical configuration (Brown-Augsburger et al., 1995). Although alanine tracts within other proteins are predisposed to α-helix formation (Yang and Honig, 1995; Avbelj, 2000), high helical content within tropoelastin's KA domains was primarily demonstrated to persist in solvents that stabilize secondary structure, such as trifluoroethanol, rather

than aqueous solution (Luo and Baldwin, 1997; Tamburro et al., 2006). More recently, it has been demonstrated that KA domains consist of random coil content prior to self-assembly and become more ordered as molecules aggregate, marrying the observations discussed above into a cohesive model within the context of assembly and the requirements of higher-order structures (Reichheld et al., 2014).

The first successful experiments to define the 3D envelope of tropoelastin utilized small angle X-ray scattering (SAXS) and small-angle neutron scattering (SANS) (Baldock et al., 2011). Tropoelastin was revealed to be an asymmetric molecule with distinct N- and C-terminal regions that are respectively referred to as the "head" and "foot" of the molecule. The N-terminal head caps an extended coil region that consists of domains 2–18. Below the coil is a flexible "hinge" region made up of domains 20–24, which are directly adjacent to the "bridge" regions of domains 25–26. Domains 27–36 make up tropoelastin's foot, which are labeled as such due to their spatial arrangement, forming an almost claw-like component of the molecule. However, higher resolution data were required to map out its elusive properties and performance within a hierarchical assembly (Tarakanova et al., 2018; Ozsvar et al., 2019).

COMPUTATIONAL MODELS OF TROPOELASTIN

Computational approaches have gained popularity in recent decades as their methodologies have been refined to provide accurate atomistic scale insights into molecular structure and movement (Tarakanova et al., 2018). Thus, computational approaches can be considered as important means to complement wet bench experiments. By leveraging the advantages of computational models, such as elastic network models, full-atomistic models and coarse grained models, as depicted in **Figure 2**, the correlation between the structure, motions, and the functionality of tropoelastin have recently been explored in depth (Yeo et al., 2016; Tarakanova et al., 2018, 2019a).

The full-atomistic model of tropoelastin was developed based on replica exchange molecular dynamics (REMD) simulations, an accelerated sampling method for molecular dynamics (Tarakanova et al., 2018). This model revealed that tropoelastin maintains a canonical or "average" structure based on the distribution of its possible conformations in spite of its flexible nature (**Figure 2**), as well as the possible roles that local structures play in biological processes, specifically, elastogenesis (Tarakanova et al., 2019b). This canonical computational structure was determined to be highly similar to the envelope found via SAXS/SANS, where both consist of an extended molecular body accompanied by a protruding foot (Baldock et al., 2011). The computational model uncovered the contributions of each molecular region to the flexibility of the molecule. For example, the highly flexible domains 2–5 that were noted to generate a twisting motion in N-terminus, were positioned beside domain 6, a relatively immobile region that may assist in stabilizing the subsequent regions. The flexibility of the mid-region of the molecule was proposed to drive the overall elasticity of the resultant fibers. Closer to the base of the molecule, the flexible hinge region between domains 21 and 23 presented with a scissors-like bending, which is now believed to contribute to elasticity and multimeric assembly through enhanced conformational space sampling (Tarakanova et al., 2019b). Further down the molecule, the cell-interactive C-terminus was noted to be highly flexible, indicating that high conformational sampling could be conducive to tropoelastin's interactions between cell-surface receptors and elastic fiber-associated proteins. Thus, the current computational model unifies the global and regional characteristics of tropoelastin, inferring mechanisms that complement observed experimental phenomena.

Computational models have also been leveraged to pinpoint the molecular consequences of synthetic and disease mutations of tropoelastin. For example, models involving single point mutations at negatively charged residues demonstrated both regional and global destabilization of tropoelastin's structure, which were validated by SAXS structures (Yeo et al., 2012; Tarakanova et al., 2018). The reduction in solvent accessible surface area of the mutant molecules suggests that the underlying mechanism for their altered self-assembly properties observed in experiments is due to less exposure of the appropriate hydrophobic domains required for coacervation. Similarly, a mutation model associated with cutis laxa, or "loose skin disease" (Hu et al., 2006), was found to exhibit higher stability compared with the wild-type molecule due to the increased longevity of its salt bridges (Hu et al., 2006; Tarakanova et al., 2018). The resultant bending motion – rather than scissors-twist motion – that stemmed from this stabilization highlights the mutant's diminished flexibility as a key driver of impaired fiber assembly in cutis laxa (Tarakanova et al., 2018). By probing mutations in computational studies that resolve the atomistic structure of the molecule, the deduction of mechanisms associated with changes to functional roles of specific domains has become feasible, and a connection between local structures and biological performance can be established (**Figure 2**; Tarakanova et al., 2018).

Stiffness within the context of self-assembly has also been examined with both coarse grained and full-atomistic simulations using polypeptides derived from tropoelastin's hydrophobic domains. The stiffness that arose due to amino acid substitutions partially determined resultant secondary structure which, in turn, impacted assembly (Prhashanna et al., 2019). Such models could be used in conjunction with the full molecular model of tropoelastin to examine the self-assembly of discrete regions to understand the impacts of amino acid substitutions in disease. Unsubstituted models are also critical to understanding self-assembly. Modeling utilizing tropoelastin derivatives has demonstrated that structural compaction into both coils and globules occurs above the transition temperature of self-assembly, which may assist in explaining the anisotropic nature of mature elastin (Baul et al., 2020).

The importance of tropoelastin's flexibility during self-assembly has also been examined in the light of natural allysine modifications, which condense to give cross-links within mature

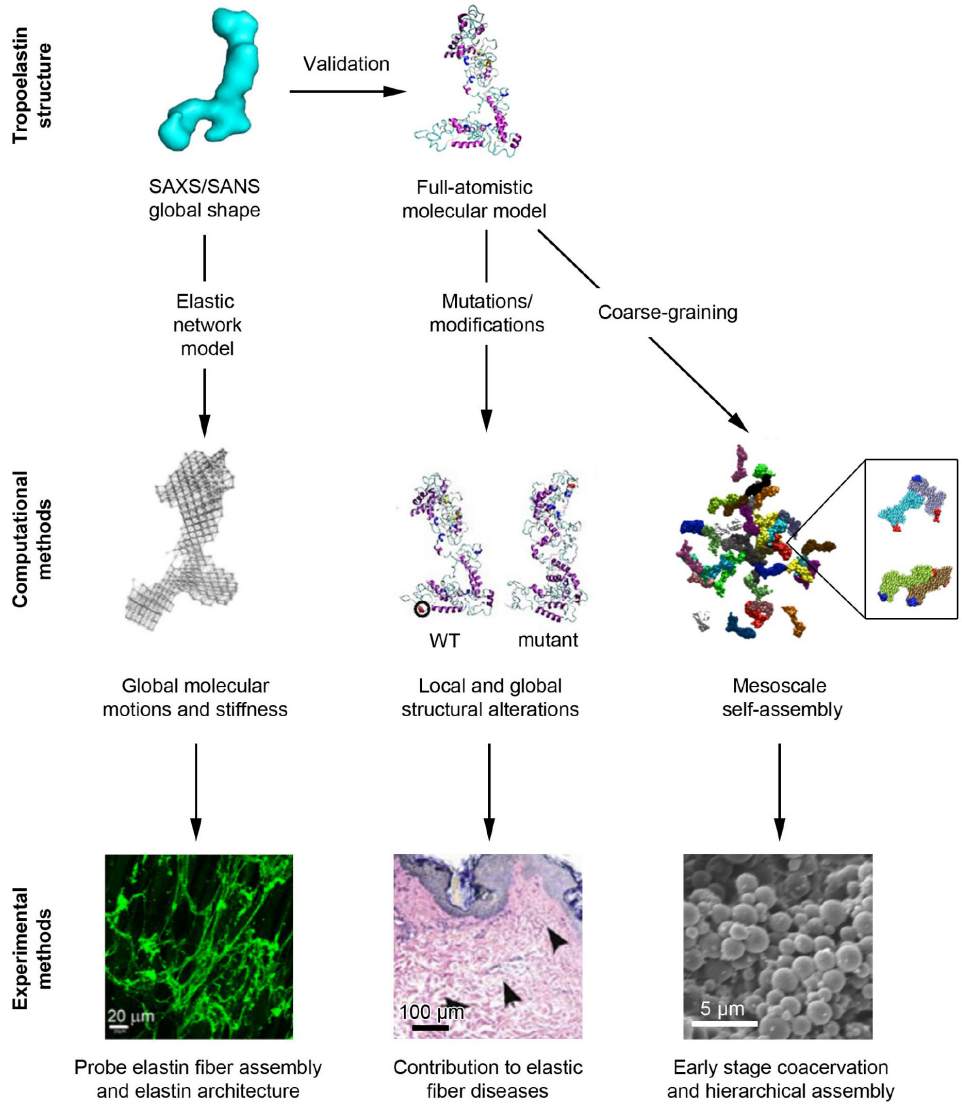

FIGURE 2 | Overview of the computational and experimental methodologies that have recently contributed to our understanding of elastic fiber assembly. The SAXS/SANS global shape of tropoelastin (Baldock et al., 2011) has been used to validate the full-atomistic computational model of tropoelastin through a geometric and topological comparison (Tarakanova et al., 2018). Furthermore, the SAXS/SANS structure has been mapped to an elastic network model with tunable stiffness to probe the role of tropoelastin's flexibility in fiber assembly (Yeo et al., 2016). Meanwhile, modifications to the full-atomistic model have revealed the mechanisms that contribute to aberrant fiber structure (Tarakanova et al., 2018) that have been hypothesized to predispose patients to diseases such as acquired cutis laxa (Hu et al., 2006). Additionally, coarse-graining the full-atomistic model has allowed for the examination of mesoscale tropoelastin assembly and, in particular, deciphered the orientation of tropoelastin molecules that occurs during early stage assembly (inset image) (Tarakanova et al., 2019a). Future investigations will allow the bridging of the gap between mesoscale simulations and microscopically observed coacervation (Clarke et al., 2006).

elastin (discussed further in the following section) (Ozsvar et al., 2019). The conversion of a single lysine to an allysine results in structural stabilization, which may serve as a checkpoint during self-assembly to ensure that molecules incapable of forming multiple cross-links are not incorporated into the growing chain. This deduction has been corroborated by the observation that tropoelastin with multiple allysine modifications displays conformational sampling comparable to that of the wild-type molecule, suggesting it is more likely to readily participate in self-assembly.

ELASTOGENESIS

Elastogenesis is the term that collectively describes the hierarchical process of elastic fiber formation, and is comprised of distinct phases: tropoelastin synthesis, coacervation, cross-linking, and deposition.

Elastogenic cells, such as fibroblasts (Mecham et al., 1985) and smooth muscle cells (Narayanan et al., 1976), synthesize and secrete tropoelastin. The majority of tropoelastin synthesis occurs during perinatal development (Myers et al.,

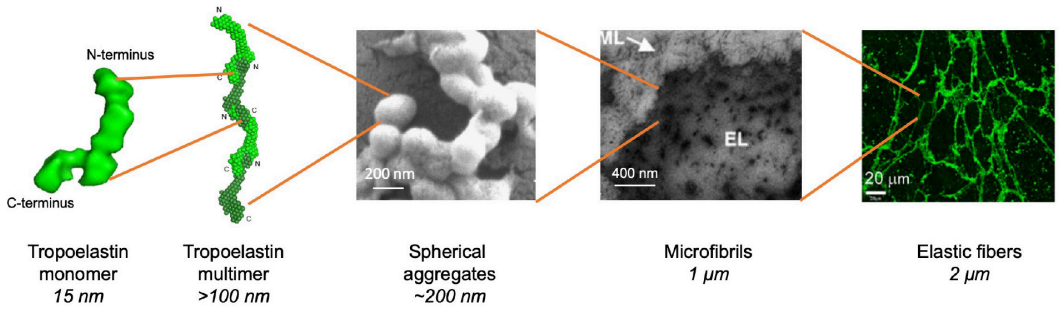

FIGURE 3 | Stages of hierarchical assembly of elastic fibers. Tropoelastin monomers undergo self-assembly upon reaching the transition temperature through the aggregation of their hydrophobic domains (Wise et al., 2014). Assembly proceeds from a nucleation event and undergoes elongation in a step-wise manner to form a multimer which can occur in a head-to-tail fashion (Wise et al., 2014). Multimers may undergo further transitions, such as branching, to form spherules made of multimer aggregates (Tu et al., 2010). The spherules grow in size and are deposited onto the microfibril scaffold where they fuse into fibrillar structures (Sherratt et al., 2001). Elastic fibers are eventually formed after extensive cross-linking through a process termed maturation (Yeo et al., 2016).

1983; Noguchi et al., 1990), however, synthesis may be triggered in response to tissue damage (Parks et al., 1992) or during diseases such as atherosclerosis (Phinikaridou et al., 2018). Tropoelastin is secreted as a ∼60–70 kDa protein to the cell surface where it participates in self-assembly (Hinek and Rabinovitch, 1994; **Figure 3**).

Coacervation is an endothermic, entropically favorable process through which tropoelastin monomers self-assemble into higher order n-mer structures. Coacervation optimally occurs at physiological temperature, however, *in vitro* coacervation can also occur at lower temperatures depending on experimental conditions and the choice of tropoelastin isoform or derivative (Yeo et al., 2011). This temperature is also known as the transition temperature. Initially, *in vitro* coacervation is characterized by the rapid aggregation of tropoelastin. into 200 nm then 1–2 μm spherules, which eventually grow and stabilize into spherules 2–6 μm in diameter (Clarke et al., 2006; Kozel et al., 2006; Tu and Weiss, 2010; Tu et al., 2010). Tropoelastin spherules assemble at the cell surface before deposition onto the microfibrillar scaffold in cell culture systems at physiological temperature (Kozel et al., 2006). The process of tropoelastin aggregation is initially reversible, as spherules dissipate if the temperature is lowered (Clarke et al., 2006), however, maintenance of a physiological temperature results in maturation, which is indicated by spherule coalescence and the irreversible formation of fibrillar structures (Cox et al., 1974; Bressan et al., 1983; Mithieux et al., 2005). The presence of tropoelastin spherules fusing to fibrils has been noted in native tissue, demonstrating marked similarities between *in vitro* and *in vivo* coacervation (Haust et al., 1965; Albert, 1972; Kozel et al., 2006).

Tropoelastin's hydrophobic domains are primarily responsible for facilitating coacervation (Tamburro et al., 1992; Miao et al., 2003; Muiznieks et al., 2003). Non-polar residues are a major contributor to protein folding, as their unfavorable interactions with water drive them to bury into the protein core, however, as tropoelastin is comprised of numerous hydrophobic domains, it has been demonstrated that many of these domains will be at least partially solvent exposed (Dyksterhuis et al., 2007). Thus, at lower temperatures, the water surrounding these domains forms ordered, clathrate-like shells that prevent aggregation until the appropriate temperature is reached (Wu and Weiss, 1999; Miao et al., 2003; Dandurand et al., 2015). In contrast, higher temperatures allow the breaking of the hydrogen bonds of the ordered water, dissipating the clathrate shells and permitting the association of the hydrophobic domains (Yeo et al., 2011). The prevention of early self-aggregation *in vitro* is thought to be mediated by chaperone proteins (Hinek and Rabinovitch, 1994; Miao et al., 2013). Further to this, the flexibility of the hydrophobic domains may also play a key role in self-assembly. Molecular dynamics modeling of aggregating tropoelastin-derived peptide chains points to the maintenance of a hydrated, disordered, liquid-like state due to the formation of short-lived inter-chain bonds (Rauscher and Pomes, 2017; Reichheld et al., 2020), mostly likely due to the inducement of random coils by PG repeats (*vide supra*). This phenomenon is supported by *in vitro* peptide studies, which note that increasing the space between PG motifs or removing prolines results in more ordered structures (Rauscher et al., 2006).

Similar to other ECM proteins, such as collagen, tropoelastin covalently cross-links via its lysines. Approximately 90% of tropoelastin's lysines undergo modification and/or participate in cross-links, indicating that mature elastin is extensively cross-linked (Kozel et al., 2003; Schmelzer et al., 2019). Cross-linking requires the modification of at least one of the lysine participants by a member of the copper-containing LOX or lysine oxidase-like (LOXL) enzyme families. LOX and LOXL convert the ε-amino group of lysine to α-aminoadipic acid δ-semialdehyde (allysine) (Schmelzer et al., 2019), which spontaneously undergo either a Schiff base reaction with a lysine, or two allysines crosslink through aldol condensation, to give rise to bifunctional crosslinks (Franzblau et al., 1969; Lent et al., 1969). The bifunctional cross-links can undergo further condensation to form tetrafunctional desmosine or isodesmosine (Partridge, 1966). A series of mapping studies have been recently conducted to pinpoint the locations of these cross-links (Schrader et al., 2018; Hedtke et al., 2019; Schmelzer et al., 2019) as their placements are crucial to understanding the resultant molecular orientation of tropoelastin within cross-linked elastin. Molecular docking studies utilizing

tropoelastin and the 3D structure of LOX1 (Vallet et al., 2018) may assist in our understanding as to whether the enzyme has a preference for modifying particular tropoelastin residues.

The next stage of elastin assembly involves the deposition of tropoelastin spherules onto the microfibril scaffold of elastic fibers. Microfibrils comprise multiple proteins, of which fibrillin-1 is the most common. Tropoelastin interacts with microfibril components including fibrillin-1, fibulin-4, and -5, and other associated molecules such as latent transforming growth factor β binding protein-4 (Visconti et al., 2003; McLaughlin et al., 2006; Urban et al., 2009; Yamauchi et al., 2010; Noda et al., 2013; Lockhart-Cairns et al., 2020). It has recently been suggested that fibrillins are capable of stabilizing tropoelastin, possibly for the purpose of selecting conformations that are favorable for elastin assembly (Lockhart-Cairns et al., 2020). In addition to interacting with tropoelastin, fibulin-4 and -5 are capable of also binding LOX and fibrillin-1 and, thus, have key roles in facilitating elastogenesis (Hinderer et al., 2015). Moreover, fibulins are essential for elastic fiber directionality, as fibroblasts with fibulin-4 and -5 knockdowns generate poorly formed elastic fibers (Yamauchi et al., 2010), and fibulin-4 –/– mice display aberrant, poorly cross-linked, and non-fibrous elastin (McLaughlin et al., 2006).

CURRENT MODEL OF TROPOELASTIN ASSEMBLY

It was first hypothesized that tropoelastin assembles in a head-to-tail manner similar to that of other ECM proteins such as collagen, which assembles into fibrils that subsequently associate laterally to form sheets and thicker fibers (Kadler, 2017). Solving tropoelastin's global structure (Baldock et al., 2011) allowed for 3D mapping on tropoelastin of the approximate locations of domains 10, 19, and 25, which were the first unequivocally cross-linked domains to be discovered (Brown-Augsburger et al., 1995). The alignment of these three domains indicates that at least two tropoelastin molecules are required to form this tetrafunctional cross-link, thus, giving rise to the head-to-tail model of assembly involving the growth of a linear chain that can assemble laterally to form sheets and eventually form spherules (Baldock et al., 2011).

However, there are aspects of this model that warrant further investigation. For example, the tetrafunctional cross-link, on which the model is based, is derived from porcine elastin (Brown-Augsburger et al., 1995). Although there is no 3D structure for porcine tropoelastin, porcine tropoelastin differs from that of humans (Sandberg et al., 1977), leaving it unclear as to whether these domains align as expected in human tissue. Further to this, the current model of elastin assembly does not account for how long strings or sheets of tropoelastin are capable of forming spherules on a macroscopic scale (Tu et al., 2010).

More recently, the computational model of tropoelastin has been leveraged to characterize higher-order structures and probe self-assembly (Tarakanova et al., 2019a). Forty tropoelastin molecules were subjected to simulations using a MARTINI-based coarse-grained model, integrated with an elastic network model (Tarakanova et al., 2019a). The advantage of coarse-grained methodologies is that they allow for the simulation of timescales of large molecular systems on the order of microseconds, which are otherwise computationally infeasible with classical full-atomistic molecular dynamics. Dominant driving factors of assembly were examined, including water, temperature and domain pair orientations. Crucially, these simulations revealed that self-assembly starts with a nucleation event and elongation proceeds via both globular and fibrillar structures (Tarakanova et al., 2019a). This suggests a high level of conformational sampling during this phase of coacervation, indicating that the flexibility of tropoelastin plays a key role in assembly that may persist, to some extent, into later stages of assembly (Reichheld et al., 2020). Importantly, the presence of fibrils indicates that the nanostructures formed during initial assembly contribute to the supramolecular structures that arise during both early (spherule) and later (fibril) stages of elastogenesis. Interestingly, the location and orientation of different domains that contacted each other during self-assembly was noted to be heterogeneous, resulting in head-to-head, tail-to-tail, head-to-tail, and lateral interactions (Tarakanova et al., 2019a). This reflects the experimentally observed heterogeneity of cross-links in mature elastin, again giving weight to the hypothesis that the flexibility of tropoelastin is imperative for assembly (Schrader et al., 2018; Tarakanova et al., 2019a).

TROPOELASTIN-CELL RECEPTOR INTERACTIONS AND IMPLICATIONS FOR ASSEMBLY

Tropoelastin promotes cell attachment and migration of several cell types including fibroblasts, endothelial cells and mesenchymal stem cells. Cellular activities are mediated through interactions between tropoelastin or EDPs and specific receptors on the cell surface. These interactions trigger a wide range of processes including wound healing, elastogenesis and maintenance of stemness (Yeo and Weiss, 2019).

Elastin binding protein (EBP) is a splice variant of β-galactosidase, that recognizes the repetitive hydrophobic sequences (VGVAPG) of tropoelastin (Tajima et al., 1997). EBP plays two roles in the assembly of elastin. The first is an intracellular role as a tropoelastin chaperone and the second is as part of the elastin receptor complex (ERC). Intracellularly, EBP is associated with tropoelastin after the release of the signal peptide and acts as a chaperone to prevent self-aggregation and proteolysis as it transported to the cell membrane, after which EBP is then recycled and serves as a reusable shuttle protein (Hinek et al., 1995).

On the cell surface, EBP forms a complex with protective protein/cathepsin A (PPCA) and neuraminidase-1 (Neu-1), giving rise to the ERC (Duca et al., 2007). The ERC binds elastin derived peptides, which are the product of proteolytic activity of soluble and insoluble elastin by various elastases. Elastases can be in the form of serine- (e.g., Ela-2), cysteine- (e.g., cathepsin I), or matrix metalloproteinases (MMP-2, -7, -9, and -12),

and bioactive peptides include the VGVAPG peptide. Binding of EDPs to the ERC induces a number of biological effects including migration, adhesion, proliferation, protease expression, and secretion. EDPs can modulate an array of signal pathways (Scandolera et al., 2016), but full-length tropoelastin does not trigger pathways through the ERC. This suggests the ERCs' primary signal pathways are involved in wound recognition through fragments of elastin, where EDPs are formed as a result of elastic tissue damage.

Glycosaminoglycans (GAGs) are negatively charged, linear polysaccharides, which can be either sulfated [heparan sulfate (HS) or chondroitin sulfate] or non-sulfated (hyaluronic acid). HS, which is present on cell surface proteoglycans (syndecans and glypicans), interacts strongly with tropoelastin (Cain et al., 2005). Positively charged lysine residues in domains 17 were identified to interact with negatively charged HS, most likely via ionic interactions (Lee et al., 2017). The last 17 amino acid residues of the C-terminus of domain 36 are also implicated in HS interactions; the last four residues are Arg-Lys-Arg-Lys and are positively charged at physiological pH which provides a charged cluster capable of binding negatively charged HS (Broekelmann et al., 2005). It has been postulated that the interaction between tropoelastin and cell surface proteoglycans is part of the assembly process of elastin before it is deposited on microfibrils. Fibrillin-1 and -2 also interact with proteoglycans (Tiedemann et al., 2001), which coupled with tropoelastin/GAG interactions provide a pathway to the formation of elastic fibers.

Integrins are a major class of cell surface receptor family, of which tropoelastin has been found to interact with two types: $\alpha_v\beta_3$ (Rodgers and Weiss, 2004) and $\alpha_v\beta_5$. Integrins canonically bind proteins containing Arg-Glu-Asp motifs, but this sequence is not found in tropoelastin (Lee et al., 2014). Instead, tropoelastin domains 14–18 and 36 (RKRK sequence) have been found to bind to both integrins. The lysines of domain 15 and 17 are believed to play key roles in this interaction. It is likely that, as a general rule, integrin binding to tropoelastin is mediated via GAGs, which is facilitated by the repetition of tropoelastin's primary sequence and the surface exposure of positively charged similar domains (Lee et al., 2017; Bochicchio et al., 2021). Interactions with these integrins on the surface of mesenchymal stem cells, either through surface bound or as soluble tropoelastin, promote MSC proliferation and phenotypic maintenance via FAK and PKB/AKT (Yeo and Weiss, 2019). The narrow specificity to $\alpha_v\beta_3$ and $\alpha_5\beta_3$ may also be beneficial compared with other ECM adhesion molecules such as fibronectin (which can adhere to up to 20 types of integrin) which may compete with and modulate binding to tropoelastin, and deliver opposing effects on cell proliferation. Furthermore, as integrins are involved in the remodeling of the ECM (Bonnans et al., 2014), this is consistent with a model where the tropoelastin-integrin interaction forms part of the wound repair process.

CONCLUSION

Tropoelastin is a unique protein with biochemical and physical properties that allow it to rapidly self-assemble into fibrous structures. It has become increasingly evident that tropoelastin's sequence, structure and subsequent functionality are in a delicate balance; thus, perturbations to tropoelastin's sequence can have far-reaching consequences for self-assembly and the resultant architecture of elastic fibers. For many years it was difficult to study tropoelastin at an atomic scale, but the application of computational methods, such as full-atomistic molecular dynamics and elastic network models, in combination with powerful low-resolution structural studies, have expanded the field and delivered an enhanced understanding of the mechanisms that contribute to self-assembly. Modeling has been verified using wet-bench methodologies, forming a robust suite of complementary methodologies that will undoubtedly become more prevalent for exploring the assembly of biological fibers over time. With leaps in the improvement of cryogenic electron microscopy to characterize flexible molecules, we predict that this approach will contribute to a deeper understanding of tropoelastin structure and self-assembly in the context of endogenous fiber formation and biomaterials fabrication.

AUTHOR CONTRIBUTIONS

All authors contributed to writing and editing the review.

FUNDING

The Wellcome Trust Centre for Cell-Matrix Research is supported by funding from Wellcome Trust (203128/Z/16/Z). CB gratefully acknowledges BBSRC funding (Ref: BB/R008221/1). AW gratefully acknowledges NHMRC funding (Ref: 1195827). The authors wrote and submitted this manuscript in response to an invitation by the Editor. AT acknowledges support from University of Connecticut's Institute for Collaboration on Health, Intervention, and Policy Faculty Research Seed Grant.

REFERENCES

Aaron, B., and Gosline, J. (1981). Elastin as a random-network elastomer: a mechanical and optical analysis of single elastin fibers. *Biopolymers* 20, 1247–1260. doi: 10.1002/bip.1981.360200611

Albert, E. N. (1972). Developing elastic tissue. An electron microscopic study. *Am. J. Pathol.* 69, 89–102.

Annabi, N., Zhang, Y. N., Assmann, A., Sani, E. S., Cheng, G., Lassaletta, A. D., et al. (2017). Engineering a highly elastic human protein-based sealant for surgical applications. *Sci. Transl. Med.* 9:eaai7466. doi: 10.1126/scitranslmed.aai7466

Avbelj, F. (2000). Amino acid conformational preferences and solvation of polar backbone atoms in peptides and proteins. *J. Mol. Biol.* 300, 1335–1359. doi: 10.1006/jmbi.2000.3901

Baldock, C., Oberhauser, A. F., Ma, L., Lammie, D., Siegler, V., Mithieux, S. M., et al. (2011). Shape of tropoelastin, the highly extensible protein that controls human tissue elasticity. *Proc. Natl. Acad. Sci. U.S.A.* 108, 4322–4327. doi: 10.1073/pnas.1014280108

Bashir, M. M., Indik, Z., Yeh, H., Ornstein-Goldstein, N., Rosenbloom, J. C., Abrams, W., et al. (1989). Characterization of the complete human elastin gene. Delineation of unusual features in the 5'-flanking region. *J. Biol. Chem.* 264, 8887–8891.

Baul, U., Bley, M., and Dzubiella, J. (2020). Thermal compaction of disordered and elastin-like polypeptides: a temperature-dependent, sequence-specific coarse-grained simulation model. *Biomacromolecules* 21, 3523–3538. doi: 10.1021/acs.biomac.0c00546

Bochicchio, B., Floquet, N., Pepe, A., Alix, A. J., and Tamburro, A. M. (2004). Dissection of human tropoelastin: solution structure, dynamics and self-assembly of the exon 5 peptide. *Chemistry* 10, 3166–3176. doi: 10.1002/chem.200305661

Bochicchio, B., Yeo, G. C., Lee, P., Emul, D., Pepe, A., Laezza, A., et al. (2021). Domains 12 to 16 of tropoelastin promote cell attachment and spreading through interactions with glycosaminoglycan and integrins alphaV and alpha5beta1. *FEBS J.* [Epub ahead of print].

Bonnans, C., Chou, J., and Werb, Z. (2014). Remodelling the extracellular matrix in development and disease. *Nat. Rev. Mol. Cell Biol.* 15, 786–801. doi: 10.1038/nrm3904

Bressan, G. M., Castellani, I., Giro, M. G., Volpin, D., Fornieri, C., and Pasquali Ronchetti, I. (1983). Banded fibers in tropoelastin coacervates at physiological temperatures. *J. Ultrastruct. Res.* 82, 335–340. doi: 10.1016/s0022-5320(83)80021-5

Broekelmann, T. J., Kozel, B. A., Ishibashi, H., Werneck, C. C., Keeley, F. W., Zhang, L., et al. (2005). Tropoelastin interacts with cell-surface glycosaminoglycans via its COOH-terminal domain. *J. Biol. Chem.* 280, 40939–40947. doi: 10.1074/jbc.M507309200

Brown-Augsburger, P., Tisdale, C., Broekelmann, T., Sloan, C., and Mecham, R. P. (1995). Identification of an elastin cross-linking domain that joins three peptide chains. Possible role in nucleated assembly. *J. Biol. Chem.* 270, 17778–17783. doi: 10.1074/jbc.270.30.17778

Cain, S. A., Baldock, C., Gallagher, J., Morgan, A., Bax, D. V., Weiss, A. S., et al. (2005). Fibrillin-1 interactions with heparin. Implications for microfibril and elastic fiber assembly. *J. Biol. Chem.* 280, 30526–30537. doi: 10.1074/jbc.M501390200

Chung, M. I., Miao, M., Stahl, R. J., Chan, E., Parkinson, J., and Keeley, F. W. (2006). Sequences and domain structures of mammalian, avian, amphibian and teleost tropoelastins: clues to the evolutionary history of elastins. *Matrix Biol.* 25, 492–504. doi: 10.1016/j.matbio.2006.08.258

Clarke, A. W., Arnspang, E. C., Mithieux, S. M., Korkmaz, E., Braet, F., and Weiss, A. S. (2006). Tropoelastin massively associates during coacervation to form quantized protein spheres. *Biochemistry* 45, 9989–9996. doi: 10.1021/bi0610092

Cordier, P., Tournilhac, F., Soulié-Ziakovic, C., and Leibler, L. (2008). Self-healing and thermoreversible rubber from supramolecular assembly. *Nature* 451, 977–980. doi: 10.1038/nature06669

Cox, B. A., Starcher, B. C., and Urry, D. W. (1974). Communication: coacervation of tropoelastin results in fiber formation. *J. Biol. Chem.* 249, 997–998. doi: 10.1016/s0021-9258(19)43030-5

Dandurand, J., Samouillan, V., Lacabanne, C., Pepe, A., and Bochicchio, B. (2015). Water structure and elastin-like peptide aggregation. *J. Therm. Anal. Calorim.* 120, 419–426. doi: 10.1007/s10973-014-4254-9

Debelle, L., and Tamburro, A. M. (1999). Elastin: molecular description and function. *Int. J. Biochem. Cell Biol.* 31, 261–272. doi: 10.1016/s1357-2725(98)00098-3

Duca, L., Blanchevoye, C., Cantarelli, B., Ghoneim, C., Dedieu, S., Delacoux, F., et al. (2007). The elastin receptor complex transduces signals through the catalytic activity of its Neu-1 subunit. *J. Biol. Chem.* 282, 12484–12491. doi: 10.1074/jbc.M609505200

Dyksterhuis, L. B., Baldock, C., Lammie, D., Wess, T. J., and Weiss, A. S. (2007). Domains 17-27 of tropoelastin contain key regions of contact for coacervation and contain an unusual turn-containing crosslinking domain. *Matrix Biol.* 26, 125–135. doi: 10.1016/j.matbio.2006.10.002

Dyksterhuis, L. B., and Weiss, A. S. (2010). Homology models for domains 21-23 of human tropoelastin shed light on lysine crosslinking. *Biochem. Biophys. Res. Commun.* 396, 870–873. doi: 10.1016/j.bbrc.2010.05.013

Elvin, C. M., Carr, A. G., Huson, M. G., Maxwell, J. M., Pearson, R. D., Vuocolo, T., et al. (2005). Synthesis and properties of crosslinked recombinant pro-resilin. *Nature* 437, 999–1002. doi: 10.1038/nature04085

Fazio, M. J., Olsen, D. R., Kuivaniemi, H., Chu, M. L., Davidson, J. M., Rosenbloom, J., et al. (1988). Isolation and characterization of human elastin cDNAs, and age-associated variation in elastin gene expression in cultured skin fibroblasts. *Lab. Invest.* 58, 270–277.

Foster, J. A., Gray, W. R., and Franzblau, C. (1973). Isolation and characterization of crosslinked peptides from elastin. *Biochim. Biophys. Acta* 303, 363–369. doi: 10.1016/0005-2795(73)90368-1

Franzblau, C., Faris, B., and Papaioannou, R. (1969). Lysinonorleucine. A new amino acid from hydrolysates of elastin. *Biochemistry* 8, 2833–2837. doi: 10.1021/bi00835a021

Gray, W. R., Sandberg, L. B., and Foster, J. A. (1973). Molecular model for elastin structure and function. *Nature* 246, 461–466. doi: 10.1038/246461a0

Haust, M. D., More, R. H., Bencosme, S. A., and Balis, J. U. (1965). Elastogenesis in human aorta: an electron microscopic study. *Exp. Mol. Pathol.* 4, 508–524. doi: 10.1016/0014-4800(65)90015-8

He, D., Chung, M., Chan, E., Alleyne, T., Ha, K. C. H., Miao, M., et al. (2007). Comparative genomics of elastin: sequence analysis of a highly repetitive protein. *Matrix Biol.* 26, 524–540. doi: 10.1016/j.matbio.2007.05.005

He, D., Miao, M., Sitarz, E. E., Muiznieks, L. D., Reichheld, S., Stahl, R. J., et al. (2012). Polymorphisms in the human tropoelastin gene modify in vitro self-assembly and mechanical properties of elastin-like polypeptides. *PLoS One* 7:e46130. doi: 10.1371/journal.pone.0046130

Hedtke, T., Schrader, C. U., Heinz, A., Hoehenwarter, W., Brinckmann, J., Groth, T., et al. (2019). A comprehensive map of human elastin cross-linking during elastogenesis. *FEBS J.* 286, 3594–3610. doi: 10.1111/febs.14929

Hinderer, S., Shena, N., Ringuette, L. J., Hansmann, J., Reinhardt, D. P., Brucker, S. Y., et al. (2015). In vitro elastogenesis: instructing human vascular smooth muscle cells to generate an elastic fiber-containing extracellular matrix scaffold. *Biomed. Mater.* 10:034102. doi: 10.1088/1748-6041/10/3/034102

Hinek, A., Keeley, F. W., and Callahan, J. (1995). Recycling of the 67-kDa elastin binding protein in arterial myocytes is imperative for secretion of tropoelastin. *Exp. Cell Res.* 220, 312–324. doi: 10.1006/excr.1995.1321

Hinek, A., and Rabinovitch, M. (1994). 67-kD elastin-binding protein is a protective "companion" of extracellular insoluble elastin and intracellular tropoelastin. *J. Cell Biol.* 126, 563–574. doi: 10.1083/jcb.126.2.563

Hu, Q., Reymond, J. L., Pinel, N., Zabot, M. T., and Urban, Z. (2006). Inflammatory destruction of elastic fibers in acquired cutis laxa is associated with missense alleles in the elastin and fibulin-5 genes. *J. Invest. Dermatol.* 126, 283–290. doi: 10.1038/sj.jid.5700047

Indik, Z., Yeh, H., Ornstein-Goldstein, N., Kucich, U., Abrams, W., Rosenbloom, J. C., et al. (1989). Structure of the elastin gene and alternative splicing of elastin mRNA: implications for human disease. *Am. J. Med. Genet.* 34, 81–90. doi: 10.1002/ajmg.1320340115

Indik, Z., Yeh, H., Ornstein-Goldstein, N., Sheppard, P., Anderson, N., Rosenbloom, J. C., et al. (1987). Alternative splicing of human elastin mRNA indicated by sequence analysis of cloned genomic and complementary DNA. *Proc. Natl. Acad. Sci. U.S.A.* 84, 5680–5684. doi: 10.1073/pnas.84.16.5680

Jensen, S. A., Vrhovski, B., and Weiss, A. S. (2000). Domain 26 of tropoelastin plays a dominant role in association by coacervation. *J. Biol. Chem.* 275, 28449–28454. doi: 10.1074/jbc.M004265200

Kadler, K. E. (2017). Fell muir lecture: collagen fibril formation in vitro and in vivo. *Int. J. Exp. Pathol.* 98, 4–16. doi: 10.1111/iep.12224

Kentsis, A., and Sosnick, T. R. (1998). Trifluoroethanol promotes helix formation by destabilizing backbone exposure: desolvation rather than native hydrogen bonding defines the kinetic pathway of dimeric coiled coil folding. *Biochemistry* 37, 14613–14622. doi: 10.1021/bi981641y

Kozel, B. A., Rongish, B. J., Czirok, A., Zach, J., Little, C. D., Davis, E. C., et al. (2006). Elastic fiber formation: a dynamic view of extracellular matrix assembly using timer reporters. *J. Cell Physiol.* 207, 87–96. doi: 10.1002/jcp.20546

Kozel, B. A., Wachi, H., Davis, E. C., and Mecham, R. P. (2003). Domains in tropoelastin that mediate elastin deposition in vitro and in vivo. *J. Biol. Chem.* 278, 18491–18498. doi: 10.1074/jbc.M212715200

Kumashiro, K. K., Ho, J. P., Niemczura, W. P., and Keeley, F. W. (2006). Cooperativity between the hydrophobic and cross-linking domains of elastin. *J. Biol. Chem.* 281, 23757–23765. doi: 10.1074/jbc.M510833200

Lee, P., Bax, D. V., Bilek, M. M., and Weiss, A. S. (2014). A novel cell adhesion region in tropoelastin mediates attachment to integrin alphaVbeta5. *J. Biol. Chem.* 289, 1467–1477. doi: 10.1074/jbc.M113.518381

Lee, P., Yeo, G. C., and Weiss, A. S. (2017). A cell adhesive peptide from tropoelastin promotes sequential cell attachment and spreading via distinct receptors. *FEBS J.* 284, 2216–2230. doi: 10.1111/febs.14114

Lent, R. W., Smith, B., Salcedo, L. L., Faris, B., and Franzblau, C. (1969). Studies on the reduction of elastin. II. Evidence for the presence of alpha-aminoadipic acid delta-semialdehyde and its aldol condensation product. *Biochemistry* 8, 2837–2845. doi: 10.1021/bi00835a022

Lockhart-Cairns, M. P., Newandee, H., Thomson, J., Weiss, A. S., Baldock, C., and Tarakanova, A. (2020). Transglutaminase-mediated cross-linking of tropoelastin to fibrillin stabilises the elastin precursor prior to elastic fibre assembly. *J. Mol. Biol.* 432, 5736–5751. doi: 10.1016/j.jmb.2020.08.023

Luan, C. H., Harris, R., Prasad, K. U., and Urry, D. W. (1990). Differential scanning calorimetry studies of the inverse temperature transition of the polypentapeptide of elastin and its analogues. *Biopolymers* 29, 1699–1706. doi: 10.1002/bip.360291403

Luo, P., and Baldwin, R. L. (1997). Mechanism of helix induction by trifluoroethanol: a framework for extrapolating the helix-forming properties of peptides from trifluoroethanol/water mixtures back to water. *Biochemistry* 36, 8413–8421. doi: 10.1021/bi9707133

MacEwan, S. R., Weitzhandler, I., Hoffmann, I., Genzer, J., Gradzielski, M., and Chilkoti, A. (2017). Phase behavior and self-assembly of perfectly sequence-defined and monodisperse multiblock copolypeptides. *Biomacromolecules* 18, 599–609. doi: 10.1021/acs.biomac.6b01759

Mackay, J. P., Muiznieks, L. D., Toonkool, P., and Weiss, A. S. (2005). The hydrophobic domain 26 of human tropoelastin is unstructured in solution. *J. Struct. Biol.* 150, 154–162. doi: 10.1016/j.jsb.2005.02.005

Martin, S. L., Vrhovski, B., and Weiss, A. S. (1995). Total synthesis and expression in *Escherichia coli* of a gene encoding human tropoelastin. *Gene* 154, 159–166. doi: 10.1016/0378-1119(94)00848-m

McLaughlin, P. J., Chen, Q., Horiguchi, M., Starcher, B. C., Stanton, J. B., Broekelmann, T. J., et al. (2006). Targeted disruption of fibulin-4 abolishes elastogenesis and causes perinatal lethality in mice. *Mol. Cell. Biol.* 26, 1700–1709. doi: 10.1128/mcb.26.5.1700-1709.2006

Mecham, R. P. (1991). Elastin synthesis and fiber assembly. *Ann. N. Y. Acad. Sci.* 624, 137–146. doi: 10.1111/j.1749-6632.1991.tb17013.x

Mecham, R. P., Levy, B. D., Morris, S. L., Madaras, J. G., and Wrenn, D. S. (1985). Increased cyclic GMP levels lead to a stimulation of elastin production in ligament fibroblasts that is reversed by cyclic AMP. *J. Biol. Chem.* 260, 3255–3258. doi: 10.1016/s0021-9258(19)83613-x

Miao, M., Bellingham, C. M., Stahl, R. J., Sitarz, E. E., Lane, C. J., and Keeley, F. W. (2003). Sequence and structure determinants for the self-aggregation of recombinant polypeptides modeled after human elastin. *J. Biol. Chem.* 278, 48553–48562. doi: 10.1074/jbc.M308465200

Miao, M., Bruce, A. E., Bhanji, T., Davis, E. C., and Keeley, F. W. (2007). Differential expression of two tropoelastin genes in zebrafish. *Matrix Biol.* 26, 115–124. doi: 10.1016/j.matbio.2006.09.011

Miao, M., Reichheld, S. E., Muiznieks, L. D., Huang, Y., and Keeley, F. W. (2013). Elastin binding protein and FKBP65 modulate in vitro self-assembly of human tropoelastin. *Biochemistry* 52, 7731–7741. doi: 10.1021/bi400760f

Miao, M., Reichheld, S. E., Muiznieks, L. D., Sitarz, E. E., Sharpe, S., and Keeley, F. W. (2017). Single nucleotide polymorphisms and domain/splice variants modulate assembly and elastomeric properties of human elastin. Implications for tissue specificity and durability of elastic tissue. *Biopolymers* 107:e23007. doi: 10.1002/bip.23007

Miao, M., Stahl, R. J., Petersen, L. F., Reintsch, W. E., Davis, E. C., and Keeley, F. W. (2009). Characterization of an unusual tropoelastin with truncated C-terminus in the frog. *Matrix Biol.* 28, 432–441. doi: 10.1016/j.matbio.2009.07.003

Mithieux, S. M., Wise, S. G., Raftery, M. J., Starcher, B., and Weiss, A. S. (2005). A model two-component system for studying the architecture of elastin assembly in vitro. *J. Struct. Biol.* 149, 282–289. doi: 10.1016/j.jsb.2004.11.005

Muiznieks, L. D., Jensen, S. A., and Weiss, A. S. (2003). Structural changes and facilitated association of tropoelastin. *Arch. Biochem. Biophys.* 410, 317–323. doi: 10.1016/s0003-9861(02)00719-1

Muiznieks, L. D., Reichheld, S. E., Sitarz, E. E., Miao, M., and Keeley, F. W. (2015). Proline-poor hydrophobic domains modulate the assembly and material properties of polymeric elastin. *Biopolymers* 103, 563–573. doi: 10.1002/bip.22663

Murata, K., and Wolf, M. (2018). Cryo-electron microscopy for structural analysis of dynamic biological macromolecules. *Biochim. Biophys. Acta Gen. Subj.* 1862, 324–334. doi: 10.1016/j.bbagen.2017.07.020

Myers, B., Dubick, M., Last, J. A., and Rucker, R. B. (1983). Elastin synthesis during perinatal lung development in the rat. *Biochim. Biophys. Acta* 761, 17–22. doi: 10.1016/0304-4165(83)90357-4

Narayanan, A. S., Sandberg, L. B., Ross, R., and Layman, D. L. (1976). The smooth muscle cell. III. Elastin synthesis in arterial smooth muscle cell culture. *J. Cell Biol.* 68, 411–419. doi: 10.1083/jcb.68.3.411

Noda, K., Dabovic, B., Takagi, K., Inoue, T., Horiguchi, M., Hirai, M., et al. (2013). Latent TGF-β binding protein 4 promotes elastic fiber assembly by interacting with fibulin-5. *Proc. Natl. Acad. Sci. U.S.A.* 110, 2852–2857. doi: 10.1073/pnas.1215779110

Noguchi, A., Firsching, K., Kursar, J. D., and Reddy, R. (1990). Developmental changes of tropoelastin synthesis by rat pulmonary fibroblasts and effects of dexamethasone. *Pediatr. Res.* 28, 379–382. doi: 10.1203/00006450-199010000-00015

Nonaka, R., Sato, F., and Wachi, H. (2014). Domain 36 of tropoelastin in elastic fiber formation. *Biol. Pharm. Bull.* 37, 698–702. doi: 10.1248/bpb.b13-00933

Ozsvar, J., Tarakanova, A., Wang, R., Buehler, M. J., and Weiss, A. S. (2019). Allysine modifications perturb tropoelastin structure and mobility on a local and global scale. *Matrix Biol. Plus* 2:100002. doi: 10.1016/j.mbplus.2019.03.001

Parks, W. C., Roby, J. D., Wu, L. C., and Grosso, L. E. (1992). Cellular expression of tropoelastin mRNA splice variants. *Matrix* 12, 156–162. doi: 10.1016/s0934-8832(11)80057-0

Partridge, S. M. (1966). Biosynthesis and nature of elastin structures. *Fed. Proc.* 25, 1023–1029.

Pepe, A., Flamia, R., Guerra, D., Quaglino, D., Bochicchio, B., Pasquali Ronchetti, I., et al. (2008). Exon 26-coded polypeptide: an isolated hydrophobic domain of human tropoelastin able to self-assemble in vitro. *Matrix Biol.* 27, 441–450. doi: 10.1016/j.matbio.2008.02.006

Phinikaridou, A., Lacerda, S., Lavin, B., Andia, M. E., Smith, A., Saha, P., et al. (2018). Tropoelastin: a novel marker for plaque progression and instability. *Circ. Cardiovasc. Imaging* 11:e007303. doi: 10.1161/circimaging.117.007303

Prhashanna, A., Taylor, P. A., Qin, J., Kiick, K. L., and Jayaraman, A. (2019). Effect of peptide sequence on the LCST-like transition of elastin-like peptides and elastin-like peptide–collagen-like peptide conjugates: simulations and experiments. *Biomacromolecules* 20, 1178–1189. doi: 10.1021/acs.biomac.8b01503

Rauscher, S., Baud, S., Miao, M., Keeley, F. W., and Pomès, R. (2006). Proline and glycine control protein self-organization into elastomeric or amyloid fibrils. *Structure* 14, 1667–1676. doi: 10.1016/j.str.2006.09.008

Rauscher, S., and Pomes, R. (2017). The liquid structure of elastin. *eLife* 6:e26526. doi: 10.7554/eLife.26526

Reichheld, S. E., Muiznieks, L. D., Huynh, Q., Wang, N., Ing, C., Miao, M., et al. (2020). The evolutionary background and functional consequences of the rs2071307 polymorphism in human tropoelastin. *Biopolymers* [Epub ahead of print].

Reichheld, S. E., Muiznieks, L. D., Keeley, F. W., and Sharpe, S. (2017). Direct observation of structure and dynamics during phase separation of an elastomeric protein. *Proc. Natl. Acad. Sci. U.S.A.* 112, E4408–E4415. doi: 10.1073/pnas.1701877114

Reichheld, S. E., Muiznieks, L. D., Lu, R., Sharpe, S., and Keeley, F. W. (2019). Sequence variants of human tropoelastin affecting assembly, structural characteristics and functional properties of polymeric elastin in health and disease. *Matrix Biol.* 84, 68–80. doi: 10.1016/j.matbio.2019.06.010

Reichheld, S. E., Muiznieks, L. D., Stahl, R., Simonetti, K., Sharpe, S., and Keeley, F. W. (2014). Conformational transitions of the cross-linking domains of elastin during self-assembly. *J. Biol. Chem.* 289, 10057–10068. doi: 10.1074/jbc.M113.533893

Reiersen, H., and Rees, A. R. (2000). Trifluoroethanol may form a solvent matrix for assisted hydrophobic interactions between peptide side chains. *Protein Eng.* 13, 739–743. doi: 10.1093/protein/13.11.739

Roberts, S., Dzuricky, M., and Chilkoti, A. (2015). Elastin-like polypeptides as models of intrinsically disordered proteins. *FEBS Lett.* 589(19 Pt A), 2477–2486. doi: 10.1016/j.febslet.2015.08.029

Rodgers, U. R., and Weiss, A. S. (2004). Integrin alpha v beta 3 binds a unique non-RGD site near the C-terminus of human tropoelastin. *Biochimie* 86, 173–178. doi: 10.1016/j.biochi.2004.03.002

Sandberg, L. B., Gray, W. R., Foster, J. A., Torres, A. R., Alvarez, V. L., and Janata, J. (1977). Primary structure of porcine tropoelastin. *Adv. Exp. Med. Biol.* 79, 277–284. doi: 10.1007/978-1-4684-9093-0_25

Scandolera, A., Odoul, L., Salesse, S., Guillot, A., Blaise, S., Kawecki, C., et al. (2016). The elastin receptor complex: a unique matricellular receptor with high anti-tumoral potential. *Front. Pharmacol.* 7:32. doi: 10.3389/fphar.2016.00032

Schmelzer, C. E. H., Heinz, A., Troilo, H., Lockhart-Cairns, M. P., Jowitt, T. A., Marchand, M. F., et al. (2019). Lysyl oxidase-like 2 (LOXL2)-mediated cross-linking of tropoelastin. *FASEB J.* 33, 5468–5481. doi: 10.1096/fj.201801860RR

Schrader, C. U., Heinz, A., Majovsky, P., Karaman Mayack, B., Brinckmann, J., Sippl, W., et al. (2018). Elastin is heterogeneously cross-linked. *J. Biol. Chem.* 293, 15107–15119. doi: 10.1074/jbc.RA118.004322

Shapiro, S., Endicott, S., Province, M., Pierce, J., and Campbell, E. (1991). Marked longevity of human lung parenchymal elastic fibers deduced from prevalence of D-aspartate and nuclear weapons-related radiocarbon. *J. Clin. Investig.* 87, 1828–1834. doi: 10.1172/jci115204

Sherratt, M., Wess, T. J., Baldock, C., Ashworth, J., Purslow, P., Shuttleworth, C., et al. (2001). Fibrillin-rich microfibrils of the extracellular matrix: ultrastructure and assembly. *Micron* 32, 185–200. doi: 10.1016/s0968-4328(99)00082-7

Tajima, S., Wachi, H., Uemura, Y., and Okamoto, K. (1997). Modulation by elastin peptide VGVAPG of cell proliferation and elastin expression in human skin fibroblasts. *Arch. Dermatol. Res.* 289, 489–492. doi: 10.1007/s004030050227

Tamburro, A. M., Bochicchio, B., and Pepe, A. (2003). Dissection of human tropoelastin: exon-by-exon chemical synthesis and related conformational studies. *Biochemistry* 42, 13347–13362. doi: 10.1021/bi034837t

Tamburro, A. M., Guantieri, V., and Gordini, D. D. (1992). Synthesis and structural studies of a pentapeptide sequence of elastin. Poly (Val-Gly-Gly-Leu-Gly). *J. Biomol. Struct. Dyn.* 10, 441–454. doi: 10.1080/07391102.1992.10508661

Tamburro, A. M., Pepe, A., and Bochicchio, B. (2006). Localizing alpha-helices in human tropoelastin: assembly of the elastin "puzzle". *Biochemistry* 45, 9518–9530. doi: 10.1021/bi060289i

Tarakanova, A., and Buehler, M. J. (2013). Molecular modeling of protein materials: case study of elastin. *Model. Simul. Mater. Sci. Eng.* 21:063001. doi: 10.1088/0965-0393/21/6/063001

Tarakanova, A., Huang, W., Weiss, A. S., Kaplan, D. L., and Buehler, M. J. (2017). Computational smart polymer design based on elastin protein mutability. *Biomaterials* 127, 49–60. doi: 10.1016/j.biomaterials.2017.01.041

Tarakanova, A., Ozsvar, J., Weiss, A. S., and Buehler, M. J. (2019a). Coarse-grained model of tropoelastin self-assembly into nascent fibrils. *Mater. Today Biol.* 3:100016. doi: 10.1016/j.mtbio.2019.100016

Tarakanova, A., Yeo, G. C., Baldock, C., Weiss, A. S., and Buehler, M. J. (2018). Molecular model of human tropoelastin and implications of associated mutations. *Proc. Natl. Acad. Sci. U.S.A.* 115, 7338–7343. doi: 10.1073/pnas.1801205115

Tarakanova, A., Yeo, G. C., Baldock, C., Weiss, A. S., and Buehler, M. J. (2019b). Tropoelastin is a flexible molecule that retains its canonical shape. *Macromol. Biosci.* 19:e1800250. doi: 10.1002/mabi.201800250

Tiedemann, K., Batge, B., Muller, P. K., and Reinhardt, D. P. (2001). Interactions of fibrillin-1 with heparin/heparan sulfate, implications for microfibrillar assembly. *J. Biol. Chem.* 276, 36035–36042. doi: 10.1074/jbc.M104985200

Toonkool, P., Jensen, S. A., Maxwell, A. L., and Weiss, A. S. (2001). Hydrophobic domains of human tropoelastin interact in a context-dependent manner. *J. Biol. Chem.* 276, 44575–44580. doi: 10.1074/jbc.M107920200

Tu, Y., and Weiss, A. S. (2010). Transient tropoelastin nanoparticles are early-stage intermediates in the coacervation of human tropoelastin whose aggregation is facilitated by heparan sulfate and heparin decasaccharides. *Matrix Biol.* 29, 152–159. doi: 10.1016/j.matbio.2009.10.003

Tu, Y., Wise, S. G., and Weiss, A. S. (2010). Stages in tropoelastin coalescence during synthetic elastin hydrogel formation. *Micron* 41, 268–272. doi: 10.1016/j.micron.2009.11.003

Urban, Z., Hucthagowder, V., Schürmann, N., Todorovic, V., Zilberberg, L., Choi, J., et al. (2009). Mutations in LTBP4 cause a syndrome of impaired pulmonary, gastrointestinal, genitourinary, musculoskeletal, and dermal development. *Am. J. Hum. Genet.* 85, 593–605. doi: 10.1016/j.ajhg.2009.09.013

Vallet, S. D., Miele, A. E., Uciechowska-Kaczmarzyk, U., Liwo, A., Duclos, B., Samsonov, S. A., et al. (2018). Insights into the structure and dynamics of lysyl oxidase propeptide, a flexible protein with numerous partners. *Sci. Rep.* 8, 1–16.

Visconti, R. P., Barth, J. L., Keeley, F. W., and Little, C. D. (2003). Codistribution analysis of elastin and related fibrillar proteins in early vertebrate development. *Matrix Biol.* 22, 109–121. doi: 10.1016/s0945-053x(03)00014-3

Vrhovski, B., Jensen, S., and Weiss, A. S. (1997). Coacervation characteristics of recombinant human tropoelastin. *Eur. J. Biochem.* 250, 92–98. doi: 10.1111/j.1432-1033.1997.00092.x

Vrhovski, B., and Weiss, A. S. (1998). Biochemistry of tropoelastin. *FEBS J.* 258, 1–18. doi: 10.1046/j.1432-1327.1998.2580001.x

Wang, Z., Liu, L., Mithieux, S. M., and Weiss, A. S. (2020). Fabricating organized elastin in vascular grafts. *Trends Biotechnol.* [Epub ahead of print]. doi: 10.1007/978-3-319-71530-8_13-1

Wen, Q., Mithieux, S. M., and Weiss, A. S. (2020). Elastin biomaterials in dermal repair. *Trends Biotechnol.* 38, 280–291. doi: 10.1016/j.tibtech.2019.08.005

Wise, S. G., and Weiss, A. S. (2009). Tropoelastin. *Int. J. Biochem. Cell Biol.* 41, 494–497. doi: 10.1016/j.biocel.2008.03.017

Wise, S. G., Yeo, G. C., Hiob, M. A., Rnjak-Kovacina, J., Kaplan, D. L., Ng, M. K., et al. (2014). Tropoelastin: a versatile, bioactive assembly module. *Acta Biomater.* 10, 1532–1541. doi: 10.1016/j.actbio.2013.08.003

Wu, W. J., and Weiss, A. S. (1999). Deficient coacervation of two forms of human tropoelastin associated with supravalvular aortic stenosis. *Eur. J. Biochem.* 266, 308–314. doi: 10.1046/j.1432-1327.1999.00891.x

Yamauchi, Y., Tsuruga, E., Nakashima, K., Sawa, Y., and Ishikawa, H. (2010). Fibulin-4 and -5, but not fibulin-2, are associated with tropoelastin deposition in elastin-producing cell culture. *Acta Histochem. Cytochem.* 43, 131–138. doi: 10.1267/ahc.10026

Yang, A. S., and Honig, B. (1995). Free energy determinants of secondary structure formation: I. alpha-Helices. *J. Mol. Biol.* 252, 351–365. doi: 10.1006/jmbi.1995.0502

Yeo, G. C., Baldock, C., Tuukkanen, A., Roessle, M., Dyksterhuis, L. B., Wise, S. G., et al. (2012). Tropoelastin bridge region positions the cell-interactive C terminus and contributes to elastic fiber assembly. *Proc. Natl. Acad. Sci. U.S.A.* 109, 2878–2883. doi: 10.1073/pnas.1111615108

Yeo, G. C., Baldock, C., Wise, S. G., and Weiss, A. S. (2017). Targeted modulation of tropoelastin structure and assembly. *ACS Biomater. Sci. Eng.* 3, 2832–2844. doi: 10.1021/acsbiomaterials.6b00564

Yeo, G. C., Keeley, F. W., and Weiss, A. S. (2011). Coacervation of tropoelastin. *Adv. Colloid Interface Sci.* 167, 94–103. doi: 10.1016/j.cis.2010.10.003

Yeo, G. C., Tarakanova, A., Baldock, C., Wise, S. G., Buehler, M. J., and Weiss, A. S. (2016). Subtle balance of tropoelastin molecular shape and flexibility regulates dynamics and hierarchical assembly. *Sci. Adv.* 2:e1501145. doi: 10.1126/sciadv.1501145

Yeo, G. C., and Weiss, A. S. (2019). Soluble matrix protein is a potent modulator of mesenchymal stem cell performance. *Proc. Natl. Acad. Sci. U.S.A.* 116, 2042–2051. doi: 10.1073/pnas.1812951116

Yue, K., Li, X., Schrobback, K., Sheikhi, A., Annabi, N., Leijten, J., et al. (2017). Structural analysis of photocrosslinkable methacryloyl-modified protein derivatives. *Biomaterials* 139, 163–171. doi: 10.1016/j.biomaterials.2017.04.050

Conflict of Interest: AW is the Scientific Founder of Elastagen Pty. Ltd., which was sold to Allergan, now a division of AbbVie.

The remaining authors declare that the research was conducted in the absence of any commercial or financial relationships that could be construed as a potential conflict of interest.

frontiers in Bioengineering and Biotechnology

REVIEW
published: 03 March 2021
doi: 10.3389/fbioe.2021.641372

Amyloid-Like Aggregation in Diseases and Biomaterials: Osmosis of Structural Information

Nicole Balasco[1†], Carlo Diaferia[2†], Giancarlo Morelli[2], Luigi Vitagliano[1‡] and Antonella Accardo[2*‡]*

[1] Institute of Biostructures and Bioimaging (IBB), CNR, Naples, Italy, [2] Department of Pharmacy, Research Centre on Bioactive Peptides (CIRPeB), University of Naples "Federico II", Naples, Italy

OPEN ACCESS

Edited by:
Ulf Olsson,
Lund University, Sweden

Reviewed by:
Vito Foderà,
University of Copenhagen, Denmark
Enrico Ferrari,
University of Lincoln, United Kingdom
Galit Fichman,
National Cancer Institute at Frederick, United States

***Correspondence:**
Luigi Vitagliano
luigi.vitagliano@cnr.it;
luigi.vitagliano@unina.it
Antonella Accardo
antonella.accardo@unina.it

[†] *These authors have contributed equally to this work*

[‡] *These authors share last authorship*

Specialty section:
This article was submitted to Nanobiotechnology, a section of the journal Frontiers in Bioengineering and Biotechnology

Received: *14 December 2020*
Accepted: *05 February 2021*
Published: *03 March 2021*

Citation:
Balasco N, Diaferia C, Morelli G, Vitagliano L and Accardo A (2021) Amyloid-Like Aggregation in Diseases and Biomaterials: Osmosis of Structural Information. Front. Bioeng. Biotechnol. 9:641372. doi: 10.3389/fbioe.2021.641372

The discovery that the polypeptide chain has a remarkable and intrinsic propensity to form amyloid-like aggregates endowed with an extraordinary stability is one of the most relevant breakthroughs of the last decades in both protein/peptide chemistry and structural biology. This observation has fundamental implications, as the formation of these assemblies is systematically associated with the insurgence of severe neurodegenerative diseases. Although the ability of proteins to form aggregates rich in cross-β structure has been highlighted by recent studies of structural biology, the determination of the underlying atomic models has required immense efforts and inventiveness. Interestingly, the progressive molecular and structural characterization of these assemblies has opened new perspectives in apparently unrelated fields. Indeed, the self-assembling through the cross-β structure has been exploited to generate innovative biomaterials endowed with promising mechanical and spectroscopic properties. Therefore, this structural motif has become the *fil rouge* connecting these diversified research areas. In the present review, we report a chronological recapitulation, also performing a survey of the structural content of the Protein Data Bank, of the milestones achieved over the years in the characterization of cross-β assemblies involved in the insurgence of neurodegenerative diseases. A particular emphasis is given to the very recent successful elucidation of amyloid-like aggregates characterized by remarkable molecular and structural complexities. We also review the state of the art of the structural characterization of cross-β based biomaterials by highlighting the benefits of the osmosis of information between these two research areas. Finally, we underline the new promising perspectives that recent successful characterizations of disease-related amyloid-like assemblies can open in the biomaterial field.

Keywords: amyloid aggregates, cross-β structure, peptide-based hydrogels, amino acid aggregation, glutamine rich structures, biomaterials

BACKGROUND AND INTRODUCTION

The ability of the carbon atom to combine easily with other elements of the periodic table through covalent bonds is universally considered as a central factor for the development of life and of its related molecular diversity and complexity (Pace, 2001). The ability of this atom to form long chains is, however, only one of the founding aspects of life. Indeed, equally important is

the capability of the building blocks of the molecules and macromolecules of life to establish a variety of non-covalent interactions that lead to the generation of the intricate architectures frequently exhibited by biomolecules and that regulate their mutual interactions. Whereas the definition of the skeleton of the covalent bonds of these molecules has progressively become a rather straightforward task despite its chemical complexity, the understanding of the bases that govern non-covalent interactions is still a matter of intense and, not rarely, unproductive work. Although many significant progresses have been recently achieved, the decrypting of the folding code of macromolecules or the prediction of intermolecular partnerships remain extremely challenging tasks (Baker, 2019; Senior et al., 2020; Lensink et al., 2020).

This intricate scenario has been further enriched by the discovery that the polypeptide chain has a remarkable and intrinsic propensity to form non-covalent aggregates, denoted as amyloid for their macroscopic reminiscence to starch-like deposits (Riek and Eisenberg, 2016; Chiti and Dobson, 2017). The interest for these particular supramolecular assemblies has been initially dictated by the discovery that in several neurodegenerative diseases, such as Parkinson and Alzheimer diseases and Huntington chorea, proteins and peptides, generally showing completely unrelated sequences, undergo structural transitions (misfolding) (Chiti and Dobson, 2017; Soto and Pritzkow, 2018). In contrast to what observed in physiological conditions where proteins are generally biochemical recyclable and degradable entities, in amyloidosis diseases, upon misfolding, specific proteins become resistant to the normal desegregation and turnover. Consequently, progressive accumulation and extracellular deposition occur in the different tissues, including brain, kidney and heart. The characterization of this proteinaceous material has unraveled a supramolecular organization in which synergic non-covalent interactions generally lead to the formation of extremely stable and low soluble structures (Soto, 2003; Chiti and Dobson, 2017). Beyond oligomers, annular and short/quiescent fibrils and protofibrils, other important forms of amyloid organization comprise superstructures, including spherulites, amyloid-crystals and microparticles (Krebs et al., 2004; Cannon and Donald, 2013; Reynolds et al., 2017).

The structural characterization of these misfolded protein states has progressively shown that both the main chain and the side chain atoms that concur to the formation of non-covalent interactions stabilize them. More specifically, the backbone moieties that participate to hydrogen bonds as hydrogen donors (CO) or acceptors (NH) generate a network of H-bonds that associates β-strands in β-sheet secondary structure. In the case of misfolded states, however, the hydrogen bond pattern is perpendicular to the growth axis of the assembly to generate the so-called cross-β structure (**Figure 1**; Sunde et al., 1997; Eisenberg et al., 2006). This structural motif presents a characteristic fiber diffraction pattern that exhibits a strong meridional reflection at 4.7–4.8 Å and a broad equatorial reflection in the resolution range 10–12 Å that correspond to the inter-strand and inter-sheet distances, respectively (**Figure 1**). Side chains contribute to the stability of these assemblies by making a variety of polar and apolar interactions that stabilize the structure of the individual β-sheets (ladder interactions) and the inter-sheet interfaces (Tsai et al., 2005).

Interestingly, the progressive molecular and structural characterization of these assemblies suggested that they could be also formed by rather small and very simple peptides (Gazit, 2007; Wang et al., 2018). This important discovery has led to the growth of a new area of research devoted to the development of innovative and bioinspired biomaterials based on small peptides assembling in cross-β structures. These biomaterials have shown excellent, and often unexpected, mechanical and spectroscopic properties that make them suitable for a myriad of applications in different biomedical and biotechnological areas (Gras, 2007; Maity et al., 2014; Kemper et al., 2015; Peralta et al., 2015; Tena-Solsona et al., 2016; Avitabile et al., 2018; Hu et al., 2018; Diaferia et al., 2019a).

Here, we analyze the state of the art about structural characterizations of cross β-sheet biomaterials and misfolded aggregates of proteins/peptides involved in neurodegenerative diseases. Although these self-assembling biomolecules share a common basic element, the methodologies used and the level of accuracy achieved for their structural characterizations present significant differences. It is important to stress that many of the topics here reported have been already illustrated in excellent literature reviews (see for example Cavalli et al., 2010; Riek and Eisenberg, 2016; Wei et al., 2017). However, it is also worth noting that new exciting results and ideas come out in literature almost daily. The present review is aimed at providing a general view of the state of the art of structural characterizations of cross β-sheet assemblies with a specific focus on the mutual benefits that each of these fields has gained from the success of the other. A particular emphasis is given to the impact that the impressive breakthroughs achieved in the structural characterization of misfolded proteins involved in neurodegeneration in the very last years could have on the possible development of innovative biomaterials.

THE TEMPORAL EVOLUTION OF THE STRUCTURAL CHARACTERIZATION OF AMYLOID-LIKE AGGREGATES INVOLVED IN DISEASE

Some of the first insightful experiments in structural biology were performed by Astbury in mid 30ties who obtained the fiber diffraction patterns of different protein samples (Astbury and Street, 1931; Astbury et al., 1935). Although he was unable to derive atomic-level models from these data, he obtained meaningful diffraction patterns for the most common motifs observed in protein structures, i.e., α- and β-structure. Astbury was also able to register data from denatured samples of proteins displaying a pattern that was similar but rotated to that associated to the β-structure (cross-β structure). For years, the diffraction data of the α- and β-structure were extensively investigated with the aim of deriving the underlying atomic models. These were eventually obtained by Linus Pauling who theoretically built

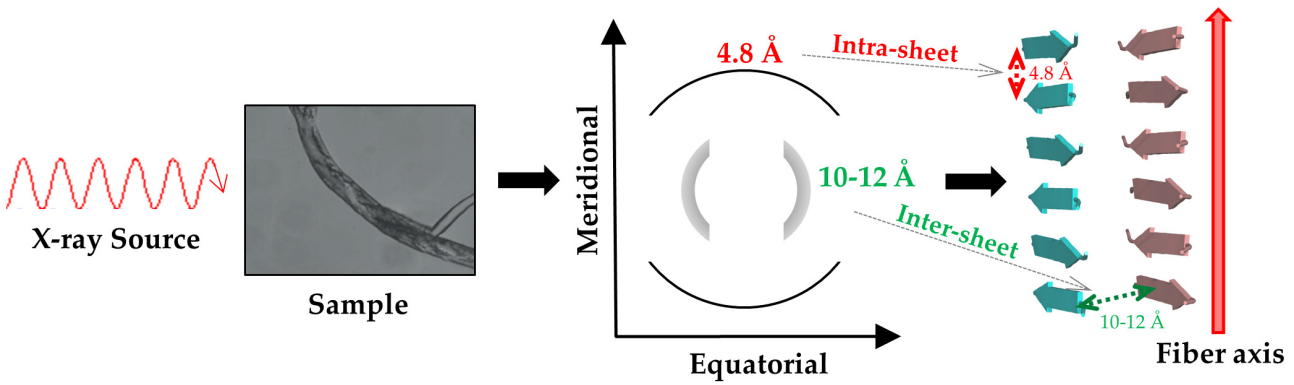

FIGURE 1 | Schematic representation of the diffraction pattern and of the structure of a typical cross-β assembly.

the correct structures for the α-helix and the β-sheet (Pauling et al., 1951; Pauling and Corey, 1951). On the other hand, the data and the possible related structure of the cross-β structure was somehow overlooked. The interest for this structural motif raised when its characteristic diffraction pattern was detected for misfolded proteins involved in neurodegeneration. Although the basic features of the cross-β structure could be straightforwardly derived from the diffraction pattern (**Figure 1**), the determination of the atomic structures of proteins/peptides adopting this motif has been a difficult process (Balbirnie et al., 2001; Eisenberg et al., 2006). As illustrated in **Figure 2**, this field has taken advantage of different experimental techniques that, in a step-by-step process started 15 years ago, have progressively led to the structural characterization of misfolded systems of increasing biological relevance. **Figure 2** also shows that the most important contributions to the field come from X-ray crystallography (Eisenberg and Sawaya, 2017) and from cryo Electron Microscopy (cryoEM) (Fitzpatrick and Saibil, 2019) with interesting results also obtained by using solid state NMR (ssNMR) (Tycko, 2011) and Electron Diffraction (ED) studies conducted on extremely tiny crystals (microED) (Nannenga and Gonen, 2019). The remarkable contribution of computational studies in unraveling the structural/dynamic properties of self-assembling systems involved in pathogenic processes has been reviewed elsewhere (Nasica-Labouze et al., 2015). These three-dimensional structural data have been also exploited to design inhibitors of amyloid-like aggregation (Seidler et al., 2018; Griner et al., 2019) and nanovaccines (Luo and Abrahams, 2014; Al-Halifa et al., 2020; Zottig et al., 2020). It is also important to note that solution studies conducted with Small-Angle X-ray Scattering (SAXS) and Small-Angle Neutron Scattering (SANS) techniques have provided a considerable contribution to the characterization of solvent structure and dynamics of cross-β assemblies (Fichou et al., 2015; Langkilde et al., 2015; Pounot et al., 2020).

Interestingly, X-ray crystallography dominated the field in the early stage of this process (**Figure 2**). Indeed, very important results were achieved using a reductionist approach that consisted in the identification and the characterization of small peptide fragments that could be crystallized and that in some way could mimic the aggregation tendency and the properties of the misfolded parent protein/polypeptide (Eisenberg et al., 2006). Obviously, the major limitation of the technique is related to the crystallization of the biological relevant misfolded biomolecules whose size and tendency to form fibers make the crystallization process difficult if not impossible. In recent years, this scenario has drastically changed due to the impressive progresses made in the structural characterization of biomacromolecules using single particle cryoEM, a technique that is revolutionizing this field and the entire structural biology. This is clearly evident from the inspection of the right side of **Figure 2** that highlights some of the milestones achieved using cryoEM.

The first experimental structural model of an amyloid-like system was the peptide corresponding to the 105-115 fragment of the amyloidogenic protein transthyretin whose structure was determined by magic angle spinning NMR spectroscopy (Jaroniec et al., 2004). The experimental data demonstrated that the peptide adopts a β-strand conformation with the main- and side-chain torsion angles close to their optimal values observed in β-sheets. Although the structural data highlighted a degree of long-range order, generally associated only with crystalline materials, no information could be derived on the lateral association of different β-sheets.

As mentioned above and highlighted by **Figure 2**, X-ray crystallography provided the most important contributions to the first characterizations of the amyloid-like structures at atomic level. Indeed, once solved the problem of handling and collecting data from the very small crystals that amyloid-like peptides tend to form due to their propensity to form fibers, a remarkable number of high resolution structures was obtained in very few years. The structure of the eptapeptide with the sequence GNNQQNY, which has become a sort of a prototype in the structural studies of amyloid-like peptides (Nelson et al., 2005), showed that the side chains of facing β-sheets interdigitated each other to form the so-called steric zipper motif (**Figure 3A**). The observed tight packing of the side chains in this motif straightforwardly explains the typical irreversibility of the formation of amyloid-like aggregates. It is worth mentioning that, although the role of the steric zipper motif in amyloid-like assemblies was experimentally discovered with the structure of GNNQQNY, a similar interdigitation of

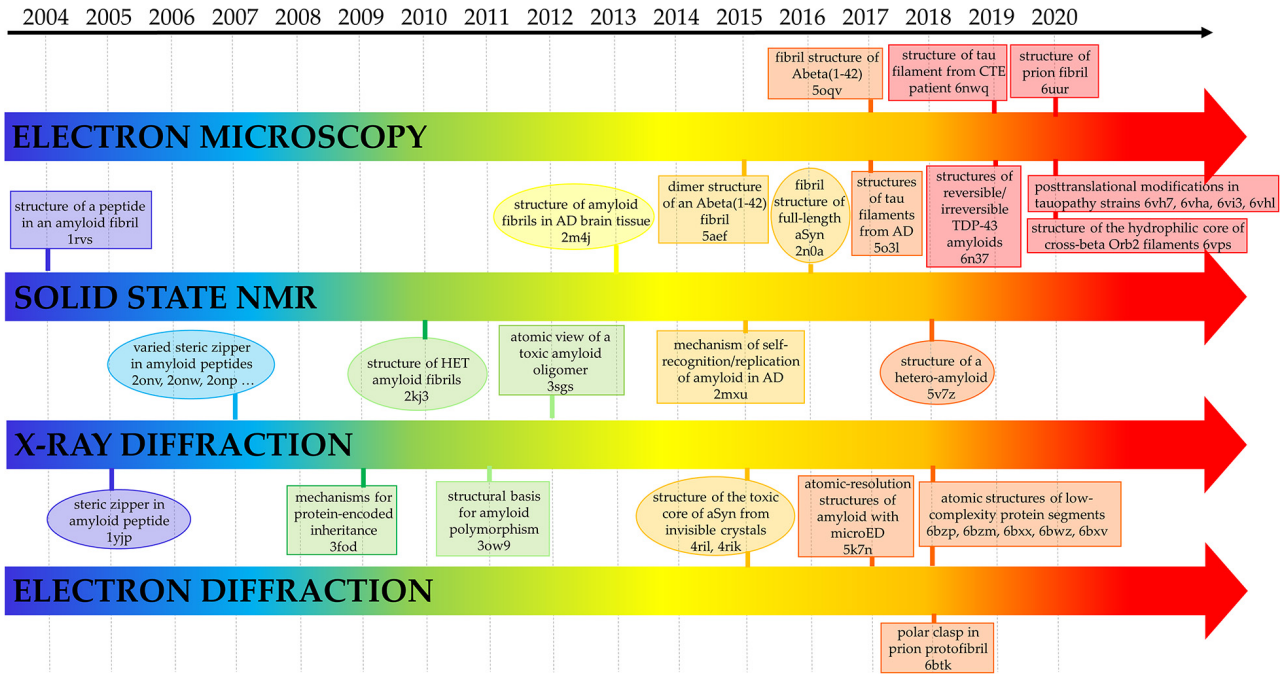

FIGURE 2 | Selected milestones in the atomic-level characterization of cross-β structures related to diseases. The Protein Data Bank code of the related structures is also reported. AD, aSyn, CTE, microED are the abbreviations for Alzheimer Disease, α-Synuclein, Chronic Traumatic Encephalopathy and micro Electro Diffraction, respectively.

the side chains was proposed for poly-glutamine aggregates on the basis of fiber diffraction data and molecular modeling (Sikorski and Atkins, 2005).

Subsequent structural studies carried out on peptide fragments taken from different proteins demonstrated that steric zipper is a frequent motif adopted by the spine of amyloid-like fibers (Sawaya et al., 2007). These structures also unraveled that this motif can be adopted in several different arrangements depending on the nature of the β-sheet (parallel or antiparallel) and on the relative orientations of the facing β-sheets. Despite their limited size, the characterization of these peptides also provided interesting insights into the (mis)function of the aggregates. Particularly relevant in this context is the discovery of polymorphic crystal structures of prion and other amyloid fragments that suggested intriguing structural mechanisms for protein-encoded inheritance (Wiltzius et al., 2009). In particular, combining the information derived from these structures that are stabilized by interactions formed between identical chains (homotypic) with those emerged from ssNMR studies (Paravastu et al., 2008) that highlighted the possibility of forming interactions between distant regions of the protein (heterotypic), packing and segmental polymorphisms were suggested (Colletier et al., 2011; Laganowsky et al., 2012; Lu et al., 2013; Cao et al., 2019).

As indicated by the histograms reported in **Figure 3** and data reported in **Supplementary Table 1**, which lists the amyloid-like structures we detected in a survey of the Protein Data Bank (PDB – release of October 2020) and classify them as function of the size of the cross-β core, the structural complexity of the characterized systems has enormously grown in the very last years. Apart from the structure of the HET amyloid fibrils (van Melckebeke et al., 2010), which actually adopt a different structural organization (β-helix), structures embodying significant fragments of the parent misfolded proteins were determined only since 2015. These achievements include the fibril structure of the Aβ peptide 1-42, of α-synuclein, of the protease resistant portion of the prion protein, of the Tau protein, and of functional amyloids such as the drosophila protein Orb2 (Schmidt et al., 2015; Xiao et al., 2015; Rodriguez et al., 2015; Tuttle et al., 2016; Gremer et al., 2017; Fitzpatrick et al., 2017; Mompean et al., 2018; Falcon et al., 2018a,b, 2019; Salinas et al., 2018, 2021; Hervas et al., 2020; Glynn et al., 2020; Röder et al., 2020; Schweighauser et al., 2020; Zhang et al., 2020).

Remarkably, some of these structural studies have been performed using protein samples directly extracted from patients. According to our survey, the largest cross-β structure present in the PBD is the doublet Tau fibril from corticobasal degeneration human brain tissue (Arakhamia et al., 2020). In line with other large amyloid-like assemblies, this structure is stabilized by many heterotypic interactions that involve distant residues of the polypeptide sequence, in which hydrophobic contacts play a major role (**Figure 4**). Interestingly, large cross-β assemblies may also be stabilized by hydrophilic interactions as in the functional filaments of the protein Orb2 (Hervas et al., 2020), a putative substrate of long-lasting memories (**Figure 5**). In this functional amyloid, the side chains of the internal glutamine residues interdigitate to form a tight inter-sheet association that is virtually identical to that observed in the assemblies involved in the

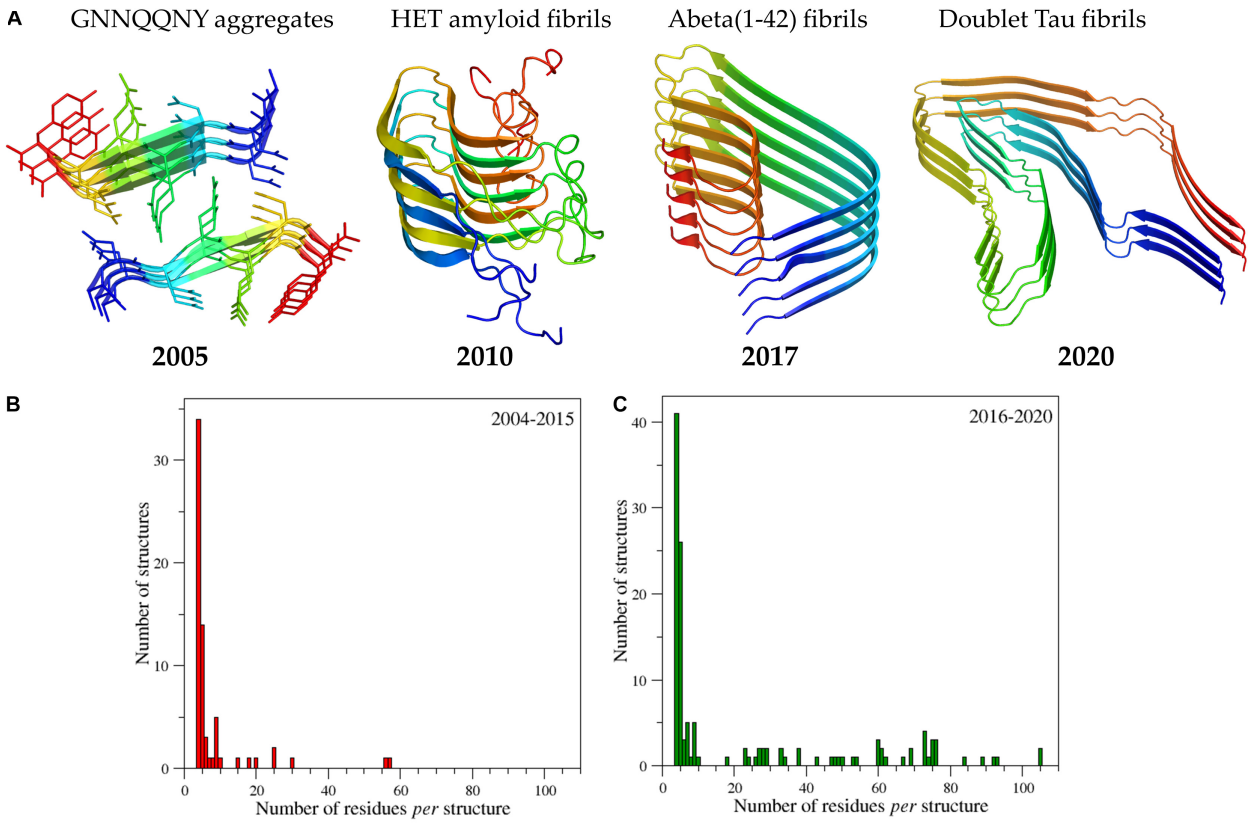

FIGURE 3 | Progressive increase of structural complexity of the cross-β systems whose structure has been determined at atomic levels starting from the GNNQQNY peptide to the human brain-derived Tau filaments **(A)**. The PDB code of the structures reported from the left to the right of panel **(A)** are 1yjp, 2kj3, 5oqv, and 6vh7. Ribbons are represented with a color code (blue to red) from the N- to the C-terminus. The panels **(B)** and **(C)** report the number of amyloid structures as function of the size deposited in the time interval 2004-2015 and 2016-2020, respectively. The initial search for amyloid-like structures was performed by interrogating the entire PDB (release of October 2020) using as a query the following criteria: Polymer Entity Type = "Protein"; Experimental Method = X-ray diffraction, electron microscopy, electron crystallography, solid-state NMR, fiber diffraction, neutron diffraction, solution scattering; Additional Structure Keywords = "amyloid"; Polymer Entity Sequence Length > 5. The PDB structures identified by the server were then manually checked and their main features were reported in the **Supplementary Table 1**.

glutamine expansion diseases (Sambashivan et al., 2005; Sikorski and Atkins, 2005; Esposito et al., 2008; Colombo et al., 2008).

Finally, the structural characterization of small protein fragments by X-ray and electron diffraction crystallography has recently provided important contributions in the emerging area of biology aimed at characterizing subcellular membrane-less assemblies that form and re-dissolve in mammalian cells in response to stimuli (de la Cruz et al., 2017; Hughes et al., 2018; Gallagher-Jones et al., 2018). This type of phase separation is frequently observed with proteins that contain low-complexity domains (LCD) and that show a tendency to form reversible semi-solid phase hydrogels at high concentration. The structural characterization at atomic level of these proteins is extremely difficult. Moreover, although X-ray diffraction analysis of these hydrogels yields a cross-β pattern, fibrils found in these hydrogels are heat sensitive in contrast to amyloid fibrils that generally resist denaturation. The crystal structures of small LCD fragments isolated from a protein that forms these hydrogels (FUS) indicate that the heat sensitivity of these cross-β aggregates is related to the less tight association of the β-sheets inside the assemblies compared to steric zipper association detected in amyloids (**Figure 6**; Hughes et al., 2018).

GOING SMALL: OLIGOPEPTIDE-BASED CROSS-β ASSEMBLIES FOR BIOMATERIALS

As outlined in the previous section, initial attempts to gain molecular and structural information on misfolded states of proteins involved in neurodegenerative diseases were performed using a reductionist approach based on the identification of the minimal peptide fragments that were able to emulate the behavior of the parent protein/polypeptide. These studies were not only useful to get structural information on these systems, but they also suggested that very small peptides could be able to self-assemble.

Early successful examples of this reductionist approach include the identification of small amyloid-forming peptides from fragments of the islet amyloid polypeptide (the hexapeptide

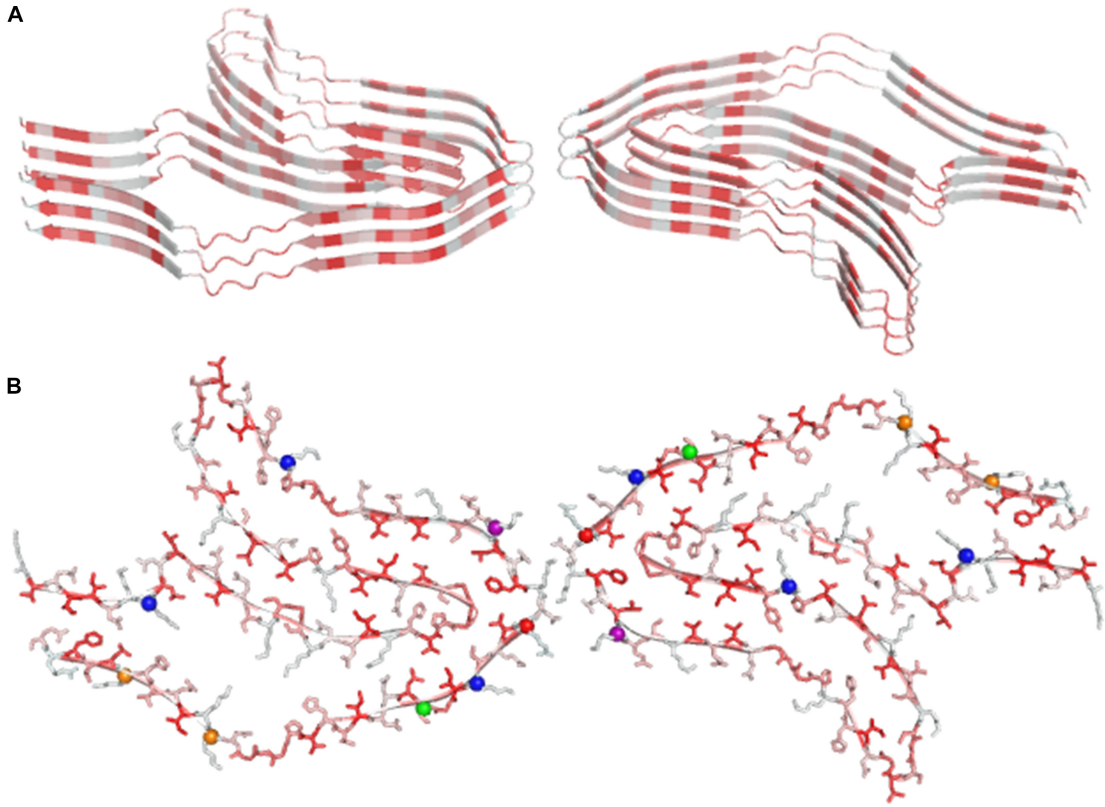

FIGURE 4 | Ribbon **(A)** and ball and stick representation **(B)** of the doublet Tau Fibril from corticobasal degeneration human brain tissue, the largest cross-β structure currently deposited in the PDB (code 6vh7). Residues are colored as function of their hydrophobicity from gray (polar) to red (apolar). In panel B, posttranslational modification sites are denoted with balls.

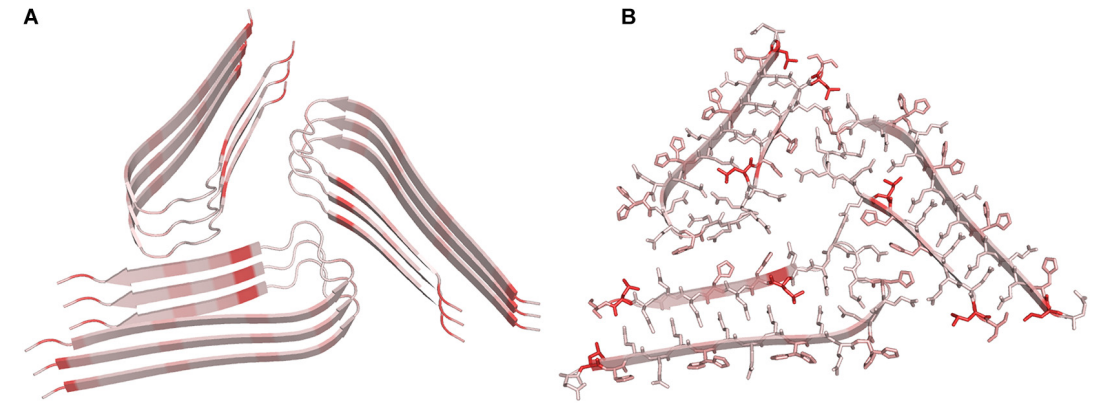

FIGURE 5 | Ribbon **(A)** and ball and stick representation **(B)** structure of the hydrophilic core of cross-beta Orb2 filaments (PDB code 6vps) Residues are colored as function of their hydrophobicity from gray (polar) to red (apolar).

with sequence FGAILK) (Tenidis et al., 2000), human calcitonin (the pentapeptide DFNKFA) (Kazantzis et al., 2002) and the Aβ1-42 polypeptide (the hexapeptide KLVFFA) (Hilbich et al., 1992; **Figure 7**). In 2003, Reches and Gazit, extending the approach used to dissect the Aβ1-42 polypeptide and starting from the KLVFFA peptide, identified the diphenylalanine (FF) peptide as the shortest motif able to self-assemble (Görbitz, 2001; Reches and Gazit, 2003; Amdursky et al., 2010). Interestingly, due to its small size, minor modifications of the FF dipeptide lead to different supramolecular assemblies. Indeed, while H-FF-OH formed tubes, spheres, and quantum-dots, the FF variants H-FF-NH_2 and Ac-FF-NH_2 formed nanotubes (Yan et al., 2007; Adler-Abramovich and Gazit, 2014). Interestingly, carbobenzoxy-FF-OH, PEGylated-FF-OH, and

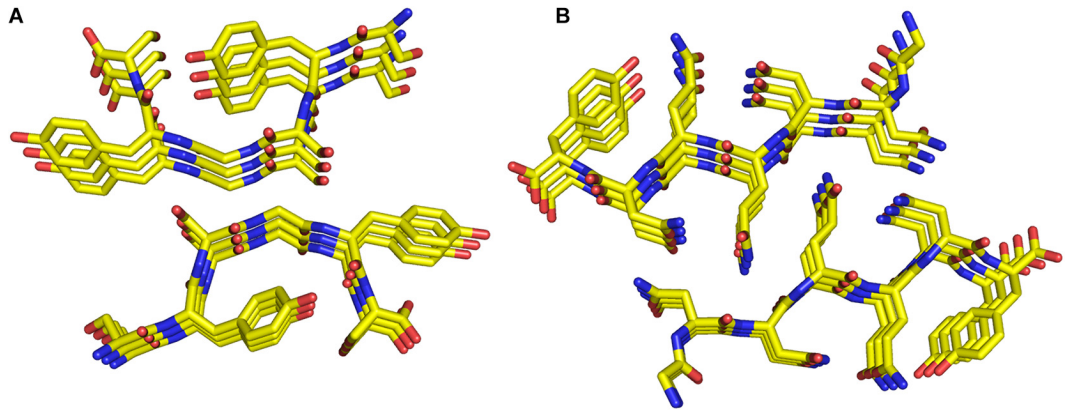

FIGURE 6 | Ball and stick representation of the SYSGYS peptide (PDB code 6bwz) from the low-complexity domain of FUS **(A)**. The structure of the GNNQQNY peptide (PDB code 1yjp) is also reported **(B)**.

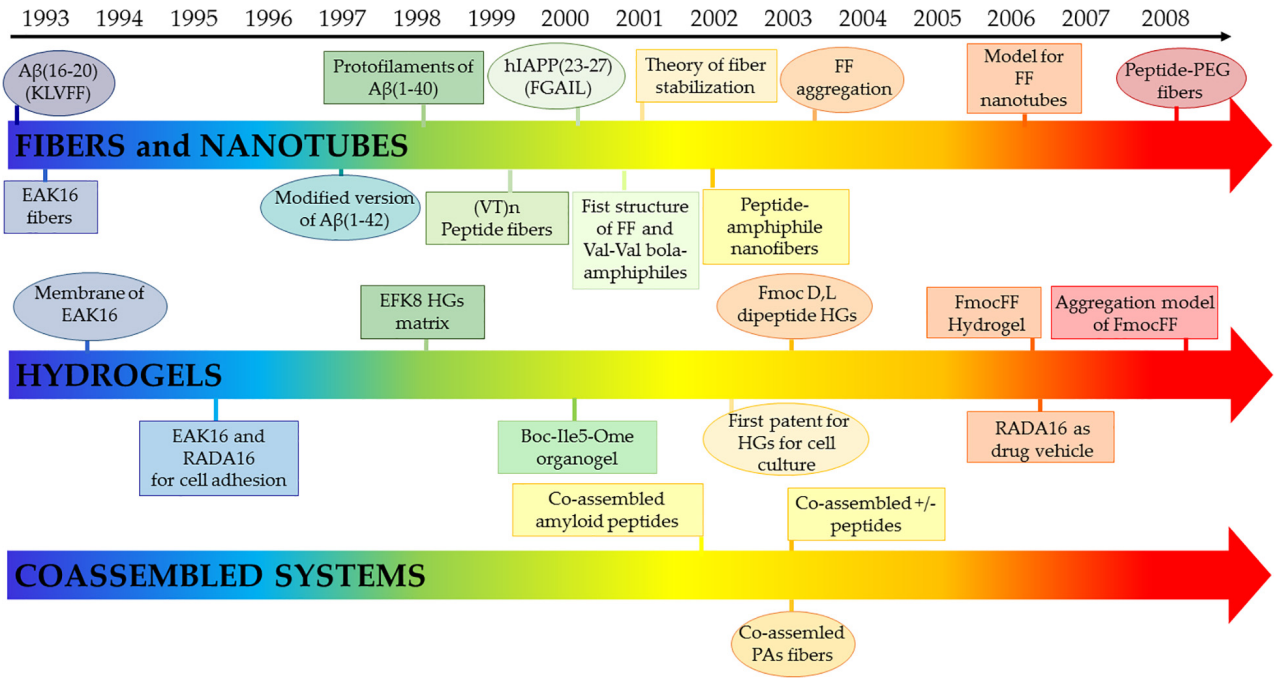

FIGURE 7 | Selected early milestones on self-assembling peptides assuming cross-β structures as elements for fibers and nanotubes, hydrogels and co-assembled biomaterials. Reference for each group are reported following. *Fibers and nanotubes:* Aβ(16-20) (KLVFF) (Hilbich et al., 1992); EAK16 fibers (Zhang et al., 1993a); modified version of Aβ(1-42) (Seilheimer et al., 1997); protofilaments of Aβ(1-40) (Malinchik et al., 1998); (VT)n peptide fibers (Janek et al., 1999); hIAPP(23-27) (FGAIL) (Tenidis et al., 2000); Val-Val bola-amphiphiles (Kogiso et al., 2000); theory of fiber stabilization (Nyrkova et al., 2000); first crystallographic structure of FF (Görbitz, 2001); peptide-amphiphile nanofibers (Hartgerink et al., 2002); FF aggregation (Reches and Gazit, 2003); model for FF nanotubes (Görbitz, 2006); peptide-PEG fibers (Hamley and Krysmann, 2008). *Hydrogels:* membranes of EAK16 (Zhang et al., 1993b); EAK16 and RADA16 for cell adhesion (Zhang et al., 1993b); EFK8 HGs matrix (Leon et al., 1998); Boc-Ile5-Ome organogel (Jayakumar et al., 2000); Fmoc *D,L* dipeptide HGs (Zhang et al., 2003); FmocFF Hydrogel (Mahler et al., 2006); RADA16 as drug vehicle (Nagai et al., 2006); aggregation model of Fmoc-FF (Smith et al., 2008). *Co-assembled systems*: co-assembled amyloid peptides (Takahashi et al., 2002); co-assemled PAs fibers (Niece et al., 2003); co-assembled ± peptides (Aggeli et al., 2003).

Fmoc-FF-OH formed amyloid-like structures, nanofibers, and β-sheet-based fibrous-hydrogel, respectively (Reches and Gazit, 2005; Jayawarna et al., 2006; Mahler et al., 2006; Castelletto and Hamley, 2009; Diaferia et al., 2019b).

The seminal discovery on the ability of FF to self-assemble originated a new research area that developed in different directions (Yan et al., 2010). On one hand, it stimulated activities aimed at characterizing oligopeptides based on aromatic residues that are known to have a remarkable propensity to self-assemble. On the other hand, it also inspired studies focused on the self-assembling properties of single amino acids. The state of the art of these research lines will be outlined in the following paragraphs from a structural perspective.

Among oligopeptides based on aromatic residues, homopeptides formed by Phe residues, including tri-, tetra-, penta- and hexa-Phe peptides, have a special role. The analysis of the literature suggests that the length of the oligopeptide significantly influences structural, morphological and functional properties of the supramolecular architecture. In particular, the higher stability of these extended oligopeptides compared to the FF homodimer is due to the extended aromatic network in the peptide sequence. Opposite to FF dipeptide, FFF tripeptide forms planar nanostructures (Han et al., 2010), whereas its protected analogs Fmoc-FFF and Boc-FFF self-assemble into nanosphere (Chronopoulou et al., 2010) and hydrogels, respectively (Tamamis et al., 2008). Theoretical density functional theory (DFT) calculations carried out on the zwitterionic FFFF indicated the formation of irregular nanotubes resembling those achieved for FF. On the contrary, its Fmoc-FFFF derivative, lacking of the positive charge on the N-terminal end, can self-organize into a variety of assemblies (nanoplates, fibrils, star-like aggregates, and nanospheres), with a preference toward fibrillary structures with an antiparallel β-sheet organization. Instead, the double protected derivative Fmoc-FFFF-OBzl brought to the formation of volcano-like structures, triaxial ellipsoid-like nodules, and nanotubes (Mayans et al., 2015). Moreover, tetraphenylalanine derivatives in which the aromatic framework is derivatized with the Fmoc group (Fmoc-FFFF) or with polymeric chains such as polyethylene glycole, polycaprolactone, or polyethylene oxide keep a β-sheet structure (Castelletto and Hamley, 2009; Tzokova et al., 2009a,b; Diaferia et al., 2015, 2016a). Analogously to tetra-Phe also penta-Phe self-assembles into fibrillary structures in acetic acid, even though spectroscopic assays made by measuring Thioflavin T fluorescence are negative and the aggregates are not able to exhibit autofluorescence (Arnon et al., 2015).

Although biophysical characterizations of these assemblies provide some information on their structural preferences, models that illustrate their structures at atomic level are difficult to be experimentally obtained. Indeed, the intrinsic propensity of these systems to form fibers, which are generally twisted, disfavors the crystallization process. Moreover, their repetitive sequences make multiple associations between monomers energetically favorable, for example through alternative staggering of the pairing chains, which also have a negative impact on the growth of ordered crystals. Moreover, for very small peptides crystal packing may have a dramatic impact on their conformation. Therefore, crystalline states may not be fully representative of the real structure of these assemblies. Finally, the limited size of the basic spine of these assemblies makes the cryoEM technique hardly applicable.

A significant contribution to this field has been provided by the application of computational approaches (see for example López-Pérez et al., 2013; Do et al., 2015). Molecular modeling and molecular dynamics (MD) studies have indeed provided an atomic level description for F_6 assemblies and demonstrated that Phe residues can tightly pack in anhydrous and rigid interfaces that stabilize the cross-β motif (Diaferia et al., 2016b, 2018a; **Figure 8**). These analyses have shown that Phe-side chains of facing β-sheets, although not interdigitated, establish repetitive and regular interactions that are quite common also in globular structures (**Figure 8B**). Similar arrangements into cross-β assemblies have been observed for other aromatic peptides based on either Tyr or Trp residues (e.g., Y_6 and W_4) (Diaferia et al., 2018b,c). MD simulations have also provided insights into the role that intra-sheet Phe-Phe interactions along with the terminal charged groups play in directing the associations of the β-strands, either parallel or antiparallel, within the β-sheets (Diaferia et al., 2018a). As mentioned above, the discovery of the FF self-assembling properties also stimulated the search for small, and even smaller than FF, aggregating systems. Limiting the size of the self-assembling entity has many synthetic

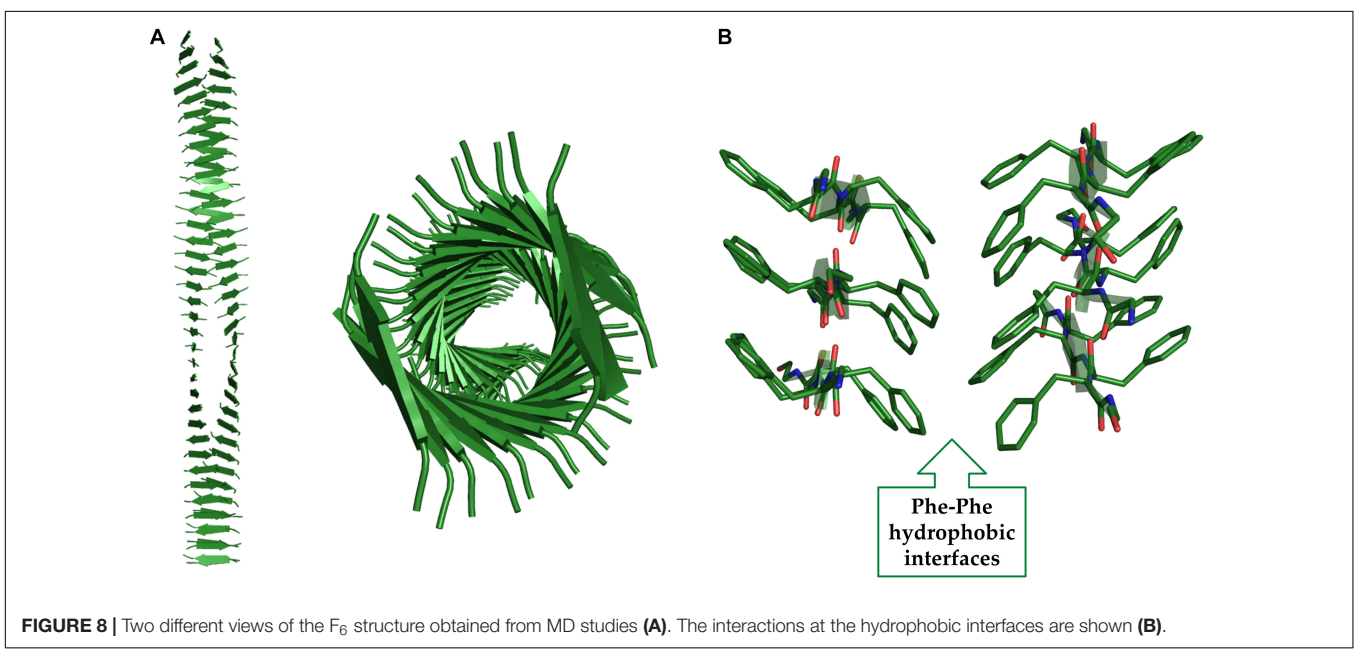

FIGURE 8 | Two different views of the F_6 structure obtained from MD studies **(A)**. The interactions at the hydrophobic interfaces are shown **(B)**.

advantages and reduces the costs of preparation of the resulting biomaterials. In this framework, many other natural occurring short and ultra-short peptide sequences demonstrated their tendency to self-assemble into ordered nanostructures (Frederix et al., 2015). For many years, it was assumed that dipeptides could represent the minimal entities able to allow generation of complex supramolecular structures due to the unique physicochemical properties of the amide bond. Only ten years after the identification of FF, Gazit and co-workers evaluated the possibility that, under specific conditions, also single amino acids could self-associate. This pioneering study was inspired by the evidence that many short amyloid-forming peptides contain non-consecutive phenylalanine residues (Gazit, 2002) as for example FGAIL and QRLANFLVH fragments of IAPP, NFGSVQFV of lactadherin protein, and SFNNGDCCFILD of gelsolin. In an independent analysis, Dobson and coworkers highlighted that aromatic amino acids, such as Phe and Trp, are the most amyloidogenic ones (Pawar et al., 2005). Although aromaticity is not an essential requirement for amyloid formation, it is clear that π-π interactions between aromatic moieties may accelerate the process of amyloid formation, especially for ultrashort peptide sequences in which the contribution of the hydrogen bonding is limited (Makin et al., 2005).

The first unmodified amino acid tested for its aggregating properties was Phe. The interest for the aggregation of this amino acid was also generated from the evidence that the congenital metabolic disorder phenylketonuria (PKU) is due to the accumulation of high levels of Phe in different portions of the brain, cerebrospinal fluid, and plasma (Kaufman, 1999). By using a series of biophysical techniques, which included electron microscopy, diffraction, thioflavin T and Congo red assays, it was demonstrated that at millimolar concentrations, phenylalanine could self-assemble into ordered nanofibrillar structures resembling amyloids (Adler-Abramovich et al., 2012). However, as detailed below, more recent studies have shown that structural characterization of Phe amyloid-like aggregation is not straightforward, thus demonstrating, once again, that the definition of the structure of assemblies formed by minimal peptide fragments may be a complicate task. In 2013, Perween et al. reported a further investigation on the aggregation properties of Phe in water solution under neutral pH. Although their analysis suggested that Phe self-assembles through different interactions such as hydrogen bonds and electrostatic interactions formed by the amino acid ends and π-π interactions established by the phenyl groups of adjacent molecules, no β-sheet structure was observed (Perween et al., 2013). The ability of the Phe amino acid to make multiple interactions was confirmed by the determination of a novel crystalline form of the zwitterionic L-phenylalanine (Mossou et al., 2014). In this monoclinic crystalline form, four Phe molecules are present in the asymmetric unit (Mossou et al., 2014). Phe layers are stabilized by alternating hydrophobic (aromatic environment) and hydrophilic interactions. Further information on the mechanism of assembly of phenylalanine oligomers and fibrils were obtained using ion-mobility mass spectrometry and theoretical calculations (Do et al., 2015). This study suggests that the Phe aggregation involves the formation of pore-like tetrameric oligomers. These layers of tetramers stack on top of each other to form an elongate structure and build multiple core structures through lateral π-stacking interactions.

Not surprisingly, later studies demonstrated the influence of the charged state of Phe ends on the morphology of the aggregates. In particular, in its zwitterionic state, Phe self-assembles into nanostructures with a fibrillary morphology, while in its cationic and anionic state, its aggregates are dominated by a flake morphology (Tomar et al., 2019). Moreover, several studies were also oriented to investigate different aggregation properties and kinetics of *L* and *D*-Phe. Both the isomers were found able to generate micrometer-long singular fiber structures, very similar to the amyloid-like assemblies. The crystal structure analysis of the pure Phe enantiomers highlighted that this aromatic amino acid self-organizes as consequence of hydrogen bonding and polar interactions between NH_3^+ and COO^- groups in neighboring molecules. On the other hand, the authors observed that both kinetics and final morphologies were significantly altered in *L/D* co-assembling samples (Bera et al., 2020). Specifically, the *DL*-Phe racemate showed inhibition of fiber organization with the formation of crystalline flake-like structural assemblies with a consequent difference also in the Young's moduli (53.5 ± 12.1 GPa for *DL*-Phe composite system respect to 5.8 ± 0.7 and 1.8 ± 0.3 GPa for L- and D-isomer one, respectively). Dynamic simulations reveal that the chirality of amino acids and the lack of central symmetry in the crystals formed by these molecules promote crystal bending. The overall picture delineated above is further complicated by the discovery that Phe aggregates exhibit optical properties with a fluorescent emission peak at 485 nm that overlaps with the fluorescence emission spectra of the ThT/β-structure adduct. This result indicates that false-positive can occur in the ThT assay, which is generally used as a probe for amyloid structure. This evidence also suggests that this assay cannot be used to assess the amyloid nature of Phe aggregates (Ziaunys and Smirnovas, 2019).

Obviously, the possibility that other amino acids could exhibit self-assembling properties has been explored in the last decade. Exactly as for Phe, Tyr accumulation, which is due to the abnormal metabolic behavior of the tyrosine transaminase (TT) enzyme, was identified as the cause of tyrosinemia type II, another neurodegenerative disorder (Banik et al., 2017). The capability of Tyr to self-assemble was initially documented by Perween at al (Perween et al., 2013). They observed the formation of straight fibers with a flat ribbon-like texture from an aqueous solution of Tyr at a concentration of 1 mM, although the authors were not able to detect any typical signature of secondary structure adopted by the amino acid in these assemblies. No evidence for amyloid formation was found on different aggregates (fiber, dendrimeric structures and nanoribbon strip-like nanostructures) of Tyr obtained by varying its concentration (Mènard-Moyon et al., 2015). On the other hand, Gazit and coworkers pointed out the capability of Tyr to form amyloid resembling fibers, when aggregation occurs under different experimental conditions of pH (PBS), temperature (90°C), and concentration (∼22 mM) (Shaham-Niv et al., 2015). It seems, however, that the formation of Tyr amyloid fibers follows a different self-assembly process

compared to that observed for Phe. Indeed, Banik et *al.* (Banik et al., 2017) demonstrated that in Tyr assemblies the H-bonding partner of the COO^- group is the OH present in its side chain whereas the carboxylate interacts with the NH_3^+ group in Phe aggregates. The self-assembling properties of unmodified tryptophan, which accumulates in pathological conditions related to two inborn errors of metabolism (hypertryptophanemia and Hartnup disease), were studied (Singh et al., 2017). On analogy with Tyr and Phe, this amino acid may form amyloid-like assemblies in specific conditions (at a concentration of ∼19.5 mM in phosphate buffer) (Shaham-Niv et al., 2017). On the other hand, in ethanol Trp self-assembles in nanotubes able to emit fluorescence when excited at 385 (blue), 488 (green), and 561 (red) nm (Babar and Sarkar, 2017). Several reports suggest that, despite the absence of π-π stacking interactions, also other amino acids like glycine, cysteine, methionine, and histidine can form ordered amyloid-like structures at millimolar concentrations (Gour et al., 2019). Structural studies highlighted that in these amino acids the fibril formation is prompted by hydrogen bonding occurring between the charged terminal groups NH_3^+ and COO^-. This suggestion is supported by the observation that Cys and Met aggregates are amorphous in nature and can be obtained only under neutral pH conditions.

Finally, the growing evidences that pathological states of some inborn metabolic diseases could be correlated to the increase of endogenous metabolites prompted the researchers to evaluate the possibility that these metabolites could self-aggregate into amyloid-like structures (Shaham-Niv et al., 2015). In this scenario, Gazit and co-workers studied aggregation phenomena of some metabolites (adenine, orotic acid, cystine, tyrosine, uracil, and phenylalanine). Based on their observations, they suggest that the concept of amyloid aggregation could be also extended to non-peptidic chemical entities.

CROSS-β HYDROGELS FORMED BY PROTEINS AND PEPTIDES

The β-structure in general and the cross-β motif in particular have also played a remarkable role in the development of peptide-based hydrogels (HG). HGs are self-supporting materials, structured as a supramolecular hydrophilic network associated with the construction of space-spanning structures characterized by a non-Newtonian behaviour (De Leon Rodriguez M. R. et al., 2016; Rivas et al., 2019). Their hydrophilic nature allows the entrapping of a high volume of biological fluids and water in the swelling process. Due to their appealing features, in the last years HGs have been exploited as versatile and innovative tools in nanomedicine as 3D-extracellular matrices for tissue engineering and regeneration, wound healing systems, ophthalmic compatible materials, and drug delivery systems (Yan and Pochan, 2010; Draper and Adams, 2017; Diaferia et al., 2019c). The specific 3D-connectivity of HGs may be generated by either a chemical irreversible junction (e.g., chemical bonds) or *via* non-covalent interactions (e.g., π-stacking, cation-π interaction, Van der Waals forces, and hydrogen bonding). Based on the different association modes of their basic components, HGs are broadly categorized as physically or chemically cross-linked materials. Moreover, based on their origin, HGs can be also classified as synthetic [e.g., poly(acrylic acid), poly(ε-caprolactone), poly(lactic acid), poly(glycolic acid)] or natural hydrogels (e.g., glycosaminoglycans, fibrin, chitosan, collagen) (Li et al., 2020).

Protein-Based Hydrogels With Cross-β Structure

Proteins are attractive systems for generating HGs due to some specific properties that include biocompatibility, biodegradability, tunable mechanical properties, molecular binding abilities, and responses to external stimuli. They contain several functional and reactive groups that can be exploited for cross-linking. Interestingly, some proteins can form HGs without any chemical modification. Indeed, HGs may be occasionally formed by proteins in their misfolded states. Interesting examples include elastin (Flamia et al., 2007), α-synuclein (Bhak et al., 2010), lysozyme (Yan et al., 2006; Mains et al., 2013), Escherichia coli inner membrane protein YajC (YajC-CT) (Fang et al., 2011), and β-lactoglobulin (Gosal et al., 2004; Bolisetty et al., 2012), which were found able to self-aggregate, under specific conditions, into amyloid hydrogels of different nature in terms of stiffness, elasticity and biodegradability.

The low level of order of these HGs makes their atomic-level characterizations virtually unfeasible. A number of different biophysical techniques such as Thioflavin-T binding fluorescence, Congo red birefringence, Fourier Transform Infrared (FTIR), Transmission Electron Microscopy (TEM), Atomic Force Microscopy (AFM), cryo-Scanning Electron Microscopy (cryo-SEM) and Small-Angle Neutron Scattering (SANS) are generally used to assess their amyloid-like state. The molecular complexity of proteins and their articulated sequences make also difficult to identify their aggregation prone regions that constitute the spine of the HG. For elastin, some structural information on the aggregating region has been obtained through the characterization of the VGGVG pentapeptide and of the amyloids formed by poly(VGGVG) (Flamia et al., 2007).

Peptide-Based Hydrogels With Cross-β Structure

The ability of peptides to self-assemble in cross-β structures has also been exploited for the development of innovative HGs (De Leon Rodriguez M. R. et al., 2016). Synthetic peptides exhibit a variable capability to gelificate depending on their amino acid sequence, hydrophilic/hydrophobic balance, net charge, and length. Experimental conditions such as peptide concentration, presence and concentration of electrolytes, the pH of the solution, and temperature can differently affect the functional and structural properties of the resulting hydrogel.

The gelation properties of peptides are also strongly affected by specific conjugations and modifications. A strategy that has been proposed for controlling mechanical and degradation properties of hydrogels, as well as to enhance their biocompatibility, is the functionalization of the peptide sequence with polymeric moieties. The advantage provided by the use of peptide-polymer

conjugates is the chance to combine the features of each component into a unique building block (Redvar and Azevedo, 2019). Due to its high biocompatibility, water solubility and, long circulation time *in vivo*, poly(ethylene glycol) (PEG) has been exploited as polymer for derivatization of peptides to employ in the hydrogel formulation (Hamley, 2014). Peptide derivatization with PEG moiety was performed according to two different architectures of the conjugate: triblock (peptide-PEG-peptide) or diblock (PEG-peptide). However, it is worth noting that all peptides derivatized with PEG gelificate forming soft hydrogels with a storage modulus ranged between 10 and 100 Pa at a concentration < 5wt%. The gelation tendency of peptides may be deeply affected by their conjugation to aromatic groups such as Fmoc (fluorenylmethylcarbonyl) or naphthyl group. In this case, the hydrogelation process is favored by the additional stabilization effect (π–π stacking) due to the aromaticity of these molecules. Owing to this further stabilization effect, also very short peptide sequences containing either aromatic or non-aromatic amino acids were found to be able to gelificate. In extreme cases, the derivatization with the Fmoc group allows gelification of single amino acids (See also below). (Dasgupta et al., 2013; Fleming and Ulijn, 2014; Adler-Abramovich and Gazit, 2014).

Due to their simpler molecular complexity compared to proteins, the inspection of the sequences of peptides able to form HGs may provide insights into the structure of the final assemblies. In the most frequent cases, hydrogels are formed by peptides that present an alternation of amino acids in their sequences, typically polar/charged residues with apolar ones.

In addition to these peptides with alternating sequences, other HG forming peptides are made of stretches of hydrophobic and hydrophilic residues with the former assuring the formation of the cross-β structure and the latter contributing to the solubilization and to the interactions with the solvent. In the following paragraphs, HG-forming peptides are categorized and subcategorized using this conceptual framework. A specific section is dedicated to the HGs formed by very small peptides (dipeptides) and single amino acids (**Table 1**).

TABLE 1 | Classification of peptide-based hydrogels assuming a cross-β structure with the relative reference.

HGs formed by peptides with alternating sequences	
Alternation of apolar residues with both positively and negatively charged residues	**Alternation of apolar residues with either positively or negatively charged residues**
Ac-(AEAEAKAK)$_2$-NH$_2$ [1]	PE(LE)$_5$P-OH[12]
Ac-RADARADARADARADA-NH$_2$[2]	Ac-(IKIK)$_2$-NH$_2$[13]
Ac-RARADADARARADADA-NH$_2$[2]	Ac-(FKFK)$_2$-NH$_2$[13]
Ac-(FKFE)$_n$-NH$_2$; n = 2,3,4[3]	Ac-(F5FKF5FK)$_2$-NH$_2$[13]
FEFEFKFK-OH [4]	Ac-(ChaKChaK)$_2$-NH$_2$[13]
(FEFEFKFK)$_2$-OH[5]	Ac-(VK)$_5$-NH$_2$[13]
Ac-(VKVE)$_3$-NH$_2$[6]	(VK)$_4$V-NH$_2$[13]
VKVKVEVK-OH[7]	(VK)$_5$V-NH$_2$[13]
VEVKVEVK-OH[7]	(VK)$_6$V-NH$_2$[13]
VEVEVEVK-OH[7]	(VR)$_6$V-NH$_2$[14]
Ac-(IKIE)$_3$-NH$_2$[8]	(IK)$_6$I-NH$_2$[14]
Ac-RLDLRLALRLDLR-NH$_2$[9]	(LK)$_6$L-NH$_2$[14]
FFKLVFF-PEG2k[10]	Ac-(AAAK)$_3$-NH$_2$[15–17]
FFKLVFF-PEG3k[10]	Ac-(AAAK)$_4$-NH$_2$[15–17]
VEQLTEEQKNEFKAAFDIFVLGA-OH[11]	VKVKVKVKV^{D}PPTKVKVKVKV-NH$_2$[18]
Alternation of apolar and uncharged polar residues	**Gln-rich peptides**
PEG8-(FY)$_3$-NH$_2$[19]	Ac-QQRQQQQQEQQ-NH$_2$[23]
H-(Nal-DOPA)$_3$-NH$_2$[20]	Ac-QQRFQWQFEQQ-NH$_2$[23]
Ac-K$_2$(SL)$_6$K$_2$-NH$_2$[21]	Ac-QQKFQFQFEQQ-NH$_2$[24]
Ac-K$_2$(QL)$_6$K$_2$-NH$_2$[21]	
Ac-K$_2$(TL)$_6$K$_2$-NH$_2$[21]	
GSFSIQYTYHV-OH[22]	
HGs formed by blocks of polar/apolar stretchs	**HGs formed by conjugating single amino acids or dipeptides**
Ac-LIVAGD-OH[25]	Fmoc-F[30]
Ac-LIVAGDD-OH[25]	Fmoc-Y[31]
Ac-IVAGD-OH[25]	Fmoc-FF-OH[32,33]
Ac-IVD-OH[25]	Fmoc-FG-OH[34]
Ac-ILVAGD-OH[25]	Fmoc-DOPA-DOPA[35]
Ac-ILVAGS-OH[25]	Fmoc-F-Nphe[36]
Pal-VVVAA-EEE-OH[26]	Fmoc-Nphe-F[36]
Pal-VVAAA-EEE-OH[26]	Fmoc-Nphe-Nphe[36]
Pal-AAAVVV-EEE-OH[26]	Nvoc-FF[37]
Pal-VVVAAAA-EEE-OH[26]	
Pal-VVVAAA-EEE-OH[26]	
Pal-VVAA-EEE-OH[26]	
Pal-VVVVAA-EEE-OH[26]	
Pal-VVAAAA-EEE-OH[26]	
Pal-AAAVVV-EEE-OH[26]	
Pal-GGGGGGG-ERGDS-OH[27]	
Pal-GGGGGGNMeG-ERGDS-OH[27]	
Pal-GGGGGNMeGG-ERGDS-OH[27]	
Pal-GGGGNMeGGG-ERGDS-OH[27]	
Pal-GGGGGNMeGNMeG-ERGDS-OH[27]	
Pal-V$_3$K$_2$-NH$_2$[28]	
Lar-V$_3$K$_2$-NH$_2$[28]	
Myr-V$_3$K$_2$-NH$_2$[28]	
Myr-AA-OH[28]	
GSSAAAAAAAASGPGGYGPENQG PSGPGGYGPGGP[29]	

[1] Zhang et al. (1993a,b), [2] Yokoi et al. (2005), [3] Swanekamp et al. (2014), [4] Saiani et al. (2009), [5]Wang et al. (2005), [6] Bowerman et al. (2011), [7] Roberts et al. (2012), [8] Caplan et al. (2002): [9] Nagai et al. (2012), [10] Castelletto et al. (2010), [11] De Leon-Rodriguez L. M. et al. (2016), [12] Rapaport et al. (2008), [13] Bowerman et al. (2011), [14] Geisler and Schneider (2012), [15] Measey and Schweitzer-Stenner (2006), [16] Measey et al. (2010), [17] Jang et al. (2009), [18] Nagy-Smith et al. (2015), [19] Diaferia et al. (2018b), [20] Diaferia et al. (2020), [21] Galler et al. (2010), [22] Frohm et al. (2015), [23] Davies et al. (2006): [24] Dawson et al. (1994), [25] Mishra et al. (2011), [26] Pashuck (2010): [27] Paramonov et al. (2006), [28] Wang et al. (2015), [29] Schacht and Scheibel (2011), [30] Singh et al. (2015), [31] Yang et al. (2021), [32] Mahler et al. (2006), [33] Jayawarna et al. (2006), [34] Tang et al. (2011), [35] Fichman et al. (2014a), [36]Rajbhandary and Nilsson (2017), [37] Roth-Konforti et al. (2018).

Hydrogels Formed by Peptides With Alternating Sequences

In the β-structure arrangement, peptide sequences with an alternation of apolar and polar/charged residues direct their side chain in opposite directions, thus forming a hydrophobic and a hydrophilic face. The tight and rigid association of the two apolar faces generates the basic cross-β motif that constitutes the spine of the filaments within the HG. On the other hand, the hydrophilic interfaces interact with the solvent and mediate the interaction of different filaments in a non-regular way. However, it is worth noting that the nature of the polar/charged residues can strongly affect the possible interactions between the solvent and the exposed faces. The polar/charged residues may also stabilize the cross-β structure by making inter-sheet interactions with residues of adjacent strands. This class may be further subdivided based on the type of polar/charged residues present in the sequence. Indeed, the nature of these residues strongly affects the possible interactions between the solvent and the exposed faces. Since,

within the same sheet, these residues can interact with those of adjacent strands, their presence also influences the type (parallel or antiparallel) of β-structure. It is likely that the simultaneous presence of both positively and negatively charged residues in the sequence may stabilize the cross-β motif and the formation of antiparallel β-sheets. On the other hand, the presence of only negatively or positively charged residues in the sequence may interfere with the association of the cross-β filaments in the HG. These evidences are detailed in the two next sections.

Alternation of Apolar Residues With Both Positively and Negatively Charged Residues

The prototype of this class of self-assembling peptides is EAK [Ac-$(AEAEAKAK)_2$-NH_2], which was designed and characterized by Zhang and co-authors (Zhang et al., 1993a). The sequence of this peptide exhibits an alternation of aliphatic (Ala) and ionic (Lys and Glu) residues. The dry interface of this peptide is built through the interdigitating of the methyl group of Ala side chains, a residue that has the well-defined ability to make this kind of assemblies. MD analyses indicate that this inter-sheet interface, which is approximately 6.5 Å wide, is rather rigid and confers a remarkable stability to the assembly (Calvanese et al., 2020). This study also indicates that interactions formed at the hydrophilic interface by the charged side chains contribute to the stabilization of the individual sheets present in the assembly. Over the years, EAK inspired the development of self-assembling peptides based on the same basic features i.e., the alternation in the sequence of Ala residues with positively or negatively charged residues. The peptides RADA16-I (Ac-RADARADARADARADA-NH_2) and RAD16-II (Ac-RARADADARARADADA-NH_2) are widely studied variants of EAK that share with the parent peptide the overall structural organization (Yokoi et al., 2005).

A similar conceptual approach has been used to develop new classes of self-assembling peptides by replacing Ala with other hydrophobic residues such as Phe (FEFEFKFK-OH, $(FEFEFKFK)_2$, Ac-$(FKFE)_2$-NH_2, Ac-$(FKFE)_3$-NH_2, and Ac-$(FKFE)_4$-NH_2), Val (Ac-$(VKVE)_3$-NH_2, VKVKVEVK-OH, VEVKVEVK-OH, and VEVEVEVK-OH), Ile (Ac-$(IKIE)_3$-NH_2), and Leu (Ac-RLDLRLALRLDLR-NH_2) (**Table 1**; Caplan et al., 2002; Wang et al., 2005; Saiani et al., 2009; Nagai et al., 2012; Roberts et al., 2012; Swanekamp et al., 2014). To this class, it can also be associated the peptide isolated from the protein troponin C (VEQLTEEQKNEFKAAFDIFVLGA-OH) (De Leon-Rodriguez L. M. et al., 2016). Although this peptide does not display a repetitive sequence, hydrophobic residues that can generate the hydrophobic interface can be identified in the sequence (H-KNEFKAAFDIFV-OH). These residues are surrounded by several charged ones that will be located on the hydrophilic face of the assembly.

Alternation of Apolar Residues With Either Positively or Negatively Charged Residues

A variation on the theme of the peptides displaying an alternation of hydrophobic residues with positively and negatively charged ones is represented by the class of peptides in which the apolar residues alternate exclusively with either negative or positive residues. The absence in these peptides of pair of residues that can form electrostatic interactions has an impact on both the stabilization of the individual sheets and on the lateral association of independent cross-β filaments.

Examples of peptides presenting only negative residues include the acidic β-sheet forming peptides (AAβP) that present the sequence $PY(XY)_5P$, where Y is either Glu or Asp and X is either Phe or Leu. The pH value often plays a key role in the assembling of these alternating peptides into HGs. For example, the $PE(LE)_5P$-OH peptide is able to form hydrogel only at a neutral pH value, where deprotonation of the acidic side chains occurs (Rapaport et al., 2008). As alternative, gelification of these negatively charged peptides was observed at low concentration in presence of Ca^{2+} ions. The coordination of this metal by the negatively charged side chains is an effective way to crosslink different cross-β filaments.

Positively charged β-sheet forming octapeptides with general sequence Ac-$(XKXK)_2$-NH_2, where X is Val, Ile, Phe, pentafluorophenylalanine (F5-Phe) or cyclohexylalanine (Cha), were able to gelificate in soft or hard hydrogels for non-aromatic or aromatic residue containing sequences, respectively. It is worth noting that gel formation by all these peptides, with the exception of Ac-$(VKVK)_2$-NH_2, occurs only at high values of ionic strength, where the electrostatic repulsions between the positive charges on lysine side chains are minimized (Bowerman et al., 2011). Lack of gelification in Ac-$(VKVK)_2$-NH_2 was attributed to the low hydrophobic interactions established by the valine residues. Indeed, it was observed that longer variants of this peptide such as (VK)nV-NH_2 (with n = 4, 5, 6) and $(VR)_6$V-NH_2 were able to self-assemble into hydrogels (Geisler and Schneider, 2012). Successively, a systematic analysis of the aggregation properties of peptides obtained by replacing the valine residues in the sequence of the hydrogelator Ac-$(VK)_n$V-NH_2 with other aliphatic residues such as Ala, Ile or Leu highlighted the role of the hydrophobicity in the gelification process (Bowerman et al., 2011).

Later, other nine peptides presenting an alternation of hydrophobic (Leu and Ala) and hydrophilic positively charged (Lys and Arg) residues in their sequence were exploited as starting building blocks for the preparation of self-supporting hydrogels (Geisler and Schneider, 2012). Although these peptides exist in a random coil conformation in water, they undergo to aggregation phenomena upon addition of a buffered saline solution, by initially forming a β-sheet rich network of fibrils, ultimately leading to hydrogelation. Others two amphipathic variants of positively charged peptides (e.g., Ac-$(AAAK)_3$-NH_2 and Ac-$(AAAK)_4$-NH_2) that were able to form hydrogels at particularly low concentrations were then reported by Schweitzer-Stenner and coworkers (Measey and Schweitzer-Stenner, 2006; Jang et al., 2009; Measey et al., 2010).

The MAX1 peptide and its analogs also belong to this class (Dasgupta et al., 2013). MAX1 sequence (VKVKVKVK-V^DPPT-KVKVKVKV-NH_2) contains a tetrapeptide (V^DPPT) assuming type II' β-turn conformation in the middle of two extended strands with alternating hydrophobic (Val) and positively charged (Lys) residues (**Table 1**). Solid-state NMR characterization on self-assembled MAX1 in its fibrillary state

pointed out that the peptide in the gel adopts a β-hairpin conformation and self-assembles into a double-layered cross-β structure (Nagy-Smith et al., 2015). Moreover, hairpins assemble with four probable structures differing in the nature of intermolecular alignments within and between the β-sheets.

Alternation of Apolar and Uncharged Polar Residues

The presence of charged residues in the peptides whose sequence presents an alternation of polar and apolar residues is not essential for aggregation and gelation. A remarkable example in this context is represented by the peptide H-$(FY)_3$-NH_2 (Diaferia et al., 2018b). This peptide presents a strong tendency to form fibrillar solid aggregates whose three-dimensional structure has been derived by combining Wide Angle X-ray Scattering (WAXS) data with molecular modeling and dynamics. The basic structural element of these assemblies formed by H-$(FY)_3$-NH_2 contain two distinct interfaces: a hydrophobic and highly rigid one made by the interactions of Phe residues and an hydrophilic one constituted by interacting Tyr side chains of facing strands (**Figure 9**). The conjugation of this peptide with the PEG moiety increases its solubility and leads to the formation of a hydrogel in which the Phe interface is likely retained in this state while the Tyr one is probably destabilized by the interaction with the solvent. In this conceptual framework it is not surprising that the peptide analogue H-$(Nal\text{-}DOPA)_3$-NH_2 (in which Nal is the 2-naphthylalanine and DOPA is the 3,4-dihydroxy-L-phenylalanine), designed as more hydrophilic variant of H-$(FY)_3$-NH_2 is able to form HGs without any type of PEG conjugation (Diaferia et al., 2020). The series of SL peptides (Ac-$K_2(SL)_6K_2$-NH_2, Ac-$K_2(QL)_6K_2$-NH_2 and Ac-$K_2(TL)_6K_2$-NH_2) also belongs to this type of HG-forming peptides, in which Leu and Ser residues make the hydrophobic and hydrophilic interfaces, respectively (Galler et al., 2010). Finally, an alternation of apolar/aromatic and non-charged polar residues may be identified in the natural peptide extracted from the semenolegin I protein (GSFSIQYTYHV-OH) that can be also associated to this class (Frohm et al., 2015).

Gln-rich peptides deserves a special description as they present some peculiar sequence features. Indeed, the capability of Gln to be part of both the internal and the external face of the cross-β motif (see for example **Figure 6**) makes these peptides particularly appealing. This ability is evident in the sequences of the cross-β peptides denoted as P11-I (Ac-QQRQQQQQEQQ-NH_2) and P11-II (Ac-QQRFQWQFEQQ-NH_2) in which Gln residues are frequently consecutive in the sequences (Davies et al., 2006). In P11-I the external face of the sheet includes the charged residues Arg and Glu that also favor the antiparallel orientation of the β-strands within the sheet. In P11-II, the cross-β motif is reinforced by replacing some internal Gln residues with other hydrophobic residues such as Phe and Trp. Above a critical concentration, P11 peptides are able to assemble into hydrogen-bonded β-sheet tapes. The further increase of concentration can lead to higher order structures compared to tapes. Indeed, since the amphiphilic tapes are endowed with both hydrophilic and hydrophobic faces, they can pair into ribbons which, in turn, can stack into fibrils and fibers through further intermolecular interactions (Collier and Messersmith, 2003). Based on P11–II, Collier and coworkers developed the β-sheet-forming peptide Q11 (Ac-QQKFQFQFEQQ-NH_2), which can be covalently bound to bioactive molecules containing Lysine residues via tissue transglutaminase (Dawson et al., 1994). In this uncharged peptide the combination of the alternating FQFQF core and the short polyglutamine repeats allows the formation of stiff hydrogels.

Hydrogels Formed by Blocks of Polar/Apolar Stretchs

Another important class of peptides that can self-organize into β-sheet hydrogels is represented by amphiphilic peptides that present stretches of hydrophobic and hydrophilic residues. This class of peptides can be further sub-classified into: (i) surfactant like peptides (SLPs), and (ii) classical peptide amphiphiles (PAs). SLPs have a general formula X_mY_n, where X is a hydrophobic amino acid (e.g., Gly, Ile, Leu, Val) and Y a polar charged amino acid (e.g., Asp, Glu, His, Lys, or Arg) and m and n are ranged between 3 to 8 and 1 to 2, respectively. Example of SLPs able to self-assemble into stiff hydrogels are Ac-LIVAGD-OH, Ac-LIVAGDD-OH, Ac-IVAGD-OH, Ac-IVD-OH, Ac-ILVAGD-OH, and Ac-ILVAGS-OH (Mishra et al., 2011). The rheological

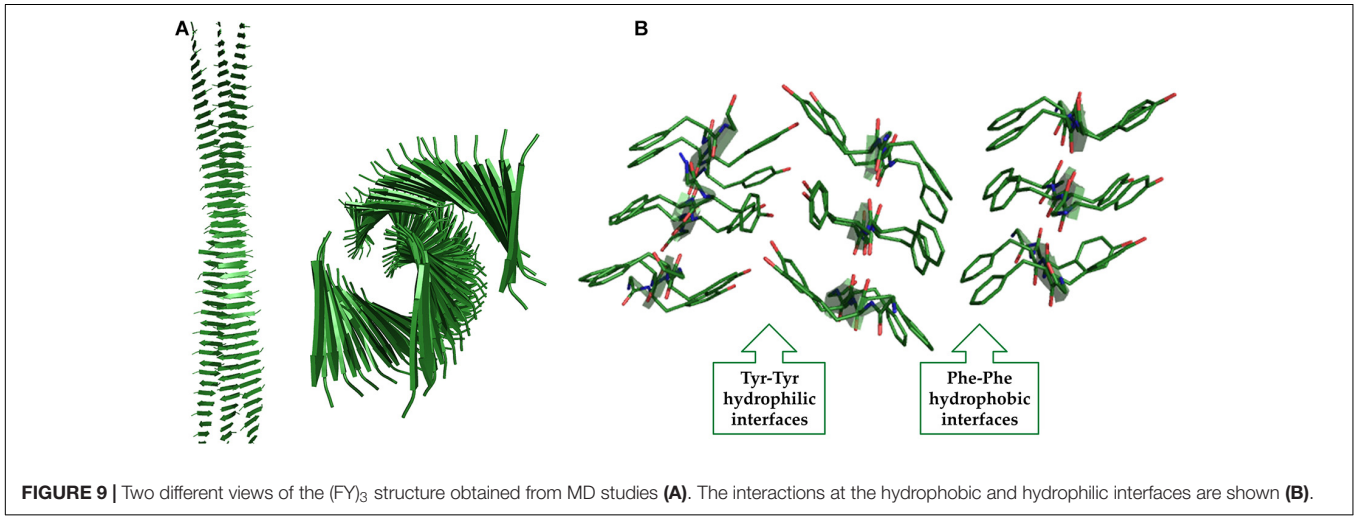

FIGURE 9 | Two different views of the $(FY)_3$ structure obtained from MD studies **(A)**. The interactions at the hydrophobic and hydrophilic interfaces are shown **(B)**.

characterization of these gels highlighted that the length of the hydrophobic moiety and the polarity of the head group drastically affect the stiffness of the resultant hydrogel.

On the other hand, PAs contain a peptide sequence composed by a head group and a β-sheet inducer segment, which is in turn connected to a hydrophobic aliphatic tail of variable length. Nanofibers formation in PAs is allowed by the combination of hydrophobic interactions between the alkyl tails and hydrogen bonds between the side chains of the head group. A significant number of PA-based hydrogels have been described in literature for biomedical applications (De Leon Rodriguez M. R. et al., 2016; Machado et al., 2019; Diaferia et al., 2019d). Examples of PAs able to form hard hydrogels characterized by a cross-β sheet motif, with the general formula Pal-V_nA_n-EEE-OH (where n = 2, 3, 4), are Pal-VVVVAA-EEE-OH, Pal-VVAAAA-EEE-OH, and Pal-AAAVVV-EEE-OH, in which the hydrophobic tail is represented by the palmitoyl and the peptide sequence contains a variable number of Ala and Val residues and a tri-Glu head peptide, which promotes a stimuli-triggered peptide assembly (Pashuck et al., 2010). A similar structural transformation from twisted to helical ribbons was also observed in the PA containing three Phe residues (Pashuck and Stupp, 2010; Pashuck et al., 2010). As expected, in the series Pal-V_nA_n-EEE-OH, the hydrogel rigidity was found to be the highest for the longest peptide sequences, whereas the substitution of Val with Ala (as for example Pal-VVAAAA-EEE-OH compared to Pal-VVVVAA-EEE-OH) causes a dramatic decrease of the mechanical properties of the resulting hydrogels. This result is obviously due to the lower propensity of Ala residue to favor β-sheet assembly than Val. On the other hand, it was observed that the length of the aliphatic tail does not significantly affect the mechanical properties of PA-based hydrogels (Wang et al., 2015).

Other examples of PAs able to generate hydrogels are those containing the hepta-Gly peptide (Pal-GGGGGGG-ERGDS-OH) and its analogs in which one or more Gly residues in the sequence are replaced with NMeGly (N-Methyl-Glycine) (Paramonov et al., 2006). Due to the lower tendency of Gly to self-assemble into β-sheet, hepta-Gly peptides form soft hydrogels.

In 2011, Schacht et al. described another hydrogel based on the β-sheet forming peptide sequence from silk proteins, eADF4(C16) (GSSAAAAAAAASGPGGYGPENQGP SGPGGYGPGGP) containing 16 repeat units of module C. (Schacht and Scheibel, 2011). The eADF4 hydrogel formation occurs through a transformation from an initial random coil structure to α-helices, and eventually to β-sheets. The authors achieved an increase of stability and of mechanical stiffness in the hydrogels by chemically cross-linking tyrosine side chains.

Hydrogels Formed by Conjugating Single Amino Acids or Dipeptides

As mentioned above, the derivatization with Fmoc-group of small peptides and even single amino acids allows gelification (Dasgupta et al., 2013; Adler-Abramovich and Gazit, 2014; Fichman and Gazit, 2014; Fleming and Ulijn, 2014; Singh et al., 2015; Yang et al., 2021). Indeed, it is well known that the capability of small molecules to gelificate is strictly related to their hydrophobicity. Commonly, the total hydrophobicity is reported as logP, where P (repartition coefficient) is the ratio of concentrations at equilibrium of a compound in the two phases of a mixture made by two immiscible solvents. In line with this consideration, some of the Fmoc peptide derivatives have been deeply investigated as suitable building blocks for self-supporting hydrogels preparation. One of the most studied and promising dipeptide is Fmoc-FF-OH. The interest toward Fmoc-FF is to research into its capability of gelificate at physiological pH, compatible with biomedical applications (such as tissue engineering and drug delivery). Fmoc-FF firstly synthesized by Reches and Gazit (2005), self-assembles into macroscopic fibrous hydrogels above a critical concentration of 0.5%wt. Hydrogel formation is achieved either using the "solvent switch" method (Mahler et al., 2006), or as reported by Ulijn and co-workers, using the "pH-switch" method (Jayawarna et al., 2006). Structural studies on Fmoc-FF hydrogels allowed the proposal of a plausible theoretical aggregation model, in which peptide copies are arranged into a nanocylindrical structure (with a diameter of ∼3.0 nm) due to the interlocking through lateral π-π interactions of four twisted anti-parallel β-sheets. Under optimal pH conditions, lateral assembly of the nanostructures causes the formation of large flat ribbons. In the attempt to design novel simple peptide based materials, many others hydrogels based on Fmoc-dipeptides have been synthetized and characterized using both natural and unnatural amino acids. As for the long peptide sequences, it was observed that also for dipeptides both the number and the position of the aromatic residues in the peptide sequence played a key role in the self-assembling process and in the mechanical properties of the final material. In this context, the couple Fmoc-FG-OH and Fmoc-GF-OH represents an example in which the simple inversion between Phe and Gly (FG to GF) causes the loss of hydrogelation, thus indicating that the hydrogelation is favored for peptides containing adjacent aromatic groups (Tang et al., 2011). The importance of the primary peptide sequence in the hydrogel preparation was further evidenced by Adam's group in their comparative study of the assembly process and of the mechanical properties of a small Fmoc-dipeptide library (Adams et al., 2010). Their results pointed out that only dipeptides with a logP value between 3.4 and 5.5 were able to form self-supporting hydrogels and the gel rigidity proportionally increases with the hydrophobicity. Moreover, the more hydrophilic Fmoc-FF variant, Fmoc-DOPA-DOPA, forms self-supporting hydrogels in which catechol groups are exposed to the solvent (Fichman et al., 2014b).

Successively, Rajbhandary and Nilsson synthetized three Fmoc-FF analogs (Fmoc-F-Nphe, Fmoc-Nphe-F and Fmoc-Nphe-Nphe) in which one or both the Phe residues were replaced with the N-benzyl glycine peptoid (Nphe) derivative, where the benzyl group in the amino acid is shifted from the C^{α} to the N^{α} atom (Rajbhandary and Nilsson, 2017). Their structural characterization indicated that only the two peptide/peptoid hybrids, keeping at least one Phe residue were able to gelificate, although with a lower propensity compared to Fmoc-FF. This result underlines the critical role played by the intermolecular H-bonding and the geometry of aromatic interactions in the gelation process. The effect of other aromatic groups on FF homodimer was also evaluated. For example, Adler-Abramovic et al. synthetized the Nvoc-FF

(6-nitroveratryloxycarbonyl-diphenylylalanine), a Fmoc-FF analog in which the Fmoc group is replaced by the Nvoc one, a well-known ultraviolet (UV)-sensitive photo-trigger. This peptide forms light responsive hard hydrogels that can promote a controlled drug release upon UV irradiation (Roth-Konforti et al., 2018).

Analogously to Fmoc-dipeptides, also single amino acids derivatized with the Fmoc group have been found to be able to gelificate. In this case, hydrogelation is pH dependent and thermally reversible. The first example of fibrillation and subsequent hydrogelation by Fmoc protected single amino acids, alone or in combination, was reported by Xu and coworkers that described the hydrogelation of a mixture of Fmoc-Lys and Fmoc-Val upon basification (Yang et al., 2004). In order to exploit this small hydrogelator for industrial and biomedical applications, the hydrogelation of Fmoc-Phe and its aromatic analogues were also studied by other research groups (Sutton et al., 2009; Ryan et al., 2010aRyan et al., 2010b; Ryan et al., 2011). Fmoc-Phe gelificates by carefully adjusting the pH of the peptide solution from basic to neutral/acidic, whereas Fmoc-Tyr gelificates by diluting in water the peptide predissolved in an organic solvent at very high concentration. As alternative, the formation of self-assembled Fmoc-Y hydrogels can be promoted by a dephosphorylation reaction catalyzed by a phosphatase (Yang et al., 2008). Moreover, Shi et al. demonstrated that Phe can undergo to the gelification process also when functionalized with aromatic group alternative to Fmoc (e.g., naphthyl, naphthalenoxyl, or cinnamoyl) (Shi et al., 2011). The single crystal structure of Fmoc-F and Fmoc-Y gelators has been determined and the resulting data compared to the fiber X-ray diffraction data (Draper et al., 2015). Results indicated that there is a good match between data obtained on the fiber phase and on the crystalline phase of Fmoc-F. On the contrary, there are substantial differences between the two phases for Fmoc-Y. Indeed, in the crystal structure of Fmoc-Y the packing is mediated by π-π interactions between the aromatic rings of the Fmoc groups, whilst in the fiber the self-aggregation is prompted by hydrogen bonding within the gel. Analogously to Fmoc-F and Fmoc-Y also DOPA derivative self-assemble into hydrogels. Fmoc-DOPA is a non-coded analog of Fmoc-Y in which the catechol group replaces the phenol group of the tyrosine. Using a multistage and multiscale analysis, Fishman et *al.* proposed a model for the Fmoc-DOPA assembly mechanism, in which building blocks undergo to a progressive rearrangement from metastable spheres, in equilibrium with their monomeric form, up to thermodynamically favorable ultrastructures. The mechanism is based on three distinct stages: hydrophobic association in solution, self-assembly into ordered nanofibrils and crystallization due to the spatial locking and to the stabilization by hydrogen bonds (Fichman et al., 2016).

OTHER APPLICATIONS OF PROTEIN AND PEPTIDE BASED MATERIALS WITH β-STRUCTURE

With the advent of biosynthetic and efficient methods of purification, protein-based materials (recombinant, punctual chemically modified or engineered) are at the cutting-edge of materials science, electronics, and medicine (Vasconcelos et al., 2008; Abascal and Regan, 2018). Indeed, these materials are characterized by peculiar physical properties. Among these, their intrinsic biodegradability allows the process of circular economy that returns them to the total biomass. Moreover, as the cross-β motif represents a stable architecture in water-soluble polypeptides, it can be properly designed (Biancalana et al., 2010).

Different methodologies were developed to produce fibrils from protein-rich and renewable sources (*e.g.,* plant proteins) (Kamada et al., 2017; Josefsson et al., 2020).This aspect can explain the currently interest in both manufacturing and obtaining innovative protein-based systems. In this context, the first examples are related to natural fibers, including silk fibroin and resilin. Electrospunned into nanofibers, fibroin, corresponding to the protein of silk core, was proposed to prepare filaments for clothing (Aigner et al., 2018). This protein can be also wet-spun or self-organized to form microfibers, solvent cast into mesoporous foams for local dermal applications, used as enhancer for optoelectronic chips and nanorods or used as component of films. A solvent-based process can be used to form silk-based biodegradable screws or plates or to produce artificial skin and nanodots (Kishimoto et al., 2013; Saravanan et al., 2018; Maniglio et al., 2018; Cazares Vargas et al., 2019; Guo et al., 2020; Zheng and Zuo, 2021).

Resilin and elastin, together with their related materials, have been shaped properly for potential use in tissue engineering, in wound healing as porous scaffolds or films and as drug delivery systems. Aside from the reported applications, protein-based materials have shown potential use as conductive elements (Pena-Francesch et al., 2018). Protein- and peptide-based nanofibrils display interesting mechanical and functional properties in forming nanotubular scaffolding for bionanotechnology. For example, amyloid fibers were found to be mechanically strong (Lara et al., 2012; Bortolini et al., 2015; Paul et al., 2016), thus suggesting their potential use as constituents of functional systems and materials (Nuno et al., 2014; Knowles and Mezzenga, 2016). Moreover, they can be properly decorated by assembling antibody, fusion proteins or ligand to obtain biochemical sensors and chips (Men et al., 2010; Sakono et al., 2012; Kim et al., 2015; Oliveri et al., 2018). For instance, fibril aggregates have been proposed as potential tools for the next-generation of photovoltaic and organic solar cells (Barrau et al., 2008; Hauser et al., 2014), catalytic chemistry (Bolisetty et al., 2015; Al-Garawi et al., 2017) and energy-harvesting devices (Slabov et al., 2019). 2D amyloid hybrids fibrils were also used as immobilization platform for Au and enzymes (Pilkington et al., 2010; Fernández et al., 2016). These systems have also been applied as bioassay to clarify the mechanism of bacterial biofilm formation and of amyloid aggregation (Taglialegna et al., 2016; Taricska et al., 2020).

Peptide-based fibers were also proposed as innovative materials for biomedical applications, such as diagnostic agents, bioimaging agents and tissue engineering. For example, peptide nanofibers opportunely derivatized with gadolinium complexes were exploited as potential contrast agents for Magnetic Resonance Imaging (MRI) technique (Kim et al., 2016;

Diaferia et al., 2019a; Gallo et al., 2020). On the other hand, the intrinsic blue/green photoluminescence recently associated to amyloid and amyloid-like structures has brought to the investigation of peptide and protein fibrils as fluorescent sources for monitoring the *in vitro* kinetics of aggregation (Liu et al., 2015; Gao et al., 2019). These photoluminescent materials (including peptide films and fibers), opportunely engineered, were evaluated as constituents for the development of integrated optoelectronic systems or waveguiding tools (Bo et al., 2019; Apter A. et al., 2020, Apter B. et al., 2020). Moreover, the chemical access, the biocompatibility and the high loading capacity of both hydrophobic and hydrophilic drugs displayed by these peptide and protein nanostructures make them appealing tools for drug delivery applications (Stie et al., 2020). Furthermore, fibrillary objects could be properly planned and decorated with bioactive motifs to achieve an active targeting of the drug. Stimuli-responsive, prolonged and triggered drug release profiles can also be obtained by modifying their primary sequence (Choi et al., 2016; Wei et al., 2017).

The unique physiochemical properties of amyloid fibrils make them attractive materials in a myriad of applications (Gras, 2007; Fichman et al., 2014a; Peralta et al., 2015), not just in biomedical and regenerative medical fields. Relevant applications were proposed in environmental sciences and liquid crystals (Corrigan et al., 2006; Castelletto and Hamley, 2009). For instance, amyloid fibrils, blended with activated carbon amyloid and forming macroscopic membranes, were proposed as purifying tools for a variety of contaminants from wastewater samples (Li and Mezzenga, 2012; Bolisetty and Mezzenga, 2016; Bolisetty et al., 2017). Modified lysozyme amyloid fibrils were also proposed as Chromium(VI) ions absorbent or as component for liquid crystal phases (Leung et al., 2016).

CONCLUDING REMARKS AND FUTURE PERSPECTIVES

The intrinsic ability of the polypeptide chains to form β-rich structures, almost regardless of their length, has a tremendous impact in different research areas. As detailed in the previous sections, the interplay between the structural characterizations of small and large cross-β assemblies has been crucial to achieve an atomic level understanding of the aggregates involved in neurodegeneration and to develop innovative biomaterials. The reductionist approach has been fundamental for gaining the first information on structural bases of the aggregation modes of proteins. On the other hand, the structural characterization of protein/peptides assemblies in their misfolded states have provided important information for the definition of the atomic structures of self-assembling peptides.

This osmosis is likely to endure in the future, as the recent elucidation of the intricate structures of misfolded proteins will probably be exploited to create new biomaterials. In particular, the analysis of these structures reveals the presence of several heterotypic regions (see for example **Figure 4**) that could allow the design of couples of peptides whose mixing may generate novel self-assembling systems. Indeed, there is a growing interest toward hybrid hydrogels that can be generated by simply mixing two or more hydrogelators (Halperin-Sternfeld et al., 2017; Diaferia et al., 2019d; Zhai et al., 2019). This strategy may allow the creation of novel materials with improved mechanical properties, desired morphologies, implemented structural and functional complexity and enhanced stability. Moreover, the hydrophilic core of Orb2 filaments indicates that glutamine-based oligopeptides may represent an attractive source for the generation of innovative biomaterials due to the versatility of this residue that can be involved in both the anhydrous and the solvent exposed face of the sheet in the cross-β motif (**Figure 5**). Finally, new classes of peptide-based hydrogels may come from the characterization of peptides mimicking low-complexity domains of proteins involved in phase separation.

AUTHOR CONTRIBUTIONS

NB and CD performed the bibliographic research and arranged the graphical fashion. AA, GM, and LV conceptualized the topic and organized the manuscript. All the authors contributed to the writing steps and revisions.

FUNDING

This work was supported by the grant from Regione Campania-POR Campania FESR 2014/2020 "Combattere la resistenza tumorale: piattaforma integrata multidisciplinare per un approccio tecnologico innovative alle oncoterapie-Campania Oncoterapie" (Project No. B61G18000470007).

SUPPLEMENTARY MATERIAL

The Supplementary Material for this article can be found online at: https://www.frontiersin.org/articles/10.3389/fbioe.2021.641372/full#supplementary-material

Supplementary Table 1 | Reports the list of amyloid-like structure detected in a survey of the PDB (release of October 2020) including the PDB entry, the title, method, resolution, date of release and number of residues involved in cross-β core.

REFERENCES

Abascal, N. C., and Regan, L. (2018). The past, present and future of protein-based materials. *Open Biol.* 8:180113. doi: 10.1098/rsob.180113

Adams, D. J., Mullen, L. M., Berta, M., Chen, L., and Frith, W. J. (2010). Relationship between molecular structure, gelation behaviour and gel properties of Fmoc-dipeptides. *Soft Matter* 6, 1971–1980. doi: 10.1039/B921863G

Adler-Abramovich, L., and Gazit, E. (2014). The physical properties of supramolecular peptide assemblies: from building block association to technological applications. *Chem. Soc. Rev.* 43:7238. doi: 10.1039/c4cs00164h

Adler-Abramovich, L., Vaks, L., Carny, O., Trudler, D., Magno, A., Caflisch, A., et al. (2012). Phenylalanine assembly into toxic fibrils suggests amyloid etiology in phenylketonuria. *Nat. Chem. Biol.* 8, 701–706. doi: 10.1038/nchembio.1002

Aggeli, A., Bell, M., Boden, N., Carrick, M. L., and Strong, A. E. (2003). Self-assembling peptide polyelectrolyte β-sheet complexes form nematic

hydrogels. *Angew. Chem. Int. Ed.* 42, 5603–5606. doi: 10.1002/anie.200352207

Aigner, T. B., De Simone, E., and Scheibel, T. (2018). Biomedical applications of recombinant silk-based materials. *Adv. Mater.* 30:e1704636. doi: 10.1002/adma.201704636

Al-Garawi, Z. S., McIntosh, B. A., Neill-Hall, D., Hatimy, A. A., Sweet, S. M., Bagleya, M. C., et al. (2017). The amyloid architecture provides a scaffold for enzyme-like catalysts. *Nanoscale* 9, 10773–10783. doi: 10.1039/C7NR02675G

Al-Halifa, S., Zottig, X., Babych, M., Côté-Cyr, M., Bourgault, S., and Archambault, D. (2020). Harnessing the activation of toll-like receptor 2/6 by self-assembled cross-β fibrils to design adjuvanted nanovaccines. *Nanomaterials* 10:1981. doi: 10.3390/nano10101981

Amdursky, N., Molotskii, M., Gazit, E., and Rosenman, G. (2010). Elementary building blocks of self-assembled peptide nanotubes. *J. Am. Chem. Soc.* 132, 15632–15636. doi: 10.1021/ja104373e

Apter, A., Fainberg, B., Handelman, A., Lapsker, I., Accardo, A., Diaferia, C., et al. (2020). Long−range fluorescence propagation in amyloidogenic β−sheet films and fibers. *Adv. Opt. Mater.* 8:2000056. doi: 10.1002/adom.202000056

Apter, B., Lapshina, N., Barhom, H., Fainberg, B., Handelman, A., Accardo, A., et al. (2020). Long−range fluorescence propagation in amyloidogenic β−sheet films and fibers. *Crystals* 10:668. doi: 10.3390/cryst10080668

Arakhamia, T., Lee, C. E., Carlomagno, Y., Duong, D. M., Kundinger, S. R., Wang, K., et al. (2020). Posttranslational modifications mediate the structural diversity of tauopathy strains. *Cell* 180, 633–644. doi: 10.1016/j.cell.2020.01.027

Arnon, Z., Adler-Abramovich, L., Levin, A., and Gazit, E. (2015). Solvent−induced self−assembly of highly hydrophobic tetra−and pentaphenylalanine peptides. *Isr. J. Chem.* 55, 756–762. doi: 10.1002/ijch.201400184

Astbury, W. T., Dickinson, S., and Bailey, K. (1935). The X-ray interpretation of denaturation and the structure of the seed globulins. *Biochem. J.* 29, 2351–2360. doi: 10.1042/bj0292351

Astbury, W. T., and Street, A. (1931). X-ray studies of the structures of hair, wool, and related fibres. I. General. *Phil. Trans. R. Soc. Ser. A* 230, 75–101. doi: 10.1098/rsta.1932.0003

Avitabile, C., Diaferia, C., Della Ventura, B., Mercurio, F. A., Leone, M., Roviello, V., et al. (2018). Self−assembling of Fmoc−GC peptide nucleic acid dimers into highly fluorescent aggregates. *Chem. Eur. J.* 24, 4729–4735. doi: 10.1002/chem.201800279

Babar, D. G., and Sarkar, S. (2017). Self-assembled nanotubes from single fluorescent amino acid. *Appl. Nanosci.* 7, 101–107. doi: 10.1007/s13204-017-0551-5

Baker, D. (2019). What has de novo protein design taught us about protein folding and biophysics? *Prot. Sci.* 28, 678–683. doi: 10.1002/pro.3588

Balbirnie, M., Grothe, R., and Eisenberg, D. S. (2001). An amyloid-forming peptide from the yeast prion Sup35 reveals a dehydrated β-sheet structure for amyloid. *Proc. Natl. Acad. Sci. U.S.A.* 98, 2375–2380. doi: 10.1073/pnas.041617698

Banik, D., Kundu, S., Banerjee, P., Dutta, R., and Sarkar, N. (2017). Investigation of fibril forming mechanisms of L-Phenylalanine and L-Tyrosine: microscopic insight toward phenylketonuria and tyrosinemia type II. *J. Phys. Chem. B* 121, 1533–1543. doi: 10.1021/acs.jpcb.6b12220

Barrau, S., Zhang, F., Herland, A., Mammo, W., Andersson, M. R., and Inganas, O. (2008). Integration of amyloid nanowires in organic solar cells. *App. Phys. Lett.* 93:023307. doi: 10.1063/1.2949073

Bera, S., Xue, B., Rehak, P., Jacoby, G., Ji, W., Shimon, L. J. W., et al. (2020). Self-assembly of aromatic amino acid enantiomers into supramolecular materials of high rigidity. *ACS Nano* 14, 1694–1706. doi: 10.1021/acsnano.9b07307

Bhak, G., Lee, S., Park, J. W., Cho, S., and Paik, S. R. (2010). Amyloid hydrogel derived from curly protein fibrils of alpha-synuclein. *Biomater* 31, 5986–5995. doi: 10.1016/j.biomaterials.2010.03.080

Biancalana, M., Makabe, K., and Koide, S. (2010). Minimalist design of water-soluble cross-β architecture. *Proc. Natl. Acad. Sci. U.S.A.* 107, 3469–3474. doi: 10.1073/pnas.0912654107

Bo, J., Aliyan, A., Cook, N. P., Augustine, A., Bhak, G., Maldonado, R., et al. (2019). Monitoring the formation of amyloid oligomers using photoluminescence anisotropy. *J. Am. Chem. Soc.* 141, 15605–15610. doi: 10.1021/jacs.9b06966

Bolisetty, S., Arcari, M., Adamcik, J., and Mezzenga, R. (2015). Hybrid amyloid membranes for continuous flow catalysis. *Langmuir* 31, 13867–13873. doi: 10.1021/acs.langmuir.5b03205

Bolisetty, S., Harnau, L., Jung, J. M., and Mezzenga, R. (2012). Gelation, phase behavior, and dynamics of β-lactoglobulin amyloid fibrils at varying concentrations and ionic strengths. *Biomacromol* 13, 3241–3252. doi: 10.1021/bm301005w

Bolisetty, S., and Mezzenga, R. (2016). Amyloid–carbon hybrid membranes for universal water purification. *Nat. Nanotech.* 11, 365–371. doi: 10.1038/nnano.2015.310

Bolisetty, S., Reinhold, N., Zeder, C., Orozcob, M. N., and Mezzenga, R. (2017). Efficient purification of arsenic-contaminated water using amyloid–carbon hybrid membranes. *Chem. Commun.* 53, 5714–5717. doi: 10.1039/c7cc00406k

Bortolini, C., Jones, N. C., Hoffmann, S. V., Wang, C., Besenbachera, F., and Dong, M. (2015). Mechanical properties of amyloid-like fibrils defined by secondary structures. *Nanoscale* 7, 7745–7752. doi: 10.1039/C4NR05109B

Bowerman, C. J., Liyanage, W., Federation, A. J., and Nilsson, B. L. (2011). Tuning β-sheet peptide self-assembly and hydrogelation behavior by modification of sequence hydrophobicity and aromaticity. *Biomacromol* 12, 2735–2745. doi: 10.1021/bm200510k

Calvanese, L., Brun, P., Messina, G. M. L., Russo, T., Zamuner, A., Falcigno, L., et al. (2020). EAK hydrogels cross-linked by disulfide bonds: cys number and position are matched to performances. *ACS Biomater. Sci. Eng.* 6, 1154–1164. doi: 10.1021/acsbiomaterials.9b01556

Cannon, D., and Donald, A. M. (2013). Control of liquid crystallinity of amyloid-forming systems. *Soft Matter* 9, 2852–2857. doi: 10.1039/C2SM26946E

Cao, Q., Boyer, D. R., Sawaya, M. R., Ge, P., and Eisenberg, D. S. (2019). Cryo-EM structures of four polymorphic TDP-43 amyloid cores. *Nat. Struct. Mol. Biol.* 26, 619–627. doi: 10.1038/s41594-019-0248-4

Caplan, M. R., Schwartzfarb, E. M., Zhang, S., Kamm, R. D., and Lauffenburger, D. A. (2002). Control of self-assemblingoligopeptide matrix formation through systematic variation of amino acid sequence. *Biomaterials* 23, 219–227. doi: 10.1016/S0142-9612(01)00099-0

Castelletto, V., and Hamley, I. W. (2009). Self-assembly of a model amphiphilic phenylalanine peptide/polyethylene glycol block copolymer in aqueous solution. *Biophys. Chem.* 141, 169–174. doi: 10.1016/j.bpc.2009.01.008

Castelletto, V., Newby, G. E., Zhu, Z., Hamley, I. W., and Noirez, L. (2010). Self-assembly of PEGylated peptide conjugates containing a modified amyloid β-peptide fragment. *Langmuir* 26, 9986–9999. doi: 10.1021/la100110f

Cavalli, S., Albericio, F., and Kros, A. (2010). Amphiphilic peptides and their cross-disciplinary role as building blocks for nanoscience. *Chem. Soc. Rev.* 39, 241–263. doi: 10.1039/B906701A

Cazares Vargas, E., Cohen Stuart, M. A., de Vries, R., and Hernandez-Garcia, A. (2019). Template−free self−assembly of artificial de novo viral coat proteins into nanorods: effects of sequence, concentration, and temperature. *Chem. Eur. J.* 25, 11058–11065. doi: 10.1002/chem.201901486

Chiti, F., and Dobson, C. M. (2017). Protein misfolding, amyloid formation, and human disease: a summary of progress over the last decade. *Ann. Rev. Biochem.* 86, 27–68. doi: 10.1146/annurev-biochem-061516-045115

Choi, H., Jeena, M. T., Palanikumar, L., Jeong, Y., Park, S., Lee, E., et al. (2016). The HA-incorporated nanostructure of a peptide-drug amphiphile for targeted anticancer drug delivery. *Chem. Commun.* 52, 5637–5640. doi: 10.1039/c6cc00200e

Chronopoulou, L., Lorenzoni, S., Masci, G., Dentini, M., Togna, A. R., Togna, G., et al. (2010). Lipase-supported synthesis of peptidic hydrogels. *Soft Matter* 6, 2525–2532. doi: 10.1039/C001658F

Colletier, J. P., Laganowsky, A., Landau, M., Zhao, M., Soriaga, A. B., Goldschmidt, L., et al. (2011). Molecular basis for amyloid-beta polymorphism. *Proc. Natl. Acad. Sci. U.S.A.* 108, 16938–16943. doi: 10.1073/pnas.1112600108

Collier, J. H., and Messersmith, P. B. (2003). Enzymatic modification of self-assembled peptide structures with tissue transglutaminase. *Bioconj. Chem.* 14, 748–755. doi: 10.1021/bc034017t

Colombo, G., Meli, M., and De Simone, A. (2008). Computational studies of the structure, dynamics and native content of amyloid-like fibrils of ribonuclease A. *Proteins* 70, 863–872. doi: 10.1002/prot.21648

Corrigan, A. M., Müller, C., and Krebs, M. R. H. (2006). The formation of nematic liquid crystal phases by hen lysozyme amyloid fibril. *J. Am. Chem. Soc.* 128, 14740–14741. doi: 10.1021/ja064455l

Dasgupta, A., Mondal, J. H., and Das, D. (2013). Peptide hydrogels. *RSC Adv.* 2013, 9117–9149. doi: 10.1039/C3RA40234G

Davies, R. P. W., Aggeli, A., Beevers, A. J., Boden, N., Carrick, L., Fishwick, M. C. W. G., et al. (2006). Self-assembling β-sheet tape forming peptides. *Supramol. Chem.* 18, 435–443. doi: 10.1080/10610270600665855

Dawson, P. E., Muir, T. W., Clark-Lewis, I., and Kent, S. B. (1994). Synthesis of proteins by native chemical ligation. *Science* 266, 776–779. doi: 10.1126/science.7973629

de la Cruz, M. J., Hattne, J., Shi, D., Seidler, P., Rodriguez, J., Reyes, F. E., et al. (2017). Atomic-resolution structures from fragmented protein crystals with the cryoEM method MicroED. *Nat. Methods* 14, 399–402. doi: 10.1038/nmeth.4178

De Leon Rodriguez, M. R., Hemar, Y., Cornishc, J., and Brimblead, M. A. (2016). Structure-mechanical property correlations of hydrogel forming β-sheet peptides. *Chem. Soc. Rev.* 45, 4797–4824. doi: 10.1039/C5CS00941C

De Leon-Rodriguez, L. M., Kamalov, M., Hemar, Y., Mitra, A. K., Castelletto, V., Hermida-Merino, D., et al. (2016). A peptide hydrogel derived from a fragment of human cardiac troponin C. *Chem. Commun.* 52, 4056–4059. doi: 10.1039/C6CC00209A

Diaferia, C., Balasco, N., Altamura, D., Sibillano, T., Gallo, E., Roviello, V., et al. (2018a). Assembly modes of hexaphenylalanine variants as function of the charge states of their terminal ends. *Soft Matter* 14, 8219–8230. doi: 10.1039/C8SM01441H

Diaferia, C., Balasco, N., Sibillano, T., Giannini, C., Vitagliano, L., Morelli, G., et al. (2018c). Structural characterization of self-assembled tetra-tryptophan based nanostructures: variations on a common theme. *ChemPhysChem* 19, 1635–1642. doi: 10.1002/cphc.201800026

Diaferia, C., Balasco, N., Sibillano, T., Gosh, M., Adler-Avramovich, L., Giannini, C., et al. (2018b). Amyloid-like fibrillary morphology originated by tyrosine-containing aromatic hexapeptides. *Chem. Eur. J.* 24, 6804–6817. doi: 10.1002/chem.201800351

Diaferia, C., Gianolio, E., and Accardo, A. (2019a). Peptide−based building blocks as structural elements for supramolecular Gd−containing MRI contrast agents. *J. Pept. Sci.* 25:e3157. doi: 10.1002/psc.3157

Diaferia, C., Gianolio, E., Palladino, P., Arena, F., Boffa, C., Morelli, G., et al. (2015). Peptide materials obtained by aggregation of polyphenylalanine conjugates as gadolinium-based magnetic resonance imaging contrast agents. *Adv. Funct. Mater.* 25, 7003–7016. doi: 10.1002/adfm.201502458

Diaferia, C., Gosh, M., Sibillano, T., Gallo, E., Stornaiuolo, M., Giannini, C., et al. (2019c). Fmoc-FF and hexapeptide-based multicomponent hydrogels as scaffold materials. *Soft Matter* 15, 487–496. doi: 10.1039/C8SM02366B

Diaferia, C., Mercurio, F. A., Giannini, C., Sibillano, T., Morelli, G., Leone, M., et al. (2016a). Self-assembly of PEGylated tetra-phenylalanine derivatives: structural insights from solution and solid state studies. *Sci. Rep.* 6:26638. doi: 10.1038/srep26638

Diaferia, C., Morelli, G., and Accardo, A. (2019d). Fmoc-diphenylalanine as a suitable building block for the preparation of hybrid materials and their potential applications. *J. Mater. Chem. B* 7, 5142–5155. doi: 10.1039/C9TB01043B

Diaferia, C., Netti, F., Ghosh, M., Sibillano, T., Giannini, C., Morelli, G., et al. (2020). Bi-functional peptide-based 3D hydrogel-scaffolds. *Soft Matter* 16, 7006–7017. doi: 10.1039/D0SM00825G

Diaferia, C., Roviello, V., Morelli, G., and Accardo, A. (2019b). Self-assembly of PEGylated diphenylalanines into photoluminescent fibrillary aggregates. *ChemPhysChem* 20, 2774–2782. doi: 10.1002/cphc.201900884

Diaferia, C., Sibillano, T., Balasco, N., Giannini, C., Roviello, V., Vitagliano, L., et al. (2016b). Hierarchical analysis of self-assembled PEGylated hexaphenylalanine photoluminescent nanostructures. *Chem. Eur. J.* 22, 16586–16597. doi: 10.1002/chem.201604107

Do, T. D., Kincannon, W. M., and Bowers, M. T. (2015). Phenylalanine oligomers and fibrils: the mechanism of assembly and the importance of tetramers and counterions. *J. Am. Chem. Soc.* 137, 10080–10083. doi: 10.1021/jacs.5b05482

Draper, E. R., and Adams, D. J. (2017). Low-molecular-weight gels: the state of the art. *Chem* 3, 390–410. doi: 10.1016/j.chempr.2017.07.012

Draper, E. R., Morris, K. L., Little, M. A., Raeburn, J., Colquhoun, C., Cross, E. R., et al. (2015). Hydrogels formed from Fmoc amino acids. *Cryst. Eng. Comm.* 17, 8047–8057. doi: 10.1039/C5CE00801H

Eisenberg, D. S., Nelson, R., Sawaya, M. R., Balbirnie, M., Sambashivan, S., Ivanova, M. I., et al. (2006). The structural biology of protein aggregation diseases: fundamental questions and some answers. *Acc. Chem. Res.* 39, 568–575. doi: 10.1021/ar0500618

Eisenberg, D. S., and Sawaya, M. R. (2017). Structural studies of amyloid proteins at the molecular level. *Annu. Rev. Biochem.* 20, 69–95.

Esposito, L., Paladino, A., Pedone, C., and Vitagliano, L. (2008). Insights into structure, stability, and toxicity of monomeric and aggregated polyglutamine models from molecular dynamics simulations. *Biophys. J.* 94, 4031–4040. doi: 10.1529/biophysj.107.118935

Falcon, B., Zhang, W., Murzin, A. G., Murshudov, G., Garringer, H. J., Vidal, R., et al. (2018a). Structures of filaments from Pick's disease reveal a novel tau protein fold. *Nature* 561, 137–140. doi: 10.1038/s41586-018-0454-y

Falcon, B., Zhang, W., Schweighauser, M., Murzin, A. G., Vidal, R., Garringer, H. J., et al. (2018b). Tau filaments from multiple cases of sporadic and inherited Alzheimer's disease adopt a common fold. *Acta Neuropathol.* 136, 699–708. doi: 10.1007/s00401-018-1914-z

Falcon, B., Zivanov, J., Zhang, W., Murzin, A. G., Garringer, H. J., Vidal, R., et al. (2019). Novel tau filament fold in chronic traumatic encephalopathy encloses hydrophobic molecules. *Nature* 568, 420–423. doi: 10.1038/s41586-019-1026-5

Fang, J., Zhang, X., Cai, Y., and Wei, Y. (2011). Small globular protein motif forms particulate hydrogel under various pH conditions. *Biomacromoleculesol* 12, 1578–1584. doi: 10.1021/bm101571r

Fernández, C., González-Rubio, G., Langer, J., Tardajos, G., Liz-Marzán, L. M., Giraldo, R., et al. (2016). Nucleation of amyloid oligomers by RepA-WH1-prionoid-functionalized gold nanorods. *Angew Chem. Int. Ed.* 55, 11237–11241. doi: 10.1002/anie.201604970

Fichman, G., Adler-Abramovich, L., Manohar, S., Mironi-Harpaz, I., Guterman, T., Seliktar, D., et al. (2014a). Seamless metallic coating and surface adhesion of self-assembled bioinspired nanostructures based on di-(3,4-dihydroxy-L-phenylalanine) peptide motif. *ACS Nano* 8, 7220–7228. doi: 10.1021/nn502240r

Fichman, G., and Gazit, E. (2014). Self-assembly of short peptides to form hydrogels: design of building blocks, physical properties and technological applications. *Acta Biomater.* 10, 1671–1682. doi: 10.1016/j.actbio.2013.08.013

Fichman, G., Guterman, T., Adler-Abramovich, L., and Gazit, E. (2014b). The use of the calcitonin minimal recognition module for the design of DOPA-containing fibrillar assemblies. *Nanomaterials* 4, 726–740. doi: 10.3390/nano4030726

Fichman, G., Guterman, T., Damron, J., Adler-Abramovich, L., Schmidt, J., Kesselman, E., et al. (2016). Spontaneous structural transition and crystal formation in minimal supramolecular polymer model. *Sci. Adv.* 2:e1500827. doi: 10.1126/sciadv.500827

Fichou, Y., Schirò, G., Gallat, F. X., Laguri, C., Moulin, M., Combet, J., et al. (2015). Hydration water mobility is enhanced around tau amyloid fibers. *Proc. Natl. Acad. Sci. U.S.A.* 112, 6365–6370. doi: 10.1073/pnas.1422824112

Fitzpatrick, A. W. P., Falcon, B., He, S., Murzin, A. G., Murshudov, G., Garringer, H. J., et al. (2017). Cryo-EM structures of tau filaments from Alzheimer's disease. *Nature* 547, 185–190. doi: 10.1038/nature23002

Fitzpatrick, A. W. P., and Saibil, H. R. (2019). Cryo-EM of amyloid fibrils and cellular aggregates. *Curr. Opin. Struct. Biol.* 58, 34–42. doi: 10.1016/j.sbi.2019.05.003

Flamia, R., Salvi, A. M., D'Alessio, D., Castle, J. E., and Tamburro, A. M. (2007). Transformation of amyloid-like fibers, formed from an elastin-based biopolymer, into a hydrogel: an X-ray photoelectron spectroscopy and atomic force microscopy study. *Biomacromoleculesmol* 8, 128–138. doi: 10.1021/bm060764s

Fleming, S., and Ulijn, R. V. (2014). Design of nanostructures based on aromatic peptide amphiphiles. *Chem. Soc. Rev.* 43, 8150–8177. doi: 10.1039/C4CS00247D

Frederix, P. W., Scott, G. G., Abul-Haija, Y. M., Kalafatovic, D., Pappas, C. G., Javid, N., et al. (2015). Exploring the sequence space for (tri-)peptide self-assembly to design and discover new hydrogels. *Nat. Chem.* 7, 30–37. doi: 10.1038/nchem.2122

Frohm, B., Denizio, J. E., Lee, D. S. M., Gentile, L., Olsson, U., Malm, J., et al. (2015). A peptide from human semenogelin I self-assembles into a pH-responsive hydrogel. *Soft Matter* 11:414. doi: 10.1039/C4SM01793E

Gallagher-Jones, M., Glynn, C., Boyer, D. R., Martynowycz, M. W., Hernandez, E., Miao, J., et al. (2018). Sub-angstrom cryo-EM structure of a prion protofibril reveals a polar clasp. *Nat. Struct. Mol. Biol.* 25, 131–134. doi: 10.1038/s41594-017-0018-0

Galler, K. M., Aulisa, L., Regan, K. R., D'Souza, R. N., and Hartgerink, J. D. (2010). Self-assembling multidomain peptide hydrogels: designed susceptibility

to enzymatic cleavage allows enhanced cell migration and spreading. *J. Am. Chem. Soc.* 132, 3217–3223. doi: 10.1021/ja910481t

Gallo, E., Diaferia, C., Di Gregorio, E., Morelli, G., Gianolio, E., and Accardo, A. (2020). Peptide-based soft hydrogels modified with gadolinium complexes as MRI contrast agents. *Pharmaceuticals* 13:19. doi: 10.3390/ph13020019

Gao, Y., Liu, Q., Xu, L., Zheng, N., He, X., and Xu, F. (2019). Imaging and spectral characteristics of amyloid plaque autofluorescence in brain slices from the APP/PS1 mouse model of Alzheimer's disease. *Neurosci. Bull.* 35, 1126–1137. doi: 10.1007/s12264-019-00393-6

Gazit, E. (2002). A possible role for π-stacking in the self-assembly of amyloid fibrils. *FASEB J.* 16, 77–83. doi: 10.1096/fj.01-0442hyp

Gazit, E. (2007). Self assembly of short aromatic peptides into amyloid fibrils and related nanostructures. *Prion* 1, 32–35. doi: 10.4161/pri.1.1.4095

Geisler, I. M., and Schneider, J. P. (2012). Evolution-based design of an injectable hydrogel. *Adv. Funct. Mater.* 22, 529–537. doi: 10.1002/adfm.201102330

Glynn, C., Sawaya, M. R., Ge, P., Gallagher-Jones, M., Short, C. W., Bowman, R., et al. (2020). Cryo-EM structure of a human prion fibril with a hydrophobic, protease-resistant core. *Nat. Struct. Mol. Biol.* 27, 417–423. doi: 10.1038/s41594-020-0403-y

Gosal, W. S., Clark, A. H., and Ross-Murphy, S. B. (2004). Fibrillar β-lactoglobulin gels: part 3. dynamic mechanical characterization of solvent-induced systems. *Biomacromol* 5, 2420–2429. doi: 10.1021/bm0496615

Gour, N., Kanth, P. K., Koshti, B., Kshtriya, V., Shah, D., Patel, S., et al. (2019). Amyloid-like structures formed by single amino acid self-assemblies of cysteine and methionine. *ACS Chem. Neurosci.* 10, 1230–1239. doi: 10.1021/acschemneuro.8b00310

Gras, S. L. (2007). Amyloid Fibrils: from disease to design. New biomaterial applications for self-assembling cross-β fibrils. *Austr. J. Chem.* 60, 333–342. doi: 10.1071/CH06485

Gremer, L., Schölzel, D., Schenk, C., Reinartz, E., Labahn, J., Ravelli, R. B. G., et al. (2017). Fibril structure of amyloid-β(1-42) by cryo-electron microscopy. *Science* 358, 116–119. doi: 10.1126/science.aao2825

Griner, S. L., Seidler, P., Bowler, J., Murray, K. A., Yang, T. P., Sahay, S., et al. (2019). Structure-based inhibitors of amyloid beta core suggest a common interface with tau. *eLife* 8:e46924. doi: 10.7554/eLife.46924.001

Guo, X., Liu, Y., Bera, H., Zhang, H., Chen, Y., Cun, D., et al. (2020). α-Lactalbumin-based nanofiber dressings improve burn wound healing and reduce scarring. *ACS Appl. Mater. Interfaces* 41, 45702–45713. doi: 10.1021/acsami.0c05175

Görbitz, C. H. (2001). Nanotube formation by hydrophobic dipeptides. *Chem. Eur. J.* 7, 5153–5159. doi: 10.1002/1521-3765(20011203)7:233.0.CO;2-N

Görbitz, C. H. (2006). The structure of nanotubes formed by diphenylalanine, the core recognition motif of Alzheimer's β-amyloid polypeptide. *Chem. Commun.* 2332–2334. doi: 10.1039/B603080G

Halperin-Sternfeld, M., Ghosh, M., Sevostianov, R., Grigoriants, I., and Adler-Abramovich, L. (2017). Molecular co-assembly as a strategy for synergistic improvement of the mechanical properties of hydrogels. *Chem. Commun.* 53, 9586–9589. doi: 10.1039/C7CC04187J

Hamley, I. W. (2014). PEG-peptide conjugates. *Biomacromolecules* 15, 1543–1559. doi: 10.1021/bm500246w

Hamley, I. W., and Krysmann, M. J. (2008). Effect of PEG crystallization on the self-assembly of peg/peptide copolymers containing amyloid peptide fragments. *Langmuir* 24, 8210–8214. doi: 10.1021/la8005426

Han, T. H., Ok, T., Kim, J., Shin, D. O., Ihee, H., Lee, H.-S., et al. (2010). Bionanosphere lithography via hierarchical peptide self-assembly of aromatic triphenylalanine. *Small* 6, 945–951. doi: 10.1002/smll.200902050

Hartgerink, J. D., Beniash, E., and Stupp, S. I. (2002). Peptide-amphiphile nanofibers: a versatile scaffold for the preparation of self-assembling materials. *Proc. Natl. Acad. Sci. U.S.A.* 99, 5133–5138. doi: 10.1073/pnas.072699999

Hauser, C. A. E., Maurer-Stroh, M., and Martins, I. C. (2014). Amyloid-based nanosensors and nanodevices. *Chem. Soc. Rev.* 43, 5326–5345. doi: 10.1039/C4CS00082J

Hervas, R., Rau, M. J., Park, S., Zhang, W., Murzin, A. G., Fitzpatrick, J. A. J., et al. (2020). Cryo-EM structure of a neuronal functional amyloid implicated in memory persistence in *Drosophila*. *Science* 367, 1230–1234. doi: 10.1126/science.aba3526

Hilbich, C., Kisterswoike, B., Reed, J., Masters, C. L., and Beyreuther, K. (1992). Substitutions of hydrophobic amino acids reduce the amyloidogenicity of Alzheimer's disease beta A4 peptides. *J. Mol. Biol.* 228, 460–473. doi: 10.1016/0022-2836(92)90835-8

Hu, X.-Y., Ehlers, M., Wang, T., Zellermann, E., Mosel, S., Jiang, H., et al. (2018). Formation of twisted β−sheet tapes from a self−complementary peptide based on novel pillararene−GCP host–guest interaction with gene transfection properties. *Chem. Eur. J.* 24, 9754–9759. doi: 10.1002/chem.201801315

Hughes, M. P., Sawaya, M. R., Boyer, D. R., Goldschmidt, L., Rodriguez, J. A., Cascio, D., et al. (2018). Atomic structures of low-complexity protein segments reveal kinked beta sheets that assemble networks. *Science* 359, 698–701. doi: 10.1126/science.aan6398

Janek, K., Behlke, J., Zipper, J., Fabian, H., Georgalis, Y., Beyermann, M., et al. (1999). Water-soluble β-sheet models which self-assemble into fibrillar structures. *Biochemistry* 38, 8246–8252. doi: 10.1021/bi990510

Jang, S., Yuan, J.-M., Shin, J., Measey, T. J., Schweitzer-Stenner, R., and Li, F.-Y. (2009). Energy landscapes associated with the self-aggregation of an alanine-based oligopeptide (AAKA)4. *J. Phys. Chem. B* 113, 6054–6061. doi: 10.1021/jp809279r

Jaroniec, C. P., MacPhee, C. E., Bajaj, V. S., McMahon, M. T., Dobson, C. M., and Griffin, R. G. (2004). High-resolution molecular structure of a peptide in an amyloid fibril determined by magic angle spinning NMR spectroscopy. *Proc. Natl. Acad. Sci. U.S.A.* 101, 711–716. doi: 10.1073/pnas.0304849101

Jayakumar, R., Murugesan, M., Asokan, C., and Scibioh, M. A. (2000). Self-assembly of a peptide Boc-(Ile)5-OMe in chloroform and N,N-dimethylformamide. *Langmuir* 16, 1489–1496. doi: 10.1021/la990004l

Jayawarna, V., Ali, M., Jowitt, T. A., Miller, F. A., Saiani, A., Gough, J. E., et al. (2006). Nanostructured hydrogels for three−dimensional cell culture through self−assembly of fluorenylmethoxycarbonyl–dipeptides. *Adv. Mater.* 18, 611–614. doi: 10.1002/adma.200501522

Josefsson, L., Ye, X., Brett, C. J., Meijer, J., Olsson, C., Sjögren, A., et al. (2020). Potato protein nanofibrils produced from a starch industry sidestream. *ACS Sustainable Chem. Eng.* 8, 1058–1067. doi: 10.1021/acssuschemeng.9b05865

Kamada, K., Mittal, N., Söderberg, L. D., Ingverud, T., Ohm, W., Roth, S. V., et al. (2017). Flow-assisted assembly of nanostructured protein microfibers. *Proc. Natl. Acad. Sci. U.S.A.* 114, 1232–1237. doi: 10.1073/pnas.1617260114

Kaufman, S. (1999). A model of human phenylalanine metabolism in normal subjects and in phenylketonuric patients. *Proc. Natl. Acad. Sci. U.S.A.* 96, 3160–3164. doi: 10.1073/pnas.96.6.3160

Kazantzis, A., Waldner, M., Taylor, J. M., and Kapurniotu, A. (2002). Conformationally constrained human calcitonin (hCt) analogues reveal a critical role of sequence 17–21 for the oligomerization state and bioactivity of hCt. *Eur. J. Biochem.* 269, 780–791. doi: 10.1046/j.0014-2956.2001.02689.x

Kemper, B., Hristova, Y. R., Tacke, S., Stegemann, L., van Bezowen, L. S., Stuart, M. C. A., et al. (2015). Facile synthesis of a peptidic Au(I)-metalloamphiphile and its self-assembly into luminescent micelles in water. *Chem. Commun.* 51, 5253–5256. doi: 10.1039/c4cc03868a

Kim, I., Han, E. H., Ryu, J., Min, J. Y., Ahn, H., Chung, Y.-H., et al. (2016). One−dimensional supramolecular nanoplatforms for theranostics based on co−assembly of peptide amphiphiles. *Biomacromolecules* 17, 3234−3243. doi: 10.1021/acs.biomac.6b00966

Kim, S., Kim, J. H., Lee, J. S., and Park, C. B. (2015). Beta-sheet-forming, self-assembled peptide nanomaterials towards optical, energy, and healthcare applications. *Small* 11, 3623–3640. doi: 10.1002/smll.201500169

Kishimoto, Y., Ito, F., Usamia, H., Togawa, E., Tsukada, M., Morikawa, M., et al. (2013). Nanocomposite of silk fibroin nanofiber and montmorillonite: fabrication and morphology. *Int. J. Macromol.* 57, 124–128. doi: 10.1016/j.ijbiomac.2013.03.016

Knowles, T. P. J., and Mezzenga, R. (2016). Amyloid fibrils as building blocks for natural and artificial functional materials. *Adv. Mater.* 28, 6546–6561. doi: 10.1002/adma.201505961

Kogiso, M., Okada, Y., Hanada, T., Yase, K., and Shimizu, T. (2000). Self-assembled peptide fibers from valylvaline bola-amphiphiles by a parallel β-sheet network. *Biochim. Biophys. Acta* 1475, 346–352. doi: 10.1016/S0304-4165(00)00088-X

Krebs, M. R. H., MacPhee, C. E., Miller, A. F., Dunlop, I. E., Dobson, C. M., and Donald, A. M. (2004). The formation of spherulites by amyloid fibrils of bovine insulin. *Proc. Natl. Acas. Sci. U.S.A.* 101, 14420–14424. doi: 10.1073/pnas.0405933101

Laganowsky, A., Liu, C., Sawaya, M. R., Whitelegge, J. P., Park, J., Zhao, M., et al. (2012). Atomic view of a toxic amyloid small oligomer. *Science* 335, 1228–1231. doi: 10.1126/science.1213151

Langkilde, A. E., Morris, K. L., Serpell, L. C., Svergun, D. I., and Vestergaard, B. (2015). The architecture of amyloid-like peptide fibrils revealed by X-ray scattering, diffraction and electron microscopy. *Acta Crystallogr. D Biol. Crystallogr.* 71(Pt 4), 882–895. doi: 10.1107/S1399004715001674

Lara, C., Gourdin-Bertin, S., Adamcik, J., Bolisetty, S., and Mezzenga, R. (2012). Self-assembly of ovalbumin into amyloid and non-amyloid fibrils. *Biomacromolecules* 13, 4213–4221. doi: 10.1021/bm301481v

Lensink, M. F., Nadzirin, N., Velankar, S., and Wodak, S. J. (2020). Modeling protein interactions and complexes in CAPRI: seventh CAPRI evaluation meeting. *Prot. Struc. Funct. Bioinf.* 88, 913–915. doi: 10.1002/prot.25975

Leon, E. J., Verma, N., Zhang, S., Lauffenburger, D. A., and Kamm, R. D. (1998). Mechanical properties of a self-assembling oligopeptide matrix. *J. Biomat. Sci. Pol. Ed.* 9, 297–312. doi: 10.1163/156856298X00668

Leung, W. H., Lo, W. H., and Chan, P. H. (2016). Amyloid fibrils as rapid and efficient nano-biosorbents for removal of dye pollutants. *RSC Adv.* 6, 58363–58364. doi: 10.1039/C6RA90054B

Li, C. X., and Mezzenga, R. (2012). Functionalization of multiwalled carbon nanotubes and their pH-responsive hydrogels with amyloid fibrils. *Langmuir* 28, 10142–10146. doi: 10.1021/la301541d

Li, Y., Xue, B., and Cao, Y. (2020). 100th Anniversary of macromolecular science viewpoint: macromolecular materials for additive manufacturing. *ACS Macro Lett.* 9, 512–524. doi: 10.1021/acsmacrolett.0c00200

Liu, X., Zhu, P., Fei, J., Zhao, J., Yan, X., and Li, J. (2015). Synthesis of peptide−based hybrid nanobelts with enhanced color emission by heat treatment or water induction. *J. Chem. Eur. J.* 21, 9461–9467. doi: 10.1002/chem.201500580

López-Pérez, D. E., Revilla-López, G., Hamley, I. W., and Alemán, C. (2013). Molecular insights into aggregates made of amphiphilic Fmoc-tetrapeptides. *Soft Matter* 9, 11021–11032. doi: 10.1039/C3SM51826D

Lu, J. X., Qiang, W., Yau, W. M., Schwieters, C. D., Meredith, S. C., and Tycko, R. (2013). Molecular structure of β-amyloid fibrils in Alzheimer's disease brain tissue. *Cell* 154, 1257–1268. doi: 10.1016/j.cell.2013.08.035

Luo, J., and Abrahams, J. P. (2014). Cyclic peptides as inhibitors of amyloid fibrillation. *Chem. Eur. J.* 20, 2410–2419. doi: 10.1002/chem.201304253

Machado, C. A., Smith, I. R., and Savin, D. A. (2019). Self-assembly of oligo- and polypeptide-based amphiphiles: recent advances and future possibilities. *Macromolecules* 52, 1899–1911. doi: 10.1021/acs.macromol.8b02043

Mahler, A., Reches, M., Rechter, M., Cohen, S., and Gazit, E. (2006). Rigid, self−assembled hydrogel composed of a modified aromatic dipeptide. *Adv. Mater.* 18, 1365–1370. doi: 10.1002/adma.200501765

Mains, J., Lamprou, D. A., McIntosh, L., Oswald, I. D. H., and Urquhart, A. J. (2013). Beta-adrenoceptor antagonists affect amyloid nanostructure; amyloid hydrogels as drug delivery vehicles. *Chem. Commun.* 49, 5082–5084. doi: 10.1039/C3CC41583J

Maity, S., Nir, S., Zada, T., and Reches, M. (2014). Self-assembly of a tripeptide into a functional coating that resists fouling. *Chem. Commun.* 50, 11154–11157. doi: 10.1039/C4CC03578J

Makin, O. S., Atkins, E., Sikorski, P., Johansson, J., and Serpell, L. C. (2005). Molecular basis for amyloid fibril formation and stability. *Proc. Natl. Acad. Sci. U.S.A.* 102, 315–320. doi: 10.1073/pnas.0406847102

Malinchik, S. B., Inouye, H., Szumowski, K. E., and Kirschner, D. A. (1998). Structural analysis of Alzheimer's β(1-40) amyloid: protofilament assembly of tubular fibrils. *Biophys. J.* 74, 537–545. doi: 10.1016/S0006-3495(98)77812-9

Maniglio, D., Bonani, W., Migliaresi, C., and Motta, A. (2018). Silk fibroin porous scaffolds by N_2O foaming. *J.Biomats Sci. Pol. Ed.* 29, 491–506. doi: 10.1080/09205063.2018.1423811

Mayans, E., Ballano, G., Casanovas, J., Díaz, A., Pérez-Madrigal, M. M., Estrany, F., et al. (2015). Self-assembly of tetraphenylalanine peptides. *Chem. Eur. J.* 21, 16895–16905. doi: 10.1002/chem.201501793

Measey, T. J., and Schweitzer-Stenner, R. (2006). Aggregation of the amphipathic peptides (aaka)n into antiparallel β-Sheets. *J. Am. Chem. Soc.* 128, 13324–13325. doi: 10.1021/ja0632411

Measey, T. J., Schweitzer-Stenner, R., Sa, V., and Kornev, K. (2010). Anomalous conformational instability and hydrogel formation of a cationic class of self-assembling oligopeptides. *Macromolecules* 43, 7800–7806. doi: 10.1021/ma101450b

Men, D., Zhang, Z.-P., Guo, J.-C., Zhu, D.-H., Bi, L.-J., Deng, Y.-J., et al. (2010). An auto-biotinylated bifunctional protein nanowire for ultra-sensitive molecular biosensing. *Biosens. Bioelectron.* 26, 1137–1141. doi: 10.1016/j.bios.2010.07.103

Mènard-Moyon, C., Venkatesh, V., Krishna, K. V., Bonachera, F., Verma, S., and Bianco, A. (2015). Self-assembly of tyrosine into controlled supramolecular nanostructures. *Chem. Eur. J.* 2015, 11681–11686. doi: 10.1002/chem.201502076

Mishra, A., Loo, Y., Deng, R., Chuah, Y. J., Hee, H. T., Ying, J. Y., et al. (2011). Ultrasmall natural peptides self-assemble to strong temperature-resistant helical fibers in scaffolds suitable for tissue engineering. *Nano Today* 6, 232–239. doi: 10.1016/j.nantod.2011.05.001

Mompean, M., Li, W., Li, J., Laage, S., Siemer, A. B., Bozkurt, G., et al. (2018). The structure of the necrosome RIPK1-RIPK3 core, a human hetero-amyloid signaling complex. *Cell* 173, 1244–1253.e10. doi: 10.1016/j.cell.2018.03.032

Mossou, E., Teixeira, S. C. M., Mitchell, E. P., Mason, S. A., Adler-Abramovich, L., Gazit, E., et al. (2014). The self−assembling zwitterionic form of L−phenylalanine at neutral pH. *Acta Crystallogr. Sect. C Struct. Chem.* 70, 326–331. doi: 10.1107/S2053229614002563

Nagai, Y., Unsworth, L. D., Koutsopoulos, S., and Zhang, S. (2006). Slow release of molecules in self-assembling peptide nanofiber scaffold. *J. Contr. Rel.* 115, 18–25. doi: 10.1016/j.jconrel.2006.06.031

Nagai, Y., Yokoi, H., Kaihara, K., and Naruse, K. (2012). The mechanical stimulation of cells in 3D culture within a self-assembling peptide hydrogel. *Biomaterials* 33, 1044–1051. doi: 10.1016/j.biomaterials.2011.10.049

Nagy-Smith, K., Moore, E., Schneider, J., and Tycko, R. (2015). Molecular structure of monomorphic peptide fibrils within a kinetically trapped hydrogel network. *Proc. Natl. Acad. Sci. U.S.A.* 112, 9816–9821. doi: 10.1073/pnas.1509313112

Nannenga, B., and Gonen, T. (2019). The cryo-EM method microcrystal electron diffraction (MicroED). *Nat. Methods* 16, 369–379. doi: 10.1038/s41592-019-0395-x

Nasica-Labouze, J., Hguyen, P. H., Sterpone, F., Berthoumieu, O., Buchete, N.-V., Coté, S., et al. (2015). Amyloid β Protein and Alzheimer's disease: when computer simulations complement experimental studies. *Chem. Rev.* 115, 3518–3563. doi: 10.1021/cr500638n

Nelson, R., Sawaya, M. R., Balbirnie, M., Madsen, A. O., Riekel, C., Grothe, R., et al. (2005). Structure of the cross-beta spine of amyloid-like fibrils. *Nature* 435, 773–778. doi: 10.1038/nature03680

Niece, K. L., Hartgerink, J. D., Donners, J. J. J. M., and Stupp, S. I. (2003). Self-assembly combining two bioactive peptide-amphiphile molecules into nanofibers by electrostatic attraction. *J. Am. Che. Soc.* 125, 7146–7147. doi: 10.1021/ja028215r

Nuno, H. C. S., Silva, N. H. C. S., Vilela, C., Marrucho, I. M., Freire, C. S. R., Neto, C. P., et al. (2014). Protein-based materials: from sources to innovative sustainable materials for biomedical applications. *J.Mater. Chem. B* 2, 3715–3740. doi: 10.1039/C4TB00168K

Nyrkova, I. A., Semenov, A. N., Aggeli, A., and Boden, N. (2000). Fibril stability in solutions of twisted β-sheet peptides: a new kind of micellization in chiral systems. *Eur. Phys. J. B* 17, 481–497. doi: 10.1007/s100510070127

Oliveri, V., Zimbone, S., Giuffrida, M. L., Bellia, F., Tomasello, M. F., and Vecchio, G. (2018). Porphyrin cyclodextrin conjugates modulate amyloid beta peptide aggregation and cytotoxicity. *Chem. Eur. J.* 24, 6349–6353. doi: 10.1002/chem.201800807

Pace, N. R. (2001). The universal nature of biochemistry. *Proc. Natl. Acad. Sci. U.S.A.* 98, 805–808. doi: 10.1073/pnas.98.3.805

Paramonov, S. E., Jun, H. W., and Hartgerink, J. D. (2006). Self-assembly of peptide-amphiphile nanofibers: the roles of hydrogen bonding and amphiphilic packing. *J. Am. Chem. Soc.* 128, 7291–7298. doi: 10.1021/ja060573x

Paravastu, A. K., Leapman, R. D., Yau, W. M., and Tycko, R. (2008). Molecular structural basis for polymorphism in Alzheimer's beta-amyloid fibrils. *Proc. Natl. Acad. Sci. U.S.A.* 105, 18349–18354. doi: 10.1073/pnas.0806270105

Pashuck, E. T., Cui, H., and Stupp, S. I. (2010). Tuning supramolecular rigidity of peptide fibers through molecular structure. *J. Am. Chem. Soc.* 132, 6041–6046. doi: 10.1021/ja908560n

Pashuck, E. T., and Stupp, S. I. (2010). Direct observation of morphological transformation from twisted ribbons into helical ribbons. *J. Am. Chem. Soc.* 132, 8819–8821. doi: 10.1021/ja100613w

Paul, T. J., Hoffmann, Z., Wang, C., Shanmugasundaram, M., De Joannis, J., Shekhtman, A., et al. (2016). Structural and mechanical properties of amyloid

beta fibrils: a combined experimental and theoretical approach. *Phys. Chem. Lett.* 7, 2758–2764. doi: 10.1021/acs.jpclett.6b01066

Pauling, L., and Corey, R. B. (1951). The pleated sheet, a new layer configuration of polypeptide chains. *Proc. Natl. Acad. Sci. U.S.A.* 37, 251–256. doi: 10.1073/pnas.37.5.251

Pauling, L., Corey, R. B., and Branson, H. R. (1951). The structure of proteins: two hydrogen-bonded helical configurations of the polypeptide chain. *Proc. Natl. Acad. Sci. U.S.A.* 37, 205–211. doi: 10.1073/pnas.37.4.205

Pawar, A. P., DuBay, K. F., Zurdo, J., Chiti, F., Vendruscolo, M., and Dobson, C. M. (2005). Prediction of "aggregation-prone" and "aggregation-susceptible" regions in proteins associated with neurodegenerative diseases. *J. Mol. Biol.* 350, 379–392. doi: 10.1016/j.jmb.2005.04.016

Pena-Francesch, A., Jung, H., Hickner, M. A., Tyagi, M., Allen, B. D., and Demirel, M. C. (2018). Programmable proton conduction in stretchable and self-healing proteins. *Chem. Mater.* 30, 898–905. doi: 10.1021/acs.chemmater.7b04574

Peralta, M. D. R., Karsai, A., Ngo, A., Sierra, C., Fong, K. T., Hayre, N. R., et al. (2015) Engineering amyloid fibrils from β-solenoid proteins for biomaterials applications. *ACS Nano* 9, 449–463. doi: org/10.1021/nn5056089

Perween, S., Chandanshive, B., Kotamarthi, H. C., and Khushalani, D. (2013). Single amino acid based self-assembled structure. *Soft Matter* 9, 10141–10145. doi: 10.1039/C3SM51054A

Pilkington, S. M., Roberts, S. J., Meade, S. J., and Gerrard, J. A. (2010). Amyloid fibrils as a nanoscaffold for enzyme immobilization. *Biotechnol. Prog.* 26, 93–100. doi: 10.1002/btpr.309

Pounot, K., Chaaban, H., Foderà, V., Schirò, G., Weik, M., and Seydel, T. (2020). Tracking internal and global diffusive dynamics during protein aggregation by high-resolution neutron spectroscopy. *J. Phys. Chem. Lett.* 11, 6299–6304. doi: 10.1021/acs.jpclett.0c01530

Rajbhandary, A., and Nilsson, B. L. (2017). Investigating the effects of peptoid substitutions in self-assembly of Fmoc-diphenylalanine derivatives. *Biopolymers* 108:e22994. doi: 10.1002/bip.22994

Rapaport, H., Grisaru, H., and Silberstein, T. (2008). Hydrogel scaffolds of Amphiphilic and Acidic β−Sheet peptides. *Adv. Funct. Mater.* 18, 2889–2896. doi: 10.1002/adfm

Reches, M., and Gazit, E. (2003). Casting metal nanowires within discrete self-assembled peptide nanotubes. *Science* 300, 625–627. doi: 10.1126/science.1082387

Reches, M., and Gazit, E. (2005). Self−assembly of peptide nanotubes and amyloid−like structures by charged−termini−capped diphenylalanine peptide analogues. *Isr. J. Chem.* 45, 363–371. doi: 10.1560/5MC0-V3DX-KE0B-YF3J

Redvar, E., and Azevedo, H. S. (2019). Supramolecular peptide/polymer hybrid hydrogels for biomedical applications. *Macromol. Biosci.* 19:e1800221. doi: 10.1002/mabi.201800221

Reynolds, N. P., Adamcik, J., Berryman, J. T., Handschin, S., Asghar, A., Zanjani, H., et al. (2017). Competition between crystal and fibril formation in molecular mutations of amyloidogenic peptides. *Nat. Commun.* 8:1338. doi: 10.1038/s41467-017-01424-4

Riek, R., and Eisenberg, D. S. (2016). The activities of amyloids from a structural perspective. *Nature* 539, 227–235. doi: 10.1038/nature20416

Rivas, M., del Valle, L. J., Alemán, C., and Puiggalí, J. (2019). Peptide self-assembly into hydrogels for biomedical applications related to hydroxyapatite gels. *Gels* 5:14. doi: 10.3390/gels5010014

Roberts, D., Rochas, C., Saiani, A., and Miller, A. F. (2012). Effect of peptide and guest charge on the structural, mechanical and release properties of β-sheet forming peptides. *Langmuir* 28, 16196–16206. doi: 10.1021/la303328p

Röder, C., Kupreichyk, T., Gremer, L., Schäfer, L. U., Pothula, K. R., Ravelli, R. B. G., et al. (2020). Cryo-EM structure of islet amyloid polypeptide fibrils reveals similarities with amyloid-β fibrils. *Nat. Struct. Mol. Biol.* 27, 660–667. doi: 10.1038/s41594-020-0442-4

Rodriguez, J. A., Ivanova, M. I., Sawaya, M. R., Cascio, D., Reyes, F. E., Shi, D., et al. (2015). Structure of the toxic core of α-synuclein from invisible crystals. *Nature* 525, 486–490. doi: 10.1038/nature15368

Roth-Konforti, M. E., Comune, M., Halperin-Sternfeld, M., Grigoriants, I., Shabat, D., and Adler-Abramovich, L. (2018). UV light-responsive peptide-based supramolecular hydrogel for controlled drug delivery. *Macromol. Rapid Comm.* 39:1800588. doi: 10.1002/marc.201800588

Ryan, D. M., Anderson, S. B., and Nilsson, B. L. (2010a). The influence of side-chain halogenation on the self-assembly and hydrogelation of Fmoc-phenylalanine derivatives. *Soft Matter* 6, 3220–3231. doi: 10.1039/C0SM00018C

Ryan, D. M., Anderson, S. B., Senguen, F. T., Youngman, R. E., and Nilsson, B. L. (2010b). Self-assembly and hydrogelation promoted by F5-phenylalanine. *Soft Matter* 6, 475–479. doi: 10.1039/B916738B

Ryan, D. M., Doran, T. M., and Nilsson, B. N. (2011). Stabilizing self-assembled Fmoc–F5–Phe hydrogels by co-assembly with PEG-functionalized monomers. *Chem. Commun.* 47, 475–477. doi: 10.1039/C0CC02217A

Saiani, A., Mohammed, A., Frielinghausc, H., Collins, R., Hodson, N., Kielty, C. M., et al. (2009). Self-assembly and gelation properties of α-helix versus β-sheet forming peptides. *Soft Matter* 5, 193–202. doi: 10.1039/B811288F

Sakono, M., Zako, T., and Maeda, M. (2012). Naked-eye detection of amyloid aggregates using gold nanoparticles modified with amyloid beta antibody. *Anal. Sci.* 28:73. doi: 10.2116/analsci.28.73

Salinas, N., Colletier, J. P., Moshe, A., and Landau, M. (2018). Extreme amyloid polymorphism in Staphylococcus aureus virulent PSMα peptides. *Nat. Commun.* 9:3512. doi: 10.1038/s41467-018-05490-0

Salinas, N., Povolotsky, T. L., Landau, M., and Kolodkin-Gal, I. (2021). Emerging roles of functional bacterial amyloids in gene regulation, toxicity, and immunomodulation. *Microbiol. Mol. Biol. Rev.* 85:e00062-20. doi: 10.1128/MMBR.00062-20

Sambashivan, S., Liu, Y., Sawaya, M. R., Gingery, M., and Eisenberg, D. (2005). Amyloid-like fibrils of ribonuclease A with three-dimensional domain-swapped and native-like structure. *Nature* 437, 266–269. doi: 10.1038/nature03916

Saravanan, A., Huang, B.-R., and Kathiravan, D. (2018). Bio−industrial waste silk fibroin protein and carbon nanotube−induced carbonized growth of one−dimensional ZnO−based bio−nanosheets and their enhanced optoelectronic properties. *Chem. Eur. J.* 24, 12574–12583. doi: 10.1002/chem.201800702

Sawaya, M. R., Sambashivan, S., Nelson, R., Ivanova, M. I., Sievers, S. A., Apostol, M. I., et al. (2007). Atomic structures of amyloid cross-β spines reveal varied steric zippers. *Nature* 447, 453–457. doi: 10.1038/nature05695

Schacht, K., and Scheibel, T. (2011). Controlled hydrogel formation of a recombinant spider silk protein. *Biomacromolecules* 12, 2488–2495. doi: 10.1021/bm200154k

Schmidt, M., Rohou, A., Lasker, K., Yadav, J. K., Schiene-Fischer, C., Fändrich, M., et al. (2015). Peptide dimer structure in an Aβ(1–42) fibril visualized with cryo-EM. *Proc. Natl. Acad. Sci. U.S.A.* 112, 11858–11863. doi: 10.1073/pnas.1503455112

Schweighauser, M., Shi, Y., Tarutani, A., Kametani, F., Murzin, A. G., Ghetti, B., et al. (2020). Structures of α-synuclein filaments from multiple system atrophy. *Nature* 585, 464–469. doi: 10.1038/s41586-020-2317-6

Seidler, P. M., Boyer, D. R., Rodriguez, J. A., Sawaya, M. R., Cascio, D., Murray, K., et al. (2018). Structure-based inhibitors of tau aggregation. *Nat. Chem.* 10, 170–176. doi: 10.1038/nchem.2889

Seilheimer, B., Bohrmann, B., Bondolfi, L., Muller, F., Stuber, S., and Dobeli, H. (1997). The toxicity of the Alzheimer's β-amyloid peptide correlates with a distinct fiber morphology. *J. Struct. Biol.* 119, 59–71. doi: 10.1006/jsbi.1997.3859

Senior, A. W., Evans, R., Jumper, J., Kirkpatrick, J., Sifre, L., Green, T., et al. (2020). Improved protein structure prediction using potentials from deep learning. *Nature* 577, 706–710. doi: 10.1038/s41586-019-1923-7

Shaham-Niv, S., Adler-Abramovich, L., Schnaider, L., and Gazit, E. (2015). Extension of the generic amyloid hypothesis to nonproteinaceous metabolite assemblies. *Sci. Adv.* 1:e1500137. doi: 10.1126/sciadv.1500137

Shaham-Niv, S., Rehak, P., Vuković, L., Adler-Abramovich, L., Kràl, P., and Gazit, E. (2017). Formation of apoptosis-inducing amyloid fibrils by tryptophan. *Isr. J. Chem.* 57, 729–737. doi: 10.1002/ijch.201600076

Shi, J., Gao, Y., Yang, Z., and Xu, B. (2011). Exceptionally small supramolecular hydrogelators based on aromatic–aromatic interactions. *Beilstein J. Org. Chem.* 7, 167–172. doi: 10.3762/bjoc.7.23

Sikorski, P., and Atkins, E. (2005). New model for crystalline polyglutamine assemblies and their connection with amyloid fibrils. *Biomacromolecules* 6, 425–432. doi: 10.1021/bm0494388

Singh, P., Brar, S. K., Bajaj, M., Narang, N., Mithu, V. S., Katare, O. P., et al. (2017). Self-assembly of aromatic α-amino acids into amyloid inspired nano/micro

scaled architects. *Mater. Sci. Eng.* 72, 590–600. doi: 10.1016/j.msec.2016.11.117

Singh, V., Snigdha, K., Singh, C., Sinhad, N., and Thakur, A. K. (2015). Understanding the self-assembly of Fmoc–phenylalanine to hydrogel formation. *Soft Matter* 11, 5353–5364. doi: 10.1039/c5sm00843c

Slabov, V., Kopyl, S., Soares dos Santos, M. P., and Kholkin. (2019). "A. piezoelectricity in self-assembled peptides: a new way towards electricity generation at nanoscale," in *Nanogenerators*, eds S. J. Kim, A. Chandrasekhar, and N. R. Alluri (London: InTech). doi: 10.5772/intechopen.89703

Smith, A. M., Williams, R. J., Tang, C., Coppo, P., Collins, R. F., Turner, M. L., et al. (2008). Fmoc-diphenylalanine self assembles to a hydrogel via a novel architecture based on π-π interlocked β-sheets. *Adv. Mater.* 20, 37–41. doi: 10.1002/adma.200701221

Soto, C. (2003). Unfolding the role of protein misfolding in neurodegenerative diseases. *Nat. Rev. Neurosci.* 4, 49–60. doi: 10.1038/nrn1007

Soto, C., and Pritzkow, S. (2018). Protein misfolding, aggregation, and conformational strains in neurodegenerative diseases. *Nat. Neurosci.* 21, 1332–1340. doi: 10.1038/s41593-018-0235-9

Stie, M. B., Corezzi, M., Bombin, A. D. J., Ajallouеian, F., Attrill, E., Pagliara, S., et al. (2020). Waterborne electrospinning of α-lactalbumin generates tunable and biocompatible nanofibers for drug delivery. *ACS Appl. Nano Mater.* 3, 1910–1921. doi: 10.1021/acsanm.9b02557

Sunde, M., Serpell, L. C., Bartlam, M., Fraser, P. E., Pepys, M. B., and Blake, C. F. (1997). Common core structure of amyloid fibrils by synchrotron X-ray diffraction. *J. Mol. Biol.* 273, 729–739. doi: 10.1006/jmbi.1997.1348

Sutton, S., Campbell, N. L., Cooper, A. I., Kirkland, M., Frith, W. J., and Adams, D. J. (2009). Controlled release from modified amino acid hydrogels governed by molecular size or network dynamics. *Langmuir* 25, 10285–10291. doi: 10.1021/la9011058

Swanekamp, R. J., Welch, J. J., and Nilsson, B. L. (2014). Proteolytic stability of amphipathic peptide hydrogels composed of self-assembled pleated b-sheet or coassembled rippled β-sheet fibrils. *Chem. Commun.* 50, 10133–10136. doi: 10.1039/c4cc04644g

Taglialegna, A., Lasa, I., and Valle, J. (2016). Amyloid structures as biofilm matrix scaffolds. *J. Bacter.* 198, 2579–2588. doi: 10.1128/JB.00122-16

Takahashi, Y., Ueno, A., and Mihara, H. (2002). Amyloid architecture: complementary assembly of heterogeneous combinations of three or four peptides into amyloid fibrils. *ChemBioChem* 3, 637–642. doi: 10.1002/1439-7633(20020703)3:7<637::AID-CBIC637<3.0.CO;2-9

Tamamis, P., Adler-Abramovich, L., Gazit, E., and Archontis, G. (2008). "Insights into the self-assembly of phenylalanine oligopeptides by replica exchange md simulations with the gbsw implicit-Solvent Model," in *From Computational Biophysics to Systems Biology (CBSB08)*, Vol. 40, eds U. H. E. Hansmann, J. H. Meinke, S. Mohanty, W. Nadler, and O. Zimmermann (Ho Chi Minh: John von Neumann Institute for Computing (Jilich), NIC Series), 393–396.

Tang, C., Ulijn, R. V., and Saiani, A. (2011). Effect of Glycine Substitution on Fmoc-Diphenylalanine Self-Assembly and Gelation Properties. *Langmuir* 27, 14438–14449. doi: 10.1021/la202113j

Taricska, N., Horváth, D., Menyhárd, D. K., Ákontz−Kiss, H., Noji, M., So, M., et al. (2020). The route from the folded to the amyloid state: exploring the potential energy surface of a drug−like miniprotein. *Chem. Eur. J.* 26, 1968–1978. doi: 10.1002/chem.201903826

Tena-Solsona, M., Nanda, J., Díaz-Oltra, S., Chotera, A., Ashkenasy, G., and Escuder, B. (2016). Emergent catalytic behavior of self−assembled low molecular weight peptide−based aggregates and hydrogels. *Chem. Eur. J.* 22, 6687–6694. doi: 10.1002/chem.201600344

Tenidis, K., Waldner, M., Bernhagen, J., Fischle, W., Bergmann, M., Weber, M., et al. (2000). Identification of a penta- and hexapeptide of islet amyloid polypeptide (IAPP) with amyloidogenic and cytotoxic properties. *J. Mol. Biol.* 295, 1055–1071. doi: 10.1006/jmbi.1999.3422

Tomar, D., Chaudharya, S., and Jena, K. C. (2019). Self-assembly of L-phenylalanine amino acid: electrostatic induced hindrance of fibril formation. *RSC Adv.* 9, 12596–12605. doi: 10.1039/C9RA00268E

Tsai, H.-H. G., Reches, M., Tsai, C.-J., Gunasekaran, K., Gazit, E., and Nussinov, R. (2005). Energy landscape of amyloidogenic peptide oligomerization by parallel-tempering molecular dynamics simulation: significant role of Asn ladder. *Proc. Natl. Acad. Sci. U.S.A.* 102, 8174–8179. doi: 10.1073/pnas.0408653102

Tuttle, M. D., Comellas, G., Nieuwkoop, A. J., Covell, D. J., Berthold, D. A., Kloepper, K. D., et al. (2016). Solid-state NMR structure of a pathogenic fibril of full-length human α-synuclein. *Nat. Struct. Mol. Biol.* 23, 409–415. doi: 10.1038/nsmb.3194

Tycko, R. (2011). Solid state NMR studies of amyloid fibril structure. *Annu. Rev. Phys. Chem.* 62, 279–299. doi: 10.1146/annurev-physchem-032210-103539

Tzokova, N., Fernyhough, C., Butler, M. F., Armes, S. P., Ryan, A. J., Topham, P. D., et al. (2009a). The effect of PEO length on the self-assembly of poly(ethylene oxide)-tetrapeptide conjugates prepared by "click" chemistry. *Langmuir* 25, 11082–11089. doi: 10.1021/la901413n

Tzokova, N., Fernyhough, C. M., Topham, P. D., Sandon, N., Adams, D. J., Butler, M. F., et al. (2009b). Soft hydrogels from nanotubes of poly (ethylene oxide)- tetraphenylalanine conjugates prepared by click chemistry. *Langmuir* 25, 2479–2485. doi: 10.1021/la8035659

van Melckebeke, H., Wasmer, C., Lange, A., Ab, E., Loquet, A., Böckmann, A., et al. (2010). Atomic-resolution three-dimensional structure of HET-s(218-289) amyloid fibrils by solid-state NMR spectroscopy. *J. Am. Chem. Soc.* 132, 13765–13775. doi: 10.1021/ja104213j

Vasconcelos, A., Freddi, G., and Cavaco-Paulo, A. (2008). Biodegradable materials based on silk fibroin and keratin. *Biomacromolecules* 9, 1299–1305. doi: 10.1021/bm7012789

Wang, J. Q., Sun, Y. J., Dai, J. R., Zhao, Y. R., Cao, M. W., Wang, D., et al. (2015). Effects of alkyl chain length and peptide charge distribution on self-assembly and hydrogelation of lipopeptide amphiphiles. *Acta Phys. Chim. Sin.* 31, 1365–1373. doi: 10.3866/PKU.WHXB201505051

Wang, K., Keasling, J. D., and Muller, S. J. (2005). Effects of the sequence and size of non-polar residues on self-assembly of amphiphilic peptides. *Int. J. Biol. Macromol.* 36, 232–240. doi: 10.1016/j.ijbiomac.2005.06.006

Wang, M., Wang, J., Zhou, P., Deng, J., Zhao, Y., Sun, Y., et al. (2018). Nanoribbons self-assembled from short peptides demonstrate the formation of polar zippers between β-sheets. *Nat. Commun.* 9:5118. doi: 10.1038/s41467-018-07583-2

Wei, G., Su, Z., Reynolds, N. P., Arosio, P., Hamley, I. W., Gazit, E., et al. (2017). Self-assembling peptide and protein amyloids: from structure to tailored function in nanotechnology. *Chem. Soc. Rev.* 46, 4661–4708. doi: 10.1039/c6cs00542j

Wiltzius, J. J., Landau, M., Nelson, R., Sawaya, M. R., Apostol, M. I., Goldschmidt, L., et al. (2009). Molecular mechanisms for protein-encoded inheritance. *Nat. Struct. Mol. Biol.* 16, 973–978. doi: 10.1038/nsmb.1643

Xiao, Y., Ma, B., McElheny, D., Parthasarathy, S., Long, F., Hoshi, M., et al. (2015). Aβ(1-42) fibril structure illuminates self-recognition and replication of amyloid in Alzheimer's disease. *Nat. Struct. Mol. Biol.* 22, 499–505. doi: 10.1038/nsmb.2991

Yan, C., and Pochan, D. J. (2010). Rheological properties of peptide-based hydrogels for biomedical and other applications. *Chem. Soc. Rev.* 39, 3528–3540. doi: 10.1039/B919449P

Yan, H., Saiani, A., Gough, J. E., and Miller, A. F. (2006). Thermoreversible protein hydrogel as cell scaffold. *Biomacromolecules* 7, 2776–2782. doi: 10.1021/bm0605560

Yan, X., He, Q., Wang, K., Duan, L., Cui, Y., and Li, J. (2007). Transition of cationic dipeptide nanotubes into vesicles and oligonucleotide delivery. *Angew. Chem. Int. Ed.* 46, 2431–2434. doi: 10.1002/anie.200603387

Yan, X., Zhu, P., and Li, J. (2010). Self-assembly and application of diphenylalanine-based nanostructures. *Chem. Soc. Rev.* 39, 1877–1890. doi: 10.1039/B915765B

Yang, Z., Gu, H., Fu, D., Gao, P., Lam, J.K., and Xu, B. (2004). Enzymatic formation of supramolecular hydrogels. *Adv. Mater.* 16, 1440–1444. doi: 10.1002/adma.200400340

Yang, Z., Liang, G., and Xu, B. (2008). Enzymatic hydrogelation of small molecules. *Acc. Chem. Res.* 41, 315–326. doi: 10.1021/ar7001914

Yang, Z-Y., Zhong, Y-Y., Zheng, J., Liu, Y., Li, T., Hu, E., et al. (2021). Fmoc-amino acid-based hydrogel vehicle for delivery of amygdalin to perform neuroprotection. *Smart Mat. Med.* 2, 56–64. doi: 10.1016/j.smaim.2020.10.004

Yokoi, H., Kinoshita, T., and Zhang S. (2005). Dynamic reassembly of peptide RADA16 nanofiber scaffold. *Proc. Natl. Acad. Sci. U.S.A.* 102, 8414–8419. doi: 10.1073/pnas.0407843102

Zhai, Z., Xu, K., Mei, L., Wu, C., Liu, J., Liu, Z., et al. (2019). Co-assembled supramolecular hydrogels of cell adhesive peptide and alginate for rapid hemostasis and efficacious wound healing. *Soft Matter* 15, 8603–8610. doi: 10.1039/C9SM01296F

Zhang, S., Holmes, T. C., di Persio, C. M., Hynes, R. O., Su, X., and Rich, A. (1993a) Self-complementary oligopeptide matrices support mammalian cell attachment. *Biomaterials* 16, 1385–1393. doi: 10.1016/0142-9612(95)96874-Y

Zhang, S., Holmes, T. C., Lockshin, C., and Rich, A. (1993b) Spontaneous assembly of a self-complementary oligopeptide to form a stable macroscopic membrane. *Proc. Natl. Acad. Sci. U.S.A.* 90, 3334–3338. doi: 10.1073/pnas.90.8.3334

Zhang, W., Tarutani, A., Newell, K. L., Murzin, A. G., Matsubara, T., Falcon, B., et al. (2020). Novel tau filament fold in corticobasal degeneration. *Nature* 580, 283–287. doi: 10.1038/s41586-020-2043-0

Zhang, Y., Gu, H., Yang, Z., and Xu, B. (2003). Supramolecular hydrogels respond to ligand-receptor interaction. *J. Am. Chem Soc.* 125, 13680–13681. doi: 10.1021/ja036817k

Zheng, H., and Zuo, B. (2021). Functional silk fibroin hydrogels: preparation, properties and applications. *J. Mater. Chem. B*. doi: 10.1039/D0TB02099K

Ziaunys, M., and Smirnovas, V. (2019). Emergence of visible light optical properties of L-phenylalanine aggregates. *PeerJ* 7:e6518. doi: 10.7717/peerj.6518

Zottig, X., Côté-Cyr, M., Arpin, D., Archambault, D., and Bourgault, S. (2020). Protein supramolecular structures: from self-assembly to nanovaccine design. *Nanomaterials* 10:1008. doi: 10.3390/nano1005 1008

Conflict of Interest: The authors declare that the research was conducted in the absence of any commercial or financial relationships that could be construed as a potential conflict of interest.

frontiers in Bioengineering and Biotechnology

BRIEF RESEARCH REPORT
published: 24 March 2021
doi: 10.3389/fbioe.2021.654349

SAXS/WAXS Investigation of Amyloid-β(16-22) Peptide Nanotubes

Theyencheri Narayanan[1]*, *Axel Rüter*[2] and *Ulf Olsson*[2]

[1] ESRF-The European Synchrotron, Grenoble, France, [2] Division of Physical Chemistry, Lund University, Lund, Sweden

This brief report presents an X-ray scattering investigation of self-assembled nanotubes formed by a short peptide. X-ray scattering methods enable multiscale structural elucidation of these nanotubes in solution under the same conditions involved in the self-assembly process. In particular, the dimensions of nanotubes and the crystalline organization within their walls can be determined quantitatively. This is illustrated in the case of amyloid-β(16-22) peptide nanotubes.

Keywords: peptide self-assembly, peptide nanotubes, peptide nanoribbons, X-ray scattering, SAXS

OPEN ACCESS

Edited by:
Maria Gazouli, National and Kapodistrian University of Athens, Greece

Reviewed by:
Vasil M. Garamus, Helmholtz Centre for Materials and Coastal Research (HZG), Germany
Angelina Angelova, UMR8612 Institut Galien Paris Sud (IGPS), France

***Correspondence:**
Theyencheri Narayanan
narayan@esrf.fr

Specialty section:
This article was submitted to Nanobiotechnology, a section of the journal Frontiers in Bioengineering and Biotechnology

Received: *16 January 2021*
Accepted: *24 February 2021*
Published: *24 March 2021*

Citation:
Narayanan T, Rüter A and Olsson U (2021) SAXS/WAXS Investigation of Amyloid-β(16-22) Peptide Nanotubes. Front. Bioeng. Biotechnol. 9:654349. doi: 10.3389/fbioe.2021.654349

1. INTRODUCTION

The hierarchical self-assembly of short peptides to form well-defined nanotubes of nearly macroscopic dimension has been the subject of numerous investigations (Childers et al., 2009; Valéry et al., 2011; Hamley, 2014). Most often short peptides self-assemble to form fibrillar morphologies but under certain specific conditions the ribbon-like fibrillar structure curls and form nanotubes of uniform dimension. This self-assembly is governed by the delicate interplay of hydrogen bonding, electrostatic, and entropic interactions. Both helical ribbons and nanotubes have similar mean curvature and zero Gaussian curvature (Ke et al., 2020). The size uniformity and tunability make them suitable for templated growth of functional nanomaterials with potential applications in modern technologies (Valéry et al., 2011; Hamley, 2014; Levin et al., 2020). The preceding article presented a short review of X-ray scattering investigations of different peptide systems forming similar nanotubes (Narayanan et al., 2021).

A well-known example for the nanotube forming peptide system is the $CH_3CO-KLVFFAE-NH_2$, a sequence from the amyloid-β peptide [Aβ(16-22)] (Lu et al., 2003; Mehta et al., 2008). This short peptide self-assembles in acetonitrile/water binary liquid mixture at pH 2 forming well-defined nanotubes with mean diameter and wall thickness about 52 and 4.3 nm, respectively. This system has been the subject of many structural investigations (Childers et al., 2009). Instead at pH 6, this peptide exhibits fibrillar morphology (Mehta et al., 2008). Using electron diffraction and complementary spectroscopic methods, the packing of peptides into bilayer leaflets within the tube wall was demonstrated (Mehta et al., 2008, 2013). A model for the lamination of peptides involving antiparallel β-sheets and the curling of peptide bilayers to form nanotubes was proposed (Childers et al., 2009).

This report presents a small and wide angle X-ray scattering (SAXS and WAXS, respectively) investigation of the Aβ(16-22) self-assembly over a wider peptide concentration range. A combination of SAXS and WAXS methods elucidates the different hierarchical levels exhibiting by the self-assembled structure. The improvement in the detection capability of scattering techniques now enable deciphering weak structural features submerged beneath a high background as illustrated here. In addition, a coexistence of two different structural moieties is observed at higher peptide concentrations.

2. MATERIALS AND METHODS

The Aβ(16-22) peptide ($CH_3CO-KLVFFAE-NH_2$) nanotubes were formed in 40 weight % acetonitrile/water solvent mixture with 0.1% trifluoroacetic acid (TFA) at pH close to 2 (Lu et al., 2003; Mehta et al., 2008). The peptide was purchased from CPC Scientific Inc. (purity of 97 %) and was used without further purification. The pH of the solvent was adjusted to 2 by the addition of TFA. Nanotubes were aged for several weeks prior to SAXS and WAXS measurements. The X-ray scattering experiments were performed on the ID02 beamline at the ESRF (Narayanan, 2014). The samples were loaded in a flow-through capillary cell (diameter $\sim$ 2 mm and wall thickness $\sim$ 10 μm) maintained at 25^{o}C, which enabled accurate background measurements from the capillary filled with the solvent as well as limited flow alignment of the nanotubes. To cover the broad size scales relevant to the self-assembled structure, two sample-to-detector distances of 8 and 1.2 m were used for SAXS and the WAXS detector was placed at 0.11 m from the sample. The measured two dimensional scattering patterns were normalized to an absolute intensity scale after applying detector specific corrections and isotropic patterns were azimuthally averaged to obtain the one-dimensional scattering profiles (Narayanan, 2014). After subtraction of the corresponding normalized background, one-dimensional profiles from different sample-to-detector distances were merged together to obtain the scattered intensity, $I(q)$ as a function of the magnitude of scattering vector (q). Where $q = (4\pi/\lambda)sin(\theta/2)$, with λ the wavelength of the X-rays ($\simeq$ 1 Å) and θ the scattering angle. The SAXS data were modeled in terms of core-shell cylinders (with the core scattering length density set to the same as the solvent) and rectangular parallelepiped form factors using the SasView software (Doucet et al., 2017). The helical ribbon form factor was adapted from the models presented in Pringle and Schmidt (1971) and Hamley (2008).

3. RESULTS AND DISCUSSION

Figure 1 presents the partially oriented 2D SAXS and WAXS patterns for four concentrations of the peptide over a restricted q range. At 0.1 % (by weight), the peptide was fully soluble without any features of nanotube scattering function. The 0.2 and 0.5% samples clearly showed the scattering form factor of nanotubes as indicated by the oscillations in SAXS intensity and corresponding WAXS patterns displayed weak Bragg peaks from the peptide packing within the nanotube walls. The 0.5% sample maintained the alignment of nanotubes induced by the flow while in 0.2% sample the orientation was lost upon cessation of the flow. The clear alignment of WAXS peaks in the 0.5% sample indicates that the β-sheets are oriented around the nanotube axis along a helical path with a pitch angle of 23^o. A distinguishing hallmark between the tubular and fibrillar morphologies is this azimuthal tilt in the β-sheet reflections. The SAXS patterns from 1.5 and 3.0% samples did not show the characteristic features of nanotube scattering form factor though some anisotropy is maintained in the former. Corresponding WAXS patterns displayed stronger Bragg peaks without clear azimuthal orientation. The observed SAXS features suggest a morphological transition but WAXS confirms that the molecular packing of peptides has not changed. This peptide is known to form nanotubes only around pH 2, whereas at higher pH a fibrillar assembly has been observed (Mehta et al., 2008). Here, the pH is fixed at 2 by the presence

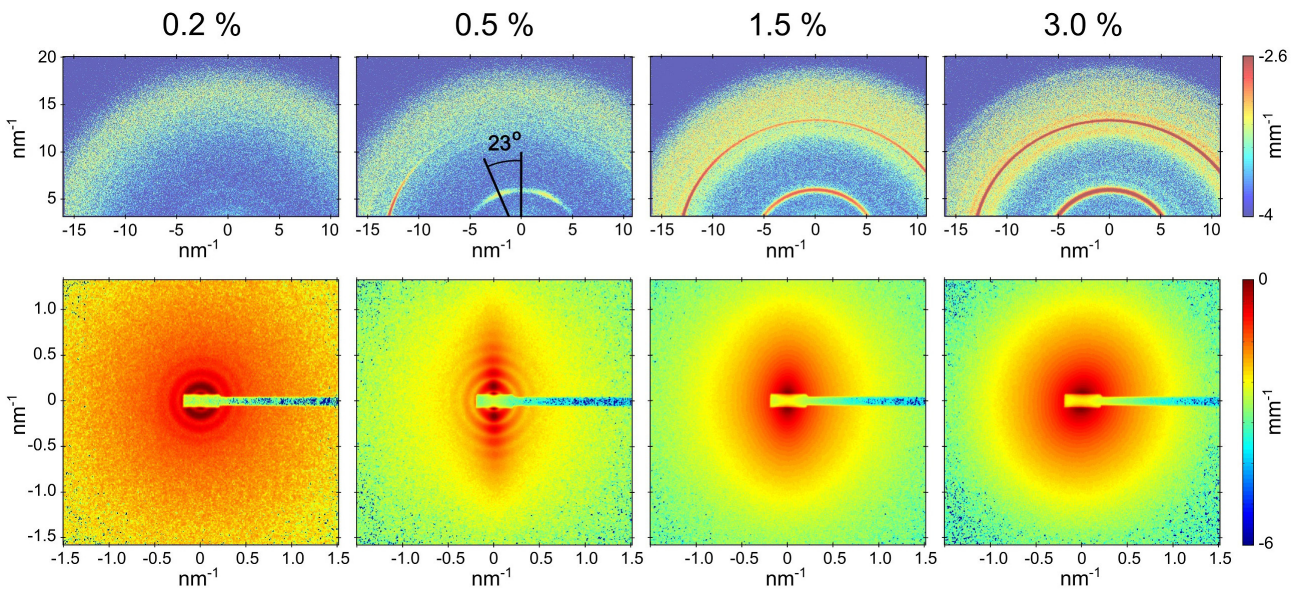

FIGURE 1 | Partially aligned SAXS and WAXS patterns (lower and upper panels, respectively) from Aβ(16-22) peptide samples at four different concentrations after the solvent background subtraction. In the case of 0.5% sample, the nanotubes are aligned along the horizontal axis and the relative orientation of nanotube radius and β-sheet laminations is shown. The SAXS sample-detector distance was 1.2 m.

of the strong acid TFA, and the lysine side group remains fully protonated at all concentrations studied.

Figures 2A,B depict the azimuthal average of the normalized SAXS and WAXS intensities, respectively over the full q range of measurements. To derive the structural parameters of the nanotubes, SAXS profiles were modeled by polydisperse core-shell (hollow) cylinder scattering function in SASView. The corresponding parameters, outer radius (R) and wall thickness (δ), were 24.8 and 5.2 nm, respectively for 0.2% sample and 24.6 and 4.4 nm, respectively for 0.5% sample. The mean length of the nanotubes was larger than the q range covered by these measurements. In the fits, it was kept in the range of 3,000–5,000 nm but from the alignment behavior, it is clear that the nanotubes are much longer. The obtained size parameters are consistent with previously reported values (Lu et al., 2003; Mehta et al., 2008). In the modeling, the wall thickness is constrained by the scattering minimum around q of 1–2 nm^{-1}, which was not resolved in previous studies. The inset of **Figure 2A** shows that the determination of this high q minimum critically depends on the accuracy of the solvent background subtraction. Due to concentration fluctuations, the acetonitrile/water solvent mixture background is a Lorentzian function (Narayanan, 2014) and not flat like that of pure water. The high q minimum of the nanotube scattering falls on the decaying part of the Lorentzian function with a correlation length $\simeq$ 0.8 nm. Nevertheless, the shift in the minimum is evident even in the background unsubtracted data. Although the outer diameter is nearly the same, the packing of peptides in the 0.5% sample appears to be tighter. The SAXS profiles of 1.5 and 3.0% samples showed only weak oscillations and the minima and maxima are less defined. This suggests a coexistence of two morphologies, which are likely nanotubes and nanofibrils. As a result, SAXS profiles were modeled by a linear combination of polydisperse hollow cylinder and monodisperse parallelepiped scattering functions. In addition, the weak minima and maxima have shifted to lower q values than in the 0.5% case implying an increase in the diameter of nanotubes or partial unwinding (helical ribbons). The model curve for 3.0% sample represents nanotube radius and wall thickness of 33.6 and 4.0 nm, respectively, and parallelepiped length, width, and thickness of 3,900, 36.0, and 3.5 nm, respectively. The corresponding nanotube and nanofibril number density fractions are 0.23 and 0.77, respectively. **Table 1** summarizes the main structural parameters derived from the SAXS modeling in terms of a linear combination of tube (hollow cylinder) and flat ribbon (parallelepiped) scattering functions.

For the 1.5 and 3.0% samples, the SAXS profiles can also be described by a linear combination of helical and flat ribbons with parameters of helix, mean radius, polydispersity, width, and length; 62, 0.06, 80, and 2,000 nm, respectively. The pitch was fixed at the same value as that of the tube (364 nm), determined by its radius and angle from the WAXS pattern (67^o). The helical ribbon form factor alone is not sufficient to describe the SAXS profiles and a clear power law decay of $I(q)$ at the high q region is absent (Hamley, 2008). The lack of significant orientation suggests that the nanotubes and nanofibrils are shorter than the nanotubes in the 0.5% sample. This is also consistent with the tendency of scattering profiles to flatten at lower q region. The structure factor of interparticle interactions (Narayanan, 2014) is neglected as the data do not display the signature of such an effect in 1.5 and 3.0% samples. Moreover, for a given peptide volume fraction (ϕ_p), the hollow nanotubes occupy a larger volume than ribbons as they also contain enclosed solvent. The nanotube volume fraction, ϕ_{tube}, is approximately given by $\phi_{tube} = (R/2\delta)\phi_p$ (Bucak et al., 2009). For the parameters in **Table 1**, nanotubes are roughly 3 times more voluminous than flat ribbons for the same ϕ_p.

The azimuthally averaged WAXS profiles are shown in **Figure 2B**. The inset displays the corresponding background unsubtracted data and shows the weak Bragg peaks superimposed on the strong structure factor of the solvent mixture. In addition, the perfect overlap of the solvent scattering confirms that the composition of the solvent remained the same in all four samples. The stronger Bragg peaks at 13.1 and 6.0 nm^{-1} corresponding to spacings of 0.479 and 1.046 nm represent the orthogonal β-strand periodic repeat and stacking of the antiparallel β-sheets, respectively. Interestingly, both these periodicities are very similar to the two orthogonal cross-β spacings, meridional and equatorial, respectively, observed in the fiber diffraction diagram of full length Aβ peptide (Serpell, 2000). These Bragg peaks can be assigned to the (1,0) and (0,1) reflections from a 2D rectangular lattice (Childers et al., 2009), schematically shown in **Figure 3**. The higher order peaks of the stacking or lamination can be found at 12 and 18 nm^{-1}, corresponding to spacings of 0.523 and 0.348 nm, respectively. In the case of nanofibrils, two additional weak peaks at 7.7 and 15 nm^{-1} (spacings 0.819 and 0.419 nm) are also observed, which may be from out of registry β strands. The observed peak positions in the WAXS are consistent with that reported by electron diffraction (Mehta et al., 2008), except for 5–10% dilation of spacings, which can be attributed to the drying effect in the latter. The advantage of WAXS is that the information is deduced in the solution condition that is more relevant in functional studies. **Figure 3** schematically illustrates the semi-crystalline organization within the nanotube walls and different crystallographic planes of the 2D lattice.

A transition from nanotubes to helical ribbons and then to nanofibrils has been observed in the case of amphiphilic peptide KI_4K with increasing acetonitrile in a similar aqueous solvent (Zhao et al., 2015). However, a large change in the relative concentration of acetonitrile (20–80 %) was required. These transformations have been attributed to the changes in the hydrophobic interaction in the side chains while the peptide backbone hydrogen bonding remained intact (Zhao et al., 2015). The amphiphilic peptide system A_6R is another example, where a coexistence of nanotubes and nanosheets has been observed at higher peptide concentrations (> 15%) (Hamley et al., 2013). In that case, the transition is attributed to enhanced screening of the electrostatic repulsion between the arginine units and C-terminal carboxyls, which stabilizes the planar geometry. For the related peptide A_6K a coexistence of nanotube and a high concentration planar lamellar phase has been reported (Cenker et al., 2011). The mechanism for the concentration induced structural transition from nanotubes to nanofibrils in the present case is not fully clear. The relative stabilities of nanotubes and twisted ribbons were recently discussed within a model considering different

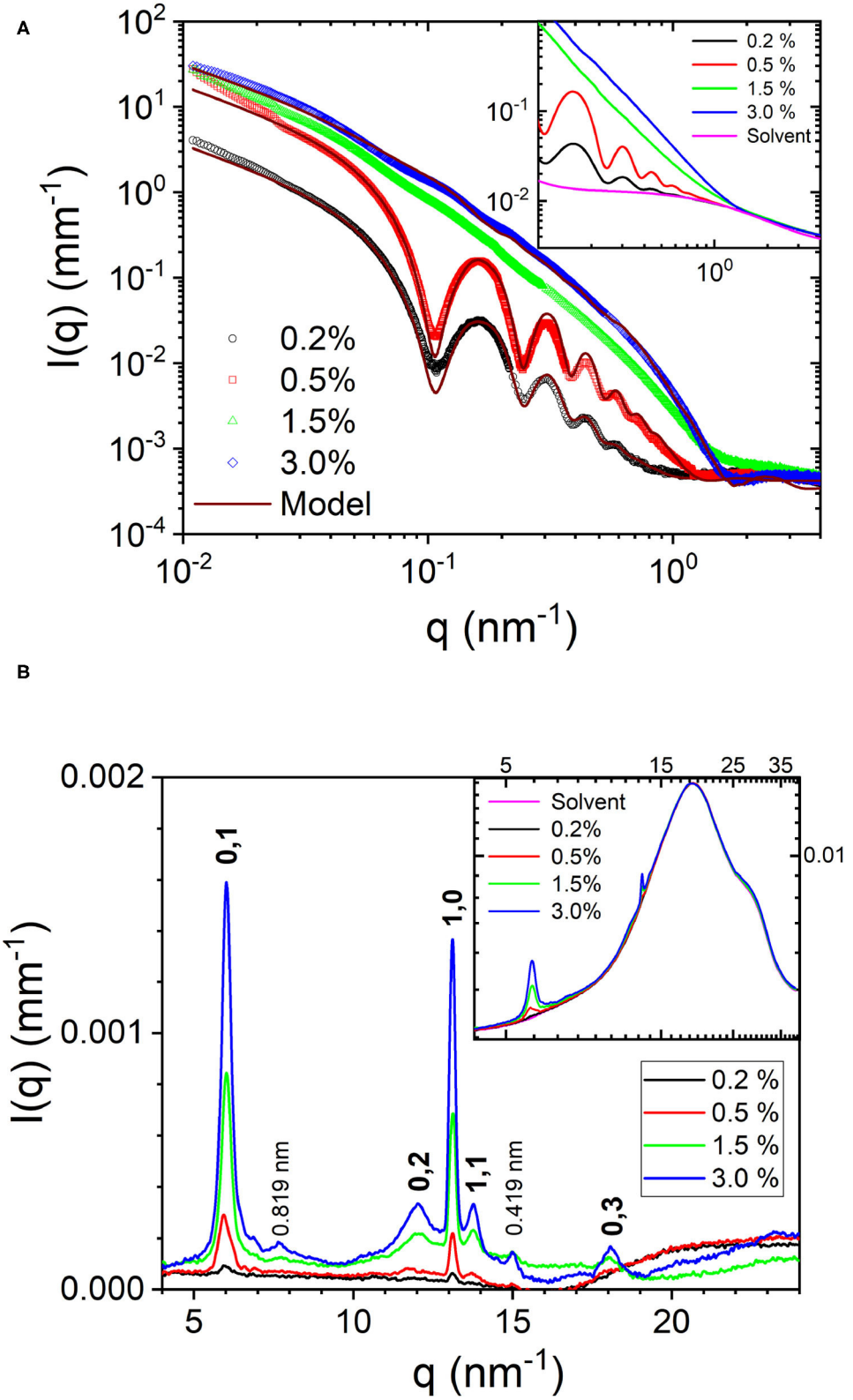

FIGURE 2 | (A) Normalized SAXS profiles from Aβ(16-22) peptide at four concentrations over the full q range of measurement. The inset displays the background unsubtracted profiles and highlights the importance of accurate background subtraction. **(B)** Corresponding WAXS profiles for the four peptide concentrations and indexation of the Bragg peaks (the spacings of which are specified in the text). The inset depicts the strong solvent background scattering.

TABLE 1 | Model parameters from the SAXS analysis of Aβ(16-22) peptide samples shown in **Figure 2A**.

Concentration (weight %)	Mean radius (nm)	Wall thickness (nm)	Polydispersity	Fraction	Length (nm)	Width (nm)	Thickness (nm)
0.2	24.8	5.2	0.09	1.0			
0.5	24.6	4.4	0.07	1.0			
1.5	34.0	4.0	0.06	0.63	3,900	36.0	3.5
3.0	34.0	4.0	0.06	0.23	3,900	36.0	3.5

Columns 2-5 correspond to nanotubes and the remaining (6-8) for nanofibrils. The number density fraction is a relative quantity with total nanotube and nanofibril fractions summing to 1. The error bars are in the last significant digit.

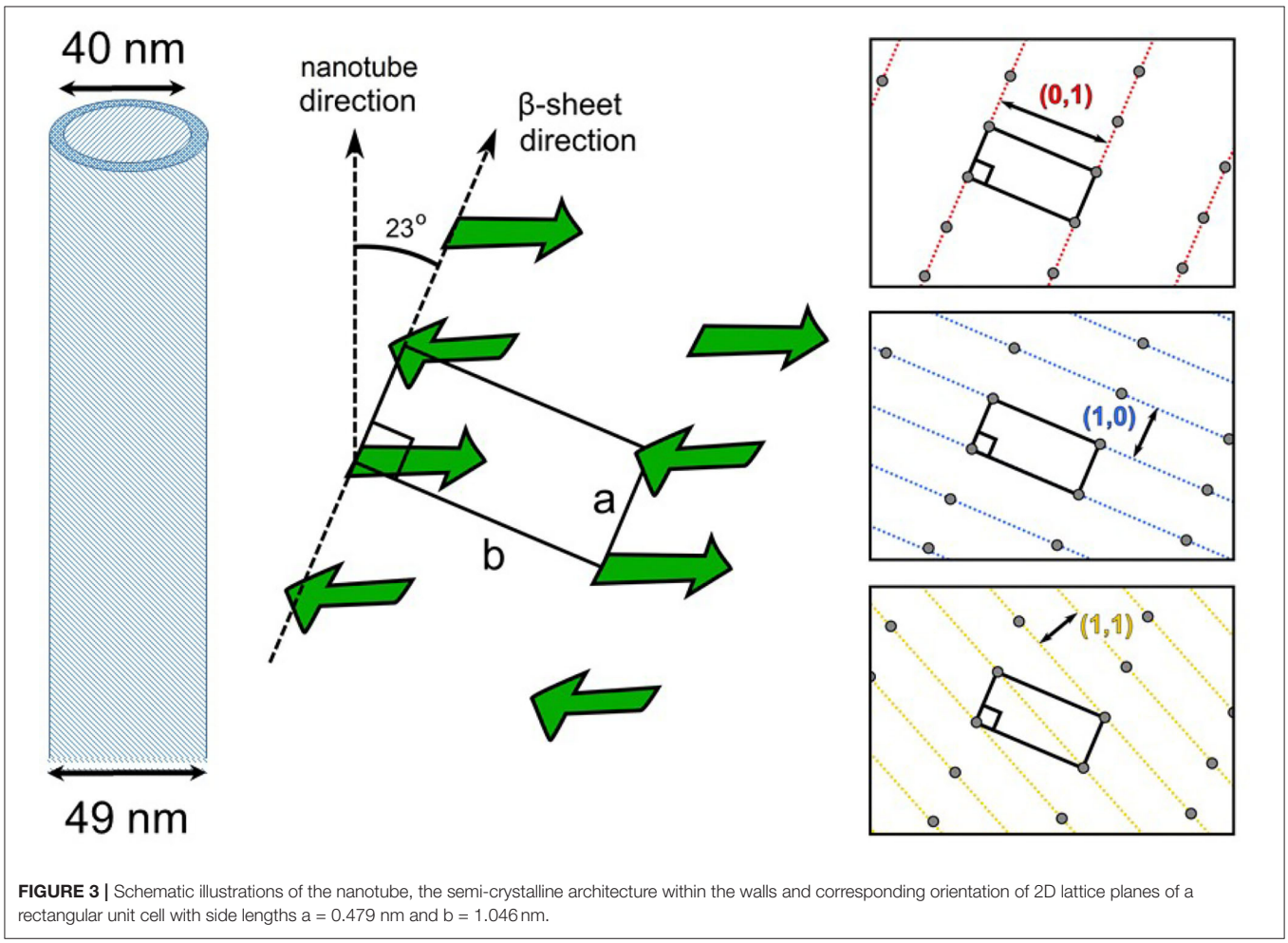

FIGURE 3 | Schematic illustrations of the nanotube, the semi-crystalline architecture within the walls and corresponding orientation of 2D lattice planes of a rectangular unit cell with side lengths a = 0.479 nm and b = 1.046 nm.

β-sheet deformations in the two structures in addition to a preferred β-sheet twist and an interfacial tension term (Rüter et al., 2020). The peptide chemical potential in the two structures can be very similar, and small perturbations (e.g., translational and rotational entropies) may shift the relative stability from nanotubes to nanofibrils.

4. CONCLUSION

Overall, the presented SAXS and WAXS data are in good agreement with the nanotube model derived from complementary electron microscopy and diffraction, an array of spectroscopic methods, and molecular dynamics simulations (Mehta et al., 2008, 2013; Childers et al., 2009). The nanotube diameter and wall thickness are consistent with the values reported earlier (Lu et al., 2003; Mehta et al., 2008) and compatible with an interdigitated bilayer arrangement of peptides in the nanotube walls. However, as the peptide concentration is increased, there is a gradual unwinding of the nanotubes, and partially unwound tubes or helical ribbons coexist with flat ribbons.

The example presented in the previous section illustrates the capability of scattering methods to decipher weak structural signals submerged beneath a large solvent background. This aspect could be further exploited in functional studies of self-assembled peptide systems. A combination of SAXS and WAXS methods enable hierarchical structural elucidation from the molecular packing up to the macroscopic dimension of the nanotubes simultaneously. In addition, the coexistence of different structural moieties can be identified on a quantitative scale.

DATA AVAILABILITY STATEMENT

The raw data supporting the conclusions of this article will be made available by the authors, without undue reservation.

AUTHOR CONTRIBUTIONS

UO and TN designed the research and TN performed X-ray measurements. TN and AR analyzed the data and all authors involved in the discussion of the results. TN wrote the first draft of the manuscript. All authors contributed in the revisions of the manuscript.

FUNDING

This study was funded by ESRF, and the Swedish Research Council.

ACKNOWLEDGMENTS

C.C. Cenker was thanked for the preparation of the Aβ peptide solutions investigated in this work and ESRF was acknowledged for the provision of synchrotron beam time.

SUPPLEMENTARY MATERIAL

The Supplementary Material for this article can be found online at: https://www.frontiersin.org/articles/10.3389/fbioe.2021.654349/full#supplementary-material

REFERENCES

Bucak, S., Cenker, C., Nasir, I., Olsson, U., and Zackrisson, M. (2009). Peptide nanotube nematic phase. *Langmuir* 25, 4262–4265. doi: 10.1021/la804175h

Cenker, Ç. Ç., Bucak, S., and Olsson, U. (2011). Nanotubes and bilayers in a model peptide system. *Soft Matter* 7, 4868–4875. doi: 10.1039/c0sm01186j

Childers, W. S., Ni, R., Mehta, A. K., and Lynn, D. G. (2009). Peptide membranes in chemical evolution. *Curr. Opin. Chem. Biol.* 13, 652–659. doi: 10.1016/j.cbpa.2009.09.027

Doucet, M., Cho, J. H., Alina, G., Bakker, J., Bouwman, W., Butler, P., et al. (2017). *SasView Version 4.1.2*. Available online at: http://www.sasview.org.

Hamley, I. W. (2008). Form factor of helical ribbons. *Macromolecules* 41, 8948–8950. doi: 10.1021/ma8014917

Hamley, I. W. (2014). Peptide nanotubes. *Angew. Chem. Int. Ed.* 53, 6866–6881. doi: 10.1002/anie.201310006

Hamley, I. W., Dehsorkhi, A., and Castelletto, V. (2013). Self-assembled arginine-coated peptide nanosheets in water. *Chem. Commun.* 49, 1850–1852. doi: 10.1039/c3cc39057h

Ke, P. C., Zhou, R., Serpell, L. C., Riek, R., Knowles, T. P., Lashuel, H. A., et al. (2020). Half a century of amyloids: past, present and future. *Chem. Soc. Rev.* 49, 5473–5509. doi: 10.1039/C9CS00199A

Levin, A., Hakala, T. A., Schnaider, L., Bernardes, G. J., Gazit, E., and Knowles, T. P. (2020). Biomimetic peptide self-assembly for functional materials. *Nat. Rev. Chem.* 4, 615–634. doi: 10.1038/s41570-020-0215-y

Lu, K., Jacob, J., Thiyagarajan, P., Conticello, V. P., and Lynn, D. G. (2003). Exploiting amyloid fibril lamination for nanotube self-assembly. *J. Am. Chem. Soc.* 125, 6391–6393. doi: 10.1021/ja0341642

Mehta, A. K., Lu, K., Childers, W. S., Liang, Y., Dublin, S. N., Dong, J., et al. (2008). Facial symmetry in protein self-assembly. *J. Am. Chem. Soc.* 130, 9829–9835. doi: 10.1021/ja801511n

Mehta, A. K., Rosen, R. F., Childers, W. S., Gehman, J. D., Walker, L. C., and Lynn, D. G. (2013). Context dependence of protein misfolding and structural strains in neurodegenerative diseases. *Peptide Sci.* 100, 722–730. doi: 10.1002/bip.22283

Narayanan, T. (2014). "Small-angle scattering," in *Structure From Diffraction Methods*, eds D. W. Bruce, D. O'Hare, and R. I. Walton (Chichester: Wiley Online Library), 259–324.

Narayanan, T., Rüter, A., and Olsson, U. (2021). Multiscale structural elucidation of peptide nanotubes by x-ray scattering methods. *Front. Bioeng. Biotechnol.* 9:654339. doi: 10.3389/fbioe.2021.654339

Pringle, O., and Schmidt, P. (1971). Small-angle x-ray scattering from helical macromolecules. *J. Appl. Crystallogr.* 4, 290–293.

Rüter, A., Kuczera, S., Stenhammar, J., Zinn, T., Narayanan, T., and Olsson, U. (2020). Tube to ribbon transition in a self-assembling model peptide system. *Phys. Chem. Chem. Phys.* 22, 18320–18327. doi: 10.1039/D0CP03204B

Serpell, L. C. (2000). Alzheimer's amyloid fibrils: structure and assembly. *Biochim. Biophys. Acta* 1502, 16–30. doi: 10.1016/S0925-4439(00)00029-6

Valéry, C., Artzner, F., and Paternostre, M. (2011). Peptide nanotubes: molecular organisations, self-assembly mechanisms and applications. *Soft Matter* 7, 9583–9594. doi: 10.1039/c1sm05698k

Zhao, Y., Deng, L., Wang, J., Xu, H., and Lu, J. R. (2015). Solvent controlled structural transition of KI_4K self-assemblies: from nanotubes to nanofibrils. *Langmuir* 31, 12975–12983. doi: 10.1021/acs.langmuir.5b02303

Conflict of Interest: The authors declare that the research was conducted in the absence of any commercial or financial relationships that could be construed as a potential conflict of interest.

frontiers in Bioengineering and Biotechnology

MINI REVIEW
published: 29 March 2021
doi: 10.3389/fbioe.2021.654339

Multiscale Structural Elucidation of Peptide Nanotubes by X-Ray Scattering Methods

Theyencheri Narayanan[1]*, *Axel Rüter*[2] and *Ulf Olsson*[2]

[1] ESRF-The European Synchrotron, Grenoble, France, [2] Division of Physical Chemistry, Lund University, Lund, Sweden

This mini-review presents the structural investigations of the self-assembled peptide nanotubes using X-ray scattering techniques. As compared to electron microscopy, scattering methods enable studies of nanotubes in solution under the appropriate physicochemical conditions and probe their formation mechanism. In addition, a combination of X-ray scattering methods allow the elucidation of structural organization from the molecular scale to the dimension of nanotubes.

Keywords: peptide self-assembly, peptide nanotubes, peptide nanoribbons, X-ray scattering, SAXS

OPEN ACCESS

Edited by:
Wojciech Chrzanowski,
The University of Sydney, Australia

Reviewed by:
Hiroshi Sekiguchi,
Japan Synchrotron Radiation Research Institute, Japan
Michela Pisani,
Marche Polytechnic University, Italy

***Correspondence:**
Theyencheri Narayanan
narayan@esrf.fr

Specialty section:
This article was submitted to Nanobiotechnology, a section of the journal Frontiers in Bioengineering and Biotechnology

Received: *16 January 2021*
Accepted: *16 February 2021*
Published: *29 March 2021*

Citation:
Narayanan T, Rüter A and Olsson U (2021) Multiscale Structural Elucidation of Peptide Nanotubes by X-Ray Scattering Methods. Front. Bioeng. Biotechnol. 9:654339. doi: 10.3389/fbioe.2021.654339

1. INTRODUCTION

The aggregation of proteins can lead to a variety of complex structures, which are at the origin of many degenerative diseases (Ke et al., 2020). A well-known example is the fibrillar assemblies of amyloid peptides, formed by cleavage from a larger amyloid precursor protein, involved in neurodegenerative disorders (Serpell, 2000; Hamley, 2012). In the vast majority of cases, peptides self-assemble to fibrillar morphologies but under specific solvent and pH conditions, oligopeptides may form more organized nanotubes of nearly macroscopic dimension in length (Hartgerink et al., 1996; Valéry et al., 2011; Hamley, 2014). At the molecular level, both amyloid fibers and peptide nanotubes display the same characteristic feature, orthogonal antiparallel β-sheet structure, and sheet laminations (Mehta et al., 2008; Morris et al., 2013; Hamley, 2014). This unique structural signature shared by both pathogenic amyloid forming peptides and artificial functional peptides contrast their macroscopic properties, for example, the undesired effects of amyloid peptides in neurodegenerative diseases but beneficial roles of synthetic peptides in modern technologies (Ke et al., 2020). In particular, the self-assembly of synthetic biomimetic peptides enables a broader exploration of specific interactions and sequences than those possible with conventional amphiphilic molecules (Schneider et al., 2002; Zhao et al., 2013; Dasgupta and Das, 2019). As a result, relatively simple model peptide systems can be used to mimic more complex biological systems and processes (Ke et al., 2020; Levin et al., 2020).

The hierarchical self-assembly of short peptides to form uniform nanotubes of nearly macroscopic dimension has been the subject of numerous investigations (Valéry et al., 2011; Hamley, 2014). In specific cases due to the delicate interplay of hydrogen bonding, electrostatic and entropic interactions, the ribbon-like fibrillar structure curls and forms nanotubes of well-defined dimension. The wide range of polymorphism exhibited by peptide self-assemblies can be rationalized in terms of the free-energy landscape in which helical ribbons and nanotubes occupy closely located minima, with crystals at the lowest energy state (Adamcik and Mezzenga, 2018). Both helical ribbons and nanotubes have similar mean curvature and zero Gaussian curvature (Ke et al., 2020). The homogeneity in the diameter and limited tunability make them interesting candidates for templated growth of functional nanomaterials with potential applications in the

biotechnology and nanotechnology (Reches and Gazit, 2003; Pouget et al., 2007; Valéry et al., 2011; Hamley, 2014; Levin et al., 2020).

This short review presents some of the recent studies of self-assembled peptide nanotube systems using X-ray scattering methods. In particular, small and wide angle X-ray scattering (SAXS and WAXS, respectively) elucidate the different hierarchical levels involved in the self-assembly process albeit lacking the chemical sensitivity (Narayanan et al., 2017). Indeed, the morphology of the peptide nanotubes is directly revealed by imaging methods such as cryogenic transmission electron microscopy (cryo-TEM) and atomic force microscopy (AFM) (Valéry et al., 2011; Hamley, 2014; Adamcik and Mezzenga, 2018), which is a decisive input for the quantitative X-ray modeling of the nanotubes in solution.

2. X-RAY SCATTERING STUDIES OF PEPTIDE NANOTUBE SELF-ASSEMBLY

A prototypical case of the hierarchical self-assembly has been illustrated with the lanreotide octapeptide developed by Beaufour-Ipsen laboratory that forms a therapeutic gel (autogel®) (Valéry et al., 2003, 2011). At a lower lanreotide concentration than in the gel, monodisperse nanotubes of diameter about 25 nm are spontaneously formed. The supramolecular and molecular organizations within the tube wall were elucidated by SAXS and WAXS, and complementary techniques of electron microscopy and vibrational spectroscopies (Valéry et al., 2003). In this case, the exceptionally well-aligned fiber diffraction patterns revealed that the structural organization within the nanotubes wall is crystalline with low mosaicity, that in turn allowed constructing their electron density maps, which indicated a 2.07 nm alternation of aliphatic and aromatic residues that formed amyloid-β like fibers. The nanotubes are constituted by 26 of these fibers and consequently their diameter is very uniform. High-resolution SAXS further revealed the hexagonal packing of these nanotubes at high volume fractions (Valéry et al., 2003). The feasibility of serving these nanotubes as templates for biomineralization has been illustrated with a silica precursor resulting in double-walled silica nanotubes of uniform diameter and bundles of which assemble to centimeter-sized fibers (Pouget et al., 2007). Mutations in the peptide sequence can lead to different packing of aromatic residues, and modification of a single aromatic residue enabled a four-fold increase in nanotube diameter in the range of 10–36 nm (Tarabout et al., 2011). Further studies involving the effect of counterions revealed the specificity of anion size, demonstrating that counterions are not only regulating the charges on the surface of the nanotubes but also playing an important structural role, varying their diameter in the range of 19–26 nm (Gobeaux et al., 2012). By substituting monovalent by divalent counterions, double-walled nanotubes were observed and this morphological change has been attributed to competition between the adhesion force generated by divalent counterions and the mechanical stiffness of the peptide wall (Gobeaux et al., 2013).

Another nanotube forming peptide system investigated in detail from the structural perspective is the $CH_3CO-KLVFFAE-NH_2$, a sequence from the amyloid-β peptide, Aβ(16-22) (Lu et al., 2003; Childers et al., 2009). This short peptide self-assembles in acetonitrile/water solution at pH 2 into well-defined nanotubes with mean diameter about 52 nm and wall thickness 4.3 nm. Instead at pH 6, the peptide forms fibrils (Mehta et al., 2008). Using electron diffraction and complementary spectroscopic methods, the packing of peptides into bilayer leaflets within the tube wall was elucidated (Mehta et al., 2008, 2013). A model for the lamination of peptides involving antiparallel β-sheets and the curling of peptide bilayers to form nanotubes was proposed (Childers et al., 2009). Further work using peptides differing only in their N-terminal residue, phosphotyrosine vs. lysine, showed a coassembly as stacks of antiparallel β-sheets with precisely patterned charged lattices stabilizing the bilayer leaflet interface, creating nanotubes with dense negative external and positive internal surfaces (Li et al., 2016). Another sequence Aβ(13-22) with different N-terminal extensions enhanced the propensity for β-sheet laminations and transformed into nanotubes over a wider pH range (Liu et al., 2008).

The nanotubes formed by surfactant-like peptides are another case subjected to X-ray scattering investigations (Hamley, 2014). A well-studied system is the peptide without endcaps $AAAAAAK$ (A_6K) that self-assembles into nanotubes in water (Bucak et al., 2009). At higher concentrations, nanotubes orient to form a nematic-like phase. At even higher concentrations corresponding to a volume fraction in excess of 0.4, a lamellar phase has been reported (Cenker et al., 2011). The initial SAXS modeling suggested a wall thickness $\leq$ 1 nm and proposed a model involving the parallel packing of peptides in the nanotube walls (Castelletto et al., 2010). However, this model has been revised on the basis of other experimental evidences to that comprising bilayers of peptides perpendicular to the nanotube wall similar to that in the case of Aβ(16-22) (Hamley, 2014). Time evolution of SAXS intensity during the formation of nanotubes showed an exponential growth similar to a crystal growth process (Cenker et al., 2012). Further investigation of the homologous series A_nK with $n = 4$, 6, 8, and 10 revealed that while A_6K forms single-walled nanotubes in water above a threshold concentration (10%), A_4K is fully soluble, and A_8K and $A_{10}K$ assemble to rod-like aggregates even in dilute concentrations (Cenker et al., 2014). The latter structure has been revised to twisted ribbon with laminations of single stretched peptide molecules (Rüter et al., 2019) and a thermodynamic model has been presented for the transition between tube to ribbon structures (Rüter et al., 2020). The arginine-rich peptide R_3L_{12} (arginine$_3$-leucine$_{12}$) forms a variety of nanostructures including nanotubes in aqueous solutions as a function of pH (Castelletto et al., 2020). These structures are supposedly built from α-helical antiparallel coiled-coil peptide dimers arranged perpendicular to the nanotube axis in a cross-α configuration.

3. RECENT EXAMPLES OF X-RAY SCATTERING STUDIES OF PEPTIDE NANOTUBES

A state-of-the-art example for X-ray diffraction investigation of peptide nanotube self-assembly has been presented by Valery et al. in the case of a decapeptide, triptorelin (Valéry et al., 2015). This peptide self-assembles to form monodisperse nanotubes (diameter $\simeq 50$ nm and wall thickness 2.6 nm) at higher pH (> 7.5). The organization within the nanotube wall is crystalline (2D monoclinic) as indicated by low mosaicity fiber diffraction patterns. These authors exploited a smart crystallization strategy to enable atomic resolution structural elucidation (Valéry et al., 2015). The conformational change of the peptide with pH was exploited to derive a deeper functional insight. At the atomic scale, it was revealed that the globular conformation at high pH is stabilized through a strong histidine-serine H-bond and a tight histidine-aromatic packing (Valéry et al., 2015). Lowering the pH induced histidine protonation, disrupting these interactions and triggering a large change to an extended β-sheet-based conformation. At lower pH (< 6.5), triptorelin assemblies exhibit in the form of twisted nanotubes of smaller diameter ($\simeq 11$ nm). High resolution small and wide angle X-ray diffraction was used to derive a molecular level structural model of the nanotube assembly. **Figure 1** illustrates typical X-ray diffraction pattern from an oriented bundle of nanotubes and corresponding structural models at different hierarchical levels (Valéry et al., 2015). The well-defined meridional layerlines at 4.85 Å shows that the β-sheet H-bond network lies along the nanotube axis and forms protofilaments. The repeat distance along the nanotube axis is the size of the β-hairpin. The large number of Bragg peaks in the equatorial layer indicate the crystalline six-fold ordering of protofilments and 30 of which constitute a nanotube. The small-angle equatorial intensity is modeled in terms of hexagonal packing of nanotubes within the bundles. Furthermore, the nanotube wall thickness is about 2.6 nm, which is similar to that at higher pH but with an outer shell of 1 nm having an excess electron density than the inner layer. This corresponds to more aromatic residues located on the outer surface of the nanotube, which are likely involved in the close contact between nearest neighbors to form the twisted bundle.

As mentioned before, in the A_nK model peptide system the self-assembled structure is strongly dependent on the number of alanine residues in the chain, n, resulting in assemblies of tubes or twisted ribbons (Rüter et al., 2020). **Figure 2A** presents SAXS profiles of the nanotube forming A_6K above and below the solubility limit (10%). The SAXS profile of dissolved peptides is well-described by the scattering function of Gaussian polymer coils with a radius of gyration of about 0.55 nm. At higher concentrations, the scattering profile shows the characteristic features from a tubular structure, which can be described by a hollow cylinder model with mean radius 30.8 nm, polydispersity 4% and wall thickness 3.3 nm. The deviations at lower q region is attributed to the packing of oriented tubes in domains. **Figure 2B** depicts the WAXS pattern from oriented nanotubes. The orientation of the peaks shows the helical pitch angle (52^o) with β-sheets arranged on helical paths along the tube surface. The peaks in the WAXS pattern were assigned to a 2D oblique unit cell with the first peak at 1.16 nm^{-1} corresponding to the alanine stacking distance (Middleton et al., 2013). Considering the length of an extended peptide monomer, $l_p = 2.5$ nm and the tilt angle, the wall thickness of 3.3 nm may correspond to an interdigitated bilayer arrangement (Hamley, 2014). A similar bilayer architecture has been employed to model nanotubular morphologies formed by short peptides Aβ(16–22) (Mehta et al., 2013) and $\alpha S\beta 1$ ($NH_2 - VLYVGSKT - COOH$) (Morris et al., 2013).

4. OTHER SYSTEMS FORMING SELF-ASSEMBLED NANOTUBES

Not only short peptides but also a variety of amphiphilic molecules self-assemble to form nanotubes of comparable dimension. In many cases, SAXS has proven valuable for the elucidation of their structure and pathways of self-assembly in solution. An example is lithocholic bile acid in aqueous sodium or ammonium hydroxide solutions forming well-defined nanotubes of diameter in the range of 50 nm (Terech et al., 2006). In this case, SAXS revealed that the pathway of their formation is via helical ribbons. In concentrated suspensions, the oriented tubes self-organize to 2D hexagonal lattice with *p6m* symmetry (Terech et al., 2006). Using SAXS, cryo-TEM, and AFM, derivatives of cholic acid (Travaglini et al., 2013) and sodium lithocholate (Gubitosi et al., 2014) have been shown to self-assemble into nanotubes. Furthermore, in mixtures of sodium lithocholate and its mannose derivative, the nanotube radius could be tuned by the mixing ratio (Gubitosi et al., 2015). Certain amino acid amphiphiles, like N-α-lauryl-lysyl-aminolauryl-lysyl-amide, have also been shown to form nanotubes in solution (Ziserman et al., 2011). Here, nanotubes were observed to form slowly, over a period of several weeks. Following the process using cryo-TEM, it was demonstrated how nanotubes evolved from originally thin fibers via twisted and helical ribbons (Ziserman et al., 2011). Besides, some sterols and γ-oryzanol in edible oils form nanotubes with diameters ranging from 6 to 8 nm (Bot et al., 2009) and the network of these tubes resulting in an organogel. Another case is the self-assembly of DNA minor groove-binding heterocyclic ligand DB921 in aqueous solutions containing chloride or bromide salts (Mizuta et al., 2018). The single-walled nanotubes of diameters 26–32 nm are developed from helical ribbons which close to form tubes only in the presence of chloride or bromide counterions.

Amphiphilic diblock copolypeptoids having domains chemically distinct and congruent in size and shape self-assemble in water into nanotubes with crystalline walls (Sun et al., 2016). These peptoids are like molecular tiles and their length determines the nanotube diameter (4–10 nm). The nanotube wall is composed of stacked, porous crystalline rings, which are held together primarily by side-chain van der Waals interactions. Bolaamphiphiles consisting of a sugar residue, an alkyl chain, and an amino group (NKNT2-C18) are another type of molecules exhibiting propensity to self-assemble and form nanotubes in aqueous solution with diameters in the range of 18–20 nm (Takahashi et al., 2019). In this case, the

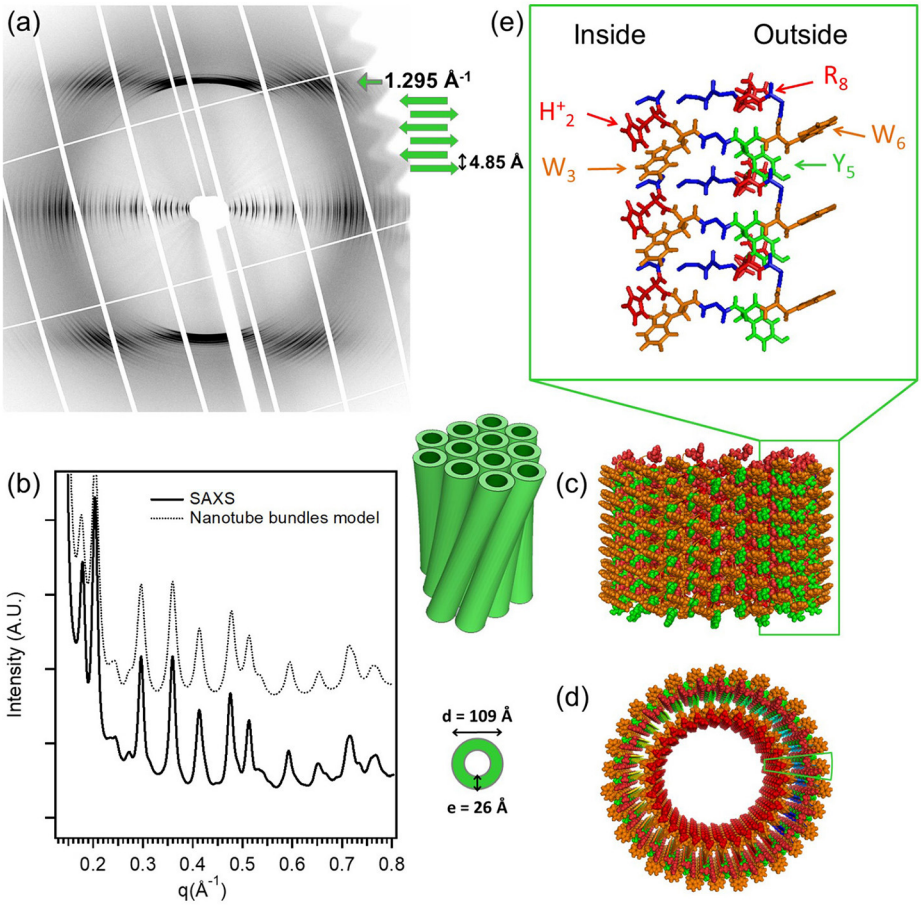

FIGURE 1 | The molecular structure of the low-pH triptorelin nanotubes. Aligned **(a)** fiber diffraction pattern and **(b)** SAXS profile of bundles of small nanotubes. **(c)** Side and **(d)** top schematic views of the small nanotubes built from 30 protofilaments. **(e)** Molecular structure of the protofilaments forming the nanotube walls. Color code: W (orange), Y (green), protonated histidine $(H_2)^+$, and $(R_8)^+$ (red). The two green boxes in **(c,d)** underline the position of one protofilament that is enlarged in **(e)**. Reproduced from Valéry et al. (2015) licensed under a Creative Commons Attribution 4.0 International License.

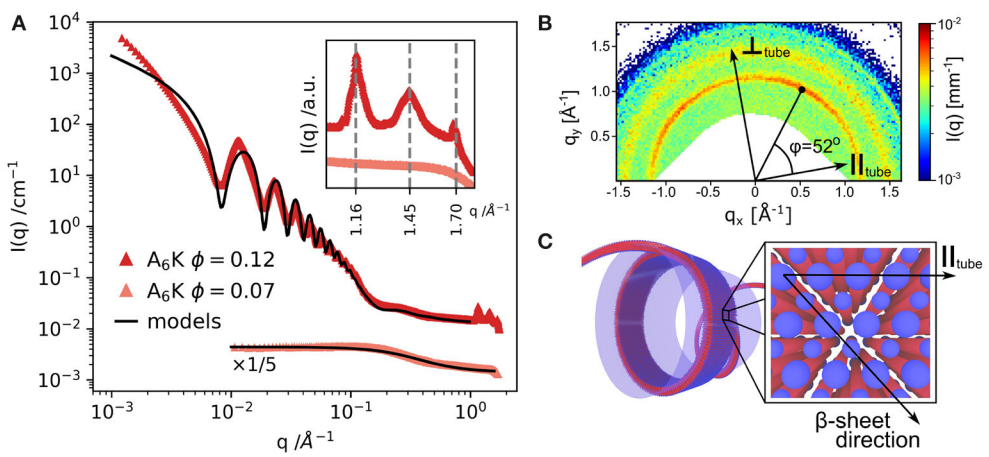

FIGURE 2 | (A) SAXS and WAXS (inset) profiles from A_6K peptide for two concentrations above and below the peptide solubility limit. **(B)** WAXS pattern from partially aligned nanotubes showing the peptide packing and helical pitch angle of 52°. **(C)** Model of the nanotube wall architecture: blue: hydrophilic peptide ends, red: hydrophobic core of the peptide sequence. Reproduced from Rüter et al. (2020) licensed under a Creative Commons Attribution 3.0 Unported License.

formation mechanism is not via helical ribbons but more like by closure of the well-organized monolayer membranes. Finally, the programmable route to design nanotubes of tailored diameter and desired chirality is via single-stranded DNA bricks strategy (Sun et al., 2019). In this case, the width of DNA helical tubes is controlled by the rigidity and curvature of repeating units through their thickness and helical twist density, respectively. Nanotubes, as well as the twisted or helical ribbons, that form in these self-assembling systems, are considered to be consequences of molecular chirality (Helfrich and Prost, 1988; Chung et al., 1993; Selinger et al., 2001). However, achiral gemini-tartrate amphiphiles complexed with chiral tatrate anions form ribbons and tubes due to induced chirality at a supramolecular level (Brizard et al., 2007). It has been possible to resolve the molecular structure of such self-assembled systems and correlate to the macroscopic properties (Oda et al., 2008).

5. SUMMARY

This mini review presented a brief overview of X-ray scattering investigations of self-assembled peptide nanotube systems. The key advantage of X-ray scattering method is that the structural information can be elucidated in real solvent and under appropriate thermodynamic conditions, over a broad range of concentrations. In addition, external perturbations such as temperature (Cenker et al., 2011), shear flow (Narayanan et al., 2020), and electric or magnetic fields (Pandey et al., 2017) can easily be imposed. A combination of SAXS and WAXS methods enable hierarchical structural elucidation from the crystalline molecular packing up to the micron scale dimension of the nanotubes. In addition, the coexistence of different structural moieties can be identified on a quantitative scale (Narayanan et al., 2021). Complementary real space information from cryo-TEM and AFM provide decisive input for constraining the solution structural model. Although, both cryo-TEM (Ziserman et al., 2011) and frequency modulation AFM (Sugihara et al., 2013) are capable of revealing subnanometer molecular structure of nanotubes, X-ray modeling yields more quantitative structural parameters averaged over a large ensemble.

High brilliance SAXS and WAXS methods enable deciphering of weak structural features superimposed on a large background, which could be useful in studies involving self-assembled functional peptide systems. One potential avenue is exploring the complex pathways of self-assembly involving the coexistence of multiple structural motifs. A particular challenge is formulating theoretical models that can predict structural parameters from molecular properties (Nyrkova and Semenov, 2010; Zhang et al., 2019). The analysis software tools need to be better optimized for complete modeling of the self-assembled structures from the known molecular architecture.

AUTHOR CONTRIBUTIONS

TN wrote the first draft of the manuscript. All authors contributed in the subsequent revisions of the manuscript.

FUNDING

ESRF and Knut and Alice Wallenberg Foundation (KAW 2014.0052).

REFERENCES

Adamcik, J., and Mezzenga, R. (2018). Amyloid polymorphism in the protein folding and aggregation energy landscape. *Angew. Chem. Int. Ed.* 57, 8370–8382. doi: 10.1002/anie.201713416

Bot, A., Den Adel, R., Roijers, E. C., and Regkos, C. (2009). Effect of sterol type on structure of tubules in sterol+ γ-oryzanol-based organogels. *Food Biophys.* 4, 266–272. doi: 10.1007/s11483-009-9124-9

Brizard, A., Aimé, C., Labrot, T., Huc, I., Berthier, D., Artzner, F., et al. (2007). Counterion, temperature, and time modulation of nanometric chiral ribbons from gemini-tartrate amphiphiles. *J. Am. Chem. Soc.* 129, 3754–3762. doi: 10.1021/ja0682172

Bucak, S., Cenker, Ç. Ç., Nasir, I., Olsson, U., and Zackrisson, M. (2009). Peptide nanotube nematic phase. *Langmuir* 25, 4262–4265. doi: 10.1021/la804175h

Castelletto, V., Nutt, D. R., Hamley, I. W., Bucak, S., Cenker, Ç. Ç., and Olsson, U. (2010). Structure of single-wall peptide nanotubes: in situ flow aligning x-ray diffraction. *Chem. Commun.* 46, 6270–6272. doi: 10.1039/c0cc00212g

Castelletto, V., Seitsonen, J., Ruokolainen, J., Piras, C., Cramer, R., Edwards-Gayle, C. J. C., et al. (2020). Peptide nanotubes self-assembled from leucine-rich alpha helical surfactant-like peptides. *Chem. Commun.* 56, 11977–11980. doi: 10.1039/D0CC04299D

Cenker, Ç. Ç., Bomans, P. H., Friedrich, H., Dedeoğlu, B., Aviyente, V., Olsson, U., et al. (2012). Peptide nanotube formation: a crystal growth process. *Soft Matter* 8, 7463–7470. doi: 10.1039/c2sm25671a

Cenker, Ç. Ç., Bucak, S., and Olsson, U. (2011). Nanotubes and bilayers in a model peptide system. *Soft Matter* 7, 4868–4875. doi: 10.1039/c0sm01186j

Cenker, Ç. Ç., Bucak, S., and Olsson, U. (2014). Aqueous self-assembly within the homologous peptide series a_nk. *Langmuir* 30, 10072–10079. doi: 10.1021/la5016324

Childers, W. S., Ni, R., Mehta, A. K., and Lynn, D. G. (2009). Peptide membranes in chemical evolution. *Curr. Opin. Chem. Biol.* 13, 652–659. doi: 10.1016/j.cbpa.2009.09.027

Chung, D. S., Benedek, G. B., Konikoff, F. M., and Donovan, J. M. (1993). Elastic free energy of anisotropic helical ribbons as metastable intermediates in the crystallization of cholesterol. *Proc. Natl. Acad. Sci. U.S.A.* 90, 11341–11345. doi: 10.1073/pnas.90.23.11341

Dasgupta, A., and Das, D. (2019). Designer peptide amphiphiles: self-assembly to applications. *Langmuir* 35, 10704–10724. doi: 10.1021/acs.langmuir.9b01837

Gobeaux, F., Fay, N., Tarabout, C., Meneau, F., Mériadec, C., Delvaux, C., et al. (2013). Experimental observation of double-walled peptide nanotubes and monodispersity modeling of the number of walls. *Langmuir* 29, 2739–2745. doi: 10.1021/la304862f

Gobeaux, F., Fay, N., Tarabout, C., Mériadec, C., Meneau, F., Ligeti, M., et al. (2012). Structural role of counterions adsorbed on self-assembled peptide nanotubes. *J. Am. Chem. Soc.* 134, 723–733. doi: 10.1021/ja210299g

Gubitosi, M., Travaglini, L., D'Annibale, A., Pavel, N., Vázquez, J. T., Obiols-Rabasa, M., et al. (2014). Sugar-bile acid-based bolaamphiphiles: from scrolls to monodisperse single-walled tubules. *Langmuir* 30, 6358–6366. doi: 10.1021/la500908r

Gubitosi, M., Travaglini, L., di Gregorio, M. C., Pavel, N. V., Vázquez Tato, J., Sennato, S., et al. (2015). Tailoring supramolecular nanotubes by bile salt based surfactant mixtures. *Angew. Chem.* 127, 7124–7127. doi: 10.1002/ange.201500445

Hamley, I. W. (2012). The amyloid beta peptide: a chemist's perspective. Role in Alzheimer's and fibrillization. *Chem. Rev.* 112, 5147–5192. doi: 10.1021/cr3000994

Hamley, I. W. (2014). Peptide nanotubes. *Angew. Chem. Int. Ed.* 53, 6866–6881. doi: 10.1002/anie.201310006

Hartgerink, J. D., Granja, J. R., Milligan, R. A., and Ghadiri, M. R. (1996). Self-assembling peptide nanotubes. *J. Am. Chem. Soc*. 118, 43–50. doi: 10.1021/ja953070s

Helfrich, W., and Prost, J. (1988). Intrinsic bending force in anisotropic membranes made of chiral molecules. *Phys. Rev. A* 38:3065. doi: 10.1103/PhysRevA.38.3065

Ke, P. C., Zhou, R., Serpell, L. C., Riek, R., Knowles, T. P., Lashuel, H. A., et al. (2020). Half a century of amyloids: past, present and future. *Chem. Soc. Rev*. 49, 5473–5509. doi: 10.1039/C9CS00199A

Levin, A., Hakala, T. A., Schnaider, L., Bernardes, G. J., Gazit, E., and Knowles, T. P. (2020). Biomimetic peptide self-assembly for functional materials. *Nat. Rev. Chem*. 4, 615–634. doi: 10.1038/s41570-020-0215-y

Li, S., Mehta, A. K., Sidorov, A. N., Orlando, T. M., Jiang, Z., Anthony, N. R., et al. (2016). Design of asymmetric peptide bilayer membranes. *J. Am. Chem. Soc*. 138, 3579–3586. doi: 10.1021/jacs.6b00977

Liu, P., Ni, R., Mehta, A. K., Childers, W. S., Lakdawala, A., Pingali, S. V., et al. (2008). Nucleobase-directed amyloid nanotube assembly. *J. Am. Chem. Soc*. 130, 16867–16869. doi: 10.1021/ja807425h

Lu, K., Jacob, J., Thiyagarajan, P., Conticello, V. P., and Lynn, D. G. (2003). Exploiting amyloid fibril lamination for nanotube self-assembly. *J. Am. Chem. Soc*. 125, 6391–6393. doi: 10.1021/ja0341642

Mehta, A. K., Lu, K., Childers, W. S., Liang, Y., Dublin, S. N., Dong, J., et al. (2008). Facial symmetry in protein self-assembly. *J. Am. Chem. Soc*. 130, 9829–9835. doi: 10.1021/ja801511n

Mehta, A. K., Rosen, R. F., Childers, W. S., Gehman, J. D., Walker, L. C., and Lynn, D. G. (2013). Context dependence of protein misfolding and structural strains in neurodegenerative diseases. *Peptide Sci*. 100, 722–730. doi: 10.1002/bip.22283

Middleton, D. A., Madine, J., Castelletto, V., and Hamley, I. W. (2013). Insights into the molecular architecture of a peptide nanotube using ftir and solid-state nmr spectroscopic measurements on an aligned sample. *Angew. Chem*. 125, 10731–10734. doi: 10.1002/ange.201301960

Mizuta, R., Devos, J., Webster, J., Ling, W.-L., Narayanan, T., Round, A., et al. (2018). Dynamic self-assembly of dna minor groove-binding ligand db921 into nanotubes triggered by an alkali halide. *Nanoscale* 10, 5550–5558. doi: 10.1039/C7NR03875E

Morris, K. L., Zibaee, S., Chen, L., Goedert, M., Sikorski, P., and Serpell, L. C. (2013). The structure of cross-β tapes and tubes formed by an octapeptide, $\alpha s\beta 1$. *Angew. Chem*. 125, 2335–2339. doi: 10.1002/ange.201207699

Narayanan, T., Dattani, R., Möller, J., and Kwaśniewski, P. (2020). A microvolume shear cell for combined rheology and x-ray scattering experiments. *Rev. Sci. Instrum*. 91:085102. doi: 10.1063/5.0012905

Narayanan, T., Rüter, A., and Olsson, U. (2021). SAXS/WAXS investigation of amyloid-β(16-22) peptide nanotubes. *Front. Bioeng. Biotechnol*. 9:654349. doi: 10.3389/fbioe.2021.654349

Narayanan, T., Wacklin, H., Konovalov, O., and Lund, R. (2017). Recent applications of synchrotron radiation and neutrons in the study of soft matter. *Crystallogr. Rev*. 23, 160–226. doi: 10.1080/0889311X.2016.1277212

Nyrkova, I., and Semenov, A. (2010). Twisted surfactant structures: an advanced theoretical model. *Soft Matter* 6, 501–516. doi: 10.1039/B914067K

Oda, R., Artzner, F., Laguerre, M., and Huc, I. (2008). Molecular structure of self-assembled chiral nanoribbons and nanotubules revealed in the hydrated state. *J. Am. Chem. Soc*. 130, 14705–14712. doi: 10.1021/ja8048964

Pandey, G., Saikia, J., Sasidharan, S., Joshi, D. C., Thota, S., Nemade, H. B., et al. (2017). Modulation of peptide based nano-assemblies with electric and magnetic fields. *Sci. Rep*. 7, 1–9. doi: 10.1038/s41598-017-02609-z

Pouget, E., Dujardin, E., Cavalier, A., Moreac, A., Valéry, C., Marchi-Artzner, V., et al. (2007). Hierarchical architectures by synergy between dynamical template self-assembly and biomineralization. *Nat. Mater*. 6, 434–439. doi: 10.1038/nmat1912

Reches, M., and Gazit, E. (2003). Casting metal nanowires within discrete self-assembled peptide nanotubes. *Science* 300, 625–627. doi: 10.1126/science.1082387

Rüter, A., Kuczera, S., Pochan, D. J., and Olsson, U. (2019). Twisted ribbon aggregates in a model peptide system. *Langmuir* 35, 5802–5808. doi: 10.1021/acs.langmuir.8b03886

Rüter, A., Kuczera, S., Stenhammar, J., Zinn, T., Narayanan, T., and Olsson, U. (2020). Tube to ribbon transition in a self-assembling model peptide system. *Phys. Chem. Chem. Phys*. 22, 18320–18327. doi: 10.1039/D0CP03204B

Schneider, J. P., Pochan, D. J., Ozbas, B., Rajagopal, K., Pakstis, L., and Kretsinger, J. (2002). Responsive hydrogels from the intramolecular folding and self-assembly of a designed peptide. *J. Am. Chem. Soc*. 124, 15030–15037. doi: 10.1021/ja027993g

Selinger, J., Spector, M., and Schnur, J. (2001). Theory of self-assembled tubules and helical ribbons. *J. Phys. Chem. B* 105, 7157–7169. doi: 10.1021/jp010452d

Serpell, L. C. (2000). Alzheimer's amyloid fibrils: structure and assembly. *Biochim. Biophys. Acta Mol. Basis Dis*. 1502, 16–30. doi: 10.1016/S0925-4439(00)00029-6

Sugihara, T., Hayashi, I., Onishi, H., Kimura, K., and Tamura, A. (2013). Sub-nanometer-resolution imaging of peptide nanotubes in water using frequency modulation atomic force microscopy. *Chem. Phys*. 419, 74–77. doi: 10.1016/j.chemphys.2013.02.021

Sun, J., Jiang, X., Lund, R., Downing, K. H., Balsara, N. P., and Zuckermann, R. N. (2016). Self-assembly of crystalline nanotubes from monodisperse amphiphilic diblock copolypeptoid tiles. *Proc. Natl. Acad. Sci. U.S.A*. 113, 3954–3959. doi: 10.1073/pnas.1517169113

Sun, S., Yang, Y., Li, D., and Zhu, J. (2019). Large chiral nanotubes self-assembled by DNA bricks. *J. Am. Chem. Soc*. 141, 19524–19528. doi: 10.1021/jacs.9b08737

Takahashi, R., Kawauchi, H., Kameta, N., Lee, J. H., Fujii, S., Shimizu, T., et al. (2019). Observing the kinetic pathway of nanotube formation from bolaamphiphiles by time-resolved small-angle x-ray scattering. *J. Phys. Chem. B* 123, 4340–4345. doi: 10.1021/acs.jpcb.9b01746

Tarabout, C., Roux, S., Gobeaux, F., Fay, N., Pouget, E., Meriadec, C., et al. (2011). Control of peptide nanotube diameter by chemical modifications of an aromatic residue involved in a single close contact. *Proc. Natl. Acad. Sci. U.S.A*. 108, 7679–7684. doi: 10.1073/pnas.1017343108

Terech, P., Jean, B., and Ne, F. (2006). Hexagonally ordered ammonium lithocholate self-assembled nanotubes with highly monodisperse sections. *Adv. Mater*. 18, 1571–1574. doi: 10.1002/adma.200502358

Travaglini, L., D'Annibale, A., di Gregorio, M. C., Schillén, K., Olsson, U., Sennato, S., et al. (2013). Between peptides and bile acids: self-assembly of phenylalanine substituted cholic acids. *J. Phys. Chem. B* 117, 9248–9257. doi: 10.1021/jp405342v

Valéry, C., Artzner, F., and Paternostre, M. (2011). Peptide nanotubes: molecular organisations, self-assembly mechanisms and applications. *Soft Matter* 7, 9583–9594. doi: 10.1039/c1sm05698k

Valéry, C., Deville-Foillard, S., Lefebvre, C., Taberner, N., Legrand, P., Meneau, F., et al. (2015). Atomic view of the histidine environment stabilizing higher-ph conformations of ph-dependent proteins. *Nat. Commun*. 6:7771. doi: 10.1038/ncomms8771

Valéry, C., Paternostre, M., Robert, B., Gulik-Krzywicki, T., Narayanan, T., Dedieu, J.-C., et al. (2003). Biomimetic organization: Octapeptide self-assembly into nanotubes of viral capsid-like dimension. *Proc. Natl. Acad. Sci. U.S.A*. 100, 10258–10262. doi: 10.1073/pnas.1730609100

Zhang, M., Grossman, D., Danino, D., and Sharon, E. (2019). Shape and fluctuations of frustrated self-assembled nano ribbons. *Nat. Commun*. 10:3565. doi: 10.1038/s41467-019-11473-6

Zhao, Y., Wang, J., Deng, L., Zhou, P., Wang, S., Wang, Y., et al. (2013). Tuning the self-assembly of short peptides via sequence variations. *Langmuir* 29, 13457–13464. doi: 10.1021/la402441w

Ziserman, L., Lee, H.-Y., Raghavan, S. R., Mor, A., and Danino, D. (2011). Unraveling the mechanism of nanotube formation by chiral self-assembly of amphiphiles. *J. Am. Chem. Soc*. 133, 2511–2517. doi: 10.1021/ja107069f

Conflict of Interest: The authors declare that the research was conducted in the absence of any commercial or financial relationships that could be construed as a potential conflict of interest.

frontiers in Bioengineering and Biotechnology

REVIEW
published: 27 April 2021
doi: 10.3389/fbioe.2021.644595

Mimicking the Hierarchical Organization of Natural Collagen: Toward the Development of Ideal Scaffolding Material for Tissue Regeneration

Luca Salvatore[1], Nunzia Gallo[1], Maria Lucia Natali[1], Alberta Terzi[2], Alessandro Sannino[1] and Marta Madaghiele[1]*

[1] Department of Engineering for Innovation, University of Salento, Lecce, Italy, [2] Institute of Crystallography, National Research Council, Bari, Italy

OPEN ACCESS

Edited by:
Maria Grazia Raucci, Institute of Polymers, Composites and Biomaterials, National Research Council (IPCB-CNR), Italy

Reviewed by:
Barbara Barboni, University of Teramo, Italy
Simone Sprio, Institute of Science and Technology for Ceramics, Italian National Research Council, Italy

***Correspondence:**
Luca Salvatore
luca.salvatore@unisalento.it

Specialty section:
This article was submitted to Nanobiotechnology, a section of the journal Frontiers in Bioengineering and Biotechnology

Received: *21 December 2020*
Accepted: *15 March 2021*
Published: *27 April 2021*

Citation:
Salvatore L, Gallo N, Natali ML, Terzi A, Sannino A and Madaghiele M (2021) Mimicking the Hierarchical Organization of Natural Collagen: Toward the Development of Ideal Scaffolding Material for Tissue Regeneration. Front. Bioeng. Biotechnol. 9:644595. doi: 10.3389/fbioe.2021.644595

Biological materials found in living organisms, many of which are proteins, feature a complex hierarchical organization. Type I collagen, a fibrous structural protein ubiquitous in the mammalian body, provides a striking example of such a hierarchical material, with peculiar architectural features ranging from the amino acid sequence at the nanoscale (primary structure) up to the assembly of fibrils (quaternary structure) and fibers, with lengths of the order of microns. Collagen plays a dominant role in maintaining the biological and structural integrity of various tissues and organs, such as bone, skin, tendons, blood vessels, and cartilage. Thus, "artificial" collagen-based fibrous assemblies, endowed with appropriate structural properties, represent ideal substrates for the development of devices for tissue engineering applications. In recent years, with the ultimate goal of developing three-dimensional scaffolds with optimal bioactivity able to promote both regeneration and functional recovery of a damaged tissue, numerous studies focused on the capability to finely modulate the scaffold architecture at the microscale and the nanoscale in order to closely mimic the hierarchical features of the extracellular matrix and, in particular, the natural patterning of collagen. All of these studies clearly show that the accurate characterization of the collagen structure at the submolecular and supramolecular levels is pivotal to the understanding of the relationships between the nanostructural/microstructural properties of the fabricated scaffold and its macroscopic performance. Several studies also demonstrate that the selected processing, including any crosslinking and/or sterilization treatments, can strongly affect the architecture of collagen at various length scales. The aim of this review is to highlight the most recent findings on the development of collagen-based scaffolds with optimized properties for tissue engineering. The optimization of the scaffolds is particularly related to the modulation of the collagen architecture, which, in turn, impacts on the achieved bioactivity.

Keywords: type I collagen, hierarchical organization, tissue engineering, regenerative medicine, scaffold, collagen processing, fibrous assemblies

INTRODUCTION

Biological tissues are made of cells embedded in a tissue-specific extracellular matrix (ECM). The ECM is an intricate network of macromolecules, including proteins, glycosaminoglycans, proteoglycans, and glycoproteins, which are able to hold a high amount of water (Gelse et al., 2003; Birk and Bruckner, 2011). This provides the ECM with gel-like texture and gel-like mechanical properties. While the ECM was originally thought as a passive system responsible for the structural and functional integrity of tissues and organs, it is now clear that the ECM actually plays a pivotal role as an active regulator of cell phenotype (Birk and Bruckner, 2011; Pawelec et al., 2016). Cell surface receptors recognize specific ligands on the ECM, attach to them, and then transduce signals from the ECM. This type of signaling, including biochemical, topographical, and mechanical cues, regulates various cell functions, such as cellular growth, migration, and differentiation. The interplay between cells and ECM also includes the turnover or remodeling of the ECM by the cells during both normal and pathological conditions through the secretion of several ECM-degrading enzymes, along with the secretion and deposition of ECM components. Very briefly, it can be stated that cells and ECM constitute a highly dynamic and finely regulated system that controls the development, maintenance, and repair of tissues and organs.

Among the ECM proteins, collagen definitely holds the lion's share. In humans, it is indeed estimated to account for about 30% of the total body protein content (Nimni and Harkness, 1998). The unique fingerprint of collagen molecules is a right-handed triple-helical domain, called tropocollagen, which is formed by three left-handed polypeptide helices, called polyproline-II (PPII) helices (Gelse et al., 2003; Shoulders and Raines, 2009; Birk and Bruckner, 2011). So far, at least 28 proteins having this specific fingerprint have been identified as members of the collagen family, which are differently located within the body and progressively named from type I to type XXVIII according to the time of discovery (Shoulders and Raines, 2009; Birk and Bruckner, 2011). The differences among the collagen types are related to their submolecular, molecular, and supramolecular features, which confer them distinct structural and biological functions (Shoulders and Raines, 2009; Birk and Bruckner, 2011). Type I collagen, which has been the first collagen to be identified (hence being the most widely investigated), is the predominant fibrous component of connective tissues such as the dermis, bones, tendons, ligaments, and cornea, accounting for approximately 70% of the total collagens found in the body (Gelse et al., 2003).

Therefore, it is not surprising that tissue engineering and regenerative medicine, which respectively aim at achieving tissue regeneration *in vitro* and *in vivo*, make extensive use of type I collagen (mostly derived from animal tissues, e.g., bovine) as the biomaterial of choice for the manufacture of cell-instructive scaffolds (Walters and Stegemann, 2014; Terzi et al., 2020). Scaffolds are artificial matrices designed to work as temporary ECM substitutes, i.e., designed to deliver specific structural and biochemical signals to the cells, in order to stimulate the cellular processes involved in tissue regeneration and matrix remodeling. Hence, the scaffold design takes inspiration from the ECM, attempting to mimic as closely as possible the tissue-specific ECM composition and architecture, at various length scales.

Being a major ECM component, type I collagen is intrinsically bioactive and biodegradable. It also possesses low immunogenicity (i.e., the ability to trigger an immune response) and weak antigenicity (i.e., the ability to interact with antibodies) (Bianchini and Parma, 2001; Lynn et al., 2004; Delgado et al., 2017). Furthermore, its versatile processing allows the production of a wide range of tissue engineering scaffolds of various sizes and shapes, e.g., hydrogels, sponges, and fibrous mats (Friess, 1998; Dong and Lv, 2016). However, the cellular interaction with a processed collagen-based scaffold is largely affected by how closely the scaffold is able to recapitulate the structure of native collagen on different length scales (Walters and Stegemann, 2014). In tissues, type I collagen exhibits a peculiar multilevel hierarchical structure, moving from the nanoscale to the macroscale, with each structural level inducing or controlling given biological processes, in addition to providing the tissue (e.g., skin, bone, tendon) with appropriate mechanical strength. Several processing steps, performed during both collagen isolation and scaffold manufacturing, can impact the native collagen assembly to various extents, thus potentially affecting the cellular response and the overall biological activity *in vivo*.

In this review, after presenting the structural hierarchy of type I collagen in tissues and discussing the related biological activity, we address the most recent findings on the development of collagen-based scaffolds with optimized regenerative capability. In particular, our aim is to emphasize that the scaffold optimization goes through a deeper understanding of the structural modifications of collagen induced by processing, along with a detailed analysis of the cellular response(s) elicited by such changes. To this purpose, we first discuss, on a general basis, the effects of the collagen source and the subsequent processing on the scaffold structure and the related biological activity. Then, we focus on the optimization of collagen-based scaffolds for the regeneration of specific tissues (such as skin, cornea, bone, and tendon) by presenting some exemplary attempts to modulate the scaffold biological activity to improve the *in vitro* and/or *in vivo* regenerative performance.

Abbreviations: ECM, extracellular matrix; PPII, polyproline-II; Gly, glycine; Pro, proline; Hyp, hydroxyproline; CRPs, proline-rich collagen-related peptides; Phe, phenylalanine; Glu, glutamate; Arg, arginine; Asp, aspartate; Ala, alanine; TEM, transmission electron microscopy; SIS, small intestinal submucosa; FMD, foot and mouth disease; BSE, bovine spongiform encephalopathy; WAXS, wide-angle X-ray scattering; SAXS, small-angle X-ray scattering; AFM, atomic force microscopy; PFM, piezoresponse force microscopy; US-DSC, ultrasensitive differential scanning calorimetry; CD, circular dichroism; micro-CT, X-ray micro-computed tomography; SEM, scanning electron microscopy; DHT, dehydrothermal treatment; DHS, dry heat; EtO, ethylene oxide; β-ray, beta irradiation; γ-ray, gamma irradiation; DRT, dermis regeneration template; TGF-β1, transforming growth factor beta 1; BMP, bone morphogenetic protein; PCL, polycaprolactone; PLGA, poly(lactide-co-glycolide); COMP, cartilage oligomeric matrix protein; TNC, tenascin-C; PLLA, poly-L-lactic acid; PLCL, poly(lactide-co-caprolactone); PU, polyurethane; SCX, tendon-associated gene scleraxis; COL1, type I collagen gene.

HIERARCHICAL STRUCTURE OF TYPE I COLLAGEN AND RELATED BIOACTIVITY

Together with collagen types II, III, V, XI, XXIV, and XXVII (**Table 1**), type I collagen is a fibril-forming protein. Fibril-forming collagens are the most widespread in vertebrates, representing about 90% of the total collagens (Gelse et al., 2003).

Briefly, the triple-helical molecular domains (with length ≈300 nm and diameter ≈1.5 nm) assemble to form cylindrical structures known as fibrils (with length ≈μm and diameter ≈100 nm), which are, in turn, organized into fibers (length ≈mm and diameter ≈10 μm). Within tissues (length scale ≈cm), collagen fibers are then either randomly oriented or preferentially arranged in given directions in order to provide the tissue with proper architecture to ensure structural and functional integrity (**Figure 1**).

Along with this hierarchy at the microscale and macroscale (i.e., at the fibril, fiber, and tissue levels), the single collagen fibrils also show a peculiar hierarchical structure. Similarly to other proteins, four different structural levels can be identified for type I collagen, with one level (i.e., primary) at the atomic/submolecular scale, two levels at the molecular scale (i.e., secondary and tertiary), and one level at the supramolecular scale (i.e., quaternary). These structural levels are concisely described in the following before addressing the tissue architecture. As then summarized in **Table 2**, some hints on the interplay between the collagen structure and the biological activities are also provided.

Primary Structure

The primary structure of collagen refers to the amino acid sequence in the polypeptide chains (called α chains) that make up the collagen molecule and univocally identify the collagen isoform. Type I collagen, for example, is a hetero-trimer consisting of two identical α1 chains and one α2 chain (**Table 1**), where α1 and α2 chains differ for the amino acid sequence. The primary structure of collagen is tissue-specific, i.e., provides the protein with peculiar biochemical and physical properties that affect cell attachment and other biological functions (Walters and Stegemann, 2014).

TABLE 1 | Fibril-forming collagens found in vertebrates (Shoulders and Raines, 2009; Sorushanova et al., 2019).

Type	Composition	Molecular weight α chain (kDa)	Distribution
I	$2\alpha_1$(I) α_2(I)	95	Dermis, bone, tendon, ligament, cornea
II	$3\alpha_1$(II)	95	Cartilage, vitreous body
III	$3\alpha_1$(III)	95	Skin, blood vessels, intestine
V	$3\alpha_1$(V) $2\alpha_1$(V) α_2(V) α_1(V) α_2(V) α_3(V)	120–145	Bone, dermis, cornea, placenta
XI	α_1(XI) α_2(XI) α_3(XI)	110–145	Cartilage, intervertebral disks
XXIV	$3\alpha_1$(XXIV)	–	Bone, cornea
XXVII	$3\alpha_1$(XXVII)	–	Cartilage

In general, collagen can be represented as a repetition of the Gly-X-Y triplet, where glycine (Gly), i.e., the smallest amino acid, occupies every third position in the peptide sequence of the single chain, so as it can be positioned in the core of the triple helix, closely packing the structure. Conversely, side groups in the X and Y positions are exposed to the surface for the sterical interaction with other residues and are frequently occupied by proline (Pro) and hydroxyproline (Hyp), respectively (Shoulders and Raines, 2009). Since each α chain contains about 1,000 amino acid residues, approximately 330 repeating Gly-X-Y triplets per chain can be estimated. In particular, the triplet Gly-Pro-Hyp, unique to collagen molecules, is reported to occur with a frequency of about 12%, while 44% of triplets are in the forms Gly-X-Hyp and Gly-Pro-Y, and the remaining 44% in the general form Gly-X-Y (Sorushanova et al., 2019).

The high content of Gly (higher than 30%) is fundamental to stabilize the triple-helical domain through the formation of inter-chain hydrogen bonds that are perpendicular to the chain axis. These bonds include both direct hydrogen bonds between the backbone -NH group of Gly and the backbone –C = O group of a residue in the X position of the neighboring chain and indirect hydrogen bonds mediated by water bridges, such as those involving the hydroxyl group of Hyp in the Y position (Rich and Crick, 1961; Ramachandran and Chandrasekharan, 1968).

Pro and Hyp contribute to stabilize the triple helix and also stiffen the α chains by preventing rotation around the C-N bond (Sorushanova et al., 2019). It is estimated that about 22% of all residues in the strands of human collagen are either Pro or Hyp (Shoulders and Raines, 2009). Hyp is typical of collagen, thus it is commonly used as a marker to detect and quantify collagen in tissues (Ignat'eva et al., 2007). Remaining residues in the primary structure of collagen include a variety of amino acids that provide the protein tissue-specific bioactivity.

Secondary and Tertiary Structures

The secondary structure of proteins refers to the peculiar local arrangement of the single polypeptide chains forming the molecule. For collagen, the secondary structure is thus represented by the left-handed PPII helical conformation of the α chains. However, single α chains only have this conformation when associated with the other two chains, with a one-residue staggering, to form a right-handed triple-helical unit (Brodsky and Ramshaw, 1997; Bella, 2016). This triple helix, stabilized by inter-chain hydrogen bonds, represents the tertiary structure of collagen. Since PPII helices would not exist in the absence of the triple helix, the secondary and tertiary structures of collagen are sometimes considered a unique structure (termed "secondary"). It is important to note that the single chains also comprise two short non-helical regions at both the amino (N–) and carboxy (C–) termini, which measure about 9–26 residues (Shoulders and Raines, 2009; Sorushanova et al., 2019) and do not have a repeating Gly-X-Y structure (Kadler et al., 1996). Therefore, the collagen molecule (about 300 nm long and 1.5 nm in diameter) is made of a central tropocollagen unit and two short non-helical ends, called telopeptides.

Zooming into the triple-helical conformation, two models are reported in the literature to describe this structure

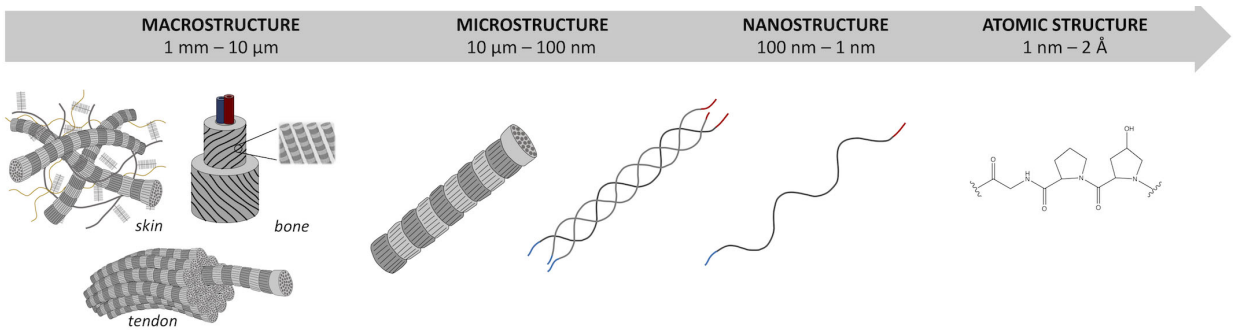

FIGURE 1 | Hierarchical organization of type I collagen skin, tendon, and bone from macroscale to atomic scale.

TABLE 2 | Hierarchical structure of fibril-forming collagens: identification of the different structural levels and the related biological activity.

Structural level	Length scale	Collagen's feature	Biological activity
Primary	2 Å–1 nm	Amino acid sequence	• Cell ligand identity
Secondary and tertiary	≈10–100 nm	Molecular conformation • PPII helices–secondary • Triple helix–tertiary	• Cell ligand exposure • Enzymatic resistance and degradation mechanism • Mechanical strength/mechanotransduction* • Antigenicity (for animal-derived collagen used as a biomaterial)
Quaternary	≈1 μm	Packing of molecules • Fibril structure – banding	• Enzymatic resistance • Mechanical strength/mechanotransduction* • Activation of blood clotting
Architecture	≈1–10 mm	Packing of fibrils • Fiber structure • Fiber arrangement or orientation	• Tissue mechanical properties (e.g., stiffness)/mechanotransduction* • Tissue functionality

**By means of mechanotransduction, cells can detect mechanical stimuli from their microenvironment and respond by performing biological processes.*

(Rich and Crick, 1961; Okuyama et al., 2006). The Rich and Crick model (Rich and Crick, 1961), based on fiber diffraction studies on native type I collagen, considers a single inter-chain hydrogen bond per triplet and a 10-fold helical symmetry with a 10/3 pitch (i.e., 10 repeating triplets in three turns, 3.33 triplets/turn), a 28.6-Å axial repeat, and a pitch length of 86 Å. Another more recent model proposed by Okuyama et al. (2006) is based on crystallographic analyses of proline-rich collagen-related peptides (CRPs) and shows a sevenfold helical symmetry with a 7/2 pitch (i.e., seven triplets in two turns, 3.5 triplets/turn), a 20.0-Å axial repeat, and a 60-Å pitch length. In order to match the two models, it has been postulated that the helical pitch of collagen could be 10/3 in proline-poor regions and 7/2 in proline-rich regions. However, it is now acknowledged that a range of helical symmetries can be found in native collagen and among different collagen types (Shoulders and Raines, 2009; Orgel et al., 2014). This variability could also play a role in the interaction of collagen with other biomolecules (Shoulders and Raines, 2009).

Regardless of the helical symmetry, the rope-like triple helix conformation is fundamental to provide collagen with proper biochemical and biophysical properties, including adequate mechanical stiffness, susceptibility to collagenase, and exposure of selected cell ligands, e.g., GFOGER (Gly-Phe-Hyp-Gly-Glu-Arg), to collagen-specific integrin receptors, such as $\alpha_1\beta_1$, $\alpha_2\beta_1$, $\alpha_3\beta_1$, $\alpha_{10}\beta_1$, and $\alpha_{11}\beta_1$ (Knight et al., 2000; Khew and Tong, 2007; Grover et al., 2012a,b).

The denatured counterpart of collagen, i.e., gelatin, is obtained from the disruption of the triple-helical structure by cleavage of the hydrogen bonds, e.g., by thermal heating (Bigi et al., 2004). The consequent molecular unfolding (i.e., helix-to-coil transition) is mostly irreversible and leads to a loss of structural order, which results in much lower stiffness and much higher susceptibility to proteases compared to native collagen. This is why particular care is needed to avoid denaturation during the processing of collagen-based scaffolds, since tissue regeneration requires the scaffolds to be mechanically stable for a given time length. With regard to cell adhesion, several cell types are able to attach to both native and denatured collagen, suggesting the presence of conformation-independent binding sites that are masked in the triple-helical conformation but exposed to cells upon molecular unfolding. Cellular attachment to gelatin is likely due to the interaction of several integrin receptors, e.g., $\alpha_5\beta_1$, $\alpha_v\beta_3$, and $\alpha_2\beta_1$, with RGD (Arg-Gly-Asp) and DGEA (Asp-Gly-Glu-Ala) ligands (Davis, 1992; Yamamoto and Yamamoto, 1994; Grover et al., 2012a,b).

As for enzymatic degradation, it is worth recalling that the secondary and tertiary structures of collagen are specific substrates for collagenase, thus playing a pivotal role in the ECM (or scaffold) remodeling. Indeed, collagenase is able to cleave the tropocollagen unit through all three α chains, specifically at a single point that is located at about three quarters of the length from the N-terminus (Sunada and Nagai, 1983). The resulting

triple-helical fragments then undergo spontaneous denaturation at physiological temperature, thus becoming susceptible to various proteases.

As an additional general note on the biological response to a collagen-based implant, it is also worth mentioning that collagen antigenicity is related to its molecular (secondary and tertiary) structure. Antigenic determinants of collagen can be classified into one of three categories, respectively: (a) helical, i.e., dependent on triple-helical conformation; (b) central, i.e., located within the triple helix, but dependent only on the peptide sequence; (c) terminal, i.e., located in the telopeptides (Lynn et al., 2004). While collagen antigenicity has been attributed mostly to its terminal telopeptides, it is important to note that the location of the major antigenic sites actually depends on the specific donor/recipient species pair being considered, e.g., bovine/human (Lynn et al., 2004).

Quaternary Structure

In native collagen, rope-like collagen molecules spontaneously assemble to form a three-dimensional crystalline lattice. As mentioned above, collagen fibrils are formed, in which the molecules are quasi-hexagonally packed and super-twisted in a right-handed structure along the longitudinal axis of the fibril (Collins et al., 2019). Interestingly, the super-twisted structure of the fibrils is maintained also through the non-helical telopeptide regions (Shoulders and Raines, 2009).

Based on the X-ray diffraction patterns of native collagen, Orgel et al. (2006) proposed a "microfibril" structural model having a triclinic unit cell formed by parts of five different collagen molecules (Collins et al., 2019). This is quite consistent with the simplified microfibril model previously proposed by Hodge and Petruska (1963), who envisaged a bidimensional stack of five collagen molecules aligned parallel to one another with a staggering of about 67 nm (**Figure 2**). This longitudinal or axial stagger represents the characteristic D-periodicity of the fibrils detected by transmission electron microscopy (TEM), which is the sum of gap and overlap regions between collagen molecules (**Figure 2**). Indeed, because the molecule length (≈300 nm) is about 4.4–4.5D, a fibril contains a gap or low-electron density regions (about 0.54D long), with some space between the ends of longitudinally lined-up molecules, as well as an overlap or high-electron density regions (about 0.46D long) where side-by-side overlapping of adjacent triple helices occurs (Shoulders and Raines, 2009; Sorushanova et al., 2019). In TEM imaging, gap regions are visualized as the darker ones.

Type I collagen fibrils can be even greater than 500 μm in length and 500 nm in diameter (Shoulders and Raines, 2009; Sorushanova et al., 2019), which suggests the assembly of a huge number of molecules (more than 10^7). Fibril formation or fibrillogenesis is basically a spontaneous self-assembly process, in which hydrophobic and electrostatic interactions between adjacent molecules occur to minimize the surface area/volume ratio of the final assembly (Kadler et al., 1996; Sorushanova et al., 2019). However, fibril formation can be also cell-regulated, especially in developing or repairing tissues (Kadler et al., 1996). More in general, fibrillogenesis is a tissue-specific process, since different fibril structures and organization are needed to provide the tissue with given functions.

While single triple helices would be unstable at body temperature (i.e., the random coil conformation would be the preferred one) (Shoulders and Raines, 2009), the formation of supramolecular fibrils allows stabilizing the molecular domains. Moreover, this supramolecular assembly is essential to provide collagen with resistance to multidirectional mechanical loading, as well as with enhanced resistance to proteolysis, compared to single molecules.

Although triple helices lacking telopeptides might assemble into fibrils, the C-terminal telopeptides of collagen molecules appear to be involved in the initiation of fibrillogenesis, thus being able to accelerate the process of fibril assembly (Shoulders and Raines, 2009). More importantly, telopeptides play a key role in the mechanical stabilization of fibrils, as they contain sites for both intramolecular and intermolecular crosslinking (Terzi et al., 2020). Subsequently to fibril formation, Lys side chains in the telopeptides are covalently crosslinked forming hydroxylysil pyridinoline and lysil pyridinoline crosslinks between Lys and hydroxylysine residues (Shoulders and Raines, 2009). Covalent crosslinks between triple helices repeat at regular intervals along the fibril, following the fixed stagger pattern. Such a crosslinking provides the fibrils with enhanced strength and stability, as well as higher resistance to proteolysis. Therefore, while telopeptides might not be essential for fibrillogenesis, they are fundamental to strengthen the fibrils *via* the formation of crosslinks (Shoulders and Raines, 2009).

Within the final crystalline lattice, water molecules surround each triple helix, forming a cylinder of hydration that contributes to stabilize the molecular structure (Collins et al., 2019; Terzi et al., 2020). In addition to this "bound" water, free water is also found in the intra-fibrillar spaces. The intra-fibrillar level of hydration clearly affects the intermolecular distance between lateral and longitudinal neighbors (Birk and Bruckner, 2011). Drying of fibrils is indeed known to lead to a shortening of the D-periodicity, as well as a reduction of the lateral packing. For example, the intrafibrillar lateral packing of collagen molecules is reported to vary from 1.6 nm for wet bovine cornea to 1.8 nm for dry rat tail tendon (Terzi et al., 2020). Intermolecular center-to-center distances are also affected by the diameter of the single triple helices, which is in turn dependent on the extent of glycosylation, i.e., the galactosylation and glucosyl-galactosylation of hydroxylysine residues. Differences in the extent of glycosylation are thus a mode of physiological regulation of fibril organization, as it occurs in corneal type I collagen (Birk and Bruckner, 2011).

In addition to determining the structural and mechanical properties of collagen within given tissues, the organization of the collagen molecules into fibrils is actively involved in the process of blood clotting or hemostasis. Indeed, when fibrous collagens, such as type I collagen, are exposed to the blood flow due to injury, platelets recognize specific collagen sequences and interact with the protein, giving rise to the process of blood clot formation (Brass and Bensusan, 1974; Kehrel et al., 1998). Such

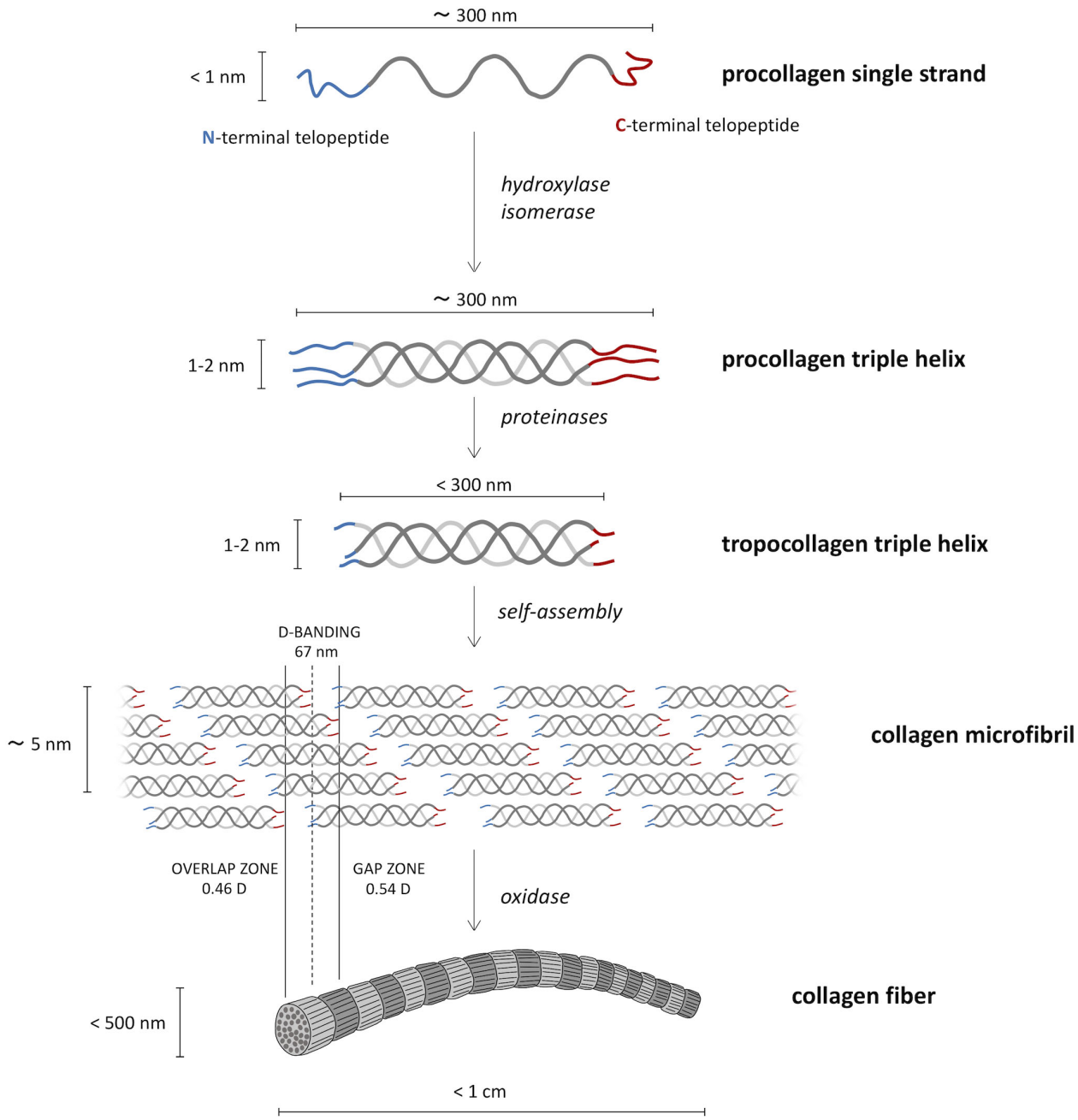

FIGURE 2 | Biosynthetic route from the molecular procollagen to collagen fibers. Three helical left-handed procollagen single strands form a right-handed triple helix of roughly 300 nm in length, named procollagen triple helix. The tropocollagen molecules, resulting from proteinases cut of N- and C-termini, go toward the supramolecular assembly in the so-called collagen microfibrils in the characteristic quarter-staggered form that causes the characteristic appearance of the collagen type I fibrils on the ultrastructural level.

collagen-induced platelet activation requires both the tertiary and the quaternary structures of collagen (Kehrel et al., 1998).

Fibers and Tissue Architecture

At the next hierarchical level, collagen fibrils are bound together by interfibrillar proteoglycans that are orthogonal to the fibrils in order to form fibers that have a typical packing distance $\geq$ 100 nm (Brodsky and Ramshaw, 1997; Shoulders and Raines, 2009). Proteoglycans form crossing bridges between adjacent fibrils by binding collagen at specific sites located at regular intervals of about 60 nm (Terzi et al., 2020). Along with interfibrillar proteoglycans, intrafibrillar proteoglycans are also

found, which are oriented along the fibril axis and contribute to the maintenance of the rope-like structure (Terzi et al., 2020). The residual presence of strongly bound proteoglycans, upon the extraction of collagen from animal tissues, is a factor known to affect the antigenicity of the biomaterial (Lynn et al., 2004).

Similarly to the tissue-specific fibril structure, collagen fibers are also tissue-specific and arranged in a peculiar architecture in order to ensure structural and functional ECM performance. For example, in the cornea, all collagen fibrils have small diameters (≈30 nm) and are regularly packed in orthogonal lamellae, which provide not only mechanical stability but also transparency (Birk and Bruckner, 2011). On the contrary, tendon fibrils show a heterogeneous distribution of large diameters (≈50–250 nm), and the fibers are all arranged along the longitudinal axis of the tendon (Birk and Bruckner, 2011; Chen et al., 2017).

In general, heterogeneity is an intrinsic feature of biological tissues, which is present at various length scales and originates at the level of the collagen molecule (Chen et al., 2017). While heterotrimeric triple helices (such as those of type I collagen) are more prevalent than homotrimeric ones (Shoulders and Raines, 2009), it is also important to note that heterotypic fibrils exist, which are assembled from mixtures of two or more fibril-forming collagens (Birk and Bruckner, 2011). Indeed, connective tissues consisting of collagen types I, II, and III (i.e., the quantitatively major fibril-forming collagens) contain minor amounts of collagen types V and XI. The latter are regulatory fibril-forming collagens that are critical for fibrillogenesis and co-assemble with the major fibril-forming collagens to form heterotypic fibrils. The resulting fibril organization and assembly then result in tissue-specific fibril differences (Birk and Bruckner, 2011). For instance, type V collagen is commonly associated with type I collagen in most tissues, especially in the cornea, while type XI collagen is commonly found with type II collagen in cartilage tissues. Additional heterogeneity of the collagen fibrils can also depend on the extent of the lysil oxidase crosslinking (Chen et al., 2017). All of these inherent sources of chemical and structural heterogeneity found at the nanoscale and microscale induce heterogeneity at higher hierarchical levels, thus making the detailed characterization of tissues quite challenging. Heterogeneity at all length scales clearly affects also the mechanical properties of the tissue-specific ECM (Chen et al., 2017).

While the ECM mechanical properties provide structural integrity to tissues, it is worth recalling that they may directly affect the cellular behavior. Upon mechanical loading of the ECM, strain is differently distributed over the distinct hierarchical levels of collagen (from fibers down to molecules) (Gautieri et al., 2011). Cells are continuously exposed to local mechanical cues, arising from their ECM as well as from neighboring cells. By means of mechanotransduction, i.e., a series of molecular processes that transform a physical/mechanical cue into a biological process, cells can perceive a given mechanical stimulus and respond to it (Martino et al., 2018). Mechanical signals, in addition to biochemical and topographical cues, are thus pivotal regulators of cell function. This is the most important reason why cell-instructive scaffolds for tissue engineering should be designed to match as closely as possible the mechanical properties of the target tissue. On the contrary, changes of the compliance of the ECM, which are related to changes of its nanostructure and composition, are commonly associated with the progression of degenerative diseases (Martino et al., 2018).

MANUFACTURING OF TYPE I COLLAGEN-BASED SCAFFOLDS: IMPACT ON STRUCTURE AND BIOLOGICAL ACTIVITY

Due to the intrinsic complexity and heterogeneity of the ECM at various length scales, the scaffolds currently adopted to recapitulate the ECM composition and structure actually represent oversimplified ECM substitutes. Generally speaking, two strategies can be implemented to produce scaffolds for tissue engineering, respectively a top-down strategy, inherent to the use of decellularized ECMs (Gouveia and Connon, 2016), and a bottom-up strategy, regarding the assembly of scaffolds from molecular building blocks. Whereas the decellularization of the ECMs is successfully applied in some clinical settings [e.g., the use of porcine small intestinal submucosa (SIS) for chronic wounds or the use of decellularized nerve grafts for peripheral nerve injuries], it still poses concerns on reproducibility and sterilization (Garreta et al., 2017). Moreover, although the process of decellularization is claimed to retain the structure of the native ECM, the chemical processes that are involved, if not properly controlled, may have some impact on the collagen structure, in addition to removing key soluble ECM components (Gouveia and Connon, 2016).

Compared to the use of decellularized ECMs, the assembly of scaffolds is much more challenging but advantageous, as it allows building artificial ECM substitutes with tunable and reproducible properties. However, the reconstitution of the native collagen architecture within a scaffold is challenged by the available processing techniques: while the control of the collagen organization on multiple length scales is hard to achieve, the scaffold processing can also impact on the collagen structure on multiple levels. Interestingly, in spite of providing oversimplified ECM substitutes, this close interplay between processing and structure, as detailed in the following, offers the great opportunity to modulate the structure-related biological activity of the scaffolds in order to optimize their capability to induce and sustain tissue regeneration (**Table 3**).

Collagen Source

The choice of the collagen source represents the first step in the production of collagen-based scaffolds and plays a pivotal role in the subsequent processing, as well as in the determination of the physicochemical, mechanical, and biological properties of the scaffolds (Zeugolis et al., 2008b; Parenteau-Bareil et al., 2011; Perez-Puyana et al., 2019). In general, the collagen used for the manufacturing of scaffolds can be obtained either from recombinant production systems or from animal tissues. Recombinant human collagen can be expressed by both prokaryotic (i.e., bacteria) and eukaryotic

TABLE 3 | Impact of processing on the structure-related biological activity of collagen-based scaffolds: overview of the main structural properties (or parameters) modulated by a given processing step and the *in vitro/in vivo* biological properties (or processes) that could be concurrently affected.

Processing step	Modulated structural properties/parameters	Modulated biological properties/processes	References
Choice of the collagen source	*Thermal stability* *Enzymatic resistance* *Mechanical properties*	*Antigenicity/immunogenicity* *Cell response (via biochemical, mechanical, and topographical cues)*	*Zeugolis et al., 2008b; Parenteau-Bareil et al., 2011; Perez-Puyana et al., 2019; Sorushanova et al., 2021*
Collagen extraction	Triple helix content Telopeptides Fibril network	Antigenicity/immunogenicity Cell response (*via* biochemical, mechanical, and topographical cues)	Delgado et al., 2017; Xu et al., 2017; Bak et al., 2018; Terzi et al., 2020
Aqueous processing of raw material	Banding Triple helix content	Blood clotting Cell response (*via* biochemical and mechanical cues)	Sylvester et al., 1989; Ding et al., 2014; Böhm et al., 2017; Terzi et al., 2018; Stanton et al., 2019
Scaffold shaping/fabrication	Porous/fibrous assembly Macroscopic size and shape Mechanical properties	Cell response (*via* mechanical and topographical cues) Remodeling Vascularization	O'Brien et al., 2005; Antoine et al., 2015; Metavarayuth et al., 2016; Offeddu et al., 2016; Pawelec et al., 2016
Scaffold crosslinking	Thermal stability Enzymatic resistance Mechanical properties	Cell response (*via* biochemical and mechanical cues) Remodeling Foreign body response Vascularization	Chan et al., 2014; Aamodt and Grainger, 2016; Bax et al., 2017; Maternini et al., 2019; Nair et al., 2020a
Scaffold sterilization	Thermal stability Enzymatic resistance Mechanical properties	Cell response (*via* biochemical and mechanical cues) Remodeling	Noah et al., 2003; Wiegand et al., 2009; Proffen et al., 2015; Monaco et al., 2017

The choice of the collagen source is highlighted (italics), since it affects the subsequent processing steps, as well as the final scaffold properties. The generic term "cell response" is used in this table to address the potential effects on multiple cell processes, such as proliferation, migration, and differentiation, with reference to the cell type(s) needed for the regeneration of the target tissue/organ.

hosts (i.e., yeast, mammalian, plant, and insect cells) and offers the potential for consistent collagen production at large scale (Dong and Lv, 2016; Wang et al., 2017). However, recombinant collagen is still far from being similar to native human collagen in a multitude of parameters, since hosts are not able to reproduce the full-length molecule with the native amount of posttranslational modifications (i.e., hydroxylation, glycosylation) (Wang et al., 2017). The incorporation attempts of non-native hydroxylases in *ad hoc* engineered hosts revealed to be unable to adequately hydroxylate collagen molecules (Wang et al., 2017). Although this issue can be overcome by the use of mammalian cells, which require a less extent of genetic manipulation, thanks to the naturally owing of the necessary posttranslational modification apparatus, the yield improvement is very challenging. The genetic manipulation by the introduction of stronger promoter for the increment of collagen production unpairs with the prolyl hydroxylase activity that is thus unable to fully hydroxylate collagen (Wang et al., 2017). Additionally, apart from that, large-scale production is limited by the high cost of mammalian cell culture and the long production time required.

Among eukaryotic systems, it is worth mentioning the outcomes reached by the CollPlant Ltd. company that was able to reproduce a transgenic type I collagen from engineered tobacco plant with hydroxylation levels of both proline and lysine similar to that of human type I collagen (Merle et al., 2002; Stein et al., 2009). Furthermore, they demonstrated how the tobacco-derived type I collagen was able to organize in fibrils, although they did not show the characteristic axial periodicity (Stein et al., 2009). Based on these promising results, CollPlant Ltd. administered two preclinical trials (Shilo et al., 2013; Abir et al., 2020) and one clinical trial[1] (Identifier: NCT02309307) with plant-derived recombinant human collagen for wound healing and tissue repair.

Despite the potential of recombinant collagens, unresolved issues make them expensive and thus less attractive than animal-derived collagen, which is still the gold standard for use. Therefore, in an attempt to mimic the structure of native collagen as closely as possible, the majority of the collagen currently used in the biomedical field is derived from animal tissues.

Large terrestrial mammals (such as cows, pigs, sheep, and horses) are currently the preferred sources for collagen extraction in the biomedical industry, owing to the high sequence homology with human collagen, as well as the possibility to breed them domestically in large numbers (Silvipriya et al., 2015; Gallo et al., 2020b). In particular, bovine and porcine collagens are the most widely available, being derived from the by-products of the slaughter of beef and pork. Among tissues, tendons and skins are the most commonly used for collagen extraction because of their high collagen content. Up to 85% of the dry mass of the Achilles tendon is reported to be collagen, while in skin, the collagen content is about 70% (Gallo et al., 2020b). The collagen yield from these tissues can be highly variable, depending on the extraction method and on specific characteristics of the animal source (e.g., species, age of animals) but can reach values of 70% or higher (Ghodbane and Dunn, 2016). For research-only applications, collagens from small mammals find also wide use, e.g., the collagen from rat-tail tendon (Davison-Kotler et al., 2019).

In spite of being the current gold standard for biomedical applications, mammalian collagen is not free from risks or limitations. Firstly, it has the potential to induce an undesired

[1] ClinicalTrials.gov

immune response; about 2–4% of the population shows allergy to bovine and porcine collagen (Silvipriya et al., 2015). Moreover, it holds the risk of cross-species transmission of infectious diseases, such as foot and mouth disease (FMD) and bovine spongiform encephalopathy (BSE). In this regard, all the sources used for the production of medical-grade collagens are required to be veterinary controlled, traceable, and certified as "disease-free." Additionally, it is worth noting that the xenogeneic origin often dictates the cultural accommodation of collagen-based products. For example, the use of porcine and equine collagens is not acceptable for Muslim and Jewish people, while the use of bovine collagen is prohibited by the Hindu faith.

In this context, animal sources other than mammals, although showing "immunological distance" from humans (Peng et al., 2010), have been investigated for collagen extraction. While collagen of avian origin (e.g., from chicken skin and feet) may be suitable for biomedical usage (Peng et al., 2010; Li et al., 2017; Perez-Puyana et al., 2019), it still presents the risk of zoonotic diseases, e.g., the avian influenza. On the contrary, collagen from aquatic animals, such as fish, jellyfish, marine sponges, and mollusks, seems safer and more attractive for use (Salvatore et al., 2020a). Indeed, this collagen holds a lower likelihood of transmitting infectious diseases, in addition to being free from any religious or cultural concerns and easily harvested from waste by-products of the fish processing industry. Although the incidence of fish allergy is variable, it is estimated that only 1% of the general population present immune reactions due to fish and fish-based products (Kourani et al., 2019). This further contributes to the common perception that collagen from aquatic animals is safer than collagen from terrestrial mammals. However, the use of this collagen for the production of scaffolds is mainly restricted to research settings, since for most aquatic sources, medical-grade collagen is not yet available. This limitation is due to the need to improve the extraction yields for large-scale production and, most of all, to enhance the batch-to-batch consistency, which is pivotal for clinical implementation (Salvatore et al., 2020a).

In the choice of the optimal collagen source for given tissue engineering applications, the advantages and limitations of each source should be taken into account (**Table 4**), together with the effects of the source on both the related processing and the final scaffold properties. First of all, the amino acid composition of collagen varies considerably between species (Yamada et al., 2014; Perez-Puyana et al., 2019). The different primary structures directly impact on the biological activity of the protein (i.e., the integrin-binding motifs), as well as the structure at higher length scales and the physicochemical and mechanical properties, including thermal stability, degradation rate, solubility, viscosity, crosslinking, and elastic modulus (Zeugolis et al., 2008b). For example, collagen from aquatic animals demonstrated to have chemical and physical properties significantly different from those of mammalian collagen, such as a lower denaturation temperature (related to a lower amount of imino acids) and a greater degradation rate (Salvatore et al., 2020a). These properties affect the extraction protocols and the subsequent processing phases while requiring the adoption of specific treatments (e.g., crosslinking) to improve the thermal and mechanical stability of the collagen scaffolds for potential clinical use (Salvatore et al., 2020a).

In addition to the animal species, the specific tissue and the age of the animals are further variables that determine the qualitative features of collagen and collagen-based products (Sorushanova et al., 2021). Indeed, the function-related structural role that collagen covers in tissues, along with the increase of collagen crosslinking with age, deeply influences its hierarchical organization, mechanical properties, and enzymatic resistance

TABLE 4 | Comparison of the main collagen sources utilized and/or investigated for the production of collagen-based scaffolds.

Source	Immunogenicity/ Antigenicity	Risk of zoonosis	Religious issues	Availability/ Supply	Price**	References
Recombinant	*Low*	*No*	*No*	*Limited*	*Very high*	*Davison-Kotler et al., 2019; He et al., 2021*
Bovine	*Low*	*Yes*	*Yes*	*Very high*	*Low*	*Ellingsworth et al., 1986; Charriere et al., 1989; Michaeli and MacPherson, 1990; Lynn et al., 2004; Zhang et al., 2017; Avila Rodriguez et al., 2018*
Porcine	*Low*	*Yes*	*Yes*	*Very high*	*Low*	Lynn et al., 2004; Silvipriya et al., 2015; Avila Rodriguez et al., 2018
Ovine	*Low*	*Yes*	*No*	*Limited**	*Moderate*	*Banerjee et al., 2012; Busra et al., 2019*
Equine	*Low*	*Yes*	*Yes*	*High*	*Moderate*	*Adelmann-Grill and Otto, 1987; Bianchini and Parma, 2001; Steel and Twenhafel, 2010; Abdal-Hameed, 2014; Silverstein et al., 2014; Gallo et al., 2020b*
Poultry	Variable	Yes	No	High	High	Pantin-Jackwood et al., 2017; Grønlien et al., 2019
Fish	Variable	Yes (but lower than mammalian and avian sources)	No	Very high	High	Sakaguchi et al., 2000; Kobayashi et al., 2016; Milovanovic and Hayes, 2018; Kourani et al., 2019; Salvatore et al., 2020a
Jellyfish	*Low*	*No*	*No*	*Limited**	*High*	*Putra et al., 2014; Flaig et al., 2020*

For the sources in italics, medical-grade collagen is commercially available, which ensures the safety and the quality of the protein in terms of traceability and batch-to-batch consistency (for scaffold production, fish and poultry collagens have been so far used only in research settings). The limited supply highlighted with (*) indicates a very low number of companies providing that collagen. As for the price (**), a commercially competitive cost of collagen for healthcare uses is in the range 5,000–50,000 USD/kg (Silva et al., 2014).

(Terzi et al., 2020). With regard to mammalian sources, collagens isolated from skin and tendons exhibit significantly different properties. Tendon collagen fibers are indeed strictly packed and aligned in the main load-bearing direction, in a high hierarchical organization that results in a greater physicochemical, enzymatic, and mechanical stability, while skin collagen fibers, with their anisotropic distribution along Langer lines, are arranged in a loose network that is more easily susceptible to the enzymatic cleavage (Gallo et al., 2020b; Sorushanova et al., 2021). As for the effect of aging, the higher amount of collagen crosslinks with age makes the collagen less flexible and more acid-insoluble (Gautieri et al., 2014).

Collagen Processing

As already mentioned, the processing of collagen, from the extraction process to the sterilization of the end product, strongly influences its conformational structure and thus its biological, physicochemical, and mechanical performances. In this respect, a recent study by Böhm et al. (2017), who investigated the *in vitro* response of fibroblasts and platelets to collagen matrices obtained from different sources and processing conditions, suggested that the processing of collagen may have a stronger effect on the cell response than the collagen source.

As widely known, the development of a collagen-based device could be divided into five macro-steps of manufacturing, including the extraction process, the raw material processing in aqueous solutions, the fabrication of the collagen-based product with given microstructure and macrostructure, its customization by the application of physical and/or chemical crosslinking, and the final sterilization (**Figure 3**). Terminal sterilization is indeed preferred over aseptic manufacturing due to enhanced repeatability (Monaco et al., 2017). All process parameters of each step could be varied to manufacture a structurally versatile material with varying properties with regard to morphology, mechanics, degradation rate, and behavior in the physiological environment. The possibility to act on all levels allows to finely tune the properties of the collagen-based device in order to achieve the desired final features.

The application of material science and engineering principles to biology for the in-depth understanding of cell interaction with collagen forms led to the identification of several products with specific bioactive properties. Generally, scientific and industrial research focused on the development of three main kinds of reconstituted collagen in the form of native triple helix, gelatin, or peptides of a wide range of molecular weights, according to the application. Although the bioactive properties of gelatin and peptides made them valid raw materials for the cosmetic and food sectors, great relevance has native-like collagen in the biomedical field, attributed to the generally accepted concept that the protein entirely performs its biological function only when it retains its tertiary structure or above. Because of the important role in cell signaling, the collagen triple-helical molecule is characterized by the presence of a high number of integrin binding sites (i.e., the "GFOGER" sequence) that are fundamental for cell adhesion and interaction, proliferation, and differentiation (Davidenko et al., 2016b, 2018). The crucial structural role of collagen in the tissues' architecture and shape maintenance and its regulatory functions

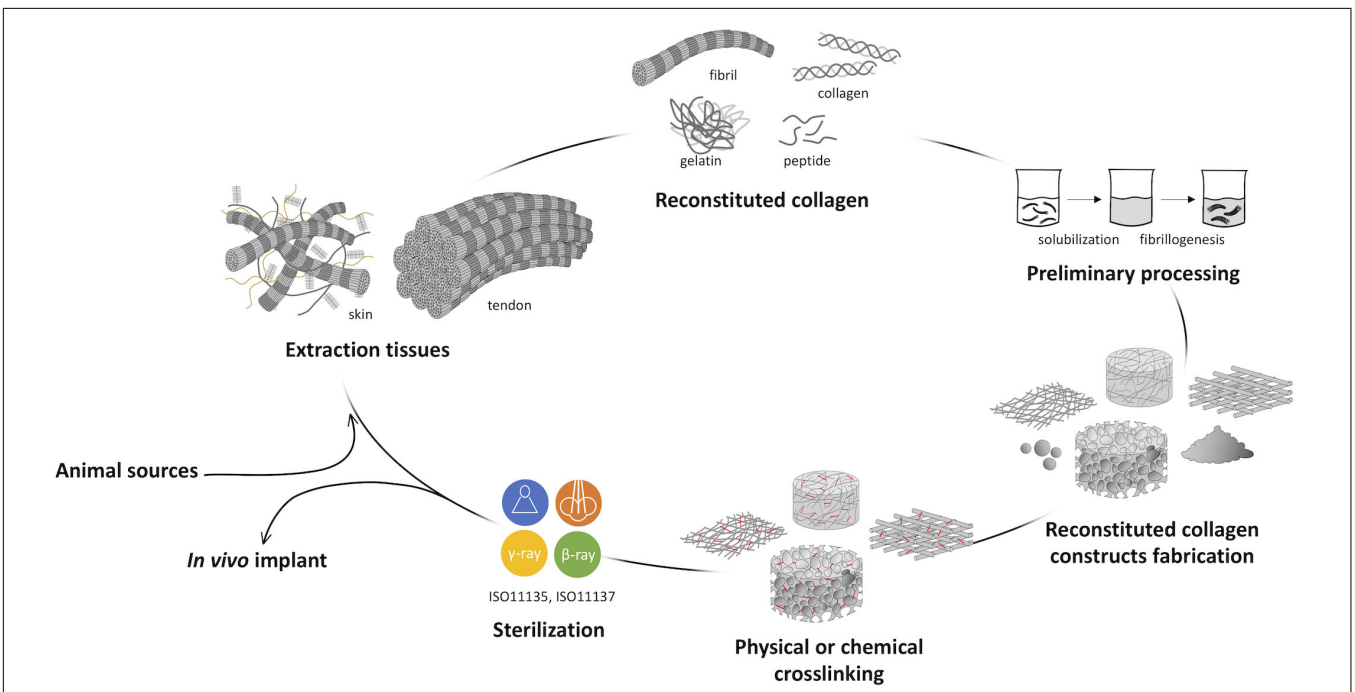

FIGURE 3 | Representative scheme of collagen processing steps from the animal source harvesting to the *in vivo* implant. The development of a collagen-based product can be divided into five macro steps: (i) the extraction or isolation from animal tissues, (ii) the preliminary raw material processing, (iii) the fabrication of the collagen-based product, (iv) its customization by the application of physical and/or chemical crosslinking, and (v) the final sterilization.

(Gelse et al., 2003; Makareeva and Leikin, 2014) suggested how mimicking the native tissue, by *ex vivo* reorganizing a native-like multiscale and hierarchically organized building blocks, could provide the possibility to finely control the cellular microenvironment and the cell response, enabling functional tissue regeneration. In this attempt, a key role is covered by the investigation techniques employed to correlate collagen structure to its *in vitro* bioactivity. The recent application of new and advanced imaging techniques such as wide-angle X-ray scattering (WAXS), small-angle X-ray scattering (SAXS), TEM, atomic force microscopy (AFM), piezoresponse force microscopy (PFM) allowed to deeply understand the impact of the processing on collagen spatial conformation at the nanoscale level and its interaction with cells.

Impact on Submolecular and Molecular Structure

In the manufacturing of a collagen-based product, the extraction of collagen from animal tissues is the preliminary step that, more than all further processing, influences the final properties of the device (Delgado et al., 2017; Xu et al., 2017; Bak et al., 2018). By means of several procedures with specific processing conditions, including exposure times, kind and concentration of chemicals, temperature, and pH, it is possible to obtain different types of reconstituted collagen, from the native protein extracts to peptides, with finely controlled properties at the submolecular and molecular levels. Among them, after the preliminary tissue mincing and milling, a crucial role is covered by the successive chemical and the enzymatic treatments. The exposure time, chemical agent concentration, and temperature deeply control reconstituted collagen structure.

The chemical treatment, usually performed in acetic acid solutions, allows to achieve only a partial solubilization of collagen fibers with a high level of native structure conservation, since intermolecular crosslinked collagen fibrils are not cleaved (Delgado et al., 2017). The enzymatic and non-enzymatic crosslinks present in mature collagen that give it resistance to degradation and chemical cleavage are the main causes of its low solubility in buffers and weak acids usually employed for its extraction. Despite this, long-lasting chemical treatment or high concentrations of chemicals are prevented when the extraction of collagen in native form is required, since long exposure times to acids do not increase collagen yield but damage the protein folding.

For this reason, the enzymatic treatment is almost always routinely performed after the chemical treatment to increase collagen extraction yield (Mocan et al., 2011). The chosen enzyme and its specific cut strictly direct toward the specific type of molecule that will be obtained. Usually, native collagen extraction involves the use of pepsin, an enzyme that cleaves the collagen non-helical telopeptide regions without disrupting its triple-helical structure, thanks to its affinity to unfolded proteins rather than folded. The effective removal of telopeptides can be controlled through the quantification by mass spectroscopy of the tyrosine residues that could be found only in the N-terminal and C-terminal positions. Despite the fact that the enzymatic treatments modify the native length of the collagen by cutting its extremities, the ultrastructural investigation by means of WAXS, SAXS, and Fourier-transform infrared spectroscopy (FT-IR) analyses demonstrated how the finely tuned chemical and enzymatic treatments allowed to retain a partial lateral packing arrangement despite the disruptive treatments of the extraction process (Falini et al., 2004; Terzi et al., 2018, 2019, 2020).

The production of peptides of specific molecular weights and therefore with specific bioactivity occurs through the use of different types of enzymes such as trypsin, chymotrypsin, alcalase, bromelin, collagenase, ficin, Flavourzyme, neutrase, pancreatin, thrombin, papain, and others that have high affinity to collagen in its native form and cut in specific points of the chain (Jung et al., 2014; Hong et al., 2019; Semenycheva et al., 2020). Also in this case, the fine-tuning of digestion parameters (pretreatments, enzyme type and concentration, time, temperature, pH) allows to have peptides with a variable and selective molecular weight distribution and isoelectric points (Zhang et al., 2013; Chi et al., 2015; Hong et al., 2019).

It is essential not to forget the role played by temperature, which must be kept below the collagen denaturation temperature during the whole extraction process when the preparation aims to save the triple-helical structure. On the contrary, the production of gelatin and peptides could involve raising of the working temperature above the denaturation temperature in acidic or alkaline environment with or without enzymes (Gorgieva and Kokol, 2011; Mokrejs et al., 2012).

The length of the collagen fibers could be controlled by tuning the dry matter content during homogenization. "Wet" homogenization (dry matter content in an aqueous system lower than 5%) allows to isolate fibers of several hundred micrometers, while with the "dry" homogenization (10–15% of dry matter contents in an aqueous system), thicker fibers of several centimeters long are achieved (Meyer, 2019).

The influence of the dialysis on collagen and thus on collagen-based scaffold properties and cell behavior was recently investigated by Bak et al. (2018). Supported by Raman spectroscopy and X-ray diffraction analysis, they demonstrated that the presence of acetic acid residues in collagen dialyzed with acetic acid presents a major extent on denatured molecules that directly impacted on mesenchymal stem cell proliferation rate (Bak et al., 2018). Complete elimination of acetic acid residues from collagen by performing dialysis with deionized water is recommended to preserve collagen nativeness and bioactivity.

As previously discussed, the entire extraction process and the physicochemical properties of the final material are strongly dependent on the selected animal source and tissue. More in general, various factors, such as animal age and interspecies variability, make collagen chemical and physical properties highly variable but customizable within a range of values (Gallo et al., 2020b). Keeping in mind all these aspects (i.e., age, tissue, animal, interspecies variability) and the variability of extraction protocols and the sensibility of the instruments and techniques used for collagen characterization, it is not surprising to find literature reports about the mechanical properties (e.g., stiffness) of the different hierarchical levels of collagen, which fall within a very wide range of values, sometimes overlapping (**Table 5**). Another factor that might lead to discrepancies is the fibril hydration level.

TABLE 5 | Young modulus of type I collagen in wet state at microscale and nanoscale, calculated as the slope of the tangent to the linear elastic region of stress–strain curves obtained by means of AFM or tensile test.

Organization level	Type I collagen state		Young modulus	References
Submolecular and supramolecular	Collagen molecule		3–5 GPa	Lorenzo and Caffarena, 2005; Gautieri et al., 2011
	Collagen microfibril		1–2 MPa	Yadavalli et al., 2010; Gautieri et al., 2011
Microstructure and macrostructure	Film	Not-crosslinked	∼5 MPa	Grover et al., 2012a
		Physically crosslinked	2–5 MPa	Terzi et al., 2018
		Chemically crosslinked	30–300 MPa	Grover et al., 2012a; Nair et al., 2020b
	Electrospun mat	Not crosslinked	–	–
		Physically crosslinked	0.2–1.0 MPa	Drexler and Powell, 2011
		Chemically crosslinked	3 kPa–5 MPa	Drexler and Powell, 2011; Lin et al., 2013; Elamparithi et al., 2016
	Porous membrane	Not crosslinked	∼0.7 MPa	Proffen et al., 2015
		Physically crosslinked	1–5 kPa	Davidenko et al., 2016a; Monaco et al., 2017
		Chemically crosslinked	20–50 kPa	Salvatore et al., 2014; Zhang et al., 2014; Monaco et al., 2017
	Hydrogel	Not crosslinked	0.2–10.0 kPa	Raub et al., 2010; Mason et al., 2013
		Physically crosslinked	0.5–20.0 kPa	Achilli and Mantovani, 2010; Antoine et al., 2015
		Chemically crosslinked	0.4–80.0 kPa	Raub et al., 2010; McBane et al., 2013; Yunoki et al., 2013; Contessi Negrini et al., 2018

AFM, atomic force microscopy.

Some recent studies confirmed that hydration plays an important role in the elastic modulus of collagen, which in the hydrated state is about 1,000-fold decreased than in the dry state (Yadavalli et al., 2010; Gautieri et al., 2011). However, although high standard deviations are found, it is clear that fiber bundles are the most flexible structural unit (slightly more than whole tissue), four times less stiff than microfibrils and 20 times less stiff than a collagen molecule (Meyer, 2019).

Impact on Supramolecular Structure

The conformational organization of the isolated collagen in the form of fiber, fibril, single molecule, or peptide could be further modulated after the extraction process by its preliminary handling prior to its manufacturing by means of further mechanical, chemical, and physical treatments. Several works report that the solubilization step, the solvent used and its concentration, and the homogenization procedures and times strongly affect the collagen supramolecular organization (Gopinath et al., 2014; Bak et al., 2018; Terzi et al., 2018; Zubal et al., 2018; Stanton et al., 2019).

One of the most important aspects in the manufacturing of collagen-based products is to produce devices with reproducible and constant properties. To do this, collagen is usually dispersed in acid aqueous solutions in such a way to form a homogeneous suspension, named "*slurry*." Obviously, the solvent concentration and type strongly influence its structure and thus its interaction with other molecules. From a biological point of view, the use of acid solutions is reported to disrupt the periodic banding (**Figure 2**) of the collagen fibrils, thus potentially affecting the related platelet response (Sylvester et al., 1989; Böhm et al., 2017). In addition, despite existing strategies for the removal of excess acid, the presence of non-negligible residues heavily affects the cellular response, as the release of acids is directly responsible for pH changes in the medium, which lead to cell growth slowdown or cell death.

While some types of less packed collagen are soluble in aqueous environment and do not require special precautions, other highly structured ones require a slightly acidic environment as well as the application of mechanical forces to break the strong interaction forces that keep collagen microfibers and do not allow them to uniformly solubilize or disperse in solution. Incomplete solubilization may induce non-homogeneous slurry properties, which would then be responsible for non-homogeneous or non-reproducible properties of the final device. Thus, collagen slurries are usually subjected to several cycles of mechanical homogenization (Terzi et al., 2019; Nair et al., 2020b). The modulation of the homogenization parameters allows to obtain more or less extensive fragmentation of the collagen fibers, thus controlling the supramolecular structure of collagen and, as a result, its bioactivity. In this regard, the tuning of the homogenization process in aqueous solution has been recently found by our team to lead to structural collagen modifications, as well as to control Schwann cell differentiation into myelinating cells (Terzi et al., 2018).

A significant in-depth study was then conducted by Ding et al. (2014), who explored collagen aggregation behavior in acid environment, related to concentration and temperature, to provide information on its use or processing. By means of ultrasensitive differential scanning calorimetry (US-DSC), AFM, and fluorescence techniques, they demonstrated that collagen molecular state was different in solutions with different collagen concentrations. In particular, they found that the denaturation temperature and the corresponding enthalpy slightly decreased with the increase of collagen concentration. The increment of collagen concentration reflects the formation of more hydrophobic interactions among collagen molecules and less water-mediated hydrogen bonds that tend to reduce the stability of collagen and increase the formation of aggregates (Ding et al., 2014). Furthermore, the thermal denaturation of collagen might be influenced by the heat transfer rate: the shorter distance between collagen molecules in aggregates may lead

to a higher rate of heat transfer, thus to an easier thermal denaturation (Ding et al., 2014). Additionally, collagen elastic modulus was reported to be strongly influenced by the type and concentration of monovalent salt (e.g., sodium chloride, potassium chloride, ammonium chloride) dissolved into the collagen suspension, which revealed to have a dose-dependent stiffening effect (Grant et al., 2009).

Insoluble collagen, which is usually more structured and more resistant to enzymatic degradation and mechanical load, has the disadvantages to need a more complex manufacturing and to result in a narrower application range. Indeed, the fact that it is soluble in weakly acid solutions, while aggregating and precipitating at physiological values of pH, drastically limits its use for the formulation of hydrogels or injectable suspensions. Some manufacturing "tricks" were developed in order to make native-like ultrastructured insoluble collagen soluble at neutral pH (Li et al., 2015; Zhang M. et al., 2018; Yang et al., 2020a,b). Among these, acylation and desamidation were set up to induce shifts of the collagen isoelectric point to lower values. The acylation of ε-amino group of lysine by means of succinic or glutaric anhydrides makes collagen molecules polyanionic and thus soluble at physiological pH, without affecting its triple-helical structure (Sripriya et al., 2011; Xu et al., 2017). By means of advanced analytical techniques such as XRD, AFM, FT-IR, and circular dichroism (CD), Xu et al. (2017) demonstrated how the collagen conformation was still preserved after acylation. Moreover, this kind of structural modification influences not only collagen solubility but also its resistance against enzymatic degradation, since lysine is one of the recognition residues for the proteases (Sripriya et al., 2011). The biocompatibility of such a treatment has been widely evaluated, and the treatment is currently used for ophthalmic applications due to the high level of thin film transparency (Hadassah et al., 2008, 2010). Less known is the alkaline (i.e., sodium sulfate) treatment of collagen fibrils that progressively hydrolyzes the amide groups of glutamine and asparagine side chains of collagen, resulting in the increase in the number of free carboxyl group and consequently in the sharpening of the isoelectric point (Radhika and Sehgal, 1997; Radhika et al., 1999). While acylation increases collagen thermal stability (Sripriya et al., 2011; Li et al., 2013), desamidation induces a decrement of collagen denaturation temperature (Radhika and Sehgal, 1997). Although the partial destructuration due to the breaking of intermolecular and intramolecular crosslinks between alpha chains and collagen molecules, the alkali treatment apparently does not affect cell behavior, since abnormal cell morphology and cytotoxic phenomena were not detected, confirming the absolute biocompatibility of the so treated collagen (Radhika and Sehgal, 1997; Radhika et al., 1999). However, the lack of in-depth cellular studies on this type of structural modification prevents from defining its long-term effects on cellular behavior.

The last supramolecular structure control, before further processing, could be done by inducing *in vitro* fibrillogenesis. Despite collagen extraction protocols are commonly set up to preserve its native structure as much as possible, the application of mechanical, chemical, and enzymatic treatments brings to a partial destructuration of the strict hierarchical organization of collagen fibrils (Gallo et al., 2020b) that is reflected in fibrils characterized by smaller diameter and length. Thus, the structural organization of the native tissue is not completely preserved in the extracted product. In this regard, some attempts were made in order to *in vitro* reorganize collagen fibrils in fibers that could resemble the natural ones by mimicking the entropy-driven process through which collagen molecules naturally assemble into fibrils.

Fiber packing can be controlled based on solution parameters such as concentration, temperature, pH, and ionic strength (Yadavalli et al., 2010; Harris et al., 2013; Li and Douglas, 2013; Moraes and Cunha, 2013; Ding et al., 2014). The exposure of collagen gels to relatively high temperature (32°C) below the denaturation temperature allows to obtain thicker fibers compared to those at room temperature (Ding et al., 2014). However, at temperatures close to or above the denaturation temperature, the fibers become thinner, suggesting that collagen disaggregation process occurs (Ding et al., 2014). Of key importance is the pH of the collagen suspensions, since it could promote or inhibit the collagen self-assembly process (Yadavalli et al., 2010). However, depending on collagen extraction source and type, different results could be obtained. Additionally, a high number of studies tried to enhance collagen assembly, depending on salt and ion concentration in solution. TEM and AFM revealed that collagen self-assembled into fibrils in the presence of multivalent ions that are able to induce the like-charge attraction and facilitate monomers' longitudinal registration to form fibrils with the native banding (Li and Douglas, 2013). In particular, Li and Douglas (2013) demonstrated that native fibrils could be reconstituted at pH 7.4 in salts with divalent anions and at pH 9.0 in salts with divalent cations. Some alternative strategies achieved high fibrillation levels by means of the presence of functionalized surfaces. For example, a hyaluronic acid surface coating was found to facilitate the self-reconstitution of collagen, leading to a more mature fibrous network with a twisted structure and enhanced lateral aggregation of fibrils. This fibrous network resulted in enhanced mesenchymal stem cell adhesion and spreading (He et al., 2013).

It is worth noting that, although a partial realignment could be obtained, to date, it is not possible to completely reassemble the extracted collagen fibrils in the ordered hierarchical natural organization.

Impact on Microstructure and Macrostructure

As previously mentioned, biological systems are highly hierarchical organized structures constituted by building blocks that enable and regulate the tissue function. To engineer such complex tissues, biomanufacturing tools are necessary to manufacture and model multiscale building blocks. The high versatility of collagen allows it to be manufactured in many different forms whose properties can be adjusted in a broad range. The last processing level that comprises collagen-based device fabrication and sterilization offers another tool for architecture control on the microscale and macroscale. Clearly, the former processing at the submolecular, molecular, and supramolecular level has a strong impact on this step. The manufacturing

techniques most frequently used for the production of temporary nanostructured and microstructured substitutes are, but are not limited to, freeze-drying, electrospinning, sol–gel transitions, and the new strategies enclosed in the additive manufacturing. It should not be neglected that the techniques accessible for collagen manufacturing are limited to those that allow handling it at temperatures lower than the denaturation one. However, it is worth noting that, in dry and vacuum conditions, the denaturation temperature can be even exceeded to induce a physical crosslink or to sterilize the collagen-based products.

The porous 3D structure, highly required for tissue engineering applications to promote cell survival, infiltration, and vascularization, could be produced and tuned according to the needs in terms of micro- and macro-architecture (e.g., pore size, shape, orientation, pore wall thickness and roughness) by acting on the manufacturing parameters (Offeddu et al., 2016; Pawelec et al., 2016). Advanced techniques, such as X-ray micro-computed tomography (micro-CT) and scanning electron microscopy (SEM), allowed in-depth investigation on collagen concentration effect on pore features and swelling behavior, revealing an increase of pore wall thickness, closed pore number, and swelling volume with collagen density (Offeddu et al., 2016). Besides to act on the technique, the modulation of the morphological parameters can occur through the addition of solutes to the collagen slurry. By means of SEM imaging investigation, sucrose was found to lead to the formation of smaller pore size, while sodium chloride was found able to stabilize collagen fibrils that became more fibrillar and led to the detection of scaffold pore walls with a more fiber-like surface (Pawelec et al., 2016), in accordance with Grant et al. (2009). Ideally, the porous or fibrous assembly of the scaffold should be tuned to match as much as possible the structural organization of collagen fibers within the target tissue. Indeed, topographical cues are fundamental to promote the desired cell phenotype/differentiation and to direct cell migration, as shown *in vitro* for multiple cell types, e.g., dermal fibroblasts (Poole et al., 2005), mesenchymal (Metavarayuth et al., 2016) and embryonic stem cells (Natale et al., 2020), and corneal keratocytes (Wilson et al., 2012). Moreover, the substrate topography can drive the remodeling of the scaffold, where the secretion of degrading enzymes by the cells and the deposition of new ECM components, in a native tissue-like architecture, may be assisted by the spatial arrangement of the scaffold in a similar pattern (Ahearne et al., 2020).

In this regard, the possibility to develop 3D hydrogel constructs *via* reproducible and flexible molding procedures such as the sol–gel transition is of great interest for the creation of constructs of a variety of shapes and size with a 3D network resembling that of soft tissues. The high number of variables implicated in hydrogel synthesis such as solubilization method, pH and temperature of polymerization, solution components, crosslinker, ionic strength, and collagen concentration allows to control and optimize hydrogel properties in order to better replicate the ones of the target tissue. To this aim, Antoine et al. (2015) developed an empirical predictive model by correlating multiple fabrication parameters in order to facilitate *a priori* design of collagen hydrogels with prescribed properties. An in-depth insight into the features of collagen hydrogels was done by means of a novel optical tweezers-based micro-rheometer technique, which demonstrated the presence of local inhomogeneities in the length scales of 25 μm or larger (Latinovic et al., 2010). The presence of areas of sparse and dense regions reflected the variability of the structural and viscoelastic properties on the microscale, since differences in the elastic properties of the collagen network, of three orders of magnitude higher than the less dense parts, were registered (Latinovic et al., 2010).

Another strategy to resemble an ECM-like architecture is provided by electrospinning, a well-established fabrication technique able to produce submicron non-woven fibers. Various advantages such as high surface–volume ratio, adjustable porosity, and easy surface functionalization made electrospun collagen matrices extremely useful for applications in the fields of tissue engineering, drug delivery, and wound dressing. By means of different strategies, electrospinning allows to manufacture collagen nanofiber networks similar to that present in the ECM in terms of fiber directionality and dimensions. However, native-like collagen suspensions cannot be spun because of inadequate viscosity, solubility, and insufficient solvent evaporation. As such, the electrospinning of gelatin or gelatin/collagen blends is more commonly performed (Monroy et al., 2017; Campiglio et al., 2019).

In the manufacture of implantable devices, key properties are mechanical resistance and enzymatic degradability. Unfortunately, the advantages of collagen biocompatibility, low antigenicity, and high bioactivity collide with disadvantages including low mechanical stiffness and poor resistance to enzymatic degradation. A chance to overcome this issue is offered by the post-fabrication formation of crosslinking bonds between the collagen chains by means of physical, chemical, or enzymatic methods (**Table 5**). Physical treatments that include ionizing, UV irradiation, dehydrothermal treatment (DHT), and dye-mediated photo-oxidation (Weadock et al., 1996; Gu et al., 2019) allow to achieve low values of crosslink density that restrict their range of application. Hence, a wide range of chemicals such as aldehydes (formaldehyde, glutaraldehyde, acrolein, glyoxal, malondialdehyde, succinaldehyde, dialdehyde starch), isocyanates (hexamethylene diisocyanate), carbodiimides [ethyl-3(3-dimethylamino)propylcarbodiimide], epoxides (1,4-butanediol diglycidyl ether, ethylene glycol diglycidyl ether), and some natural agents extracted from plants (gallic acid, glucose, quinones, genipin, oleuropein) were investigated as crosslinking agents in order to enhance the residence time and the mechanical performances of collagen-based devices (Madaghiele et al., 2009; Salvatore et al., 2014, 2020c; Madaghiele et al., 2016; Snider et al., 2017; Gallo et al., 2018; Terzi et al., 2018; Adamiak and Sionkowska, 2020; Gallo et al., 2020a). Recently, some enzymes such as tyrosinase, laccase, and mostly transglutaminase have also been investigated as non-toxic agents (Gu et al., 2019; Adamiak and Sionkowska, 2020). Depending on the clinical application and the function of implants, crosslinking seems to be advantageous with regard to physical properties such as strength over time, the integration in the surrounding tissue, and the rate

and type of remodeling. Each crosslinking method is able to induce different degrees of structural and mechanical stability, which are largely dependent on the crosslinking mechanisms, concentration, and exposure time. Advanced microscopy techniques such as AFM and PFM allowed to investigate the amino acid level modification of collagen piezoelectricity, as well as the ability to modify it using chemical crosslinkers, in order to tailor the electromechanical properties and the related biological response (Nair et al., 2019). Carbodiimide crosslinking of collagen films was found to result in local alignment of collagen fibrils to form thicker fiber bundles, with a perceptible enhanced and localized piezoelectric response; on the contrary, transglutaminase and genipin crosslinked films displayed a non-localized enhanced piezoelectric response (Nair et al., 2019).

Although numerous investigations focus on chemical crosslinking optimization, from a clinical point of view, various authors recommend to avoid chemical crosslinking because of the intensive proinflammatory reaction to crosslinked materials. During resorption, chemical crosslinking affects matrix metalloproteinase (MMP) bioactivity and produce an imbalance in ECM turnover (Aamodt and Grainger, 2016) that results in scar formation. Additionally, resulting collagen degradation fragments are recognized as antigens and amplify the foreign body response (Sandor et al., 2008; Maternini et al., 2019). However, in contrast to the general assumption, Dunn (2012) recently argued that *in vivo* trials often lack comparable conditions and long-term clinical investigations are still missing. One of the most important effects of crosslinkers is their modification of the GFOGER integrin binding sites of collagen helical structure. The hiding or the removal of such recognition sites significantly alters cell differentiation, adhesion, and migration, since cell response is mediated by integrin bonding in a mechanosensing and ligand density-dependent way (Bax et al., 2017). Nair et al. (2020b) demonstrated that the long-term proliferation of human dermal fibroblasts is dependent on the availability of integrin binding sites regardless of the mechanical cues, and that it can be effectively modulated by choosing the appropriate crosslinking. Thus, it is of fundamental importance to consider the mechanism of action and the amount of crosslinker used in order to tune the biological response according to the intended application. In the light of these pieces of evidence, collagen scaffold crosslinking has been customized to direct stem cells toward differentiation (Keogh et al., 2010), organoid formation (Mason et al., 2013; Abbas et al., 2019; Yang et al., 2020c), or to develop 3D cancer models for drug development and testing (Campbell et al., 2017). Interestingly, the crosslinking and stiffening of collagen gels have been also reported to promote the *in vitro* stability of tubular structures, such as blood and lymphatic vessels (Chan et al., 2014).

The considerable advantages offered by crosslinking pushes the research toward the identification of a potential "gold standard" crosslinking protocol for collagen-based devices, to date not yet found. A key problem when comparing different crosslinking treatments is that used protocols often differ greatly. Moreover, additional variations could be ascribed to the different collagens (i.e., extraction source, selected tissue) used as starting materials as well as to their peculiar processing. Indeed, both factors have been shown to have a large effect on crosslinking efficacy and cellular response. While numerous researches demonstrated that mechanical properties and degradation rate could be finely tuned as a function of the crosslinking method, optimized crosslinking methods for collagen-based materials still needs to be developed not only to achieve an adequate balance between stability and functional tissue remodeling but also to affect and control key cell–matrix interactions (e.g., adhesion and migration) required for proper tissue synthesis.

Sterilization of collagen-based devices is the last key process to accurately perform prior to *in vivo* implant. Traditional sterilization methods utilizing heat (autoclaving) are not applicable, since collagen is irreversibly denatured over 60°C (Proffen et al., 2015). Therefore, the most frequently used methods include dry heat (DHS), ethylene oxide (EtO), and high-energy radiations such as beta (β-ray) or gamma irradiation (γ-ray). The major issue in sterilization methods is that all of them induce molecular alteration of the collagen triple-helical structure, with a consequent decrease of mechanical and enzymatic resistance (Noah et al., 2003; Wiegand et al., 2009; Proffen et al., 2015; Monaco et al., 2017). A variety of studies have shown that an unsuitable sterilization process can destroy the structure of collagen, break chemical bonds, and alter physical, chemical, and biological properties substantially (Noah et al., 2003). Therefore, the choice of the sterilization technique is fundamental to preserve the collagen structural and biological role in the ECM-like reconstituted construct.

The treatment with EtO induces changes in the protein structure, a decrement of mechanical properties and a reduction of cell metabolic activity due to the possible presence of toxic residues (Proffen et al., 2015). As well, β-ray can alter the protein structure by directly cleaving the protein chains (Proffen et al., 2015). However, EtO sterilization and β-ray irradiation induce less damage than γ-ray (Parenteau-Bareil et al., 2010; Monaco et al., 2017). The latter indeed is able to break chemical bonds and decrease tensile strength even severely so as to induce a rapid enzyme degradation (Noah et al., 2003). Still, when comparing EtO with β-ray sterilization, the former seems to have less effect on the decrease of mechanical properties (Proffen et al., 2015). The chain scission occurring upon β-ray exposure leads to protein fragmentation and overall increased enzymatic degradability compared to EtO. With respect to EtO and β-ray, DHS treatment resulted in the slowest enzymatic degradation, thanks to the further heat-induced crosslinking that makes the collagen-based scaffold less vulnerable to proteolysis (Monaco et al., 2017).

The modification of the structural properties of the manufactured scaffold could affect the cell response, since the native cell binding sites may be no more available due to collagen triple helix denaturation or chain scissions. With regard to sterilization, conversely to what was expected, Wiegand et al. (2009) demonstrated that γ- and β-ray as well as EtO sterilization did not influence the binding capacity of type I collagen for selected proteases and cytokines associated with non-healing wounds, as no significant loss in the binding affinity for polymorphonuclear elastase, matrix metalloproteinase-2, and interleukin-1β or in the antioxidant capacity was found. However, while these modifications were not reported to

significantly affect cell response *in vitro* and *in vivo* (Proffen et al., 2015; Monaco et al., 2017), evidences by Noah et al. (2003) showed a higher proliferation in EtO-sterilized sponges compared to γ-ray-treated ones.

OPTIMIZATION OF TYPE I COLLAGEN-BASED SCAFFOLDS FOR THE DEVELOPMENT OF SPECIFIC TISSUE SUBSTITUTES

The manufacturing and the optimization of collagen-based scaffolds for tissue regeneration have been the subject of a large number of studies over the last 40 years. Since the pioneering work by Yannas et al. (1982) on the synthesis of collagen-based sponges for skin regeneration, which dates back to early 1980s, extensive research has been performed *in vitro* and *in vivo*, with the multiple aims of (a) investigating the cellular processes underlying tissue regeneration; (b) understanding the guidance cues (e.g., biochemical, mechanical, and topographical) provided by the scaffold to instruct and orient cells toward tissue regeneration; (c) improving the extent and the quality of induced regeneration in terms of size of the regenerated tissue and restoration of the native tissue structure and functionality. This multidisciplinary research has been enabled and boosted by several technological advancements in both the biology and materials science sectors, such as the optimization of cell culture procedures and the development of more accurate manufacturing technologies and analytical methods.

An exhaustive review on the use of type I collagen-based scaffolds for tissue regeneration would go beyond the scope of this article. Here, we only discuss the optimization of the scaffold structure for improved biological activity by focusing on exemplary cases inherent to the regeneration of skin, cornea, bone, and tendon tissues. Several attempts to develop functional tissue substitutes are described, highlighting, where applicable, critical features due to inappropriate or poor mimesis of the native tissue structure.

Skin (Dermal Templates)

Skin is the largest organ of the human body, composed of an outer cell-based epithelial layer, i.e., the epidermis, and an inner ECM-based connective tissue, i.e., the dermis. In the dermal ECM, type I collagen is the most abundant fibrous component (80%), along with type III collagen (15%) and elastin (Kaur et al., 2019; Rahmati et al., 2020). Glycosaminoglycans are also found, which form the so-called ground substance, i.e., an amorphous gel in which cells and fibrous components are embedded. The dermis is also highly vascularized and innervated and contains several appendages, i.e., hair follicles, sweat glands, and sebaceous glands, which contribute to skin functionality (Vig et al., 2017; Kaur et al., 2019). Furthermore the dermis is responsible for the different thicknesses of the skin in different parts of the body in relation to the function of the tissue.

Skin constantly deals with intrinsic and extrinsic forces. The effect of mechanical forces is dependent upon the stiffness and biomechanical properties of the skin, which vary between anatomical locations (Wong et al., 2012). As a physical force is applied to the skin, mechanical signals are converted into chemical ones and transmitted to cells in order to trigger a further signaling cascade of responses (Kuehlmann et al., 2020; Urbanczyk et al., 2020). In doing this, ECM components and in particular type I collagen cover an essential role in the transduction of mechanical forces to cell mechanosensors such as cytoskeleton (e.g., actin and transforming protein RhoA), ion channels, catenin complexes, cell adhesion molecules (e.g., focal adhesions and integrins), and several signaling pathways [e.g., Wnt, focal adhesion kinase (FAK)-extracellular signal-regulated kinase (ERK), mitogen-activated protein kinase (MAPK)/ERK] (Alenghat and Ingber, 2002; Kuehlmann et al., 2020; Urbanczyk et al., 2020). Thus, besides the biomechanical aspects, type I collagen is involved in a plethora of additional functions. Signaling by specific receptors that mediate the interaction with collagens, such as integrins, discoidin-domain receptors, glycoprotein VI, or specialized proteoglycan receptors defines adhesion, differentiation, growth, and cell reactivity.

In case of severe injuries, the spontaneous healing response of the dermis consists of a repair process, where the injured site is closed by wound contraction and deposition of an irregular collagenous "scar" tissue. Repair thus leads to the formation of a tissue that is structurally and functionally different from the native one. On the contrary, induced skin regeneration aims to restore the physiologic organ structure and function by using a dermal template (or scaffold) capable of limiting or suppressing spontaneous contraction and scar formation while enabling the synthesis of new dermal tissue (Yannas, 2009; Soller et al., 2012). The understanding of mechanotransduction processes revealed to be important in the manufacturing of a temporary scaffold for tissue regeneration, since mechanical stimuli contribute to alterations in the wound healing process and scar formation (Kuehlmann et al., 2020). Clinical evidence confirmed how the application of mechanomodulatory procedures by the use of a compression device is able to relax skin tension at the site of the wound and effectively reduce scar development, although there remains room for improvement (Lim et al., 2014; Longaker et al., 2014; Orgill and Ogawa, 2014). To date, a multitude of temporary skin substitutes are available for clinical use, which consist of cell-free and/or cell-seeded biomaterial templates (Vig et al., 2017). However, the so-obtained skin is only partially regenerated, as it lacks appendages and does not show the full recovery of biofunctional properties, such as thermoregulation, sensation, and pigmentation (Vig et al., 2017). Therefore, the optimization of dermal templates for improved regeneration is currently the subject of extensive ongoing research.

In the context of skin regeneration, various type I collagen-based templates have been developed and tested in research and/or clinical settings. Groundbreaking studies performed by Yannas et al. (1982) showed that a collagen/glycosaminoglycan-based freeze-dried sponge, crosslinked with glutaraldehyde, could partially regenerate the dermis in animal models and in humans. Although being an oversimplified ECM substitute, this cell-free dermis regeneration template (DRT) (later commercialized as Integra® skin graft) was notably able

to induce significant regenerative outcomes. In particular, by modulating some structural parameters of the DRT, it was possible to demonstrate that induced regeneration was strongly correlated to the scaffold ability to delay wound contraction (Yannas et al., 1982). In this regard, two evidence-based mechanisms have been later proposed to explain how the scaffold may hinder contraction, i.e., the reduction of the number of contractile cells (myofibroblasts) in the wound bed and the reduction of the overall contraction forces (Soller et al., 2012). The observed decrease of the number of myofibroblasts in the wound, in the presence of the scaffold (Murphy et al., 1990), could be due to the scaffold ability to non-specifically bind the transforming growth factor beta 1 (TGF-β1), which is a promoter of the myofibroblast phenotype (Yannas, 2009) while preventing platelet aggregation (Sylvester et al., 1989). Indeed, the DRT scaffold is processed by dispersion of bovine tendon collagen in an acid solution, which disrupts the native collagen fiber banding. The consequent inhibition of platelet aggregation may thus lead to inhibition of platelet degranulation and to the concomitant reduction of TGF-β1 from the wound bed (Sylvester et al., 1989). As for the reduction of the contractile force, this may be related to the scaffold ability to bind most of the contractile cells along its randomly oriented collagen struts, thus resulting in ineffective contractile forces, oriented out of the plane of the wound (Yannas, 2005; Soller et al., 2012). Noteworthy, this mechanism would explain why the DRT leads to a maximum delay of wound contraction, i.e., maximum biological activity, only when having specific mean pore size (in the range 20–120 μm, achieved by tuning the freezing rate and temperature in the freeze-drying process) and specific degradation rate (with an *in vivo* residence time of approximately 3 weeks, yielded by tuning the crosslinking) (Yannas, 2005). The requirement of an optimal pore size that suggests an optimal surface area per unit volume may be due to the need for the scaffold to bind an adequate number of contractile cells (O'Brien et al., 2005). Similarly, the requirement of an optimal residence time may be due to the need for the scaffold to persist at least over the period of wound healing (about 3 weeks) during which contraction remains active (Yannas et al., 1989). At the same time, a too long persistence of the scaffold would likely interfere with the synthesis of new tissue. Indeed, the inhibition of contraction is necessary but not sufficient for regeneration, since regeneration also requires tissue formation (Yannas, 2009).

Based on such observations, the following structural determinants of the scaffold biological activity have been identified (Yannas, 2005), which are mostly linked to the scaffold ability to establish direct interactions with the hosted cells: (a) the chemical composition (i.e., the ligand identity); (b) the mean pore size (i.e., the ligand density); (c) the crosslink density (i.e., the ligand duration); and (d) the local spatial arrangement or microstructure (i.e., the ligand orientation). Moreover, collagen banding is an additional structural feature that likely plays a major role in modulating the *in vivo* response. With regard to pore size and crosslink density, it is worth mentioning that the optimal values found by the Yannas team for their DRT are currently used as a gold standard for the development of alternative dermal substitutes. However, the DRT does not present the native collagen banding (it is estimated to have only a 5% residual banding) (Yannas, 2005) while having a microporous sponge-like structure that does not really mimic the fibrillar network of the skin ECM (Dill and Mörgelin, 2020). This relatively poor mimesis of the native collagen architecture may be one of the critical features leading to suboptimal skin regeneration.

Indeed, more recent studies seem to suggest that the preservation of the native tissue structure is highly desirable for improved skin regeneration (Böhm et al., 2017; De Angelis et al., 2018; Tati et al., 2018; Dill and Mörgelin, 2020). When comparing different collagen-based dermal substitutes, all obtained by freeze-drying but varying for the collagen source and the related processing steps (e.g., collagen extraction, aqueous processing, and crosslinking), those with a dermis-like fibrillar network and/or those retaining the native collagen banding have been shown to promote *in vitro* important biological processes involved in tissue regeneration, such as the binding and inactivation of proteases (Tati et al., 2018), an accelerated adhesion, migration and proliferation of cells in the scaffolds (Böhm et al., 2017; Dill and Mörgelin, 2020), an improved cell morphology (Dill and Mörgelin, 2020), and a higher downregulation of the myofibroblast phenotype (Dill and Mörgelin, 2020). Interestingly, in a recent clinical study, an alternative dermal template based on native type I collagen has been shown to lead to accelerated angiogenesis and tissue formation in the short term, as well as to a better clinical outcome in the long term, compared to the Integra® DRT (De Angelis et al., 2018). In that study, the two investigated templates had similar glutaraldehyde-based crosslinking and were both obtained by freeze-drying but mainly differed for the chemical composition (collagen from bovine skin vs. collagen from bovine tendon and glycosaminoglycan) and the related microstructure.

Although requiring further exploration, these findings indicate that the scaffold capability to recapitulate at least some of the structural features of collagen in native dermis may suffice to enhance the scaffold regenerative potential. From a clinical point of view, accelerated angiogenesis is a key factor to improve the outcome of skin regeneration, also considering that the kinetics of angiogenesis is inversely related to the incidence of infections (Yannas, 2009). Therefore, research efforts to improve skin regeneration include the functionalization of cell-free scaffolds with angiogenic molecules, as well as the induction of simultaneous dermis and epidermis regeneration (Oh et al., 2012; do Amaral et al., 2019). For example, it has been recently shown that a DRT added with platelet-rich plasma holds potential for both enhanced vascularization and simultaneous epidermis regeneration (do Amaral et al., 2019). Sophisticated manufacturing techniques, such as 3D bioprinting, are being explored to produce functional full-thickness skin equivalents, starting from cells embedded in collagen-based gels (Ramasamy et al., 2021). While these complex skin substitutes may be particularly useful for *in vitro* studies related to pharmaceutical and cosmetics purposes, they do not appear competitive or easily translatable to the clinical setting, where relatively simple

and functional skin substitutes (although yet suboptimal) are already available.

As a final note on skin regeneration, it is worth mentioning that, in spite of the well-known importance of mechanical signals on the cell behavior (e.g., fibroblasts migrating from softer to stiffer substrates) (Kidoaki and Matsuda, 2008), the mechanical properties of the various skin substitutes developed so far have not been widely addressed (Kaur et al., 2019). As an example, the DRT discussed above has a quite low tensile modulus in the wet state (about 500 Pa) (do Amaral et al., 2019), which has not been optimized to match the skin modulus. The measured modulus of human skin is actually quite variable, in the range 0.004–150 MPa, based on body location, age, orientation of the skin sample with respect to the Langer lines, and testing method (Nì Annaidh et al., 2012). The scaffold mechanical properties are thus likely to be critical features that deserve future optimization for an improved regenerative outcome. In this respect, scaffolds with stiffness gradients have been recently proposed to simulate the stiffness gradient between different skin layers (epidermis and dermis), so as to better resemble the mechanical cues that cells in each layer receive from their microenvironment (Rahmati et al., 2020). In addition, the identification of an optimal crosslinking agent is worth a future investigation, considering that toxic glutaraldehyde is still widely used. The effects of various crosslinking agents on both the mechanical properties and the actual availability of cell ligands on the scaffold surface should be properly addressed.

Cornea

The cornea is a rigid, transparent, and multilayered organ on the eye surface that protects the eye and focuses light onto the crystalline lens, thus ensuring vision. The epithelium is the outermost cell-based tissue, in contact with the external environment, which accounts for ≈10% of the corneal thickness; the stroma (≈90% of the thickness) is the supportive avascular but highly innervated ECM-based tissue mainly responsible for the functional properties of the cornea, such as mechanical strength and transparency; the innermost endothelium is composed of a single layer of endothelial cells that regulate the cornea hydration (Gouveia and Connon, 2016; Ahearne et al., 2020; Mahdavi et al., 2020). Proteoglycans and type I collagen, which are secreted by keratocytes, form the stromal ECM with its unique structural pattern: collagen fibrils, having a diameter of about 35 nm (Raspanti et al., 2018), are regularly arranged in orthogonal layers (or lamellae), in which fibrils lie in a quasi-hexagonal lattice, like a liquid crystal, which enable transmittance of visible light wavelengths and confer suitable mechanical properties to resist the tension exerted by the intraocular pressure (Sibillano et al., 2016). Fratzl and Daxer (1993) also observed that hydration of the fibrils and layers influence corneal mechanical features.

In the anterior part, the fibrils are highly interwoven and dictate the precise curvature of the cornea, which allows to properly focus light for vision (Gouveia and Connon, 2016). Optical clarity of the cornea is also ascribable, in part, to its stromal cells. Indeed, keratocytes, which reside between the lamellae, express corneal crystallins, i.e., proteins that are thought to match the refractive index of the cell cytoplasm with that of the surrounding ECM (Shah et al., 2008).

Considering that damage to corneal stroma results in scarring and impaired or lost vision, great efforts are directed to the development of stromal substitutes *via* scaffold-based tissue engineering approaches, as recently detailed in several reviews (Zhang et al., 2019; Ahearne et al., 2020; Mahdavi et al., 2020). Among the scaffolds proposed for corneal regeneration, those based on type I collagen are largely investigated, in an attempt to mimic the composition of the stromal ECM. Some of the earliest trials to produce corneal substitutes involved the use of collagen-based gels (Germain et al., 1999), sponges (Orwin and Hubel, 2000), and films (Crabb and Hubel, 2008), with the collagen derived from animal tissues, such as bovine or porcine skin or tendon. However, the achievement of suitable strength and transparency, prerequisites for corneal function, soon represented major challenges in the development of practical corneal substitutes. Young's modulus and tensile strength of the human cornea are reported in the wide ranges 0.1–110.0 MPa and 3–6 MPa, respectively, based on tissue anisotropy, donor variability, and testing methods (Fagerholm et al., 2014; Shih et al., 2017; Ahearne et al., 2020). While several crosslinking methods could be utilized to effectively enhance the stiffness of the collagen substrates without impairing the transparency, the cytotoxicity of the crosslinking agents could limit the cell proliferation (Ahearne et al., 2020). Collagen sponges, obtained by freeze-drying and DHT crosslinking, were found to support the growth of corneal epithelial, stromal, and endothelial cells but also to induce a myofibroblast phenotype of stromal cells over time in culture (Orwin and Hubel, 2000). Interestingly, when comparing DHT-crosslinked collagen sponges and films (with the latter being stiffer than the former), this shift in phenotype was less pronounced on the films, on which cells could grow but not migrate into. This confirmed the utmost importance of both topographical and mechanical cues on cell behavior (Crabb et al., 2006).

Indeed, critical limitations of those earliest corneal substitutes were mostly ascribable to their inability to mimic the dense and sophisticated quasi-hexagonal packing of the collagen fibrils in the corneal ECM, which also led to a mismatch of the mechanical properties. Preliminary studies on the analysis of corneal cell behavior on aligned 2D substrates demonstrated that topographical features could modulate the proliferation of epithelial and stromal cells, in addition to controlling cell alignment, migration, and phenotype (Liliensiek et al., 2006). The development of aligned and dense 3D collagen scaffolds, inspired by the native corneal architecture, has attracted much attention in the last 15 years. With reference to collagen gels, one of the simplest methods to improve the mimesis of native tissue density and mechanical properties is to utilize plastic compression under load. In compressed gels, collagen dehydration and mechanical/physical crosslinking occur, so as to increase both the collagen concentration and the gel stiffness (Cheema et al., 2007; Gouveia and Connon, 2016). Interestingly, cyclic loading has been investigated and found to control the collagen fibril diameter (Cheema et al., 2007). In spite of the simplicity of this approach, compressed gels

have been shown to represent a significant improvement over conventional gels for the production of epithelial, stromal, and endothelial constructs (Cheema and Brown, 2013; Levis et al., 2015). Recently, compressed gels containing human corneal stromal stem cells have been reported to suppress scar formation and improve regeneration in a mouse model (Shojaati et al., 2018).

Noteworthy, compressed collagen gels have been utilized to reproduce the native corneal curvature, which is an additional structural requirement deeply affecting cell behavior (Gouveia et al., 2017; Miotto et al., 2019). Indeed, curvature alone has been shown to control the alignment of human corneal stromal cells and their biosynthesis of stromal tissue (Gouveia et al., 2017). While curved substrates are commonly obtained using contact lens molds (Merrett et al., 2008; Gouveia et al., 2017), the self-curvature of compressed collagen gels has been recently induced by patterning the gels with a peptide amphiphile, able to inhibit the contractile activity of stromal cells *via* specific Arg-Gly-Asp (RGD) sequence–integrin interactions (Gouveia et al., 2014). The spatial modulation of the substrate contraction activated by stromal cells has been found to promote the tissue self-curvature over time in culture, then resulting in the formation of a tissue substitute with both native-like curvature and ultrastructure (Miotto et al., 2019).

Other attempts to mimic the native corneal architecture, in order to enhance the biological activity of the tissue substitute, have involved the use of advanced manufacturing techniques that allow controlling the diameter and orientation of the collagen fibers upon deposition. For example, electrospun collagen-based substrates with aligned fibers, in the diameter range 30–500 nm, have been shown *in vitro* to downregulate the myofibroblast phenotype while improving the optical properties of the tissue construct (Phu et al., 2011). However, since electrospinning may have a significant impact on the collagen triple helix conformation, alternative techniques have been explored to produce oriented collagen scaffolds, such as oriented flow casting (Tanaka et al., 2011) and the magnetic alignment of collagen fibrils (Torbet et al., 2007). Electrospun nanofibers based on synthetic polymers have been coupled to collagen gels (Wilson et al., 2012) and compressed collagen gels (Kong et al., 2017), respectively, resulting in downregulation of the myofibroblast phenotype and enhancement of mechanical properties while supporting cell growth.

Bioprinting is an additional manufacturing method that has gained much interest for the production of corneal substitutes due to its ability to control the hierarchical assembly of biological constructs while allowing the fast synthesis of thick and customizable constructs (Isaacson et al., 2018; Sorkio et al., 2018; Zhang et al., 2019; Fuest et al., 2020). Several collagen-based bioinks are being explored to encapsulate and deposit corneal cells upon printing (Isaacson et al., 2018; Sorkio et al., 2018; Duarte Campos et al., 2019; Kim et al., 2019), some of which based on human type I collagen (derived from neonatal fibroblast cells) for better mimesis of the human corneal stroma and higher compatibility with human stem cells (Sorkio et al., 2018). Notably, it has been shown that printed constructs with aligned collagen fibrils and cells can be obtained by properly controlling the shear stress on the bioink upon extrusion (Kim et al., 2019). Compared to non-oriented constructs, the oriented ones were shown to induce the creation of a structure similar to the native cornea upon their remodeling *in vivo* (in a rabbit model) (Kim et al., 2019).

While most substrates investigated for corneal regeneration involve the use of animal-derived collagen, it is worth noting that recombinant human collagens have been explored as safer alternatives for the development of implantable cell-free tissue substitutes. Preliminary studies compared the *in vivo* performance of recombinant type I and type III collagen gels, stabilized *via* carbodiimide crosslinking, in an animal model (Lagali et al., 2008; Merrett et al., 2008). Type III collagen was used due to its ability to form smaller fibrils than type I in an attempt to enhance the fibril packing in the hydrogels. The studies showed that both gel substitutes had similar chemical and mechanical properties, although the ones based on recombinant type III collagen had superior optical clarity. Moreover, both substitutes were effectively integrated into the host corneas 12 months after surgery, maintaining transparency and ensuring regeneration of corneal cells, tear film, and nerve endings (Lagali et al., 2008; Merrett et al., 2008). Following clinical data then demonstrated that the implantation of recombinant type III collagen gels promoted, over 4 years of observation, the endogenous recruitment and regeneration of corneal tissue and nerves, without any rejection episode (Fagerholm et al., 2014). To the best of our knowledge, these findings are the first and only documenting the use of cell-free collagen-based scaffolds for corneal regeneration on humans.

However, despite being so far the most promising devices for a future clinical translation, recombinant collagen gels still need further improvements to optimize their regenerative performance and functional outcome. In particular, some critical features of the gels have emerged in the abovementioned studies, which appear related to their poor mimesis of the native tissue structure and/or properties. First of all, the gels do not have mechanical properties comparable to those of the human cornea (Fagerholm et al., 2014). Although being sufficiently robust for grafting, the gels need particular care for surgical manipulation and suturing, and sutures may result in local surface thinning or indentation of the implants, which compromise the achievable visual acuity (Fagerholm et al., 2014). Moreover, a detailed characterization of the structural and optical properties of the gels showed that these corneal substitutes have a substantially different architecture than the native tissue, as well as a high and undesired transmission of UV light (in addition to visible light), which is potentially damaging to the lens and the retina (Hayes et al., 2015). With regard to the structural properties, compared to the native corneal tissue, the hydrogels were found to show collagen fibers or filaments with smaller diameter and more sparsely distributed, with the absence of stacked lamellae and the absence of fiber interweaving in the anterior part (Hayes et al., 2015). Furthermore, no periodic D-banding was observed, which indicated the lack of native collagen fibrils in the synthetic hydrogels (Hayes et al., 2015). Future structural modifications of the gels, directed to optimize the extent of mimesis of the native tissue (e.g., by

implementing more advanced manufacturing techniques for a higher control of the collagen patterning, or by optimizing the crosslinking for suitable strength), may show promise to enhance the therapeutic potential.

Bone

Bone is a complex, living, constantly changing tissue. With its peculiar architecture and composition, it performs an essential mechanical function besides playing a critical role in diverse metabolic processes mediated by calcium delivery as well as in hematopoiesis. Natural bone is a heterogeneous and anisotropic nanocomposite, the principal components of which are a mineral phase and an organic phase, hierarchically organized into several structural levels from the nanoscale to the macroscale. Thus, bone is principally composed of calcium phosphates (69–80 wt.%, mainly hydroxyapatite and β-tricalcium phosphate), collagens (17–20 wt.%, mainly types I, III, and V), and other minor components (5 wt.%; biglycan, fibronectin, osteonectin, osteopontin, thrombospondin, osteocalcin, alkaline phosphatase, and others) (Filippi et al., 2020; Lin et al., 2020). Type I collagen accounts for the 90% of the total collagen in bone tissue (Lin et al., 2020), and it covers an important role not only in the tissue mechanical supporting but also in biological processes fundamental for bone homeostasis (Lin et al., 2020). Indeed, the lack of type I collagen or mutation of collagen structure (i.e., osteogenesis imperfecta, osteoporosis, osteoarthritis) results in ECM property changes and, more specifically, in the significant reduction of mechanical properties and in the increase of the related fracture risk (Giannini et al., 2014; Lin et al., 2020). Types III and V collagens, present in smaller amounts, regulate the fiber diameter and fibrillogenesis of type I collagen (Garnero, 2015). At the nanoscale level, collagen fibrils assembled from type I collagen molecules (1.5 nm in diameter, 300 nm in length) are infiltered and surrounded by mineral nanocrystals (plate or needle-shaped, 1.5–4.0 nm in thickness) oriented along the axial direction of the fibril (Filippi et al., 2020). Scaling up from the nanostructural to the microstructural frame, collagen fibrils interact with other collagenous and non-collagenous proteins to assemble higher-ordered fibril bundles and fibers organized in 3–7-μm-wide planar sheets, called lamellae (Filippi et al., 2020; Lin et al., 2020). Concentric layers of lamellae of about 200–250 μm of diameter form cylindrical structures that run parallel to the bone long axis, named osteons or Haversian systems (Filippi et al., 2020).

Although bone is constantly remodeled in physiological conditions and presents a strong regenerative capacity, in case of extensive traumas, repairing processes are not able to fully regenerate the injured tissue and surgical interventions are needed. Actually, autograft is the gold standard for repairing defective tissue, but it may lead to donor tissue degeneration and dysfunction (Ma et al., 2021). However, the limited access to autologous bone, donor site morbidity, surgical complications, fitting irregular defect difficulties, as well as inconsistent repair limited its execution (Dewey et al., 2021). On the other side, allotransplantation can cause immune rejection (Ma et al., 2021). Thus, the high number of shortcomings of current treatments headed research for tissue engineering solutions.

Being one of the major bone components and one of the key factors for mineralization beginning and propagation, several collagen-based templates were proposed. Beyond processing, if the regeneration of other tissues is influenced by collagen structure, in the case of bone regeneration, different collagen forms direct osteoblast proliferation and differentiation. In particular, in contrast to soluble and fibrillar forms, denatured forms of type I collagen inhibit the proliferation of osteoblast-like cells and stimulate osteoblastic differentiation, a stage indicated by higher alkaline phosphatase activity and osteopondin expression (Tsai et al., 2010). However, a long-term study showed opposite results, with the delay of proliferation and mineralization mediated by the fibrillar form (Hanagata et al., 2006). The discrepancy between these two studies might be due to collagen sources, processing, and manufacturing but also by the different stages of osteoblastic maturation, a parameter that deeply affects the cell–material interaction.

The arrangement of collagen fibers in bone is much more complex than in other tissues, and it is very difficult to achieve ECM-like bottom-up temporal bone substitutes. To this, oriented collagen fiber scaffolds were not widely investigated for use in bone tissue engineering (Ma et al., 2021). Thus, the challenging goal is to develop scaffolds able to mimic the microenvironment of native bone *in vivo* and to: (i) provide a temporary mechanical support; (ii) have an appropriate porous architecture to promote bone cell migration and differentiation into the scaffold; (iii) encourage osteoinduction; (iv) and enhance osteointegration with the host tissue. Collagen-based freeze-dried scaffolds revealed to have a bone pro-regenerative effect. A huge number of studies investigated the possibility to control the pore size by tuning manufacturing processes in order to develop scaffolds with particular pore features, since osteogenic cells revealed to respond to pore size and orientation (Murphy et al., 1990; Abbasi et al., 2020). While small pore sizes (<100 μm) are associated with the formation of non-mineralized osteoid or fibrous tissue, larger pore sizes (from 100 to 800 μm) are more appropriate to support bone formation (Roosa et al., 2010; Cheng et al., 2016; Liu et al., 2018; Iviglia et al., 2019). Regarding the individuation of the best pore size, several studies reported different ranges but all higher than 100 μm. For Murphy et al. (1990), a pore size of 100–325 μm was optimal. Cheng et al. (2016) reported how a pore size of about 400 μm leads to greater formation of mature bone by promoting vascularization compared to 250 μm. The formation of blood vessels supplies sufficient oxygen and nutrients for osteoblastic activity, leading to the upregulation of osteopontin and collagen type I, and subsequently to a better regeneration level of the bone mass (Cheng et al., 2016).

However, reconstituted collagen physical strength is not high enough to withstand alone the regeneration of large bone defects. Although mechanical and physical properties of collagen can be modified by chemical crosslinking, the combination with stiffer materials allows to significantly improve mechanical properties and bone conductivity. Mineralized collagen scaffolds own better mechanical properties and

osteoconductivity and exhibit higher levels of osteogenic gene expression than unmineralized ones (Liu et al., 2011). In this regard, extensive research has been conducted on the fabrication of both intrafibrillar and extrafibrillar mineralized collagen scaffolds from nanoscale to macroscale to promote bone repair, demonstrating solid advantages in intrafibrillar mineralized collagen fibrils (Weisgerber et al., 2015; Weiss-Bilka et al., 2019; Yu et al., 2020). Due to exceptional outcomes, currently, several collagen-mineral scaffolds are approved and commercially available, such as Collagraft^{TM} (Collagen Corp., United States) (Leupold et al., 2006), OssiMend^{TM} Bone Graft Matrix (Collagen Matrix Inc., United States) (Ferreira et al., 2021), and Healos (DePuy Spine, United States) (Carter et al., 2009; Kunakornsawat et al., 2013).

Although good efficacy levels, the lack of an adequate level of osteoinductivity and/or osteoconductivity led to the addition of other components such as metals, in particular iron, manganese (Yu et al., 2020), and strontium (Montalbano et al., 2020; Wei et al., 2021), or cytokines belonging to β-TGF superfamily, namely, bone morphogenetic proteins (BMPs) (Dawson et al., 2009; Lu et al., 2012; Oryan et al., 2014). Among metals, Fe/Mn-enriched collagen-hydroxyapatite scaffolds manifested enhanced adhesion and proliferation of osteoblasts, promoted bone sialoprotein, dentin matrix acidic phosphoprotein 1 expressions, alkaline phosphatase activity, and increased osteogenic-specific gene expression in *in vitro* osteogenic culture and much better *in vivo* bone-regenerating capability compared to scaffolds without Fe/Mn or Healos, a commercial collagen-hydroxyapatite-based scaffold (Yu et al., 2020). As a further example, Infuse^{TM} Bone Graft (Medtronic Sofamor Danek Inc., United States) is a collagen sponge loaded with recombinant human BMP-2 for tibial fracture repair procedures and oral maxillofacial and dental regenerative bone grafting procedures (Dawson et al., 2009). Despite BMP-positive effects, their use is going to be limited due to their high costs, safety, and efficacy concerns, high doses needed, and osteolysis (Oryan et al., 2014).

Recently, 3D printing and the annex potential of computer-aided design and computer-aided manufacturing (CAD-CAM) technology in scaffold according to patient-specific bone defect were investigated (Bahraminasab, 2020). Several biomaterials were printed in blend with collagen such as hydroxyapatite (Keriquel et al., 2017), β tricalcium-phosphate (Bian et al., 2012), polycaprolactone (PCL) (Ciocca et al., 2014), poly(lactide-co-glycolide) (PLGA) (Dewey et al., 2021) in order to improve temporal substitutes' mechanical strength (Bahraminasab, 2020). Although having promising outcomes, 3D technology is still far from transforming research know-how into clinical products. Printable material properties and the insertion of biomolecules and cells are still challenging in the manufacture of bone tissue scaffold. In the inkjet and extrusion-based bioprinting, the viscosity of the bioink, print speed, nozzle diameter, and dispensing pressure are important factors that affect the mechanical stability of a scaffold and the fate of cells that therefore still need to be standardized (Bahraminasab, 2020).

To date, significant challenges remain in terms of biomaterial strength optimization, osteogenic activity improvement, and ability to fit complex defect geometries. Moreover, mechanical stability and the ability to limit micromotion at the host–implant interface is still a crucial aspect to unravel since osseointegration and bone regeneration directly affect the healing outcome (Dewey et al., 2021).

Tendon

Tendon belongs to the musculoskeletal system and is principally characterized by highly hierarchically organized type I collagen fascicles (60–85% of tendon dry weight), parallel to the long axis of the tendon (Thorpe and Screen, 2016). Each hierarchical level, from microfibril to fascicles, provides the tissue with non-linear, viscoelastic, anisotropic mechanical properties necessary to afford the strength necessary to translate loads from muscle-to-bone and bone-to-bone (Puetzer et al., 2021). Tendon also contains a range of non-collagenous proteins, present in low amounts, which nevertheless have important functional roles. Proteoglycans (in particular decorin, but also lubricin, versican) represent the 1–5% of tendon dry weight and are the primary component of the matrix interspersing the collagenous units. By binding type I collagen at all organization levels, they cover a particular role in the tissue development and maturation (i.e., fibrillogenesis), and they also contribute to the mechanical properties of the mature tendon (i.e., sliding, lubrication) (Thorpe and Screen, 2016). With regard to glycoproteins, cartilage oligomeric matrix protein (COMP) and tenascin-C (TNC) are known to bind type I collagen, but their function is yet to be established. Lastly, elastic fibers are also found in varying amounts throughout the tendon matrix, with reported concentrations from 1 to 10% of tendon dry weight, with the role to give to the tissue high elasticity, fatigue resistance, and the ability to store and return energy (Thorpe and Screen, 2016). In tendons, fascicles of fibers are longitudinally and transversally oriented, guaranteeing the absorption of the tensile stress, strain limitation, and keeping tendon in the anatomic site during mechanical load. Furthermore, SAXS and WAXS techniques allow to observe additional mechanisms for strain control, i.e., the fibrils sliding and rearrangement that act as buffers against strain (Bianchi et al., 2016). Within tendon, tenocytes are organized in linear arrays aligned with and interspersed between collagen fibers as a 3D network of cells and their processes distributed throughout the tendon (Lavagnino et al., 2015). Cells are in direct contact with collagen bundles: the deformation of tendon ECM from applied loading (i.e., tension, compression, hydrostatic pressure, and fluid shear stress) is transduced to tendon cells. Thus, mechanical signals stimulate cell biochemical pathways and effect cellular processes, such as differentiation, proliferation, tissue development, as in details reported by James et al. (2008) and Lavagnino et al. (2015).

Tendon injuries due to inappropriate physical training, excessive repetitive stretch, or trauma often lead to collagen organization disruption, resulting in loss of function, pain, and decreased mobility (Puetzer et al., 2021). Because of low blood supply, low oxygen consumption, and low metabolism, the self-healing capacity of tendon is very poor (Zhang B. et al., 2018).

While small tendon injuries spontaneously heal, larger defects undergo a repair-mediated process generating fibrocartilagenous scar tissue with inferior structural and biomechanical properties that led to the loss of motion and strength along with high rates of injury recurrence (Grier et al., 2017). Current treatments consist of autograft or allograft transplants, but limited availability, risk of immune response, high risk of reinjury, limited long-term function recovery, and donor site morbidity limited their execution (Puetzer et al., 2021; Yuan et al., 2021).

Actually, how to manage damaged tendon is still a great challenge in the clinic. However, tissue engineering offered promising alternatives. Collagen is the principal load-bearing component of tendon ECM and confers high mechanical strength to the tissue. Being theoretically capable of providing the structural properties required for load bearing in musculoskeletal tissues is thus the most employed biomaterial for tendon tissue engineering. As it happens with all other tissues, also in the case of the tendon regeneration, the architecture and the mechanical properties of a collagen-based construct profoundly influence tenocyte response.

The hierarchical organization of collagen fiber is crucial for the mechanical integrity and function of tendons. Therefore, the reproduction of aligned, mechanically strong collagen fibers constitutes an attractive step for the development of bottom-up scaffold able to mimic both the mechanical and biological tendon environment. Several attempts were made by exploiting various principles and techniques with the aim to artificially reproduce the structural organization of type I collagen in tendon. Early attempts were based on the exploitation of the natural phenomenon of the self-assembly, recreating *in vitro* the physiological conditions for the formation of micrometric fibers. To enhance and control this phenomenon, the use of electrochemical control to direct the pH of the collagen fiber assembly microenvironment was used to produce fibrous structures with particularly aligned pattern, microscopically comparable with native tendon tissue (Cheng et al., 2008). Electrostatically and magnetically aligned multilayer collagen membranes characterized by the presence of collagen fibers of 50–400 μm diameter and several inches length were produced by pouring successive layers of collagen gel in electrostatically charged plates and allowing each layer to partially dry before pouring on the next (Gigante et al., 2009). A hybrid attempt, firstly made by Kato et al. (1989) but followed by other researchers, consisted in the reproduction of collagen pseudo-native structure by extruding an insoluble collagen suspension into a neural buffer as a fiber (from 10 to 2,000 μm) and subsequently performing fibrillogenesis *in vitro* (Kato et al., 1989; Zeugolis et al., 2008a). In this regard, it was found that the nature of the collagen type chosen for the extrusion impacted on the final mechanical properties of extruded collagen fiber: compared to insoluble collagen, soluble collagen conferred improved mechanical properties and uniaxial alignment perhaps owing to improved assembly kinetic (Wang et al., 1994; Pins and Silver, 1995). Although these strategies allow to partially recreate the organized structure of tendon collagen, unfortunately, they are not scalable and are therefore limited to *in vitro* applications.

Alternatively, electrospinning was considered an attractive method to fabricate and handle submicron-diameter fibers (100–500 nm) with native D-banding (Matthews et al., 2002), potentially providing the topographical cues that mimic the architecture of native tendon comprising primarily of parallel collagen fibers, which are beneficial for tenogenic differentiation (Cardwell et al., 2014; Yunoki et al., 2015). However, electrospinning of collagen, besides using non-benign solvents (e.g., 1,1,1,3,3,3 hexafluoro-2-propanol, tricloroacetic acid, 2,2,2-trifluoroethanol) that may have a denaturing effect on the triple-helix structure and a deleterious effect on the biological environment, does not allow to reproduce sheets of aligned fibers with native-like mechanical resistance despite the application of different crosslinking methods (Bazrafshan and Stylios, 2019). Thus, the impossibility to replicate the mechanical strength of native collagen and thus to achieve adequate mechanical properties led to the exploration of collagen/synthetic composites. Thus, the enhanced mechanical properties of synthetic materials were coupled with the bioactivity of collagen (Sahoo et al., 2007; Xu et al., 2014; Salvatore et al., 2018; Sensini et al., 2018). A variety of representative synthetic materials, such as poly-L-lactic acid (PLLA), poly(lactide-co-caprolactone) (PLCL), polyurethane (PU), PCL, and PLGA, were successfully electrospun into aligned ultrafine fibers to engineer tendon tissues. The surface modification of aligned ultrafine fibers with bioactive molecules such as collagen allowed to partially overcome the synthetic material poor cellular responses and the lack of cell recognition motif by improving cell attachment, spreading, and proliferation (Sahoo et al., 2007; Xu et al., 2014; Sensini et al., 2018). Moreover, the incorporation of another tendon ECM component such as chondroitin sulfate in collagen-enriched synthetic fibers increased both biomechanical properties and cell response in terms of upregulation of type I collagen, decorin, and fibronectin gene expression, tenocyte alignment and bioactivity, peritendinous adhesion formation, and inflammatory response (Bhavsar et al., 2010; Kinneberg et al., 2010; Caliari and Harley, 2011; Caliari et al., 2012). It is therefore reasonable to assume that the presence of native tendon ECM principal components in electrospun aligned fibers, by recapitulating the biochemical and topographical features of the tendon tissue, could lead to enhanced tenogenic differentiation and *in vivo* tendon regeneration. In this regard, the expression of the tendon-associated gene scleraxis (SCX) and type I collagen gene (COL1) as well as protein tenomodulin was significantly increased (Yuan et al., 2021). Additionally, the expression of TGF-β2, TGFβR-II, and Smad3 indicated the ability to dictate tenogenic differentiation through the activation of the TGF-β signaling pathway (Yuan et al., 2021). Moreover, animal study in rat Achilles tendon repair model corroborated the promoting role of synthetic fiber enriched with type I collagen and chondroitin sulfate in regenerating a tendon-like tissue (Yuan et al., 2021).

All the production techniques for aligned micrometric fibers lead to the formation of such structures with a high degree of organization, very similar to the native one. However, the mechanical properties of these constructs are by no means comparable to those of the natural tissue. For this reason,

rather than trying to recreate the nano-fibrous structure, scientific research directed toward the mimicry of the natural mechanical stimuli using collagen scaffolds with a high degree of postprocessing conservation of the biomaterial native structure. Grier et al. (2017) demonstrated that the structural properties (i.e., pore size and collagen fiber crosslinking density) of anisotropic freeze-dried scaffolds with an aligned ellipsoidal pore structure deeply affect tenocyte bioactivity, viability, and gene expression. Anisotropic scaffolds with high crosslinking densities and small pore sizes (about 50 μm) were more able to resist cell-mediated contraction forces, promote tenocyte metabolic activity, and increase the expression of tenogenic genes (i.e., SCX, TNC) (Grier et al., 2017). Also, Sandri et al. (2016) demonstrated the ability of a collagen-based 3D scaffold exhibiting a "core-shell" architecture to induce tendon regeneration in a rat tendon lesion model by the synergistic association of the requirements of strength and bioactivity through the coupling of two components differing in their morphological and mechanical properties: (i) the core component, made of enlaced non-porous collagen-based strips responsible for the mechanical; and (ii) the shell component, made of a highly porous hollow tube exhibiting an aligned and interconnected porous microstructure and suitable cell permeability, able to support and guide tendon cell infiltration and migration during the regenerative process and promote the scaffold integration and vascularization. Moreover, a study by Di Giancamillo et al. (2017) showed how, with the same processing treatment, the collagen extraction source greatly influences the cell response: a porous scaffold made of type I collagen extracted from animal tendon induced a better tenocyte response compared to that one generated by an analogous porous scaffold consisting of collagen extracted from animal skin. The cellular response clearly indicates how collagen extracted from a highly structurally organized tissue such as the tendon, although subjected to disruptive treatments during the extraction process, maintains a greater fiber diameter, length, and alignment than those of extracted from skin, which are thus able to more faithfully mimic the native tendon ECM.

Although the control of scaffold structural and flexural rigidity *via* crosslinking and porosity could provide an ideal framework to resolve structure–function maps by identifying the most compliant levels of anisotropy, stiffness, and nutrient biotransport for tenocyte-mediated scaffold remodeling and long-term phenotype maintenance, the mechanical properties of collagen gels or porous collagen temporal substitutes are vastly inferior to those of tendon. With the aim of improving the mechanical properties of collagen-based scaffolds and above all of providing cells the right mechanostimulation, external forces were applied. To this, physiologic loads required to maintain tendon homeostasis have been identified with both *in vitro* and *in vivo* models since mechanobiology of tendon cells is vital for the maintenance of tissue homeostasis and for the triggering of regenerative processes. Several studies reported how certain loading patterns induce cellular anabolic adaptation of tendon (Hannafin et al., 1995; Cousineau-Pelletier and Langelier, 2010; Magnusson et al., 2010; Galloway et al., 2013). However, overstimulation or hypostimulation led to tendinopathy (Arnoczky et al., 2007). Repetitive loading may lead to overstimulation of tendon cells and to the initiation of a catabolic degenerative response, collagen fibril damage, microdamage, or laxity (Lavagnino et al., 2006, 2014; Arnoczky et al., 2007). Hypostimulation of tendon cells resulting from altered cell–matrix interactions demonstrated to have similar outcomes, such as collagen disruption, hypocellularity, increased matrix metalloproteinase levels, and cell apoptosis (Arnoczky et al., 2007; Egerbacher et al., 2008; Magnusson et al., 2010). A recent work of Zhang B. et al. (2018) reported how a tendon replacement tissue based on a collagen sponge and mesenchymal stem cells by coupled mechano-chemical induction (cyclic stretch and TGF-β1) was effectively able to enhance Achilles tendon regeneration in a rat model.

Efforts to produce aligned hierarchical collagen fibers concentrated on the application of mechanical boundary conditions on collagen hydrogels to guide cells to produce aligned fibrils. In this attempt, a strong influence was covered by collagen concentration: as the concentration of collagen gels increases, cellular contraction of the gel decreases and mechanical properties increase (Puetzer et al., 2015, 2021). Cell-loaded low-density collagen hydrogels (1–5 mg/ml) allowed the production of organized collagen fibrils resembling embryonic tissue (<1 μm in diameter) (Henshaw et al., 2006; Herchenhan et al., 2013). However, the immature form of fibrils and the low density of the material are respectively responsible of inferior mechanical properties and significant contraction, resulting in a lack of therapeutic applications and early rupture (Puetzer et al., 2021). Cell-loaded high-density collagen hydrogel (10–20 mg/ml) instead allowed to develop native sized (30–40 μm diameter) collagen fibers (Puetzer and Bonassar, 2016; McCorry and Bonassar, 2017). Puetzer et al. (2021) was one of the first to reproduce fiber organization similar to bovine juvenile collagen with native fibril banding patterns, hierarchical fiber bundles 50–350 μm in diameter in 6 weeks, and improved tensile properties of about 1 MPa. Although these are some of the largest fibers developed to date in engineered tissues, the mechanical properties were lacking in comparison to native tissue, suggesting a need for further maturation (Puetzer et al., 2021).

Thus, the application of mechanical external forces in addition to the customized structure of the scaffolds allowed adding another piece to the complex development attempt of a multidisciplinary system capable of supporting the regeneration of native tendon tissue. However, the precise magnitude, frequency, and duration of stimulation required for normal tendon homeostasis remain unknown. In addition, despite numerous *in vivo*, *in vitro*, and *ex vivo* studies on tendon mechanical properties and the development of prediction models (Galloway et al., 2013; Fang and Lake, 2016; Herod et al., 2016; Thorpe and Screen, 2016; Thompson et al., 2017; Chen et al., 2018; Carniel and Fancello, 2019; Theodossiou and Schiele, 2019), the precise *in vivo* loading levels required to induce tendon repair are yet unspecified. In this regard, further understanding of the *in vivo* loading of tendons is vital to understand the mechanobiological stimuli required to induce anabolic or reduce catabolic activity (Lavagnino et al., 2015).

CONCLUSION

Type I collagen is largely used as biomaterial for the manufacture of cell-instructive devices for tissue engineering and regenerative medicine. Its versatile processing (ranging from the choice of the collagen source and the protein extraction to the fabrication of given devices and several post-fabrication treatments, including crosslinking and sterilization) allows the production of a wide range of scaffolds for tissue regeneration. Notably, the manufacturing affects not only the macroscopic physicochemical and mechanical properties of the final device but also the *in vitro*/*in vivo* cellular response due to changes of the collagen structure occurring at the submolecular, molecular, and supramolecular scales. This strong interplay among processing, structure, and cellular response can be conveniently exploited to optimize the scaffold biological activity and regenerative outcome. In particular, based on the most recent findings on the development of specific tissue substitutes (i.e., skin, cornea, bone, and tendon), the quality of induced regeneration appears to be enhanced when the scaffold exhibits a higher mimesis of the hierarchical organization of native collagen in the target tissue. In this respect, a fundamental role in scaffold optimization is currently played by advanced investigative techniques such as WAXS, SAXS, FT-IR, AFM, PFM, which allow to accurately study collagen structure and its modifications, so as to correlate the direct effects of processing parameters on the microstructure and nanostructure of collagen with macroscopic phenomena, such as the mechanical behavior and the cellular response.

AUTHOR CONTRIBUTIONS

All authors listed have made a substantial, direct and intellectual contribution to the work, and approved it for publication.

FUNDING

This work was partially supported by SAPIENT project "A system approach for identifying connective tissue degeneration in diabetic analogues" (CUP: B54I19002520001).

REFERENCES

Aamodt, J. M., and Grainger, D. W. (2016). Extracellular matrix-based biomaterial scaffolds and the host response. *Biomaterials* 86, 68–82. doi: 10.1016/j.biomaterials.2016.02.003

Abbas, Y., Brunel, L. G., Hollinshead, M. S., Fernando, R. C., Gardner, L., Duncan, I., et al. (2019). Generation of a three-dimensional collagen scaffold-based model of the human endometrium. *Interface Focus* 10:20190079. doi: 10.1098/rsfs.2019.0079

Abbasi, N., Hamlet, S., Love, R. M., and Nguyen, N.-T. (2020). Porous scaffolds for bone regeneration. *J. Sci. Adv. Mater. Dev.* 5, 1–9.

Abdal-Hameed, I. A. (2014). Clinical and radiographical assessment of topical application of collagen fibrils on tooth socket healing. *Al–Rafidain Dent. J.* 14, 244–251. doi: 10.33899/rden.2014.160892

Abir, R., Stav, D., Taieb, Y., Gabbay-Benziv, R., Kirshner, M., Ben-Haroush, A., et al. (2020). Novel extra cellular-like matrices to improve human ovarian grafting. *J. Assist. Reprod. Genet.* 37, 2105–2117. doi: 10.1007/s10815-020-01832-4

Achilli, M., and Mantovani, D. (2010). Tailoring mechanical properties of collagen-based scaffolds for vascular tissue engineering: the effects of pH, temperature and ionic strength on gelation. *Polymers* 2, 664–680. doi: 10.3390/polym2040664

Adamiak, K., and Sionkowska, A. (2020). Current methods of collagen cross-linking: review. *Int. J. Biol. Macromol.* 161, 550–560. doi: 10.1016/j.ijbiomac.2020.06.075

Adelmann-Grill, B. C., and Otto, K. (1987). Immunological safety evaluation of a haemostatic agent and wound dressing made of horse collagen fibrils. *Arzneimittelforschung* 37, 802–805.

Ahearne, M., Fernandez-Perez, J., Masterton, S., Madden, P. W., and Batthacharjee, P. (2020). Designing scaffolds for corneal regeneration. *Adv. Funct. Mater.* 30:1908996. doi: 10.1002/adfm.201908996

Alenghat, F. J., and Ingber, D. E. (2002). Mechanotransduction: all signals point to cytoskeleton, matrix, and integrins. *Sci. STKE* 119:e6.

Antoine, E. E., Vlachos, P. P., and Rylander, M. N. (2015). Tunable collagen I hydrogels for engineered physiological tissue micro-environments. *PLoS One* 10:e0122500. doi: 10.1371/journal.pone.0122500

Arnoczky, S. P., Lavagnino, M., and Egerbacher, M. (2007). The mechanobiological aetiopathogenesis of tendinopathy: is it the over-stimulation or the under-stimulation of tendon cells? *Int. J. Exp. Pathol.* 88, 217–226. doi: 10.1111/j.1365-2613.2007.00548.x

Avila Rodriguez, M. I., Rodriguez Barroso, L. G., and Sanchez, M. L. (2018). Collagen: A review on its sources and potential cosmetic applications. *J. Cosmet. Dermatol.* 17, 20–26. doi: 10.1111/jocd.12450

Bahraminasab, M. (2020). Challenges on optimization of 3D-printed bone scaffolds. *BioMed. Eng. Online* 19:69.

Bak, S. Y., Lee, S. W., Choi, C. H., and Kim, H. W. (2018). Assessment of the influence of acetic acid residue on type I collagen during isolation and characterization. *Materials* 11:2518. doi: 10.3390/ma11122518

Banerjee, I., Mishra, D., Das, T., Maiti, S., and Maiti, T. K. (2012). Caprine (goat) collagen: a potential biomaterial for skin tissue engineering. *J. Biom. Sci. Polym. Ed.* 23, 355–373. doi: 10.1163/092050610x551943

Bax, D. V., Davidenko, N., Gullberg, D., Hamaia, S. W., Farndale, R. W., Best, S. M. C., et al. (2017). Fundamental insight into the effect of carbodiimide crosslinking on cellular recognition of collagen-based scaffolds. *Acta Biomater.* 49, 218–234. doi: 10.1016/j.actbio.2016.11.059

Bazrafshan, Z., and Stylios, G. K. (2019). Spinnability of collagen as a biomimetic material: A review. *Int. J. Biol. Macromol.* 129, 693–705. doi: 10.1016/j.ijbiomac.2019.02.024

Bella, J. (2016). Collagen structure: new tricks from a very old dog. *Biochem. J.* 473, 1001–1025. doi: 10.1042/BJ20151169

Bhavsar, D., Shettko, D., and Tenenhaus, M. (2010). Encircling the tendon repair site with collagen-GAG reduces the formation of postoperative tendon adhesions in a chicken flexor tendon model. *J. Surg. Res.* 159, 765–771. doi: 10.1016/j.jss.2009.10.010

Bian, W., Li, D., Lian, Q., Li, X., Zhang, W., Zhang, K., et al. (2012). Fabrication of a bio-inspired beta-tricalcium phosphate/collagen scaffold based on ceramic stereolithography and gel casting for osteochondral tissue engineering. *Rapid Prototyping J.* 18, 68–80. doi: 10.1108/13552541211193511

Bianchi, F., Hofmann, F., Smith, A. J., and Thompson, M. S. (2016). Probing multi-scale mechanical damage in connective tissues using X-ray diffraction. *Acta Biomater.* 45, 321–327. doi: 10.1016/j.actbio.2016.08.027

Bianchini, P., and Parma, B. (2001). Immunological safety evaluation of a horse collagen haemostatic pad. *Arzneimittelforschung* 51, 414–419. doi: 10.1055/s-0031-1300056

Bigi, A., Panzavolta, S., and Rubini, K. (2004). Relationship between triple-helix content and mechanical properties of gelatin films. *Biomaterials* 25, 5675–5680. doi: 10.1016/j.biomaterials.2004.01.033

Birk, D. E., and Bruckner, P. (2011). "Collagens, suprastructures and collagen fibril assembly," in *The Extracellular Matrix: An Overview, Biology of Extracellular*

Matrix, ed. R. P. Mecham (Berlin: Springer-Verlag), 77–115. doi: 10.1007/978-3-642-16555-9_3

Böhm, S., Straub, C., Stoiber, S., Kasper, C., and Charwat, V. (2017). Impact of source and manufacturing of collagen matrices on fibroblast cell growth and platelet aggregation. *Materials* 10:1086. doi: 10.3390/ma10091086

Brass, L. F., and Bensusan, H. B. (1974). The role of collagen quaternary structure in the platelet:collagen interaction. *J. Clin. Invest.* 54, 1480–1487. doi: 10.1172/jci107896

Brodsky, B., and Ramshaw, J. A. (1997). The collagen triple-helix structure. *Matrix Biol.* 15, 545–554.

Busra, F. M., Rajab, N. F., Tabata, Y., Saim, A. B., Idrus, R. B. H., and Chowdhury, S. R. (2019). Rapid treatment of full-thickness skin loss using ovine tendon collagen type I scaffold with skin cells. *J. Tissue Eng. Regen. Med.* 13, 874–891. doi: 10.1002/term.2842

Caliari, S. R., and Harley, B. A. C. (2011). The effect of anisotropic collagen-GAG scaffolds and growth factor supplementation on tendon cell recruitment, alignment, and metabolic activity. *Biomaterials* 32, 5330–5340. doi: 10.1016/j.biomaterials.2011.04.021

Caliari, S. R., Weisgerber, D. W., Ramirez, M. A., Kelkhoff, D. O., and Harley, B. A. C. (2012). The influence of collagen-glycosaminoglycan scaffold relative density and microstructural anisotropy on tenocyte bioactivity and transcriptomic stability. *J. Mech. Behav. Biomed.* 11, 27–40. doi: 10.1016/j.jmbbm.2011.12.004

Campbell, J. J., Husmann, A., Hume, R. D., Watson, C. J., and Cameron, R. E. (2017). Development of three-dimensional collagen scaffolds with controlled architecture for cell migration studies using breast cancer cell lines. *Biomaterials* 114, 34–43. doi: 10.1016/j.biomaterials.2016.10.048

Campiglio, C. E., Contessi Negrini, N., Farel̀, S., and Draghi, L. (2019). Cross-linking strategies for electrospun gelatin scaffolds. *Materials* 12:2476. doi: 10.3390/ma12152476

Cardwell, R. D., Dahlgren, L. A., and Goldstein, A. S. (2014). Electrospun fibre diameter, not alignment, affects mesenchymal stem cell differentiation into the tendon/ ligament lineage. *J. Tissue Eng. Regen. Med.* 8, 937–945. doi: 10.1002/term.1589

Carniel, T. A., and Fancello, E. A. (2019). A variational homogenization approach applied to the multiscale analysis of the viscoelastic behavior of tendon fascicles. *Continuum Mech. Thermodyn.* 31, 607–626. doi: 10.1007/s00161-018-0714-y

Carter, J. D., Swearingen, A. B., Chaput, C. D., and Rahm, M. D. (2009). Clinical and radiographic assessment of transforaminal lumbar interbody fusion using HEALOS collagen-hydroxyapatite sponge with autologous bone marrow aspirate. *Spine J.* 9, 434–438. doi: 10.1016/j.spinee.2008.11.004

Chan, K. L. S., Khankhel, A. H., Thompson, R. L., Coisman, B. J., Wong, K. H. K., Truslow, J. G., et al. (2014). Crosslinking of collagen scaffolds promotes blood and lymphatic vascular stability. *J. Biomed. Mater. Res. Part. A* 102A, 3186–3195. doi: 10.1002/jbm.a.34990

Charriere, G., Bejot, M., Schnitzler, L., Ville, G., and Hartmann, D. J. (1989). Reactions to a bovine collagen implant–clinical and immunological study in 705 patients. *J. Am. Acad. Dermatol.* 21, 1203–1208. doi: 10.1016/s0190-9622(89)70330-3

Cheema, U., and Brown, R. A. (2013). Rapid fabrication of living tissue models by collagen plastic compression: undestanding three-dimensional cell matrix repair in vitro. *Adv. Wound Care* 2, 176–185. doi: 10.1089/wound.2012.0392

Cheema, U., Chuo, C.-B., Sarathchandra, P., Nazhat, S. N., and Brown, R. A. (2007). Engineering functional collagen scaffolds: cyclical loading material strength and fibril aggregation. *Adv. Funct. Mater.* 17, 2426–2431. doi: 10.1002/adfm.200700116

Chen, J., Ahn, T., Colon-Bernal, I. D., Kim, J., and Banaszak Holl, M. M. (2017). The relationship of collagen structural and compositional heterogeneity to tissue mechanical properties: a chemical perspective. *ACS Nano* 11, 10665–10671. doi: 10.1021/acsnano.7b06826

Chen, K., Hu, X., Blemker, S. S., and Holmes, J. W. (2018). Multiscale computational model of Achilles tendon wound healing: untangling the effects of repair and loading. *PLoS Comput. Biol.* 14:e1006652. doi: 10.1371/journal.pcbi.1006652

Cheng, M.-Q., Wahafu, T. E. H. J., Jiang, G. F., Liu, W., Qiao, Y. Q., Peng, X. C., et al. (2016). A novel open-porous magnesium scaffold with controllable microstructures and properties for bone regeneration. *Sci. Rep.* 6:24134.

Cheng, X., Gurkan, U. A., Dehen, C. J., Tate, M. P., Hillhouse, H. W., Simpson, G. J., et al. (2008). An electrochemical fabrication process for the assembly of anisotropically oriented collagen bundles. *Biomaterials* 29, 3278–3288. doi: 10.1016/j.biomaterials.2008.04.028

Chi, C., Hu, F., Li, Z., Wang, B., and Luo, H. (2015). Influence of different hydrolysis processes by trypsin on the physicochemical, antioxidant, and functional properties of collagen hydrolysates from *Sphyrna lewini*, *Dasyatis akjei*, and *Raja porosa*. *J. Aquat. Food Prod. Technol.* 25, 616–632. doi: 10.1080/10498850.2014.898004

Ciocca, L., Donati, D., Lesci, I. G., BDozza, B., Duchi, S., Mezini, O., et al. (2014). Custom-made novel biomimetic composite scaffolds for the bone regenerative medicine. *Mater. Lett.* 136, 393–396. doi: 10.1016/j.matlet.2014.08.097

Collins, C. J., Andriotis, O. G., Nedelkovski, V., and Frank, M. (2019). "Bone micro- and nanomechanics," in *Encyclopedia of Biomedical Engineering*, ed. N. Roger (Amsterdam: Elsevier), 22–44.

Contessi Negrini, N., Tarsini, P., Tanzi, M. C., and Farel̀, S. (2018). Chemically crosslinked gelatin hydrogels as scaffolding materials for adipose tissue engineering. *J. Appl. Polym. Sci.* 136:47104. doi: 10.1002/app.47104

Cousineau-Pelletier, P., and Langelier, E. (2010). Relative contributions of mechanical degradation, enzymatic degradation, and repair of the extracellular matrix on the response of tendons when subjected to under- and over-mechanical stimulations in vitro. *J. Orthop. Res.* 28, 204–210. doi: 10.1002/jor.20982

Crabb, R. A., Chau, E. P., Decoteau, D. M., and Hubel, A. (2006). Microstructural characteristics of extracellular matrix produced by stromal fibroblasts. *Ann. Biomed. Eng.* 34, 1615–1627. doi: 10.1007/s10439-006-9181-x

Crabb, R. A., and Hubel, A. (2008). Influence of matrix processing on the optical and biomechanical properties of a corneal stroma equivalent. *Tissue Eng.* 14, 173–181. doi: 10.1089/ten.2007.0139

Davidenko, N., Bax, D. V., Schuster, C. F., Farndale, R. W., Hamaia, S. W., Best, S. M., et al. (2016a). Optimisation of UV irradiation as a binding site conserving method for crosslinking collagen-based scaffolds. *J. Mater. Sci. Mater. Med.* 27:14.

Davidenko, N., Hamaia, S., Bax, D. V., Malcor, J. D., Schuster, C. F., Gullberg, D., et al. (2018). Selecting the correct cellular model for assessing of the biological response of collagen-based biomaterials. *Acta Biomater.* 65, 88–101. doi: 10.1016/j.actbio.2017.10.035

Davidenko, N., Schuster, C. F., Bax, D. V., Farndale, R. W., Hamaia, S., Best, S. M., et al. (2016b). Evaluation of cell binding to collagen and gelatin: a study of the effect of 2D and 3D architecture and surface chemistry. *J. Mater. Sci. Mater. Med.* 27:148. doi: 10.1007/s10856-016-5763-9

Davis, G. E. (1992). Affinity of integrins for damaged extracellular-matrix - alpha-V-beta-3 binds to denatured collagen type-I through RGD sites. *Biochem. Biophys. Res. Commun.* 182, 1025–1031. doi: 10.1016/0006-291x(92)91834-d

Davison-Kotler, E., Marshall, W. S., and Garcia-Gareta, E. (2019). Sources of collagen for biomaterials in skin wound healing. *Bioengineering* 6:56. doi: 10.3390/bioengineering6030056

Dawson, E., Bae, H. W., Burkus, J. K., Stam-bough, J. L., and Glassman, S. D. (2009). Recombinant human bone morphogenetic protein-2 on an absorbable collagen sponge with an osteoconductive bulk-ing agent in posterolateral arthrodesis with instrumentation. A prospective randomized trial. *J. Bone Joint Surg. Am.* 91:7.

De Angelis, B., Orlandi, F., Fernandes Lopes Morais D'Autilio, M., Scioli, M. G., Orlandi, A., Cervelli, V., et al. (2018). Long-term follow-up comparison of two different bi-layer dermal substitutes in tissue regeneration: clinical outcomes and histological findings. *Int. Wound J.* 15, 695–706. doi: 10.1111/iwj.12912

Delgado, L. M., Shologu, N., Fuller, K., and Zeugolis, D. I. (2017). Acetic acid and pepsin result in high yield, high purity and low macrophage response collagen for biomedical applications. *Biomed. Mater.* 12:065009. doi: 10.1088/1748-605x/aa838d

Dewey, M. J., Nosatov, A. V., Subedi, K., Shah, R., Jakus, A., and Harley, B. A. C. (2021). Inclusion of a 3D-printed hyperelastic bone mesh improves mechanical and osteogenic performance of a mineralized collagen scaffold. *Acta Biomater.* 121, 224–236. doi: 10.1016/j.actbio.2020.11.028

Di Giancamillo, A., Deponti, D., Gervaso, F., Salvatore, L., Scalera, F., Mangiavini, L., et al. (2017). The analysis of different scaffolds and the benefit of fibrin

glue for tendon tissue engineering at different culture times. *J. Biol. Regul. Homeostatic Agents* 31, 67–73.

Dill, V., and Mörgelin, M. (2020). Biological dermal templates with native collagen scaffolds provide guiding ridges for invading cells and may promote structured dermal wound healing. *Int. Wound J.* 17, 618–630. doi: 10.1111/iwj.13314

Ding, C., Zhang, M., Wu, K., and Li, G. (2014). The response of collagen molecules in acid solution to temperature. *Polymers* 55, 5751–5759. doi: 10.1016/j.polymer.2014.09.011

do Amaral, R. J. F. C., Zayed, N. M. A., Pascu, E. I., Cavanagh, B., Hobbs, C., Santarella, F., et al. (2019). Functionalising collagen-based scaffolds with platelet-rich plasma for enhanced skin wound healing potential. *Front. Bioeng. Biotechnol.* 7:371.

Dong, C., and Lv, Y. (2016). Application of collagen scaffold in tissue engineering: recent advances and new perspectives. *Polymers* 8:42. doi: 10.3390/polym8020042

Drexler, J. W., and Powell, H. M. (2011). Dehydrothermal crosslinking of electrospun collagen. *Tissue Eng. Part C* 17, 9–17. doi: 10.1089/ten.tec.2009.0754

Duarte Campos, D. F., Rohde, M., Ross, M., Anvari, P., Blaeser, A., Vogt, M., et al. (2019). Corneal bioprinting utilizing collagen - based bioinks and primary human keratocytes. *J. Biomed. Mater. Res. A* 107, 1945–1953. doi: 10.1002/jbm.a.36702

Dunn, R. M. (2012). Cross-linking in biomaterials: a primer for clinicians. *Plast. Reconstr. Surg.* 130, 18S–26S.

Egerbacher, M., Arnoczky, S. P., Caballero, O., Lavagnino, M., and Gardner, K. L. (2008). Loss of homeostatic tension induces apoptosis in tendon cells: an in vitro study. *Clin. Orthop. Relat. Res.* 466, 1562–1568. doi: 10.1007/s11999-008-0274-8

Elamparithi, A., Punnoose, A. M., and Kuruvilla, S. (2016). Electrospun type 1 collagen matrices preserving native ultrastructure using benign binary solvent for cardiac tissue engineering. *Artif. Cells Nanomed. Biotechnol.* 44, 1318–1325. doi: 10.3109/21691401.2015.1029629

Ellingsworth, L. R., De Lustro, F., Brennan, J. E., Sawamura, S., and Mc Pherson, J. (1986). The human immune response to reconstituted bovine collagen. *J. Immunol.* 136, 877–882.

Fagerholm, P., Lagali, N. S., Ong, J. A., Merrett, K., Jackson, W. B., Polarek, J. W., et al. (2014). Stable corneal regeneration four years after implantation of a cell-free recombinant human collagen scaffold. *Biomaterials* 35, 2420–2427. doi: 10.1016/j.biomaterials.2013.11.079

Falini, G., Fermani, S., Foresti, E., Parma, B., Rubini, K., Sidoti, M. C., et al. (2004). Films of self-assembled purely helical type I collagen molecules. *J. Mater. Chem.* 14, 2297–2302. doi: 10.1039/b401393j

Fang, F., and Lake, S. P. (2016). Modelling approaches for evaluating multiscale tendon mechanics. *Interface Focus* 6:20150044. doi: 10.1098/rsfs.2015.0044

Ferreira, S. A., Young, G., Jones, J. R., and Rankin, S. (2021). Bioglass/carbonate apatite/collagen composite scaffold dissolution products promote human osteoblast differentiation. *Mater. Sci. Eng. C* 118:111393. doi: 10.1016/j.msec.2020.111393

Filippi, M., Born, G., Chaaban, M., and Scherberich, A. (2020). Natural polymeric scaffolds in bone regeneration. *Front. Bioeng. Biotechnol.* 8:474.

Flaig, I., Radenkovic, M., Naiman, S., Prohl, A., Jung, O., and Barbeck, M. (2020). In vivo analysis of the biocompatibility and immune response of jellyfish collagen scaffolds and its suitability for bone regeneration. *Int. J. Mol. Sci.* 21:4518. doi: 10.3390/ijms21124518

Fratzl, P., and Daxer, A. (1993). Structural transformation of collagen fibrils in corneal stroma during drying. An x-ray scattering study. *Biophys. J.* 64, 1210–1214. doi: 10.1016/s0006-3495(93)81487-5

Friess, W. (1998). Collagen - biomaterial for drug delivery. *Eur. J. Pharm. Biopharm.* 45, 113–136.

Fuest, M., Yam, G. H.-F., Mehta, J. S., and Duarte Campos, D. F. (2020). Prospects and challenges of translational corneal bioprinting. *Bioengineering* 7:71. doi: 10.3390/bioengineering7030071

Gallo, L. C., Madaghiele, M., Salvatore, L., Barca, A., Scialla, S., Bettini, S., et al. (2018). Integration of PLGA microparticles in collagen-based matrices: tunable scaffold properties and interaction between microparticles and human epithelial-like cells. *Int. J. Polym. Mater. Polym. Biomater* 69, 137–147. doi: 10.1080/00914037.2018.1552857

Gallo, N., Lunetti, P., Bettini, S., Barca, A., Madaghiele, M., Valli, L., et al. (2020a). Assessment of physico-chemical and biological properties of sericin-collagen substrates for PNS regeneration. *Int. J. Polym. Mater. Polym. Biomater.* 70, 403–413. doi: 10.1080/00914037.2020.1725755

Gallo, N., Natali, M., Sannino, A., and Salvatore, L. (2020b). An overview of the use of equine collagen as emerging material for biomedical applications. *J. Funct. Biomater.* 11:79. doi: 10.3390/jfb11040079

Galloway, M. T., Lalley, A. L., and Shearn, J. T. (2013). The role of mechanical loading in tendon development, maintenance, injury, and repair. *J. Bone Joint Surg. Am.* 95, 1620–1628. doi: 10.2106/jbjs.l.01004

Garnero, P. (2015). The role of collagen organization on the properties of bone. *Calcif. Tissue Int.* 97, 229–240. doi: 10.1007/s00223-015-9996-2

Garreta, E., Oria, R., Tarantino, C., Pla-Roca, M., Prado, P., Fernandez-Avilés, F., et al. (2017). Tissue engineering by decellularization and 3D bioprinting. *Materials Today* 20, 166–178. doi: 10.1016/j.mattod.2016.12.005

Gautieri, A., Redaelli, A., Buehler, M. J., and Vesentini, S. (2014). Age- and diabetes-related nonenzymatic crosslinks in collagen fibrils: candidate amino acids involved in advanced glycation end-products. *Matrix Biol.* 34, 89–95. doi: 10.1016/j.matbio.2013.09.004

Gautieri, A., Vesentini, S., Redaelli, A., and Buehler, M. J. (2011). Hierarchical structure and nanomechanics of collagen microfibrils from the atomistic scale up. *Nano Lett.* 11, 757–766. doi: 10.1021/nl103943u

Gelse, K., Poschl, E., and Aigner, T. (2003). Collagens–structure, function, and biosynthesis. *Adv. Drug Delivery Rev.* 55, 1531–1546. doi: 10.1016/j.addr.2003.08.002

Germain, L., Auger, F. A., Grandbois, E., Guignard, R., Giasson, M., Boisjoly, H., et al. (1999). Reconstructed human cornea produced in vitro by tissue engineering. *Pathobiology* 67:140. doi: 10.1159/000028064

Ghodbane, S. A., and Dunn, M. G. (2016). Physical and mechanical properties of cross-linked type I collagen scaffolds derived from bovine, porcine and ovine tendons. *J. Biomed. Mater. Res. A* 104, 2685–2692. doi: 10.1002/jbm.a.35813

Giannini, C., Siliqi, D., Ladisa, M., Altamura, D., Diaz, A., Beraudi, A., et al. (2014). Scanning SAXS-WAXS microscopy on osteoarthritis-affected bone - an age-related study. *J. Appl. Cryst.* 47, 110–117. doi: 10.1107/s1600576713030215

Gigante, A., Cesari, E., Busilacchi, A., Manzotti, S., Kyriakidou, K., Greco, F., et al. (2009). Collagen I membranes for tendon repair: effect of collagen fiber orientation on cell behavior. *J. Orthop. Res.* 27, 826–832. doi: 10.1002/jor.20812

Gopinath, A., Reddy, S. M. M., Madhan, B., Shanmguam, G., and Rao, J. R. (2014). Effect of aqueous ethanol on the triple helical structure of collagen. *Eur. Biophys. J.* 43, 643–652. doi: 10.1007/s00249-014-0994-5

Gorgieva, S., and Kokol, V. (2011). "Collagen- vs. gelatine-based biomaterials and their biocompatibility: review and perspectives," in *Biomaterials Applications for Nanomedicine*, ed. R. Pignatello (London: IntechOpen).

Gouveia, R. M., and Connon, C. J. (2016). *Collagen Scaffolds for Corneal Regeneration. Biomaterials and Regenerative Medicine in Ophthalmology*, 2nd Edn. Amsterdam: Elsevier, 151–177.

Gouveia, R. M., Jones, R. R., Hamley, I. W., and Connon, C. J. (2014). The bioactivity of composite Fmoc-RGDS-collagen gels. *Biomater. Sci.* 2:1222. doi: 10.1039/c4bm00121d

Gouveia, R. M., Koudouna, E., Jester, J., Figueiredo, F., and Connon, C. J. (2017). Template curvature influences cell alignment to create improved human corneal tissue equivalents. *Adv. Biosyst.* 1, 1700135. doi: 10.1002/adbi.201700135

Grant, C. A., Brockwell, D. J., Radford, S. E., and Thomson, N. H. (2009). Tuning the elastic modulus of hydrated collagen fibrils. *Biophys. J.* 97, 2985–2992. doi: 10.1016/j.bpj.2009.09.010

Grier, W. K., Iyoha, E. M., and Harley, B. A. C. (2017). The influence of pore size and stiffness on tenocyte bioactivity and transcriptomic stability in collagen-GAG scaffolds. *J. Mech. Behav. Biomed. Mater.* 65, 295–305. doi: 10.1016/j.jmbbm.2016.08.034

Grønlien, K. G., Pedersen, M. E., Sanden, K. W., Høst, V., Karlsen, J., and Tønnesen, H. H. (2019). Collagen from Turkey (*Meleagris gallopavo*) tendon: a promising sustainable biomaterial for pharmaceutical use. *Sustainable Chem. Pharm.* 13:100166. doi: 10.1016/j.scp.2019.100166

Grover, C. N., Farndale, R. W., Best, S. M., and Cameron, R. E. (2012a). The interplay between physical and chemical properties of protein films affects their bioactivity. *J. Biomed. Mater. Res. A* 100, 2401–2411.

Grover, C. N., Gwynne, J. H., Pugh, N., Hamaia, S., Farndale, R. W., Best, S. M., et al. (2012b). Crosslinking and composition influence the surface properties, mechanical stiffness and cell reactivity of collagen-based films. *Acta Biomater.* 8, 3080–3090.

Gu, L., Shan, T., Ma, Y. X., Tay, F. R., and Niu, L. (2019). Novel biomedical applications of crosslinked collagen. *Trends Biotechnol.* 37, 464–491. doi: 10.1016/j.tibtech.2018.10.007

Hadassah, J., Bhuvaneshwari, N., Singh, D., and Sehgal, P. K. (2010). Preparation and clinical evaluation of succinylated collagen punctal plugs in dry eye syndrome: a pilot study. *Ophthalmic Res.* 2010, 185–192. doi: 10.1159/000272022

Hadassah, J., Prakash, D., Sehgal, P. K., Agarwal, A., and Bhuvaneshwari, N. (2008). Clinical evaluation of succinylated collagen bandage lenses for ophthalmic applications. *Ophthalmic Res.* 40, 257–266. doi: 10.1159/000127833

Hanagata, N., Taro, T., Monkawa, A., Ikoma, T., and Junzo, T. (2006). Pre-adsorbed type-I collagen structure-dependent changes in osteoblastic phenotype. *Biochem. Biophys. Res. Commun.* 344, 1234. doi: 10.1016/j.bbrc.2006.04.021

Hannafin, J. A., Arnoczky, S. P., Hoonjan, A., and Torzilli, P. A. (1995). Effect of stress deprivation and cyclic tensile loading on the material and morphologic properties of canine flexor digitorum profundus tendon: an in vitro study. *J. Orthop. Res.* 13, 907–914. doi: 10.1002/jor.1100130615

Harris, J. R., Soliakov, A., and Lewis, R. J. (2013). In vitro fibrillogenesis of collagen type I in varying ionic and pH conditions. *Micron* 49, 60–68. doi: 10.1016/j.micron.2013.03.004

Hayes, S., Lewis, P., Islam, M. M., Doutch, J., Sorensen, T., White, T., et al. (2015). The structural and optical properties of type III human collagen biosynthetic corneal substitutes. *Acta Biomater.* 25, 121–130. doi: 10.1016/j.actbio.2015.07.009

He, J., Su, Y., Huang, T., Jiang, B., Wu, F., and Gu, Z. (2013). Effects of material and surface functional group on collagen self-assembly and subsequent cell adhesion behaviors. *Coll. Surf. B Bioint.* 116, 303–308. doi: 10.1016/j.colsurfb.2014.01.009

He, Y., Wang, J., Si, Y., Wang, X., Deng, H., Sheng, Z.-G., et al. (2021). A novel gene recombinant collagen hemostatic sponge with excellent biocompatibility and hemostatic effect. *Int. J. Biol. Macromol.* 178, 296–305. doi: 10.1016/j.ijbiomac.2021.02.162

Henshaw, D. R., Attia, E., Bhargava, M., and Hannafin, J. A. (2006). Canine ACL fibroblast integrin expression and cell alignment in response to cyclic tensile strain in three- dimensional collagen gels. *J. Orthop. Res.* 24, 481–490. doi: 10.1002/jor.20050

Herchenhan, A., Bayer, M. L., Svensson, R. B., Magnusson, S. P., and Kjær, M. (2013). In vitro tendon tissue development from human fibroblasts demonstrates collagen fibril diameter growth associated with a rise in mechanical strength. *Dev. Dynam.* 242, 2–8. doi: 10.1002/dvdy.23896

Herod, T. W., Chambers, N. C., and Veres, S. P. (2016). Collagen fibrils in functionally distinct tendons have differing structural responses to tendon rupture and fatigue loading. *Acta Biomater.* 42, 296–307. doi: 10.1016/j.actbio.2016.06.017

Hodge, A. J., and Petruska, J. A. (1963). "Recent studies with the electron microscope on ordered aggregates of the tropocollagen macromolecules," in *Aspects of Protein Structure*, ed. G. N. Ramachandran (London: London Academic), 289–300.

Hong, G.-P., Min, S.-G., and Jo, Y.-J. (2019). Anti-oxidative and anti-aging activities of porcine by-product collagen hydrolysates produced by commercial proteases: effect of hydrolysis and ultrafiltration. *Molecules* 24:1104. doi: 10.3390/molecules24061104

Ignat'eva, N. Y., Danilov, N. A., Averkiev, S. V., Obrezkova, M. V., Lunin, V. V., and Sobol', E. N. (2007). Determination of hydroxyproline in tissues and the evaluation of the collagen content of the tissues. *Sci. J. Anal. Chem.* 62, 51–57. doi: 10.1134/s106193480701011x

Isaacson, A., Swioklo, S., and Connon, C. J. (2018). 3D bioprinting of a corneal stroma equivalent. *Exp. Eye Res.* 173, 188–193. doi: 10.1016/j.exer.2018.05.010

Iviglia, G., Kargozar, S., and Baino, F. (2019). Biomaterials, current strategies, and novel nano-technological approaches for periodontal regeneration. *J. Funct. Biomater.* 10:3. doi: 10.3390/jfb10010003

James, E., Kesturu, G., Balian, G., and Chhabra, A. B. (2008). Tendon: biology, biomechanics, repair, growth factors, and evolving treatment options. *J. Hand. Surg.* 33, 102–112. doi: 10.1016/j.jhsa.2007.09.007

Jung, K.-H., Choi, Y.-C., Chun, J.-Y., Min, S.-G., and Hong, G.-P. (2014). Effects of concentration and reaction time of trypsin, pepsin, and chymotrypsin on the hydrolysis efficiency of porcine placenta. *Korean J. Food Sci. Anim. Resour.* 34, 151–157. doi: 10.5851/kosfa.2014.34.2.151

Kadler, K. E., Holmes, D. F., Trotter, J. A., and Chapman, J. A. (1996). Collagen fibril formation. *Biochem. J.* 316, 1–11.

Kato, Y. P., Christiansen, D. L., Hahn, R. A., Shieh, S. J., Goldstein, J. D., and Silver, F. H. (1989). Mechanical properties of collagen fibres: a comparison of reconstituted and rat tail tendon fibres. *Biomaterials* 10, 38–42. doi: 10.1016/0142-9612(89)90007-0

Kaur, A., Midha, S., Giri, S., and Mohanty, S. (2019). Functional skin grafts: where biomaterials meet stem cells. *Stem Cells Int.* 2019:1286054.

Kehrel, B., Wierwille, S., Clemetson, K. J., Anders, O., Steiner, M., Knight, C. G., et al. (1998). Glycoprotein VI is a major collagen receptor for platelet activation: it recognizes the platelet-activating quaternary structure of collagen, whereas CD36, glycoprotein IIb/IIIa and von Willebrand factor do not. *Blood* 91, 491–499. doi: 10.1182/blood.v91.2.491

Keogh, M. B., O'Brien, F. J., and Daly, J. S. (2010). Substrate stiffness and contractile behaviour modulate the functional maturation of osteoblasts on a collagen-gag scaffold. *Acta Biomater.* 6, 4305–4313. doi: 10.1016/j.actbio.2010.06.001

Keriquel, V., Oliveira, H., Rémy, M., Ziane, S., Delmond, S., Rousseau, B., et al. (2017). In situ printing of mesenchymal stromal cells, by laser-assisted bioprinting, for in vivo bone regeneration applications. *Sci. Rep.* 7, 1–10.

Khew, S. T., and Tong, Y. W. (2007). The specific recognition of a cell binding sequence derived from type I collagen by Hep3B and L929 cells. *Biomacromolecules* 8, 3153–3161. doi: 10.1021/bm700587j

Kidoaki, S., and Matsuda, T. (2008). Microelastic gradient gelatinuos gels to induce cellular mechanotaxis. *J. Biotechnol.* 133, 225–230. doi: 10.1016/j.jbiotec.2007.08.015

Kim, H., Jang, J., Park, J., Lee, K.-P., Lee, S., Lee, D.-M., et al. (2019). Shear-induced alignment of collagen fibrils using 3D cell printing for corneal stroma tissue engineering. *Biofabrication* 11:035017. doi: 10.1088/1758-5090/ab1a8b

Kinneberg, K. R. C., Nirmalanandhan, V. S., Juncosa-Melvin, N., Powell, H. M., Boyce, S. T., Shearn, J. T., et al. (2010). Chondroitin-6-sulfate incorporation and mechanical stimulation increase MSC-collagen sponge construct stiffness. *J. Orthop. Res.* 28, 1092–1099. doi: 10.1002/jor.21095

Knight, C. G., Morton, L. F., Peachey, A. R., Tuckwell, D. S., Farndale, R. W., and Barnes, M. J. (2000). The collagen-binding A-domains of integrins alpha(1)beta(1) and alpha(2)beta(1) recognize the same specific amino acid sequence, GFOGER, in native (triple-helical) collagens. *J. Biol. Chem.* 275, 35–40. doi: 10.1074/jbc.275.1.35

Kobayashi, Y., Kuriyama, T., Nakagawara, R., Aihara, M., and Hamada-Sato, N. (2016). Allergy to fish collagen: thermostability of collagen and IgE reactivity of patients' sera with extracts of 11 species of bony and cartilaginous fish. *Allergol. Int.* 65, 450–458. doi: 10.1016/j.alit.2016.04.012

Kong, B., Sun, W., Chen, G., Tang, S., Li, M., Shao, Z., et al. (2017). Tissue-engineered cornea constructed with compressed collagen and laser-perforated electrospun mat. *Sci. Rep.* 7:970.

Kourani, E., Corazza, F., Michel, O., and Doyen, V. (2019). What we know about fish allergy by the end of the decade? *J. Investig. Allergol. Clin. Immunol.* 29, 414–421. doi: 10.18176/jiaci.0381

Kuehlmann, B., Bonham, C. A., Zucal, I., Prantl, L., and Gurtner, G. C. (2020). Mechanotransduction in wound healing and fibrosis. *J. Clin. Med.* 9:1423. doi: 10.3390/jcm9051423

Kunakornsawat, S., Kirinpanu, A., Piyaskulkaew, C., and Sathira-Angkura, V. (2013). A comparative study of radiographic results using HEALOS collagen-hydroxyapatite sponge with bone marrow aspiration versus local bone graft in the same patients undergoing posterolateral lumbar fusion. *J. Med. Assoc. Thai.* 96, 929–935.

Lagali, N., Griffith, M., Fagerholm, P., Merrett, K., Huynh, M., and Munger, R. (2008). Innervation of tissue-engineered recombinant human collagen-based corneal substitutes: a comparative in vivo confocal microscopy study. *Invest. Ophthalmol. Vis. Sci.* 49, 3895–3902. doi: 10.1167/iovs.07-1354

Latinovic, O., Hough, L. A., and Ou-Yang, H. D. (2010). Structural and micromechanical characterization of type I collagen gels. *J. Biomechanics* 43, 500–505. doi: 10.1016/j.jbiomech.2009.09.041

Lavagnino, M., Arnoczky, S. P., Egerbacher, M., Gardner, K. L., and Burns, M. E. (2006). Isolated fibrillar damage in tendons stimulates local colla- genase mRNA expression and protein synthesis. *J. Biomech.* 39, 2355–2362. doi: 10.1016/j.jbiomech.2005.08.008

Lavagnino, M., Bedi, A., Walsh, C. P., Enselman, E. R. S., Sheibani-Rad, S., and Arnoczky, S. P. (2014). Tendon contraction after cyclic elongation is an age-dependent phenomenon: in vitro and in vivo comparisons. *Am. J. Sports Med.* 42, 1471–1477. doi: 10.1177/0363546514526691

Lavagnino, M., Wall, M. E., Little, D., Banes, A. J., Guilak, F., and Arnoczky, S. P. (2015). Tendon mechanobiology: current knowledge and future research opportunities. *J. Orthop. Res.* 33, 813–822. doi: 10.1002/jor.22871

Leupold, J. A., Barfield, W. R., An, Y. H., and Hartsock, L. A. (2006). A comparison of ProOsteon, DBX, and collagraft in a rabbit model. *J. Biomed. Mater. Res. B Appl. Biomater.* 79B, 292–297. doi: 10.1002/jbm.b.30541

Levis, H. J., Kureshi, A. K., Massie, I., Morgan, L., Vernon, A. J., and Daniels, J. T. (2015). Tissue engineering the cornea: the evolution of RAFT. *J. Funct. Biomater.* 6, 50–65. doi: 10.3390/jfb6010050

Li, C., Tian, H., Duan, L., Tian, Z., and Li, G. (2013). Characterization of acylated pepsin-solubilized collagen with better surface activity. *Int. J. Biol. Macromol.* 57, 92–98. doi: 10.1016/j.ijbiomac.2013.02.021

Li, C., Tian, Z., Liu, W., and Li, G. (2015). Structural properties of pepsin-solubilized collagen acylated by lauroyl chloride along with succinic anhydride. *Mater. Sci. Eng. C* 55, 327–334. doi: 10.1016/j.msec.2015.05.055

Li, H., Yun, H.-Y., Baek, K. J., Kwon, N. S., Choi, H.-R., Park, K.-C., et al. (2017). Avian collagen is useful for the construction of skin equivalents. *Cell Tissue Organs* 204, 261–269. doi: 10.1159/000480659

Li, Y., and Douglas, E. P. (2013). Effects of various salts on structural polymorphism of reconstituted type I collagen fibrils. *Coll. Surf. B Bioint.* 112, 42–50. doi: 10.1016/j.colsurfb.2013.07.037

Liliensiek, S. J., Campbell, S., Nealey, P. F., and Murphy, C. J. (2006). The scale of substratum topographic features modulates proliferation of corneal epithelial cells and corneal fibroblasts. *J. Biomed. Mater. Res. A* 79, 185–192. doi: 10.1002/jbm.a.30744

Lim, A. F., Weintraub, J., Kaplan, E. N., Januszyk, M., Cowley, C., McLaughlin, P., et al. (2014). The embrace device significantly decreases scarring following scar revision surgery in a randomized controlled trial. *Plast. Reconstr. Surg.* 133, 398–405. doi: 10.1097/01.prs.0000436526.64046.d0

Lin, H.-Y., Kuo, Y.-J., Chang, S.-H., and Ni, T.-S. (2013). Characterization of electrospun nanofiber matrices made of collagen blends as potential skin substitutes. *Biomed. Mater.* 8:025009. doi: 10.1088/1748-6041/8/2/025009

Lin, X., Patil, S., Gao, Y.-G., and Qian, A. (2020). The bone extracellular matrix in bone formation and regeneration. *Front. Pharmacol.* 11:757.

Liu, J., Chen, G., Xu, H., Hu, K., Sun, J. F., Liu, M., et al. (2018). Pre-vascularization in fibrin Gel/PLGA microsphere scaffolds designed for bone regeneration. *NPG Asia Mater.* 10, 827–839. doi: 10.1038/s41427-018-0076-8

Liu, Y., Li, N., Qi, Y.-P., Dai, L., Bryan, T. E., Mao, J., et al. (2011). Intrafibrillar collagen mineralization produced by biomimetic hierarchical nanoapatite assembly. *Adv. Mater.* 23, 975–980. doi: 10.1002/adma.201003882

Longaker, M. T., Rohrich, R. J., Greenberg, L., Furnas, H., Wald, R., Bansal, V., et al. (2014). A randomized controlled trial of the embrace advanced scar therapy device to reduce incisional scar formation. *Plast Reconstr. Surg.* 134, 536–546. doi: 10.1097/prs.0000000000000417

Lorenzo, A. C., and Caffarena, E. R. (2005). Elastic properties, Young's modulus determination and structural stability of the tropocollagen molecule: a computational study by steered molecular dynamics. *J. Biomech.* 38, 1527–1533. doi: 10.1016/j.jbiomech.2004.07.011

Lu, H., Kawazoe, N., Kitajima, T., Myoken, Y., Tomita, M., Umezawa, A., et al. (2012). Spatial immobilization of bone morphogenetic protein-4 in a collagen-PLGA hybrid scaffold for enhanced osteoinductivity. *Biomaterials* 33, 6140–6146. doi: 10.1016/j.biomaterials.2012.05.038

Lynn, A. K., Yannas, I. V., and Bonfield, W. (2004). Antigenicity and immunogenicity of collagen. *J. Biomed. Mater. Res. B Appl. Biomater.* 71, 343–354. doi: 10.1002/jbm.b.30096

Ma, C., Wang, H., Chi, Y., Wang, Y., Jiang, L., Xu, N., et al. (2021). Preparation of oriented collagen fiber scaffolds and its application in bone tissue engineering. *Appl. Mater. Today* 22:100902. doi: 10.1016/j.apmt.2020.100902

Madaghiele, M., Calo, E., Salvatore, L., Bonfrate, V., Pedone, D., Frigione, M., et al. (2016). Assessment of collagen crosslinking and denaturation for the design of regenerative scaffolds. *J. Biomed. Mater. Res. A* 104, 186–194. doi: 10.1002/jbm.a.35554

Madaghiele, M., Piccinno, A., Saponaro, M., Maffezzoli, A., and Sannino, A. (2009). Collagen- and gelatine-based films sealing vascular prostheses: evaluation of the degree of crosslinking for optimal blood impermeability. *J. Mater. Sci. Mater. Med.* 20, 1979–1989. doi: 10.1007/s10856-009-3778-1

Magnusson, S. P., Langberg, H., and Kjaer, M. (2010). The pathogenesis of tendinopathy: balancing the response to loading. *Nat. Rev. Rheumatol.* 6, 262–268. doi: 10.1038/nrrheum.2010.43

Mahdavi, S., Abdekhodaie, M. J., Mashayekhan, S., Baradaran-Rafii, A., and Djalilian, A. R. (2020). Bioengineering approaches for corneal regenerative medicine. *Tissue Eng. Regen. Med.* 17, 567–593. doi: 10.1007/s13770-020-00262-8

Makareeva, E., and Leikin, S. (2014). "Collagen structure, folding and function," in *Osteogenesis Imperfecta - A Translational Approach to Brittle Bone Disease*, eds J. Kassim and P. Sponseller (Cambridge, MA: Academic Press).

Martino, F., Perestrelo, A. R., Vinarsky, V., Pagliari, S., and Forte, G. (2018). Cellular mechanotransduction: from tension to function. *Front. Physiol.* 9:824.

Mason, B. N., Starchenko, A., Williams, R. M., Bonassar, L. J., and Reinhart-King, C. A. (2013). Tuning three-dimensional collagen matrix stiffness independently of collagen concentration modulates endothelial cell behavior. *Acta Biomater.* 9, 4635–4644. doi: 10.1016/j.actbio.2012.08.007

Maternini, M., Guttadauro, A., Mascagni, D., Milito, G., Stuto, A., Renzi, A., et al. (2019). Non cross-linked equine collagen (Salvecoll-E gel) for treatment of complex ano-rectal fistula. *Asian J. Surgery* 43, 401–404. doi: 10.1016/j.asjsur.2019.06.009

Matthews, J. A., Wnek, G. E., Simpson, D. G., and Bowlin, G. L. (2002). Electrospinning of collagen nanofibers. *Biomacromolecules* 3, 232–238. doi: 10.1021/bm015533u

McBane, J. E., Vulesevic, B., Padavan, D. T., McEwan, K. A., Korbutt, G. S., and Suuronen, E. J. (2013). Evaluation of a collagen-chitosan hydrogel for potential se as a pro-angiogenic site for islet transplantation. *PLoS One* 8:e77538. doi: 10.1371/journal.pone.0077538

McCorry, M. C., and Bonassar, L. J. (2017). Fiber development and matrix production in tissue engineered menisci using bovine mesenchymal stem cells and fibrochondrocytes. *Connect. Tissue Res.* 58, 329–341. doi: 10.1080/03008207.2016.1267152

Merle, C., Perret, S., Lacour, T., Jonval, V., Hudaverdian, S., Garrone, R., et al. (2002). Hydroxylated human homotrimeric collagen I in *Agrobacterium tumefaciens*-mediated transient expression and in transgenic tobacco plant. *FEBS Lett.* 515, 114–118. doi: 10.1016/s0014-5793(02)02452-3

Merrett, K., Fagerholm, P., McLaughli, C. R., Dravida, S., Lagali, N. S., Shinozaki, N., et al. (2008). Tissue-engineered recombinant human collagen-based corneal substitutes for implantation: performance of type I versus type III collagen. *Invest. Ophthalmol. Vis. Sci.* 49, 3887–3894. doi: 10.1167/iovs.07-1348

Metavarayuth, K., Sitasuwan, P., Zhao, X., Lin, Y., and Wang, Q. (2016). Influence of surface topographical cues on the differentiation of mesemchymal stem cells in vitro. *ACS Biomater. Sci. Eng.* 2, 142–151. doi: 10.1021/acsbiomaterials.5b00377

Meyer, M. (2019). Processing of collagen based biomaterials and the resulting materials properties. *Biomed. Eng. Online* 18:24. doi: 10.1186/s12938-019-0647-0

Michaeli, D., and MacPherson, M. (1990). Immunologic study of artificial skin used in the treatment of thermal injuries. *J. Burn Care Rehabil.* 11, 21–26. doi: 10.1097/00004630-199001000-00005

Milovanovic, I., and Hayes, M. (2018). Marine gelatine from rest raw materials. *Appl. Sci.* 8:2407. doi: 10.3390/app8122407

Miotto, M., Gouveia, R. M., Ionescu, A. M., Figueiredo, F., Hamley, I. W., and Connon, C. J. (2019). 4D Corneal tissue engineering: achieving time-dependent tissue self-curvature through localized control of cell actuators. *Adv. Funct. Mater.* 29:1807334. doi: 10.1002/adfm.201807334

Mocan, E., Tagadiuc, O., and Nacu, V. (2011). Aspects of collagen isolation procedures. *Curierul Med.* 2, 3–5.

Mokrejs, P., Sukop, S., and Svoboda, P. (2012). Three-stage extraction of gelatines from tendons of abattoir cattle: 2 - properties of gelatines. *Appl. Biochem. Biotechnol.* 168, 434–445. doi: 10.1007/s12010-012-9787-4

Monaco, G., Cholas, R., Salvatore, L., Madaghiele, M., and Sannino, A. (2017). Sterilization of collagen scaffolds designed for peripheral nerve regeneration: effect on microstructure, degradation and cellular colonization. *Mater. Sci. Eng. C Mater. Biol. Appl.* 71, 335–344.doi: 10.1016/j.msec.2016.10.030

Monroy, D. A. P., Bravo, J. M. C., Mercado, I. E. S., and Gómez, L. J. V. (2017). "Gelatin and collagen nanofiber scaffolds for tissue engineering," in *Tssue Regeneration*, ed. H.A.h.E.-S. Kaoud (London: IntechOpen).

Montalbano, G., Borciani, G., Cerqueni, G., Licini, C., Banche-Niclot, F., Janner, D., et al. (2020). Collagen hybrid formulations for the 3D printing of nanostructured bone scaffolds: an optimized genipin-crosslinking strategy. *Nanomaterials* 10:1681. doi: 10.3390/nano10091681

Moraes, M. C., and Cunha, R. L. (2013). Gelation property and water holding capacity of heat-treated collagen at different temperature and pH values. *Food Res. Int.* 50, 213–223. doi: 10.1016/j.foodres.2012.10.016

Murphy, G. F., Orgill, D. P., and Yannas, I. V. (1990). Partial dermal regeneration is induced by biodegradable collagen-glycosaminoglycan grafts. *Lab. Invest.* 62, 305–313.

Nair, M., Best, S. M., and Cameron, R. E. (2020a). Crosslinking collagen constructs: achieving cellular selectivity through modifications of physical and chemical properties. *Appl. Sci.* 10:6911. doi: 10.3390/app10196911

Nair, M., Calahorra, Y., Kar-Narayan, S., Best, S. M., and Cameron, R. C. (2019). Self-assembly of collagen bundles and enhanced piezoelectricity induced by chemical crosslinking. *Nanoscale* 11, 15120–15130. doi: 10.1039/c9nr04750f

Nair, M., Johal, R. K., Hamaia, S. W., Best, S. M., and Cameron, R. E. (2020b). Tunable bioactivity and mechanics of collagen-based tissue engineering constructs: A comparison of EDC-NHS, genipin and TG2 crosslinkers. *Biomaterials* 254:120109. doi: 10.1016/j.biomaterials.2020.120109

Natale, C. F., Angrisano, T., Pistelli, L., Falco, G., Calabrò, V., Netti, P. A., et al. (2020). Topographic cues impact on embryonic stem sell Zscan4-metastate. *Front. Bioeng. Biotechnol.* 8:178.

Nì Annaidh, A., Bruyere, K., Destrade, M., Gilchrist, M. D., and Ottenio, M. (2012). Characterization of the anisotropic mechanical properties of excised human skin. *J. Mech. Behav. Biomed. Mater.* 5, 139–148. doi: 10.1016/j.jmbbm.2011.08.016

Nimni, M. E., and Harkness, R. D. (1998). "Molecular structures and functions of collagen," in *Collagen*, ed. M. E. Nimni (Boca Raton, FL: CRC Press), 1–78. doi: 10.1201/9781351070799-1

Noah, E. M., Chen, J., Jiao, X., Heschel, I., and Pallua, N. (2003). Impact of sterilization on the porous design and cell behavior in collagen sponges prepared for tissue engineering. *Biomaterials* 23, 2855–2861. doi: 10.1016/s0142-9612(01)00412-4

O'Brien, F. J., Harley, B. A., Yannas, I. V., and Gibson, L. J. (2005). The effect of pore size on cell adhesion in collagen-GAG scaffolds. *Biomaterials* 26, 433–441. doi: 10.1016/j.biomaterials.2004.02.052

Offeddu, G. S., Ashworth, J. C., Cameron, R. E., and Oyen, M. L. (2016). Structural determinants of hydration, mechanics and fluid flow in freeze-dried collagen scaffolds. *Acta Biomater.* 41, 193–203. doi: 10.1016/j.actbio.2016.05.024

Oh, H. H., Lu, H., Kawazoe, N., and Chen, G. (2012). Spatially guided angiogenesis by three-dimensional collagen scaffolds micropatterned with vascular endothelial growth factor. *J. Biomater. Sci. Polym. Ed.* 23, 2185–2195. doi: 10.1163/092050611x611693

Okuyama, K., Xu, X., Iguchi, M., and Noguchi, K. (2006). Revision of collagen molecular structure. *Biopolymers* 84, 181–191. doi: 10.1002/bip.20381

Orgel, J. P. R. O., Irving, T. C., Miller, A., and Wess, T. J. (2006). Microfibrillar structure of type I collagen in situ. *Proc. Natl. Acad. Sci. U.S.A.* 103, 9001–9005. doi: 10.1073/pnas.0502718103

Orgel, J. P. R. O., Persikov, A. V., and Antipova, O. (2014). Variation in the helical structure of native collagen. *PLoS One* 9:e89519. doi: 10.1371/journal.pone.0089519

Orgill, D. P., and Ogawa, R. (2014). Discussion: the embrace device significantly decreases scarring following scar revision surgery in a randomized controlled trial. *Plast Reconstr. Surg.* 133, 406–407. doi: 10.1097/01.prs.0000436812.73412.a4

Orwin, E., and Hubel, A. (2000). In vitro culture characteristics of corneal epithelial, endothelial, and keratocyte cells in a native collagen matrix. *Tissue Eng.* 6:307. doi: 10.1089/107632700418038

Oryan, A., Alidadi, S., Moshiri, A., and Bigham-Sadegh, A. (2014). Bone morphogenetic proteins: a powerful osteoinductive compound with non-negligible side effects and limitations. *Biofactors* 40, 459–481. doi: 10.1002/biof.1177

Pantin-Jackwood, M. J., Stephens, C. B., Bertran, K., Swayne, D. E., and Spackman, E. (2017). The pathogenesis of H7N8 low and highly pathogenic avian influenza viruses from the United States 2016 outbreak in chickens, turkeys and mallards. *PLoS One* 12:e0177265. doi: 10.1371/journal.pone.0177265

Parenteau-Bareil, R., Gauvin, R., and Berthod, F. (2010). Collagen-based biomaterials for tissue engineering applications. *Materials* 3, 1863–1887. doi: 10.3390/ma3031863

Parenteau-Bareil, R., Gauvin, R., Cliche, S., Gariepy, C., Germain, L., and Berthod, F. (2011). Comparative study of bovine, porcine and avian collagens for the production of a tissue engineered dermis. *Acta Biomater.* 7, 3757–3765. doi: 10.1016/j.actbio.2011.06.020

Pawelec, K. M., Best, S. M., and Cameron, R. E. (2016). Collagen: a network for regenerative medicine. *J. Mater. Chem. B* 4:6484. doi: 10.1039/c6tb00807k

Peng, Y. Y., Glattauer, V., Ramshaw, J. A. M., and Werkmeister, J. A. (2010). Evaluation of the immunogenicity and cell compatibility of avian collagen for biomedical applications. *J. Biomed. Mater. Res. A* 93, 1235–1244.

Perez-Puyana, V. M., Jimenez-Rosado, M., Romero, A., and Guerrero, A. (2019). Highly porous protein-based 3D scaffolds with different collagen concentrates for potential application in tissue engineering. *J. Appl. Poly. Sci.* 136:47954. doi: 10.1002/app.47954

Phu, D., Wray, L. S., Warren, R. W., Haskell, R. C., and Orwin, E. J. (2011). Effect of substrate composition and alignment on corneal cell phenotype. *Tissue Eng. A* 17, 799–807. doi: 10.1089/ten.tea.2009.0724

Pins, G. D., and Silver, F. H. (1995). A self-assembled collagen scaffold suitable for use in soft and hard tissue replacement. *Mater. Sci. Eng. C* 3, 101–107. doi: 10.1016/0928-4931(95)00109-3

Poole, K., Khairy, K., Friedrichs, J., Franz, C., Cisneros, D. A., Howard, J., et al. (2005). Molecular-scale topographic cues induce the orientation and directional movement of fibroblasts on two-dimensional collagen surfaces. *J. Mol. Biol.* 349, 380–386. doi: 10.1016/j.jmb.2005.03.064

Proffen, B. L., Perrone, G. S., Fleming, B. C., Sieker, J. T., Kramer, J., Hawes, M. L., et al. (2015). Effect of low-temperature ethylene oxide and electron beam sterilization on the in vitro and in vivo function of reconstituted extracellular matrix-derived scaffolds. *J. Biomat. Appl.* 30, 435–449. doi: 10.1177/0885328215590967

Puetzer, J. L., and Bonassar, L. B. (2016). Physiologically distributed loading patterns drive the formation of zonally organized collagen structures in tissue-engineered meniscus. *Tissue Eng.* 22, 907–916. doi: 10.1089/ten.tea.2015.0519

Puetzer, J. L., Koo, E., and Bonassar, L. J. (2015). Induction of fiber alignment and mechanical anisotropy in tissue engineered menisci with mechanical anchoring. *J. Biomech.* 48:1967.

Puetzer, J. L., Ma, T., Sallent, I., Gelmi, A., and Stevens, M. M. (2021). Driving hierarchical collagen fiber formation for functional tendon, ligament, and meniscus replacement. *Biomaterials* 269:120527. doi: 10.1016/j.biomaterials.2020.120527

Putra, A. B., Nishi, K., Shiraishi, R., Doi, M., and Sugahara, T. (2014). Jellyfish collagen stimulates production of TNF-α and IL-6 by J774.1 cells through activation of NF-κB and JNK via TLR4 signaling pathway. *Mol. Immunol.* 58, 32–37. doi: 10.1016/j.molimm.2013.11.003

Radhika, M., Babu, M., and Sehgal, P. K. (1999). Cellular proliferation on desamidated collagen matrices. *Comp. Biochem. Physiol. C* 124, 131–139. doi: 10.1016/s0742-8413(99)00042-0

Radhika, M., and Sehgal, P. K. (1997). Studies on the desamidation of bovine collagen. *J. Biomed. Mater. Res.* 35, 497–503. doi: 10.1002/(sici)1097-4636(19970615)35:4<497::aid-jbm9>3.0.co;2-c

Rahmati, M., Blaker, J. J., Lyngstadaas, S. P., Mano, J. F., and Haugen, H. J. (2020). Designing multigradient biomaterials for skin regeneration. *Mater. Today Adv.* 5:100051. doi: 10.1016/j.mtadv.2019.100051

Ramachandran, G. N., and Chandrasekharan, R. (1968). Interchain hydrogen bonds via bound water molecules in the collagen triple helix. *Biopolymers* 6, 1649–1658. doi: 10.1002/bip.1968.360061109

Ramasamy, S., Davoodi, P., Vijayavenkataraman, S., Teoh, J. H., Thamizhchelvan, A. M., Robinson, K. S., et al. (2021). Optimised construction of a full thickness human skin equivalent using 3D bioprinting and a PCL/collagen dermal scaffold. *Bioprinting* 21:e00123. doi: 10.1016/j.bprint.2020.e00123

Raspanti, M., Reguzzoni, M., Protasoni, M., and Basso, P. (2018). Not only tendons: The other architecture of collagen fibrils. *Int. J. Biol. Macromol.* 107, 1668–1674. doi: 10.1016/j.ijbiomac.2017.10.037

Raub, C. B., Putnam, A. J., Tromberg, B. J., and George, S. C. (2010). Predicting bulk mechanical properties of cellularized collagen gels using multiphoton microscopy. *Acta Biomater.* 6, 4657–4665. doi: 10.1016/j.actbio.2010.07.004

Rich, A., and Crick, F. H. (1961). The molecular structure of collagen. *J. Mol. Biol.* 3, 483–506. doi: 10.1016/s0022-2836(61)80016-8

Roosa, S. M. M., Kemppainen, J. M., Moffitt, E. N., Krebsbach, P. H., and Hollister, S. J. (2010). The pore size of polycaprolactone scaffolds has limited influence on bone regeneration in an in vivo model. *J. Biomed. Mater. Res.* 92A, 359–368. doi: 10.1002/jbm.a.32381

Sahoo, S., Cho-Hong, J. G., and Siew-Lok, T. (2007). Development of hybrid polymer scaffolds for potential applications in ligament and tendon tissue engineering. *Biomed. Mater.* 2, 169–173. doi: 10.1088/1748-6041/2/3/001

Sakaguchi, M., Toda, M., Ebihara, T., Irie, S., Hori, H., Imai, A., et al. (2000). IgE antibody to fish gelatin (type I collagen) in patients with fish allergy. *J. Allergy Clin. Immunol.* 106, 579–584. doi: 10.1067/mai.2000.108499

Salvatore, L., Calo', E., Bonfrate, V., Pedone, D., Gallo, N., Natali, M. L., et al. (2020c). Exploring the effects of the crosslink density on the physicochemical properties of collagen-based scaffolds. *Polymer Testing* 93:106966.

Salvatore, L., Carofiglio, V. E., Stufano, P., Bonfrate, V., CaloÌ, E., Scarlino, S., et al. (2018). Potential of electrospun poly(3-hydroxybutyrate)/collagen blends for tissue engineering applications. *J. Healthcare Eng.* 2018, 6573947.

Salvatore, L., Gallo, N., Natali, M. L., Campa, L., Lunetti, P., Madaghiele, M., et al. (2020a). Marine collagen and its derivatives: versatile and sustainable bio-resources for healthcare. *Mat. Sci. Eng. C* 113:110963. doi: 10.1016/j.msec.2020.110963

Salvatore, L., Madaghiele, M., Parisi, C., Gatti, F., and Sannino, A. (2014). Crosslinking of micropatterned collagen-based nerve guides to modulate the expected half-life. *J. Biomed. Mater. Res. A* 102, 4406–4414. doi: 10.1002/jbm.a.35124

Sandor, M., Xu, H., Connor, J., Lombardi, J., Harper, J. R., Silverman, R. P., et al. (2008). Host response to implanted porcine-derived biologic materials in a primate model of abdominal wall repair. *Tissue Eng. Part A* 14, 2021–2031. doi: 10.1089/ten.tea.2007.0317

Sandri, M., Filardo, G., Kon, E., Panseri, S., Montesi, M., Iafisco, M., et al. (2016). Fabrication and pilot in vivo study of a collagen-BDDGE-elastin core-shell scaffold for tendon regeneration. *Front. Bioeng. Biotechnol.* 4:52.

Semenycheva, L. L., Egorikhina, M. N., Chasova, V. O., Valetova, N. B., Podguzkova, M. V., Astanina, M. V., et al. (2020). Enzymatic hydrolysis of collagen by pancreatin and thrombin as a step in the formation of scaffolds. *Russ. Chem. Bull.* 69, 164–168. doi: 10.1007/s11172-020-2738-2

Sensini, A., Gualandi, C., Zucchelli, A., Boyle, L. A., Kao, A. P., Reilly, G. C., et al. (2018). Tendon fascicle-inspired nanofibrous scaffold of polylactic acid/collagen with enhanced 3D-structure and biomechanical properties. *Sci. Rep.* 8:17167.

Shah, A., Brugnano, J., Sun, S., Vase, A., and Orwin, E. (2008). The development of a tissue-engineered cornea: biomaterials and culture methods. *Pediatric Res.* 63, 535–544. doi: 10.1203/pdr.0b013e31816bdf54

Shih, P.-J., Huang, C.-J., Huang, T. H., Lin, H.-C., Yen, J.-Y., Wang, I.-J., et al. (2017). Estimation of the corneal Young's modulus in vivo based on a fluid-filled spherical shell-model with Scheimpflug imaging. *J. Ophthalmol.* 2017:5410143.

Shilo, S., Roth, S., Amzel, T., Harel-Adar, T., Tamir, E., Grynspan, F., et al. (2013). Cutaneous wound healing following treatment with plant-derived human recombinant collagen flowable gel. *Tissue Eng. A* 19, 1519–1526. doi: 10.1089/ten.tea.2012.0345

Shojaati, G., Khandaker, I., Sylakowsky, K., Funderburgh, M. L., Du, Y., and Funderburgh, J. L. (2018). Compressed collagen enhances stem cell therapy for corneal scarring. *Stem Cells Transl. Med.* 7, 487–494. doi: 10.1002/sctm.17-0258

Shoulders, M. D., and Raines, R. T. (2009). Collagen structure and stability. *Ann. Rev. Biochem.* 78, 929–958. doi: 10.1146/annurev.biochem.77.032207.120833

Sibillano, T., De Caro, L., Scattarella, F., Scarcelli, G., Siliqi, D., Altamura, D., et al. (2016). Interfibrillar packing of bovine cornea by table-top and synchrotron scanning SAXS microscopy. *J. Appl. Crystallogr.* 49, 1231–1239. doi: 10.1107/s1600576716010396

Silva, T. H., Moreira-Silva, J., Marques, A. L., Domingues, A., Bayon, Y., and Reis, R. L. (2014). Marine origin collagens and its potential applications. *Mar. Drugs* 12, 5881–5901. doi: 10.3390/md12125881

Silverstein, R. M., Webster, F. X., Kiemle, D. J., and Bryce, D. L. (2014). *Spectrometric Identification of Organic Compounds*. Hoboken, NJ: Wiley.

Silvipriya, K., Kumar, K., Bhat, A., Kumar, B., John, A., and Lakshmanan, P. (2015). Collagen: animal sources and biomedical application. *J. Appl. Pharm. Sci.* 5, 123–127. doi: 10.7324/japs.2015.50322

Snider, S., Cavalli, A., Colombo, F., Gallotti, A. L., Quattrini, A., Salvatore, L., et al. (2017). A novel composite type I collagen scaffold with micropatterned porosity regulates the entrance of phagocytes in a severe model of spinal cord injury. *J. Biomed. Mater. Res. B Appl. Biomater.* 105, 1040–1053. doi: 10.1002/jbm.b.33645

Soller, E. C., Tzeranis, D. S., Miu, K., So, P. T. C., and Yannas, I. V. (2012). Common features of optimal collagen scaffolds that disrupt wound contraction and enhance regeneration both in peripheral nerves and in skin. *Biomaterials* 33, 4783–4791. doi: 10.1016/j.biomaterials.2012.03.068

Sorkio, A., Koch, L., Koivusalo, L., Deiwick, A., Miettinen, S., Chichkov, B., et al. (2018). Human stem cell based corneal tissue mimicking structures using laser-assisted 3D bioprinting and functional bioinks. *Biomaterials* 171, 57–71. doi: 10.1016/j.biomaterials.2018.04.034

Sorushanova, A., Delgado, L. M., Wu, Z., Shologu, N., Kshirsagar, A., Raghunath, R., et al. (2019). The collagen suprafamily: from biosynthesis to advanced biomaterial development. *Adv. Mater.* 31:e1801651. doi: 10.1002/adma.201801651

Sorushanova, A., Skoufos, I., Tzora, A., Mullen, A. M., and Zeugolis, D. I. (2021). The influence of animal species, gender and tissue on the structural, biophysical, biochemical and biological properties of collagen sponges. *J. Mater. Sci. Mater. Med.* 31:12.

Sripriya, R., Kumar, R., Balaji, S., Senthil Kumar, M., and Sehgal, P. K. (2011). Characterizations of polyanionic collagen prepared by linking additional carboxylic groups. *React. Funct. Polym.* 71, 62–69. doi: 10.1016/j.reactfunctpolym.2010.11.005

Stanton, A. E., Tong, X., and Yang, F. (2019). Varying solvent type modulates collagen coating and stem cell mechanotransduction on hydrogel substrates. *APL Bioeng.* 3:036108. doi: 10.1063/1.5111762

Steel, K. E., and Twenhafel, N. A. (2010). Review paper: pathology of animal models of alphavirus encephalitis. *Vet. Pathol.* 47, 790–805. doi: 10.1177/0300985810372508

Stein, H., Wilensky, M., Tsafrir, Y., Rosenthal, M., Amir, R., Avraham, T., et al. (2009). Production of bioactive, post-translationally modified, heterotrimeric, human recombinant type-I collagen in transgenic tobacco. *Biomacromolecules* 10:2640. doi: 10.1021/bm900571b

Sunada, H., and Nagai, Y. (1983). Mechanism of collagen degradation by collagenase: a transition process of the collagen molecule from collagenase-substrate to gelatinase-substrate. *Biomed. Res.* 4, 61–70. doi: 10.2220/biomedres.4.61

Sylvester, M. F., Yannas, I. V., Salzman, E. W., and Forbes, M. J. (1989). Collagen banded fibril structure and the collagen-platelet reaction. *Thrombosis Res.* 55, 135–148. doi: 10.1016/0049-3848(89)90463-5

Tanaka, Y., Baba, K., Duncan, T. J., Kubota, A., Asahi, T., Quantock, A. J., et al. (2011). Transparent, tough collagen laminates prepared by oriented flow casting, multi-cyclic vitrification and chemical cross-linking. *Biomaterials* 32, 3358–3366. doi: 10.1016/j.biomaterials.2010.11.011

Tati, R., Nordin, S., Abdillahi, S. M., and Mörgelin, M. (2018). Biological wound matrices with native dermis-like collagen efficiently modulate protease activity. *J. Wound Care* 27, 199–209. doi: 10.12968/jowc.2018.27.4.199

Terzi, A., Gallo, N., Bettini, S., Sibillano, T., Altamura, D., Campa, L., et al. (2019). Investigations of processing-induced structural changes in horse type-I collagen at sub and supramolecular levels. *Front. Bioeng. Biotechnol.* 7:203. doi: 10.3389/fbioe.2019.00203

Terzi, A., Gallo, N., Bettini, S., Sibillano, T., Altamura, D., Madaghiele, M., et al. (2020). Sub- and supramolecular X-ray characterization of engineered tissues from equine tendon, bovine dermis, and fish skin type-I collagen. *Macromol. Biosci.* 20:2000017. doi: 10.1002/mabi.202000017

Terzi, A., Storelli, E., Bettini, S., Sibillano, T., Altamura, D., Salvatore, L., et al. (2018). Effects of processing on structural, mechanical and biological properties of collagen-based substrates for regenerative medicine. *Sci. Rep.* 8:1429. doi: 10.1038/s41598-018-19786-0

Theodossiou, S. K., and Schiele, N. R. (2019). Models of tendon development and injury. *BMC Biomed. Eng.* 1:32.

Thompson, M. S., Bajuri, M. N., Khayyeri, H., and Isaksson, H. (2017). Mechanobiological modelling of tendons: Review and future opportunities. *Proc. Inst. Mech. Eng. H.* 231, 369–377. doi: 10.1177/095441191769 2010

Thorpe, C. T., and Screen, H. R. C. (2016). Tendon structure and composition. *Adv. Exp. Med. Biol.* 920, 3–10. doi: 10.1007/978-3-319-33943-6_1

Torbet, J., Malbouyres, M., Builles, N., Justin, V., Roulet, M., Damour, O., et al. (2007). Orthogonal scaffold of magnetically aligned collagen lamellae for corneal stroma reconstruction. *Biomaterials* 28, 4268–4276. doi: 10.1016/j.biomaterials.2007.05.024

Tsai, S. W., Cheng, Y. H., Chang, Y., Liu, H. L., and Tsai, W. B. (2010). Type I collagen structure modulates the behavior of osteoblast-like cells. *J. Taiwan Inst. Chem. Eng.* 41, 247–251. doi: 10.1016/j.jtice.2009.10.002

Urbanczyk, M., Layland, S. L., and Schenke-Layland, K. (2020). The role of extracellular matrix in biomechanics and its impact on bioengineering of cells and 3D tissues. *Matrix Biol.* 8, 1–14. doi: 10.1016/j.matbio.2019.11.005

Vig, K., Chaudari, A., Tripathi, S., Dixit, S., Sahu, R., Pillai, S., et al. (2017). Advances in skin regeneration using tissue engineering. *Int. J. Mol. Sci.* 18:798.

Walters, B. D., and Stegemann, J. P. (2014). Strategies for directing the structure and function of three-dimensional collagen biomaterials across length scales. *Acta Biomater.* 10, 1488–1501. doi: 10.1016/j.actbio.2013.08.038

Wang, M.-C., Pins, G. D., and Silver, F. H. (1994). Collagen fibres with improved strength for the repair of soft tissue injuries. *Biomaterials* 15, 507–512. doi: 10.1016/0142-9612(94)90016-7

Wang, T., Lew, J., Premkumar, J., Poh, C. L., and Naing, M. W. (2017). Production of recombinant collagen: state of the art and challenges. *J. Biol. Eng.* 1, 18–23. doi: 10.1049/enb.2017.0003

Weadock, K. S., Miller, E. J., Keuffel, E. L., and Dunn, M. G. (1996). Effect of physical crosslinking methods on collagen-fiber durability in proteolytic solutions. *J. Biomed. Mater. Res.* 32, 221–226. doi: 10.1002/(sici)1097-4636(199610)32:2<221::aid-jbm11>3.0.co;2-m

Wei, X., Zhang, X., Yang, Z., Li, L., and Sui, H. (2021). Osteoinductive potential and antibacterial characteristics of collagen coated iron oxide nanosphere containing strontium and hydroxyapatite in long term bone fractures. *Arabian J. Chem.* 14:102984. doi: 10.1016/j.arabjc.2020.102984

Weisgerber, D. W., Caliari, S. R., and Harley, B. A. (2015). Mineralized collagen scaffolds induce hMSC osteogenesis and matrix remodeling. *Biomater. Sci.* 3, 533–542. doi: 10.1039/c4bm00397g

Weiss-Bilka, H. E., Meagher, M. J., Gargac, J. A., Nierbur, G. L., Roeder, R. K., and Wagner, D. R. (2019). Mineral deposition and vascular invasion of hydroxyapatite reinforced collagen scaffolds seeded with human adipose-derived stem cells. *Biomater. Res.* 23:15.

Wiegand, C., Abel, M., Ruth, P., Wilhelms, T., Schulze, D., Norgauer, J., et al. (2009). Effect of the sterilization method on the performance of collagen type I on chronic wound parameters in vitro. *J. Biomed. Mater. Res. B Appl. Biomater.* 90, 710–719. doi: 10.1002/jbm.b.31338

Wilson, S. L., Wimpenny, I., Ahearne, M., Rauz, S., El Haj, A. J., and Yang, Y. (2012). Chemical and topographical effects on cell differentiation and matrix elasticity in a corneal stromal layer model. *Adv. Funct. Mater.* 22, 3641–3649. doi: 10.1002/adfm.201200655

Wong, V. W., Levi, K., Akaishi, S., Schultz, G., and Dauskardt, R. H. (2012). Scar zones: Region-specific differences in skin tension may determine incisional scar formation. *Plast Reconstr. Surg.* 129, 1272–1276. doi: 10.1097/prs.0b013e31824eca79

Xu, Y., Dong, S., Zhou, Q., Mo, X., Song, L., Hou, T., et al. (2014). The effect of mechanical stimulation on the maturation of TDSCs-poly(L-lactide-co-e-caprolactone)/collagen scaffold constructs for tendon tissue engineering. *Biomaterials* 35, 2760–2772. doi: 10.1016/j.biomaterials.2013.12.042

Xu, Z., Guan, X., Liu, J., Fan, H., and Chen, Y. (2017). Improving collagen extraction through an alternative strategy based on succinic anhydride pretreatment to retain collagen's triple-helix structure. *J. Appl. Polym. Sci.* 134:45424. doi: 10.1002/app.45424

Yadavalli, V. K., Svintradze, D. V., and Pidaparti, R. M. (2010). Nanoscale measurements of the assembly of collagen to fibrils. *Int. J. Biol. Macromol.* 46, 458–464. doi: 10.1016/j.ijbiomac.2010.02.012

Yamada, S., Yamamoto, K., Ikeda, T., Yanagiguchi, K., and Hayashi, Y. (2014). Potency of fish collagen as a scaffold for regenerative medicine. *Biomed. Res. Int.* 2014:3029322014.

Yamamoto, K., and Yamamoto, M. (1994). Cell-adhesion receptors for native and denatured type-I collagens and fibronectin in rabbit arterial smooth-muscle cells in culture. *Exp. Cell Res.* 214, 258–263.

Yang, J., Ding, C., Tang, L., Deng, F., Yang, Q., Wu, H., et al. (2020a). Novel modification of collagen: realizing desired water solubility and thermostability in a conflict-free way. *ACS Omega* 5, 5772–5780.

Yang, J., Xiao, Y., Tang, Z., Luo, Z., Li, D., Wang, Q., et al. (2020b). The negatively charged microenvironment of collagen hydrogels regulates the chondrogenic differentiation of bone marrow mesenchymal stem cells in vitro and in vivo. *J. Mater. Chem. B* 8, 4680–4693.

Yang, K.-C., Chen, I.-H., Yang, Y.-T., Hsiao, J.-K., and Wang, C.-C. (2020c). Effects of scaffold geometry on chondrogenic differentiation of adipose-T derived stem cells. *Mater. Sci. Eng. C* 110:110733.

Yannas, I. V. (2005). Similarities and differences between induced organ regeneration in adults and early foetal regeneration. *J. R. Soc. Interf.* 2, 403–417.

Yannas, I. V. (2009). "Principles of skin regeneration," in *Biomaterials for Treating Skin Loss*, eds D. P. Orgill and C. Blanco (Nashville, TN: W. Publishing), 212–230.

Yannas, I. V., Burke, J. F., Orgill, D. P., and Skrabut, E. M. (1982). Wound tissue can utilize a polymeric template to synthesize a functional extension of skin. *Science* 215, 174–176.

Yannas, I. V., Lee, E., Orgill, D. P., Skrabut, E. M., and Murphy, G. F. (1989). Synthesis and characterization of a model extracellular matrix which induces partial regeneration of adult mammalian skin. *Proc. Natl. Acad. Sci. U.S.A.* 86, 93–97.

Yu, L., Rowe, D. W., Perera, I. P., Zhang, J., Sui, S. L., Xin, X., et al. (2020). Intrafibrillar mineralized collagen-hydroxyapatite-based scaffolds for bone regeneration. *ACS Appl. Mater. Interf.* 12, 18235–18249.

Yuan, H., Li, X., Lee, M.-S., Zhang, Z., Li, B., Xuan, H., et al. (2021). Collagen and chondroitin sulfate functionalized bioinspired fibers for tendon tissue engineering application. *Int. J. Biol. Macromol.* 170, 248–260.

Yunoki, S., Hatayama, H., Ebisawa, M., Kondo, E., and Yasuda, K. (2015). A novel fabrication method to create a thick collagen bundle composed of uniaxially aligned fibrils: an essential technology for the development of artificial tendon/ ligament matrices. *J. Biomed. Mater. Res.* 103, 3054–3065.

Yunoki, S., Ohyabu, Y., and Hatayama, H. (2013). Temperature-responsive gelation of type I collagen solutions involving fibril formation and genipin crosslinking as a potential injectable hydrogel. *Int. J. Biomat.* 2013:620765.

Zeugolis, D. I., Paul, R. G., and Attenburrow, G. (2008a). Engineering extruded collagen fibers for biomedical applications. *J. Appl. Polym. Sci.* 108, 2886–2894.

Zeugolis, D. I., Paul, R. G., and Attenburrow, G. (2008b). Factors influencing the properties of reconstituted collagen fibers prior to self-assembly: animal species and collagen extraction method. *J. Biomed. Mater. Res. A* 86, 892–904.

Zhang, B., Luo, Q., Deng, B., Morita, Y., Ju, Y., and Song, G. (2018). Construction of tendon replacement tissue based on collagen sponge and mesenchymal stem cells by coupled mechano-chemical induction and evaluation of its tendon repair abilities. *Acta Biomater.* 74, 247–259.

Zhang, B., Xue, Q., Li, J., Ma, L., Yao, Y., Ye, H., et al. (2019). 3D bioprinting of artificial cornea: challenges and perspectives. *Med. Eng. Phys.* 71, 68–78.

Zhang, L., Niu, X., Sun, L., She, Z., Tan, R., and Wang, W. (2017). Immune response of bovine sourced cross-linked collagen sponge for hemostasis. *J. Biom. Appl.* 32, 920–931.

Zhang, M., Yang, J., Ding, C., Huang, L., and Chen, L. (2018). A novel strategy to fabricate water-soluble collagen using poly(γ-glutamic acid)-derivatives as dual-functional modifier. *React. Funct. Polym.* 122, 131–139.

Zhang, X., Chen, X., Yang, T., Zhang, N., Dong, L., Ma, S., et al. (2014). The effects of different crossing-linking conditions of genipin on type I collagen scaffolds: an in vitro evaluation. *Cell Tissue Bank* 15, 531–541.

Zhang, Y., Olsen, K., Grossi, A., and Otte, J. (2013). Effect of pretreatment on enzymatic hydrolysis of bovine collagen and formation of ACE-inhibitory peptides. *Food Chem.* 141, 2343–2354.

Zubal, L., Bonani, W., Maniglio, D., Ceccato, R., Renciuk, D., Hampl, A., et al. (2018). Soluble collagen dissolution and assembling in pressurized carbon dioxide water solutions. *eXPRESS Polym. Lett.* 12, 159–170.

Conflict of Interest: The authors declare that the research was conducted in the absence of any commercial or financial relationships that could be construed as a potential conflict of interest.

frontiers in Bioengineering and Biotechnology

ORIGINAL RESEARCH
published: 10 June 2021
doi: 10.3389/fbioe.2021.653033

Bombyx mori Silk Fibroin Regeneration in Solution of Lanthanide Ions: A Systematic Investigation

Giorgio Rizzo[1], Marco Lo Presti[2], Cinzia Giannini[3], Teresa Sibillano[3], Antonella Milella[1], Giulia Guidetti[2], Roberta Musio[1], Fiorenzo G. Omenetto[2]* and Gianluca M. Farinola[1,2]**

[1] Dipartimento di Chimica, Università degli Studi di Bari "Aldo Moro", Bari, Italy, [2] Silklab, Department of Biomedical Engineering, Tufts University, Medford, MA, United States, [3] CNR IC–Institute of Crystallography, Bari, Italy

OPEN ACCESS

Edited by:
Yogendra Kumar Mishra, University of Southern Denmark, Denmark

Reviewed by:
Silvia Fare', Politecnico di Milano, Italy
Ratiram Gomaji Chaudhary, Seth Kesarimal Porwal College, India

***Correspondence:**
Roberta Musio
roberta.musio@uniba.it
Fiorenzo G. Omenetto
fiorenzo.omenetto@tufts.edu
Gianluca M. Farinola
gianlucamaria.farinola@uniba.it

Specialty section:
This article was submitted to Nanobiotechnology, a section of the journal Frontiers in Bioengineering and Biotechnology

Received: 13 January 2021
Accepted: 11 May 2021
Published: 10 June 2021

Citation:
Rizzo G, Lo Presti M, Giannini C, Sibillano T, Milella A, Guidetti G, Musio R, Omenetto FG and Farinola GM (2021) Bombyx mori Silk Fibroin Regeneration in Solution of Lanthanide Ions: A Systematic Investigation. Front. Bioeng. Biotechnol. 9:653033. doi: 10.3389/fbioe.2021.653033

Silk Fibroin (SF) obtained from *Bombyx mori* is a very attractive biopolymer that can be useful for many technological applications, from optoelectronics and photonics to biomedicine. It can be processed from aqueous solutions to obtain many scaffolds. SF dissolution is possible only with the mediation of chaotropic salts that disrupt the secondary structure of the protein. As a consequence, recovered materials have disordered structures. In a previous paper, it was shown that, by modifying the standard Ajisawa's method by using a lanthanide salt, $CeCl_3$, as the chaotropic agent, it is possible to regenerate SF as a fibrous material with a very ordered structure, similar to that of the pristine fiber, and doped with Ce^{+3} ions. Since SF exhibits a moderate fluorescence which can be enhanced by the incorporation of organic molecules, ions and nanoparticles, the possibility of doping it with lanthanide ions could be an appealing approach for the development of new photonic systems. Here, a systematic investigation of the behavior of degummed SF in the presence of all lanthanide ions, Ln^{+3}, is reported. It has been found that all lanthanide chlorides are chaotropic salts for solubilizing SF. Ln^{+3} ions at the beginning and the end of the series (La^{+3}, Pr^{+3}, Er^{+3}, Tm^{+3}, Yb^{+3}, Lu^{+3}) favor the reprecipitation of fibrous SF as already found for Ce^{+3}. In most cases, the obtained fiber preserves the morphological and structural features of the pristine SF. With the exception of SF treated with La^{+3}, Tm^{+3}, and Lu^{+3}, for all the fibers re-precipitated a concentration of Ln^{+3} between 0.2 and 0.4% at was measured, comparable to that measured for Ce^{+3}-doped SF.

Keywords: silk fibroin, lanthanide doped fibroin, silk fibroin dissolution, silk fibroin recovery, biomaterials

INTRODUCTION

Silk fibroin (SF) is the major component of the *Bombyx mori* cocoons (70% ca) and readily available in nature. Its peculiar structural, mechanical and biological properties make it a very attractive biopolymer (Omenetto and Kaplan, 2010; Ling et al., 2018) which offers unlimited opportunities for functionalization, processing and biological modifications (Rockwood et al., 2011; Reddy, 2020). Due to its biocompatibility and biodegradability, SF is an excellent biomaterial for a wide range

of biomedical applications, for example drug delivery, tissue engineering, including cartilage and bone, skin tissue, ligaments, cornea, tympanic membrane, and implantable devices such as artificial kidney, and vascular grafts wound dressings. (Lawrence et al., 2008; Kundu et al., 2013; Koh et al., 2015; Melke et al., 2016). It can be processed from aqueous solutions and converted into a variety of versatile systems (Qi et al., 2017; Huang et al., 2018; Guo et al., 2020), such as hydrogels sponges, foams, solid matrices, ultra-resistant, optically transparent and flexible films among others. Moreover, doping with various organic and inorganic dopants opens up the way to a wide variety of applications ranging from supported catalysts (Rizzo et al., 2020a) to environmentally sustainable devices for photonics, electronics, and optoelectronics (Tao et al., 2012; Zhu et al., 2016). In fact, SF exhibits a moderate fluorescence (it can be excited at 277 nm and emits light at 345 nm) (Georgakoudi et al., 2007) that has been ascribed to the aromatic moieties of Tryptophan and Tyrosine, commonly used, together with Phenylalanine, as fluorescent probes to study the structure of proteins. SF fluorescence can be enhanced by the incorporation of organic molecules, ions and nanoparticles within the fibers, and the possibility of doping with lanthanide (Ln) ions opens new possibilities for photonic systems (Lee et al., 2020).

The use of Ln-doped fibers in photonics is well-known, and several studies have reported that the presence of lanthanides can confer photochromic, luminescent and fluorescent properties as well as up-conversion ability to fibers. Examples could be Eu^{+3} or Dy^{+3} strontium aluminate luminescent fibers produced by a special spinning technology, with the substrate of polyester, nylon, or polypropylene resin (Guo et al., 2011), fluorescent Pr^{+3} and Dy^{+3}-doped Chalcogenide fibers (Chahal et al., 2016), $Er^{+3}/Yb^{+3}/Tm^{+3}$ tri-doped tellurite glass microsphere coupled by tapered fibers (Liu et al., 2020), fluorescent silks obtained from silkworms fed with rare-earth upconverting phosphors (Zheng et al., 2018). Moreover, Ln-doped fibers have been employed in the production of lasers (amplifiers rare-earth-doped silica and fluorozirconate fibers, particularly erbium-doped fibers) (Digonnet, 2001) and smart Dy^{+3} and Eu^{+3} doped stimuli-responsive textiles (Shen et al., 2021). In addition, Tryptophan and Tyrosine can act as sensitizers for lanthanide ions enhancing their emission (da Rocha et al., 2020). Therefore, combining the mechanical and optical properties of SF with those of lanthanides ions could be an interesting approach for the development of new photonic systems, particularly appealing due to the high biocompatibility and biodegradability of SF.

Few examples of SF films and powders doped with lanthanides have been reported so far and are limited to Eu^{+3} and Tb^{+3} (Pugina et al., 2019a,b; da Rocha et al., 2020). In a previous work (Rizzo et al., 2020b) we have described a simple method for doping fibrous SF with Ce^{+3}. In particular, in the framework of a systematic study on the effects of changing the chaotropic salt in Ajisawa's solvent ($CaCl_2$ in H_2O/EtOH in a molar ratio 1:8:2), used as standard protocol to solubilize SF (Ajisawa, 1998), we found that when replacing $CaCl_2$ with the hydrated lanthanide salt $CeCl_3{\cdot}7H_2O$ while maintaining all the other conditions unchanged, not only SF was completely dissolved, but it reprecipitated in a fibrous form very quickly and spontaneously during the dialysis purification. The structural characterization of the resulting material demonstrated that the fibers obtained preserved most of the morphological and structural properties of the original degummed SF (Marsh et al., 1955; Guo et al., 2018), with a highly ordered molecular organization, and that they were doped with Ce^{+3} ions, in a concentration of about 0.3 wt%, distributed both within its amorphous regions and the β-crystalline domains.

This protocol represents the first method to obtain SF in a fibrous form after solubilization (the fibroin is normally re-obtained as aqueous solutions or gels). In addition, the SF obtained is doped with Ce^{+3} ions. In principle, this simple process could be extended to other lanthanide ions, possibly resulting in a more generally applicable protocol to produce new silk-based doped materials.

Here we report the results of a systematic investigation of the behavior of degummed SF solution in the presence of all lanthanide ions in the Periodic Table, from Lanthanum to Lutetium, in the form of chloride salts, with the only exclusion of Promethium, due to its radioactivity. The main goals of our paper are: (i) disclosing a new protocol to obtain doped fibroin in fibrous form after solubilization in the presence of Ln^{+3} ions and (ii) characterizing structural and morphological properties of the fibrous materials obtained.

MATERIALS AND METHODS

All hydrated lanthanide chlorides were purchased from NOVA ELEMENTS SAS (Palermo, Italy). All other reagents and solvents were purchased from Sigma Aldrich and were used without any further purification.

Preparation of SF Samples

Degummed SF

Degummed SF was obtained from *Bombyx mori* cocoons purchased from Tajima Shoji (Japan), following previously described procedures (Rockwood et al., 2011). To remove sericin, the cocoons were cut into fourths, shredded and boiled for 30 min in an aqueous solution of Na_2CO_3 0.02 M, then rinsed thoroughly with bidistilled water to remove the residual sericin and the excess of salt. The fibers were dried at ambient conditions for 24 h.

Dissolution of Degummed SF With Different Lanthanide Salts by modified Ajisawa's Method

The standard Ajisawa's method (Ajisawa, 1998) was applied to dissolve degummed SF, using hydrated lanthanide chlorides ($LaCl_3{\cdot}7H_2O$, $CeCl_3{\cdot}7H_2O$, $PrCl_3{\cdot}7H_2O$, $NdCl_3{\cdot}6H_2O$, $SmCl_3{\cdot}6H_2O$, $EuCl_3{\cdot}6H_2O$, $GdCl_3{\cdot}6H_2O$, $TbCl_3{\cdot}6H_2O$, $DyCl_3{\cdot}6H_2O$, $HoCl_3{\cdot}6H_2O$, $ErCl_3{\cdot}6H_2O$, $TmCl_3{\cdot}6H_2O$, $YbCl_3{\cdot}6H_2O$, $LuCl_3{\cdot}6H_2O$) as chaotropic agents instead of $CaCl_2$. The same molar ratios of the standard Ajisawa's protocol were used (0.528 g of $CaCl_2$, corresponding to 4.76 mmol, 0.69g of H_2O and 0.44g of EtOH, molar ratio $CaCl_2$: H_2O: EtOH 1:8:2). Hence, for all the lanthanide chlorides 0.125 g of degummed SF were added to a solution prepared by dissolving 4.76 mmol of the salt (see **Supplementary Table 1**) in 0.69g of H_2O and 0.44g of

EtOH. The mixtures were heated at 60°C for 4 h. The obtained solutions were dialyzed with bidistilled water, using a regenerated cellulose dialysis membrane (MWCO 12.400 g mol^{-1}) to remove salt and ethanol. In the presence of La^{+3}, Ce^{+3}, Pr^{+3}, Er^{+3}, Tm^{+3}, Yb^{+3}, Lu^{+3}, and partially for Dy^{+3}, SF reprecipitated within the dialysis cassette after 4 h and the dialysis purification step was stopped after 12 h, changing water every 4 h. The Ln^{+3}/SF fibers were rinsed and washed with bidistilled water several times and finally air dried at room temperature. The amount of SF recovered was determined by weighting methods.

For Nd^{+3}, Sm^{+3}, Eu^{+3}, Gd^{+3}, Tb^{+3}, and partially for Dy^{+3}, clear SF aqueous solutions were obtained after dialysis and hence stored a 4°C. From these solutions, drop-casted films were obtained for further investigations.

After dialysis of SF solutions obtained with Ho^{+3} a hydrogel was obtained.

Different concentrations of $CeCl_3$ in the range 1.20–8.40 mmol gsolvent^{-1}were tested, but SF was completely dissolved only when the same molar ratio of the Ajisawa's protocol was used (Rizzo et al., 2020b). The same results were obtained for $LaCl_3$.

Methods for Structural Characterization

The regenerated SF fibers recovered after treatment with La^{+3}, Pr^{+3}, Er^{+3}, Tm^{+3}, Yb^{+3}, and Lu^{+3} were characterized by scanning electron microscopy (SEM), Wide-Angle X-ray Scattering (WAXS), birefringence, Attenuated Total Reflectance Fourier Transformed Infrared Spectroscopy (ATR-FTIR) and X-Ray Photoelectron Spectroscopy (XPS). Further, drop-casted films from SF solutions obtained by Nd^{+3}, Sm^{+3}, Eu^{+3}, Gd^{+3}, and Te^{+3} treatment were characterized by ATR-FTIR.

SEM Characterization

SEM analysis was carried out by a VP Field emission SEM EDS Zeiss Sigma 300 equipped with an in lens backscattered and secondary electron detectors. An accelerating voltage of 15 kV was used and the working distance was set to 6.5 mm. FE-SEM samples were placed onto stainless-steel sample holders with carbon tape. A carbon sputtering was performed onto samples before analyses in order to prevent electron charging due to the low sample conductivity, thus enhancing topography imaging. The EDS detector was an X-Max-Silicon Drift Detector (SDD)–Nano analysis–Oxford Instruments. The acquired images were analyzed with AZtec Software.

XPS Characterization

The surface chemical composition of regenerated SF loaded with lanthanide rare earths was investigated by X-ray Photoelectron Spectroscopy (XPS). Analyses were performed with a Scanning XPS Microprobe (PHI 5000 Versa Probe II, *Physical Electronics*), equipped with a monochromatic Al K_α X-ray source (1486.6 eV) operated at 15 kV with a spot of 100 μm and a power of 24.8 W. Survey (0–1,200 eV) and high-resolution spectra (C1s, O1s, N1s, Lu4f, Tm4d, Pr3d, Dy4d, Yb4d, Er4d, La3d) were recorded in FAT (Fixed Analyzer Transmission) mode at a pass energy of 117.40 and 29.35 eV, respectively. In the set conditions, the analyzer energy resolution (FWHM, full width at half-maximum height), measured on the silver Ag $3d_{5/2}$ photoemission line, was 0.7 eV for a pass energy of 29.35 eV. All spectra were acquired at a take-off angle of 45° with respect to the sample surface. Surface charging was compensated using a dual beam charge neutralization, with a flux of low energy electrons (∼1 eV) combined with very low energy positive Ar ions (10 eV). The hydrocarbon component of C1s spectrum was used as the internal standard for charging correction and it was fixed at 285.0 eV (Moulder et al., 1992). Scanning X-ray beam induced secondary electron images were acquired to finely select analysis areas. Furthermore, on each sample, three different spots were analyzed for statistical purposes. MultiPak (*Physical Electronics*) software was used to process acquired spectra.

WAXS Characterization

WAXS experiments were performed at the X-ray Micro Imaging Laboratory (XMI-LAB) of the Institute of Crystallography of CNR-Bari (Altamura et al., 2012; Sibillano et al., 2016; Siliqi et al., 2016). The laboratory is equipped with a Fr-E + SuperBright rotating copper anode microsource (λ = 0.154 nm, 2,475 W) coupled through a focusing multilayer optics Confocal Max-Flux to a SAXS/WAXS three pinholes camera equipped for X-ray scanning microscopy. An image plate (IP) detector (250 × 160 mm^2, with 100 μm effective pixel size), with an off-line RAXIA reader, was used to collect WAXS data. The spot size at the sample position was around 200 μm. The detector was placed at around 10 cm from the samples, giving access to a range of scattering vector moduli ($q = 4\pi\sin\vartheta/\lambda$) from 0.3 to around 3.5 $Å^{-1}$, which corresponds to 1.8–25 Å d-spacing range.

Birefringence Characterization

A customized Olympus Inverted IX71 microscope equipped with a DSLR (digital single-lens reflex) camera (Canon Rebel EOS-SL1) and with a halogen lamp (Olympus, U-LH100L-3) as light source was used to perform optical microscopy. Bright-field transmission micrographs between crossed polarizers were collected using a 20× objective (Olympus, LUCPlanFL N, NA 0.45). For each Ln^{+3} treatment individual fibers were analyzed and the most representative micrograph was reported.

ATR-FTIR Characterization

ATR-FTIR spectra were acquired with a Perkin Elmer Spectrum Two Spectrophotometer equipped with a 2 × 2 mm Diamond crystal. Spectra were recorded in the range 4,000–400 cm^{-1} with a 2 cm^{-1} resolution, using 0.25 cm^{-1} acquisition interval and acquiring 32 scans for each sample.

RESULTS

According to Ajisawa's standard method (Ajisawa, 1998), hydrated $LnCl_3$ in H_2O/EtOH (in a molar ratio 1:8:2), were used to dissolve degummed SF. The mixtures were heated at 60°C for 4 h. The resulting SF solutions were dialyzed against bidistilled water to remove the residual salt and ethanol. Regenerated fibers were rinsed several times with water and let air-dry. Solutions and hydrogel were stored at 4°C.

All lanthanides chlorides in H_2O/EtOH were able to dissolve degummed SF (**Figure 1**). As already found for $CeCl_3 \cdot 7H_2O$, when using hydrated $LaCl_3$, $PrCl_3$, $ErCl_3$, $TmCl_3$, $YbCl_3$, and $LuCl_3$ as chaotropic salts, a fibrous material reprecipitated within the dialysis cassette (**Table 1**). In all these cases the recovery of the fiber was almost quantitative. With $DyCl_3$ the recovery of the fiber was only partial (48–51%) whilst with $HoCl_3$ a hydrogel was obtained. Intermediate lanthanides of the series ($NdCl_3$, $SmCl_3$, $EuCl_3$, $GdCl_3$, and $TbCl_3$) did not induce precipitation of a regenerated fibrous material leading to, at the end of the purification process, clear and stable solutions that could be used to obtain films and/or other scaffolds.

The structural and morphological properties of the solid fibers recovered after treatment with La^{+3}, Pr^{+3}, Er^{+3}, Tm^{+3}, Yb^{+3}, and Lu^{+3} salts (hereafter indicated in the text as Ln^{+3}/SF) in H_2O/EtOH were analyzed. Further, drop-casted films from SF solutions obtained by Nd^{+3}, Sm^{+3}, Eu^{+3}, Gd^{+3}, and Te^{+3} solution treatment were characterized by ATR-FTIR. All these experiments showed that the material recovered is, in fact, SF.

Morphology of Ln^{+3}/SF Fibers by SEM

The morphological features of the solid SF fibers recovered after treatment with lanthanides were studied by SEM.

The SEM images are reported in **Figures 2C–J** (larger images are shown in **Supplementary Figure 1** of the Supporting Information) and can be compared with those obtained for degummed SF (**Figure 2A**; Shen et al., 1998; Rizzo et al., 2020b) and SF doped with Ce^{+3} (**Figure 2B**), already reported in our previous paper (Rizzo et al., 2020b). The cross-sectional views of the fibers are also reported.

As reported in the literature (Shen et al., 1998; Rizzo et al., 2020b), the fibers of degummed SF (**Figure 2A**) are uniform, with a very smooth surface and they are organized in single brins with typical hemicylindrical cross-sections and an average diameter of 9.9 ± 0.5 μm. The SEM images of Pr^{+3}/SF, Er^{+3}/SF, Tm^{+3}/SF, Yb^{+3}/SF, and Lu^{+3}/SF (**Figures 2C–G**) are comparable to those of Ce^{+3}/SF: these materials have a fibrous microstructure and retains the fiber integrity of SF, but with reduced smoothness and straightness. The typical hemicylindrical shape of the fiber cross section is also retained, but, with the exception of Lu^{+3}/SF, whose average diameter (11.2 ± 1.8 μm) is similar to that of degummed SF (9.9 ± 0.5 μm), all other lanthanide/fibers are characterized by larger cross-sections. The diameters of Ln^{+3}/SF fibers, reported in **Table 2**, were calculated as the average of the dimensions of at least 30 fibers, measured directly on the SEM images recorded.

La^{+3}/SF and Dy^{+3}/SF samples (**Figures 2H,I**) are constituted by small and disordered fragments of SF fibers, with very coarse surfaces and irregular cross-sections.

In addition, SEM analysis of the air-dried hydrogel obtained after treatment of SF with Ho^{+3} (**Figure 2J**) clearly shows a highly disordered structure with no evidence of a fibrillar structure.

Inclusion of Ln^{+3} Ions Within SF by XPS

XPS investigation was performed to assess if the regenerated SF obtained after reprecipitation from $LnCl_3/H_2O$/EtOH solutions are contaminated by lanthanide ions. In fact, the low-resolution

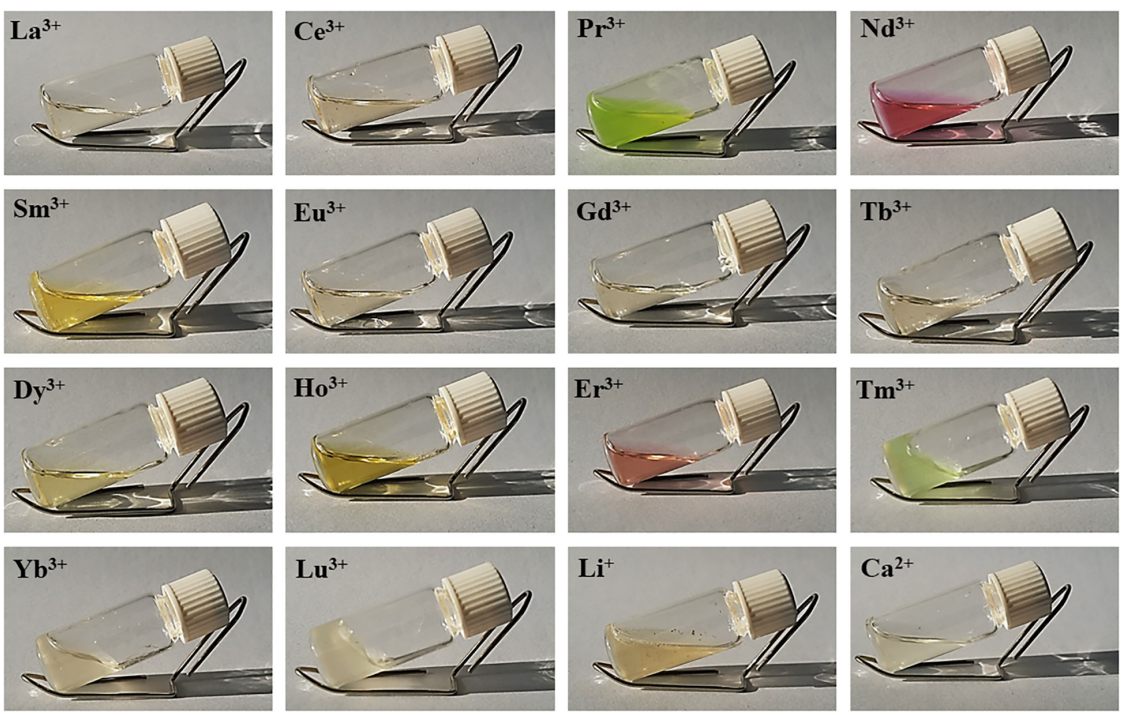

FIGURE 1 | Solutions of degummed SF dissolved in hydrated $LnCl_3/H_2O$/EtOH (1:8:2). The picture of SF dissolved in LiBr 9M in H_2O and $CaCl_2/H_2O$/EtOH (1:8:2) (standard Ajisawa's solvent) is also reported.

TABLE 1 | Lanthanide salts used for SF dissolution/regeneration protocol. For comparison, calcium chloride standard salt is listed in the last row.

Lanthanide	Salt	Ln^{+3} Ionic radius (Å) (Seaborg, 1978)	Dialysis result
Lanthanum	$LaCl_3 \cdot 7H_2O$	1.061	Fibers
Cerium	$CeCl_3 \cdot 7H_2O$	1.034	Fibers
Praseodymium	$PrCl_3 \cdot 7H_2O$	1.013	Fibers
Neodymium	$NdCl_3 \cdot 6H_2O$	0.995	Solution
Samarium	$SmCl_3 \cdot 6H_2O$	0.964	Solution
Europium	$EuCl_3 \cdot 6H_2O$	0.950	Solution
Gadolinium	$GdCl_3 \cdot 6H_2O$	0.938	Solution
Terbium	$TbCl_3 \cdot 6H_2O$	0.923	Solution
Dysprosium	$DyCl_3 \cdot 6H_2O$	0.908	Solution/Fiber
Holmium	$HoCl_3 \cdot 6H_2O$	0.894	Gel
Erbium	$ErCl_3 \cdot 6H_2O$	0.881	Fibers
Thulium	$TmCl_3 \cdot 6H_2O$	0.869	Fibers
Ytterbium	$YbCl_3 \cdot 6H_2O$	0.858	Fibers
Lutetium	$LuCl_3 \cdot 6H_2O$	0.848	Fibers
Calcium	$CaCl_2$	1.00	Solution

spectra of all regenerated fibers show photoelectron peaks originated from the lanthanide ions.

Table 3 reports the surface elemental content of Ln^{+3} ions for La^{+3}/SF, Pr^{+3}/SF, Dy^{+3}/SF, Er^{+3}/SF, Tm^{+3}/SF, Yb^{+3}/SF, and Lu^{+3}/SF regenerated fibers. High resolution spectra of Ln^{+3} are shown in **Figure 3**. Ce^{+3} spectrum of Ce^{+3}/SF is reported for comparison. The quantitative elemental composition of the fibers was also determined by high-resolution C1s, N1s, and Ln (La3d, Ce3d, Pr3d, Dy4d, Er4d, Tm4d, Yb4d, Lu4f) spectra (from peak areas, using tabulated sensitivity factors and spectrometer transmission function) as reported in the Supporting Information (**Supplementary Table 2**).

Ln^{+3} concentration ranges from less than 0.1 at%, which is the detection limit of the technique, to 0.4 at%.

These experimental data suggest that, besides Ce^{+3}, only Pr^{+3}, Dy^{+3}, Er^{+3}, and Yb^{+3} are detectable as contaminants of the SF. XPS spectra in **Figure 3** do not allow to distinguish if the ions are included within the fiber during reprecipitation or are present only as impurities, probably coordinated to the fiber surfaces.

In order to get deeper insights into the chemical environment of lanthanide ions in the regenerated fibers, XPS spectra of $DyCl_3 \cdot 6H_2O$ and $YbCl_3 \cdot 6H_2O$ salts were acquired. In fact, as previously demonstrated for Ce^{+3}/SF (Rizzo et al., 2020b), a shift toward lower binding energy (−1.3 eV) in the Ce3d spectrum of Ce^{+3}/SF compared to the spectrum of $CeCl_3 \cdot 7H_2O$ suggested the existence of interactions between Ce^{+3} ions and the oxygen atoms of fibroin aminoacids within the fiber. The same comparison was performed herein for $Dy^{+3}$and Yb^{+3}, which are those with higher concentration within the fibers and show well defined XPS spectra. For both the elements, no chemical shift was

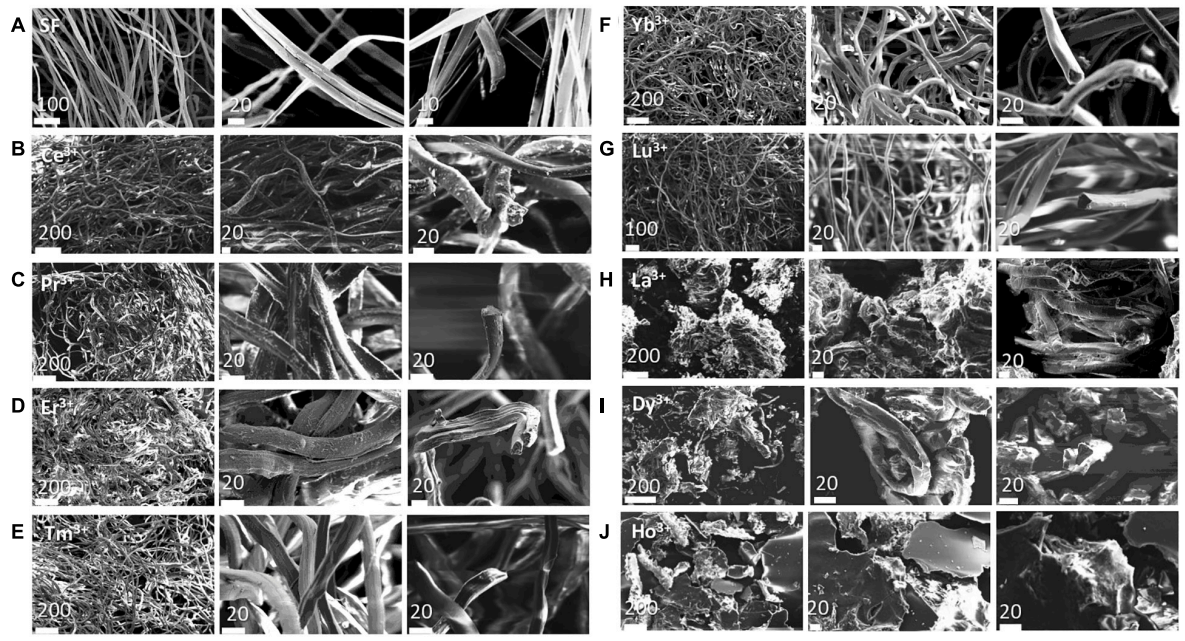

FIGURE 2 | SEM images of the Analyzed samples at two scale bars in μm (indicated on each figure) with the cross-sectional views. **(A)** degummed SF; **(B)** Ce^{+3}/SF; **(C)** Pr^{+3}/SF; **(D)** Er^{+3}/SF; **(E)** Tm^{+3}/SF; **(F)** Yb^{+3}/SF; **(G)** Lu^{+3}/SF; **(H)** La^{+3}/SF; **(I)** Dy^{+3}/SF; **(J)** Ho^{+3}/SF.

TABLE 2 | Diameters (in μm) of degummed SF and Ln^{+3}/SF fibers.

	SF	Ce^{+3}/SF	Pr^{+3}/SF	Er^{+3}/SF	Tm^{+3}/SF	Yb^{+3}/SF	Lu^{+3}/SF
Diameter	9.9 ± 0.5	20.4 ± 1.1	16.7 ± 0.5	19.4 ± 2.2	14.9 ± 1.8	17.5 ± 0.8	11.2 ± 1.8

TABLE 3 | XPS peak analyses of Ln^{+3}/SF fibers.

Sample	Peak	BE (eV)	at%
Ce^{+3}/SF	Ce3d	885.9	0.3
La^{+3}/SF	La3d	837.4	<0.1
Pr^{+3}/SF	Pr3d	933.7	0.4
Dy^{+3}/SF	Dy4d	153.2	0.3
Er^{+3}/SF	Er4d	168.9	0.2
Tm^{+3}/SF	Tm4d	177.2	<0.1
Yb^{+3}/SF	Yb4d	199.3	0.3
Lu^{+3}/SF	Lu4f	8.4	<0.1

observed between the Ln^{+3} spectra as the salt and in the fibers. Therefore, differently from Ce^{+3}, no evidence of a coordinating effect of the Ln^{+3} ions to SF was observed.

Solid State Structure of Ln^{+3}/SF by WAXS

WAXS experiments were performed on the solid fibers regenerated after La^{+3}, Dy^{+3}, Er^{+3}, Tm^{+3}, Yb^{+3}, Lu^{+3}, and Pr^{+3} treatment. The 2D WAXS patterns (**Figures 4B–F**, **5B–D**), once centered, calibrated and folded into 1D profiles, were compared with the WAXS patterns of the degummed SF and of *B. mori* cocoons (natural silk) (**Figures 4A**, **5A**, respectively), (Shen et al., 1998; Guo et al., 2018; Rizzo et al., 2020b).

As previously reported (Rizzo et al., 2020b), within the same explored area of about 200 μm, degummed SF exhibits a typical cross β-diffraction signal (**Figure 4A**) whose intensity is anisotropically distributed along two main orthogonal directions labeled as meridional, along the fiber axis, and equatorial, perpendicular to the fiber axis (Guo et al., 2018). The 1D WAXS profile was integrated around both the equatorial and the meridional directions (black curves in **Figures 4G,H**, respectively). The 2D/1D data were indexed as the fiber diffraction pattern of the *Bombyx mori* silk II structure (Fossey et al., 1991; Guo et al., 2018), which has an orthorhombic structure with unit cell dimensions a = 9.68 ± 0.20 Å, b = 9.36 ± 0.18 Å, and c = 7.02 ± 0.14 Å. *B. mori* cocoons (natural silk) does not show a WAXS pattern with clear preferential orientation but rings with uniform intensity along the azimuth (**Figure 5A**). Its 1D WAXS profile was integrated along all the azimuth and is reported in **Figure 5E** (black curve).

SF regenerated after treatment with Ln^{+3} ions showed two typical structural behaviors:

(i) samples treated with Tm^{+3}, Yb^{+3}, Lu^{+3}, and Pr^{+3} exhibit a 2D typical cross β-diffraction pattern (**Figures 4C–F**), similar to that of the degummed SF and Ce^{+3}/SF, thus indicating a partial recovery of their fibrillar nature after reprecipitation.

(ii) Samples with the addition of La^{+3}, Dy^{+3}, and Er^{+3} show 2D WAXS patterns similar to that of the natural silk cocoon, i.e., without any preferential orientation (**Figures 5B–D**). The relevant 1D WAXS profiles are shown in **Figure 5E** (orange for La^{+3}, cyan for Dy^{+3} and magenta for Er^{+3}).

The d-spacings and corresponding *q*-values for all reflections are reported in **Supplementary Table 2** of the Supporting Information. In details, the equatorial peaks at $q_1 = 0.66 \pm 0.075$ Å^{-1} ($d_1 = 9.5 \pm 1$ Å), $q_2 = 1.5 \pm 0.1$ Å^{-1} ($d_2 = 4.2 \pm 0.3$ Å), $q_3 = 1.7 \pm 0.1$ Å^{-1} ($d_3 = 3.7 \pm 0.3$ Å) were indexed as the (010), the overlap of the (020) and (210) reflections, and the (021) reflection, respectively. The latter forms an angle of about 30° with the equatorial direction (**Supplementary Figures 2, 3** in the Supporting Information). The meridional peak at $q_4 = 1.8 \pm 0.1$Å^{-1} ($d_4 = 3.5 \pm 0.2$ Å) (**Figure 5E**), indexed as the (002) reflection, indicates the β-strands distance along the fiber axis, which yields to the c = 7.0 Å axial repetition and contains two peptide units. In our previous work (Rizzo et al., 2020b), the SF sample doped with Ce^{+3} ions showed a shift of the meridional (002) reflection from $q_4 = 1.8$ Å^{-1} ($d_4 = 4.8 \pm 0.2$ Å) to $q_4 = 1.3$ Å^{-1} ($d_4 = 4.8 \pm 0.2$ Å) (blue vertical bar in **Figure 4H**). This shift corresponded to an increase in the β-strands distance from 3.5 Å, in degummed SF, to 4.8 Å for Ce^{+3}/SF and was ascribed to the incorporation of Ce^{+3} ions along the c-axis of the fiber. None of the Ln^{+3}/SF samples show such a shift of the meridional peak position. Therefore, there is no sign of inclusion of La^{+3}, Dy^{+3}, Er^{+3}, Tm^{+3}, Yb^{+3}, Lu^{+3}, and Pr^{+3} ions within the crystalline domains of the fiber.

Finally, WAXS of the Pr^{+3}/SF (**Figure 4F**) shows several additional sharp rings which are due to contamination.

Birefringence

The results of WAXS characterization are supported by birefringence measurements. For optically anisotropic fibers, birefringence can be a useful tool in structural characterization since it can give information on the orientation of crystalline regions. In fact, birefringence colors arise from the interaction of incident polarized light with the anisotropic crystalline domains of the fibers with a preferred axial orientation, i.e., β-sheet nanocrystal in SF aligned along the fiber axis (Founda and El-Tonsy, 1990; Viney et al., 1993). The effect of the lanthanides on the silk fiber birefringence can be monitored by brightfield transmission microscopy between crossed polarizers.

Birefringence results are in agreement with WAXS analyses. In fact, as shown in **Figure 6**, Ce^{+3}/SF, Tm^{+3}/SF, Yb^{+3}/SF, Lu^{+3}/SF, and Pr^{+3}/SF retain the native birefringence of the degummed SF, although with different degrees. This is evidently due to a high degree of crystallinity, with β-sheet nanocrystals highly oriented along the fiber axis, as indicated by WAXS. On the contrary, Dy^{+3}/SF, and La^{+3}/SF show poor or no birefringence, thus suggesting that regenerated fibers lose or only partially preserve the native crystallinity of degummed SF, with a significative loss in the orientation of the β-sheet domains.

FTIR-ATR

The secondary structure of Ln^{+3}/SF fibers was further characterized by FTIR-ATR spectra. FT-IR spectroscopy enables to elucidate some structural features of proteins since the amide bands are diagnostics of the secondary structure. The amide I band, in the range 1,700–1,600 cm^{-1}, mainly originates from the C = O stretching vibrations and minor contributions

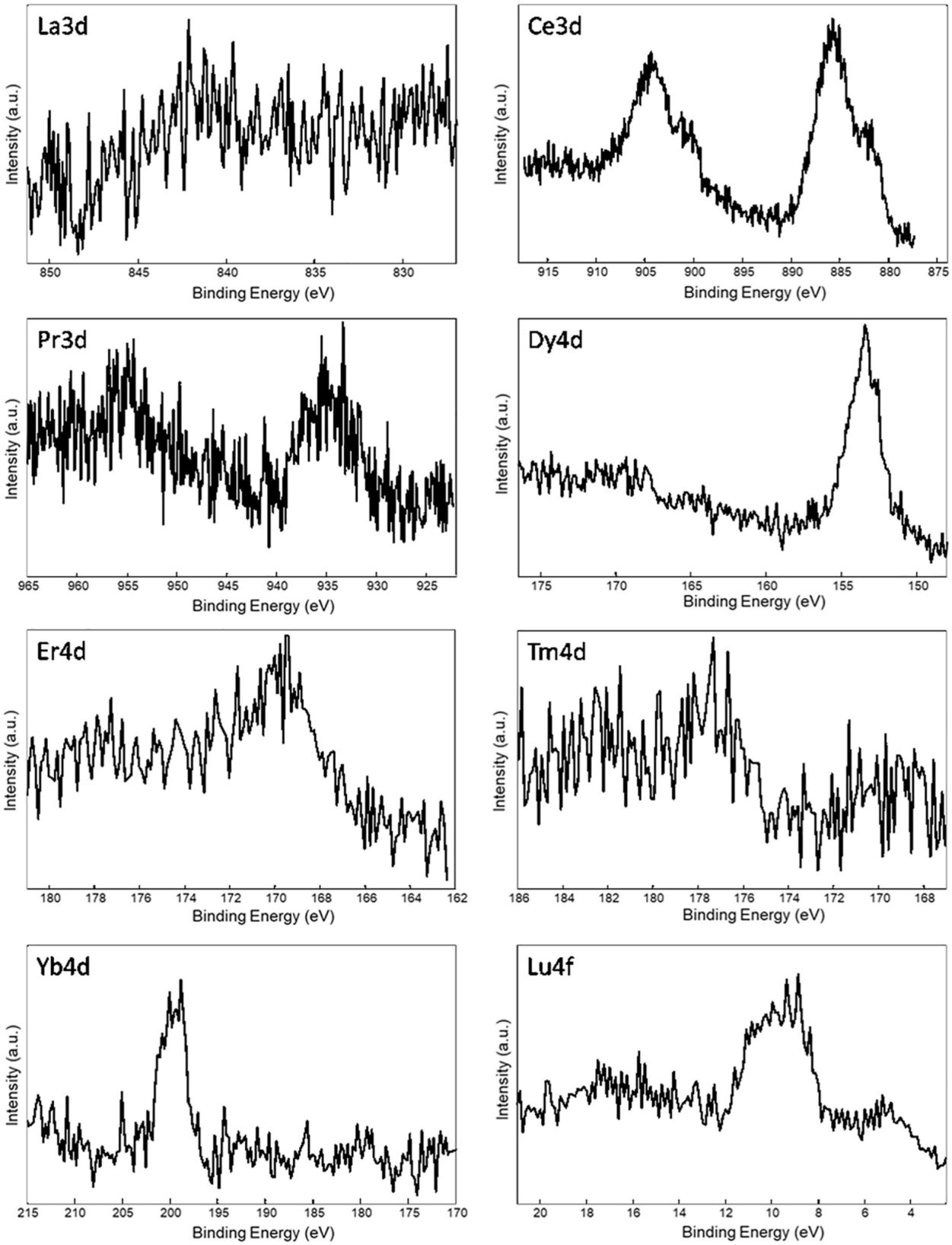

FIGURE 3 | XPS spectra of Ln^{+3}/SF regenerated fibers. Selected atomic orbital for metal investigation is indicated on each spectrum.

from the NH in-plane bending, the out of phase CN stretching vibration and the CCN deformations. The amide II band (1,600–1,500 cm^{-1}) is the result of C-N stretching and N-H in-plane bending modes whilst the amide III region (1,330–1,230 cm^{-1}) arises from N-H in-plane bending vibrations.

The complete spectra of both solid degummed SF and Ln^{+3}/SF are reported in **Figure 7**. The expansions of the amide band region (1,750–900 cm^{-1}) are shown in **Figure 8**.

The ATR-FTIR spectrum of the degummed SF (black curve in **Figures 7, 8**) shows two strong characteristic absorptions in the amide region at 1,622 cm^{-1} (amide I) and 1,511 cm^{-1} (amide II), and a medium-low intensity band at 1,232 cm^{-1} (amide III), typical of the β-sheet structure, in agreement with the IR spectra reported in the literature (Hu et al., 2006, 2008). Moreover, a very low intensity peak at 1,697 cm^{-1} and broad shoulders centered at 1,668 cm^{-1}, that can be assigned to the β-sheet structure and random coil and α-helix regions, respectively, are evident. ATR-FTIR indicated that the β-sheet content is predominant in degummed SF. The ATR-FTIR spectra of SF treated with La^{+3}, Ce^{+3}, Pr^{+3}, Dy^{+3}, Er^{+3}, Tm^{+3}, Yb^{+3}, and Lu^{+3} do not show any significant difference compared to the spectrum of the degummed SF, thus suggesting that the treatment with Ln^{+3} ions does not induce any significant variation of the secondary structure of SF.

We acquired also ATR-FTIR spectra of drop-casted films obtained from solutions of SF with Nd^{+3}, Sm^{+3}, Eu^{+3}, Gd^{+3}, Tb^{+3}, and Dy^{+3} (**Figures 9, 10**) after dialysis. The ATR-FTIR spectrum of the film obtained by drop-casting of SF solution recovered by the standard Ajisawa's method (black line in **Figures 9**, **10**), i.e., using $CaCl_2$ as chaotropic salt, was acquired for comparison.

Typical absorption bands can be identified. In addition to the typical Amide A and B bands (that originate from a Fermi resonance between the first overtone of amide II band and the

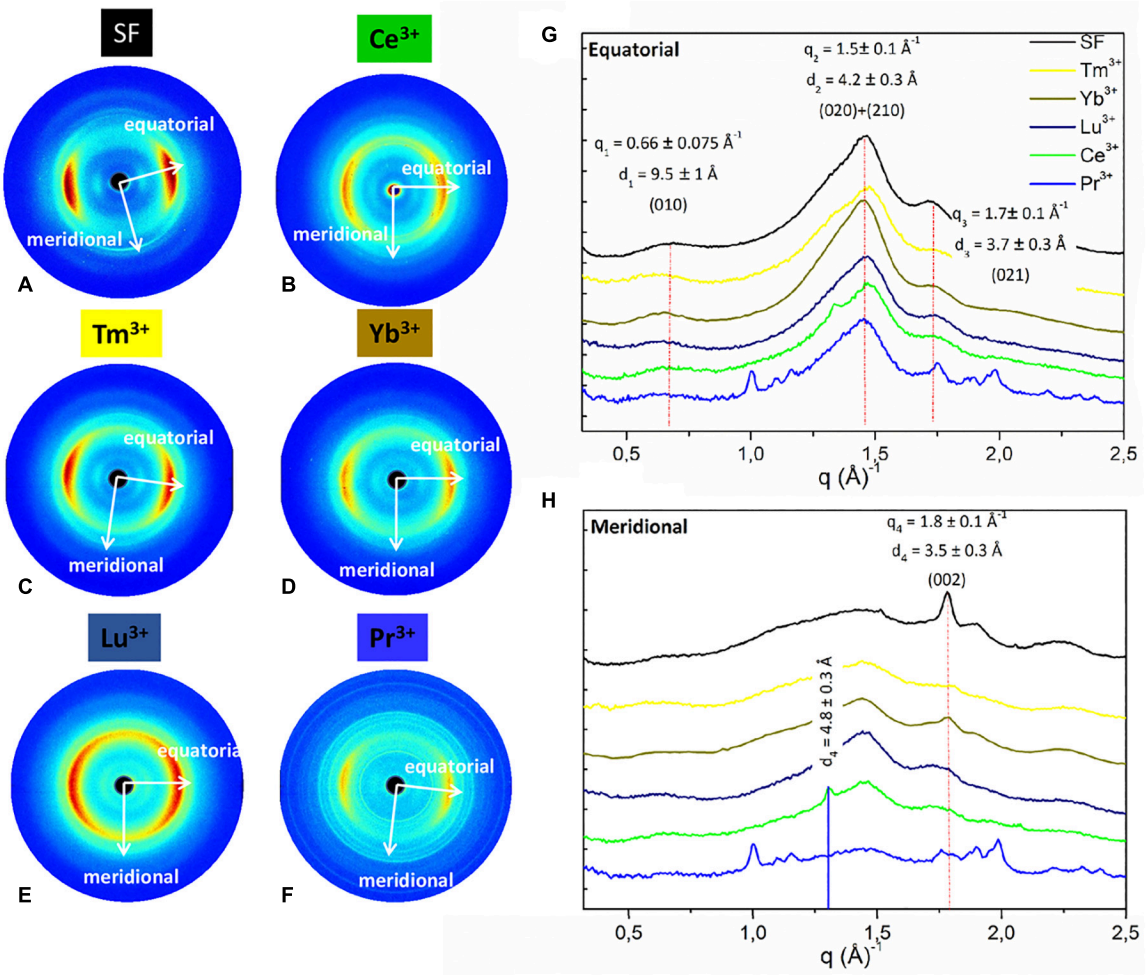

FIGURE 4 | 2D WAXS patterns of **(A)** degummed SF and regenerated fibers obtained after treatment with **(B)** Ce^{+3} **(C)** Tm^{+3}; **(D)** Y^{+3}; **(E)** Lu^{+3}; **(F)** Pr^{+3}, respectively, corresponding 1D **(G)** equatorial patterns and **(H)** meridional patterns. Vertical bars highlight the equatorial reflections at $q_1 = 0.66 \pm 0.075$ Å^{-1} ($d_1 = 9.5 \pm 1$ Å), $q_2 = 1.5 \pm 0.1$ Å^{-1} ($d_2 = 4.2 \pm 0.3$ Å), and $q_3 = 1.7 \pm 0.1$ Å^{-1} ($d_3 = 3.7 \pm 0.3$ Å) and the meridional reflection at $q_4 = 1.8 \pm 0.1$ Å^{-1} ($d_4 = 3.5 \pm 0.2$ Å) shifted at $q_4 = 1.3 \pm 0.1$ Å^{-1} ($d_4 = 4.8 \pm 0.2$ Å) only for Ce^{+3}. The equatorial and meridional peaks were indexed as follows: q_1 the (010) reflection; q_2 an overlap of the (020) and (210) reflections; q_3 the (021) reflection; q_4 the (002) reflection.

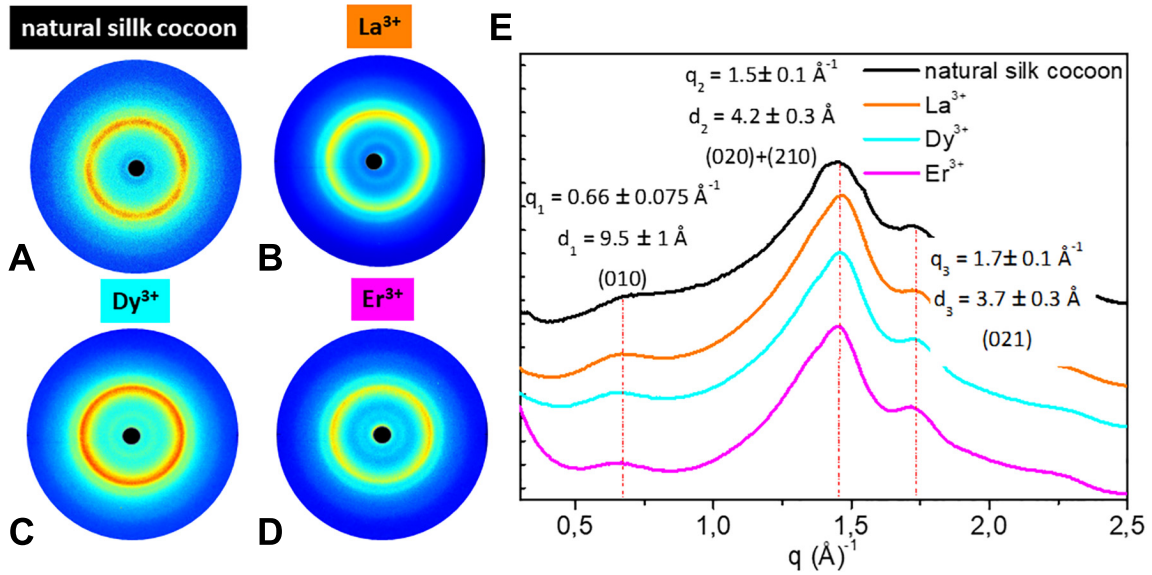

FIGURE 5 | 2D WAXS patterns of **(A)** natural silk cocoon and regenerated fibers obtained after treatment with **(B)** La^{+3}; **(C)** Dy^{+3}; **(D)** Er^{+3} respectively; **(E)** corresponding 1D WAXS patterns with vertical bars highlighting the reflections at $q_1 = 0.66 \pm 0.075$ Å^{-1} ($d_1 = 9.5 \pm 1$ Å), $q_2 = 1.5 \pm 0.1$ Å^{-1} ($d_2 = 4.2 \pm 0.3$ Å), and $q_3 = 1.7 \pm 0.1$ Å^{-1} ($d_3 = 3.7 \pm 0.3$ Å). These peaks were indexed as follows: q_1 the (010) reflection; q_2 an overlap of the (020) and (210) reflections; q_3 the (021) reflection.

N-H stretching vibrations) at 3,276 and 3,055 cm^{-1}, respectively, the asymmetric and symmetric C-H stretching frequencies at 2,920 and 2,847 cm^{-1} are evident. Amide I, Amide II and Amide III stretching frequencies bands are 1,644, 1,526, and 1,236 cm^{-1}. All films obtained from SF solutions with Nd^{+3}, Sm^{+3}, Eu^{+3}, Gd^{+3}, Tb^{+3} did not show any appreciable difference in the position and intensity of the typical IR bands. Significant differences are observed only for Dy^{+3}/SF, which exhibits an ATR-FTIR spectrum similar to that of the solid fiber with a shift of all the absorptions in the amide region toward lower wave numbers (Amide I 1,616 cm^{-1}, Amide II 1,510 cm^{-1}, and Amide III at 1,227 cm^{-1}). This lowering of the Amide band is strongly indicative of an increase in the β-sheet content in the protein and in the crystallinity of the material.

Finally, the ATR-FTIR spectrum of the SF gel obtained by dissolution with Ho^{+3} is completely superimposable to the spectrum of SF hydrogel obtained by the Ajisawa's protocol (**Figures 11**, **12**), thus suggesting that Ho^{+3} ions are capable of dissolving SF, as observed for all the lanthanides, but they are not able to regenerate the fibers.

DISCUSSION

The screening analysis of the behavior of SF solubilized by substituting the chaotropic salt $CaCl_2$ with hydrated lanthanides chlorides, $LnCl_3 \cdot nH_2O$, in the standard Ajisawa's method led to some very interesting results. First of all, all $LnCl_3 \cdot nH_2O$ are able to solubilize SF when used as chaotropic salts, but lanthanides at the beginning and at the end of the series of the Periodic Table (La^{+3}, Ce^{+3}, Pr^{+3}, Dy^{+3}, Er^{+3}, Tm^{+3}, Yb^{+3}, and Lu^{+3}) are able to induce the regeneration of the fiber during purification by dialysis. When using intermediate lanthanides (Nd^{+3}, Pr^{+3}, Sm^{+3}, Eu^{+3}, Gd^{+3}, and Tb^{+3}) aqueous solutions of SF are obtained, as in the standard Ajisawa's method. Dy^{+3} and Ho^{+3} can be considered borderline cases: using Dy^{+3} only 45% of the fiber is recovered during dialysis and the remaining part is in the aqueous solution, Ho^{+3} induces the formation of a SF hydrogel.

The fibers reprecipitated from Pr^{+3}, Er^{+3}, Tm^{+3}, Yb^{+3}, and Lu^{+3} solutions in H_2O/EtOH keep a morphology very similar to that of degummed SF and Ce^{+3}/SF: their integrity is almost recovered, although with a reduced smoothness and straightness. The typical hemicylindrical shape of the cross-section of the fibers is also retained, with an increase in the average diameter, probably due to swelling effects. Fibers obtained after treatment with La^{+3} and Dy^{+3} are constituted by small and disordered fragments with very coarse surfaces and irregular cross sections.

WAXS experiments, confirmed by ATR-FTIR and birefringence, demonstrated that in all cases the samples belonging to the SF-fiber regenerating lanthanides group retain an ordered crystalline structure, but they show two different behaviors:

(i) the fibers obtained with Pr^{+3} (at the beginning of the lanthanide series, as Ce^{+3}) and Tm^{+3}, Yb^{+3}, Lu^{+3} (at the end of the series) exhibit 2D WAXS patterns similar to degummed SF and Ce^{+3}/SF, with a typical cross β-diffraction pattern, thus indicating that, during reprecipitation, the fibers partially recover a highly oriented structure, rich of stacked β-sheet nanocrystals;

(ii) the fibers obtained with La^{+3}, Dy^{+3}, and Er^{+3} show 2D WAXS patterns similar to natural silk cocoon, i.e., without any preferential orientation.

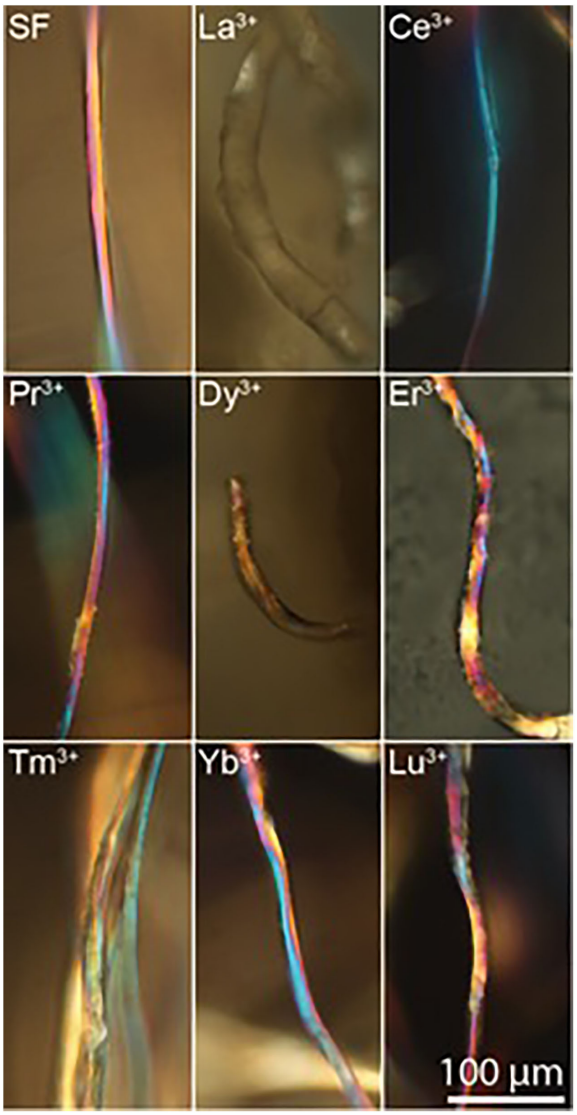

FIGURE 6 | Birefringence images of regenerated Ln^{+3}/SF fibers (degummed SF, La^{+3}/SF, Ce^{+3}/SF, Pr^{+3}/SF, Dy^{+3}/SF, Er^{+3}/SF, Tm^{+3}/SF, Yb^{+3}/SF, and Lu^{+3}/SF).

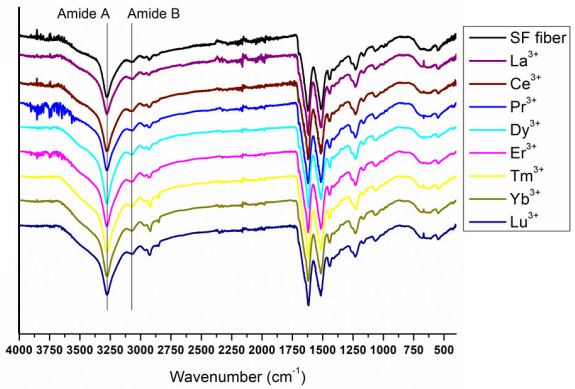

FIGURE 7 | Complete ATR-FTIR spectra of solid degummed SF (black curve) and regenerated solid Ln^{+3}/SF (La^{+3}/SF, Ce^{+3}/SF, Pr^{+3}/SF, Dy^{+3}/SF, Er^{+3}/SF, Tm^{+3}/SF, Yb^{+3}/SF, and Lu^{+3}/SF).

Anyway, WAXS experiments show no sign of inclusion of lanthanide ions within the crystalline domains of the fibers, contrary to what was found in the case of Ce^{+3}/SF.

XPS characterization indicates that the fibers with La^{+3}, Tm^{+3}, and Lu^{+3} do not show any relevant contamination of lanthanide ions, whilst in all other fibers the Ln^{+3} concentration is between 0.2 and 0.4% at, but, except for Ce^{+3}, Ln^{+3} ions are not coordinated to SF. This evidence could suggest that lanthanide ions could be present as impurities, likely on the fiber surface.

In summary, only when using $CeCl_3 \cdot 7H_2O$ as chaotropic salt in the Ajisawa's method it is possible to obtain SF doped by Ce^{+3} in a significant amount. In all other cases, SF is regenerated, but it is not doped with Ln^{+3} ions and, in some cases, it has different structural properties. Regarding intermediate lanthanide ions, it is interesting to point out that only SF aqueous solutions can be obtained at the end of the Ajisawa's process and the features of films prepared by solvent evaporation are very similar to the films obtained when using $CaCl_2$.

As already stressed when discussing the results obtained in our previous work on Ce^{+3}/SF (Rizzo et al., 2020b), this behavior is difficult to rationalize, firstly because silk solubilization and recovery are complex processes, driven by chemical and physical interactions that are not completely understood to date. It is known that SF solubilization is possible only in the presence of chaotropic salts that seemingly disrupt the hydrogen bonding network between the hydration shell of the protein and the bulk, so weakening the hydrophobic effects. However, the roles of different chaotropic salts and especially of solvent molecules have not been clarified yet.

In this context, it is necessary to consider that when using lanthanides as solubilizing agents, the situation is much more complicated due to the particular properties of lanthanides. Lanthanides series consist of 15 elements, from lanthanum ($Z = 57$) to lutetium ($Z = 71$), with high coordination numbers and characteristic oxidation state +3 (Zheng, 2012; Peters et al., 2020). It is well-known that the interactions between Ln^{+3} cations and ligands are mainly of electrostatic origin, since the formation of covalent bonds with donor atoms of ligand is virtually impossible. Due also to the absence of directionality of bonding electrons, the coordination number and the stereochemistry of Ln^{+3}-complexes are dictated by the steric requirements of the ligands and not by electronic effects. In addition, the so-called "lanthanide contraction" (Peters et al., 2020), which is a unique characteristic of lanthanide metals, must be taken into account: Ln^{+3} ionic radium decreases with increasing atomic number, that is with increasing charge density. Lanthanide contraction further affects the capability of lanthanide ions to form stable complexes. Ln coordination numbers in the range 3–12 have been observed and with 7, 8, and 9 as the most common ones. Lanthanides ions with larger ionic radii can, in principle, have larger coordination

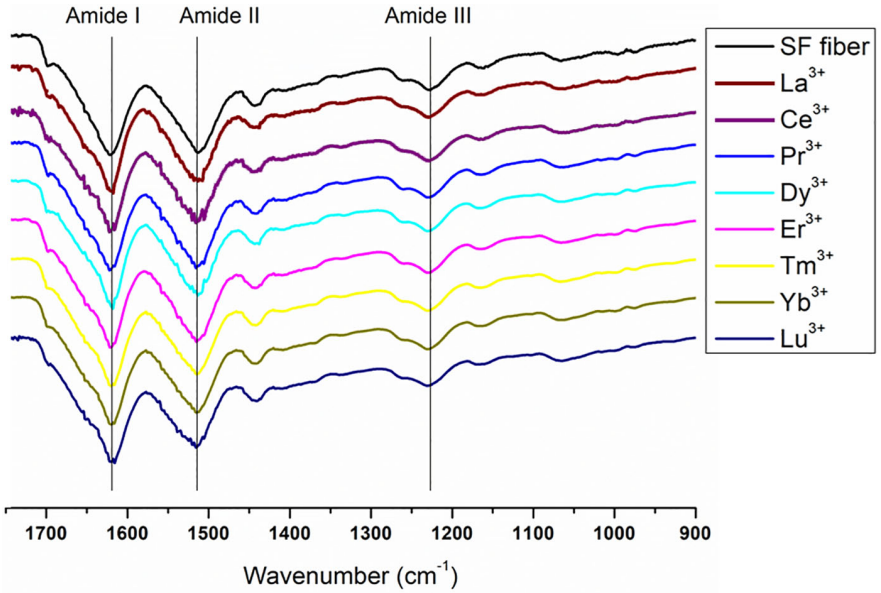

FIGURE 8 | Expansion of the amide band region, between 1750 and 900 cm^{-1}, of the spectra in **Figure 7**. Solid degummed SF (black curve) and regenerated solid Ln^{+3}/SF (La^{+3}/SF, Ce^{+3}/SF, Pr^{+3}/SF, Dy^{+3}/SF, Er^{+3}/SF, Tm^{+3}/SF, Yb^{+3}/SF, and Lu^{+3}/SF).

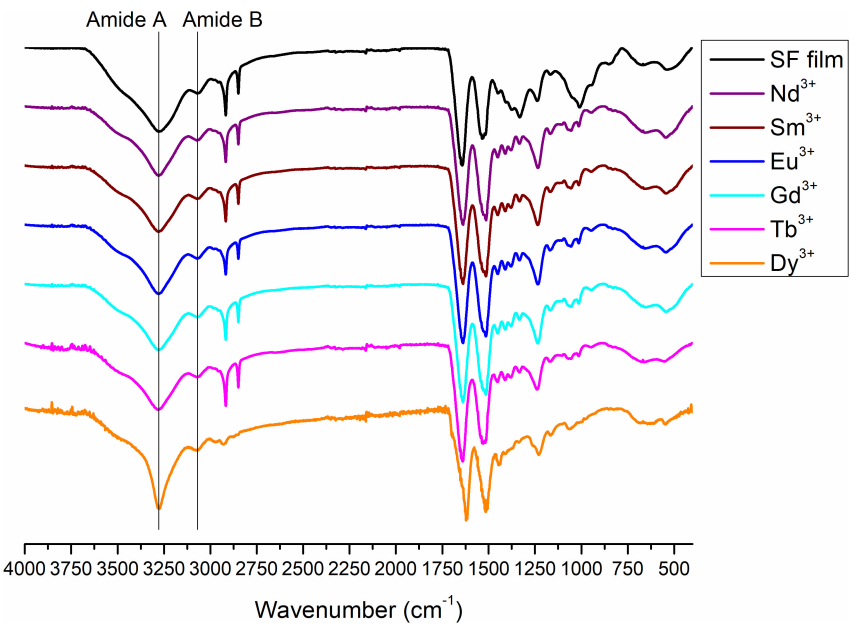

FIGURE 9 | ATR-FTIR spectra of degummed SF film (black curve) and films obtained by drop-casting of solutions of SF with Nd^{+3}, Sm^{+3}, Eu^{+3}, Gd^{+3}, Tb^{+3}, and Dy^{+3} after purification by dialysis.

numbers. On the other hand, the decrease of ionic radium with the consequent increase of charge density increases the tendency to form more stable complexes. In any case, due to their electrostatic nature, Ln^{+3}-complexes are quite labile and the coordination sphere is not well-defined, since the coordination number is primarily affected by the size of the ligands, the number of donors of each ligand that can pack around the ion and, in the case of bulky ligands, by intermolecular interactions. Because of the small radius and the high nuclear charge, the Ln^{+3} ions are strong Lewis acids that coordinate with hard bases such as carboxylates and highly electronegative donors such as N or O (Zheng, 2012), that is to say that Ln^{+3} ions are good complexing agents for amino acids and peptide bonds in proteins.

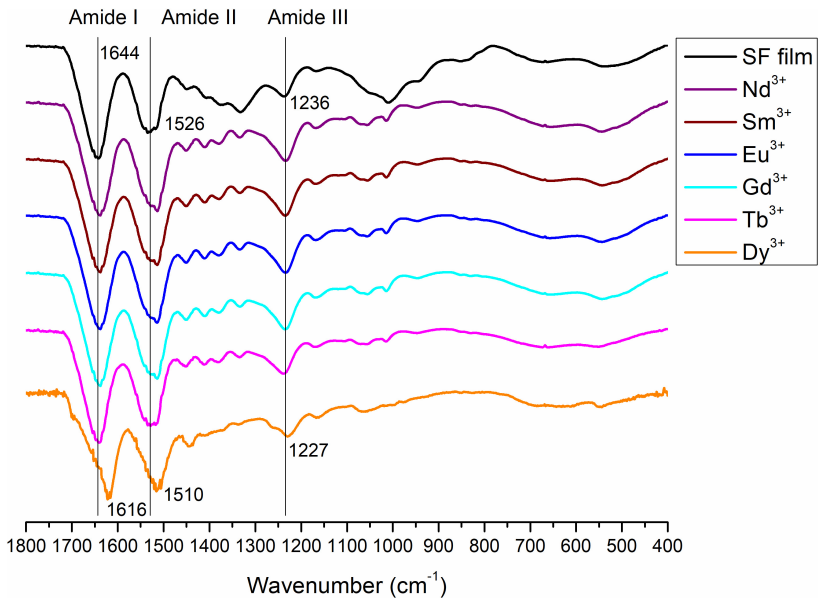

FIGURE 10 | Expansion of the amide band region, between 1,800 and 400 cm^{-1}, of the ATR-FTIR spectra of degummed SF film (black curve) and films obtained by drop-casting of solutions of SF with Nd^{+3}, Sm^{+3}, Eu^{+3}, Gd^{+3},Tb^{+3}, and Dy^{+3} after purification by dialysis.

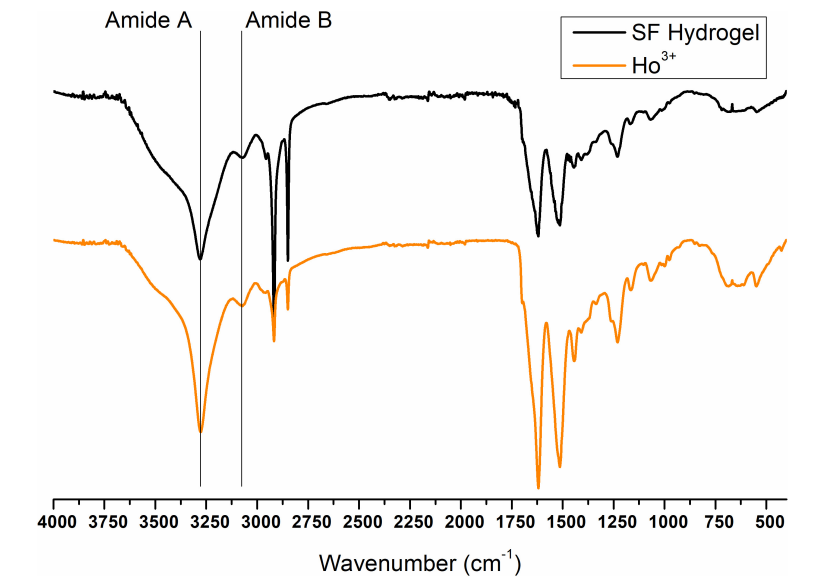

FIGURE 11 | ATR-FTIR spectra of Ho^{+3}/SF hydrogel obtained by spontaneous gelation of the dialyzed solution of SF dissolved in $HoCl_3$ according to the modified Ajisawa's protocol.

In our previous paper (Rizzo et al., 2020b), comparing the behavior of SF in the presence of Ce^{+3} ions to the results reported in the literature on the influence of other metal ions on SF, it seemed reasonable to infer that an important role is played by Ce^{+3} charge and coordination number. The results obtained for the complete series of lanthanides are consistent with this hypothesis.

The behavior of SF when Ln^{+3} ions in the middle of the lanthanide series (Nd^{+3}, Pr^{+3}, Sm^{+3}, Eu^{+3}, Gd^{+3}, and Tb^{+3}) are used as chaotropic salts is similar to the behavior observed in the presence of Ca^{+2} ions (standard Ajisawa's method). This can be explained as an effect of the ionic radius. In fact, as it can be seen in **Table 1**, the ionic radii of Ln^{+3} from Nd^{+3} to Tb^{+3}, are within 1.08 and 1.01 Å, comparable to the ionic radius of Ca^{+2} (1.03 Å).

For lanthanides at the beginning and at the end of the series, the Ln^{+3} coordination number seems to play a key role, besides the ionic radius. During the purification step after

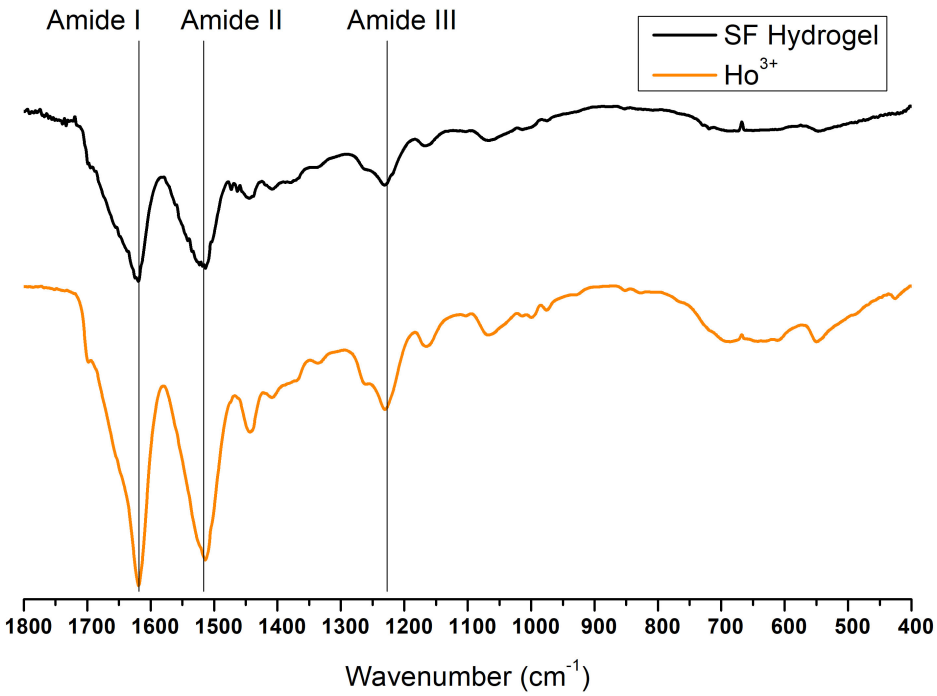

FIGURE 12 | Expansion of the amide band region, between 1,800 and 400 cm^{-1}, of the ATR-FTIR spectra of regenerated Ho^{+3}-SF hydrogel.

solubilization, the removal of Ln^{+3} ions, as already found for Ce^{+3}, seems to promote the self-assembly of the fiber in the transition from solution to solid state, with the fibers undergoing a structural transition from random coil to a highly ordered structure.

Ce^{+3} ion has ionic radius slightly larger than that of Ca^{+2}, but also a larger charge and coordination number. Pr^{+3} has an ionic radius slightly lower than Ce^{+3}, and presumably a lower coordination number. Hence, the fibers obtained at the end of the purification process are very similar to Ce^{+3}/SF, although not doped by Pr^{+3} ions, that are more easily removed during the dialysis step, due to its lower coordination number.

Ln^{+3} ions at the end of the series, from Er^{+3} to Lu^{+3}, have ionic radii that are significantly lower than Ce^{+3}. Even if their density charges are larger than Ce^{+3}, their coordination number is smaller, considering that the steric hindrance of the environment is the same. This could imply that these ions can easily induce the solubilization of SF with a mechanism very similar to the one hypothesized for Ce^{+3} ions, but can also been removed more easily than Ce^{+3} ions without remaining trapped within the fiber. The SF reprecipitated after dialysis is highly ordered, and richer of stacked β-sheet nano-crystals as the ionic radius decreases.

CONCLUSION

We have reported the results of a systematic investigation on the behavior of degummed SF when solubilized by replacing $CaCl_2$ with $LnCl_3 \cdot nH_2O$ in the standard Ajisawa's reagent. This study builds on previous work using $CeCl_3 \cdot 7H_2O$ (Rizzo et al., 2020b) and extends to all the other lanthanides in the Periodic Table, given the potential that lanthanide doping of SF holds for the manufacturing of devices for photonics and electronics.

It would seem that Cerium constitutes a unique case for obtaining lanthanide doped SF. Indeed, using $CeCl_3$ as chaotropic salt in water and ethanol, not only it is possible to regenerate SF in a fibrous form, but the fiber obtained is doped with Ce^{+3} ions and preserves the morphological and molecular structure of the pristine SF. Ce^{+3} ions should be coordinated to SF preferentially by interactions with the oxygen atoms of protein backbone and should be distributed within the highly ordered hydrophobic β-sheet regions of SF, as well as amorphous regions (Rizzo et al., 2020b). For all the other re-precipitated fibers (with the exception of La^{+3}/SF, Tm^{+3}/SF, and Lu^{+3}/SF), a surface concentration of Ln^{+3} between 0.2 and 0.4% at was measured, comparable to that measured for Ce^{+3}/SF. However, contrary to what was found in the case of Ce^{+3}/SF, there is no evidence that the ions are coordinated with the fiber fibroin, nor is the presence of Ln^{+3} ions detectable within the ordered domains. This could suggest that Ln^{+3} ions could be distributed on the fiber surface, although it is not possible to exclude their inclusion within the amorphous regions.

However, the results obtained for the other lanthanides can be considered interesting for other reasons. Indeed, our work shows that all lanthanides in H_2O/EtOH (8:1) are effective chaotropic salts for SF and that they constitute a valid alternative to $CaCl_2$ in the Ajisawa's method. Using hydrated $LnCl_3$ we have obtained a new protocol which enables to regenerate SF in the form of fibrous material by direct reprecipitation during dialysis.

A further appealing feature of the protocol described is its environmental sustainability, given both the possibility of near-full recovery of the lanthanide salts from water and the absence of toxic solvents or hazardous reagents throughout the whole process (Rizzo et al., 2020b).

Further studies are in progress to investigate the optical properties and applications of the fibers regenerated in the presence of lanthanide solutions and also to optimize possible protocols for a controlled inclusion of lanthanide ions other than Cerium into the fibers.

DATA AVAILABILITY STATEMENT

The original contributions presented in the study are included in the article/**Supplementary Material**, further inquiries can be directed to the corresponding author/s.

AUTHOR CONTRIBUTIONS

All authors listed have made a substantial, direct and intellectual contribution to the work, and approved it for publication.

ACKNOWLEDGMENTS

Dr. Adriano Bogetich is acknowledged for SEM images acquisition and elaboration.

SUPPLEMENTARY MATERIAL

The Supplementary Material for this article can be found online at: https://www.frontiersin.org/articles/10.3389/fbioe.2021.653033/full#supplementary-material

REFERENCES

Ajisawa, A. (1998). Dissolution aqueous of silk fibroin with calcium chloride / ethanol solution. *J. Sericult. Sci. Japan* 67, 91–94.

Altamura, D., Lassandro, R., Vittoria, F. A., De Caro, L., Siliqi, D., Ladisa, M., et al. (2012). X-ray microimaging laboratory (XMI-LAB). *J. Appl. Cryst.* 45, 869–873. doi: 10.1107/s0021889812025733

Chahal, R., Starecki, F., Boussard-Pledel, C., Doualan, J.-L., Michel, K., Brillard, L., et al. (2016). Fiber evanescent wave spectroscopy based on IR fluorescent chalcogenide fibers. *Sensors Act. B* 229, 209–216. doi: 10.1016/j.snb.2016.01.091

da Rocha, E. G., Pugina, R. S., and Caiut, J. M. A. (2020). Luminescent sensor based on the lanthanide-fibroin composite. *Opt. Mater.* 109, 110236–110244. doi: 10.1016/j.optmat.2020.110236

Digonnet, M. J. (2001). *Rare-Earth-Doped Fiber Lasers and Amplifiers, Revised and Expanded*. Boca Raton, FL: CRC press.

Fossey, S. A., Némethy, G., Gibson, K. D., and Scheraga H. A. (1991). Conformational energy studies of β-sheets of model silk fibroin peptides. I. Sheets of poly(Ala-Gly) chains. *Biopolymers* 31, 1529–1541. doi: 10.1002/bip.360311309

Founda, I. M., and El-Tonsy, M. M. (1990). Birefringence behavior of annealed silk fibres. *J. Mater. Sci.* 25, 4752–4757. doi: 10.1007/bf01129936

Georgakoudi, I., Tsai, I., Greiner, C., Wong, C., DeFelice, J., and Kaplan, D. (2007). Intrinsic fluorescence changes associated with the conformational state of silk fibroin in biomaterial matrices. *Opt Express* 15, 1043–1053. doi: 10.1364/oe.15.001043

Guo, C., Li, C., Mu, X., and Kaplan, D. L. (2020). Engineering silk materials: from natural spinning to artificial processing. *Appl. Phys. Rev.* 7:011313. doi: 10.1063/1.5091442

Guo, C., Zhang, J., Jordan, J. S., Wang, X., Henning, R. W., and Yarger, J. L. (2018). Structural comparison of various silkworm silks: an insight into the structure-property relationship. *Biomacromolecules* 19, 906–917. doi: 10.1021/acs.biomac.7b01687

Guo, X., Ge, M., and Zhao, J. (2011). Photochromic properties of rare-earth strontium aluminate luminescent fiber. *Fibers Polym.* 12, 875–879. doi: 10.1007/s12221-011-0875-9

Hu, X., Kaplan, D., and Cebe, P. (2006). Determining beta-sheet crystallinity in fibrous proteins by thermal analysis and Infrared Spectroscopy. *Macromolecules* 39, 6161–6170. doi: 10.1021/ma0610109

Hu, X., Kaplan, D., and Cebe, P. (2008). Dynamic protein-water relationships during β-sheet formation. *Macromolecules* 41, 3939–3948. doi: 10.1021/ma071551d

Huang, W., Ling, S., Li, C., Omenetto, F. G., and Kaplan, D. L. (2018). Silkworm silk-based materials and devices generated using bio-nanotechnology. *Chem. Soc. Rev.* 47, 6486–6504. doi: 10.1039/c8cs00187a

Koh, L. D., Cheng, Y., Teng, C. P., Khin, Y. W., Loh, X. J., Tee, S. Y., et al. (2015). Structures, mechanical properties and applications of silk fibroin materials. *Prog. Polym. Sci.* 46, 86–110.

Kundu, B., Rajkhowa, R., Kundu, S. C., and Wang, X. (2013). Silk fibroin biomaterials for tissue regenerations. *Adv. Drug Deliv. Rev.* 65, 457–470. doi: 10.1016/j.addr.2012.09.043

Lawrence, B. D., Omenetto, F., Chui, K., and Kaplan, D. L. (2008). Processing methods to control silk fibroin film biomaterial features. *J. Mater. Sci.* 43, 6967–6985. doi: 10.1007/s10853-008-2961-y

Lee, O. J., Sultan, M. D. T., Hong, H., Lee, Y. J., Lee, J. S., Lee, H., et al. (2020). Recent Advances in Fluorescent Silk Fibroin. *Front. Mater.* 7:50. doi: 10.3389/fmats.2020.00050

Ling, S., Kaplan, D. L., and Buehler, M. J. (2018). Nanofibrils in nature and materials engineering. *Nat. Rev. Mater.* 3:18016.

Liu, J., Xu, J., Guo, X., Liao, T., and Huang, Y. (2020). The up-conversion luminescence in the $Er^{+3}/Yb^{+3}/Tm^{+3}$ tri-doped tellurite glass microsphere coupled by the tapered fiber. *Opt. Sens. Imag. Technol.* 11567, 1156740–1156759.

Marsh, R. E., Corey, R. B., and Pauling, L. (1955). An investigation of the structure of silk fibroin. *Bioch. Biophys. Acta* 16, 1–34.

Melke, J., Midha, S., Ghosh, S., Ito, K., and Hofmann, S. (2016). Silk Fibroin as biomaterial for bone tissue engineering. *Acta Biomater.* 31, 1–16. doi: 10.1016/j.actbio.2015.09.005

Moulder, F., Stickle, W. F., Sobol, P. E., and Bomben, K. E. (1992). *Handbook of X-ray Photoelectron Spectroscopy*, ed. J. Chastain (Eden Prairie, MN: Perkin-Elmer Corporation).

Omenetto, F. G., and Kaplan, D. L. (2010). New opportunities for an ancient material. *Science* 329, 528–531. doi: 10.1126/science.1188936

Peters, J. A., Djanashvili, K., Geraldes, C. F. G. C., and Platas-Iglesias, C. (2020). The chemical consequences of the gradual decrease of the ionic radius along the Ln-series. *Coord. Chem. Rev.* 406:213146. doi: 10.1016/j.ccr.2019.213146

Pugina, R. S., da Rocha, E. G., and Caiut, J. M. A. (2019a). Beta-diketones in the intensification of the luminescence of the silk fibroin films doped rare earth ions. *J. Mater. Sci.: Mater. Electron.* 30, 16732–16739. doi: 10.1007/s10854-019-01181-8

Pugina, R. S., da Rocha, E. G., Ribeiro, S. J. L., and Caiut, J. M. A. (2019b). Study of the energy transfer process in rare earth-doped silk fibroin for future application in luminescent compounds. *J. Lumin.* 205, 423–428. doi: 10.1016/j.jlumin.2018.09.050

Qi, Y., Wang, H., Wei, K., Yang, Y., Zheng, R.-Y., Kim, I. S., et al. (2017). A review of structure construction of silk fibroin biomaterials form single structures to multi-level structures. *Int. J. Mol. Sci.* 18, 237–257. doi: 10.3390/ijms18030237

Reddy, N. (2020). *Silk: Materials, Processes, and Applications*. Sawston: Woodhead Publishing.

Rizzo, G., Albano, G., Lo Presti, M., Milella, A., Omenetto, F. G., and Farinola, G. M. (2020a). Palladium supported on silk fibroin for Suzuki-Miyaura cross-coupling reactions. *Eur. J. Org. Chem.* 2020, 6992–6996. doi: 10.1002/ejoc.202001120

Rizzo, G., Lo Presti, M., Giannini, C., Sibillano, T., Milella, A., Matzeu, G., et al. (2020b). Silk fibroin processing from $CeCl_3$ aqueous solution: fibers regeneration and doping with Ce(III). *Macromol. Chem. Phys.* 221:2000066. doi: 10.1002/macp.202000066

Rockwood, D. N., Preda, R. C., Yücel, T., Wang, X., Lovett, M. L., and Kaplan, D. L. (2011). Materials fabrication from Bombyx mori silk fibroin. *Nat. Protoc.* 6, 1612–1631. doi: 10.1038/nprot.2011.379

Seaborg, G. T. (1978). "Actinides and Transactinides," in *Kirk-Othmer: Encyclopedia of Chemical Technology*, Vol. 1, ed. D. Othmer (New York, NY: John Wiley and Sons), 456–488.

Shen, X., Hu, Q., and Ge, M. (2021). Fabrication and characterization of multi stimuli-responsive fibers via wet-spinning process. *Spectrochim. Acta Part A Mol. Biomol. Spectrosc.* 250, 119245.

Shen, Y., Johnson, M. A., and Martin, D. C. (1998). Microstructural characterization of *Bombyx mori* silk fibers. *Macromolecules* 31, 8857–8864.

Sibillano, T., De Caro, L., Scattarella, F., Scarcelli, G., Siliqi, D., Altamura, D., et al. (2016). Interfibrillar packing of bovine cornea by table-top and synchrotron scanning SAXS microscopy. *J. Appl. Cryst.* 49, 1231–1239.

Siliqi, D., De Caro, L., Ladisa, M., Scattarella, M., Mazzone, A., Altamura, D., et al. (2016). SUNBIM: a package for X. ray imaging of nano-and biomaterials using SAXS, WAXS, GISAXS, GIWAXS techniques. *J. Appl. Cryst.* 49, 1107–1114.

Tao, H., Kaplan, D. L., and Omenetto, F. G. (2012). Silk materials – A road to sustainable high technology. *Adv. Mater.* 24, 2824–2837.

Viney, C., Huber, A. E., Dunaway, D. L., Kerkam, K., and Case, S. T. (1993). "Optical characterization of silk secretions and fibers," in *Silk Polymers: Material Science and Biotechnology*, eds D. Kaplan, W. W. Adams, B. Farmer, and C. Viney (Washington, D.C: ACS Publication), 120–136.

Zheng, X., Zhao, M., Zhang, H., Fan, S., Shao, H., Hu, X., et al. (2018). Intrinsically fluorescent silks from silkworms fed with rare-earth upconverting phosphors. *ACS Biomater. Sci. Eng.* 4, 4021–4027.

Zheng, Z. (2012). *Lanthanides: Amino Acid Compounds. Encyclopedia of Inorganic and Bioinorganic Chemistry, Online*. Hoboken, NJ: John Wiley & Sons, Ltd,

Zhu, B., Wang, H., Leow, W. R., Cai, Y., Loh, X. J., Han, M.-Y., et al. (2016). Silk fibroin for flexible electronic devices. *Adv. Mater.* 28, 4250–4265.

Conflict of Interest: The authors declare that the research was conducted in the absence of any commercial or financial relationships that could be construed as a potential conflict of interest.

frontiers in Bioengineering and Biotechnology

REVIEW
published: 16 July 2021
doi: 10.3389/fbioe.2021.652384

Fibrous Scaffolds From Elastin-Based Materials

Jose Carlos Rodriguez-Cabello[1,2], Israel Gonzalez De Torre[1,2], Miguel González-Pérez[1,2], Fernando González-Pérez[1,2] and Irene Montequi[1,2]*

[1] BIOFORGE, University of Valladolid, Valladolid, Spain, [2] Center for Biomedical Research in the Network in Bioengineering, Biomaterials and Nanomedicine (CIBER-BBN), Madrid, Spain

Current cutting-edge strategies in biomaterials science are focused on mimicking the design of natural systems which, over millions of years, have evolved to exhibit extraordinary properties. Based on this premise, one of the most challenging tasks is to imitate the natural extracellular matrix (ECM), due to its ubiquitous character and its crucial role in tissue integrity. The anisotropic fibrillar architecture of the ECM has been reported to have a significant influence on cell behaviour and function. A new paradigm that pivots around the idea of incorporating biomechanical and biomolecular cues into the design of biomaterials and systems for biomedical applications has emerged in recent years. Indeed, current trends in materials science address the development of innovative biomaterials that include the dynamics, biochemistry and structural features of the native ECM. In this context, one of the most actively studied biomaterials for tissue engineering and regenerative medicine applications are nanofiber-based scaffolds. Herein we provide a broad overview of the current status, challenges, manufacturing methods and applications of nanofibers based on elastin-based materials. Starting from an introduction to elastin as an inspiring fibrous protein, as well as to the natural and synthetic elastin-based biomaterials employed to meet the challenge of developing ECM-mimicking nanofibrous-based scaffolds, this review will follow with a description of the leading strategies currently employed in nanofibrous systems production, which in the case of elastin-based materials are mainly focused on supramolecular self-assembly mechanisms and the use of advanced manufacturing technologies. Thus, we will explore the tendency of elastin-based materials to form intrinsic fibers, and the self-assembly mechanisms involved. We will describe the function and self-assembly mechanisms of silk-like motifs, antimicrobial peptides and leucine zippers when incorporated into the backbone of the elastin-based biomaterial. Advanced polymer-processing technologies, such as electrospinning and additive manufacturing, as well as their specific features, will be presented and reviewed for the specific case of elastin-based nanofiber manufacture. Finally, we will present our perspectives and outlook on the current challenges facing the development of nanofibrous ECM-mimicking scaffolds based on elastin and elastin-like biomaterials, as well as future trends in nanofabrication and applications.

Keywords: elastin like recombinamers, tropoelastin, fibers, tissue engineering, processing techniques

OPEN ACCESS

Edited by:
Cinzia Giannini, Institute of Crystallography, Italian National Research Council, Italy

Reviewed by:
Mustafa O. Guler, University of Chicago, United States
Vincenzo Guarino, National Research Council (CNR), Italy
Marco Lo Presti, Tufts University, United States

****Correspondence:***
Jose Carlos Rodriguez-Cabello
roca@bioforge.uva.es

Specialty section:
This article was submitted to Nanobiotechnology, a section of the journal Frontiers in Bioengineering and Biotechnology

Received: *12 January 2021*
Accepted: *25 June 2021*
Published: *16 July 2021*

Citation:
Rodriguez-Cabello JC, Gonzalez De Torre I, González-Pérez M, González-Pérez F and Montequi I (2021) Fibrous Scaffolds From Elastin-Based Materials. Front. Bioeng. Biotechnol. 9:652384. doi: 10.3389/fbioe.2021.652384

INTRODUCTION

Current cutting-edge strategies in biomaterials science are focused on mimicking the design of natural systems which, over millions of years, have evolved to exhibit extraordinary properties (Zhao et al., 2013). Based on this premise, one of the most challenging tasks in the field of tissue engineering and regenerative medicine is the development of biomaterials and scaffolds that imitate the natural extracellular matrix (ECM), due to its ubiquitous character and its crucial role in tissue integrity.

The ECM consists of a complex mixture of interconnected molecules secreted by cells that arrange to provide a physical scaffolding for cells and tissues and promote physicochemical cues for normal tissue morphogenesis, differentiation, homeostasis and healing (Frantz et al., 2010; McKee et al., 2019). ECM-mimicking scaffolds should therefore be able to reproduce the reciprocal interaction between cells and the ECM, which involves certain bio-functionalities such as cell adhesion, protease sensitivity and cytokine release, amongst others. This complex interaction also involves physical and morphological features and is not restricted exclusively to biological signals.

The anisotropic fibrillar architecture of the ECM has been reported to have a significant influence on cell behavior and function. As a consequence of the intimate relationship between the cytoskeleton and the ECM, cells are able to sense and respond to the mechanical properties of the surrounding tissue by converting mechanical inputs into chemical signals (Galbraith and Sheetz, 1998; Geiger et al., 2001). Moreover, it is known that the fibrillar structure of the matrix components causes adhesion ligand clustering, which clearly alters cell adhesion and motility (Maheshwari et al., 2000).

From a structural point of view, the natural ECM comprises protein fibrils and fibers interwoven within a hydrated network of glycosaminoglycan chains, which endows it with a fibrillar and viscoelastic character. Fibrous proteins include collagens and elastin, with the former being the most abundant and main structural component of the interstitial ECM (Gordon and Hahn, 2010; McKee et al., 2019). Elastin associates with collagen and provides complementary function, mainly as elastic fibers. It consists of tropoelastin and microfibrils (Wise and Weiss, 2009) and is responsible for the reversible extensibility (recoil properties) of tissue. Elastin is particularly abundant in tissues and organs that require elasticity or undergo cycles of elongation and shrinkage, such as the lungs [3-7%, skin (2-3%), blood vessels (28-32%), and elastic ligaments (50%)] (Uitto, 1979). Moreover, it plays a key role in the functionality of these tissues due to its involvement in many cell-signaling processes (Almine et al., 2010, 2012). In this review, we will focus our attention on fibrous assemblies of elastin and elastin-based biomaterials.

A new paradigm that pivots around the idea of incorporating both biomechanical and biomolecular cues into the design of biomaterials and systems for biomedical applications has emerged in recent years. Indeed, current trends in materials science address the development of innovative biomaterials that include the dynamics, biochemistry and structural features of the native ECM (Acosta et al., 2020a). In this context, one of the most actively studied biomaterials for tissue engineering and regenerative medicine applications are nanofiber-based scaffolds. Several advanced strategies have emerged with the aim of copying the intricate fibrillar architecture of the ECM components and manufacturing biomaterials and matrices with a similar structure. These strategies are mainly based on our understanding of supramolecular self-assembly mechanisms to form nanofibers *in situ* and in the recent progress made in polymer-processing technologies. The way these nanofiber-based scaffolds are manufactured may change their nanostructure and, hence, their function and properties.

Nanofibers have unique properties that are mostly associated with a reduction in their diameter to the nanoscale, which translates into a significant increase in the surface-to-volume ratio and greatly affects the chemical and biological reactivity, as well as the electronic and mechanical properties, of the fibers (Ko and Wan, 2014). Given their high specific surface area and porosity, nanofiber-based scaffolds exhibit an extraordinary loading capacity for biological substances and active ingredients. Moreover, these nanofibers form an interconnected network of micropores that perfectly imitates the topographical features of the natural ECM and, as a consequence, comprise a suitable scaffold for cellular growth, proliferation and differentiation (Kenry and Lim, 2017). Consequently, rational design principles should be proposed to control fiber diameters and morphology, as well as pore size, to ensure that they are compatible with the cellular processes involved in migration through the ECM (Friedl, 2004).

Since the ECM is highly heterogeneous and there are important variations between different tissues, the nature of the biomaterials employed, the method for manufacturing the nanofiber-based scaffold, and its morphological features depend closely on the desired application. Thus, materials from natural sources are widely used because of their physicochemical and mechanical properties as well as their inherent biological recognition properties, which includes the presence of receptor-binding ligands and a sensitivity to cell-triggered proteolytic degradation. Nevertheless, natural materials have some important drawbacks, such as immunogenicity and pathogen transmission issues, and have a predetermined structure that limits the possibility of functionalizing them (Acosta et al., 2020a). Most of these limitations can be overcome using recombinant protein expression technologies, which allow the production of materials with strict control of their composition and physicochemical properties and, therefore, the production of tailored scaffolds with tuneable bioactivities. In this regard, genetically engineered biomaterials based on structural proteins have emerged as outstanding candidates for the production of ECM-inspired scaffolds. In this case, a wide variety of functional building blocks, including structural, self-assembling and bioactive domains, can be merged together using molecular biology techniques, thus opening up a wide range of possibilities in the production of protein-based ECM-inspired scaffolds (Acosta et al., 2020a).

Herein we provide a broad overview of the current status, challenges, manufacturing methods and applications of nanofibers based on elastin and elastin-like biomaterials. We will start with an introduction to elastin as an inspiring

fibrous protein, as well as to the natural and synthetic elastin-based biomaterials employed to meet the challenge of developing ECM-mimicking nanofibrous-based scaffolds. This will be followed by a description of the leading strategies currently employed in nanofibrous systems production, which in the case of elastin-based materials are mainly focused on supramolecular self-assembly mechanisms and the use of advanced manufacturing technologies. Thus, we will explore the tendency of elastin-based materials to form intrinsic fibers, and the self-assembly mechanisms involved. Moreover, we will address other self-assembled motifs found in nature, such as coiled-coiled, β-sheets, and β-hairpin structures which, in combination with elastin domains, act as promoters in the formation of amyloid fibers. More specifically, we will describe the function and self-assembly mechanisms of silk-like motifs, antimicrobial peptides and leucine zippers when incorporated into the backbone of the elastin-based biomaterial. Advanced polymer-processing technologies, such as electrospinning and additive manufacturing, as well as their specific features, will be presented and reviewed for the specific case of elastin-based nanofiber manufacture. Finally, we will present our perspectives and outlook on the current challenges facing the development of nanofibrous ECM-mimicking scaffolds based on elastin and elastin-like biomaterials, as well as future trends in nanofabrication and applications.

ELASTIN-BASED BIOMATERIALS

Tropoelastin

Elastin is a fibrous and insoluble protein formed by crosslinking of its soluble precursor tropoelastin mediated by lysyl oxidase (LOX) enzymes (Brown-Augsburger et al., 1995). In nature, elastic fiber assembly starts with the production of tropoelastin in elastogenic cells. This tropoelastin is then transferred to the cell surface, where it clumps with glycosaminoglycans and accumulates as elastin aggregates. Therefore, since elastin is formed from tropoelastin, a detailed description of its properties is summarized below.

Tropoelastin is a 60-72 kDa protein comprising 750 to 800 amino acids (Brown-Augsburger et al., 1995). Its amino acid sequence is characterized by the alternation of hydrophobic and hydrophilic domains (Wise and Weiss, 2009). The former mainly comprise the non-polar amino acids glycine (G), proline (P), valine (V), and alanine (A). The hydrophilic domains are characterized by a high alanine (A) and lysine (K) content that promotes intra- and intermolecular crosslinking. Secreted tropoelastin normally have around 40 lysine residues, of which approximately 35 are modified by LOX-mediated crosslinking. The high degree of crosslinking confers an extraordinary stability on mature elastin and a very low turnover, which in turn can be considered to be why elastin lasts for the entire lifespan of the host (Hinek, 1997). Moreover, this crosslinking makes tropoelastin highly insoluble, thus preventing it from being manipulated and making it suitable for tissue engineering and other biomedical applications (Almine et al., 2010; Ozsvar et al., 2021).

The alternating hydrophobic and hydrophilic domains in the structure of tropoelastin confer elasticity and thermal responsiveness on the molecule (Wise and Weiss, 2009). Thus, below its transition temperature (Tt), tropoelastin remains as a monomer with an elongated conformation, whereas when the temperature rises above Tt, the hydrophobic domains of the molecule start to establish weak interactions, thus giving rise to spheroid aggregates with a diameter of around 1 to 2 μm, which subsequently coacervate to form aggregates of up to 6 μm. This process is reversible, such that when cooled below Tt, the system evolves to obtain monomers again. Nevertheless, if the temperature is maintained above Tt, the coacervates firstly undergo a maturation process, then collapse and crosslink with LOX to give rise to branched fibrillar structures (Mithieux et al., 2009). This is a complex non-reversible process that is governed by several factors, such as the number and position of the hydrophobic and hydrophilic domains, pH and ionic strength, amongst others (Kaibara et al., 1996; Vrhovski and Weiss, 1998; Wu et al., 1999; Bellingham et al., 2001; Pepe et al., 2008) (See **Figure 1**). As a consequence of the complexity of this process, the formation of tropoelastin fibers or hydrogels will require extreme reaction conditions (high pH) and/or the use of harmful chemical reagents, such as organic crosslinkers (Mithieux et al., 2009).

Elastin-Like Recombinamers (ELRs)

One interesting group of elastin-based biomaterials are elastin-like polymers (ELPs) and, especially, their recombinant versions (ELRs). These are protein-like materials whose composition is based on the repetition of conserved motifs found in the hydrophobic domains of native tropoelastin (Foster et al., 1973). Both ELPs and ELRs refer to the same kind of polypeptide, with differences in the production process.

The chemical synthesis of ELPs is a very long process involving a high number of steps and chemical reactions as well as the use of diverse precursors and solvents. Although it has been successfully performed for short ELP chains (Urry and Williams, 1985; Urry, 1988), high polydispersity was reported to be an important drawback when this synthetic strategy was applied to the production of larger or more complex elastin-like chains (McPherson et al., 1992). Recombinant DNA technology (**Figure 2**), which is based on use of state-of-the-art techniques in molecular biology to obtain cell factories, allows the production of advanced, complex and monodisperse biomaterials with absolute control over their composition. This technology opens up the possibility of producing a large number of protein polymers exhibiting any property found in nature, as well as other functions that are not present in living beings but which could be of particular technological interest. This method was first described by Conticello and coworkers for the production of ELRs (McMillan et al., 1999), and nowadays it is well-known that this technology allows the production of monodisperse ELR chains with the desired amino acid sequence and physical properties (Urry et al., 1985; Martín et al., 2010).

The amino acid sequence of ELRs generally comprises repeats of the (VPGXG) pentapeptide, where X is any amino acid except proline. All functional ELRs present a reversible LCST (lower critical solution temperature) phase transition (Urry, 1993).

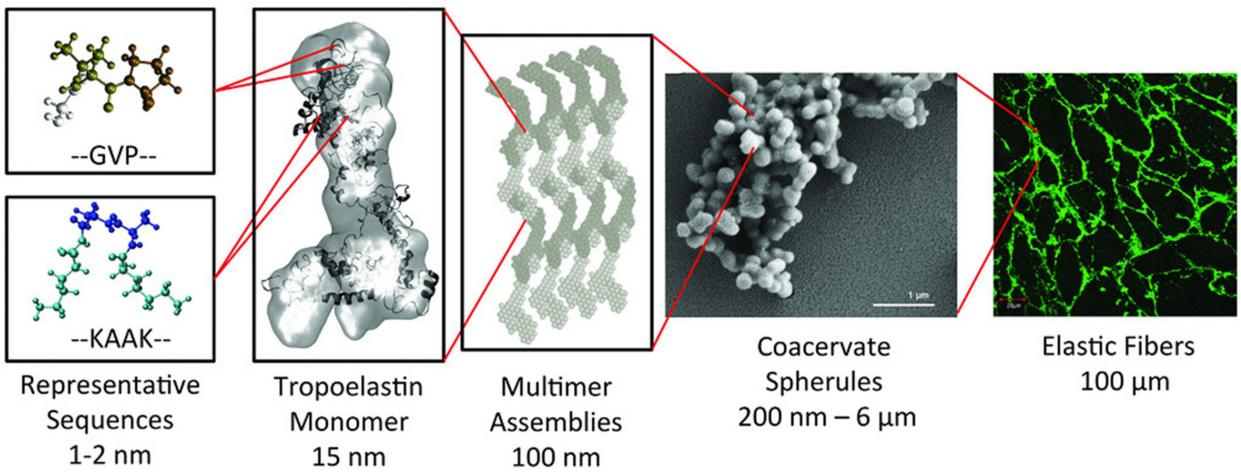

FIGURE 1 | Synopsis of the hierarchical structure of elastic fibers. The monomer of tropoelastin is composed of alternating GVP-rich hydrophobic domains and hydrophilic K-containing cross-linking domains. This monomer assembles into multimer that evolves into spherical aggregate structures. These spherules will form a microfibrillar scaffold to form an elastic fiber. Reproduced with permission from (doi.org/10.1002/mabi.201800250), copyright 2019.

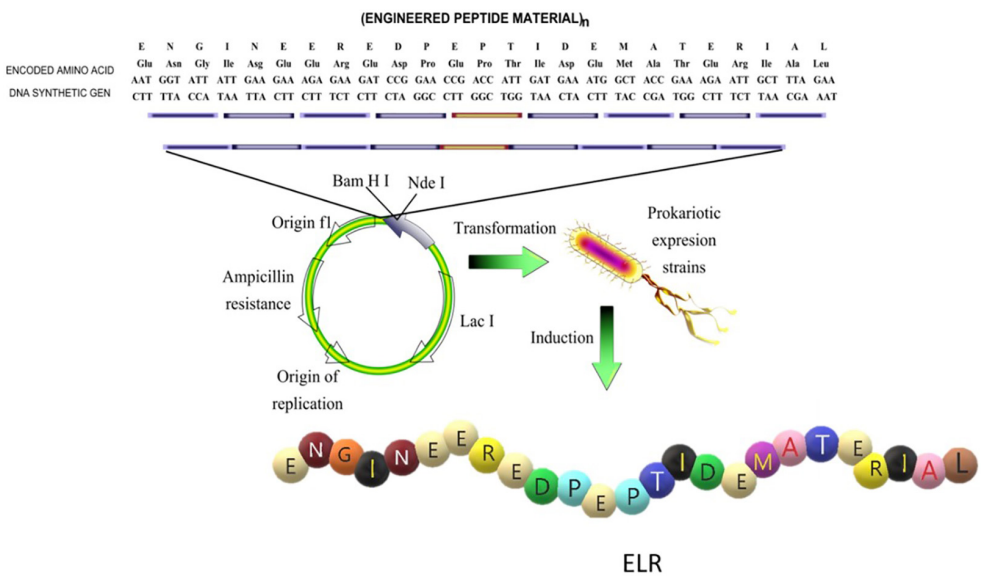

FIGURE 2 | Schematic representation of the design of the sequence and production of an elastin- like recombinamer (ELR). Reproduced with permission from (doi.org/10.1016/j.addr.2018.03.003), copyright 2018.

This means that in aqueous medium, and below the transition temperature (Tt), the polymer chain remains soluble, whereas above this temperature the ELR chains fold hydrophobically into a β-turn (Tamburro et al., 1990; Urry, 1993) and undergo a conformational transition, thus leading to phase separation (Urry et al., 1985; Manno et al., 2001). It has been shown that the LCST of ELRs depends markedly on the amino acid sequence and that, as a consequence, the Tt of an ELR sequence based on $(VPGXG)_n$ can be controlled and fitted to the desired value (within a certain range) by varying the amino acid X at the fourth position (when X is a hydrophobic amino acid, the Tt decreases, and when it is hydrophilic the Tt increases) (Ribeiro et al., 2009). Although the pentapeptide (VPGXG) itself does not confer any biofunctionality on the ELR, recombinant technologies and modular design strategies allow the inclusion of functional epitopes, such as cell-adhesion domains (i.e., RGD) (Nicol et al., 1992; Urry et al., 1998), degradation sequences (i.e., protease-sensitive domains) (Alix, 2001; Girotti et al., 2004), sequences that promote the inclusion of temperature-related or biological triggers (Ulbrich et al., 1982; Miyata et al., 1999) and cross-linking motifs, in specific positions of the ELR backbone. This cross-linking can be of either a physical or a covalent nature, and the relevant mechanisms may involve ionic and hydrophobic interactions or the chemical reaction of complementary groups

(Campoccia et al., 1998; Prestwich et al., 1998; Saha et al., 2020).

Such stimuli-responsive behavior, together with the proven biocompatibility (Urry et al., 1991) and ability to strictly control the molecular composition, and the fact that they can be functionalized, have positioned these ELRs as outstanding candidates for numerous biomedical applications (Rodriguez-Cabello et al., 2010, 2011), particularly as regards nanofiber-based scaffolds. As shown below, ELRs have been widely used to obtain nanofibers using both approaches that take advantage of their molecular self-assembly ability and advanced polymer-processing technologies.

Summarizing, ELRs are versatile materials that can be formulated with a huge variety of designs at aminoacidic level and that can tune their macromolecular appearance, physical behavior and mechanical properties depending on the molecular architecture, functional groups and the presence or absence of a concrete stimuli. Thus, ELRs can be formulated and processed in many different ways to obtain a diversity of structures such as nanoparticles, fibers, microfibers or hydrogels depending on the application field. These application fields comprise a large spectrum of areas in which the ELRs can be used, from protein or drug purification to complex systems for drug or gene-delivery or tissue regeneration through custom-designed scaffolds. González de Torre et al. (2014) obtained ELRs click hydrogels with an elastic moduli in the range 1–10 kPa, which are of widespread interest in tissue engineering application as many native tissues have moduli in this range (∼100 Pa for very soft tissues as fat or brain and ∼ 10.000 Pa for muscle). The ELR hydrogels can be engineered with a set of specific self-assembling domains that induce a sequential gelation mechanism and yield to extrudable bioinks with high printability and stability (Salinas-Fernández et al., 2020). The resulting 3D printing scaffolds, which preserve the structure long-term with high shape fidelity, are excellent candidates for the development of constructs, biological tissues or microorgans for different biomedical applications such as regenerative medicine and the validation of new drugs and therapies (Salinas-Fernández et al., 2020). ELRs have been widely used to obtain nanofibers using both approaches that take advantage of their molecular self-assembly ability and advanced polymer-processing technologies. As an example, ELR microfibrous scaffolds with a fiber width of 1.11 ± 0.45 μm and tensile strength of 0.59 ± 0.08 MPa have been obtained (González de Torre et al., 2018), which perfectly fits the values reported in the literature for fibers used as engineered ECM and, thus, are suitable candidates for tissue engineering or regenerative medicine applications.

SILK-ELASTIN-LIKE RECOMBINAMERS (SELRs) AND SILK-TROPOELASTIN BIOMATERIALS

Silk is an exceptional example of a fibrous protein found in nature (Ling et al., 2018). A variety of organisms, such as spiders and silkworms, produce an array of silk fibers that are used to build proteinaceous scaffolds for protective and hunting purposes. The most common silk sequences exceed 3000 amino acids and consist of the repetition of hydrophobic and hydrophilic blocks, thus conferring an intrinsic amphiphilicity on them. Representative models are the major ampullate spidroins (MaSp1 and MaSp2) of dragline spider silk (Gatesy et al., 2001; Motriuk-Smith et al., 2005) and the heavy chain of *Bombyx mori* (*B. mori*) silk fibroin (Xia et al., 2004). MaSp1 and MaSp2 proteins show a hydrophobic poly(GA) block, containing poly(A) domains, which are flanked by hydrophilic GGX (X = Y, L, Q) and GPGXX (X = Q, G, Y) repeats, respectively (Gaines and Marcotte, 2008). Whereas, the *B. mori* heavy chain comprises repeated GX (X = A, S, T, V) and GAGAGX (X = A, S, Y) domains interspersed by hydrophilic, aromatic and charged motifs (Zhou et al., 2001; Sehnal and Žurovec, 2004).

The combination of hydrophobic and hydrophilic blocks found in native silk proteins (Jin and Kaplan, 2003; Lu et al., 2012) results in the formation of micellar structures (Lin et al., 2017; Parent et al., 2018; Hu et al., 2020) which, by way of a coalescence process triggered by the pH change and shear stress suffered while exiting the spinning duct, evolve into aligned nanofibrils (Holland et al., 2012; Schwarze et al., 2013) comprising β-sheet secondary structures built by assembly of the recurrent poly(A), (GA), and (GAGAGS) regions (Hu et al., 2006; Lewis, 2006).

Recently, the role of the *B. mori* hexapeptide GAGAGS, which is the active motif involved in the formation of H-bonded β-sheet structures, has been investigated by Sun et al. in detail (Sun and Marelli, 2020). As reported by these authors, a multi-step self-assembly pathway is required to structure this disordered motif into β-sheeted nanofibrils. Self-assembly begins once the critical micelle concentration has been exceeded, which induces the formation of micelles that hide the hydrophobic chains from the aqueous phase and minimize the energy of the system. These structures then disassemble, leading to the formation of high energy transient conformations that are able to orderly arrange into secondary β-sheet structures. Morphogenic kinetics slows down at this stage, thus resulting in a progressive increase in the number of β-sheets and silk nanofibrils that branch out from the pre-formed fibers. As these events progress, larger, thicker and stiffer structures arise, thereby conferring remarkable mechanical properties on these silk-like fibers (Sun and Marelli, 2020).

Silk proteins reconstituted from native fibers offer a readily accessible stock with great potential for investigating advanced approaches. Reconstitution of the silk dope involves removal of the adhesive sericins found between the fibers, followed by treatment with lithium salts, which disrupts the H-bonded β-sheet structures, thus disassociating the proteins into individual entities (Heim et al., 2009). Despite the simplicity of this process, the regenerated silk fails to replicate the native properties of silk protein (Shao et al., 2003; Holland et al., 2007; Greving et al., 2010; Wang and Zhang, 2013). This has led to the development of optimized processing methods that are able to circumvent the limitations encountered (Zhou et al., 2018; Guo et al., 2020b; Rizzo et al., 2020).

Alternatively, the emergence of recombinant techniques has allowed the bioproduction and subsequent study of silk-like proteins in greater detail, further offering the possibility to develop hybrid proteinaceous designs containing alternative protein-based sequences, such as elastin (Cappello et al., 1990). This family of polypeptides, known as silk-elastin-like proteins

(SELPs) or recombinamers (SELRs) (Fernández-Colino et al., 2014; Wang et al., 2014), encompasses the silk-like GAGAGS sequence found in the heavy chain of *B. mori* fibroin (Hu et al., 2020), and the consensus elastin-like pentapeptide VPGXG (Acosta et al., 2020a), which includes any amino acid in the fourth position except proline.

The presence of silk-like domains confers the engineered SELR with the ability to self-assemble into fibrillary structures via H-bonded nanocrystalline β-sheet structures (Sun and Marelli, 2020). As such, fibrillary morphogenesis, which is not a prevailing feature of the ELRs (Misbah et al., 2015) but has been successfully imitated by the use of electrospinning techniques (Humenik et al., 2018), can be genetically encoded into the SELR constructs, thus conferring the inherent ability to form fibers comprising bundles of fibrils (Tarakanova and Buehler, 2012). In addition, molecular modeling has demonstrated that the thermoresponsive behavior of the elastin-like sequences is preserved in the SELR and favors the silk β-sheet assembly process (Tarakanova et al., 2017). Increasing the temperature induces the phase transition of the elastin-like domains, which tighten and hydrophobically fold the polypeptide backbone, thereby reducing the distance between the proteinaceous chains while fostering the formation of intramolecular H-bonds. At a molecular level, this rearrangement results in a significant shrinkage of the structure, thus enhancing the mechanical properties of the SELR in its fibrillary state.

Macroscopic evaluation of early silk-elastin-like designs revealed fibrous sponge-like structures typical of silk fibroin (Cappello et al., 1990; Dinner et al., 2000). This observation led to research focussing on understanding the role of elastin and silk-like domains in this fibrillary self-assembly. As reported by Hwang et al., when included as the guest residues in the elastin counterpart, positively charged lysine groups influence the polypeptide arrangement over mica surfaces (Hwang et al., 2009). Depending in the ionic strength, either fibrillary or spherical assemblies aggregate over the substrate. Thus, a weak ionic strength favors an ion-pairing interaction between the positively charged SELR and the negatively charged mica surface, thus providing nucleating sites that lead to the nanofibers. In contrast, an increase in salt concentration hinders this event, thereby directing the self-assembly process toward globular structures instead. Mica substrates, in combination with atomic force microscopy (AFM), can be exploited both to trigger the nucleation and to guide the direction of growth of SELR nanofibers via a bottom-up approach (Chang et al., 2011). Contacting the surface with the AFM tip initiates the nucleation of nanofibers which, given the finely applied pressure, elongate perpendicular to the scanning direction at a fast rate. This morphogenic pathway relies on events occurring at a molecular level. As described, the tip acts by stretching the stabilized and kinetically trapped SELR strands in the β-sheet, thus helping them to acquire transient conformations (Dinner et al., 2000) and therefore surpassing the high energetic barrier required to trigger the nucleation of fibrils (Varongchayakul et al., 2013). The growth stage likely continues with the self-assembly of SELRs into β-sheet structures parallel to the mica surface and perpendicular to the fibril axis drawn by the AFM tip.

Golinska et al. (2013) explored use of the octapeptide GAGAGAGE silk-like domain (Krejchi et al., 1994) to build pH-responsive SELR designs. Upon neutralization of the glutamic acid residue (Martens et al., 2009), this sequence self-assembles into β-roll assemblies (Yoder and Jurnak, 1995) from which fibrillary structures arise (Topilina et al., 2006; Werten et al., 2008). As predicted by molecular dynamics simulations, the slight differences between β-roll and β-sheet structures results in less-crystalline assemblies, and therefore semi-flexible SELR fibrils (Schor et al., 2009). On the other hand, elastin-like domains confer thermoresponsiveness on the construct. Increasing the temperature increases the number of nuclei as well as the fibril growth rate, with the morphological features remaining unaltered. However, the fibrillary structures progressively aggregate with time, undergoing an irreversible coalescence accompanied by a decrease in fiber length. Both the octapeptide GAGAGAGE and the hexapeptide GAGAGS can self-assemble into β-roll structures upon flanking four consecutive silk-like domains with lysine-rich hydrophilic elastin-like blocks in a core-sheath fashion (Zeng et al., 2014a). As reported by these authors, the presence of four consecutive silk-like domains is key to obtaining the β-roll assembly and the formation of nanofibrillar structures. Constructs containing three or fewer silk-like hexapeptides evolve into globular aggregates, whereas assembly is promoted above this threshold, thus resulting in a higher number of shorter fibrils. Switching from positively (lysine-rich) to negatively charged (glutamic acid-rich) elastin-like domains further affect the self-assembly process, via electrostatic interactions, changing the morphogenic pathway to cylindrical aggregates. Hydrophobic interactions also play a key role in the evolution of the structures formed leading, above the T_t of the elastin blocks, to the stacking of β-rolls and lateral coalescence of nanofibers over time.

Tuning the ratio of silk-to-elastin blocks further regulates the SELR self-assembly, providing access, irreversibly and reversibly, to fibrillar and micellar structures, respectively (Xia et al., 2011). As evaluated by circular dichroism (CD), an increase in the silk ratio favors β-sheet self-assembly via H-bonds, thus increasing the irreversible character of the SELR structures formed with time. Similarly, UV spectrometry suggests that an increase in the elastin ratio leads to the reversible formation of aggregates in solution that strongly absorb at 300 nm. The morphology of the structures obtained, as characterized by AFM, confirmed self-assembly of the elastin and silk-like blocks to form micellar to fibrillary structures in the micrometer range. Replica exchange molecular dynamics (REMD) and coarse-grained simulations also allow the effect of the silk-to-elastin ratio on the SELR interactions and fiber assembly to be investigated and predicted on a molecular scale. As described in the literature (Roberts et al., 2018), a high elastin content favors the structural compaction and H-bonding interaction at temperatures above the T_t, thereby reducing the exposed area while decreasing the diameter of the SELR fibers, whereas a high silk content promotes the formation of β-sheet secondary structures that increase the fiber crystallinity and mechanical strength. Both proteinaceous blocks further act synergistically, thus improving the stability and strength of the assembled fibers.

Concentration is an extra parameter that governs the growth of SELR nanofibers. Thus, the micelle-like nanoparticles that arise during the early stages of self-assembly act by increasing the polypeptide density, thus prompting close approach of the silk-like domains, which subsequently self-assemble into nanofibers (Zeng et al., 2014b). Upon reaching this state, the soluble SELR begin to add, via diffusion pathways, to the formed structures, which evolve into different arrangements depending on the concentration. Thus, low SELR concentrations result in local gradients of polypeptide toward the tip of the fibers, whereas high concentrations result in the simultaneous and uniform formation of fibrils that branch out from the formed nanofibers, thus leading to interconnected networks over time. Concentration and the ratio of silk-to-elastin blocks can be exploited together to engineer template-induced fiber formation, that is, SELR constructs that are able to self-assemble into fibrils above a concentration threshold (Willems et al., 2019). Herein, the elastin-like content determines the disordered character of the proteinaceous backbone by limiting silk self-assembly and, thereby, the growth of fibrils at low concentrations. This can be counteracted by increasing the concentration and/or silk-like content, which favors the interaction and coalescence between aggregates, thereby opposing the amorphous character induced by the elastin-like domains and leading to long fibrils.

As described by González et al., the intrinsically disordered and ordered character of SELRs can be exploited to design tailorable proteinaceous platforms for manufacturing morphologically rich fibrillary assemblies that mimic naturally occurring structures present in the natural type. These assemblies, known as biomorphs (Nakouzi and Steinbock, 2016), arise as a result of the effect of the hydrophobic, silk H-bonding and electrostatic interactions on the morphogenic pathway during the SELR desolvation stage, thus modulating and, eventually, arresting the self-assembly and transforming the transient structures into colporate biomorphic spheres (**Figure 3A**). The intrinsic disorder of the elastin-like sequence is required to structurally accommodate the three non-covalent interactions, whereas the silk-like domains kinetically trap the rearrangement of the SELR chains into the complex biomorphs by forming ordered β-sheet structures (González-Obeso et al., 2020).

SELRs have emerged as a versatile source for fibrillary scaffolds with potential applications in tissue engineering and the regenerative medicine field (Kapoor and Kundu, 2016; Aigner et al., 2018; Saric and Scheibel, 2019) as a result of their self-assembly properties and their biocompatible, biodegradable and highly tuneable character (Vepari and Kaplan, 2007; Guo et al., 2020a). For instance, injectable nanofibrillar hydrogels have been designed by combining silk and amphiphilic elastin-like blocks (Fernández-Colino et al., 2014). This configuration self-assembles, as a result of temperature, into micellar structures that evolve into nanofibrils with time. Each event is driven by a different block. Thus, the elastin-like repeats fold hydrophobically above the T_t, triggering the formation of micelles and, thereby, spatial approximation of the silk-like blocks. This reorganization facilitates assembly of the silk domains into β-sheets, thus accelerating the formation of SELR fibrils, which evolve into a fibrous hydrogel, as can be seen in **Figure 3B**.

The synergic interplay between the silk and elastin-like blocks can be further exploited to freeze intermediate self-assembled states in time. This process, termed as pre-annealing treatment, involves incubating the SELR construct at different times while maintaining the temperature above the T_t of the elastin-like block (Cipriani et al., 2018). Optimization of this process allows advanced hydrophobically folded and β-sheeted self-assembled states to be selected (**Figure 3C**), thus conferring direct control over the mechanical properties and gelation time toward fibrous injectable SELR hydrogels. This approach has been explored for cartilage repair by manufacturing scaffolds including cell adhesive RGD sequences that help regenerate the hyaline cartilage in an *ex vivo* osteochondral model. The synergic ability of the elastin-like phase transition and the silk β-sheet self-assembling domains to capture the transient states arising during the formation of fibrillary SELR hydrogels has been recently investigated (Ibáñez-Fonseca et al., 2020). As observed, the different kinetics for the self-assembly of silk and elastin-like domains affect the structure achieved in a time-dependent manner. Initially, the phase-transition of the elastin-like blocks forces the molecule to undergo a rapid and entropically driven transition to a folded state, thus pushing the system to a new energy minimum. The silk-like domains then interact by slow formation of H-bonded β-sheets, thus creating an enthalpic energy barrier that prevents complete phase separation of the SELR from water. This metastable state evolves into a porous hydrogel that becomes kinetically trapped over time and can be seeded with human mesenchymal stem cells (hMSCs) (**Figure 3D**).

Recombinant tropoelastin has also been explored together with silk fibroin for the production of fibrillary structures. A strong complementarity exists between these two proteinaceous materials as a result of their hydrophobic repeats and their opposite net charge, i.e., +38 for tropoelastin and -36 for silk fibroin (Hu et al., 2013). The resulting ion-pairing interactions prompt their spontaneous aggregation which, under the influence of hydrophobic forces, drives the formation of micellar structures from which crystalline β-sheets emerge. Mono- and tri-layered membrane-like structures for treating age-related macular degeneration have been designed using silk-tropoelastin blends (Shadforth et al., 2015). β-sheet structures arise upon 12h of annealing at 60°C, providing a strength and elasticity similar to that of native Bruch's membrane. In addition, both fabricated versions exhibit a cytocompatible character, and can be used as a potential vehicle for co-delivering retinal pigment epithelial cells and tropoelastin into the subretinal space.

ELECTROSPINNING OF ELASTIN-BASED MATERIALS

As mentioned previously, fibers can be obtained from biomaterials using different techniques. One of the most widely applied methods is electrospinning. This is not a new technique as the first reports date back to the early 20th century,

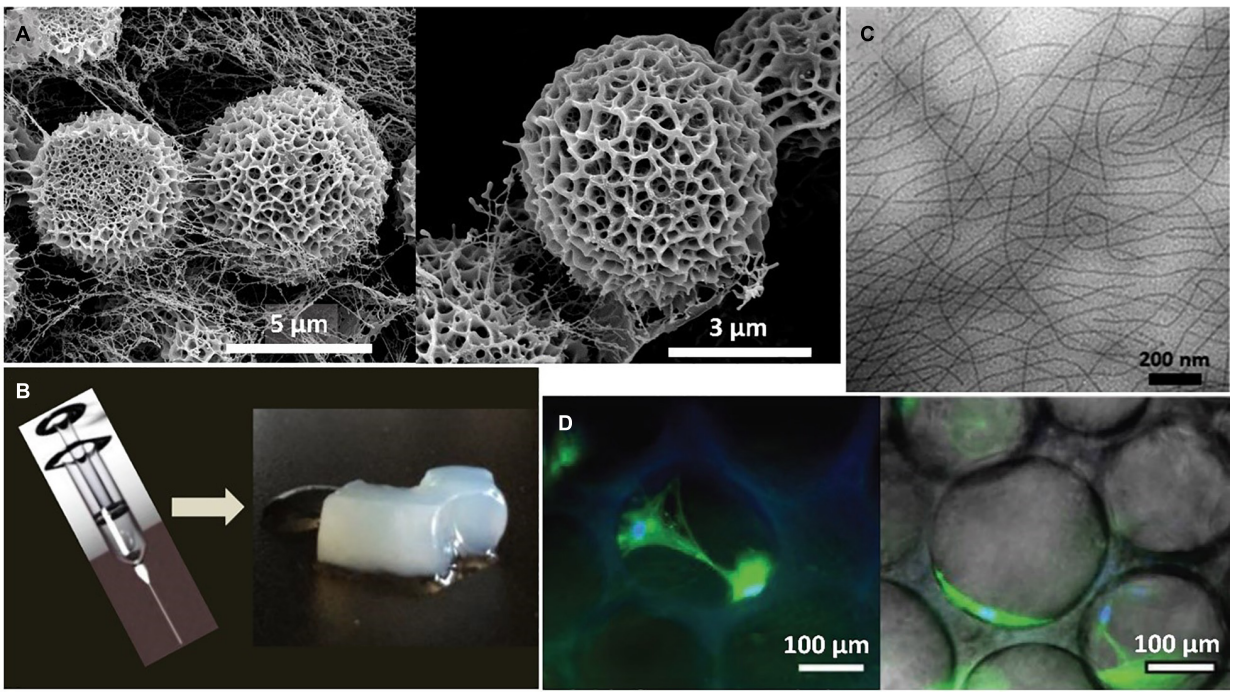

FIGURE 3 | (A) Representative SEM images of the self-assembled biomorphs generated by EI-silk-VKV SELR from 2 mg mL-1 aqueous solutions after 48 h at 37°C reproduced with permission from (doi.org/10.1002/smll.202005191), copyright 2020. **(B)** Representative macroscopic images of the self-assembled hydrogel generated by (EIS)2 SELR from 150 mg mL-1 aqueous solutions after 60 days at 37°C reproduced with permission from (doi.org/10.1021/bm501051t2014), copyright 2014. **(C)** Representative TEM images of the self-assembled fibers generated by (EIS)2-(I5R)6 SELR from 3 mg mL-1 aqueous solutions after 48 h at 37°C reproduced with permission from (doi.org/10.1021/acs.biomac.8b01211), copyright 2018. **(D)** Representative microscopic images of the self-assembled hydrogel generated by $I_{20}K_2$-RGD-$K_2S_6I_{20}$ from 175 mg mL^{-1} aqueous solutions after 14 days post-seeding with human mesenchymal stem cells (hMSCs) at 37°C reproduced with permission from (doi.org/10.1002/smll.202001244), copyright 2020."

although the electrostatic attraction of a liquid had already been observed by various scientists long before that (Tucker et al., 2012). Electrospinning technology has improved drastically since those early days, and the interest in the use of this methodology to create fibers is still increasing, as can be deduced from the large number of scientific papers published in this field every year. Electrospinning can be used to produce polymer fibers with diameters ranging from a few nanometers to several micrometers as a result of the electrical forces produced between two electrodes (Reneker and Yarin, 2008). This technique has become increasingly popular as a huge variety of polymers can be electrospun and because it offers the possibility to obtain fibers in the sub-micrometer range that can be applied in a wide variety of fields, such as filtration, optical electronics, defense, biotechnology and tissue engineering, amongst others (Bhardwaj and Kundu, 2010). Electrospinning is governed by several factors that require fine tuning to obtain fibers with the desired dimensions and properties. Briefly, these factors are applied voltage, flow rate, types of collector, distance between tip and collector, and ambient parameters such temperature and humidity (Reneker and Yarin, 2008; Bhardwaj and Kundu, 2010; Xue et al., 2017, 2019). The paramount importance of these parameters, and how to tune them to obtain the desired properties for the fibers, is beyond the scope of this review. Moreover, other excellent reviews focusing on the importance of these electrospinning parameters can be found in the literature (Reneker and Yarin, 2008; Islam et al., 2019; Xue et al., 2019).

This review is focused on the production of nano- and microfibers from elastin-based materials, especially materials made from recombinant elastin and tropoelastin, both of which have been electrospun under different conditions to obtain a wide variety of fibers for use in several biomedical applications, as will be discussed below.

ELECTROSPUN TROPOELASTIN-BASED FIBERS

As is also the case for many other materials of biological origin, tropoelastin is suitable for electrospinning, typically after dissolution in a low boiling point solvent. Electrospun tropoelastin fibers can be obtained from nano to micron scale and need to be crosslinked after deposition. The resulting scaffolds must be crosslinked prior to use as platforms for tissue regeneration. The crosslinking agent is commonly glutaraldehyde (GA), which can be directly applied in solution or as fume from a 25% aqueous solution. Although hexamethylene diisocyanate (HMDI) has also been used to crosslink these electrospun scaffolds, it has to be carefully washed out to avoid undesirable cytotoxic effects (Nivison-Smith et al., 2010). After crosslinking,

these scaffolds are extremely stable, maintaining their structural integrity for more than 180 days under physiological conditions (Almine et al., 2010). The fiber size, mechanical properties of the scaffolds, and their porosity can be precisely controlled by varying the aforementioned electrospinning parameters (Rnjak-Kovacina et al., 2011, 2012). In this way, highly elastic fibers with a Young's modulus of 265 kPa on randomly aligned fibers, and 111 kPa on aligned ones, while maintaining an ultimate stress (116 kPa) and strain of about 1.5%, have been obtained (Nivison-Smith and Weiss, 2011). Electrospun elastin fibers exhibit a characteristic thin ribbon-like morphology, with diameters ranging from 0.9 to 5.5 μm for tropoelastin and 0.6 to 3.6 μm for α-elastin (Wise et al., 2009). Tropoelastin-based scaffolds exhibit good fibroblast colonization, producing their own extracellular matrix and even obtaining good vascularization in the surrounding tissues as a result of an optimal *in vivo* interaction with the adjacent native tissues (Rnjak et al., 2009; Rnjak-Kovacina et al., 2011). These electrospun tropoelastin-based scaffolds palliate one of the greatest problems that collagen, as a biomaterial, usually exhibits, namely contraction of the scaffold after cell colonization, which in some cases is over 50% of the original size of electrospun collagen scaffolds used in wound healing (Powell and Boyce, 2009) compared with 30% for electrospun tropoelastin scaffolds. These tropoelastin scaffolds have been shown to be cytocompatible with primary human elastic-tissue derived cells such as human fibroblasts (Fb), human umbilical vein endothelial cells (HUVECs) and human coronary artery smooth muscle cells (HCASMCs). Moreover, in the case of human adipose-derived stem cells (HADSCs), the use of electrospun tropoelastin scaffolds in the field of wound healing has been shown to increase the speed of wound closure as well as the epithelial thickness when compared with the untreated controls (Machula et al., 2014). Electrospun tropoelastin scaffolds have been used as a vehicle to deliver stem cells as they mimic the biological and mechanical features of the native extracellular matrix, and electrospun scaffolds loaded with adipose-derived stem cells help the wound-healing process *in vivo* due to their low immunogenicity (Machula et al., 2014).

Another important field in which electrospun tropoelastin scaffolds have been applied is the development of cardiovascular grafts. Thus, McKenna et al. developed a tubular vascular scaffold from tropoelastin with mechanical properties similar to those of native vessels, although the mechanical strength of these scaffolds made them unsuitable for implantation (McKenna et al., 2012). To overcome this problem, tropoelastin-based scaffolds can be co-electrospun with other natural or synthetic polymers (Heydarkhan-Hagvall et al., 2008; McClure et al., 2009, 2012; Zhang X. et al., 2009; Zhang et al., 2010; Rnjak-Kovacina et al., 2012) to create new hybrid materials with improved properties (Lee et al., 2007; Zhang et al., 2007; Han et al., 2011). Such hybrid materials have mainly been used to develop vascular substitutes by electrospinning composite solutions onto a rotating mandrel that acts a cylindrical collector in order to obtain tubular scaffolds. Collagen, PDO (polydioxanone), PLGA (poly(lactide-co-glycolide)), gelatin, PLLA (poly(L-lactide) acid), PLCL (poly(lactide-co-caprolactone)), and PCL (polycaprolactone), amongst others, are the polymers most commonly used in combination with tropoelastin to create these tubular structures (Li et al., 2005, 2006; Sell et al., 2006; Lee et al., 2007; McClure et al., 2010). These co-electrospun scaffolds are intended to mimic both the natural shape of the blood vessels and the internal structure, while maintaining the mechanical properties to withstand the pressure and pulsation of the blood stream (Boland et al., 2004). Approaches based on multilayered electrospun scaffolds have been explored to that end. For instance, a tri-layer scaffold based on collagen I and tropoelastin as biomaterials was investigated by Boland et al. This scaffold had an outer electrospun layer comprising tropoelastin and collagen in a proportion of 20:80 and an internal layer with a proportion of 70:30 (tropoelastin: collagen). Fibroblasts were seeded in the outer layer and smooth muscle cells and endothelial cells were seeded in the inner part of the construct. A layer of smooth muscle cells was added between these two layers to create the third layer of the scaffold. More tri-layered tubular electrospun scaffolds with different compositions and structures have been explored, for instance a synthetic vascular graft comprising an intima layer made exclusively of electrospun tropoelastin and PCL and an adventitia layer made of collagen and a PCL, with the media comprising a mixture of tropoelastin collagen and PCL, was created by McClure et al. (2010, 2012). Similarly, Wise et al. developed a bilayer tubular scaffold based on the sequential deposition of electrospun tropoelastin fibers followed by a mixture of tropoelastin and PCL (80:20) onto a rotating mandrel then crosslinked with glutaraldehyde vapor (Wise et al., 2011). Sequential deposition of electrospun layers of tropoelastin, gelatin and polyglyconate (Thomas et al., 2007), or even more complex mixtures such as tropoelastin, gelatin, poliglecaprone and PCL (Zhang X. et al., 2009), has been used to create these artificial vascular conduits. All these approaches show the extreme versatility of this technique and the almost infinite possibilities for creating mixtures of natural and synthetic polymers with tropoelastin in order to combine the outstanding biocompatibility of tropoelastin with the mechanical properties provided by the other polymers.

Although the vascular field is perhaps the principal target of electrospun tropoelastin-based composite scaffolds, other applications in tissue engineering have been explored. Briefly, Swindle-Reilly et al. created electrospun scaffolds from elastin and PCL with fiber diameters ranging from 400 nm to 1 mm for peripheral nerve regeneration. This scaffold promoted the adhesion and alignment growth of neurites in the direction of the aligned nanofibers (Swindle-Reilly et al., 2014). Similarly, the combination of collagen and elastin has been explored by Rnjak et al. to create electrospun scaffolds as artificial skin for wound healing. These scaffolds combine the best properties of both proteins, thus resulting in optimal scaffold handling and improving the elasticity with respect to collagen-only scaffolds while maintaining excellent cell attachment and proliferation with promising *in vivo* results (Rnjak et al., 2009; Rnjak-Kovacina et al., 2011, 2012).

Electrospun ELR-Based Fibers

Elastin-like recombinamers are suitable materials for processing using different spinning techniques to obtain nano- and

microfibers. For instance, fibers with diameters of a few tens of micrometers have been obtained using ELRs functionalized with silk fibroin (Qiu et al., 2009; Zeng et al., 2014a) using a wet spinning technique. Specifically, a solution of ELR-silk in methanol/water was extruded to obtain coagulated fibers, which were then dried and crosslinked. The diameter of the fibers can be controlled by varying the spinneret size and drawing the fibers during collection. Moreover, fiber patterning can be achieved by using mechanical stimuli to induce nucleation in a specific direction (Chang et al., 2011; Johnson et al., 2012). Some ELRs have been used alone as biomaterials for electrospinning in order to create fibrous scaffolds for tissue-engineering applications (Benitez et al., 2013). For instance, Putzu et al. (2016) developed tubular scaffolds of pure ELRs by using a rotating mandrel as collector electrode. The aim of this work was to create engineered vascular grafts, particularly with an inner layer containing a peptide sequence that promotes specific adhesion of endothelial cells, such as REDV (Arg-Glu-Asp-Val). This tetrapeptide is specifically recognized by the integrin a4b1 found in endothelial cells. The outer part of the scaffold contains the general cell-adhesion sequence RGD (Arg-Gly-Asp) to induce the recruitment of structural cells, such as fibroblasts and muscle cells. These scaffolds had to be stabilized by chemical crosslinking in a 0.1% solution of genipin in acetone, then soaked in phosphate medium to eliminate any harmful residues (Putzu et al., 2016). The same group continued investigating in the same direction to eliminate the use of chemical crosslinkers in order to ensure the total cytocompatibility of the engineered vascular grafts. To that end, they electrospun ELRs containing the GAGAGS (Gly-Ala-Gly-Ala-Gly-Ser) sequence from silk. This sequence spontaneously self-assembles into b-sheets stabilized by hydrogen bonding, thereby stabilizing the whole electrospun fiber. This approach was employed to cover metal stents and catheter balloons for cardiovascular applications (Putzu et al., 2019). Also following this approach, Machado et al. electrospun fibers from two different silk-elastin like polymers (SELPs) to create three-dimensional scaffolds for tissue-engineering applications. The fibers obtained exhibited diameters much smaller than obtained previously (100 ± 12 nm) and the typical ribbon-like morphology of the ELR-based electrospun fibers, thus suggesting that the scaffolds obtained could be suitable for the aforementioned applications (Machado et al., 2013).

In 2018, Gonzalez de Torre et al. were able to create stable electrospun fibers that crosslinked during the flight of the jet from the needle to the collector by simultaneously electrospinning two complementary clickable ELRs. The scaffolds created in this way did not require any further crosslinking or stabilization step. The pure ELR-based fibers obtained exhibited a wrinkled morphology in both randomly oriented and aligned fibers (See **Figures 4**, **5**). These ELR-based click fibers opened up the possibility to creating fibers from different ELRs bearing different bifunctionalities that can be selected depending on the final application. The scaffolds obtained offered a maximum strain of 247.5 ± 36.08% and a mean Young's modulus of 1.73 ± 0.95 MPa while conserving the excellent cytocompatibility of the ELRs, as corroborated by *in vitro* experiments (González de Torre et al., 2018). Similarly, Fernandez-Colino et al. obtained stable ELR-based fibers with a mean diameter of 1.45 ± 0.32 μm from aqueous solutions (1:1 PBS/ethanol v/v). These fibers were collected on a rotating electrode, creating a small caliber tubular vascular graft.

Although recombinant tropoelastin and elastin have been blended with other natural and plastic polymers to obtain electrospun scaffolds, as described previously, ELRs have not been extensively processed together with other polymers to obtain electrospun scaffolds. However, they have been used to functionalize electrospun fibers from other synthetic polymers. Thus, Blit et al. (2012); Wong et al. (2013) modified the surface of electrospun polyurethanes with ELRs to increase the adherence of smooth muscle cells, finding a clear improvement in the cell covering of the substrate.

Table 1 has been included, in order to have a better perspective and a tentative comparation between electrospun fibers from elastin-based materials and other electrospun fibers from proteins used in the biomedical field. As can be seen, fibers from ELRs, SELPs and tropoelastin are in concordance with electrospun fibers from the other materials. Of course, in this table is only recorded a representative sample of all the works performed in this field.

In order to clarify the table the references for each biomaterials hasn't been included and can be found here: Silk references (Cunniff et al., 1994; Zarkoob et al., 2004; Wang et al., 2006; Alessandrino et al., 2008); Collagen references (Li et al., 2005; Venugopal et al., 2005; Casper et al., 2007; Yang et al., 2008); Gelatin references (Huang et al., 2004; Zhang et al., 2005; Songchotikunpan et al., 2008; Zhang S. et al., 2009); ELRs references (Huang et al., 2000; Nagapudi et al., 2002; Tan and Lim, 2006; González de Torre et al., 2018); Tropoelastin references (Li et al., 2005; Mithieux et al., 2009; Nivison-Smith et al., 2010); and SELP references (Ner et al., 2009; Machado et al., 2013).

ZIPPER-ELR

Basic mammalian leucine zipper (B-ZIP) proteins, which have been reported to complex with sequence-specific double-stranded DNA (Vinson et al., 1989), are able to dimerize as a result of the interplay between the two amphipathic alpha-helices present in the leucine zipper structure, which create a stable interhelical salt bridge. The B-ZIP motif is contained in the N-terminal half of two clusters of basic amino acids, while the C-terminal contains an amphipathic amino acid sequence of variable length with a leucine every seven positions. This amphipathic sequence is termed the "leucine zipper" (Landschulz et al., 1988) and regulates the homo- and heterodimerization of B-ZIP proteins. Herein, in order to generate a repeating helical dimerization interface, the alpha-helix overtwists from 3.6 to 3.5 amino acids per turn, allowing the structure to repeat after 7 amino acids (a heptad repeat) or two alpha-helical turns. This coiled-coil structure is described in terms of the nomenclature of seven unique amino acid positions (***a, b, c, d, e, f, and g***) (Hodges et al., 1973), with the ***a*** and ***d*** residues typically being hydrophobic and being located in the "knobs and holes" pattern (predicted by Crick, 1953) along the dimerization interface of the alpha-helix. These amino acids interact with the complementary

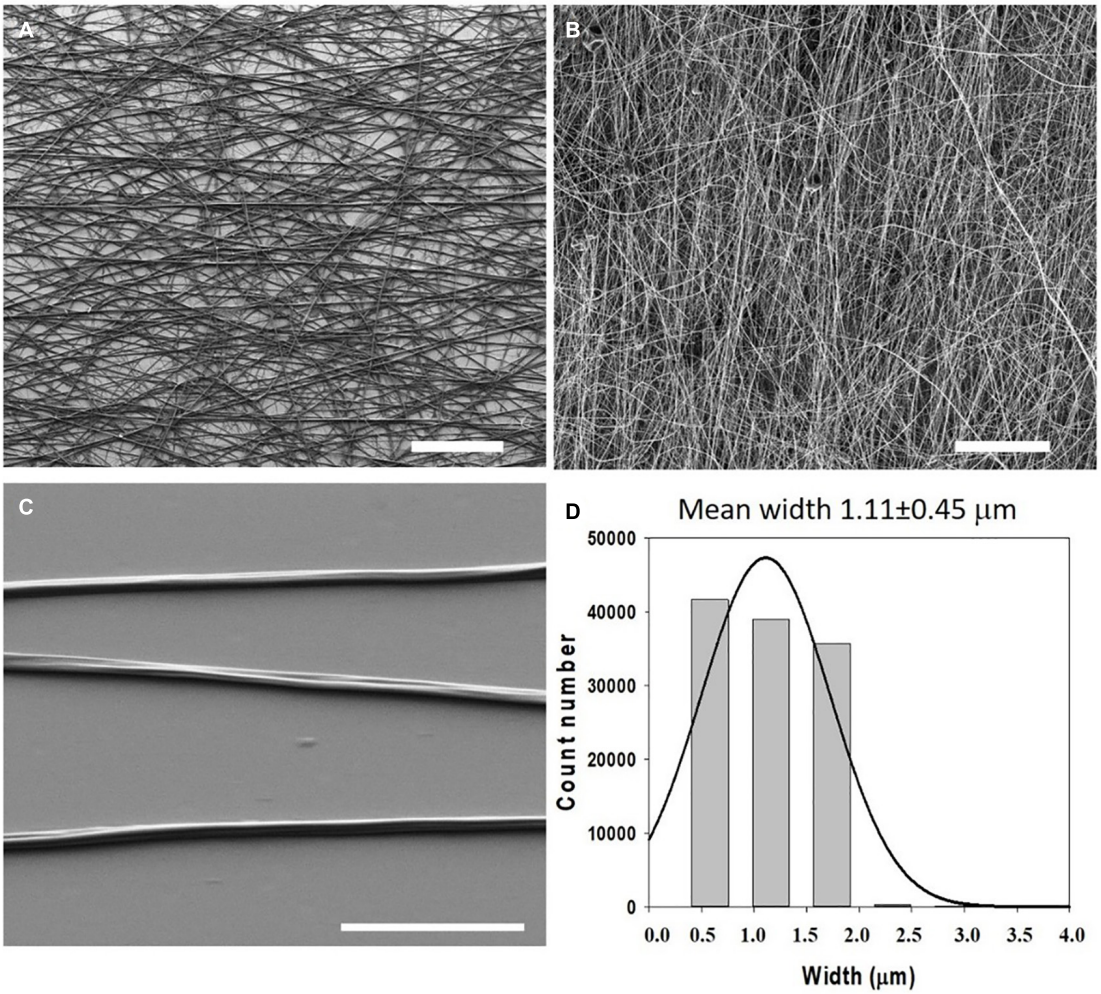

FIGURE 4 | Morphology and dimensions of the first ELR-click fibers. SEM micrographs of ELR-click fibers at different magnifications. Scale bars: **(A,B)** 100 mm, **(C)** 10 mm. **(D)** Statistical distribution of the fiber widths was obtained using the DiameterJ plug-in of Fiji (ImageJ). Fitting to a Gaussian distribution (continuous line) gave a mean width of 1.11 ± 0.45 mm. Reproduced with permission from: (doi.org/10.1016/j.actbio.2018.03.027), copyright 2018.

a′ and ***d′*** amino acid positions of the opposite monomer (refers to the second alpha-helix in the dimer), thus providing the hydrophobic core essential for dimer stability (Thompson et al., 1993). In contrast, the ***g*** and ***e*** positions are typically charged amino acids (Cohen and Parry, 1990; Vinson et al., 1993) which, when forming attractive or repulsive interhelical electrostatic interactions between ***g*** and ***e′***, referred to as i + 5 and i + 2 salt bridges (Marqusee and Baldwin, 1987; Cohen and Parry, 1990), can regulate both homo- and heterodimerization (see **Figure 6**). Furthermore, the Van der Waal interactions between ***g*** and ***e′*** methylene groups and the underlying ***a*** and ***d*** residues contribute to stability. Human B-ZIP domains have been classified into 12 families depending on the amino acids present in the ***a, d, e,*** and ***g*** positions, which appear to be critical for leucine zipper dimerization specificity (oligomerization, dimerization stability, and dimerization specificity). These have given rise to 12 families of B-ZIP with different properties, those that favor homodimerization (PAR, CREB, Oasis, and ATF6), those that favor both homo- and heterodimerization (C/EBP, ATF4, ATF2, JUN, and the small MAFs) and those that favor heterodimerization (FOS, CNC, and large MAFs; Vinson et al., 2002).

The inclusion of folded heptad repeats in the above-mentioned helical conformation can lead to the formation of fibrillary nanostructures (Herrmann and Aebi, 2004; Ryadnov et al., 2008). As described, oppositely charged sticky ends can prompt longitudinal propagation of the two-stranded α-helical coiled-coil zippers, thus yielding micrometric fibers (Pandya et al., 2000; Papapostolou et al., 2007). Specifically, the lateral association driving fibrillogenesis arises from the regularly spaced and complementary regions which, when interconnected by weak electrostatic forces, can extend and stabilize into filamentous assemblies. Indeed, the presence of salts as well as substitution of the sticky ends for blunt tails can disrupt this morphogenic pathway, thus resulting in coiled-coil assemblies that are unable to associate longitudinally. The tetrameric acidic

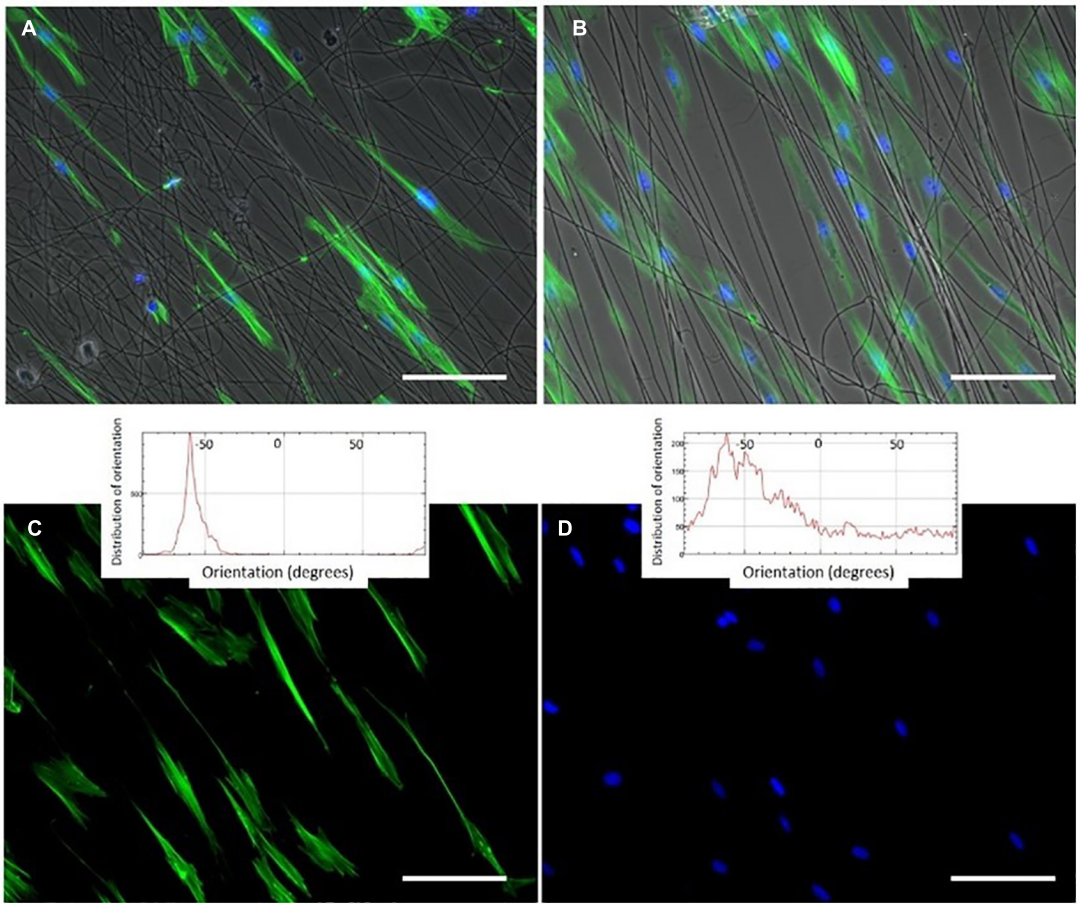

FIGURE 5 | Phalloidin and DAPI staining (green (cytoplasm) and blue (nucleus)) of oriented HFF-1 cells on ELR-click fibers. All channels are merged in panels **(A,B)**, whereas images **(C,D)** show the green and blue channels for cytoplasm and nucleus staining, respectively, for a better visualization of the extended morphology of the aligned HFF-1 cells. The inserts represent the orientation data for the cytoplasm and nucleus, respectively. Scale bars: 50 mm. Reproduced with permission from: (doi.org/10.1016/j.actbio.2018.03.027), copyright 2018.

TABLE 1 | Properties and applications of different protein-based electrospun scaffolds.

Protein	Diameter (nm)	Tensile strength (MPa)	Young's modulus (MPa)	Strain at break (%)	Applications
Silk	6.5–200	875–972	11–13	17–18	GBM, VTE, TE
Collagen	100–6000	8–12	262 ± 18	—	TE, GBM, WH, VTE
Gelatin	125–691	2.50	105	64	TE, WH
ELR	300–1500	0.59-43.3	1.73-1800	2.3-247.5	TE, GBM, WH
Tropoelastin	900–2700	13	289	—	TE
SELP	92–1593	30.8	880	7.9	GBM, TE

and basic leucine-zipper dendrimers designed by the Ghosh group (Zhou et al., 2004) are one example of molecules that can form monodisperse and fibrillar micrometric structures from zipper sequences. Upon combination of both complexes, the hydrophobic and hydrophilic, i.e., pH-sensitive, regions self-assemble, driving the formation of helical secondary structures. This process continues with the lateral and longitudinal fusion of the repeating units, thus initiating fibrillogenesis and propagating the growth of fibers width- and lengthways, respectively. The Rodriguez-Cabello group has described the molecular assembly of elastin-like recombinamers with the hepatic leukemia factor HLF B-ZIP domains from the PAR family in self-assembling, temperature-triggered systems (**Figure 6B**; Fernández-Colino et al., 2015; Salinas-Fernández et al., 2020). Herein, the leucine zipper domains form amphipathic alpha-helical structures that interact hydrophobically, thereby promoting association into a coiled-coil supramolecular structure. This structure provides initial stability to the formation of fibrous hydrogels and to

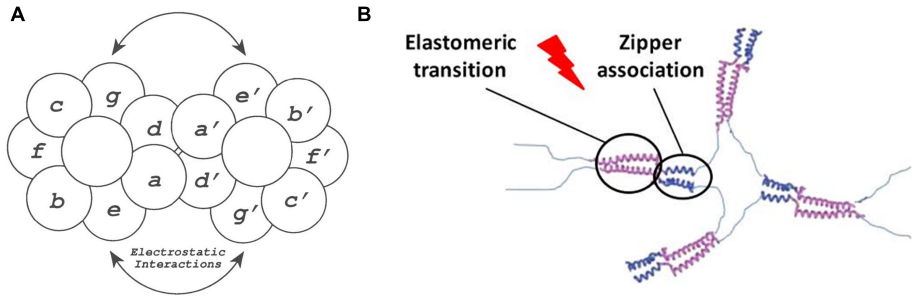

FIGURE 6 | (A) Schematic representation of the zipper dimerization interface, where the 7 amino acids forming the alpha-helical turns are represented with letters. Herein ***a*** and *d′* amino acids form the hydrophobic interactions, whereas ***e*** and ***g′*** amino acids form the electrostatic interactions reproduced with permission from (doi: 10.1101/gad.7.6.1047), copyright 1993. **(B)** Schematic representation of the elastin-like phase transition, represented in purple, and the dimerization of leucine zipper domains, represented in blue, in the formation of a ELR hydrogel reproduced with permission from (doi: 10.1021/acs.biomac.5b01103), copyright 2015.

the development of a sequential three-stage gelation bioink that demonstrated the viability and proliferation of HFF-1 cells within the printed fibers.

AMP-ELRs

Natural and engineered antimicrobial peptides (AMPs) are generally short cationic peptides (10-50 amino acids). AMPs have attracted great interest in the treatment of bacterial infections, and their amphipathic nature also opens up the possibility of developing supramolecular nanostructures, such as fibers (Liu et al., 2013), nanoparticles (Goel et al., 2018), nanoribbons, or hydrogels (Veiga et al., 2012; Jiang et al., 2015; Baral et al., 2016; Nandi et al., 2017; Ye et al., 2019). For example, the AMPs GL13K and 1018 are able to self-assemble into stable secondary β-sheet structures (Haney et al., 2017; Ye et al., 2019), which can enable the organization of intrinsically disordered protein polymers (IDPPs) into hierarchical architectures. Acosta et al. described two hybrid recombinant AMP-ELRs using the AMPs GL13K and 1018 that allowed the development of small nanofibers based on a dual-assembly process. First, the interaction between AMP domains promotes the formation of nanofibers, which evolve into fibrillary aggregates in a synergic process driven by the thermoresponsive phase transition of the ELRs above the T_t (Acosta et al., 2020b) (See **Figure 7**). These authors also observed longer fibrils in the case of 1018 AMP-ELR, probably due to the higher tendency to create β-sheet conformations in solution at the same pH (Moussa et al., 2019). Furthermore, the tailorable functionality of these AMP-ELR nanofibers broadens their use for biomedical applications.

OTHER ELR-BASED FIBERS

Incorporation of the laminin-1 sequence IKVAV into the ELR backbone has been explored to develop scaffolds capable of supporting neurotization (dos Santos et al., 2019). This sequence, which is responsible for promoting neuron cell attachment, migration and neurite outgrowth (Nomizu et al., 1995; Silva et al., 2004), confers fibrillary self-assembly properties on the elastin-based polypeptide chain, thus leading to irreversible association into fibrils. This self-assembly response and functionality, which is absent from the scrambled version including the VKAIV pentapeptide, was successfully exploited to manufacture polyethylene glycol crosslinked hydrogels that are able to support sensory neuron growth and promote neurite lengthening upon *in vivo* implantation in mice.

Finding inspiration in two hydrophobic motifs from tropoelastin (Wise et al., 2014), the Ohtsuki group designed an elastin-like pentapeptide with the ability to self-assemble into fibers (Le et al., 2017). The pentapeptide VGGVG spontaneously associates into secondary β-sheet structures, thus leading to the formation of beaded nanofibers. As electrostatic repulsion has been shown to negatively affect VGGVG fibrillogenesis, the inclusion of a positively charged tail, i.e., the KAAK tetramer, impaired the VGGVG self-assembly process, thus limiting the formation of β-sheets and slowing the kinetics toward thinner beaded nanofibers. Further addition of the cell-adhesive RGD domain conferred the intended bioactivity on the construct, although subsequent enhancement of the repulsive forces hindered the coalescence of nanoparticles on the forming nanofibers, thus decreasing the content of β-sheets. Subsequent studies revealed the dependence of self-assembly on the VGGVG content per molecule. As reported (Sugawara-Narutaki et al., 2019), an increase in the proportion of VGGVG favors the formation of β-sheet structures, thus leading to the morphogenic alignment and coalescence of nanoparticles into branched nanofibers, which laterally assemble to form bundles over time.

Alternative ELR designs, including the alanine-rich regions contained in the crosslinking domains of tropoelastin, i.e., $(APGVGV)_x$ and $(KAA(A)K)_n$ (Wise et al., 2014; Vrhovski and Weiss, 1998), have been described to undergo fibrillary morphogenesis (Djajamuliadi et al., 2020). Upon varying the temperature, this family of constructs undergoes a conformational transition from random coil to ordered secondary α-helix structures. This rearrangement, which was observed by solid-state nuclear magnetic resonance (SSNMR)

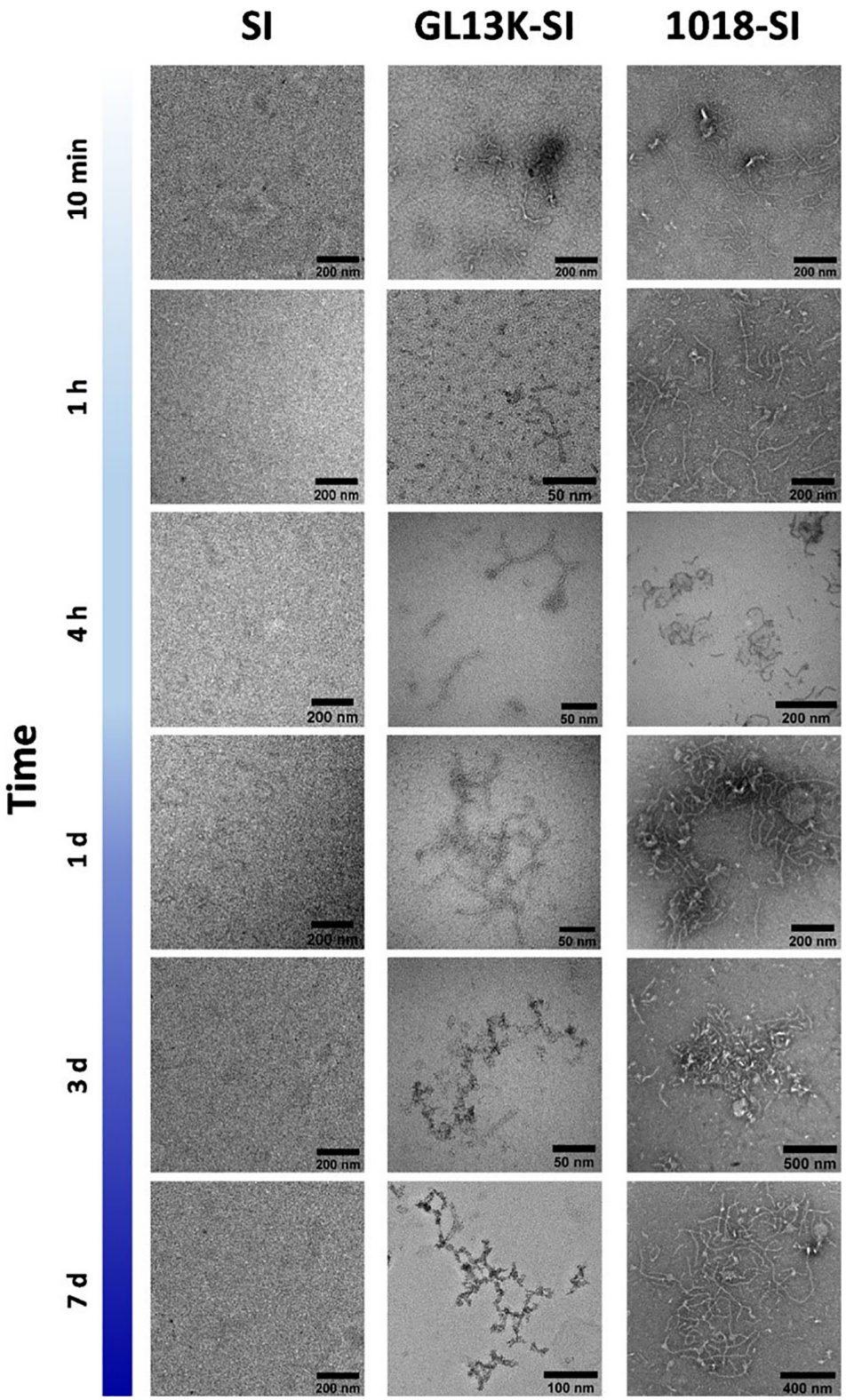

FIGURE 7 | Representative TEM micrographs of small nanofibers formed by hybrid AMP-ELRs (GL13K-SI and 1018 SI), compared with control ELR (SI), after incubation at 5°C. Reproduced with permission from (doi:10.1021/acs.biomac.0c00865), copyright 2020.

spectroscopy in tandem with strategic isotopic labeling, correlates with the association of native elastin into fibers during elastogenesis (Muiznieks et al., 2003).

Oppositely charged ELRs have also been described to serve as building blocks for the manufacture of electrostatically driven fibrillary structures (Lee et al., 2001). Thus, fibrillogenesis occurs upon mixing a glutamic acid-rich with a lysine-rich ELR designed to contain an equal number and distribution of charged residues. Carbodiimide crosslinking of the assembled filamentous structures further leads to fibrous and transparent hydrogels that show a reversible anisotropic swelling behavior, becoming cloudy with increasing temperature.

CONCLUSION

In this review, several procedures to obtain fibers and fibrous scaffolds from elastin-based materials have been described, from self-assembly processes to electrospinning. ELRs offer the possibility to modulate or adjust their structure from the designing stage which means the possibility to create new ELRs with specific properties, focused, in this case, on the formation of nanofibers. This is a huge advantage because we can obtain polymers with unique properties, but this requires designing, produce and purify new polymers that could not be an easy task and a deep molecular knowledge of the ELRs to be designed.

Although electrospinning is not a cutting-edge technology to obtain fibers and finally fibrous scaffolds to better mimic the microarchitecture of the ECM to be used in tissue engineering, it is a very versatile technique that can be used with a huge range of materials and concretely with elastin-based materials. Of course, some weaknesses can be found in this way to obtain fibers, and concretely fibers form elastin-based materials, as for instance a precise control of the spatial disposition of the nano or microfibers obtained, or the fact that many parameters (temperature, humidity, voltage, distance, and others) can affect to the quality of the fibers, but once the process is optimized the reproducibility obtaining electrospun fibrous scaffolds is quite high. Moreover, the use of potentially harmful solvent has been already avoided as was described in the previous pages. It is true that perhaps the 3D printing technologies could in a future substitute the use of electrospun scaffolds but the fiber dimensions and versatility in the use of biomaterials that electrospinning already offers to material researchers are still far from the reach of 3D printing technology and the use of it, is still a beautiful promise, at least at these levels. Therefore, electrospinning is still a technique that will continue evolving and used for the obtention of fibrous scaffolds.

AUTHOR CONTRIBUTIONS

IG, IM, MG-P, and FG-P participated in writing tasks. IG coordinated the writing tasks. JR-C directed, supervised, coordinated, and corrected the review. All authors contributed to the article and approved the submitted version.

FUNDING

The authors are grateful for the funding from the Spanish Government (MAT2016-78903-R, FPU15-00448, FPU16-04015 and PID2019-110709RB-100), Junta de Castilla y León (VA317P18, Infrared2018-UVA06), Interreg V. España Portugal POCTEP (0624_2IQBIONEURO_6_E), and Centro en Red de Medicina Regenerativa y Terapia Celular de Castilla y León.

REFERENCES

Acosta, S., Quintanilla-Sierra, L., Mbundi, L., Reboto, V., and Rodríguez-Cabello, J. C. (2020a). Elastin-like recombinamers: deconstructing and recapitulating the functionality of extracellular matrix proteins using recombinant protein polymers. *Adv. Funct. Mater.* 30:1909050. doi: 10.1002/adfm.201909050

Acosta, S., Ye, Z., Aparicio, C., Alonso, M., and Rodríguez-Cabello, J. C. (2020b). Dual self-assembled nanostructures from intrinsically disordered protein polymers with LCST behavior and antimicrobial peptides. *Biomacromolecules.* 21, 4043–4052.

Aigner, T. B., DeSimone, E., and Scheibel, T. (2018). Biomedical applications of recombinant silk-based materials. *Adv. Mater.* 30:1704636. doi: 10.1002/adma.201704636

Alessandrino, A., Marelli, B., Arosio, C., Fare, S., Tanzi, M. C., and Freddi, G. (2008). Electrospun silk fibroin mats for tissue engineering. *Eng. Life Sci.* 8, 219–225. doi: 10.1002/elsc.200700067

Alix, A. J. (2001). A turning point in the knowledge of the structure-function-activity relations of elastin. *J. Soc. Biol.* 195, 181–193.

Almine, J. F., Bax, D. V., Mithieux, S. M., Nivison-Smith, L., Rnjak, J., Waterhouse, A., et al. (2010). Elastin-based materials. *Chem. Soc. Rev.* 39:3371. doi: 10.1039/b919452p

Almine, J. F., Wise, S. G., and Weiss, A. S. (2012). Elastin signaling in wound repair. *Birth Defects Res. Part C Embryo Today Rev.* 96, 248–257. doi: 10.1002/bdrc.21016

Baral, A., Roy, S., Ghosh, S., Hermida-Merino, D., Hamley, I. W., and Banerjee, A. (2016). A peptide-based mechano-sensitive, proteolytically stable hydrogel with remarkable antibacterial properties. *Langmuir* 32, 1836–1845.

Bellingham, C. M., Woodhouse, K. A., Robson, P., Rothstein, S. J., and Keeley, F. W. (2001). Self-aggregation characteristics of recombinantly expressed human elastin polypeptides. *Biochim. Biophys. Acta - Protein Struct. Mol. Enzymol.* 1550, 6–19. doi: 10.1016/S0167-4838(01)00262-X

Benitez, P. L., Sweet, J. A., Fink, H., Chennazhi, K. P., Nair, S. V., Enejder, A., et al. (2013). Sequence-Specific crosslinking of electrospun, elastin-like protein preserves bioactivity and native-like mechanics. *Adv. Healthc. Mater.* 2, 114–118. doi: 10.1002/adhm.201200115

Bhardwaj, N., and Kundu, S. C. (2010). Electrospinning: a fascinating fiber fabrication technique. *Biotechnol. Adv.* 28, 325–347. doi: 10.1016/j.biotechadv.2010.01.004

Blit, P. H., Battiston, K. G., Yang, M., Santerre, J. P., and Woodhouse, K. A. (2012). Electrospun elastin-like polypeptide enriched polyurethanes and their interactions with vascular smooth muscle cells. *Acta Biomater.* 8, 2493–2503. doi: 10.1016/j.actbio.2012.03.032

Boland, E. D., Matthews, J. A., Pawlowski, K. J., Simpson, D. G., Wnek, G. E., and Bowlin, G. L. (2004). Electrospinning collagen and elastin: preliminary vascular tissue engineering. *Front. Biosci.* 9, 1422–1432. doi: 10.2741/1313

Brown-Augsburger, P., Tisdale, C., Broekelmann, T., Sloan, C., and Mecham, R. P. (1995). Identification of an elastin cross-linking domain that joins three peptide chains. *J. Biol. Chem.* 270, 17778–17783. doi: 10.1074/jbc.270.30.17778

Campoccia, D., Doherty, P., Radice, M., Brun, P., Abatangelo, G., and Williams, D. F. (1998). Semisynthetic resorbable materials from hyaluronan esterification. *Biomaterials* 19, 2101–2127.

Cappello, J., Crissman, J., Dorman, M., Mikolajczak, M., Textor, G., Marquet, M., et al. (1990). Genetic engineering of structural protein polymers. *Biotechnol. Prog.* 6, 198–202. doi: 10.1021/bp00003a006

Casper, C. L., Yang, W., Farach-Carson, M. C., and Rabolt, J. F. (2007). Coating electrospun collagen and gelatin fibers with perlecan domain I for increased growth factor binding. *Biomacromolecules* 8, 1116–1123. doi: 10.1021/bm061003s

Chang, J., Peng, X.-F., Hijji, K., Cappello, J., Ghandehari, H., Solares, S. D., et al. (2011). Nanomechanical stimulus accelerates and directs the self-assembly of silk-elastin-like nanofibers. *J. Am. Chem. Soc.* 133, 1745–1747. doi: 10.1021/ja110191f

Cipriani, F., Krüger, M., De Torre, I. G., Sierra, L. Q., Rodrigo, M. A., Kock, L., et al. (2018). Cartilage regeneration in preannealed silk elastin-like co-recombinamers injectable hydrogel embedded with mature chondrocytes in an ex vivo culture platform. *Biomacromolecules* 19, 4333–4347. doi: 10.1021/acs.biomac.8b01211

Cohen, C., and Parry, D. A. D. (1990). α−Helical coiled coils and bundles: how to design an α−helical protein. *Proteins Struct. Funct. Bioinforma.* 7, 1–15.

Crick, F. H. C. (1953). The packing of α-helices: simple coiled-coils. *Acta Crystallogr.* 6, 689–697.

Cunniff, P. M., Fossey, S. A., Auerbach, M. A., Song, J. W., Kaplan, D. L., Adams, W. W., et al. (1994). Mechanical and thermal properties of dragline silk from the spider Nephila clavipes. *Polym. Adv. Technol.* 5, 401–410. doi: 10.1002/pat.1994.220050801

Dinner, A. R., Šali, A., Smith, L. J., Dobson, C. M., and Karplus, M. (2000). Understanding protein folding via free-energy surfaces from theory and experiment. *Trends Biochem. Sci.* 25, 331–339. doi: 10.1016/S0968-0004(00)01610-8

Djajamuliadi, J., Ohgo, K., and Kumashiro, K. K. (2020). A two-state model describes the temperature-dependent conformational equilibrium in the alanine-rich domains in Elastin. *J. Phys. Chem. B* 124, 9017–9028.

dos Santos, B. P., Garbay, B., Pasqua, M., Chevron, E., Chinoy, Z. S., Cullin, C., et al. (2019). Production, purification and characterization of an elastin-like polypeptide containing the Ile-Lys-Val-Ala-Val (IKVAV) peptide for tissue engineering applications. *J. Biotechnol.* 298, 35–44.

Fernández-Colino, A., Arias, F. J., Alonso, M., and Carlos Rodríguez-Cabello, J. (2014). Self-organized ECM-mimetic model based on an amphiphilic multiblock silk-elastin-like corecombinamer with a concomitant dual physical gelation process. *Biomacromolecules* 15, 3781–3793. doi: 10.1021/bm501051t

Fernández-Colino, A., Arias, F. J., Alonso, M., and Rodríguez-Cabello, J. C. (2015). Amphiphilic elastin-like block co-recombinamers containing leucine zippers: cooperative interplay between both domains results in injectable and stable hydrogels. *Biomacromolecules* 16, 3389–3398. doi: 10.1021/acs.biomac.5b01103

Foster, J. A., Bruenger, E., Gray, W. R., and Sandberg, L. B. (1973). Isolation and amino acid sequences of tropoelastin peptides. *J. Biol. Chem.* 248, 2876–2879.

Frantz, C., Stewart, K. M., and Weaver, V. M. (2010). The extracellular matrix at a glance. *J. Cell Sci.* 123, 4195–4200. doi: 10.1242/jcs.023820

Friedl, P. (2004). Prespecification and plasticity: shifting mechanisms of cell migration. *Curr. Opin. Cell Biol.* 16, 14–23. doi: 10.1016/j.ceb.2003.11.001

Gaines, W. A. IV, and Marcotte, W. R. Jr. (2008). Identification and characterization of multiple Spidroin 1 genes encoding major ampullate silk proteins in Nephila clavipes. *Insect Mol. Biol.* 17, 465–474. doi: 10.1111/j.1365-2583.2008.00828.x

Galbraith, C. G., and Sheetz, M. P. (1998). Forces on adhesive contacts affect cell function. *Curr. Opin. Cell Biol.* 10, 566–571. doi: 10.1016/S0955-0674(98)80030-6

Gatesy, J., Hayashi, C., Motriuk, D., Woods, J., and Lewis, R. (2001). Extreme diversity, conservation, and convergence of spider silk fibroin sequences. *Science (80-.).* 291, 2603–2605. doi: 10.1126/science.1057561

Geiger, B., Bershadsky, A., Pankov, R., and Yamada, K. M. (2001). Transmembrane extracellular matrix-cytoskeleton crosstalk. *Nat. Rev. Mol. Cell Biol.* 2, 793–805. doi: 10.1038/35099066

Girotti, A., Reguera, J., Rodríguez-Cabello, J. C., Arias, F. J., Alonso, M., and Testera, A. M. (2004). Design and bioproduction of a recombinant multi(bio)functional elastin-like protein polymer containing cell adhesion sequences for tissue engineering purposes. *J. Mater. Sci.: Mater. Med.* 15, 479–484. doi: 10.1023/B:JMSM.0000021124.58688.7a

Goel, R., Garg, C., Gautam, H. K., Sharma, A. K., Kumar, P., and Gupta, A. (2018). Fabrication of cationic nanostructures from short self-assembling amphiphilic mixed α/β-pentapeptide: potential candidates for drug delivery, gene delivery, and antimicrobial applications. *Int. J. Biol. Macromol.* 111, 880–893. doi: 10.1016/j.ijbiomac.2018.01.079

Golinska, M. D., Pham, T. T. H., Werten, M. W. T., de Wolf, F. A., Cohen Stuart, M. A., and van der Gucht, J. (2013). Fibril formation by pH and temperature responsive silk-elastin block copolymers. *Biomacromolecules* 14, 48–55. doi: 10.1021/bm3011775

González de Torre, I., Ibáñez-Fonseca, A., Quintanilla, L., Alonso, M., and Rodríguez-Cabello, J. C. (2018). Random and oriented electrospun fibers based on a multicomponent, *in situ* clickable elastin-like recombinamer system for dermal tissue engineering. *Acta Biomater.* 72, 137–149. doi: 10.1016/j.actbio.2018.03.027

González de Torre, I., Santos, M., Quintanilla, L., Testera, A., Alonso, M., and Rodríguez Cabello, J. C. (2014). Elastin-like recombinamer catalyst-free click gels: characterization of poroelastic and intrinsic viscoelastic properties. *Acta Biomater.* 10, 2495–2505. doi: 10.1016/j.actbio.2014.02.006

González-Obeso, C., González-Pérez, M., Mano, J. F., Alonso, M., and Rodríguez-Cabello, J. C. (2020). Complex morphogenesis by a model intrinsically disordered protein. *Small* 16:2005191. doi: 10.1002/smll.202005191

Gordon, M. K., and Hahn, R. A. (2010). Collagens. *Cell Tissue Res.* 339, 247–257. doi: 10.1007/s00441-009-0844-4

Greving, I., Dicko, C., Terry, A., Callow, P., and Vollrath, F. (2010). Small angle neutron scattering of native and reconstituted silk fibroin. *Soft. Matter* 6, 4389–4395. doi: 10.1039/C0SM00108B

Guo, C., Li, C., and Kaplan, D. L. (2020a). Enzymatic degradation of bombyx mori silk materials: a review. *Biomacromolecules* 21, 1678–1686. doi: 10.1021/acs.biomac.0c00090

Guo, C., Li, C., Vu, H. V., Hanna, P., Lechtig, A., Qiu, Y., et al. (2020b). Thermoplastic moulding of regenerated silk. *Nat. Mater.* 19, 102–108. doi: 10.1038/s41563-019-0560-8

Han, J., Lazarovici, P., Pomerantz, C., Chen, X., Wei, Y., and Lelkes, P. I. (2011). Co-electrospun blends of PLGA, gelatin, and elastin as potential nonthrombogenic scaffolds for vascular tissue engineering. *Biomacromolecules* 12, 399–408. doi: 10.1021/bm101149r

Haney, E. F., Wu, B. C., Lee, K., Hilchie, A. L., and Hancock, R. E. W. (2017). Aggregation and its influence on the immunomodulatory activity of synthetic innate defense regulator peptides. *Cell Chem. Biol.* 24, 969–980.

Heim, M., Keerl, D., and Scheibel, T. (2009). Spider silk: from soluble protein to extraordinary fiber. *Angew. Chemie Int. Ed.* 48, 3584–3596. doi: 10.1002/anie.200803341

Herrmann, H., and Aebi, U. (2004). Intermediate filaments: molecular structure, assembly mechanism, and integration into functionally distinct intracellular scaffolds. *Annu. Rev. Biochem.* 73, 749–789. doi: 10.1146/annurev.biochem.73.011303.073823

Heydarkhan-Hagvall, S., Schenke-Layland, K., Dhanasopon, A. P., Rofail, F., Smith, H., Wu, B. M., et al. (2008). Three-dimensional electrospun ECM-based hybrid scaffolds for cardiovascular tissue engineering. *Biomaterials* 29, 2907–2914. doi: 10.1016/j.biomaterials.2008.03.034

Hinek, A. (1997). Elastin receptor and cell-matrix interactions in heart transplant-associated arteriosclerosis. *Arch. Immunol. Ther. Exp. (Warsz).* 45, 15–29.

Hodges, R. S., Sodek, J., Smillie, L. B., and Jurasek, L. (1973). Tropomyosin: amino acid sequence and coiled-coil structure. *Cold Spring Harbor Symp. Quant. Biol.* 37, 299–310.

Holland, C., Terry, A. E., Porter, D., and Vollrath, F. (2007). Natural and unnatural silks. *Polymer (Guildf).* 48, 3388–3392. doi: 10.1016/j.polymer.2007.04.019

Holland, C., Urbach, J. S., and Blair, D. L. (2012). Direct visualization of shear dependent silk fibrillogenesis. *Soft. Matter.* 8, 2590–2594. doi: 10.1039/C2SM06886A

Hu, L., Han, Y., Ling, S., Huang, Y., Yao, J., Shao, Z., et al. (2020). Direct observation of native silk fibroin conformation in silk gland of bombyx mori silkworm. *ACS Biomater. Sci. Eng.* 6, 1874–1879. doi: 10.1021/acsbiomaterials.9b01586

Hu, X., Kaplan, D., and Cebe, P. (2006). Determining beta-sheet crystallinity in fibrous proteins by thermal analysis and infrared spectroscopy. *Macromolecules* 39, 6161–6170. doi: 10.1021/ma0610109

Hu, X., Tang-Schomer, M. D., Huang, W., Xia, X. X., Weiss, A. S., and Kaplan, D. L. (2013). Charge-tunable autoclaved silk-tropoelastin protein alloys that control neuron cell responses. *Adv. Funct. Mater.* 23, 3875–3884. doi: 10.1002/adfm.201202685

Huang, L., McMillan, R. A., Apkarian, R. P., Pourdeyhimi, B., Conticello, V. P., and Chaikof, E. L. (2000). Generation of synthetic elastin-mimetic small diameter fibers and fiber networks. *Macromolecules* 33, 2989–2997. doi: 10.1021/ma991858f

Huang, Z. M., Zhang, Y. Z., Ramakrishna, S., and Lim, C. T. (2004). Electrospinning and mechanical characterization of gelatin nanofibers. *Polymer (Guildf).* 45, 5361–5368. doi: 10.1016/j.polymer.2004.04.005

Humenik, M., Lang, G., and Scheibel, T. (2018). Silk nanofibril self-assembly versus electrospinning. *WIREs Nanomed. Nanobiotechnol.* 10:e1509. doi: 10.1002/wnan.1509

Hwang, W., Kim, B.-H., Dandu, R., Cappello, J., Ghandehari, H., and Seog, J. (2009). Surface induced nanofiber growth by self-assembly of a silk-elastin-like protein polymer. *Langmuir* 25, 12682–12686. doi: 10.1021/la9015993

Ibáñez-Fonseca, A., Orbanic, D., Arias, F. J., Alonso, M., Zeugolis, D. I., and Rodríguez-Cabello, J. C. (2020). Influence of the thermodynamic and kinetic control of self-assembly on the microstructure evolution of silk-elastin-like recombinamer hydrogels. *Small* 16:2001244. doi: 10.1002/smll.202001244

Islam, M. S., Ang, B. C., Andriyana, A., and Afifi, A. M. (2019). A review on fabrication of nanofibers via electrospinning and their applications. *SN Appl. Sci.* 1, 1–16. doi: 10.1007/s42452-019-1288-4

Jiang, L., Xu, D., Sellati, T. J., and Dong, H. (2015). Self-assembly of cationic multidomain peptide hydrogels: supramolecular nanostructure and rheological properties dictate antimicrobial activity. *Nanoscale* 7, 19160–19169. doi: 10.1039/C5NR05233E

Jin, H.-J., and Kaplan, D. L. (2003). Mechanism of silk processing in insects and spiders. *Nature* 424, 1057–1061. doi: 10.1038/nature01809

Johnson, S., Ko, Y. K., Varongchayakul, N., Lee, S., Cappello, J., Ghandehari, H., et al. (2012). Directed patterning of the self-assembled silk-elastin-like nanofibers using a nanomechanical stimulus. *Chem. Commun.* 48, 10654–10656. doi: 10.1039/c2cc35384a

Kaibara, K., Akinari, Y., Okamoto, K., Uemura, Y., Yamamoto, S., Kodama, H., et al. (1996). Characteristic interaction of Ca2+ ions with elastin coacervate: ion transport study across coacervate layers of alpha-elastin and elastin model polypeptide, (Val-Pro-Gly-Val-Gly)n. *Biopolymers* 39, 189–198.

Kapoor, S., and Kundu, S. C. (2016). Silk protein-based hydrogels: promising advanced materials for biomedical applications. *Acta Biomater.* 31, 17–32. doi: 10.1016/j.actbio.2015.11.034

Kenry, and Lim, C. T. (2017). Nanofiber technology: current status and emerging developments. *Prog. Polym. Sci.* 70, 1–17. doi: 10.1016/j.progpolymsci.2017.03.002

Ko, F. K., and Wan, Y. (2014). *Introduction to Nanofiber Materials*. Cambridge: Cambridge University Press.

Krejchi, M. T., Atkins, E. D., Waddon, A. J., Fournier, M. J., Mason, T. L., and Tirrell, D. A. (1994). Chemical sequence control of beta-sheet assembly in macromolecular crystals of periodic polypeptides. *Science (80-.)* 265, 1427–1432. doi: 10.1126/science.8073284

Landschulz, W. H., Johnson, P. F., and McKnight, S. L. (1988). The leucine zipper: a hypothetical structure common to a new class of DNA binding proteins. *Science (80-.)* 240, 1759–1764.

Le, D. H. T., Tsutsui, Y., Sugawara-Narutaki, A., Yukawa, H., Baba, Y., and Ohtsuki, C. (2017). Double-hydrophobic elastin-like polypeptides with added functional motifs: self-assembly and cytocompatibility. *J. Biomed. Mater. Res. Part A* 105, 2475–2484.

Lee, J., Macosko, C. W., and Urry, D. W. (2001). Elastomeric polypentapeptides cross-linked into matrixes and fibers. *Biomacromolecules* 2, 170–179.

Lee, S. J., Yoo, J. J., Lim, G. J., Atala, A., and Stitzel, J. (2007). *In vitro* evaluation of electrospun nanofiber scaffolds for vascular graft application. *J. Biomed. Mater. Res. A* 83, 999–1008. doi: 10.1002/jbm.a.31287

Lewis, R. V. (2006). Spider silk:? ancient ideas for new biomaterials. *Chem. Rev.* 106, 3762–3774. doi: 10.1021/cr010194g

Li, M., Mondrinos, M. J., Chen, X., Gandhi, M. R., Ko, F. K., and Lelkes, P. I. (2006). Co-electrospun poly(lactide-co-glycolide), gelatin, and elastin blends for tissue engineering scaffolds. *J. Biomed. Mater. Res. A* 79, 963–973. doi: 10.1002/jbm.a.30833

Li, M., Mondrinos, M. J., Gandhi, M. R., Ko, F. K., Weiss, A. S., and Lelkes, P. I. (2005). Electrospun protein fibers as matrices for tissue engineering. *Biomaterials* 26, 5999–6008. doi: 10.1016/j.biomaterials.2005.03.030

Lin, T.-Y., Masunaga, H., Sato, R., Malay, A. D., Toyooka, K., Hikima, T., et al. (2017). Liquid crystalline granules align in a hierarchical structure to produce spider dragline microfibrils. *Biomacromolecules* 18, 1350–1355. doi: 10.1021/acs.biomac.7b00086

Ling, S., Kaplan, D. L., and Buehler, M. J. (2018). Nanofibrils in nature and materials engineering. *Nat. Rev. Mater.* 3:18016. doi: 10.1038/natrevmats.2018.16

Liu, Y., Yang, Y., Wang, C., and Zhao, X. (2013). Stimuli-responsive self-assembling peptides made from antibacterial peptides. *Nanoscale* 5, 6413–6421.

Lu, Q., Zhu, H., Zhang, C., Zhang, F., Zhang, B., and Kaplan, D. L. (2012). Silk self-assembly mechanisms and control from thermodynamics to kinetics. *Biomacromolecules* 13, 826–832. doi: 10.1021/bm201731e

Machado, R., Da Costa, A., Sencadas, V., Garcia-Arévalo, C., Costa, C. M., Padrão, J., et al. (2013). Electrospun silk-elastin-like fibre mats for tissue engineering applications. *Biomed. Mater.* 8:065009. doi: 10.1088/1748-6041/8/6/065009

Machula, H., Ensley, B., and Kellar, R. (2014). Electrospun tropoelastin for delivery of therapeutic adipose-derived stem cells to full-thickness dermal wounds. *Adv. Wound Care* 3, 367–375. doi: 10.1089/wound.2013.0513

Maheshwari, G., Brown, G., Lauffenburger, D. A., Wells, A., and Griffith, L. G. (2000). Cell adhesion and motility depend on nanoscale RGD clustering. *J. Cell Sci.* 113, 1677–1686.

Manno, M., Emanuele, A., Martorana, V., San Biagio, P. L., Bulone, D., Palma-Vittorelli, M. B., et al. (2001). Interaction of processes on different length scales in a bioelastomer capable of performing energy conversion. *Biopolymers* 59, 51–64. doi: 10.1002/1097-0282(200107)59:1<51::AID-BIP1005>3.0.CO;2-8

Marqusee, S., and Baldwin, R. L. (1987). Helix stabilization by Glu-. Lys+ salt bridges in short peptides of *de novo* design. *Proc. Natl. Acad. Sci. U.S.A.* 84, 8898–8902.

Martens, A. A., Portale, G., Werten, M. W. T., de Vries, R. J., Eggink, G., Cohen Stuart, M. A., et al. (2009). Triblock protein copolymers forming supramolecular nanotapes and pH-responsive gels. *Macromolecules* 42, 1002–1009. doi: 10.1021/ma801955q

Martín, L., Arias, F. J., Alonso, M., García-Arévalo, C., and Rodríguez-Cabello, J. C. (2010). Rapid micropatterning by temperature-triggered reversible gelation of a recombinant smart elastin-like tetrablock-copolymer. *Soft. Matter.* 6, 1121–1124. doi: 10.1039/b923684h

McClure, M. J., Sell, S. A., Ayres, C. E., Simpson, D. G., and Bowlin, G. L. (2009). Electrospinning-aligned and random polydioxanone–polycaprolactone–silk fibroin-blended scaffolds: geometry for a vascular matrix. *Biomed. Mater.* 4:55010.

McClure, M. J., Sell, S. A., Simpson, D. G., Walpoth, B. H., and Bowlin, G. L. (2010). A three-layered electrospun matrix to mimic native arterial architecture using polycaprolactone, elastin, and collagen: a preliminary study. *Acta Biomater.* 6, 2422–2433. doi: 10.1016/j.actbio.2009.12.029

McClure, M. J., Simpson, D. G., and Bowlin, G. L. (2012). Tri-layered vascular grafts composed of polycaprolactone, elastin, collagen, and silk: optimization of graft properties. *J. Mech. Behav. Biomed. Mater.* 10, 48–61. doi: 10.1016/j.jmbbm.2012.02.026

McKee, T. J., Perlman, G., Morris, M., and Komarova, S. V. (2019). Extracellular matrix composition of connective tissues: a systematic review and meta-analysis. *Sci. Rep.* 9, 1–15. doi: 10.1038/s41598-019-46896-0

McKenna, K. A., Hinds, M. T., Sarao, R. C., Wu, P. C., Maslen, C. L., Glanville, R. W., et al. (2012). Mechanical property characterization of electrospun recombinant human tropoelastin for vascular graft biomaterials. *Acta Biomater.* 8, 225–233. doi: 10.1016/j.actbio.2011.08.001

McMillan, R. A., Lee, T. A. T., and Conticello, V. P. (1999). Rapid assembly of synthetic genes encoding protein polymers. *Macromolecules* 32, 3643–3648.

McPherson, D. T., Morrow, C., Minehan, D. S., Wu, J., Hunter, E., and Urry, D. W. (1992). Production and purification of a recombinant elastomeric polypeptide, G-(VPGVG)19-VPGV, from *Escherichia coli*. *Biotechnol Prog* 8, 347–352. doi: 10.1021/bp00016a012

Misbah, M. H., Quintanilla, L., Alonso, M., and Rodríguez-cabello, J. C. (2015). Evolution of amphiphilic elastin-like co-recombinamer morphologies from micelles to a lyotropic hydrogel. *Polymer (Guildf)* 81, 37–44. doi: 10.1016/j.polymer.2015.11.013

Mithieux, S. M., Tu, Y., Korkmaz, E., Braet, F., and Weiss, A. S. (2009). *In situ* polymerization of tropoelastin in the absence of chemical cross-linking. *Biomaterials* 30, 431–435. doi: 10.1016/j.biomaterials.2008.10.018

Miyata, T., Asami, N., and Uragani, T. (1999). A reversibly antigen-responsive hydrogen. *Nature* 399, 766–768. doi: 10.1038/21619

Motriuk-Smith, D., Smith, A., Hayashi, C. Y., and Lewis, R. V. (2005). Analysis of the conserved N-terminal domains in major ampullate spider silk proteins. *Biomacromolecules* 6, 3152–3159. doi: 10.1021/bm050472b

Moussa, D. G., Kirihara, J. A., Ye, Z., Fischer, N. G., Khot, J., Witthuhn, B. A., et al. (2019). Dentin priming with amphipathic antimicrobial peptides. *J. Dent. Res.* 98, 1112–1121.

Muiznieks, L. D., Jensen, S. A., and Weiss, A. S. (2003). Structural changes and facilitated association of tropoelastin. *Arch. Biochem. Biophys.* 410, 317–323. doi: 10.1016/S0003-9861(02)00719-1

Nagapudi, K., Brinkman, W. T., Leisen, J. E., Huang, L., McMillan, R. A., Apkarian, R. P., et al. (2002). Photomediated solid-state cross-linking of an elastin-mimetic recombinant protein polymer. *Macromolecules* 35, 1730–1737. doi: 10.1021/ma011429t

Nakouzi, E., and Steinbock, O. (2016). Self-organization in precipitation reactions far from the equilibrium. *Sci. Adv.* 2:e1601144. doi: 10.1126/sciadv.1601144

Nandi, N., Gayen, K., Ghosh, S., Bhunia, D., Kirkham, S., Sen, S. K., et al. (2017). Amphiphilic peptide-based supramolecular, noncytotoxic, stimuli-responsive hydrogels with antibacterial activity. *Biomacromolecules* 18, 3621–3629.

Ner, Y., Stuart, J. A., Whited, G., and Sotzing, G. A. (2009). Electrospinning nanoribbons of a bioengineered silk-elastin-like protein (SELP) from water. *Polymer (Guildf)* 50, 5828–5836. doi: 10.1016/j.polymer.2009.09.017

Nicol, A., Channe Gowda, D., and Urry, D. W. (1992). Cell adhesion and growth on synthetic elastomeric matrices containing ARG-GLY-ASP-SER-3. *J. Biomed. Mater. Res.* 26, 393–413. doi: 10.1002/jbm.820260309

Nivison-Smith, L., Rnjak, J., and Weiss, A. S. (2010). Synthetic human elastin microfibers: stable cross-linked tropoelastin and cell interactive constructs for tissue engineering applications. *Acta Biomater.* 6, 354–359.

Nivison-Smith, L., and Weiss, A. S. (2011). Alignment of human vascular smooth muscle cells on parallel electrospun synthetic elastin fibers. *J. Biomed. Mater. Res. Part A* 100A, 155–161. doi: 10.1002/jbm.a.33255

Nomizu, M., Weeks, B. S., Weston, C. A., Kim, W. H., Kleinman, H. K., and Yamada, Y. (1995). Structure-activity study of a laminin α1 chain active peptide segment Ile-Lys-Val-Ala-Val (IKVAV). *FEBS Lett.* 365, 227–231. doi: 10.1016/0014-5793(95)00475-O

Ozsvar, J., Yang, C., Cain, S. A., Baldock, C., Tarakanova, A., and Weiss, A. S. (2021). Tropoelastin and Elastin assembly. *Front. Bioeng. Biotechnol.* 9:643110. doi: 10.3389/fbioe.2021.643110

Pandya, M. J., Spooner, G. M., Sunde, M., Thorpe, J. R., Rodger, A., and Woolfson, D. N. (2000). Sticky-end assembly of a designed peptide fiber provides insight into protein fibrillogenesis. *Biochemistry* 39, 8728–8734. doi: 10.1021/bi000246g

Papapostolou, D., Smith, A. M., Atkins, E. D. T., Oliver, S. J., Ryadnov, M. G., Serpell, L. C., et al. (2007). Engineering nanoscale order into a designed protein fiber. *Proc. Natl. Acad. Sci. U.S.A.* 104, 10853–10858. doi: 10.1073/pnas.0700801104

Parent, L. R., Onofrei, D., Xu, D., Stengel, D., Roehling, J. D., Addison, J. B., et al. (2018). Hierarchical spidroin micellar nanoparticles as the fundamental precursors of spider silks. *Proc. Natl. Acad. Sci. U.S.A.* 115, 11507–11512. doi: 10.1073/pnas.1810203115

Pepe, A., Flamia, R., Guerra, D., Quaglino, D., Bochicchio, B., Pasquali Ronchetti, I., et al. (2008). Exon 26-coded polypeptide: an isolated hydrophobic domain of human tropoelastin able to self-assemble *in vitro*. *Matrix Biol.* 27, 441–450. doi: 10.1016/j.matbio.2008.02.006

Powell, H. M., and Boyce, S. T. (2009). Engineered human skin fabricated using electrospun collagen-PCL blends: morphogenesis and mechanical properties. *Tissue Eng. Part A* 15, 2177–2187. doi: 10.1089/ten.tea.2008.0473

Prestwich, G. D., Marecak, D. M., Marecek, J. F., Vercruysse, K. P., and Ziebell, M. R. (1998). Controlled chemical modification of hyaluronic acid: synthesis, applications, and biodegradation of hydrazide derivatives. *J. Control. Release* 53, 93–103.

Putzu, M., Causa, F., Nele, V., de Torre, I. G., Rodriguez-Cabello, J. C., and Netti, P. A. (2016). Elastin-like-recombinamers multilayered nanofibrous scaffolds for cardiovascular applications. *Biofabrication* 8:045009. doi: 10.1088/1758-5090/8/4/045009

Putzu, M., Causa, F., Parente, M., González de Torre, I., Rodriguez-Cabello, J. C., and Netti, P. A. (2019). Silk-ELR co-recombinamer covered stents obtained by electrospinning. *Regen. Biomater.* 6, 21–28. doi: 10.1093/rb/rby022

Qiu, W., Teng, W., Cappello, J., and Wu, X. (2009). Wet-spinning of recombinant silk-elastin-like protein polymer fibers with high tensile strength and high deformability. *Biomacromolecules* 10, 602–608. doi: 10.1021/bm801296r

Reneker, D. H., and Yarin, A. L. (2008). Electrospinning jets and polymer nanofibers. *Polymer (Guildf).* 49, 2387–2425. doi: 10.1016/j.polymer.2008.02.002

Ribeiro, A., Arias, F. J., Reguera, J., Alonso, M., and Rodríguez-Cabello, J. C. (2009). Influence of the amino-acid sequence on the inverse temperature transition of elastin-like polymers. *Biophys. J.* 97, 312–320. doi: 10.1016/j.bpj.2009.03.030

Rizzo, G., Lo Presti, M., Giannini, C., Sibillano, T., Milella, A., Matzeu, G., et al. (2020). Silk fibroin processing from CeCl3 aqueous solution: fibers regeneration and doping with Ce(III). *Macromol. Chem. Phys.* 221:2000066. doi: 10.1002/macp.202000066

Rnjak, J., Li, Z., Maitz, P. K. M., Wise, S. G., and Weiss, A. S. (2009). Primary human dermal fibroblast interactions with open weave three-dimensional scaffolds prepared from synthetic human elastin. *Biomaterials* 30, 6469–6477. doi: 10.1016/j.biomaterials.2009.08.017

Rnjak-Kovacina, J., Wise, S. G., Li, Z., Maitz, P. K., Young, C. J., Wang, Y., et al. (2011). Tailoring the porosity and pore size of electrospun synthetic human elastin scaffolds for dermal tissue engineering. *Biomaterials* 32, 6729–6736. doi: 10.1016/j.biomaterials.2011.05.065

Rnjak-Kovacina, J., Wise, S. G., Li, Z., Maitz, P. K. M., Young, C. J., Wang, Y., et al. (2012). Electrospun synthetic human elastin:collagen composite scaffolds for dermal tissue engineering. *Acta Biomater.* 8, 3714–3722. doi: 10.1016/j.actbio.2012.06.032

Roberts, E. G., Rim, N.-G., Huang, W., Tarakanova, A., Yeo, J., Buehler, M. J., et al. (2018). Fabrication and characterization of recombinant silk-elastin-like-protein (SELP) fiber. *Macromol. Biosci.* 18:1800265. doi: 10.1002/mabi.201800265

Rodriguez-Cabello, J. C., Martin, L., Girotti, A., Garcia-Arevalo, C., Arias, F. J., and Alonso, M. (2011). Emerging applications of multifunctional elastin-like recombinamers. *Nanomedicine (London, U. K.)* 6, 111–122. doi: 10.2217/nnm.10.141

Rodriguez-Cabello, J. C., Pierna, M., Fernandez-Colino, A., Garcia-Arevalo, C., and Arias, F. J. (2010). Recombinamers: combining molecular complexity with diverse bioactivities for advanced biomedical and biotechnological applications. *Adv. Biochem. Eng. Biotechnol.* 125, 145–179. doi: 10.1007/10_2010_94

Ryadnov, M. G., Papapostolou, D., and Woolfson, D. N. (2008). "The leucine zipper as a building block for self-assembled protein fibers BT," in *Nanostructure Design: Methods and Protocols*, eds E. Gazit and R. Nussinov (Totowa, NJ: Humana Press), 35–51.

Saha, S., Banskota, S., Roberts, S., Kirmani, N., and Chilkoti, A. (2020). Engineering the architecture of elastin-like polypeptides: from unimers to hierarchical self-assembly. *Adv. Ther.* 3:1900164. doi: 10.1002/adtp.201900164

Salinas-Fernández, S., Santos, M., Alonso, M., Quintanilla, L., and Rodríguez-Cabello, J. C. (2020). Genetically engineered elastin-like recombinamers with sequence-based molecular stabilization as advanced bioinks for 3D bioprinting. *Appl. Mater. Today* 18:100500.

Saric, M., and Scheibel, T. (2019). Engineering of silk proteins for materials applications. *Curr. Opin. Biotechnol.* 60, 213–220. doi: 10.1016/j.copbio.2019.05.005

Schor, M., Martens, A. A., deWolf, F. A., Cohen Stuart, M. A., and Bolhuis, P. G. (2009). Prediction of solvent dependent β-roll formation of a self-assembling silk-like protein domain. *Soft. Matter.* 5, 2658–2665. doi: 10.1039/B902952D

Schwarze, S., Zwettler, F. U., Johnson, C. M., and Neuweiler, H. (2013). The N-terminal domains of spider silk proteins assemble ultrafast and protected from charge screening. *Nat. Commun.* 4:2815. doi: 10.1038/ncomms3815

Sehnal, F., and Žurovec, M. (2004). Construction of silk fiber core in Lepidoptera. *Biomacromolecules* 5, 666–674.

Sell, S. A., McClure, M. J., Barnes, C. P., Knapp, D. C., Walpoth, B. H., Simpson, D. G., et al. (2006). Electrospun polydioxanone-elastin blends: potential for bioresorbable vascular grafts. *Biomed. Mater.* 1, 72–80. doi: 10.1088/1748-6041/1/2/004

Shadforth, A., Suzuki, S., Alzonne, R., Edwards, G. A., Richardson, N. A., Chirila, T. V., et al. (2015). Incorporation of human recombinant tropoelastin into silk fibroin membranes with the view to repairing Bruch's membrane. *J. Funct. Biomater.* 6, 946–962. doi: 10.3390/jfb6030946

Shao, Z., Vollrath, F., Yang, Y., and Thøgersen, H. C. (2003). Structure and behavior of regenerated spider silk. *Macromolecules* 36, 1157–1161. doi: 10.1021/ma0214660

Silva, G. A., Czeisler, C., Niece, K. L., Beniash, E., Harrington, D. A., Kessler, J. A., et al. (2004). Selective differentiation of neural progenitor cells by high-epitope density nanofibers. *Science (80-.).* 303, 1352–1355. doi: 10.1126/science.1093783

Songchotikunpan, P., Tattiyakul, J., and Supaphol, P. (2008). Extraction and electrospinning of gelatin from fish skin. *Int. J. Biol. Macromol.* 42, 247–255. doi: 10.1016/j.ijbiomac.2007.11.005

Sugawara-Narutaki, A., Yasunaga, S., Sugioka, Y., Le, D. H. T., Kitamura, I., Nakamura, J., et al. (2019). Rheology of dispersions of high-aspect-ratio nanofibers assembled from elastin-like double-hydrophobic polypeptides. *Int. J. Mol. Sci.* 20:6262.

Sun, H., and Marelli, B. (2020). Polypeptide templating for designer hierarchical materials. *Nat. Commun.* 11:351. doi: 10.1038/s41467-019-14257-0

Swindle-Reilly, K. E., Paranjape, C. S., and Miller, C. A. (2014). Electrospun poly(caprolactone)-elastin scaffolds for peripheral nerve regeneration. *Prog. Biomater.* 3, 1–8. doi: 10.1007/s40204-014-0020-0

Tamburro, A. M., Guantieri, V., Pandolfo, L., and Scopa, A. (1990). Synthetic fragments and analogues of elastin. II. Conformational studies. *Biopolymers* 29, 855–870. doi: 10.1002/bip.360290419

Tan, E. P. S., and Lim, C. T. (2006). Mechanical characterization of nanofibers – A review. *Compos. Sci. Technol.* 66, 1102–1111. doi: 10.1016/j.compscitech.2005.10.003

Tarakanova, A., and Buehler, M. J. (2012). A materiomics approach to spider silk: protein molecules to webs. *JOM* 64, 214–225. doi: 10.1007/s11837-012-0250-3

Tarakanova, A., Huang, W., Qin, Z., Kaplan, D. L., and Buehler, M. J. (2017). Modeling and experiment reveal structure and nanomechanics across the inverse temperature transition in B. mori Silk-Elastin-like protein polymers. *ACS Biomater. Sci. Eng.* 3, 2889–2899. doi: 10.1021/acsbiomaterials.6b00688

Thomas, V., Zhang, X., Catledge, S. A., and Vohra, Y. K. (2007). Functionally graded electrospun scaffolds with tunable mechanical properties for vascular tissue regeneration. *Biomed. Mater.* 2, 224–232. doi: 10.1088/1748-6041/2/4/004

Thompson, K. S., Vinson, C. R., and Freire, E. (1993). Thermodynamic characterization of the structural stability of the coiled-coil region of the bZIP transcription factor GCN4. *Biochemistry* 32, 5491–5496.

Topilina, N. I., Higashiya, S., Rana, N., Ermolenkov, V. V., Kossow, C., Carlsen, A., et al. (2006). Bilayer fibril formation by genetically engineered polypeptides:? preparation and characterization. *Biomacromolecules* 7, 1104–1111. doi: 10.1021/bm0509016

Tucker, N., Stanger, J. J., Staiger, M. P., Razzaq, H., and Hofman, K. (2012). The history of the science and technology of electrospinning from 1600 to 1995. *J. Eng. Fiber. Fabr.* 7, 63–73. doi: 10.1177/155892501200702s10

Uitto, J. (1979). Biochemistry of the elastic fibers in normal connective tissues and its alterations in diseases. *J. Invest. Dermatol.* 72, 1–10. doi: 10.1111/1523-1747.ep12530093

Ulbrich, K., Strohalm, J., and Kopecek, J. (1982). Polymers containing enzymatically degradable bonds. VI.Hydrophilic gels cleavable by chymotrypsin. *Biomaterials* 3, 150–154.

Urry, D. W. (1988). Entropic elastic processes in protein mechanisms. II. Simple (passive) and coupled (active) development of elastic forces. *J. Protein Chem.* 7, 81–114. doi: 10.1007/BF01025240

Urry, D. W. (1993). Molecular machines: how motion and other functions of living organisms can result from reversible chemical changes. *Angew. Chemie Int. Ed. English* 32, 819–841. doi: 10.1002/anie.199308191

Urry, D. W., Parker, T. M., Reid, M. C., and Gowda, D. C. (1991). Biocompatibility of the bioelastic materials, Poly(GVGVP) and its gamma-irradiation cross-linked matrix - summary of generic biological test-results. *J. Bioact. Compat. Polym.* 6, 263–282.

Urry, D. W., Pattanaik, A., Xu, J., Woods, T. C., McPherson, D. T., and Parker, T. M. (1998). Elastic protein-based polymers in soft tissue augmentation and generation. *J. Biomater. Sci. Polym. Ed.* 9, 1015–1048.

Urry, D. W., Trapane, T. L., and Prasad, K. U. (1985). Phase-structure transitions of the elastin polypentapeptide–water system within the framework of composition–temperature studies. *Biopolymers* 24, 2345–2356. doi: 10.1002/bip.360241212

Urry, D. W., and Williams, K. U. P. D. F. (1985). *Biocompatibility of Tissue Analogues*. Boca Raton: CRC Press.

Varongchayakul, N., Johnson, S., Quabili, T., Cappello, J., Ghandehari, H., Solares, S. D. J., et al. (2013). Direct observation of amyloid nucleation under nanomechanical stretching. *ACS Nano* 7, 7734–7743. doi: 10.1021/nn402322k

Veiga, A. S., Sinthuvanich, C., Gaspar, D., Franquelim, H. G., Castanho, M. A. R. B., and Schneider, J. P. (2012). Arginine-rich self-assembling peptides as potent antibacterial gels. *Biomaterials* 33, 8907–8916. doi: 10.1016/j.biomaterials.2012.08.046

Venugopal, J., Ma, L. L., Yong, T., and Ramakrishna, S. (2005). *In vitro* study of smooth muscle cells on polycaprolactone and collagen nanofibrous matrices. *Cell Biol. Int.* 29, 861–867. doi: 10.1016/j.cellbi.2005.03.026

Vepari, C., and Kaplan, D. L. (2007). Silk as a biomaterial. *Prog. Polym. Sci.* 32, 991–1007. doi: 10.1016/j.progpolymsci.2007.05.013

Vinson, C., Myakishev, M., Acharya, A., Mir, A. A., Moll, J. R., and Bonovich, M. (2002). Classification of human B-ZIP proteins based on dimerization properties. *Mol. Cell. Biol.* 22, 6321–6335.

Vinson, C. R., Hai, T., and Boyd, S. M. (1993). Dimerization specificity of the leucine zipper-containing bZIP motif on DNA binding: prediction and rational design. *Genes Dev.* 7, 1047–1058.

Vinson, C. R., Sigler, P. B., and McKnight, S. L. (1989). Scissors-grip model for DNA recognition by a family of leucine zipper proteins. *Science (80-.)* 246, 911–916.

Vrhovski, B., and Weiss, A. S. (1998). Biochemistry of tropoelastin. *Eur. J. Biochem.* 258, 1–18. doi: 10.1046/j.1432-1327.1998.2580001.x

Wang, H., Shao, H., and Hu, X. (2006). Structure of silk fibroin fibers made by an electrospinning process from a silk fibroin aqueous solution. *J. Appl. Polym. Sci.* 101, 961–968. doi: 10.1002/app.24024

Wang, H.-Y., and Zhang, Y.-Q. (2013). Effect of regeneration of liquid silk fibroin on its structure and characterization. *Soft. Matter.* 9, 138–145. doi: 10.1039/C2SM26945G

Wang, Q., Xia, X., Huang, W., Lin, Y., Xu, Q., and Kaplan, D. L. (2014). High throughput screening of dynamic silk-elastin-like protein biomaterials. *Adv. Funct. Mater.* 24, 4303–4310. doi: 10.1002/adfm.201304106

Werten, M. W. T., Moers, A. P. H. A., Vong, T., Zuilhof, H., van Hest, J. C. M., and de Wolf, F. A. (2008). Biosynthesis of an amphiphilic silk-like polymer. *Biomacromolecules* 9, 1705–1711. doi: 10.1021/bm701111z

Willems, L., Roberts, S., Weitzhandler, I., Chilkoti, A., Mastrobattista, E., van der Oost, J., et al. (2019). Inducible Fibril formation of silk–elastin diblocks. *ACS Omega* 4, 9135–9143. doi: 10.1021/acsomega.9b01025

Wise, S. G., Byrom, M. J., Waterhouse, A., Bannon, P. G., Ng, M. K. C., and Weiss, A. S. (2011). A multilayered synthetic human elastin/polycaprolactone hybrid vascular graft with tailored mechanical properties. *Acta Biomater.* 7, 295–303. doi: 10.1016/j.actbio.2010.07.022

Wise, S. G., Mithieux, S. M., and Weiss, A. S. (2009). Engineered tropoelastin and elastin-based biomaterials. *Adv. Protein Chem. Struct. Biol.* 78, 1–24. doi: 10.1016/s1876-1623(08)78001-5

Wise, S. G., and Weiss, A. S. (2009). Tropoelastin. *Int. J. Biochem. Cell Biol.* 41, 494–497. doi: 10.1016/j.biocel.2008.03.017

Wise, S. G., Yeo, G. C., Hiob, M. A., Rnjak-Kovacina, J., Kaplan, D. L., Ng, M. K. C., et al. (2014). Tropoelastin: a versatile, bioactive assembly module. *Acta Biomater.* 10, 1532–1541. doi: 10.1016/j.actbio.2013.08.003

Wong, C. S., Liu, X., Xu, Z., Lin, T., and Wang, X. (2013). Elastin and collagen enhances electrospun aligned polyurethane as scaffolds for vascular graft. *J. Mater. Sci. Mater. Med.* 24, 1865–1874. doi: 10.1007/s10856-013-4937-y

Wu, W. J., Vrhovski, B., and Weiss, A. S. (1999). Glycosaminoglycans mediate the coacervation of human tropoelastin through dominant charge interactions involving lysine side chains. *J. Biol. Chem.* 274, 21719–21724.

Xia, Q., Zhou, Z., Lu, C., Cheng, D., Dai, F., Li, B., et al. (2004). A draft sequence for the genome of the domesticated silkworm (⁢em>Bombyx mori⁢/em&gt). *Science (80-.)* 306, 1937–1940. doi: 10.1126/science.1102210

Xia, X.-X., Xu, Q., Hu, X., Qin, G., and Kaplan, D. L. (2011). Tunable self-assembly of genetically engineered silk–elastin-like protein polymers. *Biomacromolecules* 12, 3844–3850. doi: 10.1021/bm201165h

Xue, J., Wu, T., Dai, Y., and Xia, Y. (2019). Electrospinning and electrospun nanofibers: methods, materials, and applications. *Chem. Rev.* 119, 5298–5415. doi: 10.1021/acs.chemrev.8b00593

Xue, J., Xie, J., Liu, W., and Xia, Y. (2017). Electrospun nanofibers: new concepts, materials, and applications. *Acc. Chem. Res.* 50, 1976–1987. doi: 10.1021/acs.accounts.7b00218

Yang, L., Fitié, C. F. C., van der Werf, K. O., Bennink, M. L., Dijkstra, P. J., and Feijen, J. (2008). Mechanical properties of single electrospun collagen type I fibers. *Biomaterials* 29, 955–962. doi: 10.1016/j.biomaterials.2007.10.058

Ye, Z., Zhu, X., Acosta, S., Kumar, D., Sang, T., and Aparicio, C. (2019). Self-assembly dynamics and antimicrobial activity of all l- and d-amino acid enantiomers of a designer peptide. *Nanoscale* 11, 266–275. doi: 10.1039/c8nr07334a

Yoder, M. D., and Jurnak, F. (1995). The parallel β helix and other coiled folds. *FASEB J.* 9, 335–342. doi: 10.1096/fasebj.9.5.7896002

Zarkoob, S., Eby, R. K., Reneker, D. H., Hudson, S. D., Ertley, D., and Adams, W. W. (2004). Structure and morphology of electrospun silk nanofibers. *Polymer* 45, 3973–3977. doi: 10.1016/j.polymer.2003.10.102

Zeng, L., Jiang, L., Teng, W., Cappello, J., Zohar, Y., and Wu, X. (2014a). Engineering aqueous fiber assembly into silk-elastin-like protein polymers. *Macromol. Rapid Commun.* 35, 1273–1279. doi: 10.1002/marc.201400058

Zeng, L., Teng, W., Jiang, L., Cappello, J., and Wu, X. (2014b). Ordering recombinant silk-elastin-like nanofibers on the microscale. *Appl. Phys. Lett.* 104:33702. doi: 10.1063/1.4863077

Zhang, S., Huang, Y., Yang, X., Mei, F., Ma, Q., Chen, G., et al. (2009). Gelatin nanofibrous membrane fabricated by electrospinning of aqueous gelatin solution for guided tissue regeneration. *J. Biomed. Mater. Res. A* 90, 671–679. doi: 10.1002/jbm.a.32136

Zhang, X., Thomas, V., and Vohra, Y. K. (2009). *In vitro* biodegradation of designed tubular scaffolds of electrospun protein/polyglyconate blend fibers. *J. Biomed. Mater. Res. B Appl. Biomater.* 89, 135–147. doi: 10.1002/jbm.b.31196

Zhang, X., Thomas, V., and Vohra, Y. K. (2010). Two ply tubular scaffolds comprised of proteins/poliglecaprone/polycaprolactone fibers. *J. Mater. Sci. Mater. Med.* 21, 541–549. doi: 10.1007/s10856-009-3922-y

Zhang, Y., Ouyang, H., Chwee, T. L., Ramakrishna, S., and Huang, Z. M. (2005). Electrospinning of gelatin fibers and gelatin/PCL composite fibrous scaffolds. *J. Biomed. Mater. Res. - Part B Appl. Biomater.* 72, 156–165. doi: 10.1002/jbm.b.30128

Zhang, Y. Z., Su, B., Venugopal, J., Ramakrishna, S., and Lim, C. T. (2007). Biomimetic and bioactive nanofibrous scaffolds from electrospun composite nanofibers. *Int. J. Nanomed.* 2, 623–638.

Zhao, Y., Sakai, F., Su, L., Liu, Y., Wei, K., Chen, G., et al. (2013). Progressive macromolecular self-assembly: from biomimetic chemistry to bio-inspired materials. *Adv. Mater.* 25, 5215–5256. doi: 10.1002/adma.201302215

Zhou, C., Confalonieri, F., Jacquet, M., Perasso, R., Li, Z., and Janin, J. (2001). Silk fibroin: structural implications of a remarkable amino acid sequence. *Proteins Struct. Funct. Bioinforma.* 44, 119–122.

Zhou, M., Bentley, D., and Ghosh, I. (2004). Helical supramolecules and fibers utilizing leucine zipper-displaying dendrimers. *J. Am. Chem. Soc.* 126, 734–735.

Zhou, Z., Zhang, S., Cao, Y., Marelli, B., Xia, X., and Tao, T. H. (2018). Engineering the future of silk materials through advanced manufacturing. *Adv. Mater.* 30:1706983. doi: 10.1002/adma.201706983

Conflict of Interest: The authors declare that the research was conducted in the absence of any commercial or financial relationships that could be construed as a potential conflict of interest.

Advantages of publishing in Frontiers

OPEN ACCESS
Articles are free to read for greatest visibility and readership

FAST PUBLICATION
Around 90 days from submission to decision

HIGH QUALITY PEER-REVIEW
Rigorous, collaborative, and constructive peer-review

TRANSPARENT PEER-REVIEW
Editors and reviewers acknowledged by name on published articles

Frontiers
Avenue du Tribunal-Fédéral 34
1005 Lausanne | Switzerland

Visit us: www.frontiersin.org
Contact us: frontiersin.org/about/contact

REPRODUCIBILITY OF RESEARCH
Support open data and methods to enhance research reproducibility

DIGITAL PUBLISHING
Articles designed for optimal readership across devices

FOLLOW US
@frontiersin

IMPACT METRICS
Advanced article metrics track visibility across digital media

EXTENSIVE PROMOTION
Marketing and promotion of impactful research

LOOP RESEARCH NETWORK
Our network increases your article's readership